Nikhilesh Chawla
Krishan K. Chawla

Metal Matrix Composites

Second Edition

Springer

Metal Matrix Composites

Nikhilesh Chawla • Krishan K. Chawla

Metal Matrix Composites

Second Edition

Springer

Nikhilesh Chawla
Arizona State University
Tempe, AZ, USA

Krishan K. Chawla
University of Alabama at Birmingham
Birmingham, AL, USA

ISBN 978-1-4614-9547-5 ISBN 978-1-4614-9548-2 (eBook)
DOI 10.1007/978-1-4614-9548-2
Springer New York Heidelberg Dordrecht London

Library of Congress Control Number: 2013955046

Cover Illustration: Cover image is a high speedway railroad coach bogey with four metal matrix composite brake disks produced by SAB Wabco (courtesy of H. Ruppert).

Printed on acid-free paper

Springer is part of Springer Science+Business Media (www.springer.com)

मनःप्रसादः सौम्यत्वं मौनमात्मविनिग्रहः ।
भावसंशुद्धिरित्येतत्तपो मानसमुच्यते ॥

Serenity, simplicity, gravity, self-control, and purity of thought are the austerities of the mind.

Bhagvad Gita,
Chapter 17, shloka 16

Dedicated to

Kunal Chawla and Kush Chawla Who have Brightened our Lives From the Moment they were Born

Preface to the 2nd Edition

Metal matrix composites (MMCs) represent an important category of the modern field of composites. Since the first edition, our scientific understanding and the use of MMCs have increased. With the increasing need to improve fuel economy in the transportation sector, MMCs are increasingly becoming important. Since the first edition of this book, there have been consistent and important contributions to the field from the academia and industry. These contributions involve developments in processing, microstructural characterization, testing, and analysis. In particular, the advent of many cutting-edge experimental tools, such as X-ray synchrotron tomography and focused ion beam, has significantly enhanced the community's understanding of the field. Similar improvements in computational modeling capabilities and speed have resulted in important strides in theoretical modeling of the behavior of MMCs.

The aim of the book remains the same as in the first edition: relationship among processing, microstructure, properties, and performance of MMCs. To that end, we use a balanced mechanics-materials approach supplemented with a wealth of graphics, many in color, which make it easy for the reader to grasp the underlying operating mechanisms. We emphasize our conviction that the microstructure of the composite controls its properties.

The second edition of the book, like the first, is aimed at upper division undergraduate students and beginning graduate students in departments of engineering (mechanical, electrical, materials, chemical) and physical sciences (physics and chemistry). The book will serve as a useful reference of the practicing scientist, engineer, and researcher in the industry.

We would like to acknowledge assistance from a number of sources without which this project would not have been possible. N.C. would like to acknowledge several current and former students and postdocs in his research group: N.C. Chapman, P. Hruby, J. Silva, D. Singh, S. S. Singh, J. L. Walters (Stewart), and J. J. Williams. He acknowledges many fruitful discussions and interactions with the following colleagues and collaborators: F. De Carlo, P. Portella, and

X. Xiao. N.C. would also like to thank a few key individuals in the administration at Arizona State University for providing the means and encouragement to carry out this endeavor; in particular his school's Director Kyle Squires, Dean Paul Johnson, and President Michael Crow. Peter Hruby was also instrumental in making several figures, movies, and diagrams in the 2nd edition. This work would not be possible without the unwavering encouragement and support of his wife Anita and sons Kunal and Kush.

K.K.C. would like to acknowledge the students and postdocs in his group at University of Alabama at Birmingham: K. Carlisle, Z. Chen, A. Goel, M. Koopman, R. Kulkarni, and B. V. Patel. He also thanks G. M. Gladysz, A. Mortensen, B. R. Patterson, P. D. Portella, and J. M. Rigsbee, for useful discussions.

Tempe, AZ, USA — Nikhilesh Chawla
Birmingham, AL, USA — Krishan K. Chawla

Preface to 1st Edition

Metal matrix composites (MMCs) have been around for a long time, but have only been recognized as legitimate engineering composite materials in the second half of the twentieth century. From their humble research beginnings, MMCs have gone from "niche" materials to several high-performance applications in aerospace, electronic packaging, automotive, and recreational products. Much of the significant research advances have been published in several journal articles, conference proceedings, and multi-authored volumes. It is surprising that only two texts have been published in this area. Taya and Arsenault (1989) published the first book on MMCs, which was followed by that of Clyne and Withers (1993). Thus, it has been a long time since a textbook on MMCs has been published. During this period, there has been a myriad of new and exciting advances and applications in the field. These include continuous fiber-reinforced MMCs for cables in power transmission, high-temperature superconducting wires, particulate MMCs in civilian aircraft and automotive applications, and high-volume fraction, high thermal conductivity substrates for electronic packaging. All these factors make this a very opportune time to bring out the present text.

We have several goals in writing this textbook on MMCs: (1) to provide a thorough and coherent coverage of MMCs that will be useful to the beginning student who wants to learn about this exciting field, as well as the practicing scientist or engineer who may be familiar with some aspects of MMCs, but has not been able to keep with all the exciting new developments in the field; (2) summarize and consolidate the vast body of work that has been done in the last 50 years or so; and (3) illustrate several examples of MMC applications, with the hope that this will spur further research and innovation and have an even bigger impact on MMCs for future applications.

Throughout this textbook, the reader will encounter a recurring theme, which is the synergistic relationship among processing, microstructure, and properties of MMCs. In this regard, we begin with a brief definition and introduction of metal matrix composites. This is followed by a chapter each on reinforcements and common matrix materials. A chapter on the very important topic of processing of MMC is then presented. This is followed by a chapter on interfaces in MMCs, their

characterization, and techniques to obtain interfacial properties. Next there are chapters on monotonic mechanical and physical properties, followed by cyclic fatigue, creep, and wear resistance. We conclude with a chapter on applications of MMCs.

Acknowledgments N.C. would like to acknowledge long-term support for research in the MMC arena from the Office of Naval Research (A. K. Vasudevan, Program Manager) and the US Automotive Partnership, through the Department of Energy (W. Jandeska, *GM*; R. Chernekoff, *Ford*; and J. Lynn, *Daimler–Chrysler*, Program Managers). Several individuals were instrumental in whetting his appetite and enhancing his knowledge of MMCs, through fruitful interactions, collaborations, and discussions: W. H. Hunt, Y.-L. Shen, J. J. Lewandowski, J. LLorca, J. W. Jones, and J. E. Allison. N.C. would like to thank a few key individuals in the administration at Arizona State University for providing the means and encouragement to carry out this endeavor; in particular his Department Chair S. Mahajan, Dean P. Crouch, and President M. M. Crow. This book would not have been possible without the outstanding work and inquisitive nature of his current and former students and postdocs: A. Ayyar, G. Crawford, X. Deng, M. Dudek, V. V. Ganesh, M. Kerr, G. Piotrowski, R. Saha, R. S. Sidhu, J. J. Williams, and B. Wunsch. G. Piotrowski was also instrumental in making several figures and diagrams in the text.

K.K.C. would like to acknowledge the grant of a sabbatical leave from the University of Alabama at Birmingham, part of which was spent at Arizona State University (ASU) where the hospitality of Professor S. Mahajan was a great help in the writing of this book. During other parts of the sabbatical, K.K.C. had the pleasure of stimulating discussions with P. D. Portella (BAM, Berlin), M. Elices and J. LLorca (University of Madrid), and G. M. Gladysz (Los Alamos National Laboratory). He is also grateful to the researchers in his group, K. Carlisle, M. Koopman, and R. Kulkarni at University of Alabama at Birmingham for their cheerfulness, sincerity, and hard work. He is very thankful to B. A. MacDonald, National Science Foundation, and S. Fishman and A. K. Vasudevan, Office of Naval Research, who over the years have funded his research program. He also thanks A. Mortensen, B. R. Patterson, B. V. Patel, J. M. Rigsbee, and N. Stoloff who were always there to discuss things.

The following individuals were particularly generous in providing us with micrographs and figures of their work: H. Devé, A. Dlouhy, A. Drake, G. Eggeler, J. Eldridge, D. Herling, P. Krajewski, J. Liu, J. Llorca, D. Lloyd, D. Miracle, M. Ochionero, W. Nix, S. Rawal, H. Ruppert, and T. Wang. We are very thankful to Greg Franklin and Carol Day for their patience and understanding during the course of writing this book.

Finally, for the curious reader who might be wondering about the common last names of the authors, we should let the cat out of the bag. This book is collaboration between two colleagues and friends, who happen to be father (K.K.C.) and son (N.C.). As such, it was a mutually fulfilling and special family endeavor. Furthermore, this book would not have been possible without the support and encouragement of the rest of the Chawla family: Anita Chawla (wife and daughter-in-law), Kanika Chawla (sister and daughter), and Nivedita Chawla (mother and wife). Special thanks to Anita Chawla for her invaluable assistance with formatting and index preparation.

Tempe, AZ, USA — Nikhilesh Chawla
Birmingham, AL, USA — Krishan K. Chawla

About the Authors

Nikhilesh Chawla is Fulton Professor of Materials Science and Engineering at Arizona State University. He received his Ph.D. from the University of Michigan. His research interests encompass the mechanical behavior and modeling of advanced materials at bulk and small length scales and 4D Materials Science. Professor Chawla is a fellow of ASM international. He's the recipient of the 2013 Brimacombe Medalist Award from TMS; 2011 Distinguished Lectureship given by Tsinghua University, China; 2009 Raymond Award for Best Paper by the American Institute of Mining, Metallurgical, and Petroleum Engineers (AIME); 2004 Bradley Stoughton Award for Young Teachers, given by ASM International; and the 2006 TMS Young Leaders Tutorial Lecture. He's also won the National Science Foundation Early Career Development Award and the Office of Naval Research Young Investigator Award. He serves as editor of *Materials Science and Engineering A*, as well as on the editorial board of several journals.

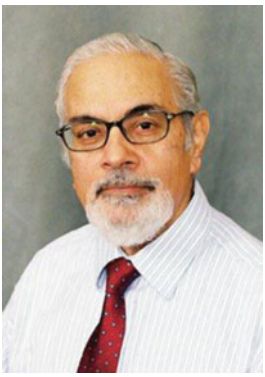

Krishan K. Chawla is Professor of Materials Science and Engineering at the University of Alabama at Birmingham, USA. He received his Ph.D. from the University of Illinois *at* Urbana-Champaign. His research interests encompass processing, microstructure, and mechanical behavior of materials. He has taught and/or done research at several universities around the world. Professor Chawla has served as a Program Director for metals and ceramics in the Division of Materials Research, National Science Foundation. He is a fellow of ASM international. Among his other awards are Distinguished Researcher Award at New Mexico Tech, Distinguished Alumnus Award from Banaras Hindu University, Eshbach Society Distinguished Visiting Scholar award at Northwestern University, President's award for Excellence in Teaching at UAB, and Faculty Fellow award at Oak Ridge National Laboratory. Professor Chawla is the author or coauthor of various textbooks in the area of materials and serves on the editorial boards of a number of journals. He is editor of the journal International Materials Reviews.

Contents

1 Introduction 1
1.1 Types of MMCs 2
1.2 Characteristics of MMCs 3

2 Reinforcements 5
2.1 Fibrous Materials 5
2.2 Fiber Flexibility 6
2.3 Carbon Fibers 8
2.3.1 Fabrication of Carbon Fibers 9
2.3.2 PAN-Based Carbon Fibers 10
2.3.3 Pitch-Based Carbon Fibers 12
2.3.4 Spinning and Rheology of Mesophase Pitch 13
2.3.5 Structure and Properties of Carbon Fibers 14
2.3.6 Structure of Carbon Fibers 15
2.3.7 Carbon Nanotubes, Nanoparticles, and Graphene 16
2.4 Boron Fibers 17
2.4.1 Residual Stresses 19
2.5 Oxide Fibers 20
2.5.1 Alumina-Type Oxide Fibers 20
2.6 Nonoxide Fibers 24
2.6.1 Silicon Carbide Fibers 24
2.6.2 Silicon Carbide Fibers Made by CVD 24
2.6.3 Nonoxide Fibers via Polymer Precursors 26
2.6.4 Structure and Properties of Nicalon Fiber 28
2.6.5 Other SiC-Type Fibers 29
2.7 Whiskers 29
2.8 Particles 30
2.8.1 Particulate Silicon Carbide 30
2.8.2 Particulate Tungsten Carbide 31
2.9 Comparison of Fibers 32
2.10 Statistical Analysis of Fiber Strength 32

3 Matrix Materials 37
3.1 Bonding and Crystalline Structure in Metals 37
3.2 Crystalline Defects in Metals 38
3.3 Strengthening Mechanisms in Metals 41
3.3.1 Dislocation Strengthening 41
3.3.2 Grain Boundary Strengthening 41
3.3.3 Solute and Precipitation Strengthening 42
3.3.4 Fracture in Metals 44
3.4 Common Matrix Materials 45
3.4.1 Aluminum and Aluminum Alloys 45
3.4.2 Titanium Alloys 46
3.4.3 Magnesium and Its Alloys 47
3.4.4 Cobalt 47
3.4.5 Copper 47
3.4.6 Silver 48
3.4.7 Nickel 48
3.4.8 Niobium 48
3.4.9 Intermetallics 48
3.5 Superconductivity 49
3.5.1 Types of Superconductors 50
3.5.2 Flux and Flux Pinning 51
3.5.3 Ductile Alloys: Niobium-Titanium Alloys 52
3.5.4 A-15 Superconductors: Nb_3Sn 53

4 Processing 55
4.1 Liquid-State Processing 55
4.1.1 Casting or Liquid Infiltration 56
4.1.2 Spray Co-deposition 62
4.1.3 In Situ Processes 64
4.1.4 Infiltration Mechanics 65
4.1.5 Microstructure Evolution During Liquid-Phase Processing 68
4.1.6 Casting 71
4.2 Solid-State Processing 75
4.2.1 Powder Metallurgy Processing 76
4.2.2 Extrusion 78
4.2.3 Forging 83
4.2.4 Pressing and Sintering 84
4.2.5 Roll Bonding and Co-extrusion 85
4.2.6 Diffusion Bonding 89
4.2.7 Explosive Shock Consolidation 91
4.3 Gaseous-State Processing 91
4.3.1 Physical Vapor Deposition 91

5 Interface 99
5.1 Crystallographic Nature of the Interface 100
5.2 Wettability 101

5.3 Types of Bonding 102
5.3.1 Mechanical Bonding 102
5.3.2 Chemical Bonding 104
5.3.3 Interactions at the Interface due to Thermal Mismatch . . . 111
5.4 Measurement of Interfacial Bond Strength 112
5.4.1 Bend Tests 112
5.4.2 Fiber Pullout and Pushout Tests 113

6 Micromechanics 121
6.1 Elastic Constants of a Fiber Reinforced Composite 121
6.1.1 Strength of Materials Approach 124
6.1.2 Micromechanical Approaches 129
6.1.3 Semiempirical Expressions 133
6.1.4 Eshelby Method or Equivalent Homogeneous Inclusion Technique 135
6.1.5 Numerical Methods 138
6.2 Physical Properties 139
6.2.1 Density 139
6.2.2 Coefficient of Thermal Expansion (CTE) 140
6.2.3 Thermal Conductivity 150
6.2.4 Electrical Conductivity 152
6.3 Thermal Stresses in Composites 153
6.3.1 Thermal Stresses in Particulate Composites 154
6.3.2 Thermal Stresses in Fiber Reinforced Composites 157

7 Monotonic Behavior 163
7.1 Strengthening Mechanisms 163
7.1.1 Direct Strengthening 164
7.1.2 Indirect Strengthening 171
7.2 Monotonic Behavior of Continuous Fiber Reinforced MMCs . . . 175
7.2.1 Criteria for Debonding and Crack Deflection at an Interface 179
7.2.2 Work Done in Fiber Pullout 182
7.2.3 Effect of Interfacial Reactions on Monotonic Behavior . . . 184
7.2.4 Modeling of Monotonic Behavior of Continuous Fiber Reinforced MMCs 187
7.3 Monotonic Behavior of Discontinuously Reinforced MMCs 191
7.3.1 Modeling of Monotonic Behavior of Particle-Reinforced MMCs 206
7.4 In Situ Metal Matrix Composites 216
7.5 Fracture Toughness 218

8 Cyclic Fatigue 227
8.1 Stress Versus Cycles (S–N) Fatigue 228
8.1.1 Continuous Fiber-Reinforced MMCs 228
8.1.2 Stiffness Loss 236
8.1.3 Particle-Reinforced MMCs 238

8.2 Fatigue Crack Growth 249
8.2.1 Continuous Fiber-Reinforced MMCs 249
8.2.2 Particle-Reinforced MMCs 260
8.2.3 Hybrid and Laminated Composites 269
8.3 Thermal Fatigue 272

9 Creep 283
9.1 Continuous Fiber Reinforced MMCs 284
9.2 Discontinuously Reinforced MMCs 290
9.3 Superplasticity 304

10 Wear and Corrosion 311
10.1 Introduction 311
10.2 Particle Reinforced Aluminum Matrix Composites 314
10.3 Tungsten Carbide/Cobalt Composites 317
10.3.1 Hardness and Strength of Cemented Carbides 317
10.3.2 Double Cemented Carbide 318
10.4 Wear in Braking Materials 321
10.5 Corrosion of MMCs 322

11 Applications 325
11.1 Aerospace 325
11.1.1 Aircraft Structures 325
11.1.2 Fiber Metal Laminates 328
11.1.3 Missiles 332
11.1.4 Space Structures 333
11.2 Transportation (Automotive and Railway) 335
11.2.1 Railroad Brakes 339
11.3 Electronics and Thermal Management 342
11.4 Filamentary Superconducting Magnets 344
11.5 Power Conductors 348
11.6 Recreational and Sporting Goods 350
11.7 Wear-Resistant Materials 352

Author Index 357

Subject Index 367

Chapter 1
Introduction

Metal matrix composites (MMCs) consist of at least two chemically and physically distinct phases, suitably distributed to give properties not obtainable with/or any one of the phases individually. Generally, there are two phases, say, a fibrous or particulate phase distributed in an appropriate manner in a matrix. Examples include continuous alumina fibers in an aluminum matrix composites used in power transmission lines, Nb–Ti filaments in a copper matrix for superconducting magnets, tungsten carbide (WC)/cobalt (Co) particulate composites used as cutting tool and oil drilling inserts.

The first legitimate question that a reader might ask is: Why MMCs? There is a two prong answer to this, advantages with respect to unreinforced metals and with respect to other composites such as polymer matrix composites (PMCs). With respect to metals, MMCs offer:

- Major weight savings due to higher specific mechanical properties
- Dimensional stability (compare, for example, SiC/Al to Al)
- Higher-temperature capabilities, i.e., creep resistance
- Improved cyclic fatigue characteristics

With respect to PMCs, MMCs offer:

- Higher strength and stiffness
- Higher service temperatures
- Higher electrical conductivity (electrical grounding, space charging)
- Higher thermal conductivity
- Better transverse properties (i.e., transverse to the fiber)
- Improved joining characteristics
- Radiation survivability (laser, UV, nuclear, etc.)
- Little or no contamination (no outgassing, no moisture absorption)

N. Chawla and K.K. Chawla, *Metal Matrix Composites*,
DOI 10.1007/978-1-4614-9548-2_1,

1.1 Types of MMCs

All MMCs have a metal or a metallic alloy as the matrix. The reinforcement can be metallic or ceramic. In an unusual case, the reinforcement is actually in the form of a fiber-reinforced PMC (a sheet of glass fiber-reinforced epoxy or aramid fiber-reinforced epoxy).

There are four kinds of MMCs:

1. Particle-reinforced MMCs
2. Short fiber- or whisker-reinforced MMCs
3. Continuous fiber- or sheet-reinforced MMCs
4. Laminated or layered MMCs

Figure 1.1 shows schematically these different types of MMCs. The reader can easily visualize that the continuous fiber-reinforced composites will be the most anisotropic of all. Table 1.1 provides examples of some important reinforcements used in MMCs as well as their aspect (length/diameter) ratios and diameters.

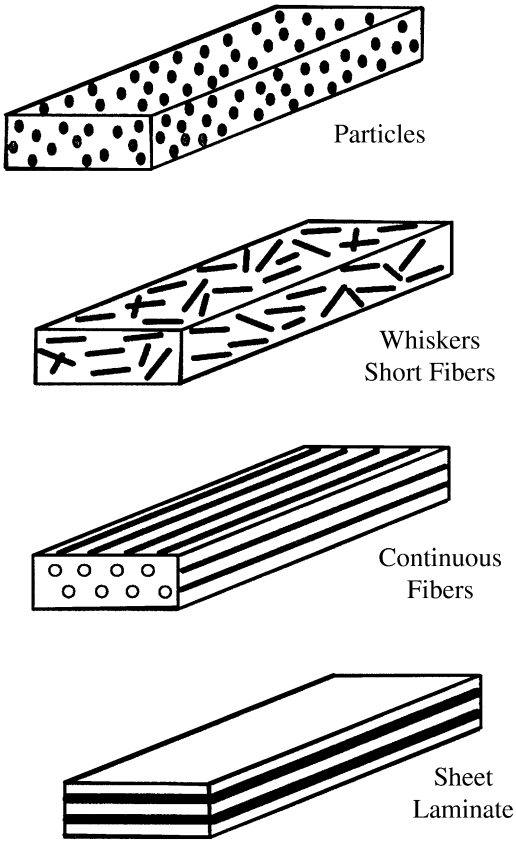

Fig. 1.1 Different types of metal matrix composites

Table 1.1 Typical reinforcements used in metal matrix composites

Type	Aspect ratio	Diameter	Examples
Particle	1–4	1–25 μm	SiC, Al_2O_3, BN, B_4C, WC
Short fiber or whisker	10–10,000	1–5 μm	C, SiC, Al_2O_3, Al_2O_3 + SiO_2
Continuous fiber	>1,000	3–150 μm	SiC, Al_2O_3, C, B, W, Nb–Ti, Nb_3Sn
Nanoparticle	1–4	<100 nm	C, Al_2O_3, SiC
Nanotube	>1,000	<100 nm	C

Particle- or discontinuously reinforced MMCs (one uses the term discontinuously reinforced MMCs to indicate MMCs having reinforcements in the form of short fibers, whiskers, or particles) have assumed special importance because of the following reasons:

- Particle-reinforced composites are inexpensive vis-à-vis continuous fiber-reinforced composites. Cost is an important and essential item for large volume usage.
- Processing by casting or powder metallurgy, followed by conventional secondary processing by rolling, forging, and extrusion, can be used.
- Higher use temperatures are possible than with the unreinforced metal.
- Enhanced modulus and strength.
- Increased thermal stability.
- Better wear resistance.
- Relatively isotropic properties compared to those of the fiber-reinforced composites.

Within the broad category of discontinuously reinforced composites, MMCs made by liquid metal casting are cheaper to produce than the powder metallurgy composites. There are two types of cast MMCs:

- Cast composite having local reinforcement.
- Cast composite in the form of a billet having general reinforcement with a wrought alloy matrix. Such composite billets are forged and/or extruded, followed by rolling or other forming operations.

1.2 Characteristics of MMCs

One of the major driving forces for MMCs is of course the enhanced stiffness and strength; there are, however, other characteristics which may be equally valuable. As an example, we can cite the ability to control the thermal expansion in applications involving electronic packaging. By adding ceramic reinforcements, one can generally reduce the coefficient of linear thermal expansion of the composite. Electrical and thermal conductivity characteristics may be important in some applications. Superconductors require obviously superconducting characteristics.

The metallic matrix provides a high thermal conductivity medium in case of an accidental quench besides holding the tiny filaments together. Other important characteristics that may be of immense values include wear resistance (e.g., in WC–Co composites used in cutting tools or oil drilling inserts SiC/Al rotor in brakes). Thus, although one commonly uses the term reinforcement, by particle or fibers in the context of MMCs, it is worth pointing out that stiffness and strength enhancement may not always be the most important characteristics in many cases.

Chapter 2
Reinforcements*

Reinforcement materials for metal matrix composites can be produced in the form of continuous fibers, short fibers, whiskers, or particles. The parameter that allows us to distinguish between these different forms of reinforcements is called the *aspect ratio*. Aspect ratio is nothing but the ratio of length to diameter (or thickness) of the fiber, particle, or whisker. Thus, continuous fibers have an aspect ratio approaching infinity while perfectly equiaxed particles have an aspect ratio of around one. Table 2.1 lists some important reinforcements available in different forms for metallic matrix materials. Ceramic reinforcements combine high strength and elastic modulus with high-temperature capability. Continuous ceramic fibers are also, however, more expensive than ceramic particulate reinforcements.

In this chapter, we describe some general features of reinforcements and then provide a more detailed description of processing, microstructure, and properties of some important ceramic reinforcements that are commonly used in metal matrix composites.

2.1 Fibrous Materials

One can transform practically any material (polymers, metals, or ceramics) into fibrous form (Chawla 1998). We can arbitrarily define a fiber as an elongated material having a more or less uniform diameter or thickness of less than 250 μm and an aspect ratio of more than 100. Note that this is not only an operational definition but also a purely geometrical one that applies to any material.

Fibers have some unique features that stem mainly from their relatively small cross-section and large aspect ratio:

- High degree of flexibility.
- Higher strength than the bulk material of the same composition.

* Portions of this chapter are taken from Chawla (2012).

N. Chawla and K.K. Chawla, *Metal Matrix Composites*,
DOI 10.1007/978-1-4614-9548-2_2, © Springer Science+Business Media New York 2013

Table 2.1 Some important reinforcements for metal matrix composites

Continuous fibers	Al_2O_3, Al_2O_3 + SiO_2, B, C, SiC, Si_3N_4, Nb–Ti, Nb_3Sn
Discontinuous fibers	
(a) Whiskers	SiC, TiB_2, Al_2O_3
(b) Short fibers	Al_2O_3, SiC, (Al_2O_3 + SiO_2), vapor-grown carbon fibers
Particles	SiC, Al_2O_3, TiC, B_4C, WC

The long length of fibers also makes it imperative, in most cases, to incorporate them in some continuous medium, which serves as the matrix to hold fiber together to make a fiber-reinforced composite. It should be emphasized that this, by no means, is the sole purpose of the matrix in a composite. The metal matrix does make important contributions to the overall performance of an MMC.

2.2 Fiber Flexibility

Flexibility is an important attribute of fine fibers. A high degree of flexibility is an intrinsic characteristic of a material having a small diameter and a low elastic modulus (Dresher 1969). Flexibility of fibers permits a variety of techniques to be employed for making fiber-reinforced composites. Consider a fiber as an elongated elastic beam, then its flexibility will be an inverse function of its elastic modulus, E, and the second moment of area or moment of inertia of its cross section, I. The elastic modulus of a material is generally independent of its form or size and is generally a material constant for a given chemical composition (assuming a fully dense material). Thus, for a given composition and density, the flexibility of a material is determined by its shape, or more precisely by its diameter, as shown below. Let us apply a bending moment, M, to the elastic beam, which will bend it to a radius R. The product of the bending moment (M) and the radius of curvature (R) is called *flexural rigidity*. We can use the inverse of this flexural rigidity as a measure of flexibility. From elementary strength of materials, we have the following relationship for a beam bent to an arbitrary radius R (see the boxed section for a derivation of this relationship):

$$\frac{M}{I} = \frac{E}{R}$$

where E is the Young's modulus of the material and the other terms are defined above. For a beam or a fiber of diameter, d, we have $I = \pi d^4/64$. Substituting this value of I in the above expression and rearranging, we can write:

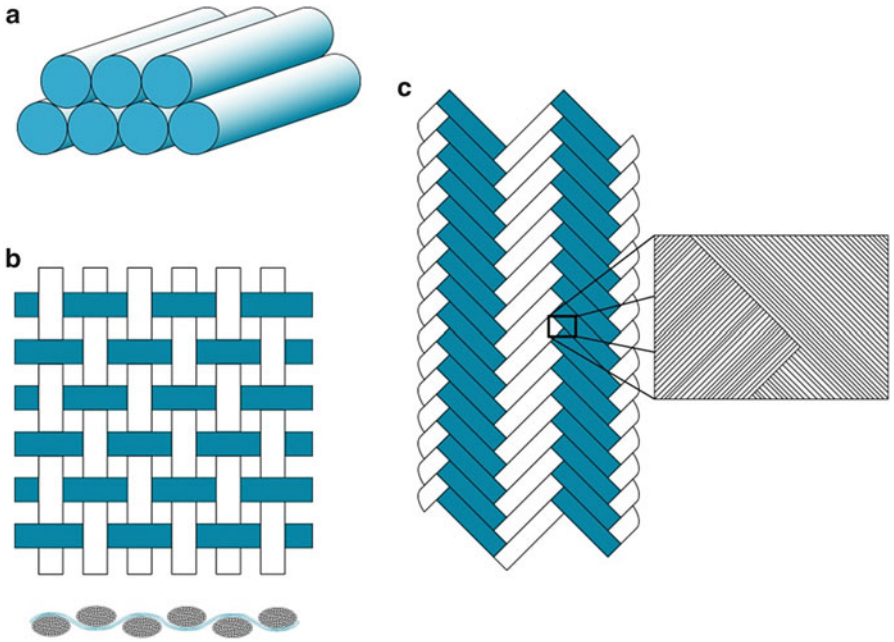

Fig. 2.1 Forms of fibrous materials (**a**) unidirectional fibers, (**b**) woven fiber fabric, and (**c**) fabric made of knitted fibers

$$\mathrm{MR} = \mathrm{EI} = \frac{E\pi d^4}{64}$$

EI (or MR) being the flexural rigidity, we have flexibility equal to 1/MR. Thus,

$$\frac{1}{\mathrm{MR}} = \frac{64}{E\pi d^4} \tag{2.1}$$

where d is the equivalent diameter and I is the moment of inertia of the beam (fiber). Equation (2.1) indicates that flexibility, 1/MR, is a very sensitive function of diameter, d. Given a sufficiently small diameter, it is possible to produce, in principle, a flexible fiber whether it is a polymer, metal, or ceramic.

Figure 2.1 shows different forms in which fibers can be used. Figure 2.1a shows unidirectionally aligned fibers in an untwisted, continuous tow or roving of fibers. Figure 2.1b shows a woven fabric in plane weave pattern, while Fig. 2.1c shows a knitted fabric. Such architectures of fibers, especially those shown in Fig. 2.1b, c are possible only with small diameter fibers which possess the required flexibility for weaving.

2.3 Carbon Fibers

Carbon is a very light element, has a theoretical density of 2.27 g/cm^3, and exists in a variety of forms. The two most important forms of carbon are diamond and graphite. Among the relatively new forms of carbon are the Buckminster Fullerene, also known as Buckyball and the drawn out version of Buckyballs, which may be in the form of nanotubes or nanowires, and graphene which is nothing but sheet of carbon atoms in the form of graphite. It is the graphitic form of carbon that is important in understanding the carbon fibers. The hexagonal structure of carbon in the graphitic form is shown in Fig. 2.2.

Consider a fiber to be a cylindrical beam under an applied moment, M,

$$M = \int y\sigma \, dA = \int y \frac{\sigma}{y} y \, dA = \frac{\sigma}{y} \int y^2 \, dA = \frac{\sigma I}{y}$$

where σ is the stress in an element of fiber a distance y from the neutral axis of the beam and dA is the cross-sectional area of the element under consideration. The term $\int y^2 \, dA = I$ is called the second moment of area of the beam. Rearranging the above expression, we get

$$\frac{M}{I} = \frac{\sigma}{Y} \tag{2.1}$$

We can write for the strain, ε, in a bent beam as

$$\varepsilon = \frac{y}{R}$$

where R is the radius of curvature of the bent beam and y is the distance from the neutral axis of the beam.
Incorporating Hooke's law,

$$\varepsilon = \frac{\sigma}{E}$$

$$\varepsilon = \frac{\sigma}{E} = \frac{y}{R}$$

$$\frac{\sigma}{y} = \frac{E}{R} \tag{2.2}$$

From (2.1) and (2.2), we get

$$\frac{M}{I} = \frac{E}{R}$$

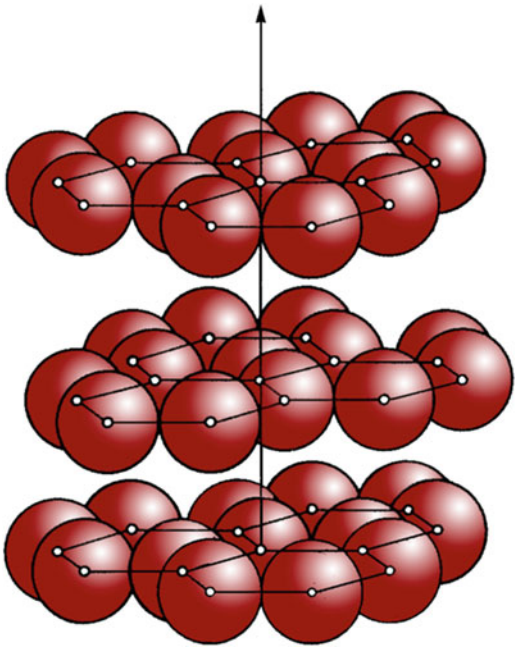

Fig. 2.2 Hexagonal structure of graphite

It should be emphasized that the term carbon fiber represents a family of fibers. It is one of the most important reinforcement fibers in all kinds of composites. The term graphite fiber is reserved for a special form of carbon fiber that is obtained after heating to a temperature greater than 2,400 °C. This process, called *graphitization*, results in a highly oriented, layered crystallographic structure, which, in turn, leads to significantly different chemical and physical properties than non-graphitic forms of carbon. An extreme case of the graphite structure is, of course, a graphite single crystal. Such a single crystal has hexagonal symmetry and, consequently, anisotropic characteristics. In particular, in a carbon fiber, properties such as elastic modulus will be different along the length of fiber and along the transverse or radial direction. The more aligned the basal planes in a carbon fiber, i.e., the more graphitic the structure, the higher the modulus in the direction of the axis and the greater the degree of anisotropy.

2.3.1 Fabrication of Carbon Fibers

Carbon fibers are fabricated by controlled pyrolysis of an organic fiber precursor (Ezekiel and Spain 1967; Watt and Johnson 1969; Johnson and Tyson 1969; Watt 1970; Diefendorf and Tokarsky 1975; Singer 1979). As it turns out, the concept of

starting with an organic precursor fiber and converting to an inorganic fiber is quite general, as we shall see for ceramic fibers. Depending on the precursor and the processing route, one can obtain a variety of carbon fibers with different strengths and moduli. Some important types of carbon fibers are high strength (HS), high modulus (HM), intermediate modulus (IM), super high modulus (SHM), etc.

Polyacrylonitrile (PAN) is commonly used as a precursor fiber for making carbon fibers. Pitch-based carbon fibers are also important; carbon fibers obtained from pitch can have much superior properties than those obtained from a PAN precursor.

The steps common to all processes of carbon fiber manufacture are as follows:

(a) Fiberization, i.e., extrusion of a polymer melt or solution into a precursor fiber.
(b) Stabilization (oxidation or thermosetting) is done at relatively low temperatures (200–450 °C), usually in air. This renders the precursor infusible during subsequent high-temperature processing.
(c) Carbonization is carried out in an inert atmosphere (pure N_2 generally) at 1,000–2,000 °C. At the end of this step, the fiber has 85–99 % carbon content.
(d) Graphitization (optional) is done in Ar or N_2 at a temperature greater than 2,500 °C. This step increases the carbon content to more than 99 % and imparts a very high degree of preferred orientation to the fiber.

2.3.2 PAN-Based Carbon Fibers

A flow diagram showing the various processing steps for PAN-based carbon fiber is shown in Fig. 2.3. The PAN precursor has a flexible polymeric chain structure, but it has an all-carbon backbone chain containing polar nitrile groups, Fig. 2.4a. During the stabilization treatment, the PAN precursor fiber is heated to 220 °C *under tension*. During this treatment, the nitrile groups form a ladder structure, a rigid and thermally stable structure, Fig. 2.4b. During this stabilization treatment, oxygen is absorbed and it cross-links the chains, the fibers turn black, and a stable ladder structure is formed. This treatment, done under tension, helps in maintaining the orientation of the ring structure even after unloading. During the carbonization treatment around 1,500 °C, well-developed hexagonal networks of carbon form and a considerable amount of gases is evolved. This gas evolution is partly responsible for some crack formation in the fiber, resulting in a lower tensile strength.

Commercially produced carbon fibers have a protective surface coating, called a *sizing or size*. The size serves two purposes: (1) ease of handling of the fiber and (2) improved adhesion with a polymeric matrix. Uncoated carbon fibers pick up surface charge easily when they come in contact with rubbing surfaces such as rollers, pulleys, guides, and spools. Handling of uncoated carbon fibers (winding, weaving, or braiding) can cause fiber breakage, and tiny fragments of carbon fibers can become airborne and short electrical machinery.

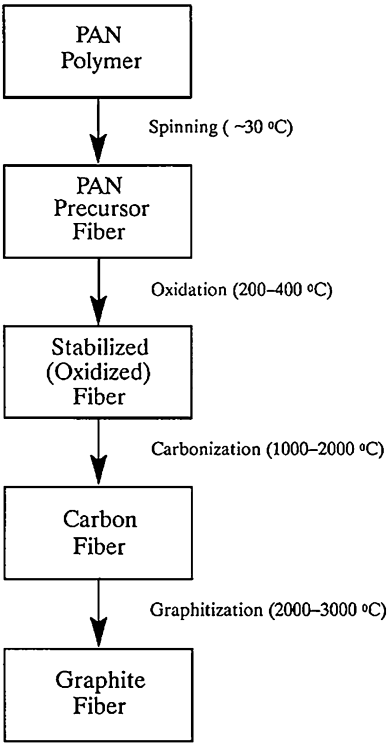

Fig. 2.3 Flow diagram for the fabrication of PAN-based carbon fiber

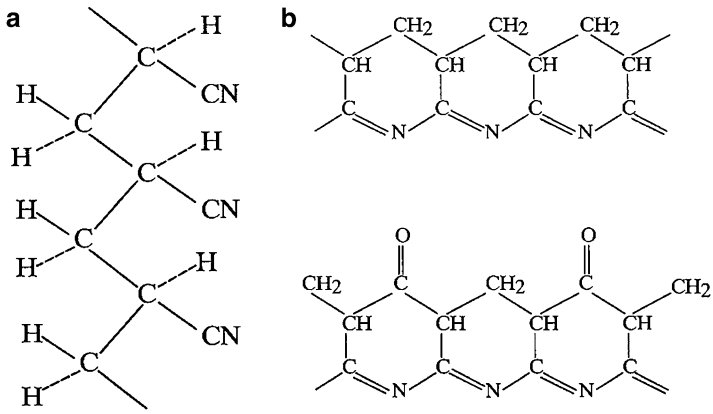

Fig. 2.4 (**a**) The carbon backbone chain structure of PAN and (**b**) the ladder structure of PAN and after stabilization

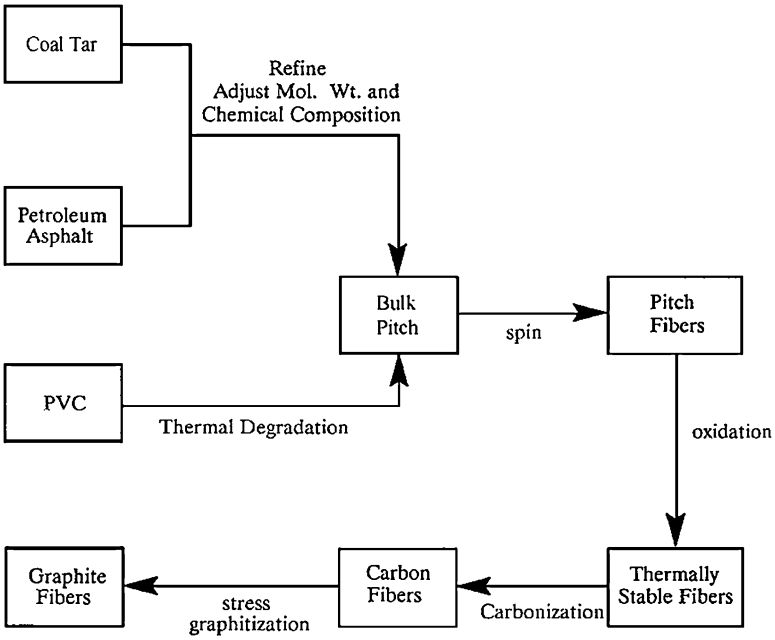

Fig. 2.5 Schematic of the process of making carbon fiber from a pitch

2.3.3 Pitch-Based Carbon Fibers

Next to PAN, pitch is an important precursor material for producing carbon fibers. Pitch is commonly obtained from one of the following three sources:

- Petroleum asphalt
- Coal tar
- Polyvinyl chloride (PVC)

All pitches, irrespective of the source, are thermoplastic in nature. This means the pitch precursor must be first stabilized against melting during pyrolysis. A schematic of the process of making carbon fibers from pitch is shown in Fig. 2.5. It involves the following steps:

- Extrusion or melt spinning into fibrous form
- Stabilization between 250 and 400 °C
- Carbonization
- Graphitization

Spinnability of the pitch and its conversion into a nonfusible state are the most important steps (Diefendorf and Tokarsky 1975). These characteristics depend on the chemical composition and molecular weight (MW) distribution of the pitch. The molecular weight (MW) of the pitch controls the viscosity and the melting range, i.e., MW controls the temperature and speed of spinning. The pitch composition depends on its source. In fact, there is tremendous variability in the composition of a pitch because it can be a mixture of hundreds of different species, varying with the source of crude oil and the processing conditions in the refinery.

Suitability of pitch for conversion to carbon fiber depends on a number of factors. The pitch should have a high carbon content (>90 %), high aromatic content (>50 %), low impurities and molecular weight, and proper molecular weight distribution, viscosity, and rheological characteristics consistent with the ease of spinning (Singer 1979).

2.3.4 Spinning and Rheology of Mesophase Pitch

Although melt spinning of a pitch to produce a precursor fiber is commercially popular, centrifugal spinning and jet spinning can also be used. Mesophase pitch, a thermoplastic, has a nematic liquid crystal structure, wherein ordered domains of rigid rodlike molecules float in an isotropic matrix. The two-phase precursor pitch is agitated prior to spinning to form a homogeneous mixture and spun into pitch filaments in the temperature range where the viscosity is in the 1–20 Pa s range. Fibers can be spun at speeds of 3–100 m min^{-1} with diameters of 10–20 μm and having the same composition as the mesophase pitch. The as-spun mesophase fibers are anisotropic because of the nematic liquid crystal structure. These fibers have large, elongated, anisotropic domains (about 4 μm diameter) aligned along the fiber axis and are thermoplastic in nature. Fibers drawn from isotropic pitch or the ones drawn from a PAN precursor do not exhibit such anisotropic domains.

An oxidation treatment is given next to thermally stabilize the pitch fibers against internal relaxation and render them infusible during the subsequent processing steps. During the stabilization treatment, oxygen enters the precursor fibers and provides cross-linking between the pitch molecules of hydrocarbons comprising pitch. There is a slight weight gain in the fibers in this step. The rest of the process is essentially similar to the PAN-based carbon fiber fabrication, except that stress is applied during graphitization. The step of carbonization serves to remove the non-carbon atoms (mostly hydrogen and oxygen) with an attendant loss in weight of the fibers.

Table 2.2 Properties of PAN-based carbon fiber (strand data) (After Riggs 1985)

Characteristic	High strength[a]	High strength[b]	Super high modulus[c]
Filament diameter (μm)	5.5–8.0	5.4–7.0	8.4
Density (g/cm^3)	1.75–1.80	1.78–1.81	1.96
Carbon content (wt.%)	92–95	99–99$^+$	99$^+$
Tensile strength (MPa)	3,100–4,500	2,400–2,550	1,865
Tensile modulus (GPa)	25–260	360–395	520
Strain at fracture (%)	1.3–1.8	0.6–0.7	0.38
Electrical resistivity (μΩm)	15–18	9–10	6.5
Thermal conductivity (W/mK)	8.1–9.3	64–70	120

[a]Thornel T-300, T-500, T-600, T-700; Celion 3000, 6000, 1200; AS2, AS4, AS6, IM6
[b]Thornel T-50, Celion G-50, HMS
[c]Celion GY-70
The "+" superscript signifies more than

Table 2.3 Properties of mesophase pitch-based carbon fiber (After Singer 1981)

Property	Thornel P555	Thornel P755	Thornel P200
Filament diameter (μm)	10	10	10
Density (g/cm^3)	2.02	2.06	2.15
Carbon content (wt.%)	99	99	99$^+$
Tensile strength (MPa)	1,895	2,070	2,240
Tensile modulus (GPa)	380	517	690
Strain at fracture (%)	0.5	0.4	0.3
Electrical resistivity (μΩm)	7.5	4.6	2.5
Thermal conductivity (W/mK)	110	185	515

The "+" superscript signifies more than

2.3.5 Structure and Properties of Carbon Fibers

Table 2.2 presents property data for three different types of PAN-based carbon fibers, while Table 2.3 gives the properties of mesophase pitch-based carbon fibers. Note the high density and high modulus of pitch-based fibers compared to PAN-based fibers. The stress applied at very high temperatures (as high as 3,000 °C) during the graphitization step (increases the degree of order in carbon fibers). This is also accompanied by a large increase in the longitudinal elastic modulus of the fiber. The tensile strength of PAN-based fibers when subjected to high-temperature treatment, however, decreases, Fig. 2.6 (Watt 1970). This is attributed to the presence of discrete flaws on the fiber surface and within the fiber. Most of the volumetric defects in carbon fibers originate from:

1. Inorganic inclusions
2. Organic inclusions
3. Irregular voids from rapid coagulation
4. Cylindrical voids precipitated by dissolved gases

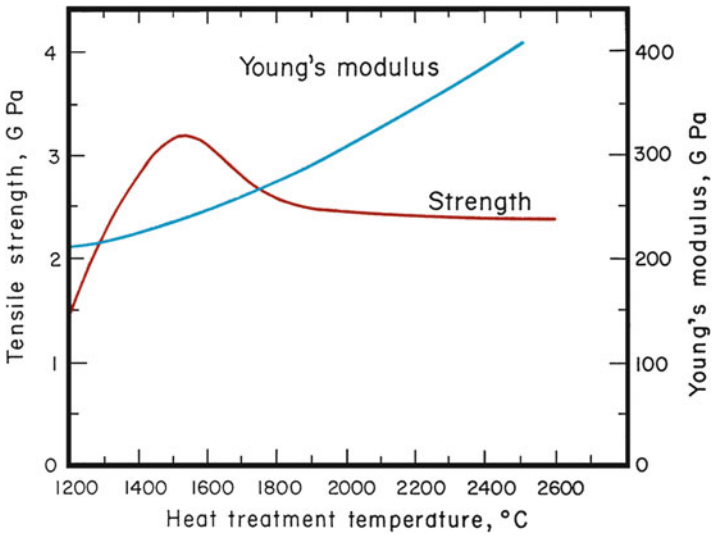

Fig. 2.6 Elastic modulus and tensile strength of carbon fiber as a function of high-temperature treatment (After Watt 1970)

These defects get transformed during the high-temperature treatment into diverse imperfections. Basal-plane cracks called *Mrozowski* cracks are perhaps the most important type of flaw that limits the tensile strength of carbon fibers. These occur as a result of anisotropic thermal contractions within the ribbon structure on cooling from the high-temperature treatment (>1,500 °C).

2.3.6 Structure of Carbon Fibers

Many researchers have studied the structure of carbon fibers; for a good summary, see, for example, Peebles (1995). Here we provide the salient features of the structure of carbon fibers. Scanning electron micrographs of pitch-based carbon fibers showing graphitic, sheet-like morphology can be seen in Fig. 2.7 (Kumar et al. 1993). At a submicrometer level, as seen in a transmission electron microscope, the microstructure of carbon fibers is quite heterogeneous. In particular, there is a pronounced irregularity in the packing of graphitic lamellae inward from the fiber surface. The basal planes are much better aligned in the near surface region of the fiber. In very general terms, the graphitic ribbons are oriented more or less parallel to the fiber axis with random interlinking of layers, longitudinally and laterally. An example of such a lamellar structure of PAN-based carbon fibers is shown in Fig. 2.8 (Deurbergue and Oberlin 1991). This is a high-resolution electron

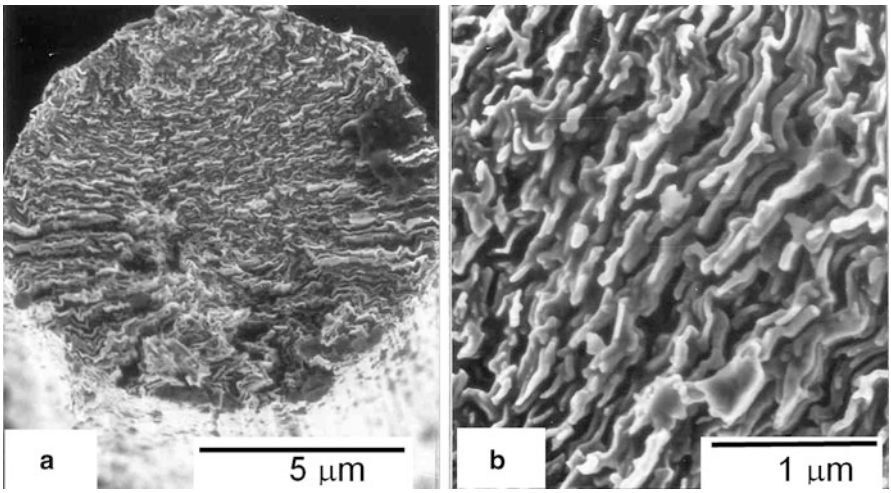

Fig. 2.7 Scanning electron micrograph of pitch-based P-100 fiber at low (**a**) and high (**b**) magnification showing graphitic sheet like morphology (Kumar et al. 1993; Courtesy of S. Kumar)

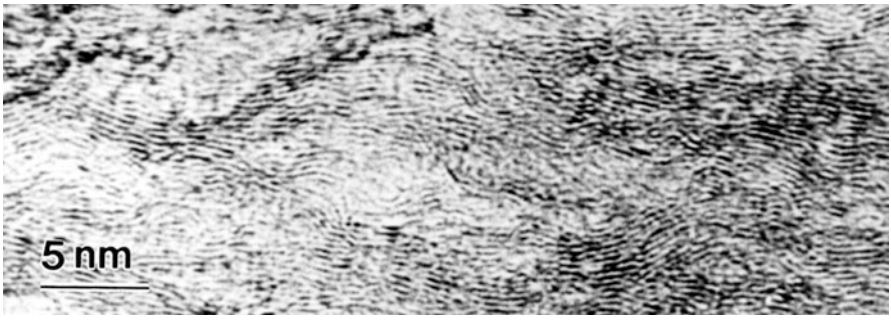

Fig. 2.8 High-resolution transmission electron micrograph showing lamellar structure of structure of PAN-based carbon fibers (Courtesy of Oberlin)

micrograph of a longitudinal section of a fiber carbonized at 1,330 °C. The micrograph shows <002> lattice fringes, which represent the graphitic planes of the carbon fiber. The degree of alignment of the basal planes increases with the final heat treatment temperature.

2.3.7 Carbon Nanotubes, Nanoparticles, and Graphene

Carbon nanotubes (CNTs) are essentially cylindrical tubes consisting of carbon atoms. The cylindrical object has a diameter on the nm scale, <50 nm. There length can be several micrometers long. There can be single walled nanotubes (SWNT) or

multi-walled nanotubes (MWNT). Since they are so small, it is not easy to determine their mechanical properties experimentally. In the literature, one finds all kinds of data. Since they have a hollow tubelike structure, their specific gravity is low (1.3–2), very high modulus (1 TPa), and strength between 10 and 50 GPa. The reader should take these values with a grain of salt.

Carbon nanoparticles are more or less spherical particles of carbon with a diameter less than 100 nm. Graphene, on the other hand, is a two-dimensional sheet structure made of carbon atoms arranged in the form of graphitic hexagons. Graphene is very thin and supposed to be very strong.

2.4 Boron Fibers

Boron is another elemental fiber, like carbon, that has high strength and high stiffness. It is commonly made by chemical vapor deposition (CVD) on a substrate such as tungsten or carbon, see Fig. 2.9. Some important characteristics of any CVD process of making fibers are:

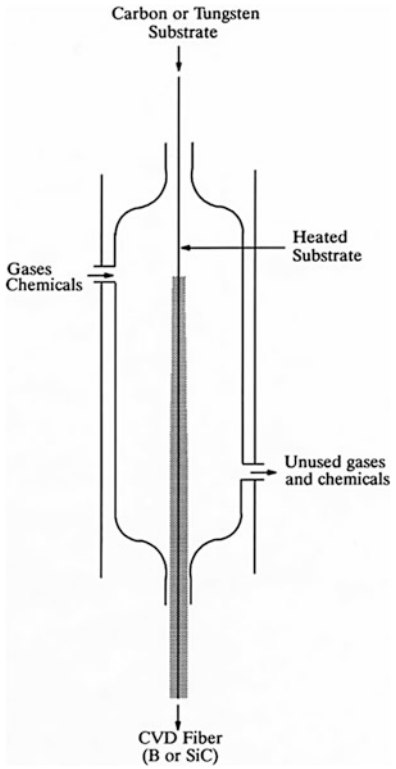

Fig. 2.9 Chemical vapor deposition (CVD) of boron or silicon carbide on a tungsten or carbon substrate

- Essentially, a coating is deposited on a fibrous substrate. The result is a fiber with a large diameter and a sheath/core structure, i.e., the fiber itself is a composite.
- Unlike conventional fiber-forming processes, the CVD fibers are not formed by stretching or drawing, i.e., there is no lengthening; instead, lateral growth by thickening occurs.
- The final diameter of the fiber may be as much as ten times that of the starting fiber substrate.

Boron on a tungsten substrate, denoted by B(W), and SiC on a carbon substrate, denoted by SiC(C), are two examples. Boron on a carbon substrate is also possible. B(W) fibers find applications mostly in aerospace and the sporting goods industry. Major drawbacks of most CVD-produced fibers are their large diameter (which makes them less flexible) and high cost.

Elemental boron is produced by the reduction of a boron halide by hydrogen:

$$2BX_3\ (g) + 3H_2\ (g) \rightarrow 2B\ (s) + 6HCl\ (g)$$

where X denotes a halogen such as Cl, Br, or I. B is deposited on a substrate of tungsten or carbon. Typically, the commercially produced boron fiber can have between 75 and 200 μm. Sometimes a surface coating of SiC or B_4C is applied by CVD on the B fiber, for use in aluminum or titanium matrix composites, to prevent chemical reaction between boron and the metal matrix.

Boron fiber made by deposition on a tungsten substrate can result in complex reaction products at the core/sheath interface. A boron fiber cross section (100 μm diameter) is shown in Fig. 2.10a while Fig. 2.10b shows, schematically, the various subparts of the cross section. Depending on the temperature conditions during deposition, the W core may consist of a series of compounds such as W, W_2B, WB, W_2B_5, and WB_4. These tungsten boride phases form by diffusion of B into W. Generally, the fiber core consists only of WB_4 and W_2B_5. On prolonged heating, the core may be converted completely into WB_4. As boron diffuses into the tungsten substrate to form borides, the core expands from its original 12.5 μm (original W wire diameter) to 17.5 μm. The SiC coating shown in Fig. 2.10b is a barrier coating used to prevent any adverse reaction between B and the matrix, such as Al or Ti, at high temperatures. The SiC barrier layer is vapor deposited onto the boron using a mixture of hydrogen and methyldichlorosilane.

As-deposited boron (β rhombohedral) has a nanocrystalline structure. The surface of boron fibers shows a corncob structure. This stems from the growth of nodules of boron, each of which starts as an individual nucleus and grows outward in a conical form. Frequently, foreign particles or inclusions are also trapped at the boundaries between nodules.

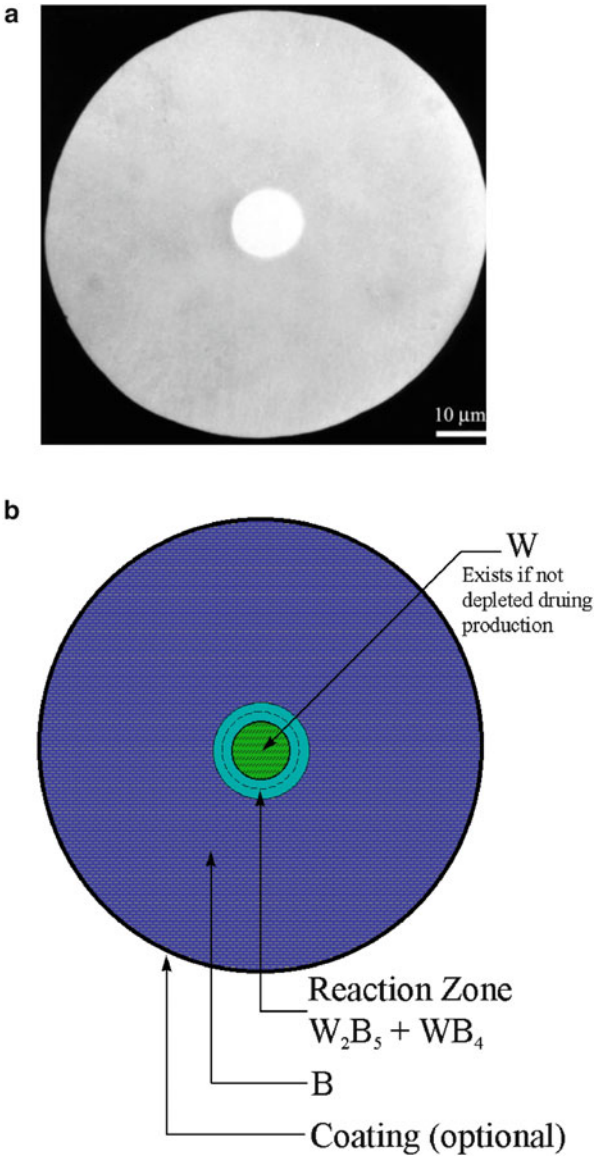

Fig. 2.10 (**a**) Boron fiber cross section (100 µm diameter) (**b**) schematic of boron fiber showing the subparts of the cross section

2.4.1 Residual Stresses

Fibers made via CVD, such as boron fiber, have inherent residual stresses which originate from the CVD process. Growth stresses in the nodules of boron, stresses introduced due to diffusion of boron into the tungsten core, and stresses generated due to the difference in the coefficient of expansion of deposited boron and

tungsten boride core contribute to the residual stresses. These internal stresses are algebraically added to the applied stresses and thus can have a considerable influence on the mechanical properties of the fiber. Morphologically, the most conspicuous aspect of these internal stresses is the frequently observed radial crack in the transverse section of these fibers.

Brittle materials such as boron show a distribution of strengths rather than a single value. Imperfections, such as inclusions or nodular boundaries on the boron fiber surface, lead to stress concentrations. As a brittle material is not capable of deforming plastically in response to these stress concentrations, fracture ensues at one or more such sites. Boron fiber is indeed a very brittle material, and cracks commonly originate at preexisting defects located at the boron–core interface or at the surface. The surface defects are due to the nodular surface which results from the growth of boron cones. In particular, when a nodule coarsens due to exaggerated growth around a contaminating particle, a crack can result from this large nodule and weaken the fiber.

2.5 Oxide Fibers

Ceramic oxide fibers, continuous and discontinuous, have been commercially available since the 1970s. We describe below some important aspects of processing and microstructure of these fibers.

2.5.1 Alumina-Type Oxide Fibers

Alumina can have different allotropic forms such as γ, δ, η, and α; α-alumina being the thermodynamically stable form. Many different alumina-based oxide fibers are available commercially. 3M Co. produces a series of oxide fibers with compositions ranging from pure alumina to mixtures of alumina and silica or alumina and mullite. Sumitomo Chemical Co. produces a fiber that can have a wide composition range: 70–100 % Al_2O_3 and 0–30 % SiO_2. A short fiber, called staple fiber, of δ-alumina (96 %) (trade name Saffil) is available commercially. Single crystal continuous aluminum oxide or sapphire fibers can be produced by drawing from molten alumina. A fiber produced by this method, called Saphikon, has a hexagonal crystal structure with its c-axis parallel to the fiber axis, i.e., the basal plane (0001) is perpendicular to the fiber axis. The diameter of this fiber is rather large, between 75 and 250 μm. We describe below the salient features of some of these fabrication methods and the properties of the fibers obtained.

Alumina + Silica Fibers and α-Alumina Fiber

A series of alumina + silica fibers made via sol–gel route is available commercially. In particular, 3M Co. has developed a series of such fibers, trade name *Nextel* fibers. In this series, *Nextel 610* is a polycrystalline, α-alumina fiber. The sol–gel process of making fibers involves the following steps common to all sol–gel processing:

(a) Formulate sol
(b) Concentrate to form a viscous gel
(c) Spin the precursor fiber
(d) Calcine to obtain the oxide fiber

Specifically, in the case of the 3M process of making Al_2O_3 fiber, the following steps are involved:

- Use an organic, basic salt solution as a precursor.
- Drive out (decompose and volatilize) the organics without causing cracking, blistering, or other defects.
- Fire at 1,400 °C under carefully controlled conditions.
- Apply a low-temperature straightening treatment.

A fine-grained α-Al_2O_3 fiber is obtained by seeding the high-temperature α-alumina with a very fine hydrous colloidal iron oxide (Wilson and Visser 2001). The fine iron oxide improves the nucleation rate of α-Al_2O_3, with the result that a high density, ultrafine, homogeneous α-Al_2O_3 fiber is obtained. The rationale for seeding with iron oxide is as follows. Basic salts of aluminum decompose into transition aluminum oxide spinels such as α-Al_2O_3 above 400 °C. These transition cubic spinels convert to hexagonal α-Al_2O_3 on heating between 1,000 and 1,200 °C. The problem is that the nucleation rate of pure α-Al_2O_3 is too low and results in large grains. Also, during the transformation to α phase, large shrinkage leads a rather large porosity (Kumagai and Messing 1985; Suwa et al. 1985). Seeding of alumina with fine particles would appear to be a solution. α-Fe_2O_3 is isostructural with α-Al_2O_3, only 5.5 % lattice mismatch (Wilson 1990). Hydrous colloidal iron oxide sol appears to be an efficient nucleating agent. According to Wilson (1990), without the seeding of iron oxide, the η-alumina to α-alumina transformation occurs at about 1,100 °C. With 1 % Fe_2O_3, the transformation temperature was decreased to 1,010 °C, while with 4 % Fe_2O_3, the transformation temperature came down to 977 °C. Concomitantly, the grain size was refined. Nextel 610 fiber has 0.4–0.7 % Fe_2O_3. Besides Fe_2O_3, about 0.5 wt.% SiO_2 is added to reduce the final grain size, although SiO_2 inhibits the transformation to the α phase. The SiO_2 addition also reduces grain growth during soaking at 1,400 °C.

Many other alumina or alumina-silica type fibers are available, most of which are made by the sol–gel process. Sumitomo Chemical Company produces a fiber that is a mixture of alumina and silica. Starting from an organoaluminum (polyaluminoxanes or a mixture of polyaluminoxanes and one or more kinds of Si-containing compounds), a precursor fiber is obtained by dry spinning. This precursor fiber is

Table 2.4 Properties of some oxide fibers (manufacturer's data)

Fiber type	Composition (wt.%)	Diameter (μm)	Density ($g/cm^{3)}$	Tensile strength (GPa)	Young's modulus (GPa)
Nextel 312	Al_2O_3-62.5, SiO_2-24.5, B_2O_3-13	10–12	2.70	1.7	150
Nextel 440	Al_2O_3-70, SiO_2-28, B_2O_3-2	10–12	3.05	2.0	190
Nextel 550	Al_2O_3-73, SiO_2-27	10–12	3.03	2.0	193
Nextel 610	Al_2O_3-99^+	10–12	3.9	3.1	370
Nextel 650	Al_2O_3-89, ZrO_2-10, Y_2O_3-1	10–12	4.10	2.5	358
Nextel 720	Al_2O_3-85, SiO_2-15	10–12	3.40	2.1	260
Saffil	Al_2O_3-96, SiO_2-4	3	2.3	1.0	100
Saphikon	Single crystal Al_2O_3	70–250	3.8	3.1	380
Sumitomo	Al_2O_3-85, SiO_2-15	9	3.2	2.6	250

calcined to produce the final fiber. The fiber structure consists of fine crystallites of spinel. SiO_2 serves to stabilize the spinel structure and prevents it from transforming to α-Al_2O_3 (Chawla 1998). Mention has been made of the Nextel series of fiber produced by the 3M Company. These fibers contain mainly Al_2O_3 + SiO_2 and some B_2O_3. The composition and properties of these fibers are given in Table 2.4. The sol–gel manufacturing process used by 3M Co. has metal alkoxides as the starting materials. Metal alkoxides are $M(OR)_n$-type compounds where M is the metal and n is the metal valence, and R is an organic compound. Selection of an appropriate organic group is very important. It should provide sufficient stability and volatility to the alkoxide so M–OR bonds are broken and MO–R is obtained to give the desired oxide ceramics. Hydrolysis of metal alkoxides results in sols which are gelled and spun. The gelled fiber is then densified at relatively low temperatures. The high surface free energy available in the pores of the gelled fiber allows for densification at a relatively low temperature. The sol–gel process provides close control over solution composition and the rheology of the fiber diameter. The disadvantage is that rather large dimensional change must be accommodated and fiber integrity conserved.

Nextel 720 fiber consists of aggregates of mullite grains embedded in α-alumina grains. The grains of each phase are small, and the aggregates of similarly aligned grains act like single grains about 0.5 μm in diameter. This gives the Nextel 720 fiber very low creep rate at temperatures above 1,000 °C.

Sol–gel method is also used to produce silica-stabilized alumina (*Saffil*) and calcia-stabilized zirconia fibers (Birchall et al. 1985). The Saffil fiber is a δ-Al_2O_3, short, staple fiber that has about 4 % SiO_2 and a very fine diameter (3 μm). The aqueous phase contains an oxide sol and an organic polymer. The sol is extruded as filaments into a coagulating (or precipitating) bath in which the extruded shape gels. The gelled fiber is then dried and calcined to produce the final oxide fiber. For alumina, aluminum oxychloride [$Al_2(OH)_5Cl$] is mixed with a medium molecular

weight polymer such as 2 wt.% polyvinyl alcohol. This solution is slowly evaporated in a rotary evaporator until a viscosity of about 80 Pa s is attained. It is then extruded through a spinneret, the fibers are wound on a drum, and fired to about 800 °C. The organic material is burned away and a fine-grained alumina fiber having 5–10 % porosity and a diameter of 3–5 μm is obtained. The fibers produced at this stage are suitable for filter applications because of their high porosity. By heating them to 1,400–1,500 °C, which causes a 3–4 % of linear shrinkage, one obtains a refractory alumina fiber suitable for reinforcement purposes.

Yet another continuous, polycrystalline, α-alumina fiber, trade name *Almax*, is prepared by dry spinning a viscous slurry consisting of an aluminum salt, a fine powder of intermediate alumina, and an organic binder to produce the precursor fiber; this is followed by prefiring (calcining) and firing (sintering) the precursor fiber to produce an alumina fiber.

Polycrystalline oxide fibers of yttrium–aluminum garnet, $Y_3Al_5O_{12}$ (YAG), composition and a composite fiber consisting of α-alumina and YAG were prepared by sol–gel method (Towata et al. 2001). The process involved the use of α-alumina or YAG seed particles. α-Alumina seed particles accelerated the phase transformation from θ-alumina to α-alumina. The YAG seed particles influenced the multistep transformation of yttrium and aluminum oxide.

A technique called *edge-defined film-fed growth* (EFG) has been used to make continuous, monocrystalline sapphire (Al_2O_3) fiber (LaBelle and Mlavsky 1967; Gasson and Cockayne 1970; LaBelle 1971; Pollack 1972; Hurley and Pollack 1972). LaBelle and Mlavsky (1967) were the first to grow sapphire (Al_2O_3) single crystal fibers using a modified Czochralski puller and radio frequency heating. In 1971, these authors devised a growth method, called the EFG method. Growth rates as high as 200 mm/min have been attained. The die material must be stable at the melting point of alumina, so a molybdenum die is typically used. A sapphire seed crystal is used. A capillary supplies a constant liquid level at the crystal interface. Molten alumina wets both molybdenum and alumina. The crystal grows from a molten film between the growing crystal and the die. The crystal shape is defined by the external shape of the die rather than the internal shape. Perhaps the most important item about the single crystal alumina fiber is that there are no grain boundaries. Thus, under creep conditions involving grain boundary-related phenomena, such as cavitation and grain boundary sliding, will not be operative, and one can expect a highly creep-resistant fiber. However, single crystal alumina can undergo dislocation creep on the basal plane. Thus, it would appear that if the basal plane can be oriented such that basal slip does not occur, then one can obtain a very creep-resistant fiber. Such will be the case for a single crystal fiber with its c-axis parallel to the fiber axis.

A *laser-heated floating zone method* can also be used to make a variety of ceramic fibers. Gasson and Cockayne (1970) used laser heating for crystal growth of Al_2O_3, Y_2O_3, $MgAl_2O_4$, and Na_2O_3. This method has been used to grow single crystal fibers of Al_2O_3, Y_2O_3, TiC, TiB_2, mullite, and Al_2O_3–YAG eutectic (Haggerty 1972; Sayir and Farmer 1995; Sayir et al. 1995). A CO_2 laser is focused on the molten zone and a source rod is brought into the focused laser beam.

A seed crystal, dipped into the molten zone, is used to control the orientation. Crystal growth starts by moving the source and seed rods simultaneously. Mass conservation dictates that the diameter is reduced as the square root of the feed rate/pull rate ratio. Mention should be made of a containerless melting technique that has been used to grow continuous fibers of alumina and YAG composition ($Y_3Al_5O_{12}$) directly from the melt. Containerless melting eliminates heterogeneous nucleation by container surfaces. A continuous-wave CO_2 laser beam is used for heating (Weber et al. 1998). Specimens are levitated in a gas jet and stabilized with an acoustic positioning device. The levitated samples are heated and melted with a CO_2 laser beam.

2.6 Nonoxide Fibers

Continuous nonoxide ceramic fibers are also available commercially. The development of silicon carbide fiber must be regarded as a major development in the field of ceramic fibers during the last quarter of the twentieth century. In particular, a process developed by the Yajima in Japan, involving controlled pyrolysis of a polycarbosilane (PCS) precursor to yield a flexible fine diameter fiber is considered to be the harbinger of making ceramic fibers from polymeric precursors. In this section we describe the processing, microstructure, and properties of silicon carbide and some other nonoxide fibers.

2.6.1 Silicon Carbide Fibers

Silicon carbide fiber is by far the most important nonoxide ceramic fiber available commercially. The two main varieties of this fiber available commercially are large-diameter fiber made by CVD and small diameter fiber made by controlled pyrolysis of a polymer. Another important type of SiC available for reinforcement purposes is SiC whiskers.

2.6.2 Silicon Carbide Fibers Made by CVD

Silicon carbide fibers can be made by CVD on a substrate heated to about 1,300 °C (DeBolt et al. 1974). The substrate can be tungsten or carbon. The reactive gaseous mixture contains hydrogen and alkyl silanes. Typically, a gaseous mixture consisting of 70 % hydrogen and 30 % silanes is introduced at the top of the reactor, where the tungsten substrate (~13 μm diameter) also enters the reactor. Mercury seals are used at both ends as contact electrodes for the filament. The substrate is heated by combined direct current (250 mA) and very high frequency

(VHF ~60 MHz) to obtain an optimum temperature profile. To obtain a 100 μm of SiC monofilament, it generally takes about 20 s in the reactor. The filament is wound on a spool at the bottom of the reactor. The exhaust gases (95 % of the original mixture + HCl) are passed around a condenser to recover the unused silanes. Efficient reclamation of the unused silanes is very important for a cost-effective production process. As described for the boron fiber, such CVD processes result in composite monofilaments which have built in residual stresses. The process is, of course, very expensive. Methyltrichlorosilane is an ideal raw material for this process as it contains one silicon and one carbon atom, i.e., a stoichiometric SiC will be deposited. The chemical reaction is

$$CH_3SiCl_3 \rightarrow SiC(s) + 3HCl$$

An optimum amount of hydrogen is required. If the hydrogen is less than sufficient, chlorosilanes will not be reduced to Si and free carbon will be present in the mixture. If too much hydrogen is present, excess Si will be present in the end product. The final monofilament (100–150 μm) consists of a sheath of mainly β-SiC with some α-SiC on the tungsten core. The {111} planes in SiC are deposited parallel to the fiber axis.

A series of surface-modified silicon carbide fibers, called SCS fibers, has been used in a variety of composites. These special fibers have a complex through-thickness gradient structure. SCS-6, for example, is a thick fiber (diameter = 142 μm) and is produced by CVD of silicon- and carbon-containing compounds onto a pyrolytic graphite-coated carbon core. The pyrolytic graphite coating is applied to a carbon monofilament to give a substrate of 37 μm. This is then coated with SiC by CVD to give a final monofilament of 142 μm diameter. The outer surface layer (about 1 μm thick) of SCS-6 fiber consists of C doped Si. Mann et al. (1999) verified the dramatic changes in mechanical characteristics of SCS-6 fiber, such as Young's modulus and hardness, as function of fiber radius using nanoindentation techniques. Besides SCS-6, there are other varieties of CVD silicon carbide fibers on a carbon core that are available commercially. Typical properties of SCS-type silicon carbide fibers are given in Table 2.5. Another SiC fiber made by CVD is called *sigma* fiber; this has a tungsten filament core.

Such fibers made by CVD on a heated substrate are composite materials themselves and can exhibit unusual behavior. Lara-Curzio and Sternstein (1993) examined the behavior of such composite fibers when subjected to thermomechanical loading. Their main conclusion was that one must take into account the strains experienced by the substrate during the CVD process of making such composite fibers. Not doing so can lead to a severe underestimate of the residual stresses in the fiber. In particular, in the case of the SCS-6 fiber, they identified the presence of large residual radial stresses at various interfaces (carbon substrate/pyrolytic graphite, pyrolytic graphite/SiC). According to these authors, the origin of rather large residual stresses lay in the high temperature of CVD and the large anisotropy in the pyrolytic graphite layer.

Table 2.5 Properties of SCS-type fibers (*Source*: Specialty Materials Inc.)

Property	SCS-6	SCS-9A	SCS-ultra
Fiber diameter (μm)	140	78	140
Density (g/cm^3)	3.0	2.8	3.0
Tensile strength (GPa)	3.45	3.45	5.86
Tensile modulus (GPa)	380	307	415
Coefficient of thermal expansion (10^{-6} K^{-1})	4.1	4.3	4.1

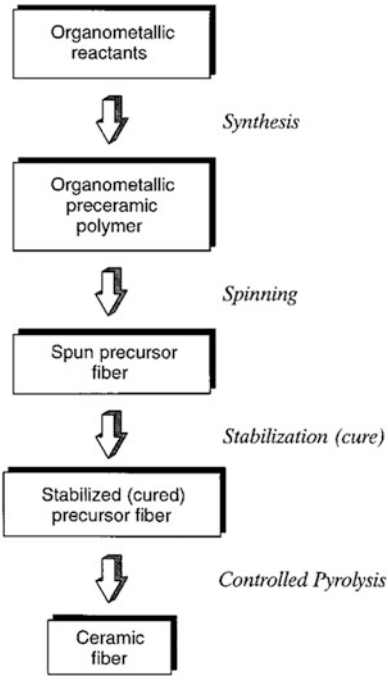

Fig. 2.11 Flow diagram for making ceramic fibers from a polymeric precursor

2.6.3 Nonoxide Fibers via Polymer Precursors

As pointed out above, the SiC fibers obtained via CVD have very large diameter and thus are not very flexible. Yajima et al. (1976) and Yajima (1980) developed a process of making fine, continuous, and flexible SiC-type fibers by controlled pyrolysis of a polymeric precursor. This method of using silicon-based polymers to produce a family of ceramic fibers having good mechanical properties, good thermal stability, and oxidation resistance has enormous potential. Figure 2.11 shows a general flow diagram for making ceramic fibers from a polymeric precursor. Note the similarity with the process of making a carbon fiber from a

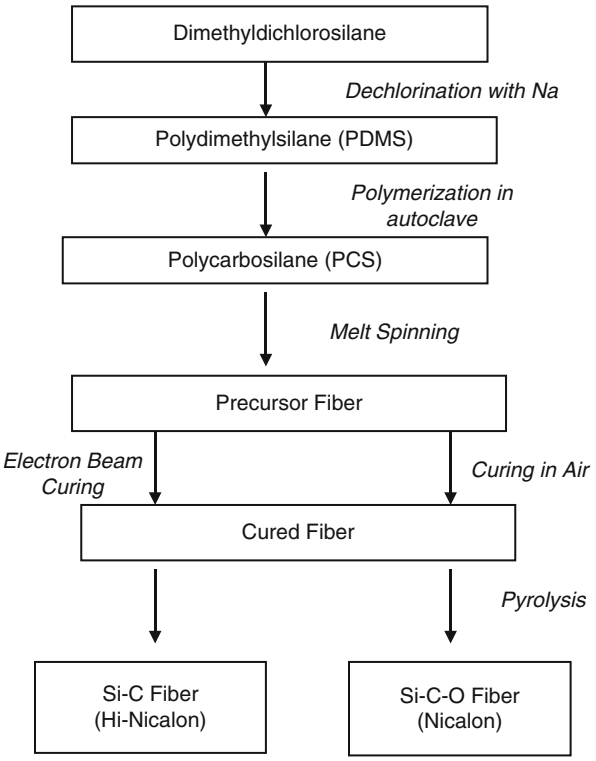

Fig. 2.12 The Yajima process of making fine diameter SiC from a polycarbosilane

polymeric precursor. The various steps involved in this polymer route can be listed as follows (Wax 1985):

(a) Characterize the polymer (yield, molecular weight, purity, etc.).
(b) Melt spin polymer into a precursor fiber.
(c) Cure the precursor fiber to cross-link the molecular chains, making it infusible during the subsequent pyrolysis.
(d) Pyrolyze the precursor fiber under controlled conditions to obtain the ceramic fiber.

Specifically, the Yajima process of making SiC fiber from a polymeric precursor fiber involves the following steps and is shown schematically in Fig. 2.12. PCS, a high molecular weight polymer, containing Si and C is synthesized. This involves the use of a commercially available material, viz., dimethylchlorosilane. Solid polydimethylsilane (PDMS) is obtained by dechlorination of dimethylchlorosilane by reacting it with sodium. PCS is obtained by thermal decomposition and polymerization of PDMS. This is carried out under high pressure in an autoclave at 470 °C in an argon atmosphere for 8–14 h. A vacuum distillation treatment at up to 280 °C follows. The average molecular weight of the resulting polymer is about 1,500. This is melt spun from a 500-hole nozzle at about 350 °C under N_2 gas to

Table 2.6 Typical properties of Nicalon SiC fiber

Property	Ceramic grade	HVR[a] grade	LVR[b] grade	Hi-Nicalon S[c]
Density (g/cm^3)	2.55	2.32	2.45–2.55	3.1
Tensile strength (MPa)	2,960	2,930	2,960	2,600
Young's modulus (GPa)	192	186	192	420
Strain-to-failure (%)	1.5	1.6	1.5	0.6
Coefficient of thermal expansion (10^{-6} K^{-1})	4	–	–	6.89
Volume resistivity (Ω cm)	10^3	$>10^6$	0.5–5.0	0.1

[a]Low dielectric fiber (high volume resistivity)
[b]Higher conductivity fiber (low volume resistivity)
[c]Hi-Nicalon S (Ichikawa 2000)

obtain the so-called pre-ceramic, continuous, precursor fiber. The precursor fiber is quite weak (tensile strength ~10 MPa). This is converted to inorganic SiC by curing in air, heating to about 1,000 °C in N_2 gas, followed by heating to 1,300 °C in N_2 under tension. During the pyrolysis, first stage of conversion occurs at around 550 °C when cross-linking of polymer chains occurs. Above this temperature, the side chains containing hydrogen and methyl groups decompose. Fiber density and mechanical properties improve sharply. The conversion to SiC occurs above about 850 °C.

2.6.4 Structure and Properties of Nicalon Fiber

The *Nicalon* multifilament fiber (single fiber diameter between 10 and 20 μm) consists of a mixture of β-SiC, free carbon, and SiO_2. The properties of Nicalon start degrading above about 600 °C because of the thermodynamic instability of composition and microstructure. Ceramic grade "Nicalon" fibers, carrying the designation NLM, HI, and HI-S having low-oxygen content, are also available. The structure of Nicalon fiber has been studied by many researchers. The commercial variety of Nicalon has an amorphous structure, while the low-oxygen variety has a microcrystalline structure (SiC grain radius of 1.7 nm) (Simon and Bunsell 1984). Microstructural analysis shows that both fibers contain, in addition to SiC, SiO_2, and free carbon. Laffon et al. (1989) proposed a model of Nicalon fiber consisting of β-SiC crystals mixed with some free carbon with a composition of SiC_xO_y, with x + y being equal to 4. The density of the fiber is about 2.6 g/cm^3 which is low compared to that of pure β-SiC. This is understandable in view of the fact that the composition is a mixture of SiC, SiO_2, and C. The properties of Nicalon fiber are summarized in Table 2.6. A quick comparison of Nicalon SiC fiber with CVD SiC fiber shows that the CVD fiber is superior in properties. In particular, it should be mentioned that CVD SiC fiber (stoichiometric) shows superior creep resistance vis-à-vis Nicalon fiber (DiCarlo 1985).

2.6.5 *Other SiC-Type Fibers*

There are other silicon carbide-type fibers that are commercially available, with elemental compositions of Si–C, Si–N–C–O, Si–B–N, Si–C–O, and Si–Ti–C–O. Almost all of them are made from polymeric precursors. A multifilament silicon carbide fiber, called *Tyranno* (Yamamura et al. 1988), is made by pyrolysis of polytitano carbosilanes, and it contains about 1.54 wt.% titanium. A textile grade silicon carbide fiber, called *Sylramic*, has, according to the manufacturer, a nanocrystalline structure (crystallite size about 0.5 μm), a density of 3.0 g/cm^3, a tensile strength of 3.15 GPa, and a Young's modulus of 405 GPa. Ichikawa (2000) reported on a Hi-Nicalon S fiber with stoichiometric SiC composition and very little free carbon. The processing feature in this case was electron beam curing. Because it has a close to stoichiometric composition, the modulus of the fiber is essentially that of SiC. The increased stiffness also comes with a reduction in strain-to-failure.

2.7 Whiskers

Whiskers are monocrystalline, short fibers with extremely high strength. This high strength, approaching the theoretical strength, comes about because of the absence of crystalline imperfections such as dislocations. Being monocrystalline, there are no grain boundaries either. Typically, whiskers have a diameter of a few μm and a length of a few mm. Thus, their aspect ratio (length/diameter) can vary between 50 and 10,000. Whiskers, however, do not have uniform dimensions or properties. This is perhaps their greatest disadvantage, i.e., the variability in properties is extremely large. Handling and alignment of whiskers in a matrix to produce a composite are other problems.

Whiskers are normally fabricated by vapor phase growth. Early in the 1970s, a new process was developed, starting from rice hulls to produce SiC particles and whiskers (Milewski et al. 1974; Lee and Cutler 1975). The SiC particles produced by this process are very fine in size. Rice hulls are a waste by-product of rice milling. For each 100 kg of rice milled, about 20 kg of rice hull is produced. Rice hulls contain cellulose, silica, and other organic and inorganic materials. Silica from soil is dissolved and transported in the plant as monosilicic acid. This is deposited in the cellulosic structure by liquid evaporation. It turns out that most of silica ends up in hull. It is the intimate mixture of silica within the cellulose that gives the near ideal amounts of silica and carbon for silica carbide production. Raw rice hulls are heated in the absence of oxygen at about 700 °C to drive out the volatile compounds. This process is called coking. Coked rice hulls, containing about equal amounts of SiO_2 and free C, are heated in inert or reducing atmosphere

(flowing N_2 or NH_3 gas) at a temperature between 1,500 and 1,600 °C for about 1 h to form silicon carbide per the following reaction:

$$3C + SiO_2 \rightarrow SiC + 2CO$$

When the above reaction is over, the residue is heated to 800 °C to remove any free C. Generally, both particles and whiskers are produced together with some excess free carbon. A wet process is used to separate the particles and the whiskers. Typically, the average aspect ratio of the as-produced whiskers is ~75.

The vapor–liquid–solid (VLS) process of growing whiskers has been known for some time (Lindemanis 1983; Milewski et al. 1985; Petrovic et al. 1985). The acronym VLS represents *vapor* feed gases, *liquid* catalyst, and *solid* crystalline whiskers. The catalyst forms a liquid solution interface with the growing crystalline phase while elements are fed from the vapor phase through the liquid–vapor interface. Whisker growth takes place by precipitation from the supersaturated liquid at the solid–liquid interface. The catalyst must take in solution the atomic species of the whisker to be grown. For SiC whiskers, transition metals and iron alloys meet this requirement. Silicon and carbon are supplied in the form of SiO and CH_4 gases, respectively. The SiO gas is obtained by carbothermal reduction of SiO_2. Generally a range of whisker morphologies is obtained. The tensile strength values have been reported in range of 1.7–23.7 GPa (Milewski et al. 1985; Petrovic et al. 1985). Whisker lengths were about 10 mm and the equivalent circular diameter averaged 5.9 μm. Their average tensile strength and modulus were 8.4 and 581 GPa, respectively. It should be pointed out that the VLS process is extremely slow.

2.8 Particles

2.8.1 Particulate Silicon Carbide

Silicon carbide in particulate form has been available for a long time. It is quite cheap and commonly used for abrasive, refractory, and chemical purposes. Particulate SiC is processed by reacting silica in the form of sand and carbon in the form of coke at 2,400 °C in an electric furnace. The SiC produced in the form of large granules is subsequently comminuted to the desired size. Two types of SiC particulate reinforcement are shown in Fig. 2.13, with angular and rounded morphology, respectively.

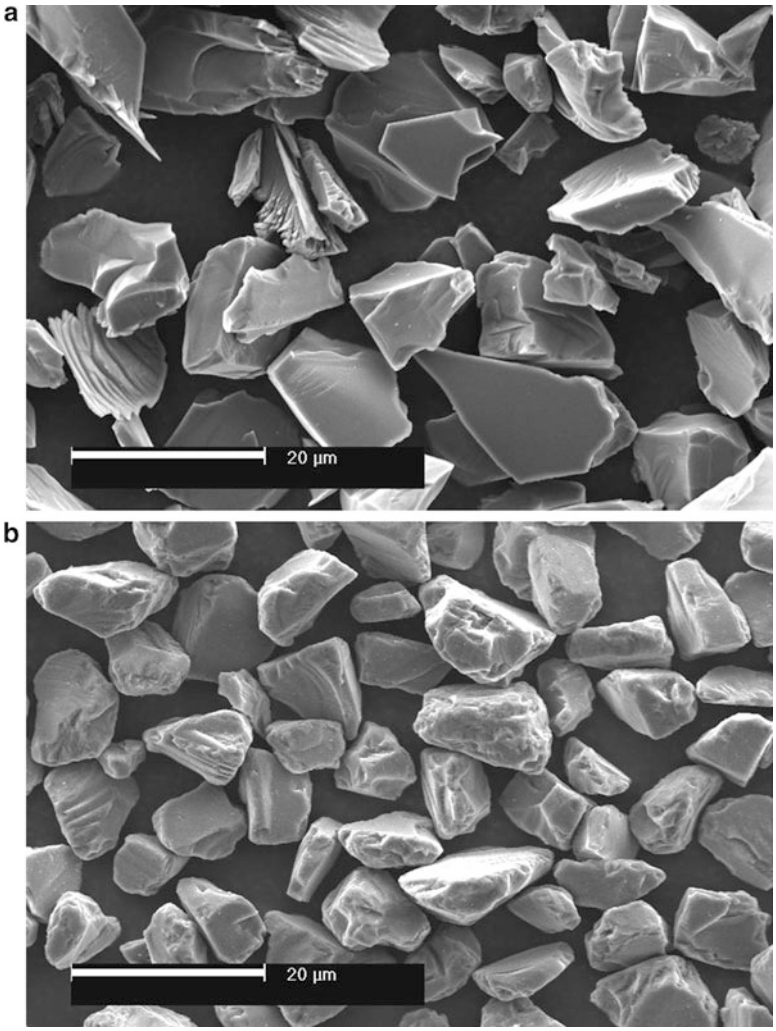

Fig. 2.13 SEM micrograph of SiC particulate reinforcement: (**a**) angular morphology and (**b**) rounded morphology (Courtesy of A. Drake and S.M.K. Emanuelsen, Saint-Gobain)

2.8.2 Particulate Tungsten Carbide

Tungsten carbide is obtained by the carburization of tungsten metal, which is obtained by hydrogen reduction of tungsten oxide. In principle, tungsten carbide can be obtained directly from ore or oxide, but gaseous carburization is usually preferred. Carbon black is added to control particle size and size distribution. A mixture of tungsten powder and carbon black in the correct particle size and distribution is subjected to ball milling or attrition milling. The goal of the

carburization process is to produce stoichiometric tungsten carbide with a small excess of free carbon to prevent the formation of the eta-phase. Carburization is performed in the presence of hydrogen at temperatures between 1,400 and 2,650 °C. The hydrogen reacts with the carbon black to form gaseous hydrocarbons, which then react to form tungsten carbide:

$$W + CH_4 \rightarrow WC + 2H_2$$

After carburization, particles are normally subjected to milling for deagglomeration. Typical particle sizes range from 0.5 to 30 μm.

2.9 Comparison of Fibers

Two most important characteristics of any reinforcement material are its strength and Young's modulus. All these high-performance reinforcements (fibers, whiskers, or particles) have very low-density values. Also, one should note that, irrespective of whether the reinforcements are in compound or elemental form, they are mostly covalently bonded which is the strongest type of bond. Generally, such light, strong, and stiff materials are very desirable in most applications, but particularly so in aerospace field, land transportation, energy-related industry, housing and civil construction, etc. Fiber flexibility is associated with the Young's modulus and the diameter (see Sect. 2.1). In the general area of high-modulus fibers, the diameter becomes the dominant parameter controlling the flexibility. For a given modulus, E, the smaller the diameter, the more flexible the fiber. Fiber flexibility is a very desirable characteristic if one wants to bend, wind, and weave a fiber in order to make a complex-shaped final product.

Some of these fibers have quite anisotropic characteristics. The strength, modulus, and thermal characteristics can vary with the direction, especially along the fiber axis and transverse to it. In particular, the thermal expansion coefficient of carbon is quite different in the radial and longitudinal directions. This would also be true of any single crystal, non-cubic, fiber or whisker, e.g., alumina single crystal fiber which has a hexagonal structure. In this respect, polycrystalline fibers such as SiC and Al_2O_3 are reasonably isotropic. Another important characteristic of these high-performance fibers is their rather low values of strain-to-fracture, generally $<$2–3 %.

2.10 Statistical Analysis of Fiber Strength

Fracture of brittle materials, in general, involves statistical considerations. Most reinforcements used in metal matrix composites are ceramic fibers. Such fibers fail in a brittle manner. Ceramic materials, fibrous or otherwise, will have randomly

distributed defects on their surfaces or in the interior. The presence of these defects results in rather large scatter in the experimentally determined strength values of ceramic materials. Ceramic fibers, in particular, exhibit a broad distribution of tensile strength, due to the distribution of processing-induced flaws, such as micropores or notches. The large surface-to-volume ratio of fibrous materials makes them particularly susceptible to surface flaws.

We can regard a fiber of a given length to be made up of a series of chain links. When such a fiber is loaded, the link or the segment containing the longest defect will fail first and cause the fiber to fracture. The longer the fiber, the higher the probability of a link having a critical flaw size required for failure. In other words, one would expect that the mean strength of a short fiber length to be greater than the mean strength of a long fiber length. The fiber failure occurs when the weakest link fails. This is called the weakest-link assumption. It turns out that such a "weak-chain" material is well described by a statistical distribution known as the Weibull distribution, named after the person who first proposed it (Weibull 1951). The basic assumption is that a fiber has a distribution of flaws (on the surface and/or in the interior). The Weibull distribution assumes that all segments or chain links have the same type of flaw but of different lengths, such a "weak-link" distribution. The Weibull distribution is a parametric distribution, i.e., it is an empirical distribution and does not concern itself with the origin of the defects.

According to the Weibull distribution, the *survival probability* $P(\sigma)$ is given by

$$P(\sigma) = \exp\left[-\left(\frac{\sigma_o}{\sigma}\right)^m\right]$$

where σ is the applied stress and σ_o and m are constants. As m increases, the distribution becomes less broad. In general, brittle materials have a lower Weibull modulus than ductile materials. Taking double logs of both sides, we have

$$\ell n \ \ell n[P(\sigma)] = m \ \ell n\left[-\frac{\sigma_o}{\sigma}\right]$$

The Weibull distribution gives the failure probability, $F(\sigma)$, of a fiber at an applied stress σ by the following expression:

$$F(\sigma) = 1 - \exp\left[-\left(\frac{\sigma_o}{\sigma}\right)^m\right]$$

where σ_o and m are statistical parameters. $F(\sigma)$ is called the cumulative frequency distribution function. The parameter m, referred to as the Weibull modulus, is a measure of the variability in the strength of the fiber. The higher the value of Weibull modulus, the higher the uniformity of strength values. The smaller the value of m, the greater the *variability* in strength. The Weibull modulus can be obtained graphically by using a double log plot of such an equation that will give a straight line of slope, m. Table 2.7 shows typical Weibull modulus for several fibers.

Table 2.7 Typical Weibull modulus (m) values for materials in fibrous form

Fiber material	Weibull modulus (m[a])
Glass	<5
SiC, Al_2O_3, C, B	5–10
Steel	>100

[a]Indicative values only

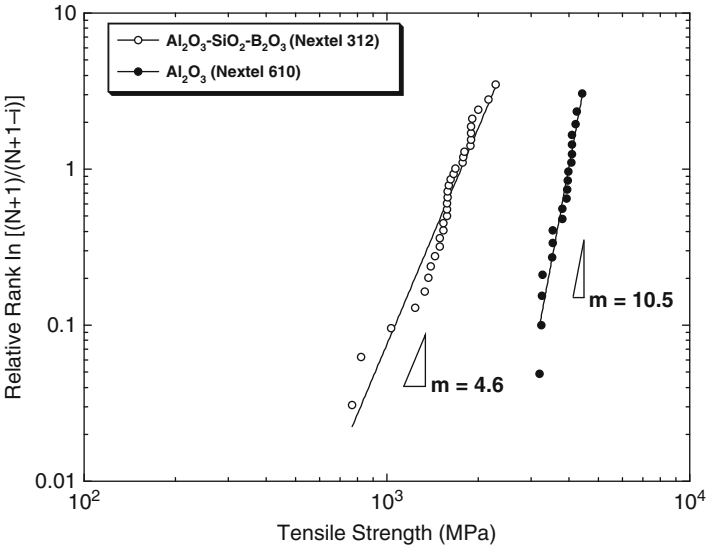

Fig. 2.14 Weibull distribution of some Nextel fibers (Chawla et al. 2005)

Experimentally, to obtain the Weibull parameters, one tests a series of identical samples (each of same volume or, in the case of fiber of constant diameter, each of a constant length) to failure. From such tests, we can obtain the fraction of samples that survives, P(σ), when loaded to a given stress, σ. We arrange the tensile strength values of the single filaments in an ascending order and assign a probability of failure using an estimator given by

$$F(\sigma_i) = \frac{i}{1+N}$$

where $F(\sigma_i)$ is the probability of failure corresponding to the *i*th strength value and N is the total number of fibers tested. Substituting this in the double log expression

$$\ell n\, \ell n \left[\frac{N+1}{N+1-i}\right] = m\ell n\sigma_i + \ell n\sigma$$

A plot of $\ell n\ [(N + 1)/(N + 1 - i)]$ versus σ_i on a log–log graph would give a straight line if the tensile strength data followed a Weibull distribution. The intercept on the y-axis will then be σ_o and the slope will be m. Figure 2.14 shows

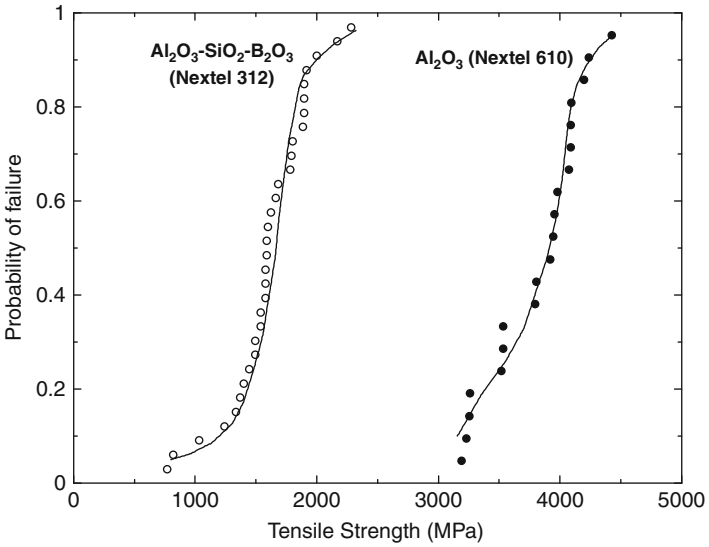

Fig. 2.15 Cumulative probability of failure of Nextel 312 fiber (Chawla et al. 2005)

such a double log plot for some Nextel fibers of (gage length = 25 mm) (Chawla et al. 2005; Kerr et al. 2005). An example of cumulative probability of failure of Nextel 312 and 610 fibers as function of fiber strength is shown in Fig. 2.15 (Chawla et al. 2005).

References

Birchall JD, Bradbury JAA, Dinwoodie J (1985) in *Strong Fibres, Handbook of Composites*, vol. 1. North Holland, Amsterdam, p. 115.
Chawla, K.K. (1998) *Fibrous Materials*, Cambridge University Press, Cambridge.
Chawla, K.K. (2012) *Composite Materials*, 3rd ed., Springer, New York.
Chawla, N., M. Kerr, and K.K. Chawla (2005) *J. Am. Ceram. Soc.*, **88**, 101.
DeBolt, H.E., V.J. Krukonis, and F.E. Wawner (1974) in *Silicon Carbide 1973*, University of South Carolina Press, Columbia, SC, p. 168.
Deurbergue, A., and A. Oberlin (1991) *Carbon*, **29**, 691.
DiCarlo, J.A. (June 1985) *J. of Metals*, **37**, 44.
Diefendorf, R.J., and E. Tokarsky (1975) *Polymer Eng. Sci.*, **15**, 150.
Dresher, W.H. (April 1969) *J. of Metals*, **21**, 17.
Ezekiel, H.N., and R. G. Spain (1967) *J. Polymer Sci. C.*, **19**, 271.
Gasson, D.G., and B. Cockayne (1970) *J. Mater. Sci.*, **5**, 100.
Haggerty, J.S. (May 1972) NASA-CR-120948.
Hurley, G.F., and J.T.A. Pollack (1972) *Metall. Trans.*, **7**, 397.
Ichikawa, H. (2000) *Ann. Chim. Sci. Mat.*, 25, 523.
Johnson, D.J., and C.N. Tyson (1969) *Brit. J. App. Phys.*, **2**, 787.
Kerr, M., N. Chawla, and K.K. Chawla (2005) *JOM*, **57**, 67.
Kumagai, M., and G.L. Messing (1985) *J. Am. Ceram. Soc.*, **68**, 500.

Kumar, S., D.P. Anderson, and A.S. Crasto (1993) *J. Mater. Sci.*, **28**, 423.
LaBelle, H.E., and A.I. Mlavsky (1967) *Nature*, **216**, 574.
LaBelle, H.E. (1971) *Mater. Res. Bull.*, **6**, 581.
Laffon, C., A.M. Flank, P. Lagarde (1989) *J. Mater. Sci.*, **24**, 1503.
Lee, J.-G., and I.B. Cutler (1975) *Am. Ceram. Soc. Bull.*, **54**, 195.
Lara-Curzio, E., and S. Sternstein (1993) *Composites Sci. & Tech.*, **46**, 265.
Lindemanis A (1983) in *Emergent Process Methods for High Technology Ceramics*, Plenum Press, New York
Mann, A.B., M. Balooch, J.H. Kinney, and T.P. Weihs (1999) *J. Amer. Ceram. Soc.*, **82**, 111.
Milewski, J.V., F.D. Gac, J.J. Petrovic, and S.R. Skaggs (1985) *J. Mater. Sci.*, **20**, 1160.
Milewski, J.V., J.L. Sandstrom, and W.S. Brown (1974) in *Silicon Carbide-1973*, University of South Carolina Press, Columbia, SC, p. 634.
Peebles, L.H. (1995) *Carbon Fibers*, CRC Press, Boca Raton, FL.
Petrovic, J.J., J.V. Milewski. D.L. Rohr, and F.D. Gac (1985) *J. Mater. Sci.*, **20**, 1167.
Pollack, J.T.A. (1972) *J. Mater. Sci.*, **7**, 787.
Riggs JP (1985) in *Encyclopedia of Polymer Science & Engineering*, 2nd ed., vol. 2. John Wiley & Sons, New York, p. 640.
Sayir, A., and S.C. Farmer (1995) in *Ceramic Matrix Composites*, *MRS proceedings*, Mater. Res. Soc., Pittsburgh, vol. 365, p. 11.
Sayir, A., S.C. Farmer, P.O. Dickerson, and H.M. Yun (1995) in *Ceramic Matrix Composites*, MRS proceedings, Mater. Res. Soc., Pittsburgh, vol. 365, p. 21.
Simon, G., and A. R. Bunsell (1984) *J. Mater. Sci.*, **19**, 3649.
Singer, L. (1979) in *Ultra-High Modulus Polymers*, Applied Sci. Pub., Essex, England, p. 251.
Singer, L. (1981) *Fuel*, **60**, 839-841.
Suwa Y, Roy R, Komarneni S (1985) *J. Am. Ceram. Soc.*, **68**, C-238.
Towata, A., H.J. Hwang, M. Yasuoka, M. Sando, and K. Niihara (2001) *Composites A*, **32A**, 1127.
Watt, W. (1970) *Proc. Roy. Soc.*, **A319**, 5.
Watt W, Johnson W (1969) *App. Polymer Symposium*, **9**, 215.
Wax, S.G. (1985) *Amer. Cer. Soc. Bull.*, **64**, 1096.
Weber, J. K. R., J. J. Felten, B. Cho, and P. C. Nordine (1998) *Nature*, **393**, 769.
Weibull, W. (1951) *J. App. Mech.*, **18**, 293.
Wilson, D.M. (1990) in *Proc. 14th Conf. On Metal Matrix, Carbon, and Ceramic Matrix Composites*, NASA Conference Publication, No. 3097, Part I, pp. 105-117.
Wilson, D.M., and L.R. Visser (2001) *Composites A*, **32A**, 1143.
Yajima, S., K. Okamura, J. Hayashi, and M. Omori (1976) *J. Amer. Ceram. Soc.*, **59**, 324.
Yajima S (1980) *Phil. Trans., R., Soc., London*, **A294**, 419.
Yamamura, T., T. Ishirkawa, M. Shibuya, T. Hiasyuki, and K. Okamura (1988) *J. Mater. Sci.*, **23**, 2589.

Chapter 3
Matrix Materials

A wide range of metals and their alloys may be used as matrix materials to make metal matrix composites (MMCs). In this chapter, we review some of the basic concepts and fundamentals of bonding and structure of common metals. Following this, we provide a summary of the characteristics of some of the most common metals that are used as matrix materials in MMCs.

3.1 Bonding and Crystalline Structure in Metals

Metals are characterized by metallic bonding, i.e., valence electrons are not bound to a particular ion in the solid. A "sea of electrons" surrounds positively charged atomic nuclei. A major result of this electron cloud surrounding the atomic nuclei is that the electronic bonding in metals is nondirectional. This nondirectionality of bonding is important in that it contributes to isotropy in many properties.

When cooled down from their molten state, most metals assume a crystalline structure below their melting point. Some metals and alloys when cooled at very high cooling rates ($>10^6$ K/s) do not undergo crystallization and assume an amorphous structure. The basic difference between a crystalline and noncrystalline structure is the degree of ordering. A fully crystalline state has a high degree of order. Metal ions are quite small (diameter ~0.25 nm), so in a crystalline structure these ions are packed in a very regular and close-packed manner. Because of nondirectional bonding, we can model the arrangement of atoms in the form of hard spheres.

There are two packing arrangements of hard, identical spheres that result in close-packed structures: face centered cubic (FCC) and hexagonal close packed (HCP). There is a third arrangement that is observed in a number of metals, namely, body centered cubic (BCC). The BCC structure is more open than the FCC or HCP structure. Figure 3.1 shows the atomic arrangement in these three cases. Both HCP and FCC structures result in close packed structures, the side of the cube or the side of the hexagon being a. The difference between the two results from the

N. Chawla and K.K. Chawla, *Metal Matrix Composites*,
DOI 10.1007/978-1-4614-9548-2_3, © Springer Science+Business Media New York 2013

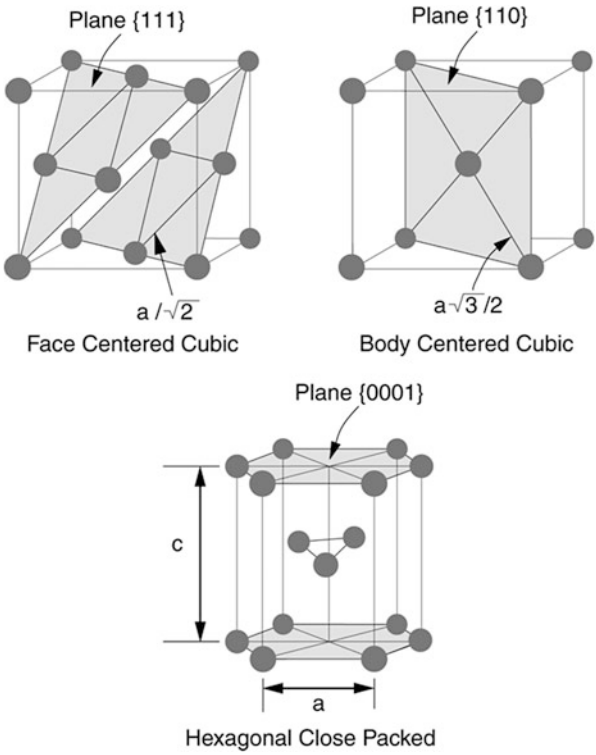

Fig. 3.1 Three common crystal structures in metals, face centered cubic (FCC), body centered cubic (BCC), and hexagonal close packed (HCP)

way the close packed planes are stacked. Figure 3.2a shows the stacking arrangement of the first layer (layer A) in a close packed structure. For the second layer of close packed atoms, one has the choice of putting the atoms at sites B or C, which are equivalent sites. The difference between FCC and HCP structures comes in the placement of the third layer of atoms. Assuming the B configuration for the second layer of atoms, one can have the third layer in A or C configuration. It turns out that the ABABAB . . . (or ACACAC . . .) results in HCP, while the ABCABCABC . . . stacking sequence results in the FCC structure. Stacking faults or planar defects may be formed, where there is an interruption of ABCABCABC stacking (FCC) sequence such that we have an HCP region in an FCC structure.

3.2 Crystalline Defects in Metals

Most metals are crystalline in their solid state. Ideally, a metal crystal has atoms arranged in a very orderly fashion in a three-dimensional lattice. Such perfect crystals are rarely seen in practice. Generally, various kinds of imperfections are present. It turns out that many of the important and interesting properties of crystalline materials are due to the presence of these imperfections or defects in

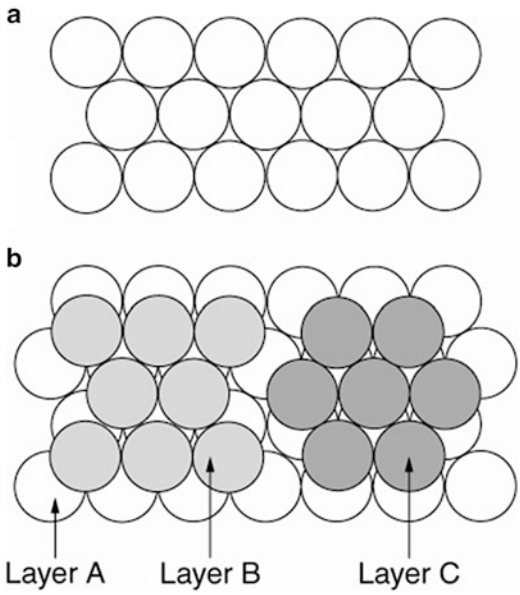

Fig. 3.2 (**a**) A layer of close-packed atoms and (**b**) positions of layers B and C on top of layer A. FCC has ABCABC stacking, while HCP has ABAB . . . stacking sequence

the crystalline lattice. These defects, called lattice defects, can be zero-, uni-, bi-, or tri-dimensional. The zero-dimensional defects are missing atoms or extra atoms at the interstitial sites in all three spatial directions. Common examples are vacancies and interstitial atoms. Unidimensional or lineal imperfections have atomic extensions in one spatial direction only. The most important example of a line defect is a dislocation. Bidimensional defects have atomic extension in two spatial directions, for example, grain boundaries, twin boundaries, and interfaces between phases. Three-dimensional defects extend into three spatial directions, for example, second phase particles and pores. These defects may result under less than ideal processing conditions.

Besides geometric differences, there is a very important physical difference between zero-dimensional defects and other higher-dimensional defects in crystals. Considering the free energy involved, only point defects (i.e., zero-dimensional defects) can be present, at a given temperature, in a state of thermal equilibrium in a crystal, while dislocations, grain boundaries, etc., represent energy much higher than energy represented by thermal fluctuations.

A dislocation can be described in terms of two vectors:

1. Dislocation line vector, **t**, which gives the direction of the dislocation line at any point. The vector **t** is tangent to the dislocation. In the case of a dislocation loop, the vector **t** runs along the loop length and will have opposite sense along the two opposite sides of the loop.
2. Burgers vector, **b**. This indicates the magnitude and direction of the displacement associated with a dislocation. It is also the displacement of the part above the slip plane of a crystal with respect to the part below the slip plane. The Burgers vector

b of a dislocation loop is constant, while the dislocation line vector **t** can change direction continuously. The Burgers vector is always an integral atomic spacing because the lattice must maintain atomic registry through the slipped and unslipped regions.

There are two special types of dislocations:

1. Edge dislocation: The dislocation line vector and the Burgers vector are orthogonal, i.e., at 90°.
2. Screw dislocation: The dislocation line vector and the Burgers vector are parallel.

Dislocations control many important characteristics of materials. In particular, dislocations occupy a position of fundamental importance in the mechanical behavior of crystalline materials. Their presence reduces the force necessary to cause displacement of atoms. In this sense, dislocations act like a lever. They allow a given quantity of work to be done by a small force moving through a large distance rather than a large force moving through a small distance. Thus, plastic flow or plastic deformation in crystalline solids is accomplished by means of movement of dislocations. The plastic strain depends on the displacement associated with each dislocation, i.e., its Burgers vector, the density of *mobile* dislocations, and the average distance moved by a dislocation. When these lineal defects move under the action of a shear stress, they result in slip or glide between crystal planes, which in turn results in permanent (plastic) deformation.

Besides plastic deformation, there are many other physical and chemical properties that are affected by the presence of dislocations. For example, dislocations can serve as easy paths for atomic diffusion (which can affect creep behavior), precipitation reactions, and order processes. They can also be very efficient sites for nucleation of solid-state phase transformations; affect thermal and electrical conductivity, especially at very low temperatures; and affect the current carrying capacity in superconductors.

Planar or two-dimensional defects include external surfaces, grain boundaries, and stacking faults. The surface is treated as a planar imperfection because the surface atoms are not bonded to the maximum number of neighbors. Thus, the surface atoms are in a higher energy state than the atoms in the interior. Small-angle grain boundaries consist of slight orientation mismatch (few degrees). Simple dislocation arrays form such boundaries; a wall of aligned edge dislocations forms a tilt boundary, while screw dislocations form twist boundaries. When the degree of misorientation between grains is too large to be accommodated by dislocations, high-angle grain boundaries are formed. These high-angle grain boundaries have a higher energy than small-angle grain boundaries. A twin boundary is a special type of grain boundary across which there is mirror symmetry of the lattice. Twin boundaries can result from mechanical shear (mechanical twins) or annealing following deformation (annealing twins). Annealing twins are commonly observed in FCC crystals, while mechanical twins are seen in BCC and HCP metals.

3.3 Strengthening Mechanisms in Metals

Metals can be strengthened in a number of ways. We provide a summary of these inasmuch as many of these mechanisms influence the behavior of the metal matrix and thus of the composite. For a more thorough treatment of strengthening mechanisms, the reader is referred to Meyers and Chawla (2009).

3.3.1 Dislocation Strengthening

The presence of dislocations generates internal stress fields. Extra work needs to be done to move a dislocation through such internal stress fields of other dislocations. Various theories have been proposed to explain the strengthening due to increased dislocation density that results, for example, from subjecting a metal to cold working. Although the dislocation structure of a deformed metal, polycrystalline or single crystal, is inhomogeneous, the strengthening due to dislocation density results in the flow stress being proportional to the square root of the dislocation density, ρ

$$\tau = \tau_o + \alpha G b \sqrt{\rho}$$

where τ is the shear flow stress, τ_o is a friction stress, G is the shear modulus, b is the Burgers vector, ρ is the dislocation density, and α is a constant on the order of 0.5. As an example, copper, in an annealed condition, has a dislocation density, $\rho = 10^7\ \text{cm}^{-2}$, while after some cold working, its dislocation density, ρ increases to $10^{12}\ \text{cm}^{-2}$ with concomitant increase in its strength.

Plastic deformation in metals commonly occurs by the movement of dislocations. In HCP metals, plastic deformation can also occur by twinning. The presence of dislocations results in what is called strain hardening or work hardening in metals. Sometimes we also refer to this as dislocation strengthening. Obstacles to dislocation motion (other dislocations, solute atoms, precipitates, grain boundaries, etc.) produce strengthening at room temperature and intermediate temperatures. At high temperatures, thermal energy can help overcome these obstacles (e.g., dislocation climb).

3.3.2 Grain Boundary Strengthening

Grain boundaries can be a very effective source of strengthening at moderate temperatures. Commonly, this is referred to as the Hall–Petch equation and is written as

$$\sigma_y = \sigma_o + \text{k}\text{d}^{-1/2}$$

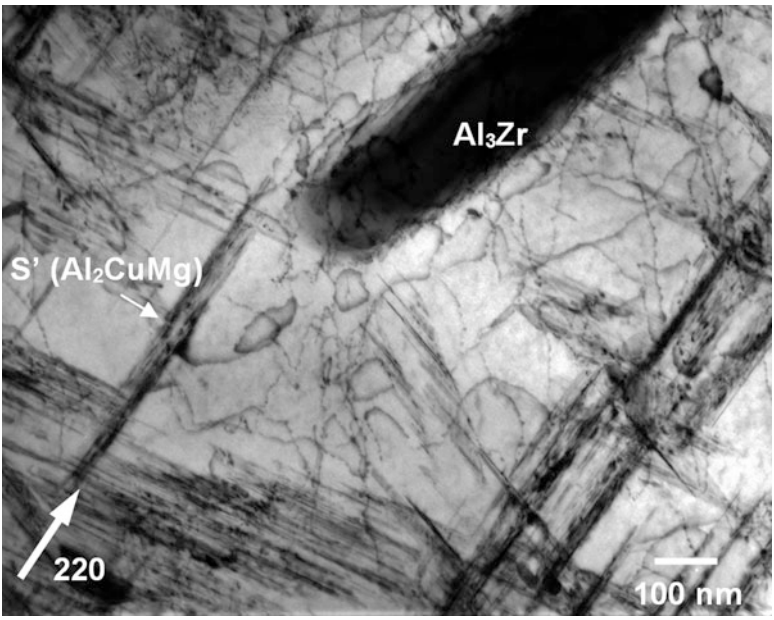

Fig. 3.3 Precipitates (S′) and dispersoids (Al_3Zr) formed in aluminum alloy 2080 (Ganesh and Chawla 2004). The transmission electron micrograph shows the precipitate structure in the matrix of a fatigued 2080/SiC/10_p composite (<220> zone axis). Dislocation motion is constrained by the precipitates and dispersoid particles

where σ_y is the yield strength, σ_o is the friction stress, k is the Hall–Petch coefficient, and d is the average grain size. The dependence of strength on inverse square root of the grain size is strictly true only over a certain range of grain sizes. At very small grain size, especially in the nanometer grain scale, this equation does not hold. The exponent of d may also change with the grain size.

3.3.3 Solute and Precipitation Strengthening

Solute atoms (solid solution strengthening), precipitates (precipitation hardening), and dispersoids (dispersion strengthening) can also impede dislocation motion and strengthen the metal.

Precipitation hardening is a versatile strengthening technique for some metallic alloys, especially aluminum, steels, and nickel-based alloys. Precipitation hardening (also called aging treatment) involves precipitation of, out of a homogeneous supersaturated solid solution, a series of metastable and stable precipitates. Various structures offer different levels of resistance to dislocation motion. An example of precipitates formed in an aluminum alloy, 2080 alloy matrix in a composite after T6 heat treatment, is shown in the transmission electron micrograph in Fig. 3.3.

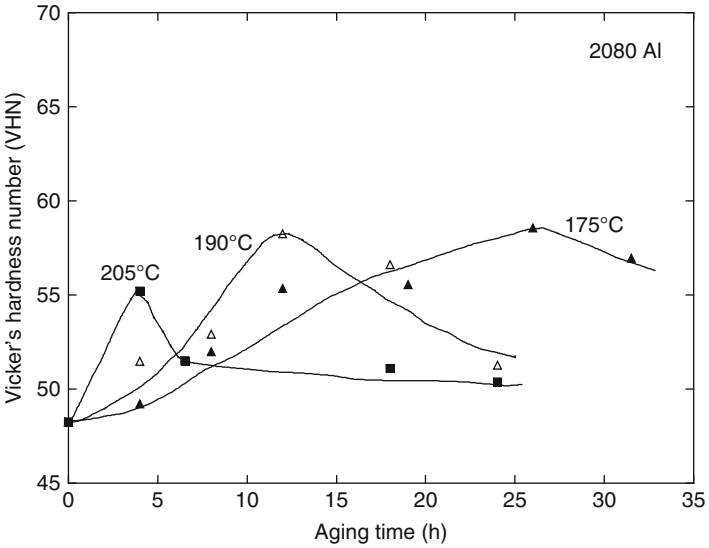

Fig. 3.4 Schematic of the variation of hardness with aging time in a 2080 (Al–Cu–Mg) aluminum alloy. Peak hardness or strength corresponds to a critical dispersion of coherent or semi-coherent precipitates. With increasing temperature, the time to peak aging decreases, because of the acceleration in aging

This material was also subjected to cyclic fatigue, and dislocations, constrained by the particles, are also shown. Figure 3.4 shows, schematically, the variation of hardness with aging time for 2080 aluminum alloy for three different temperatures. Also shown are the different precipitate types that occur during the aging treatment. Peak hardness or strength corresponds to a critical dispersion of semi-coherent precipitates.

The shape of the precipitation hardening or aging curve can be explained as follows. Immediately after quenching, only solid solution hardening is predominant. At the onset of aging, coherent zones appear in the initial stages of aging that are nothing but clusters of solute atoms on certain crystallographic plains of the matrix (e.g., clusters of copper atoms on {100} planes of aluminum). These zones are transition structures and are referred to as Guinier-Preston zones. We call them *zones* rather than precipitates in order to emphasize the fact that zones represent a small cluster of solute atoms which have not yet taken the form of precipitate particles. The very small GP zones are coherent with the matrix, i.e., the lattice planes cross the interface in a continuous manner, and small elastic, coherency strains in the matrix are present. With increasing aging time, these zones grow or thicken by diffusion. As they grow, the misfit strains between the precipitate and matrix increase. Along some planes, coherency is lost, and dislocations form at the

interface to take up the mismatch strain. Thus, the elastic energy associated with coherency strains along specific planes is reduced. The overall strain field around the particle, however, increases because of the newly formed dislocations as well as coherency strains on other planes. This increases the resistance to dislocation motion and increases the strength of the alloy. Further growth of these semi-coherent zones or precipitates results in a complete loss of coherency; an incoherent interface forms between the precipitate and the matrix.

The hardness increases as the GP zone size increases with time, making it more difficult for the dislocations to shear them. With further increase in aging time, equilibrium precipitates with incoherent interface start appearing, and the mechanism of dislocation bowing (called Orowan bowing) around the particles becomes operational. The peak hardness or strength is associated with a critical dispersion of coherent or semi-coherent precipitates. At this point, the contributions from shearing and bypass of precipitates are about equal. Further aging results in an increase of the interparticle distance, and a lower strength results as dislocation bowing becomes easier.

Dislocations move on specific slip planes in a metal under the action of a shear stress. If the slip plane has obstacles penetrating it, e.g., precipitates or dispersoids, a dislocation moving on this slip plane must interact with these obstacles. The dislocation, under the action of an applied shear stress, τ, bows between the obstacles in the slip plane. If we ignore the changes in the orientation of the dislocation because of bowing, the shear stress required to bow the dislocation to a radius r is given by

$$\tau = \frac{Gb}{2r}$$

where G is the shear modulus of the metal and b is its Burgers vector. This mechanism of dislocation bowing around particles is called Orowan bowing.

3.3.4 Fracture in Metals

Generally, metals are quite ductile and fracture by a process known as microvoid coalescence. In this process, also referred to as dimple facture, microvoids nucleate at precipitate particles, inclusions, etc. Under applied stress, these microvoids grow and coalesce leading to final fracture with characteristic dimples on the fracture surface. Figure 3.5a shows schematically the process, while Fig. 3.5b shows an SEM micrograph of an actual fracture surface obtained after tensile testing of an aluminum alloy. Note the presence of precipitates, in the center of dimples, where microvoids nucleated.

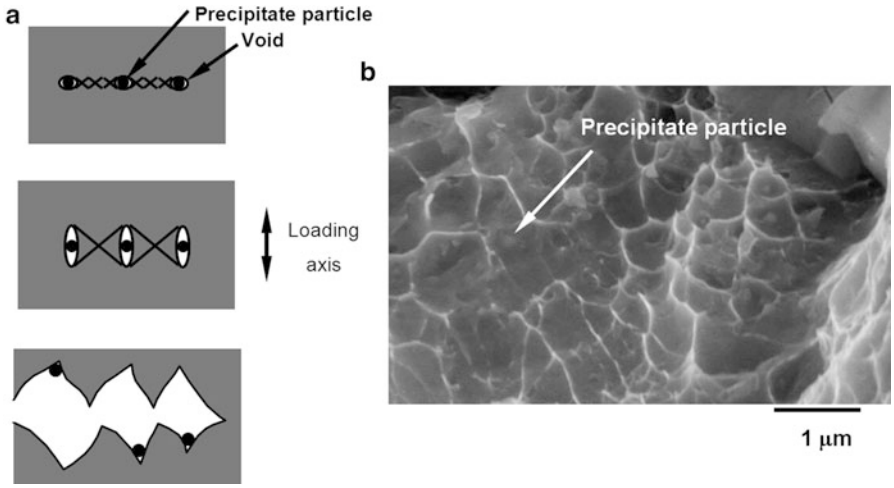

Fig. 3.5 (**a**) Schematic of nucleation, growth, and calescence of microvoids at precipitate particles in a ductile metallic alloy. (**b**) Characteristic dimples on the fracture surface in an aluminum alloy. Note the presence of precipitate particles that served as the nucleating sites for microvoids (Chawla et al. 2002)

3.4 Common Matrix Materials

3.4.1 Aluminum and Aluminum Alloys

Aluminum alloys, because of their low density and excellent strength, toughness, and corrosion resistance, have been used extensively in the automotive and aerospace fields. Of special mention are Al–Cu–Mg and Al–Zn–Mg–Cu alloys, which are very important precipitation-hardenable alloys.

Aluminum alloys can be classified as cast, wrought, or age-hardenable alloys. Some of the common age-hardening or precipitation-hardenable treatments for Al alloys are the following:

1. T4: Solutionizing and quenching, followed by aging at room temperature or "natural aging."
2. T6: Solutionizing and quenching, followed by aging at a temperature above room temperature (120–190 °C) or "peak aging."
3. T7x: Solutionizing, quenching, and overaging.
4. T8xx: Solutionizing, quenching, cold working, and peak aging.

The solutionizing temperature is typically between 440 and 540 °C, while the quenching medium can be water or a synthetic quenchant.

Liquid aluminum, like most metals, has a very low viscosity, which makes for easy casting practice. The temperature dependence of viscosity of liquid aluminum is given by (Smithells 1976)

$$\eta = 0.1492 \ \exp(1984.5/T)$$

where η is the viscosity in mPa.s, R is the gas constant (=8.3144 J/K mol), and T is the temperature in kelvin. At its melting point, pure aluminum has a viscosity of ~η = 12 mPa.s. The addition of ceramic particles or inclusions raises the viscosity very quickly. This has important implications in the processing of particle-reinforced MMCs (see Chap. 4).

3.4.2 Titanium Alloys

Titanium is one of the most important aerospace materials. Pure titanium has a density of 4.5 g/cm^3 and a Young's modulus of 115 GPa. For titanium alloys, the density can vary between 4.3 and 5.1 g/cm^3 while the Young's modulus can range between 80 and 130 GPa. Thus, titanium and its alloys have relatively high specific properties, i.e., strength/weight and modulus/weight ratios. Titanium has a relatively high melting point (1,672 °C) and retains strength to high temperatures with good oxidation and corrosion resistance. All these factors make it an ideal material for aerospace applications. Titanium alloys are used in jet engine (turbine and compressor blades), fuselage parts, etc. It is, however, an expensive material.

At extremely high speeds, such as in a supersonic military aircraft, the skin of an airplane heats up so much that aluminum alloys are no longer an option. Titanium alloys must be used at such high temperatures. In a supersonic plane, flying at speeds over Mach 2, the temperatures will be even higher than what titanium alloys can withstand. Titanium aluminides are one of the candidate materials in this case.

Titanium has two polymorphs: alpha (α) titanium has an HCP structure and is stable below 885 °C and beta (β) titanium which has a BCC structure and is stable above 885 °C. Aluminum raises the α → β transformation temperature, i.e., aluminum is an alpha stabilizer. Most other alloying elements (Fe, Mn, Cr, Mo, V, No, Ta) lower the α → β transformation temperature, i.e., they stabilize the β phase. Thus, three general alloy types can be produced, viz., α, α + β, and β titanium alloys. The Ti-6%Al-4 % V, called the *work horse* Ti alloy of the aerospace industry, belongs to the (α + β) group. Most titanium alloys are used after hot working in the (α + β) region, which breaks the structure and distributes the β phase in an extremely fine form.

Titanium has a great affinity for oxygen, nitrogen, and hydrogen. Parts per million of such interstitials in titanium can change mechanical properties drastically. In particular, microstructural changes may result in severe embrittlement. This is why welding of titanium by any technique requires protection from the atmosphere. Electron beam techniques, in vacuum, are also frequently used.

3.4.3 Magnesium and Its Alloys

Magnesium and its alloys form another group of light metals. Magnesium is one of the lightest metals, its density being 1.74 g/cm^3. Magnesium alloys, especially castings, are used in automotive and aircraft gearbox housings, chain saw housing, laptop casings, electronic equipment, etc. Magnesium has a hexagonal close-packed structure, which gives it limited ability to deform plastically by slip at room temperature.

3.4.4 Cobalt

Cobalt is a very common metal matrix that is used in WC/Co composites, also known as cemented carbides, which are used as inserts for cutting tools and in oil drilling. During processing of cemented carbides, cobalt is used in a powder form. Cobalt powder can be produced chemically by hydrogen reduction or atomization of cobalt liquid. The chemistry and crystal structure of Co powder are different from that of Co matrix in a WC/Co composite. Milling and processing by liquid-phase sintering or high-temperature, high-pressure compaction can affect the chemistry of the finished Co matrix.

Pure Co is stable below 417 °C in the HCP crystal structure. Above this temperature, the high-temperature FCC structure is stable. It turns out that the FCC cobalt becomes stable at room temperature because of dissolution of carbon from WC during processing of WC/Co composites. The FCC structure has more slip systems available, which results in higher ductility. In WC/Co composites, the small amount of Co matrix holds the WC particles in place and provides toughness, which stems from its ability to deform plastically.

3.4.5 Copper

Copper has FCC structure. Because of its high electrical conductivity (only silver and gold are better), it is used extensively as an electrical conductor. It also has good thermal conductivity, which makes it suitable for thermal management applications. It can be cast and worked easily, because it is quite ductile. One of the major applications of copper in a composite is as a matrix material in niobium-based superconductors. Copper–zinc alloys (brass) and copper–tin alloys (bronze) are solid solution strengthened and among the earliest alloy metals used.

3.4.6 Silver

Silver is another FCC metal. It is a very good electrical and thermal conductor, highly ductile, and has good corrosion resistance. It has found a new use as a matrix material in some high-temperature oxide superconductors.

3.4.7 Nickel

Nickel is also an FCC metal, which gives it good ductility. More importantly, nickel-based alloys show an excellent combination of properties. Nickel-based superalloys, primarily nickel–iron–cobalt alloys, have superior high-temperature creep resistance, making them suitable for turbine blades.

3.4.8 Niobium

Although niobium alloys are not commonly used as a matrix material in MMCs, they are used as filaments in superconducting composites. We give a brief description of these alloys in Sect. 3.5 below.

3.4.9 Intermetallics

Intermetallics (sometimes referred to as intermetallic compounds) are formed when two dissimilar metals are combined following rules of chemical valence. Generally, the bonding in intermetallics is not metallic, but ionic and covalent in nature. Such an alloy is called an intermetallic compound (Villers and Calvert 1985; Sauthoff 1995).

Intermetallics generally have a stoichiometric composition and appear as a line compound in the phase diagram. Some intermetallics have a range of composition. In general, intermetallics have a complex crystal structure and are brittle due to their ionic and covalent bonding. Some intermetallics have been identified to have rather unique attributes of high-temperature strength and stiffness, low density, and excellent oxidation resistance. Used as a matrix material for making composites, they have the potential to increase the operating temperatures over conventional materials.

Intermetallics can have a disordered or ordered structure. Ordered intermetallic alloys possess structures characterized by long-range ordering, i.e., different atoms occupy specific positions in the lattice. Because of their ordered structure, motion of dislocations in intermetallics is much more restricted than in disordered alloys.

This results in retention (and, in some cases, even an increase) in strength at elevated temperatures, a very desirable feature. For example, nickel aluminide shows a marked increase in strength up to 800 °C. An undesirable feature of intermetallics is their extremely low ambient temperature ductility.

An important disordered intermetallics is molybdenum disilicide ($MoSi_2$). It has a high melting point and shows good stability at temperatures greater than 1,200 °C, in an oxidizing atmosphere. It is commonly used as a heating element in furnaces. The high oxidation resistance comes from a protective SiO_2 film that is formed at high temperatures.

3.5 Superconductivity

Since one of the major applications of MMCs is as filamentary superconducting composites, we briefly describe the materials related aspects of the phenomenon of superconductivity.

Certain metals and alloys lose all resistance to flow of electricity when cooled to within a few degrees of absolute zero. This phenomenon is called superconductivity, and the materials exhibiting this phenomenon are called superconductors. Unlike normal metals, these superconductors can carry a high current density without any electrical resistance. Superconductors can potentially carry as much as 100 times the amount of electricity of ordinary copper or aluminum wires of the same size. This, in turn, can be exploited in devices such as motors and generators and to transmit electricity in power lines. Superconductors can generate very high magnetic fields that are common in high-energy physics and fusion energy programs. Other fields of application include magnetic resonance imaging (MRI), magneto hydrodynamic generators, rotating machines, magnetic levitation vehicles, and magnets in general.

Conventional superconductors require cooling in liquid helium (4.2 K), a very costly proposition. In 1986, however, a new class of ceramic superconductors was discovered which exhibited a critical temperature above that of liquid nitrogen (77 K). These are called the high-temperature superconductors, and the phenomenon is referred to as high-temperature superconductivity (HTS). Unlike the low-temperature superconductors, which are metallic or semimetallic, these new compounds are ceramics. The first HTS discovered had a critical temperature of 35 K (−238 °C). Then in 1987, a compound that became superconducting at 94 K (−179 °C) was discovered. This discovery was particularly significant because this compound could be cooled with cheap and readily available liquid nitrogen. This was followed by the discovery of bismuth-based compounds; thallium- and yttrium-based compounds with even higher critical temperature were discovered. The high-temperature superconductors (HTS) can function at temperatures as high as 140 K (−133 °C). This allows cooling to be done more economically and efficiently by liquid nitrogen, compared with conventional or low-temperature superconductors which need liquid helium as a cooling medium. In 2001, another

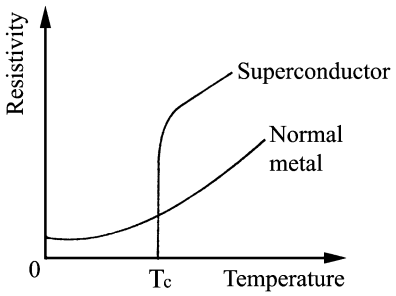

Fig. 3.6 Variation of electrical resistivity with temperature for a normal metal and that of a superconducting material

low-temperature superconductor was discovered with composition MgB_2 (Nagamatsu et al. 2001). Its T_c of 39 K is slightly higher than that of Nb-based metallic superconductors.

Niobium–titanium alloys are one of the important low-temperature superconductors. Low-temperature superconductors must be cooled to below 20 K in order to become superconducting. They are widely used in MRI machines, and in the fields of high-energy physics and nuclear fusion. Additional commercial use has been limited largely by the high refrigeration costs associated with liquid helium, which is needed to cool the materials to such low temperatures.

3.5.1 Types of Superconductors

The phenomenon of superconductivity was discovered in mercury by Onnes in 1911. Since then, many elements and hundreds of solid solutions or compounds have been discovered that show this phenomenon of total disappearance of electrical resistance below a critical temperature T_c. Figure 3.6 shows the variation of electrical resistivity with temperature of a normal metal and that of a superconducting material. T_c is the critical temperature, a characteristic constant of each material, above which the material becomes a normal conductor. Kunzler et al. (1961) discovered the high-critical-field capability of Nb_3Sn and thus opened up the field of practical, high-field superconducting magnets. Superconductors came into the realm of economic viability when techniques were developed to put the superconducting species in the form of ultrathin filaments in a copper matrix.

The technologically most important property of superconductors is their capacity to carry an electric current without normal I^2R (I is the current in amp and R is the resistance in ohm) losses up to a critical current density, J_c. This critical current is a function of the applied field and temperature. The commercially available superconductors in the 1980s could demonstrate critical current densities of $J_c > 10^6$ A/cm^2 at 4.2 K and an applied field of $H = 5$ T. There are three parameters that limit the properties of a superconductor, namely, the critical temperature (T_c), the critical electrical current density (J_c), and the critical magnetic field (H_c);

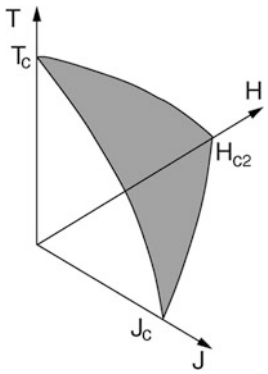

Fig. 3.7 The state of superconductivity is described by three critical parameters: magnetic field (H), temperature (T), and current density (J). As long as the material does not cross into the shaded area, it will behave as a superconductor

see Fig. 3.7. As long as the material does not cross into the shaded area indicated in Fig. 3.7, it will behave as a superconductor.

There are two types of superconductors:

Type I: These are characterized by low-T_c values, and they lose their superconductivity abruptly at H_c.

Type II: These behave as diamagnetic materials up to a field H_{c2}. Above this field, the magnetic field penetrates gradually into the material and concomitantly the superconductivity is gradually lost, until at the critical magnetic field H_{c2} the material reverts to its normal state. All major applications of superconductivity involve the use of type II superconductors.

3.5.2 Flux and Flux Pinning

When magnetic lines of force from a strong magnetic field, called flux lines, try to penetrate the surface of type II superconductor, we get what is called a flux lattice. This periodic lattice, consisting of tubular regions of flux lines, stems from the tiny magnetic moments in each flux line, which repel each other and array themselves in an orderly fashion, usually in the close-packed hexagonal arrangement. Flux pinning is required in superconductors because movement of flux, sometimes called "flux creep," is an energy-dissipative process; that is, heat is produced when flux lines move, no matter what the source. Any disturbance of a superconductor, say, by motion or a change in the applied field, leads to a rearrangement of magnetic flux lines in the superconductor. Flux movement in a superconductor, irrespective of the source of flux movement, results in a temperature increase. This leads to a reduced critical current and more flux movement. The net result is that the superconductor is heated above T_c and reverts to its normal state. A practical solution to this problem is to make the superconductor in the form of ultrathin filaments so that the amount of energy (heat) dissipated by flux motion is too small to cause this runaway

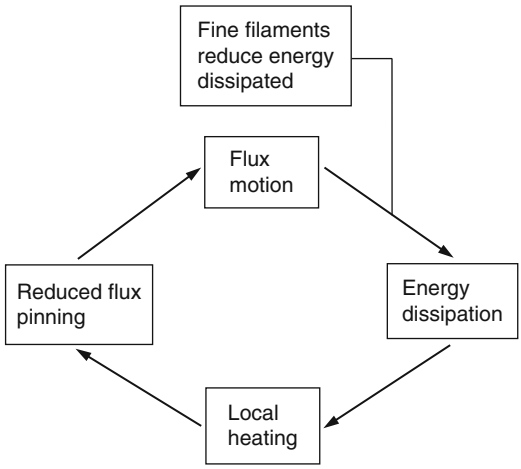

Fig. 3.8 The cryostabilization design concept: fine filaments reduce the energy dissipated due to magnetic flux movement

behavior; see Fig. 3.8. Flux pinning occurs via defects in the crystalline structure of the superconductor such as grain boundaries or impurities. The high-purity copper or silver matrix provides a high-conductivity alternate path for the current. In the case of a quench, that is, superconductor reverting to the normal state, the metal matrix carries the current without getting excessively hot. The superconductor is cooled again below its T_c and carries the electric current again. This is the so-called cryogenic stability or cryostabilization design concept; namely, the superconductor is embedded in a large volume of low-resistivity metal matrix and a coolant is in contact with all windings.

3.5.3 Ductile Alloys: Niobium-Titanium Alloys

Niobium-titanium alloys provide a good combination of superconducting and mechanical properties. A range of compositions is available commercially: Nb-44 % Ti in the UK, Nb-46.5 % Ti in the USA, and Nb–50 % Ti in Germany. Figure 3.9 shows the Nb–Ti phase diagram as well as the critical temperature and upper critical field as a function of alloy composition. Note the range (46–50 wt% Ti) for the superconducting alloys.

In all these alloys, a $J_c > 1{,}000$ A/mm^2 at 4.2 K and an applied field of 7 T can be obtained by a suitable combination of mechanical working and annealing treatments. Strong flux pinning and, therefore, high J_c are obtained in these alloys by means of dislocation cell walls and precipitates. The flux pinning by precipitates becomes important in high-Ti alloys. Extremely fine superconducting filaments embedded in a copper matrix provide flux stability and reduced losses caused by varying magnetic fields becomes important in high-Ti alloys because the Nb-Ti phase diagram indicates precipitation of α-Ti in these alloys.

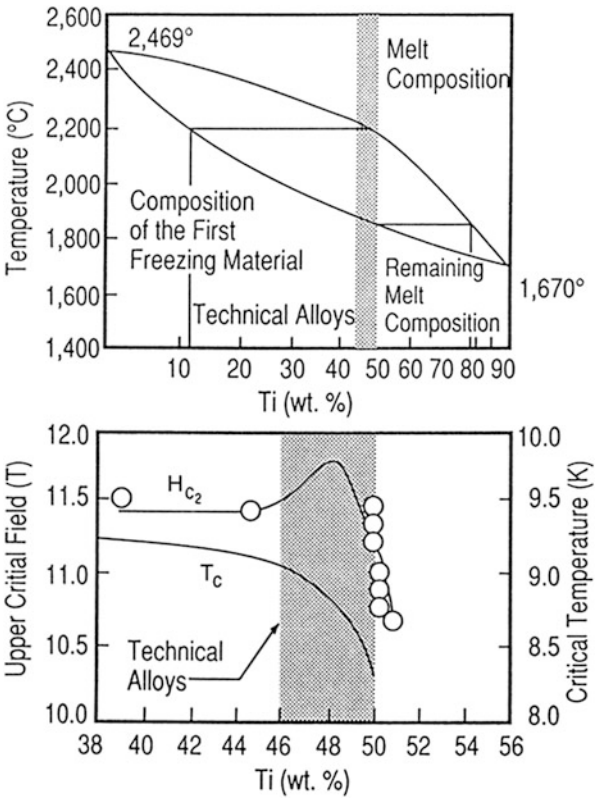

Fig. 3.9 The *top* figure shows the Nb–Ti phase diagram while the *bottom* figure shows the critical temperature and upper critical field as a function of alloy composition. Note the range (46–50 wt% Ti) for the superconducting alloys (After Hillmann 1981)

3.5.4 A-15 Superconductors: Nb_3Sn

For applications involving fields greater than 12 T, the ordered intermetallic compounds having an A-15 crystal structure are better suited than the Nb-Ti type. Nb_3Sn has a T_c of 18 K. It is easy to appreciate that the higher the T_c, the lower the refrigeration costs. Nb_3Sn is the most widely used superconductor for high fields and high temperatures. A characteristic feature of these intermetallic compounds is their extreme brittleness (typically, a strain-to-failure of 0.2 % with very little plasticity). Compare this to Nb-Ti which can be cold worked to a reduction in area over 90 %. Initially, the compound Nb_3Sn was made in the form of wires or ribbons either by diffusion of tin into niobium substrate in the form of a ribbon or by chemical vapor deposition. V_3Ga on a vanadium ribbon was also produced in this manner. The main disadvantages of these ribbon-type superconductors were (a) flux instabilities due to one wide dimension in the ribbon geometry and (b) limited flexibility in the ribbon width direction. Later on, with the realization that flux stability could be obtained by the superconductors in the form of extremely fine filaments, the filamentary composite approach to A-15 superconductor fabrication was adopted. This breakthrough involving the composite route came through early

in the 1970s. Tachikawa (1970) showed that V_3Ga could be produced on vanadium filaments in a Cu-Ga matrix, while Kaufmann and Pickett (1970) demonstrated that Nb_3Sn could be obtained on niobium filaments from a bronze (Cu-Sn) matrix. The processing of some important superconducting composite systems is described in Chap. 4, while their applications are given in Chap. 12.

References

Chawla, N., J.J. Williams, and R. Saha (2002) *Metall. Mater. Trans.*, **33A**, 3861.
Ganesh, V.V., and N. Chawla (2004) *Metall. Mater. Trans.*, **35A**, 53–62.
Hillmann, H. (1981) in *Superconductor Materials Science*, Plenum, New York, p. 275.
Kaufmann, A.R., and J.J. Pickett (1970) *Bull. Am. Phys. Soc.*, **15**, 833 (1970).
Kunzler, J.E., E. Bachler, F.S.L. Hsu, and J.E. Wernick (1961) *Phys. Rev. Lett.*, **6**, 89.
Meyers, M.A., and K.K. Chawla (2009) *Mechanical Behavior of Materials*, 2nd edition, Cambridge University Press, Cambridge.
Nagamatsu, J., N. Nakagawa, T. Muranaka, Y. Zenitani, and J. Akimitsu (2001) *Nature*, **410**, 63.
Sauthoff, G. (1995) *Intermetallics*, VCH Publishers, New York, NY.
Smithells Metals Reference Book (1976) Butterworths, Boston, p. 944.
Tachikawa, K. (1970) in *Proceedings of the 3rd ICEC*, Illife Science and Technology Publishing, Surrey, U.K., 1970.
Villers, P., and L.D. Calvert (eds.) (1985) *Pearson's Handbook of Crystallographic Data for Intermetallic Phases*, **vol. 1,2,3** ASM, Metals Park, OH, 1985.

Chapter 4
Processing

Metal matrix composites can be made by processes involving liquid, solid, or gaseous state. We describe some of the important processing techniques below.

4.1 Liquid-State Processing

Liquid-state processing of metal matrix composites involves incorporating or combining a liquid metal matrix with the reinforcement. There are several advantages to using a liquid-phase route in processing. These include near net shape (when compared to solid-state processes like extrusion or diffusion bonding), faster rate of processing, and the relatively low temperatures associated with melting most light metals, such as Al and Mg. The most common liquid-phase processing techniques can be subdivided into four major categories:

- *Casting or liquid infiltration*: This involves infiltration of a fiber or particulate preform by a liquid metal. In the case of direct introduction of short fibers or particles, the molten mixture, consisting of liquid metal and ceramic particles or short fibers, is often stirred to obtain a homogeneous distribution of particles. In centrifugal casting, a gradient in reinforcement particle loading is obtained. This can be quite advantageous in applications where the reinforcement needs to be tailored from a machining or performance perspective.
- *Squeeze casting or pressure infiltration*: This method encompasses pressure-assisted liquid infiltration of a fibrous or particulate preform. This process is particularly suited for complex shape components, selective or localized reinforcement, and where production speed is critical.
- *Spray co-deposition*: In this process the liquid metal is atomized or sprayed, while a particle injector introduces ceramic particles in the spray stream to produce a granulated mixture of composite particles.

N. Chawla and K.K. Chawla, *Metal Matrix Composites*,
DOI 10.1007/978-1-4614-9548-2_4, © Springer Science+Business Media New York 2013

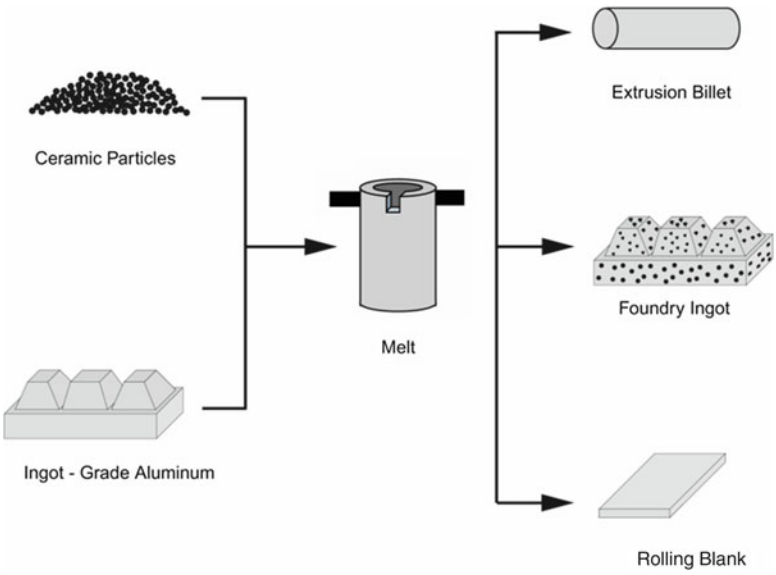

Fig. 4.1 Conventional casting route for processing particle reinforced MMCs

- *In situ processes*: In this case, the reinforcement phase is formed in situ either by reaction during synthesis or by controlled solidification of a eutectic alloy.

  We now discuss each of these processing classes in detail.

4.1.1 Casting or Liquid Infiltration

Conventional Casting

Casting of MMCs can typically be accomplished with conventional equipment used to cast aluminum alloys. It is typically used with particulate reinforcement because of the difficulty in infiltrating fibrous performs without pressure. The particles and matrix mixture are cast into ingots and secondary mechanical processing, such as extrusion or rolling, is applied to the composite (see Fig. 4.1).

Casting of MMCs requires some modifications to existing conventional casting processes, which are summarized as follows:

- Alloys that minimize reactivity with the reinforcement must be used. Al–Si alloys (with Si levels of up to 9 %) are typically used with SiC reinforcement. Figure 4.2 shows that with increasing temperature, an increase in the amount of silicon is required to prevent the formation of the undesirable compound Al_4C_3 (see Chap. 5).

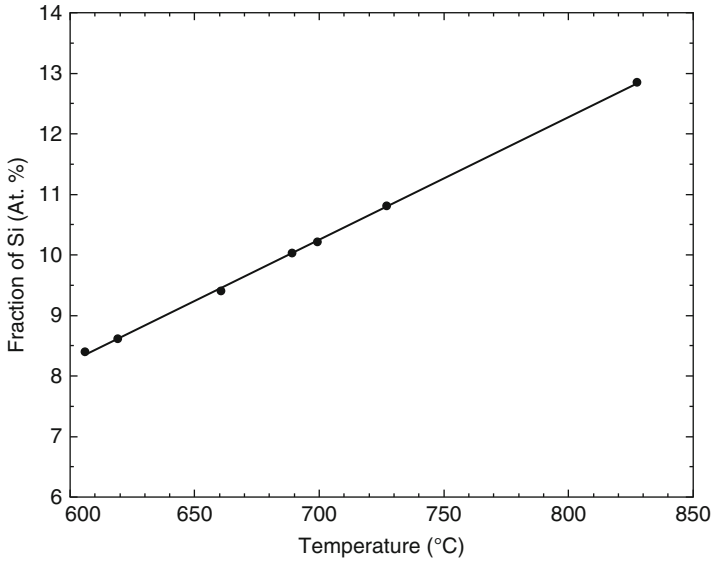

Fig. 4.2 Fraction of Si, at a given temperature, required to prevent formation of Al_4C_3 in an Al–Si–SiC composite (after Lloyd 1997)

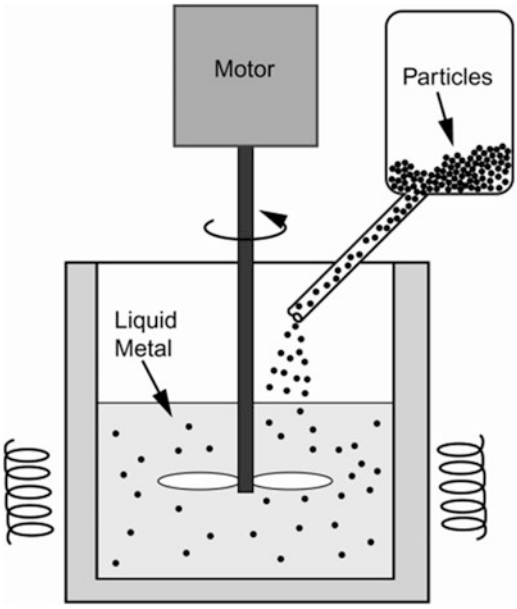

Fig. 4.3 Stirring of composite melt with ceramic particles to minimize settling of the particles during processing

- Stirring of the composite melt is often required, Fig. 4.3 (Mehrabian et al. 1974). The density of SiC (3.2 g/cm^3) is higher than that of Al (2.5 g/cm^3), so the particles will sink unless the melt is agitated. Alternating currents in a magnetic field (Katsura 1982) and mechanical vibration (Pennander and Anderson 1991)

have also been used to improve wetting and permeability of the reinforcement in the liquid matrix.

Depending on the size and concentration of the solid particles in the liquid, several models are available that describe the viscosity of the liquid as a function of volume fraction, V_p of solid particles. In the case of extremely low concentrations of fine particles, an equation due to Einstein (1906) may be used:

$$\eta_c = \eta_m \left(1 + 2.5\, V_p\right)$$

where η_c is the viscosity of the suspension, η_m is the viscosity of the liquid (i.e., the unreinforced metal), and V_p is the volume fraction of the particles. In the case of higher concentrations of particles, Guth and Simha (1936) proposed a modified equation which takes into account interaction between the solid particles:

$$\eta_c = \eta_m \left(1 + 2.5\, V_p + 14.1\, {V_p}^2\right)$$

Thomas (1965) proposed the following modification of this equation from the fitting of empirical data:

$$\eta_c = \eta_m \left(1 + 2.5\, V_p + 10.05\, {V_p}^2\right)$$

In the case of very high concentrations of smooth spherical particles, Kitano et al. (1981) give the following empirical equation:

$$\eta_c = \eta_m \left(1 - V_p/A\right)^{-2}$$

where $A = 0.68$. In view of the fact that viscosity of the liquid metal containing ceramic particles will certainly increase with the particle addition, the temperature of the composite melt should be kept above a certain limit (~745 °C for Al–Si/SiC) in order to keep the melt from becoming highly viscous. Covering the melt with an inert gas atmosphere will reduce oxidation of the melt.

Centrifugal Casting

In centrifugal casting, optimal placement of the reinforcement can be achieved by inducing a centrifugal force during casting, Fig. 4.4, to intentionally obtain a gradient in reinforcement volume fraction (Divecha et al. 1981). In brake rotors, for example, wear resistance is needed on the rotor face, but not in the hub area. Thus, in areas where reinforcement is not as crucial, such as in the hub area, easier machining may be obtained.

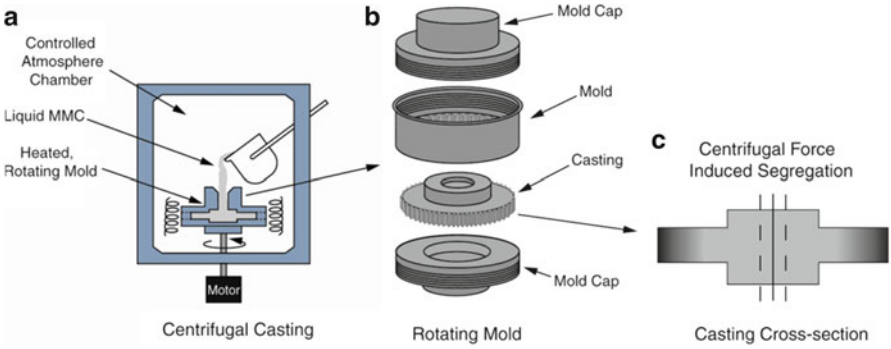

Fig. 4.4 (**a**) Schematic of centrifugal casting process, (**b**) rotating mold, and (**c**) cross section of finished casting with intentionally segregated reinforcement

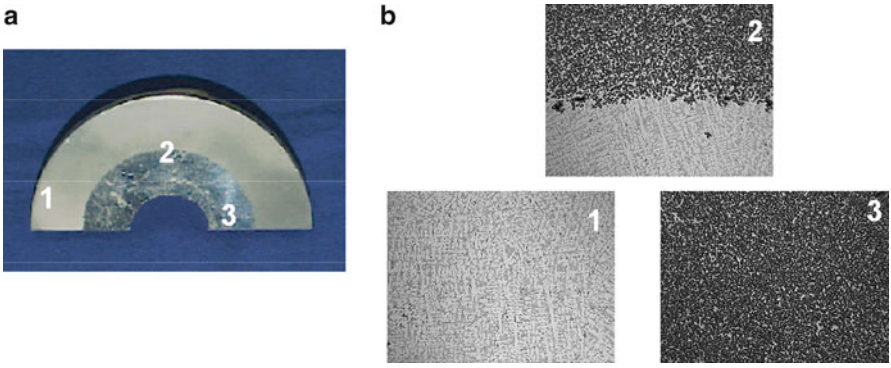

Fig. 4.5 (**a**) Centrifugally cast brake rotor with selective placement of reinforcement and (**b**) regions of the microstructure in the rotor: (1) matrix rich, (2) interface, (3) reinforcement rich (courtesy of D. Herling)

Figure 4.5 shows the microstructure at different points in a centrifugally cast brake rotor, showing the pure aluminum alloy matrix region, interface region, and reinforced region. It is reported that centrifugal casting is a relatively inexpensive process, with a potential for composite materials at as low as $2/kg.

Pressureless Liquid Infiltration (Lanxide™ Process)

Another pressureless infiltration process consists of reactive or nonreactive infiltration of a reinforcement preform. In this process a particulate filler is infiltrated with pure Al or Al–Mg alloy as shown in Fig. 4.6. When pure Al is used, Mg particles may also be intermingled with the reinforcement particles to form an Al–Mg alloy matrix. The process is conducted in N_2 atmosphere to minimize interfacial reactions, particularly since the pressureless process involves long

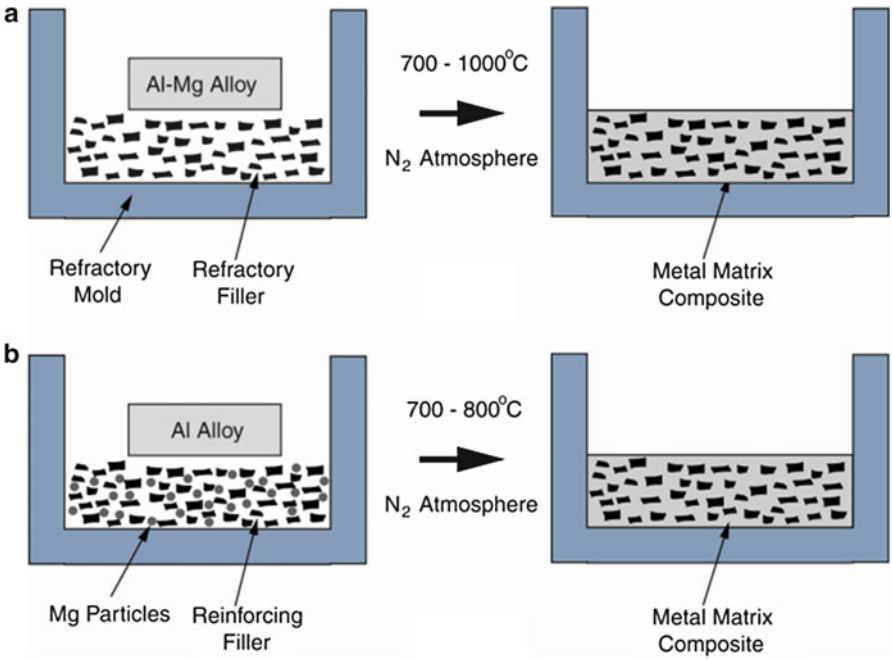

Fig. 4.6 Pressureless infiltration of MMCs: (**a**) alloy matrix infiltration of particulate preform and (**b**) pure matrix infiltration of metallic alloy particle and ceramic particulate preform

infiltration times at high temperatures (Aghajanian et al. 1989). When pure Al is infiltrated, the infiltration temperatures are between 700 and 800 °C, while infiltration of Al–Mg alloys is conducted between 700 and 1,000 °C (Lloyd 1997). Typical infiltration rates are less than 25 cm/h.

Squeeze Casting or Pressure Infiltration

Squeeze casting or pressure infiltration involves forcing the liquid metal matrix into a short fiber or particulate preform. The main advantages of this method over conventional casting are the shorter processing times (which is of particular interest for production of materials at high volumes), ability to fabricate relatively complex shapes, minimal residual porosity or shrinkage cavities due to the applied pressure, and minimization of interfacial reaction products between reinforcement and matrix, once again, due to the shorter processing times. Before infiltration takes place, the reinforcement preform must be prepared. Figure 4.7 shows two processes for making the preform: (a) press forming and (b) suction forming. In the press-forming process, an aqueous slurry of fibers is well agitated and poured into a mold, pressure is applied to squeeze the water, and the preform is dried. In the other

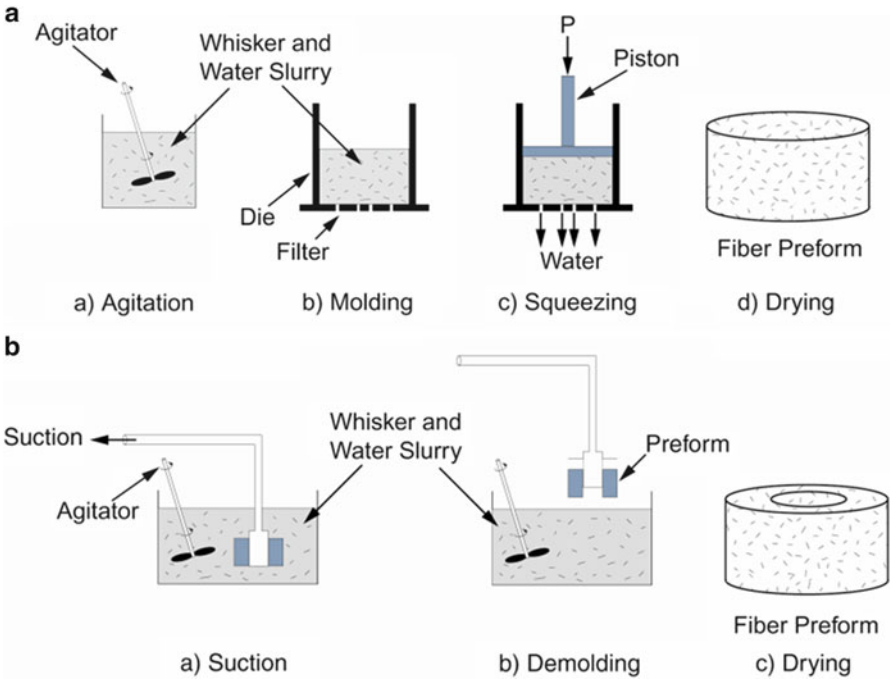

Fig. 4.7 Processes for making particulate performs: (**a**) press forming and (**b**) suction forming

process, suction is applied to a well-agitated mixture that consists of the reinforcement, fiber, and water. The mixture is then demolded and dried.

In order to obtain infiltration of the preform, clearly the molten metal must have a relatively low viscosity and good wettability with the reinforcement. A schematic of the liquid infiltration process is shown in Fig. 4.8. The reinforcement preform is placed in a mold, and the liquid is poured into a preheated die located on the bed of a hydraulic press. Infiltration takes place by mechanical force or by using a pressurized inert gas. Applied pressures on the order of 70–100 MPa are typically used. Having the preform temperature lower than that of the matrix liquidus temperature is highly desirable in order to minimize interfacial reaction and to obtain a fine matrix grain size.

Squeeze casting can also be used to obtain composites with relatively high reinforcement volume fractions (>40 %) (Saha et al. 2000). In conventional casting, achieving homogeneous particle packing and distribution at high volume fractions of reinforcement is problematic. Figure 4.9 shows the microstructure of a 6060 Al matrix composite reinforced with 50 % SiC particles. Note the fine interparticle spacing and absence of any residual porosity.

Although the squeeze casting technique has been primarily used for infiltrating low melting point metals, such as Al, continuous fiber-reinforced intermetallic matrix composites such as Al_2O_3-reinforced TiAl, Ni_3Al, and Fe_3Al have also

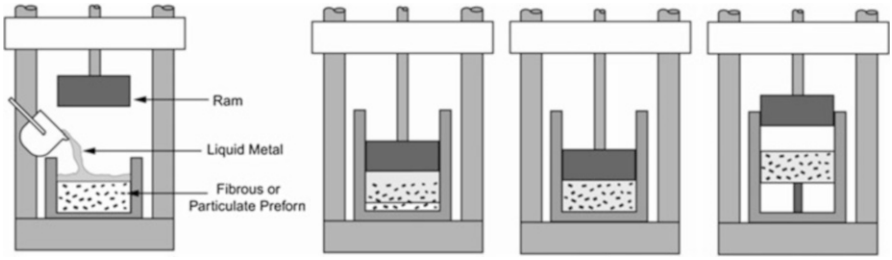

Fig. 4.8 Schematic of squeeze casting process

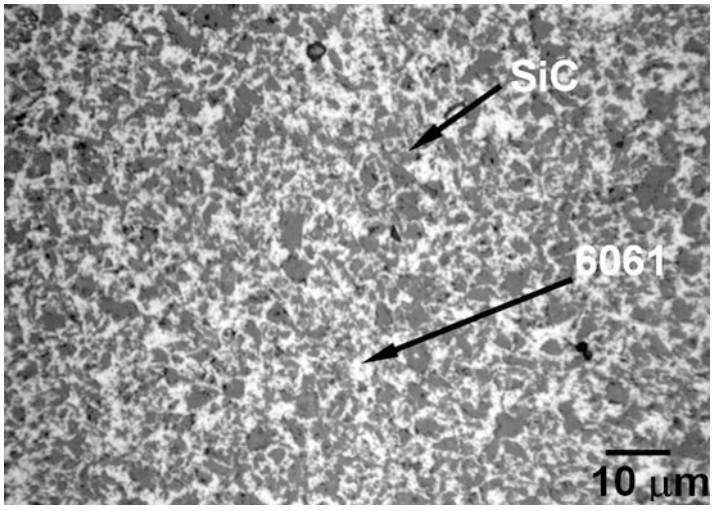

Fig. 4.9 Microstructure of 6061/SiC/50_p composite. Notice the large volume fraction of particles and relatively small interparticle spacing (Saha et al. 2000)

been processed (Nourbakhsh et al. 1990). The process is similar to that for discontinuously reinforced MMCs. A mixture of the matrix alloy with wetting-enhancing additives is melted in a crucible, while the fibrous preform is heated separately. The molten metal is then poured onto the fibers, and pressure is applied via argon gas simultaneously to infiltrate the preform.

4.1.2 Spray Co-deposition

Spray deposition can be used to fabricate metallic alloys in powder form (Lavernia et al. 1992). The metal or alloy is melted and atomized with water or an inert gas. Rapid solidification of the liquid takes place, resulting in a fine solid powder.

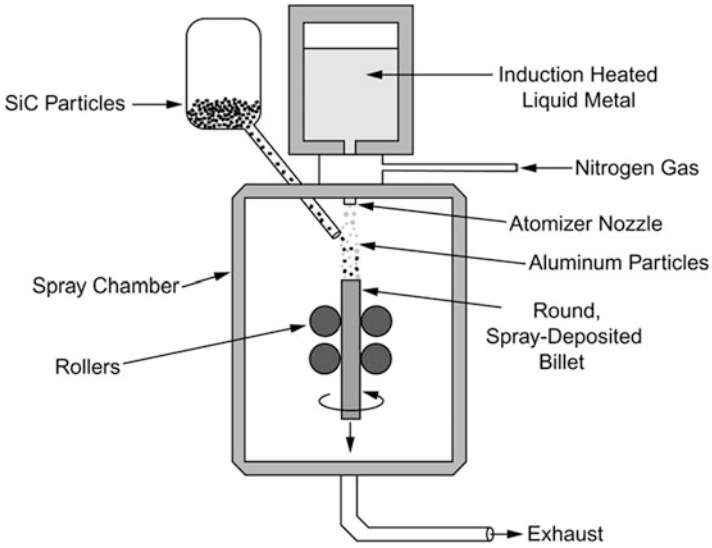

Fig. 4.10 Spray co-deposition of SiC particles and Al liquid droplets to form composite particles

This technique has been modified, by injecting reinforcement particles or co-depositing the particles with the matrix alloy, Fig. 4.10. The advantage of this technique is the high rate of production, which can approach 6–10 kg/min and the very fast solidification rate, which minimizes any reaction between particle and matrix. The as-processed billet is not fully dense, so secondary processing is required to fully densify and homogenize the composite. The distribution of particles in the liquid droplet is very much dependent on the size of the reinforcement and at what point in the process the reinforcement is injected into the matrix (Lloyd 1997). Whiskers, for example, are too fine to be optimally injected and distributed in the liquid droplets. When the particles are injected into the matrix immediately after atomization, the matrix is still liquid, so the particles are able to envelope themselves into the liquid droplet, and a relatively homogeneous distribution of particles in the matrix is obtained; see Fig. 4.11a. Injection of the particles later in the process, when the matrix droplet is semisolid, does not allow easy ingression of the particles into the matrix, causing the particles to reside along the periphery of the matrix particle, see Fig. 4.11b. A consolidated composite with the latter particle size distribution will certainly have inferior properties as a result of the high degree of particle clustering. This process is quite flexible in that the metal and reinforcement sprayers can be tailored to obtain in situ laminates or even functionally graded materials. The process can be quite expensive, however, owing to the high cost of the capital equipment.

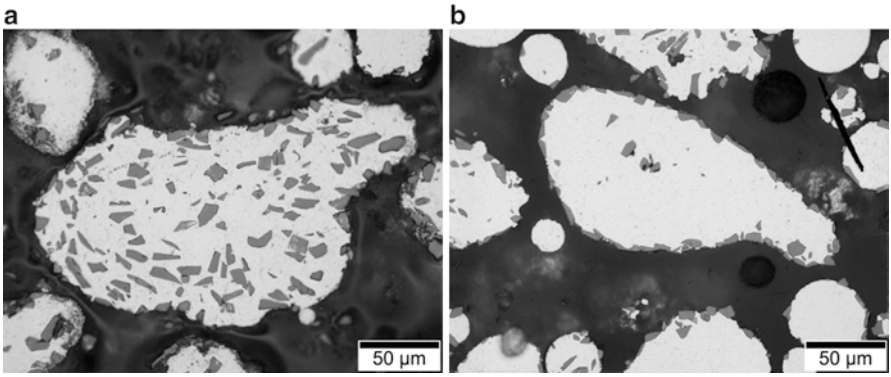

Fig. 4.11 Microstructure of composite particles obtained from spray co-deposition: (**a**) homogeneous particle distribution for particle injection, while matrix is in liquid state and (**b**) particles at periphery of matrix droplet, due to particle injection of liquid in semisolid state (courtesy of D. Lloyd)

4.1.3 In Situ Processes

In situ processes fall into two major categories, reactive and nonreactive processes. In the reactive processes two components are allowed to react exothermically to form the reinforcement phase. The XD process is an example of this process (Martin Marietta 1987). Typically, a rather high-volume fraction of ceramic particles is formed in the matrix alloy, and this master alloy is diluted with the matrix alloy to obtain a composite of desired reinforcement volume fraction. Typical examples involve TiB_2 and TiC as reinforcement particles, which are formed by the following reactions:

$$2B + Ti + Al \rightarrow TiB_2 + Al$$

and

$$C + Ti + Al \rightarrow TiC + Al$$

Processing variables such as reaction temperature can be used to tailor the desired reinforcement particle size, which is usually in the 0.25–1.5 μm range. The matrix consists of Al, Ni, or an intermetallic matrix. An alternative process that combines spray co-deposition and reaction is to atomize an Al–Ti alloy (at sufficiently high temperature) with a C-containing gas to form TiC particles (Chawla 2012).

The advantage of in situ reaction processes, in general, is that the reaction eliminates problems typically associated with wetting of the particle, so a relatively clean and strong interface is typically formed (Christodolou et al. 1988). The number of composite systems where reaction processing is beneficial, however, is limited, and the relatively fine size distribution of particles produced can significantly increase the viscosity of the melt.

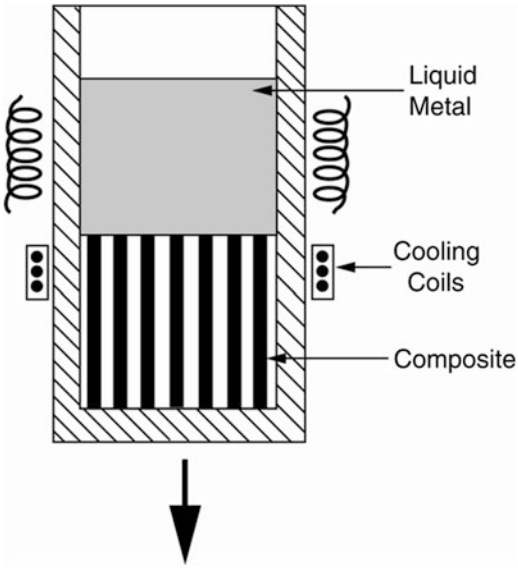

Fig. 4.12 Schematic of directional solidification process to obtain in situ composites

Nonreactive in situ processes take advantage of two-phase systems, such as eutectic or monotectic alloys, to form the fiber and matrix in situ (McLean 1983). Controlled directional solidification is conducted to separate the two phases, as shown in Fig. 4.12. A precast and homogenized material is melted in a graphite crucible and contained in a quartz tube, in vacuum, or inert gas atmosphere. Heating is typically conducted by induction and the thermal gradient is obtained by chilling the crucible. Electron beam heating may also be used, particularly when using reactive metals such as titanium. One can control the fineness of the microstructure, i.e., the size and spacing of the reinforcement (at a constant volume fraction) by controlling the solidification rate. These rates are quite slow, typically in the range of 1–5 cm/h, because one needs to maintain a stable solidification growth front. Figure 4.13 shows a cross section of the microstructure of an in situ processed composite. The matrix has been etched out locally to show the fibers. The fibers at grain boundaries are somewhat coarser due to earlier nucleation and growth, relative to the fibers within the grain.

4.1.4 Infiltration Mechanics

Infiltration of the liquid matrix through a particulate or fibrous preform can be thought of as liquid infiltration of a porous medium. As such, the infiltration characteristics through the porous reinforcement medium will be controlled by the capillarity of the liquid and the permeability of the preform. The subject of permeability of a porous medium by a fluid has been treated in several fields. In

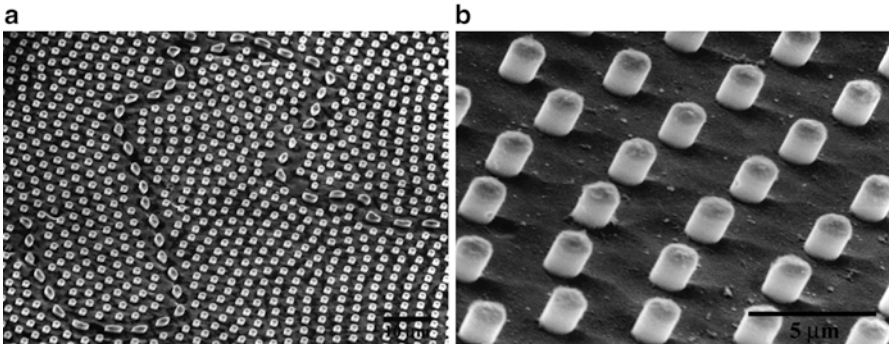

Fig. 4.13 Cross section of the microstructure of an in situ-processed composite: (**a**) lower magnification and (**b**) higher magnification. The matrix has been etched out locally to show the fibers. Note that the fibers at grain boundaries are somewhat coarser due to earlier nucleation and growth, relative to the fibers within the grain (courtesy of J.B. Andrews)

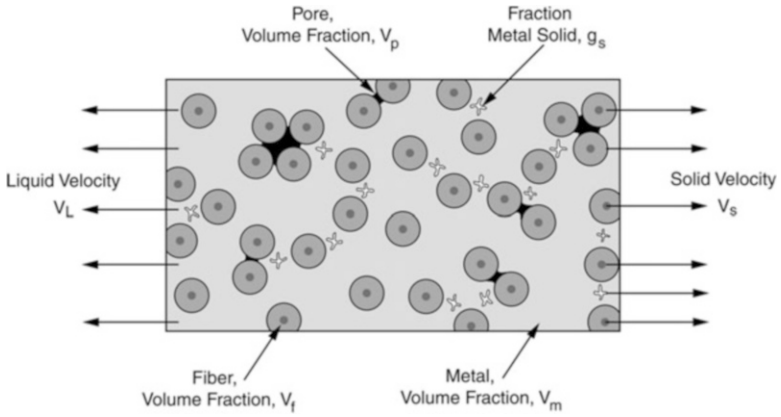

Fig. 4.14 Schematic of parameters associated with liquid infiltration of a metal matrix through a porous reinforcement preform (after Michaud 1993)

MMCs, infiltration of a liquid phase with velocity v_l through a small volume ΔV is considered, Fig. 4.14 (Michaud 1993). The total volume comprises the volumes of the fiber, matrix, and porosity, so the sum of the volume fractions, V_f, V_m, and V_p, is equal to 1. The velocity of the solid preform, v_s, is generally preform deformation which is neglected, so $v_s = 0$. A fraction of the liquid metal, g_s, will gradually solidify during infiltration so the volume fraction of the solid matter in the composite (fibers plus solidified metal) is given by $V_{sf} = V_f + g_s V_m$.

We can now discuss the liquid infiltration processes, in terms of the parameters described above, by the Forchheimer equation:

$$f - \nabla P = \left[\frac{\eta V_m (1 - g_s)}{K} + B\rho_m \sqrt{(v_l - v_s)^2}\right](v_l - v_s)$$

where f is the volumetric gravitational, centrifugal, or electromagnetic force, P is the average pressure applied in the volume ΔV, η is the viscosity of the liquid metal, ρ_m is the density of the liquid metal, and v_l and v_s are the velocity of the liquid and solid, respectively. *K* is termed the permeability of the preform and B is a constant. K is a function of the reinforcement preform microstructure, wetting characteristics, reactivity, etc., as well as V_m, the matrix volume fraction, and the characteristics of the solidified metal. It should be noted, however, that K is not dependent on the properties of the infiltrating liquid. The relevant Reynolds number for a preform with characteristic length d (e.g., fiber diameter) is given by

$$R_e = \frac{d\rho_m\sqrt{(v_l - v_s)^2}}{\eta V_f}$$

where V_f is the fiber volume fraction and the other symbols have the significance given earlier. When R_e is below a critical value of the Reynolds number, $R_{e,critical}$, (approximately equal to 1 for the preform considered here), the second term in the Forchheimer equation can be neglected, and we obtain Darcy's law:

$$v_l - v_s = \frac{K}{\eta V_m(1 - g_s)}(f - \nabla P)$$

The left-hand side of the equation can be thought of as a volumetric density of the fluid (i.e., $\frac{\text{volume}}{\text{area}\cdot\text{time}}$). It can be recognized that Darcy's law is an analog of Ohm's law for electrical conduction, i.e., permeability is analogous to electrical conductivity. Thus, in general, higher permeability, lower viscosity, and higher applied pressure will contribute to faster infiltration of the liquid matrix into the reinforcement preform.

Analysis of heat transfer during the matrix infiltration process is important because as the liquid metal infiltrates and solidifies, it will release heat into its surroundings. The heat flow will cause an increase in temperature of the system, allowing incoming liquid to remain in the liquid state, while infiltrating the preform. In practice, liquid flow ceases when enough cooling from the preform and/or partially solidified composite takes place or when the preform is completely filled. In general, heat transfer within the volume element ΔV is dictated by conduction, convection, exothermic characteristics of interfacial reactions, and the fraction of total solidified metal, g_s. The governing equation for this heat transfer is (Michaud 1993)

$$\nabla \cdot (k_c \nabla T) = \rho_c c_c \frac{\partial T}{\partial t} + \rho_m c_m V_m (1 - g_s) v_l \cdot \nabla T$$

$$+(\rho_f c_f V_f + \rho_m c_m V_m g_s) v_s \cdot \nabla T - \rho_m \Delta H \frac{\partial (g_s V_m)}{\partial t} - Q$$

where k_c is the thermal conductivity of the composite, ΔH is the latent heat of solidification of the metal, and $\dot{Q}$ is the rate of heat released from any chemical reaction. ρ and c refer to the density and heat capacity, respectively, and the subscripts f, m, and, c denote the reinforcement, metal, and composite, respectively.

Mass transfer also needs to be considered when analyzing the liquid infiltration process. Because of the relatively short time scales involved with most infiltration processes, the contribution from diffusion to mass flow within ΔV can be neglected. Rather, convection plays a more prominent role, due to solution or rejection of a solute in the metal (for an alloy) and consumption during an interfacial chemical reaction. The governing relation for mass transport is

$$\frac{\partial \overline{C}}{\partial t} = -\nabla \cdot [(1 - g_s)C_l v_l + g_s C_s v_s] + r_A$$

where $\overline{C}$ is the average matrix composition, r_A is the rate of change in solute due to the chemical reaction, and C_l and C_s are the composition of the liquid and solid phases, respectively, as determined from the phase diagram of the alloy at a given temperature.

4.1.5 *Microstructure Evolution During Liquid-Phase Processing*

The microstructure of the composite depends on the local solidification and cooling processes taking place during infiltration of the preform. In general, the liquid metal will solidify when it comes in contact with the preform, which is at a lower temperature. A schematic of the infiltration front, temperature distribution in the preform, and grain size distribution in the matrix is shown in Fig. 4.15 (Mortensen and Jin 1992). At the infiltration front, the metal will solidify first (Region 1), while in the middle of the preform (Region 2), a relatively constant temperature prevails. The semisolid metal close to the infiltration gate (Region 3), however, will continuously be in contact with the liquid metal. The situation is more complicated for a binary eutectic alloy. The infiltration front, temperature distribution, and liquid metal composition are shown for a binary alloy matrix composite, Fig. 4.15. The temperature gradient is similar to that of the pure metal, but a significant amount of solute segregation takes place at the infiltration front. Thus, the remaining incoming liquid is depleted of the solute.

The grain size distribution will also be affected by the local temperature distribution and cooling rate. For the infiltration of the pure alloy, Fig. 4.15, in Region 1, a fine matrix grain size is obtained because the molten metal comes into contact with the cooler reinforcement preform, which results in rapid solidification of the matrix. Heterogeneous nucleation at the reinforcement does not occur in most

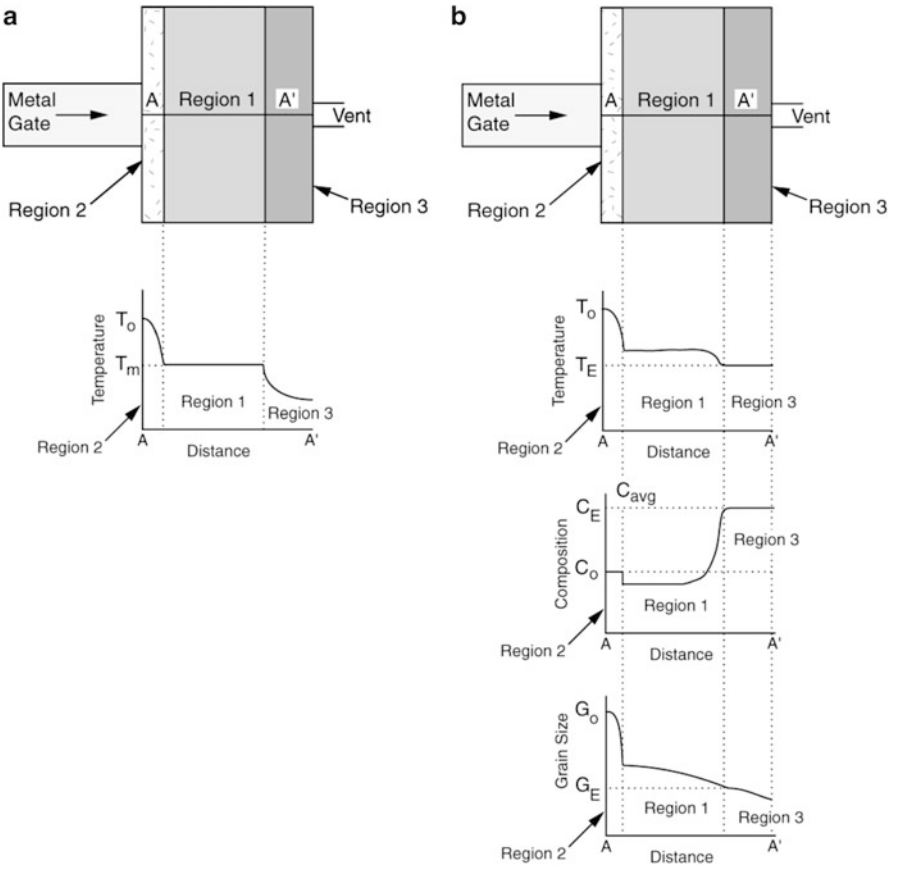

Fig. 4.15 Schematic of temperature, compositional, and grain size gradients during infiltration of reinforcement preform with (**a**) pure metal matrix and (**b**) alloy metal matrix (after Mortensen and Jin 1992)

MMCs processed by liquid phase (Mortensen and Jin 1992). In most Al matrix composites, for example, the grain size is usually much larger than the reinforcement size. The exception to this is in Al–Si matrix composites, where the primary Si phases nucleate preferentially at the reinforcement. Thus, in these composites, the composite has a finer distribution of Si phase, compared to the unreinforced alloy. Figure 4.16 shows the cell size in 6061 matrix composites, reinforced with 10 and 20 % SiC particles (Lloyd 1989). Note that the composite has a finer overall microstructure than the unreinforced alloy, at all cooling rates.

In some cases, particularly where fiber reinforcement is involved, the reinforcement actually impedes heat convection from the liquid metal, resulting in a larger degree of columnar dendritic growth than in the unreinforced alloy (Cole and Bolling 1965). In Region 2, the grain size is slightly larger because of the higher

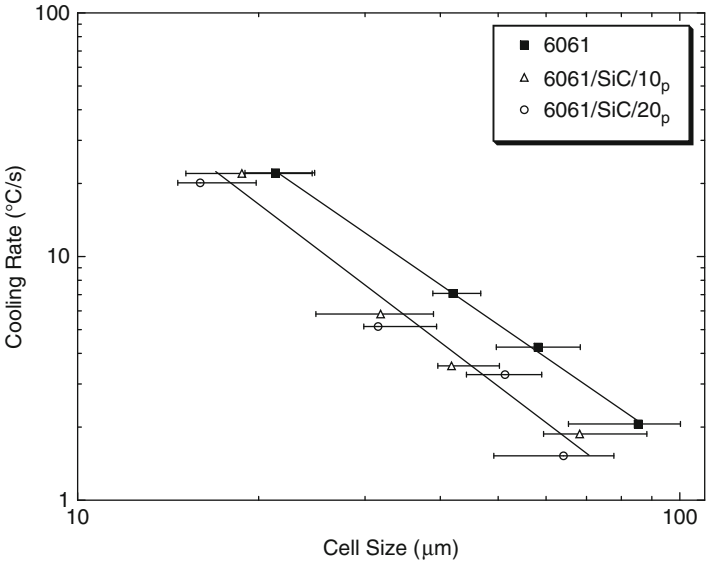

Fig. 4.16 Cooling rate versus matrix cell size in Al 6061 matrix composites, reinforced with 10 and 20 % SiC particles (Lloyd 1989). Note that the composite has a finer overall microstructure than the unreinforced alloy, at all cooling rates, because of reinforcement particle pinning

temperatures and somewhat lower cooling rate. Finally, at the gate a coarser microstructure will result, as this region will be the last to solidify and will cool at a relatively slow rate. Figure 4.17 shows the microstructure of a Saffil (Al_2O_3) fiber-reinforced Al–4.5Cu matrix, where the matrix microstructure well within the preform is much finer than that close to the infiltration gate.

The microstructure of the matrix is not only a function of the temperature and composition gradients but also on the velocity of the liquid and the interfiber spacing. Shekhar and Trivedi (1989, 1990) studied the solidification processes in model fiber and particle-containing organic transparent systems. In fiber-reinforced systems, as the interfiber spacing approaches the primary dendrite or cell spacing, perturbations in the advancing liquid cause morphological changes upon solidification. The effect of velocity and interfiber spacing (indicated by the ratio of interfiber spacing, d, to the primary dendrite spacing λ) can be represented by a microstructure map, Fig. 4.18 (Trivedi et al. 1990). For very large interfiber spacing, the morphology is dependent on the liquid velocity, going from planar to cellular to dendritic with increasing velocity. When the interfiber spacing is very small, the cellular regime is larger since both planar and dendritic structures will transform to cellular structures. At intermediate spacing, dendritic microstructures and lower velocities will be observed, when the ratio of d/λ is slightly greater than 1.

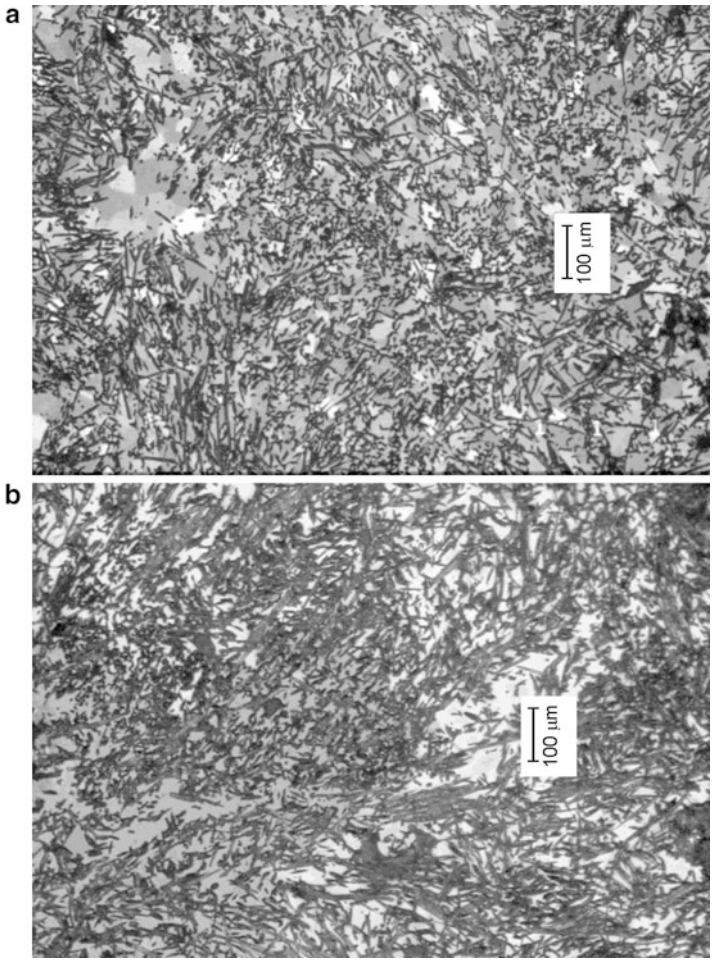

Fig. 4.17 Microstructure of a Saffil (Al_2O_3) fiber-reinforced Al-4.5 Cu matrix. The matrix grain size well within the preform (**a**) is much finer than that close to the infiltration gate (**b**), since the latter goes through remelting and much slower cooling (courtesy of V. Michaud)

4.1.6 Casting

During casting of MMCs, the reinforcement (particle or short fiber) is typically mobile, so that motion or pushing of the reinforcement, especially particles, by the liquid needs to be considered. If the particles are pushed by the solidifying liquid, the particles are segregated to the remaining liquid that solidifies. In eutectic systems, for example, the remaining liquid is highly rich in solute. The resulting microstructure, then, depends on the relative size of the primary dendrites relative to the particle size. For composites cooled at relatively slow cooling rates, the dendrite

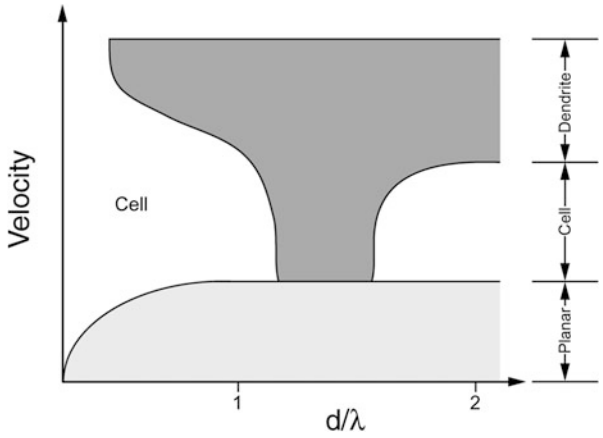

Fig. 4.18 Effect of solidification front velocity and interfiber spacing (represented by the ratio of interfiber spacing, d, to dendrite spacing, λ) on matrix microstructure. For very large d/λ, the morphology goes from planar to cellular to dendritic with increasing velocity. When the interfiber spacing is very small, the cellular regime is larger since both planar and dendritic structures will transform to cellular structures (after Trivedi et al. 1990)

size is much larger than the particle size and the solidified microstructure consists of several areas of high particle clustering, Fig. 4.19 (Lloyd 1994). For faster cooling rates, the matrix cell size is much smaller (on the order of the particle size, as shown above) so the degree of particle pushing is diminished significantly, resulting in a much more homogeneous distribution of particles, Fig. 4.20.

Experimental studies on particle pushing in particle-reinforced MMCs show the following trends: (a) in eutectic and hypereutectic matrix alloys, such as Al–Si, particle capture takes place for all growth conditions; (b) in hypoeutectic Al alloy systems, where a nonplanar solid–liquid interface is typically present, particle pushing takes place; and (c) in several systems, there is a critical velocity of the solid–liquid interface, V_c, below which particle pushing takes place and above which particle capture occurs. For a planar solid–liquid interface, V_c can be related to the particle diameter, d, by the following relationship (Mortensen and Jin 1992):

$$V_c d^n = C$$

where C is a system-dependent constant and the exponent n varies between 0.5 and 3.

Two criteria have generally been proposed for particle pushing. The first is related to the free energy change as the solid grows and comes into contact with the particle in the liquid. Uhlmann et al. (1964) and Potschke and Rogge (1989) proposed the following criterion for particle pushing, based on interfacial free energies:

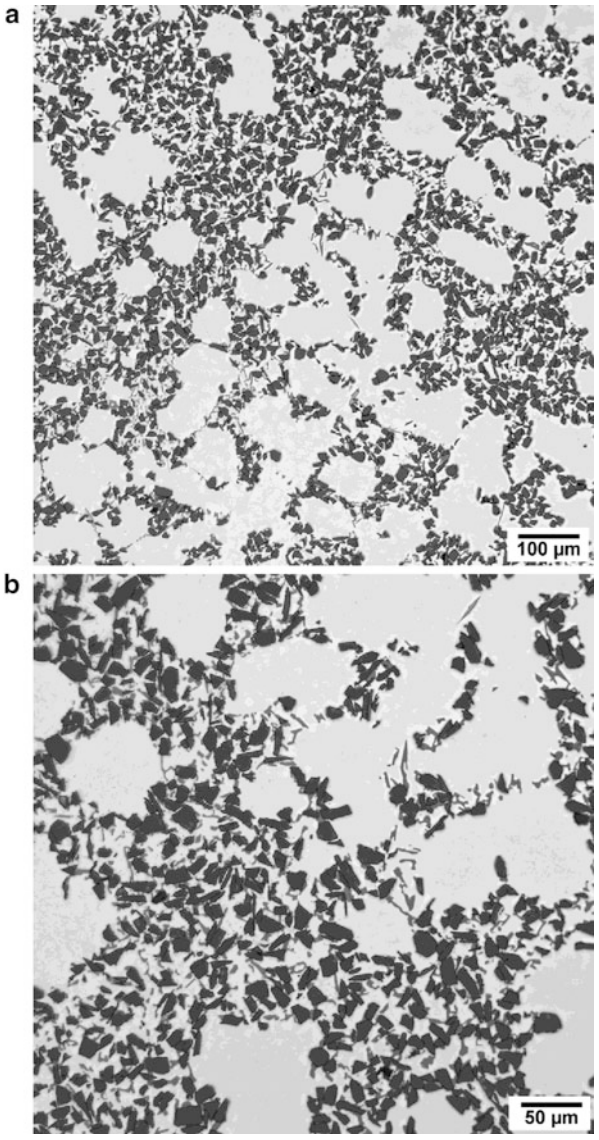

Fig. 4.19 Highly clustered reinforcement particle distribution resulting from slow cooling, due to particle pushing: (**a**) lower magnification and (**b**) higher magnification (courtesy of D. J. Lloyd)

$$\gamma_{ps} > \gamma_{pl} + \gamma_{sl}$$

where γ is the interfacial energy and ps, pl, and sl refer to particle/solid, particle/liquid, and solid/liquid interfaces, respectively. This model is generally only valid when the interface velocities are small, and it is not of great practical interest because the interfacial free energies are largely unknown.

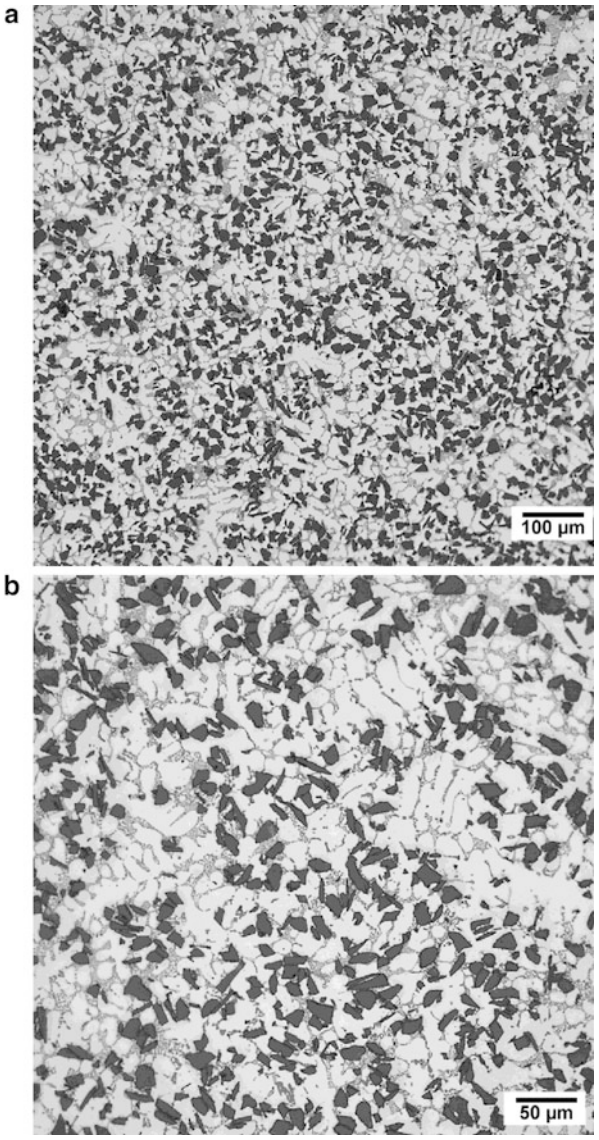

Fig. 4.20 Uniform reinforcement particle distribution resulting from faster cooling: (**a**) lower magnification and (**b**) higher magnification (courtesy of D. J. Lloyd)

Several investigators have taken a different, more practical approach of trying to predict the critical interface velocity for particle pushing (Uhlmann et al. 1964; Cisse and Bolling 1971; Stefanescu et al. 1988; Shangguan et al. 1992; and Kim and Rohatgi 1999). This approach is based on experimental observations that a critical interface velocity exists, below which the particles are pushed and above which the particles are engulfed. Cisse and Bolling (1971) modeled the balance between the viscous drag on the particle and the counteracting repulsing force exerted by

the particle on the solid/liquid interface front and arrived at the following critical velocity for particle pushing/engulfment:

$$V_c^2 = \frac{4kT\gamma_{sl}a_o}{9\pi\eta^2 R^3}\frac{\alpha(1-\alpha)^3}{1-3\alpha}$$

where η is the viscosity of the liquid, γ is the free energy of the solid/liquid interface, R is the radius of the particle, a_o is the distance between the particle and the solid/liquid interface, k is the curvature of the solid/liquid interface, and α is the ratio of particle radius to interface radius. Kim and Rohatgi (1999) modeled the shape of the solid/liquid front in terms of the ratio of thermal conductivity of the particle to that of the liquid, the temperature gradient and surface tension of the solid/liquid interface, and the heat of fusion of the liquid. They derived the following expression:

$$V_c = \frac{\Delta\gamma a_o(kR+1)}{18\eta R}$$

where $\Delta\gamma$ is the difference in interface energy, $\Delta\gamma = \gamma_{sp} - \gamma_{lp} - \gamma_{sl}$. Kim and Rohatgi (1999) showed that their model was closest to experimental measurements of the critical velocity, compared to other models, yet, their prediction was still a factor of 2 lower than the experimental values. This was attributed to the fact that (a) a constant particle temperature was used in the calculations, whereas in reality, the particle temperature may be changing with time, and (b) factors such as particle shape, particle roughness, and heat convection between the particle and the interface, were not considered in the model.

4.2 Solid-State Processing

The main drawback associated with liquid phase techniques is the difficulty in controlling reinforcement distribution and obtaining a uniform matrix microstructure (Michaud 1993). Furthermore, adverse interfacial reactions between the matrix and the reinforcement are likely to occur at the high temperatures involved in liquid processing. These reactions can have an adverse effect on the mechanical properties of the composite (Chawla et al. 1998; Sahoo and Koczak 1991), hence the interest in solid-state processing of MMCs. The most common solid-phase processes are based on powder metallurgy techniques (Ghosh 1993). These typically involve discontinuous reinforcements, due to the ease of mixing and blending, and the effectiveness of densification. The ceramic and metal powders are mixed, isostatically cold compacted, and hot pressed to full density. The fully dense compact then typically undergoes a secondary operation such as extrusion or forging (Lloyd 1997). Novel low-cost approaches, such as sinter forging, have aimed at eliminating the hot-pressing step, with promising results (Chawla et al. 2003).

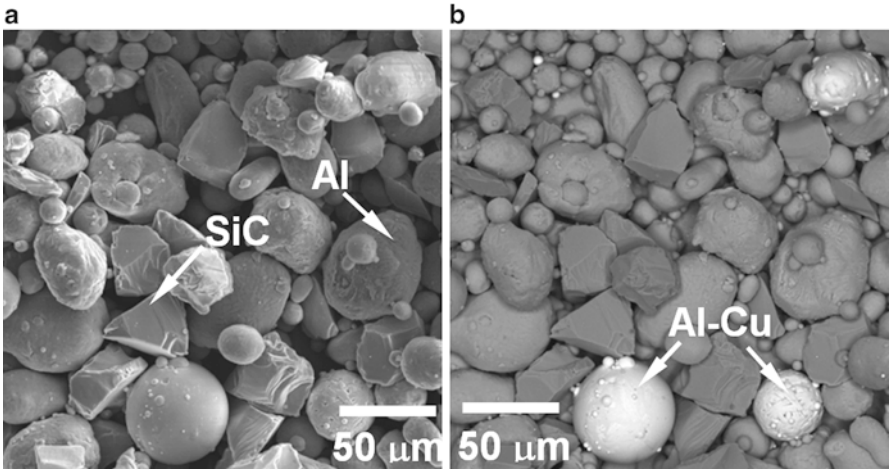

Fig. 4.21 Powder mixture of Al, SiC, and 50 wt%Al–50 wt%Cu particles: (**a**) secondary electron image and (**b**) backscattered electron image, showing the Al–Cu particles

4.2.1 Powder Metallurgy Processing

Powder processing involves cold pressing and sintering or hot pressing to fabricate primarily particle- or whisker-reinforced MMCs (Hunt 1994). The matrix and the reinforcement powders are blended to produce a homogeneous distribution. Figure 4.21 shows a blended powder mixture of Al, 50Al–50Cu (wt%), and SiC particles. The 50Al–50Cu articles are added to provide a uniform distribution of the alloying additions, while the pure Al particles enable easier cold pressing. The blending stage is followed by cold pressing to produce what is called a green body, which is about 80 % dense and can be easily handled, Fig. 4.22. The cold-pressed green body is canned in a container, sealed and degassed to remove any absorbed moisture from the particle surfaces. One of the problems with bonding metallic powder particles, such as Al particles, to ceramic particles, such as SiC, or to other Al particles is the oxide "skin" that is invariably present on the Al particle surface (Kim et al. 1985; Anderson and Foley 2001). Degassing and hot pressing in an inert atmosphere contribute to the removal of Al hydrides present on the particle surface, making the oxide skin more brittle and, thus, more easily sheared (Estrada et al. 1991; Kowalski et al. 1992). The material is hot pressed, uniaxially or isostatically, to produce a fully dense composite and extruded. The rigid particles or fibers do not deform, causing the matrix to be deformed significantly.

The ratio of the reinforcement particle size to matrix particle size is very important in achieving a homogeneous distribution of particles in the matrix.

A comparison of the effect of Al-to-SiC particle size ratio on the composite microstructure is shown in Fig. 4.23. With the larger Al particle size, the SiC particles are "pushed" and packed in the interstices between the larger Al particles,

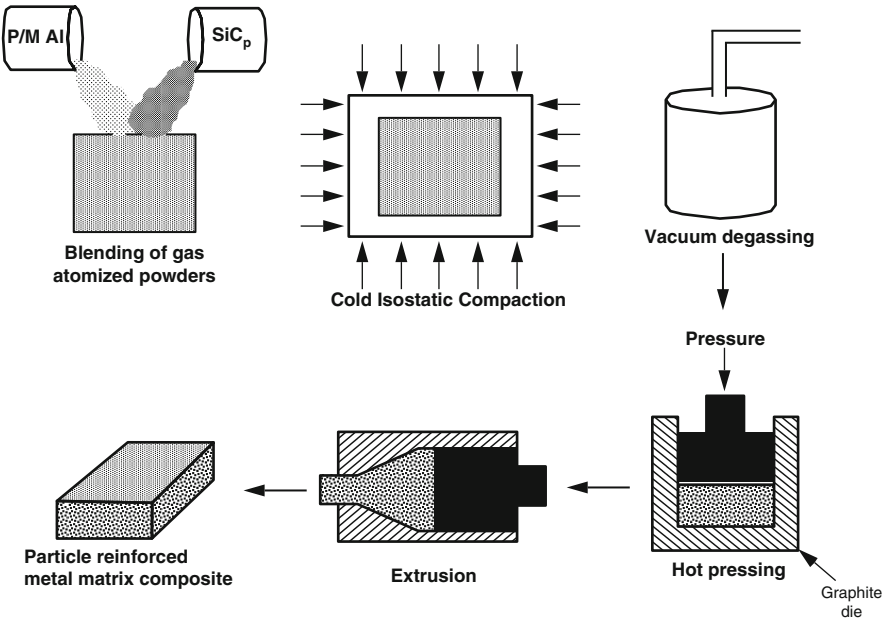

Fig. 4.22 Powder processing, hot pressing, and extrusion process for fabricating particulate or short fiber-reinforced MMCs

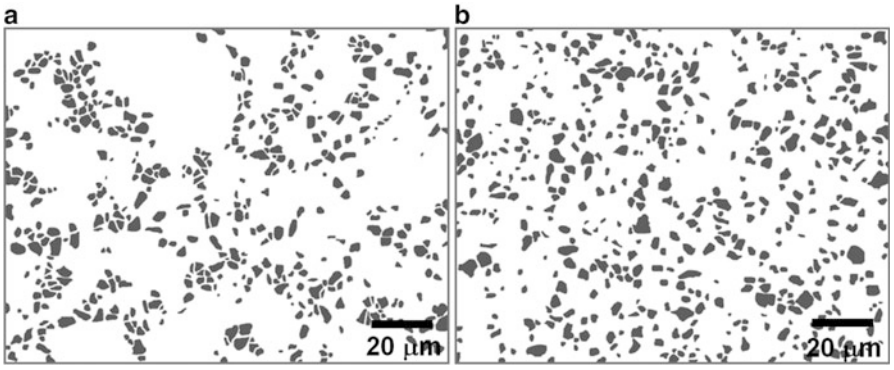

Fig. 4.23 Particle clustering in Al/SiC/15$_p$ with different Al–SiC particle size ratios: (**a**) Al–SiC ratio of 6.6 ($d_{cl} = 33$ μm, $d_{SiC} = 5$ μm) and (**b**) Al–SiC ratio of 1.4 ($d_{Al} = 7$ μm, $d_{SiC} = 5$ μm). Increasing the Al–SiC ratio results in a greater degree of SiC clustering

yielding a more clustered microstructure, Fig. 4.23a. A particle size ratio closer to one yields a more homogeneous microstructure, Fig. 4.23b. We can quantify the degree of homogeneity in particle distribution by a clustering parameter. Several techniques have been used to quantify particle (e.g., SiC) clustering in metal matrix composites (Dirichlet 1850; Lewandowski et al. 1989; Spowart et al. 2001; Yang et al. 2001). One important technique is called tessellation and is described in detail

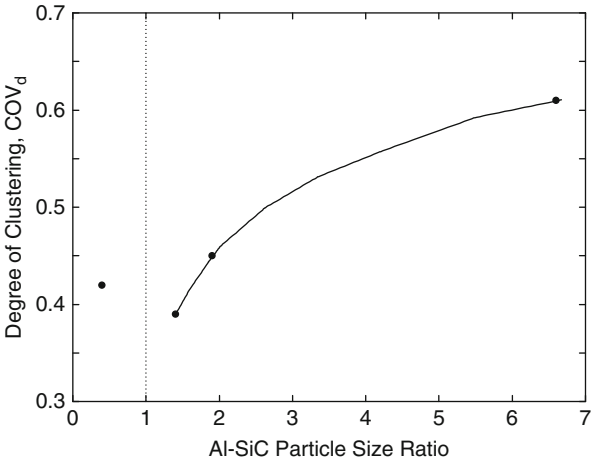

Fig. 4.24 Degree of clustering versus Al-to-SiC particle size ratio. The degree of clustering tends to a minimum at a particle size ratio close to one

in Chap. 7. Measurement of the nearest-neighbor distance of each particle is the simplest means of assessing particle clustering, but it can be deceptive, since the mean nearest-neighbor spacing ignores the distribution in nearest-neighbor spacings in the microstructure. Yang et al. (2001) showed that the coefficient of variance of the mean near-neighbor distance (COV_d) is particularly sensitive and effective in characterizing particle clustering. This parameter is also relatively insensitive to particle volume fraction, size, and morphology. COV_d can be described by the following equation (Yang et al. 2001):

$$COV_d = \frac{\sigma_d}{d}$$

where σ_d^2 is the variance in the mean nearest-neighbor distance and d is the average of the mean near-neighbor distance of the particles sampled.

The degree of clustering, as measured by COV_d, as a function of Al-SiC particle size ratio is shown in Fig. 4.24. For large particle size ratios, i.e., Al particle size much greater than SiC or vice versa, the degree of clustering is relatively high. It is interesting to note that the minimum degree of clustering (COV_d) tends to a particle size ratio of about one.

4.2.2 Extrusion

Extrusion processing has been used extensively as a means of secondary deformation processing of MMCs (Ghosh 1993; Hunt 1994; Lloyd 1997). It is particularly advantageous because the combination of extrusion pressure and temperature results in shear between Al/Al and Al/SiC particles, which contributes to fracture

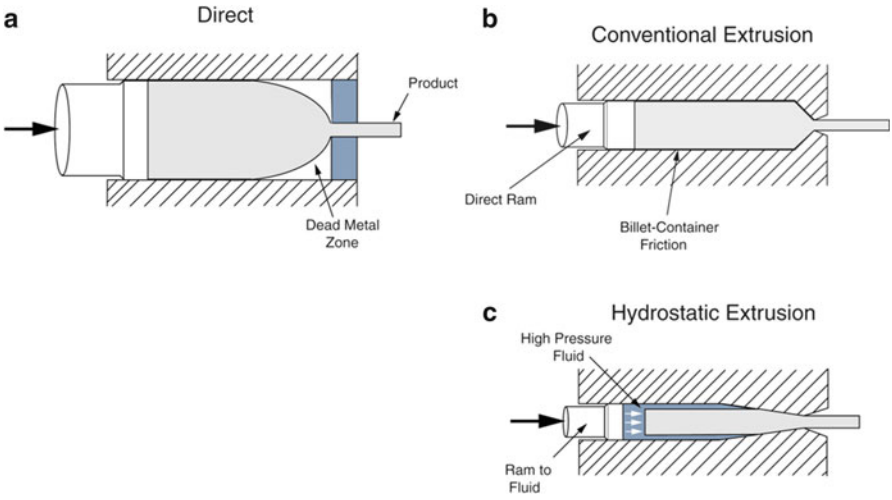

Fig. 4.25 Three types of extrusion processing: (**a**) direct, (**b**) conventional, and (**c**) hydrostatic. Hydrostatic extrusion minimizes die-friction and "dead-metal" zones

of the oxide skin on the Al particles, and the bonding between particle and matrix is enhanced. Because of the large strains associated with this process, however, extrusion has been used primarily to consolidate composites with discontinuous reinforcement, in order to minimize reinforcement fracture. Even in discontinuously reinforced materials, fracture of short fibers or particles often takes place, which can be detrimental to the properties of the composite.

Three types of extrusion are shown in Fig. 4.25, direct, conventional, and hydrostatic. In direct extrusion, the extruded material is deformed against a flat plate with a small orifice. This causes a "dead-metal zone" which consists of a region where the metal cannot flow. In conventional extrusion, the die is tapered to minimize the dead-metal zone. Die friction is present, however, which will result in higher deformation stresses at the metal/die interface. In MMCs, this effect is particularly exacerbated due to the presence of the particles and the large shear stresses at the metal/container interface result in material discontinuities. This can result in ragged edges, called the "Christmas tree" effect, Fig. 4.26. This is more predominant with an increase in reinforcement particle content, due to the increase in die friction and, thus, shear stresses. Finally, the problems of die friction can be minimized by conducting the extrusion inside a high-pressure fluid. This results in a close to hydrostatic stress state and minimal effect of friction in the billet because the contact area between material and die is minimized.

Several microstructural changes take place during extrusion. These include alignment of particles along the extrusion axis, particle fracture (depending on the reinforcement particle size and the strains involved), and refinement and recrystallization of matrix grains (Chawla et al. 1998; Tham et al. 2002; Ganesh and Chawla 2004, 2005). Figure 4.27 shows the microstructural montage of SiC

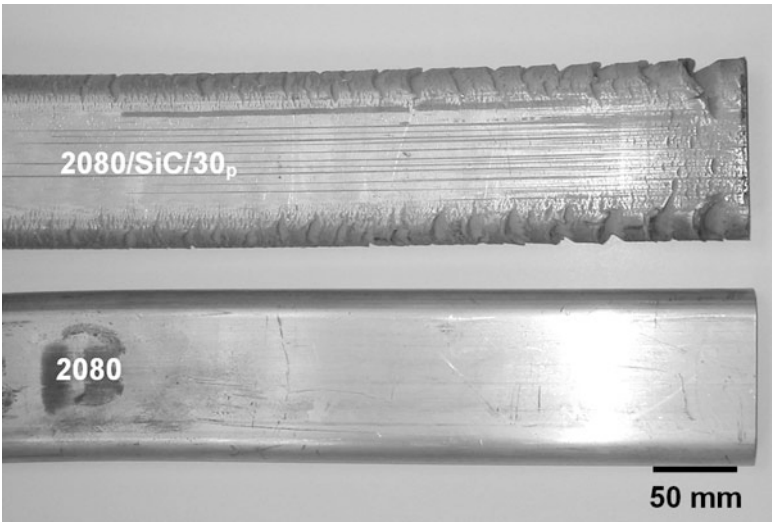

Fig. 4.26 Comparison of extruded Al 2080 alloy and 2080/SiC/30_p. Note the ragged edges or "Christmas tree" effect due to enhanced die friction in the composite

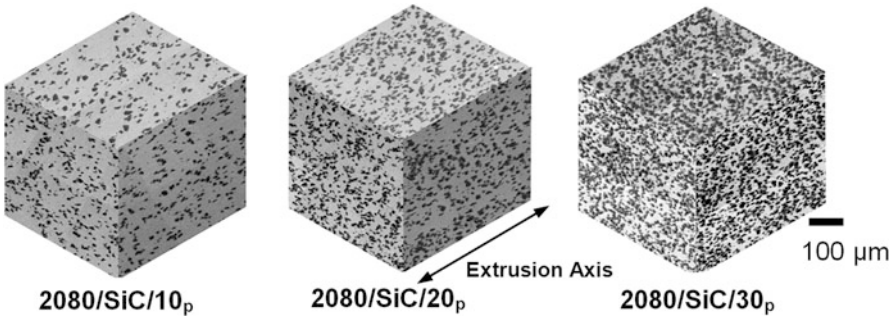

Fig. 4.27 Microstructure of SiC particle reinforced Al alloy for three reinforcement volume fractions: 10, 20, and 30 %. Note the preferred orientation of reinforcement particles along the extrusion axis (Ganesh and Chawla 2004)

particle-reinforced Al alloy at three different reinforcement volume fractions: 10, 20, and 30 %. Note the preferred orientation of reinforcement particles along the extrusion axis.

Quantitative analysis of the degree of orientation of the particles, defined as the angle of a given particle to the longitudinal or transverse axis, shows that the degree of alignment of particles in the longitudinal plane, at a given volume fraction of particles, was much higher than that in the transverse plane, Fig. 4.28. However, the degree of orientation in the longitudinal plane decreased with an increase in volume fraction of particles. This can be explained by noting that the larger the

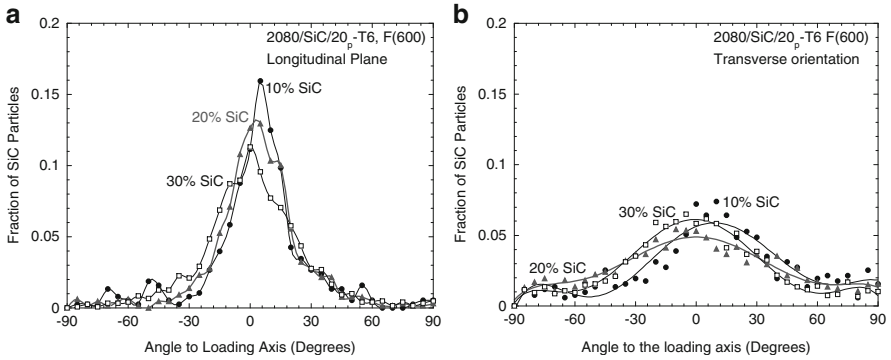

Fig. 4.28 Quantitative analysis of the degree of orientation of the particles (orientation is defined by the angle of a given particle to loading axis): (**a**) longitudinal and (**b**) transverse. The degree of alignment of particles in the longitudinal plane, at a given volume fraction of particles, is much higher than that in the transverse plane (Ganesh and Chawla 2004)

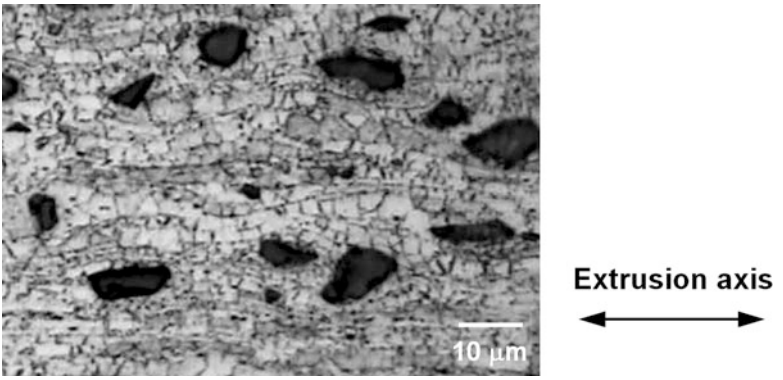

Fig. 4.29 Microstructure of extruded 2080/SiC/10_p composite (Ganesh and Chawla 2004). The matrix grain size is refined due to the constraint on deformation from the SiC particles. Dynamic recrystallization during hot extrusion results in a finger grain structure at the particle/matrix interface

volume fraction of particles, the lower the mean free path available for particle rotation and alignment along the extrusion axis. The anisotropy in particle alignment has a profound impact on Young's modulus and tensile strength (Logsdon and Liaw 1986; Ganesh and Chawla 2005), and these are described in Chap. 7. Extrusion-induced particle fracture can reduce the strength of the composite significantly, often to levels below that of the unreinforced alloy (see Chap. 6).

The incorporation of reinforcement particles has an effect on the metal matrix grain size. As described above, with the incorporation of the hard reinforcement particles, a larger degree of plastic flow is required to deform the matrix around the particles (Chawla et al. 1998). This also results in an overall refinement in matrix grain size, shown in Fig. 4.29. The grain size in the composite is also

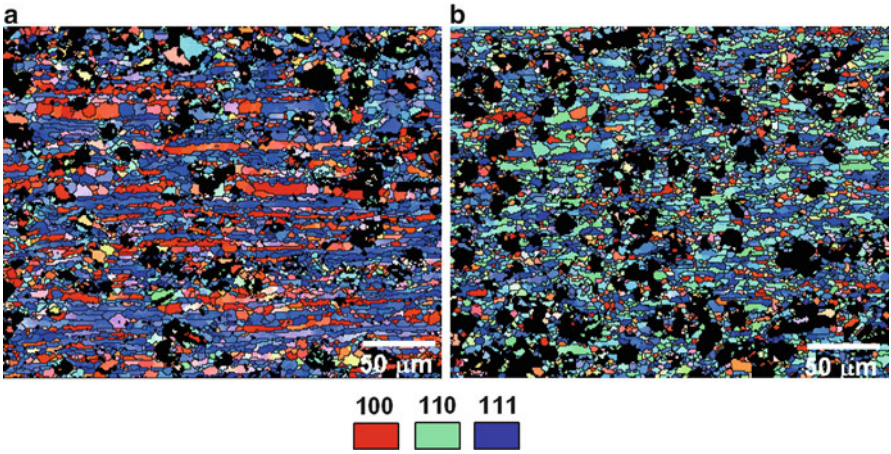

Fig. 4.30 Orientation imaging map of matrix grains in a 2080/SiC_p composite: (**a**) parallel to extrusion axis and (**b**) perpendicular to extrusion axis. The matrix exhibits a <100><111> texture, typical of deformation-processed FCC materials. Perpendicular to the extrusion direction, the texture is random, indicating an overall fibrous texture

inhomogeneous, being smaller near the particle/matrix interface and increasing in size with increasing distance from the particle/matrix interface. The large degree of shear produced by extrusion between particles and matrix is conducive to a very strong mechanical bond between the particle and matrix. A strong mechanical bond between particle and matrix is highly desirable in strengthening of MMCs, because it maximizes the degree of load transfer from the matrix to the particle, and thus, increases the chance that a given particle will be loaded to its fracture stress (Williams et al. 2002).

During hot extrusion the particles also act as nucleating sites for recrystallization of new matrix grains, which results in a much finer grain size along the particle/matrix interface (Liu et al. 1989; Humphreys et al. 1990). This is shown in the orientation imaging map of the matrix grains in the composite, Fig. 4.30. Macroscopically, the matrix exhibits a {100}<111> texture, typical of deformation-processed FCC materials. Perpendicular to the extrusion direction, the texture is random, indicating an overall fibrous texture in the material. A closer look at the grain orientation at the particle/matrix interface shows that the grains at the interface are randomly oriented, due to dynamic recrystallization, Fig. 4.31. The grains further away from the interface, however, exhibit the typical {100}<111> texture.

A disadvantage of the conventional powder metallurgy process followed by extrusion is the high cost of the process. The high cost is driven primarily by the difficulty in machining these wear-resistant composites and the material waste generated to produce a component. Thus, while the extrusion process has been used to fabricate composites for very demanding applications, particularly in the aerospace sector, it is not conducive for applications where low cost and high volume are as important as performance.

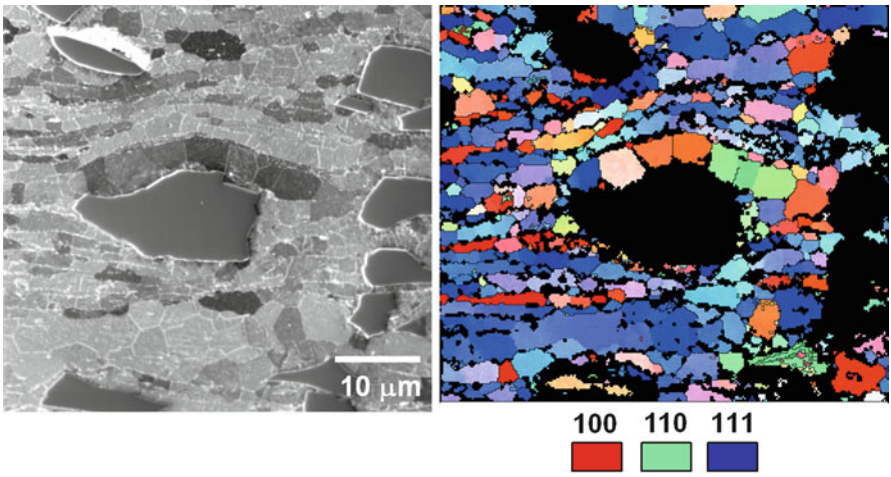

Fig. 4.31 Grain orientation at the particle/matrix interface showing that the grains at the interface are randomly oriented, due to dynamic recrystallization

4.2.3 Forging

Forging is another common secondary deformation processing technique used to manufacture metal matrix composites. Once again, this technique is largely restricted to composites with discontinuous reinforcement. In conventional forging, a hot-pressed or extruded product is forged to near-net shape (Helinski et al. 1994).

A new, low-cost sinter-forging technique has been developed whereby a mixture of the reinforcement powder and matrix powder is cold compacted, sintered, and forged to nearly full density, see Fig. 4.32 (Chawla et al. 2003). Thus, the main advantage of this technique is that forging is conducted to produce a near-net shape material, and machining operations and material waste are minimized. A similar process can be used to manufacture steel connecting rods for large volume passenger car applications (James 1985).

The microstructure of forged composites exhibits some preferential alignment of SiC particles perpendicular to the forging direction. A comparison with extruded composites, of similar particle size, indicated that the alignment in the sinter-forged composites was not as significant as that produced by extrusion (Chawla et al. 2003). This is to be expected since a much larger amount of plastic deformation can be induced during extrusion. The low-cost, sinter-forged composites have tensile and fatigue properties that are comparable to those of materials produced by extrusion (Chawla et al. 2003).

The morphology of the Al grains is also affected by forging. The grains are "pancake-shaped," Fig. 4.33, with the major axis of the grain being perpendicular to the forging axis. The observed anisotropy appears to be a direct result of the constraint on lateral deformation provided by the closed die forging, so the grains are unable to deform equally in all directions.

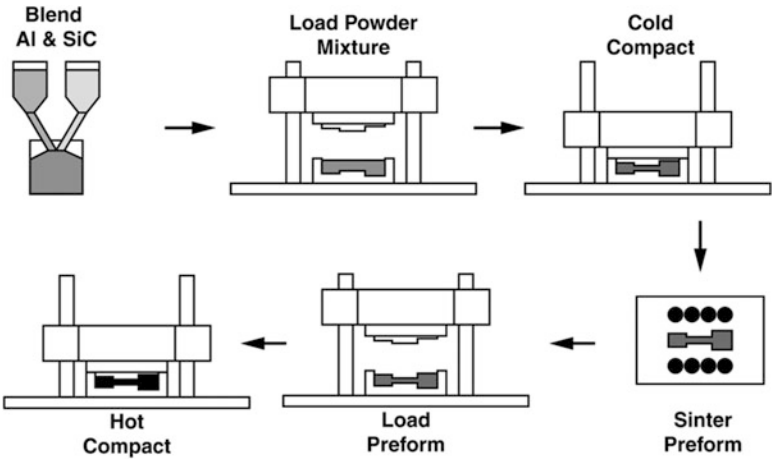

Fig. 4.32 Schematic of near-net-shape sinter-forging technique. A powder mixture of reinforcement and matrix powder is cold compacted, sintered, and forged to nearly full density (Chawla et al. 2003)

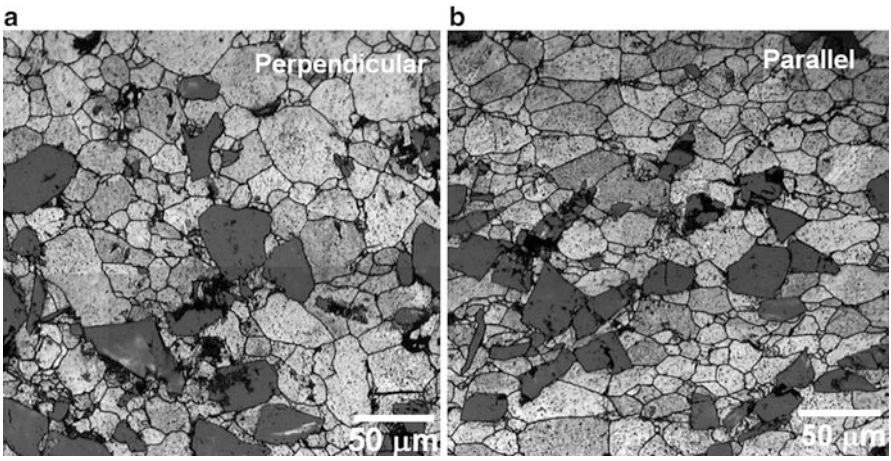

Fig. 4.33 Morphology of Al matrix grains after forging (Chawla et al. 2003): (**a**) perpendicular to forging axis and (**b**) parallel to forging axis. The latter shows that the grains are "pancake shaped," with the major axis of the grain being perpendicular to the forging axis

4.2.4 Pressing and Sintering

A relatively inexpensive and simple technique is pressing and sintering of composite powders. These composite powder systems are typically sintered at a temperature range to obtain some degree of liquid phase. The liquid phase flows through the pores in the compact resulting in densification of the composite (unless interfacial

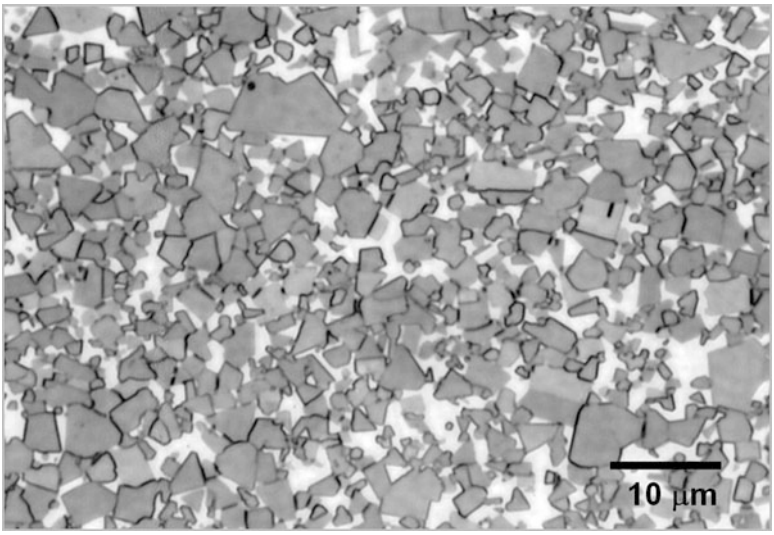

Fig. 4.34 Microstructure of liquid-phase sintered 90 % WC-reinforced Co matrix composite. Note the angular nature of the WC particles (Deng et al. 2001)

reaction takes place). Special mention should be made of WC–Co composites, commonly known as cemented carbides. They are really nothing but very high-volume fraction WC particles distributed in a soft cobalt matrix. These are used extensively for machining and rock- and oil-drilling operations. They are made by liquid-phase sintering because liquid cobalt wets WC very well, the contact angle being 0°, with little or no interfacial reaction. Figure 4.34 shows the microstructure of such a composite, 90 % WC and 10 % Co. Note the angular nature of the WC particles (Deng et al. 2001).

4.2.5 Roll Bonding and Co-extrusion

Roll bonding is a common technique used to produce a laminated composite consisting of different metals in layered form (Chawla and Godefroid 1984). Such composites are called sheet-laminated metal matrix composites. Roll bonding and hot pressing have also been used to make laminates of Al sheets and discontinuously reinforced MMCs (Hunt et al. 1991; Manoharan et al. 1990). Figure 4.35 shows the roll bonding process of making a laminated MMC. Laminated metal matrix composites of two or more dissimilar metals have been made by roll bonding to form a bidimensional composite. Figure 4.36 shows a transmission electron micrograph (TEM) of a roll-bonded Al 1100 and Al 2024-laminated composite, which exhibits the interface with very good integrity (Chawla 1991). A larger

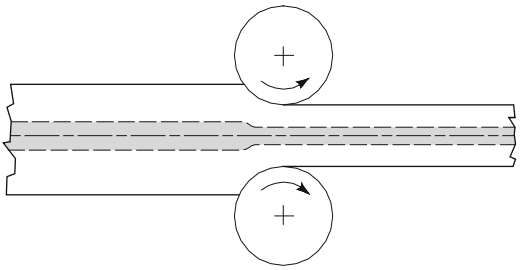

Fig. 4.35 Roll bonding process of making a laminated MMC where a metallurgical bond is produced between the layers

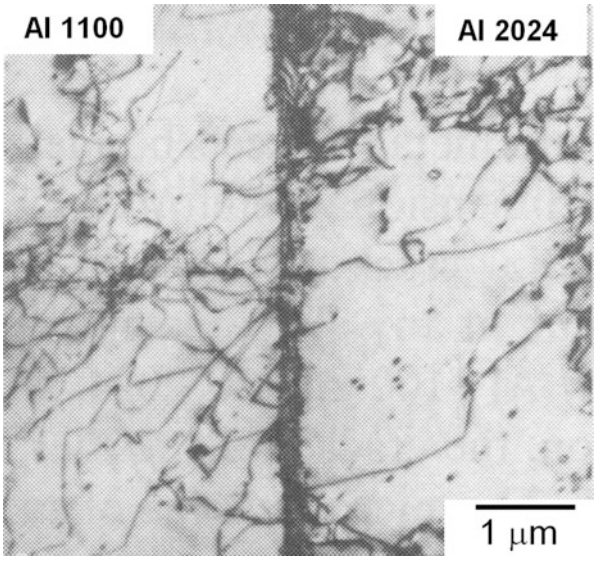

Fig. 4.36 Transmission electron micrograph (TEM) of a roll-bonded Al 1100 and Al 2024 laminated composite, which exhibits an interface with very good integrity (Chawla 1991). A larger dislocation density is observed in the Al 1100 layer, which is softer than Al 2024

dislocation density is observed in the Al 1100 layer, which underwent a larger deformation than Al 2024 during processing.

Other examples of deformation-processed metal matrix composites are niobium-based conventional filamentary superconductors with a copper matrix and high-T_C superconductors with a silver matrix. There are two main types of the conventional niobium-based superconductors: Nb–Ti/Cu and Nb_3Sn/Cu. Niobium–titanium (~50−50) form a ductile system. Rods of Nb–Ti are inserted in holes drilled in a block of copper, evacuated, sealed, and subjected to a series of drawing operations interspersed with appropriate annealing treatments to obtain the final diameter of the composite superconductor, Fig. 4.37. In the case of Nb_3Sn/Cu, a process called the bronze route is used to make this composite. Nb_3Sn, an A-15-type intermetallic, cannot be processed like Nb–Ti because of its extreme brittleness. Instead, the process starts with a bronze (Cu−13 % Sn) matrix; pure niobium rods are inserted in holes drilled in bronze, evacuated, sealed, and subjected to wire-drawing operations as in the case of Nb–Ti/Cu, Fig. 4.38. The critical step is the final heat

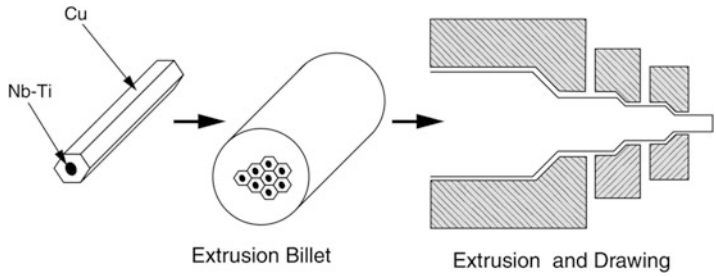

Fig. 4.37 Extrusion-drawing route for fabricating niobium–titanium superconductors. Rods of Nb–Ti are inserted in holes in a block of copper, evacuated, sealed, and subjected to a series of drawing operations interspersed with appropriate annealing treatments to obtain the final composite superconducting wire

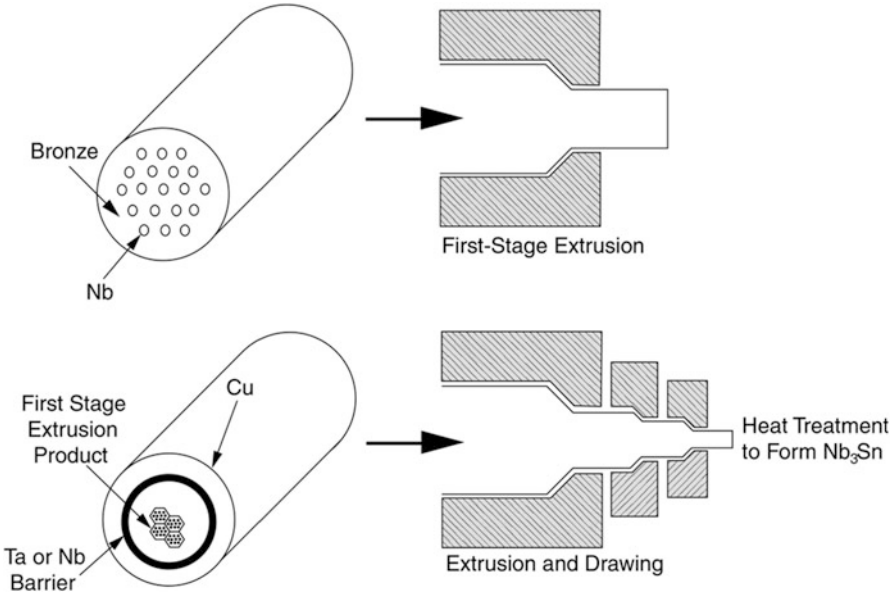

Fig. 4.38 Process for fabricating Nb_3Sn/Cu superconductors. Pure niobium rods are inserted in a bronze (Cu–13 % Sn) matrix, evacuated, sealed, and subjected to wire-drawing operations as in the case of Nb−Ti/Cu. The critical step is the final heat treatment (~700 °C) that drives out the tin from the bronze matrix to form stoichiometric, superconducting Nb_3Sn, leaving behind copper matrix

treatment (~700 °C) that drives out the tin from the bronze matrix to combine with niobium to form stoichiometric, superconducting Nb_3Sn, leaving behind copper matrix. A similar process, called the oxide-powder-in-tube (OPIT) method (Sandhage et al. 1991), can be used to fabricate silver matrix high-T_C superconducting composites. In this process, the oxide powder of appropriate composition (stoichiometry, phase content, purity, etc.) is packed inside a metal

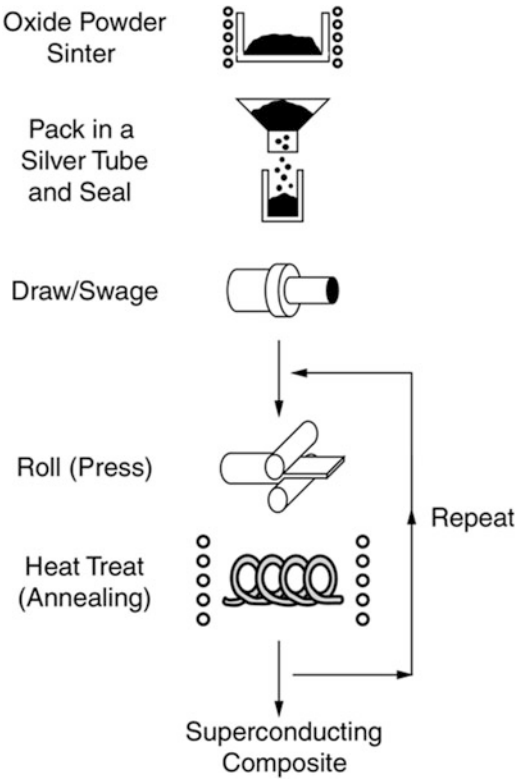

Fig. 4.39 Oxide-powder-in-tube (OPIT) method used to fabricate silver matrix high-T_C superconducting composites. The oxide powder is packed inside a metal tube (generally silver), sealed, and degassed

tube (generally silver), sealed, and degassed, Fig. 4.39. Commonly, swaging and drawing are used for making wires and rolling is used for tapes. Heat treatments, intermediate and/or subsequent to deformation, are given to form the correct phase, promote grain interconnectivity and crystallographic alignment of the oxide, and obtain proper oxygenation (Sandhage et al. 1991).

We now provide a summary of the work on the so-called second-generation (2G) high-temperature superconductor (HTS) that followed the work on first-generation HTS involving silver matrix containing superconducting filaments of $Bi_{1.8}Pb_{0.3}Sr_2Ca_2Cu_3O_{10}$ called BSCCO2223 in short. The driving force for the 2G work was the realization that an HTS with randomly oriented grains will have randomly oriented grain boundaries; such misoriented grain boundaries form obstacles to the flow of superconducting current. If the grains can be aligned, i.e., produce a textured HTS, the flow of current will improve. The approach arrived at, after a considerable amount of work, consisted of epitaxial growth of yttrium–barium–copper–oxide (YBCO) on a textured template of the substrate. The so-called second-generation HTS wire consists of a long substrate in the form of a tape that has a highly textured surface.

A technique developed at Oak Ridge National Laboratory, called RABiTS™ (rolling-assisted biaxial textured substrates), enables the superconducting phase to

have a high degree of grain alignment (Goyal et al. 1996; Goyal et al. 1999). This textured grain structure is required for an efficient flow of current through the superconductor. The RABiTS™ process results in substrates for the HTS wire that are chemically compatible with HTSs and exhibit sharp biaxial texture. Texture refers to the alignment of the grains in the wire. The process is quite complex. Tape of a metal such as nickel or nickel alloy is prepared by special rolling and heat treatment. Next, a buffer layer technology, developed specifically for these textured metals, is used to provide a chemical barrier between the nickel alloy and the superconductor while maintaining the texture. For this, a thin layer of palladium is deposited using electron beam evaporation or sputtering. Metal oxide buffer layers, for example, ceria- and yttria-stabilized zirconia (YSZ), are placed on the tapes by pulsed-laser deposition. These oxide layers maintain the biaxial texture and provide a chemical barrier between the superconductor and the metal tape. This then is a RABiTS™ substrate, ready for application of the superconductor. The HTS YBCO is then deposited on the conditioned surface by pulsed-laser deposition. On this an epitaxial YBCO coating is deposited, which is highly textured and thus achieves the desired high superconducting current density. The term epitaxy means that the orientation of the YBCO coating matches that of the underlying substrate. Thus, the second-generation (2G) HTS wires consist a tape-shaped substrate, on which a thin coating of $YBa_2Cu_3O_7$ (YBCO) is deposited epitaxially so that the grains of YBCO are highly aligned. This then is the basic principle for making of a second generation HTS wire: use a long-length substrate tape with a highly textured interface and an epitaxial YBCO coating replicating the interface texture. This results in a superconductor with high current density.

4.2.6 Diffusion Bonding

Diffusion bonding is a common solid-state processing technique for joining similar or dissimilar metals. Interdiffusion of atoms, at an elevated temperature, from clean metal surfaces in contact with each other, leads to bonding (Partridge and Ward-Close 1993; Guo and Derby 1995). The principal advantages of this technique are the ability to process a wide variety of matrix metals and control of fiber orientation and volume fraction. Among the disadvantages are long processing times, high processing temperatures and pressures (which make the process expensive), and limitation on complexity of shapes that can be produced. There are many variants of the basic diffusion bonding process, although all of them involve simultaneous application of pressure and high temperature. These include:

- Foil–fiber–foil process: A matrix alloy foil or powder cloth (a mixture of matrix powder and a fugitive organic binder) and fiber arrays (composite wire) are stacked in a predetermined order, as shown in Fig. 4.40. The stacked layers are vacuum hot pressed so that diffusion bonding may take place. Hot isostatic

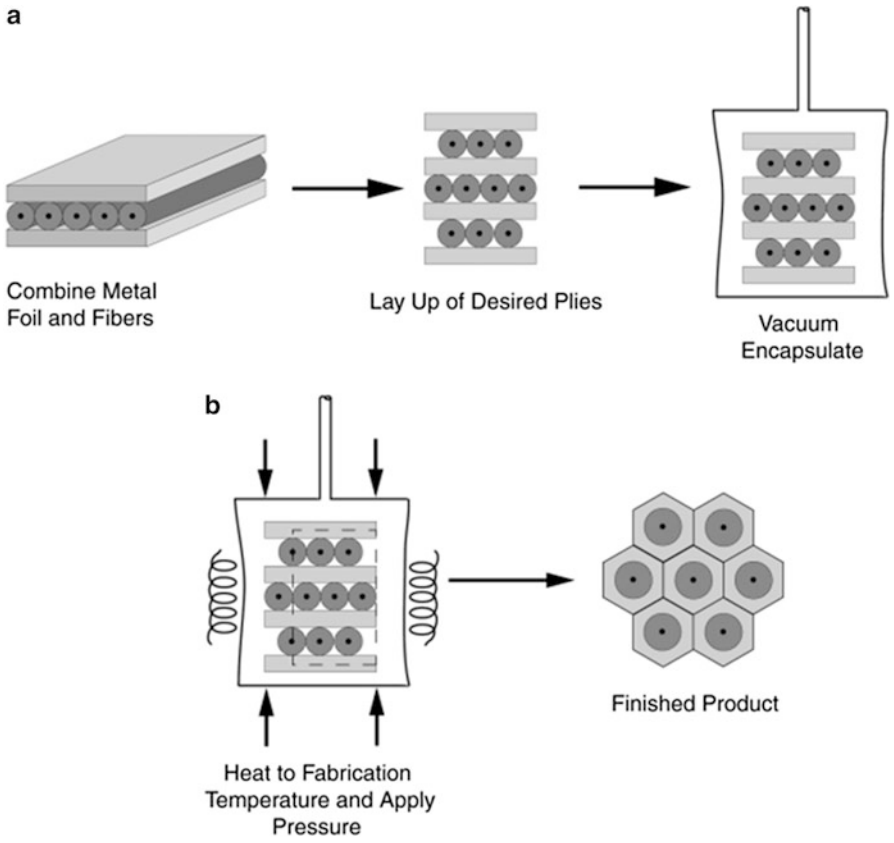

Fig. 4.40 Foil–fiber–foil diffusion bonding process: (**a**) apply metal foil and cut to shape, (**b**) lay up desired plies, (**c**) vacuum encapsulate and heat to fabrication temperature, (**d**) apply pressure and hold for consolidation cycle, and (**e**) cool, remove, and clean part

pressing (HIP), instead of uniaxial pressing, can also be used. In HIP, gas pressure against a can consolidates the composite piece inside the can. With HIP it is relatively easy to apply high pressures at elevated temperatures with variable geometries. This process is clearly suited for flat products, although corrugated structures have also been produced.

- Matrix-coated fiber process: In this, the fibers are coated with the matrix material by plasma spraying or some type of physical vapor deposition (PVD) process, Fig. 4.41. The uniformity of fiber spacing is easier to control and the fibers can be handled more easily, without inducing defects deleterious to fiber strength. Depending on the flexibility of the fibers, the coated fibers may also be wound on a drum. Since the matrix volume fraction is dependent on the thickness of matrix on each fiber, very high volume fraction loading (~80 vol.%) may be obtained. It should be noted that the fiber or fiber coatings may react or be damaged by the high impact velocity of the liquid droplets.

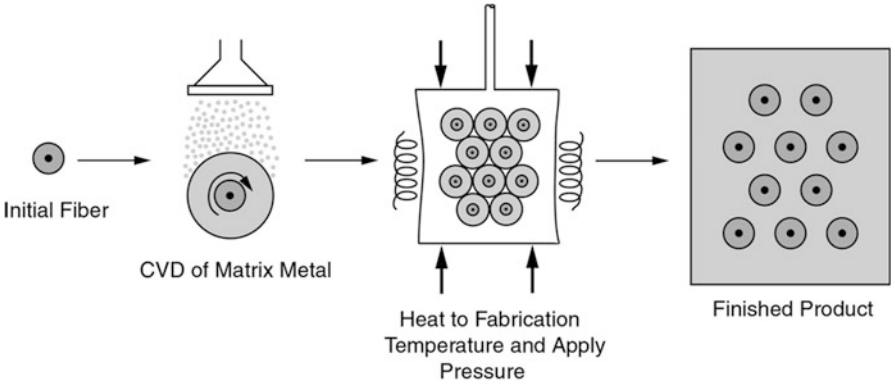

Fig. 4.41 Matrix-coated fiber process. The fibers are coated with the matrix material by plasma spraying or some type of physical vapor deposition (PVD) process

Fiber distribution is extremely important in controlling mechanical properties. In particular, fiber-to-fiber contact or very close spacing between fibers can result in very high, localized stress concentrations which will result in fiber cracking and/or matrix damage during processing, and premature damage, cracking and failure of the composite, under an applied load.

4.2.7 Explosive Shock Consolidation

A fairly novel, high strain rate, rapid solidification technique is explosive shock consolidation (Thadhani 1988; and Thadhani et al. 1991). In this technique, the dynamic compaction and/or synthesis of powders can be achieved by means of shock waves generated by either explosives in contact with the powder or high-velocity impact from projectiles, Fig. 4.42. This process is particularly attractive for consolidating hard materials such as ceramics or composites. Figure 4.43 shows an optical micrograph of a Ti_3Al particle-reinforced TiB_2 composite. In this composite, the Ti_3Al particles were mixed with TiB_2 powder. The TiB_2 then formed a continuous matrix phase around the Ti_3Al particles.

4.3 Gaseous-State Processing

4.3.1 Physical Vapor Deposition

Plasma spraying is the primary form of gaseous-state processing. The main application of plasma spraying was described above, to form matrix-coated fibers, which are subsequently hot pressed to form the final product. In addition, laminated

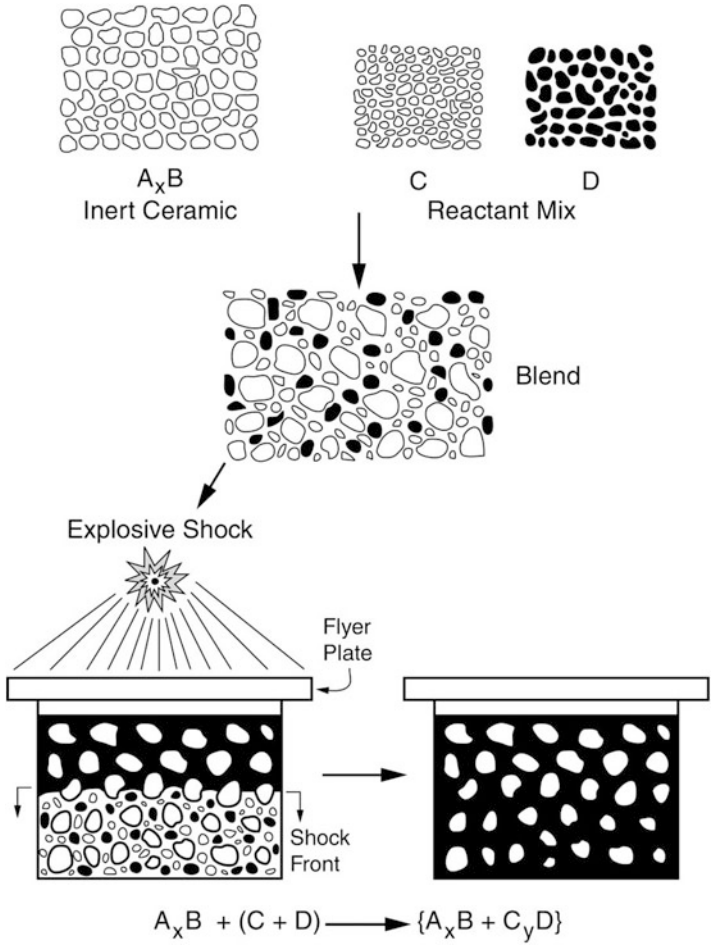

Fig. 4.42 Dynamic compaction and/or synthesis of powders achieved by means of large shock waves generated by either explosives in contact with the powder or high-velocity impact from projectiles

composites, particularly on the nanometer scale, have been processed by PVD with a great deal of success. PVD processes (specifically, sputter deposition-based processes) offer an extremely wide range of possibilities for fabricating nanolaminate microstructures with tailored chemistry, structure, and thickness of the individual layers and interfaces. Additional important PVD processing parameters include reactive deposition (Ji et al. 2001), plasma-assisted deposition (O'Keefe and Rigsbee 1994), and substrate heating (Misra et al. 1998).

Some metal/metal-layered systems, such as Ni–Cu and Ni–Ti, have been processed at the nanoscale by sputter deposition with great success (Misra et al. 1998; Misra and Nastasi 1999). An example of a nanoscale Cu–Ni multilayer

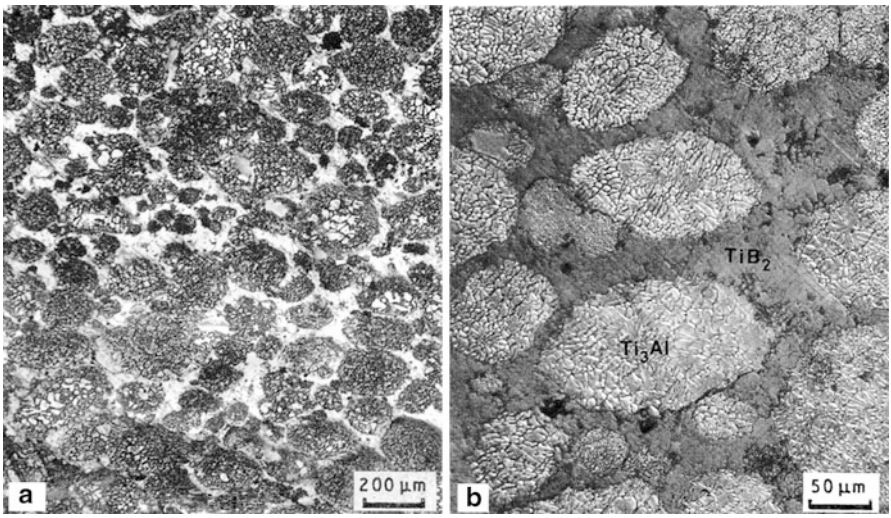

Fig. 4.43 Optical micrographs of Ti_3Al particle reinforced TiB_2 composite (Thadhani et al. 1991). Ti_3Al particles were mixed with TiB_2 powder and formed a continuous matrix phase around the Ti_3Al particles. (**a**) low magnification picture (**b**) high magnification picture with phases indicated

with a bilayer period of 5 nm is shown in Fig. 4.44 (Misra et al. 1998). Note the well-defined layered structure. The corresponding selected area diffraction pattern (inset) shows a <001> growth direction and cube-on-cube orientation relationship between FCC Cu and FCC Ni. A challenge in the synthesis of nanolaminates via the PVD approach is the control of intrinsic residual stresses. Some control over residual stresses has been achieved by energetic particle bombardment, either in situ or postdeposition using an ion source. In the case of magnetron sputtering, a negative substrate bias may be sufficient to change the residual stress from tensile to compressive (Misra and Nastasi 1999). A film deposited with low bombardment energy yields a tensile residual stress and a microstructure with nanoscale columnar porosity/cracking for a sputtered 150 nm thick Cr film. The same material sputtered with a negative bias, on the other hand, yields a nanocrystalline film with an equiaxed grain structure, near-zero residual stress, and, thus, no intergranular porosity.

While metal/metal systems exhibit high strengths, metal/ceramic systems have the advantage of combining the superior properties of both ceramics and metals (Chou et al. 1992; He et al. 1998; Meartini and Hoffman 1993; Ding et al. 1995; Deng et al. 2005; Chawla et al. 2008). Systems such as Al–SiC and Al–Al_2O_3 have been investigated. Deng et al. (2005) have fabricated nanolayered Al–SiC composites by RF magnetron sputter deposition. The deposition rates of Al and SiC are shown in Fig. 4.45. Note that because of the higher hardness of the SiC, removal of the SiC atoms from the substrate is more difficult, for a given beam energy, resulting in a lower deposition rate than for Al. The microstructure of an Al–SiC nanolayered composite is shown in Fig. 4.46. The interfaces are well bonded and the layers relatively planar.

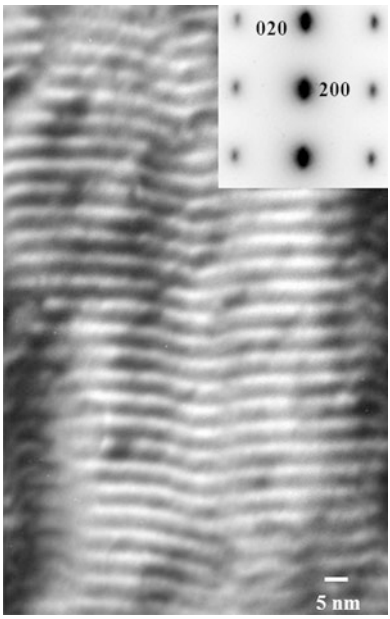

Fig. 4.44 TEM micrograph of Cu–Ni multilayer with a bilayer period of 5 nm, by PVD (courtesy of A. Misra). Note the well-defined layered structure

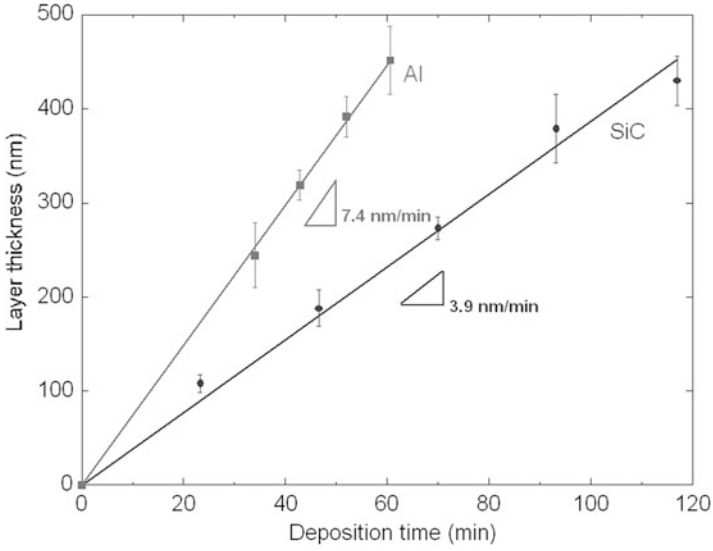

Fig. 4.45 Layer thickness versus deposition time from PVD of Al and SiC (Deng et al. 2005). Since the SiC is harder, the deposition rate is lower

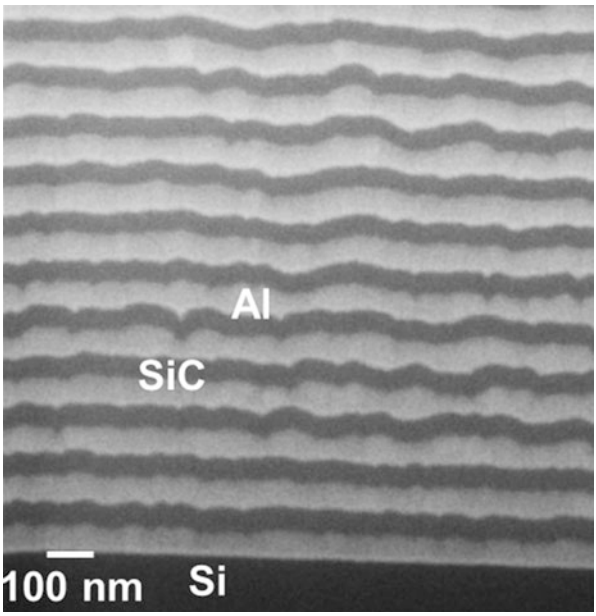

Fig. 4.46 SEM micrograph showing the microstructure of an Al/SiC-nanolayered composite (Chawla et al. 2008). The layers are approximately 50 nm in thickness. The interfaces are well bonded and the layers relatively planar

References

Aghajanian, M.K., J.T. Burke, D.R. White, and A.S. Nagelberg (1989), *SAMPE Quarterly*, **34**, 817–823.
Anderson, I.E., and J.C. Foley (2001), *Surf. Int. Anal.*, **31**, 599–608.
Chawla, K.K. (1991), in *Metal Matrix Composites*: *Mechanisms and Properties* (R.K. Everett and R.J. Arsenault, eds.) Academic Press, New York, pp. 235–253.
Chawla, K.K., and L.B. Godefroid (1984), *Proceedings of the 6th International Conference on Fracture*, Pergamon Press, Oxford, U.K., p. 2873.
Chawla, K.K. (2012), *Composite Materials: Science and Engineering*, 3rd ed., Springer, New York
Chawla, N., C. Andres, J.W. Jones, and J.E. Allison (1998), *Metall. Mater.Trans.*, **29A**, 2843.
Chawla, N., J.J. Williams, and R. Saha (2003), *J. Light Metals*, **2**, 215–227.
Chawla, N., D.R.P. Singh, Y.-L. Shen, G. Tang, and K.K. Chawla (2008), *J. Mater. Sci.*, **43**, 4383–4390.
Chou, T.C., T.G. Nieh, T.Y. Tsui, G.M. Pharr, and W.C. Oliver (1992), *J. Mater. Res.*, **7** 2765–2773.
Christodolou, L., P.A. Parrish, and C.R. Crowe (1988), *Mat. Res. Soc. Symp. Proc.*, **120**, 29.
Cisse, J., and G.F. Bolling (1971), *J. Cryst. Growth*, **11**, 25–28.
Cole, G.S., and G.F. Bolling (1965), *Trans. Metall. Soc. AIME*, **233**, 1568–1572.
Deng, X., C. Cleveland, T. Karcher, M. Koopman, N. Chawla, and K.K. Chawla (2005), *J. Mater. Eng. Perf.*, **14**, 417–423.
Deng, X., B.R. Patterson, K.K. Chawla, M.C. Koopman, Z. Fang, G. Lockwood, A. Griffo (2001) *Int. J. Refrac. Metals & Hard Mater.*, **19**, 547–552.
Ding, Y., D.O. Northwood, and A.T. Alpas (1995), *Mater. Sci. Forum*, **189**, 309–314.
Dirichlet, G.L. (1850), *J. Reine Angew. Math.* **40**, 209–227.
Divecha, A.P., S.G. Fishman, and S.D. Karmarkar (Sept. 1981), *J. Metals*, **9**, 12.

Einstein, A. (1906), *A. Ann. Phys.* **19**: 289.
Estrada, J.L., J. Duszczyk, and B.M. Korevaar (1991), *J. Mater. Sci.*, **26**, 1631–1634.
Ganesh, V.V., and N. Chawla (2004), *Metall. Mater. Trans.*, **35A**, 53–62.
Ganesh, V.V., and N. Chawla (2005), *Mater. Sci. Eng.*, **A391**, 342–353.
Ghosh, A.K. (1993), in **Fundamentals of Metal Matrix Composites**, Butterworth-Hinemann, Stoneham, MA, pp. 3–22.
Goyal, A., D.P. Norton, D.K. Christen, E.D. Specht, M. Paranthaman, D.M. Kroeger, J.D. Budai, Q. He, F.A. List, R. Feenstra, H.R. Kerchner, D.F. Lee, E. Hatfield, P.M. Martin, J. Mathis, and C. Park (1996), *Appl. Supercon.*, **4**, 403–427.
Goyal, A., R. Feenstra, F.A. List, D.P. Norton, M. Paranthaman, D.F. Lee, D.M. Kroeger, D.S. Beach, J.S. Morell, T.G. Chirayil, D.T. Verebelyi, X. Cui, E.D. Specht, D.K. Christen, and P.M. Martin (1999), *JOM*, July, 19–23.
Guo, Z.X., and B. Derby (1995), *Prog. Mater. Sci.*, **39**, 411–495.
Guth, E., Simha, R. (1936), *Kolloid Z.***74** (3): 266.
He, J.L., W.Z. Li, H.D. Li, and C.H. Liu (1998), *Surf. Coatings Tech.*, **103**, 276–280.
Helinski, E.J., J.J. Lewandowski, T.J. Rodjom, and P.T. Wang (1994), in **World P/M Congress**, **vol. 7**, (C. Lall and A. Neupaver, eds.), Metal Powder Industries Federation, Princeton, NJ, pp. 119–131.
Humphreys, F.J., W.S. Miller, and M.R. Djazeb (1990), *Mater. Sci. Tech.*, **6**, 1157–66.
Hunt, W.H., T. M. Osman, and J. J. Lewandowski (Mar. 1991), *JOM*, **43**, 30−35.
Hunt, W.H. (1994), in *Processing and Fabrication of Advanced Materials*, The Minerals and Metal Materials Society, Warrendale, PA., pp. 663−683.
James, W.B., (1985), *Int. J. Powder Metall.*, **21**, 163.
Ji, Z., J.A. Haynes, M.K. Ferber and J.M. Rigsbee (2001), *Surf. Coatings Tech.*, **135**, 109–117.
Katsura, M. (1982), Japan Pat. 57–25275.
Kim, J.K., and P.K. Rohatgi (1999), *Metall. Mater. Trans.*, **29A**, 351–358.
Kim, Y.W., W.M. Griffith, and F.H. Froes (1985), *J. Metals*, **37**, 27–33.
Kitano, T., Kataoka, T., and Shirota, T. (1981), *Rheologica Acta***20** (2): 207.
Kowalski, L., B.M. Korevaar, and J. Duszczyk (1992), *J. Mater. Sci.*, **27**, 2770–2780.
Lavernia, E.J., J.D. Ayers, and T.S. Srivatsan (1992), *Int. Mater. Rev.*, **37** 1–44.
Lewandowski, J.J., C. Liu, and W.H. Hunt (1989), *Mater. Sci. Eng.*, **A107**, 241–255.
Liu, Y.L., N. Hansen, and D.J. Jensen (1989), *Metall. Trans.*, **20A**, 1743–1753.
Lloyd, D.J. (1989), Comp. Sci. Tech., **35**, 159–179.
Lloyd, D.J. (1994), *Int. Mater. Rev.*, **39**, 1.
Lloyd, D.J. (1997), in *Composites Engineering Handbook* (P.K. Mallick, ed.), Marcel Dekker, New York, pp. 631–669.
Logsdon, W.A., and P.K. Liaw (1986), *Eng. Frac. Mech.*, **24**, 737–751.
McLean, M. (1983), *Directionally Solidified Materials for High Temperature Service*, The Metals Soc., London.
Martin Marietta Corp., U.S. Patent 4,710,348 (1987).
Manoharan, M., L. Ellis, and J. J. Lewandowski (1990), *Scripta Met. et Mater.,* **24**, 1515−1521.
Meartini, G.T., and R.W. Hoffman (1993), *J. Elec. Mater.*, **22**.
Mehrabian, R., R.G. Riek, and M.C. Flemings (1974), *Metall. Trans.*, **5**, 1899–1905.
Michaud, V.C. (1993), in *Fundamentals of Metal Matrix Composites*, Butterworth-Heinneman, Stoneham, MA, pp. 3–22.
Misra, A., M. Verdier, Y.C. Lu, H. Kung, T.E. Mitchell, M. Nastasi, and J.D. Embury (1998), *Scripta Mater.*, **39**, 555.
Misra, A., and M. Nastasi (1999), *J. Mater. Res.*, **14**, 4466.
Mortensen, A., and I. Jin (1992), *Inter. Mater. Rev.*, **37**, 101–128.
Nourbakhsh, S., F.L. Loang, and H. Margolin (1990), *Metall. Trans.*, 21A, 213.
O'Keefe, M.J., and J.M. Rigsbee (1994), *J. App. Polymer Sci.*, **53** 1631–1638.
Partridge, P.G., and C.M. Ward-Close (1993), *Int. Mater. Rev.*, **38**, 1–24.

Pennander, L., and C.-H. Anderson (1991), in *Metal Matrix Composites – Processing, Microstructure and Properties*, 12thRiso Int. Symp. On Materials Science, (N. Hansen et al., eds.) 575.

Potschke, J., and V. Rogge (1989), *J. Cryst. Growth*, **94**, 726–738.

Saha, R., E. Morris, N. Chawla, and S.M. Pickard (2000), *J. Mater. Sci. Lett.*, 337–339.

Sahoo, P., and M.J. Koczak (1991), *Mater. Sci. Eng.*, **A144**, 37–44.

Sandhage, K.H., G.N. Riley, Jr., and W. L. Carter (Mar. 1991), *J. Miner. Metal. Mater. Soc.*, **43**, 21.

Shangguan, D., S. Ahuja, and D.M. Stefanescu (1992), *Metall. Trans.*, **23A**, 669–680.

Shekhar, J.A., and R. Trivedi (1989), *Mater. Sci. Eng.*, **A114**, 133–146.

Shekhar, J.A., and R. Trivedi (1990), in *Solidification of Metal Matrix Composites*, P. Rohatgi, ed., TMS, pp. 23.

Spowart, J.E., B. Maruyama, and D.B. Miracle (2001), *Mater. Sci. Eng.*, **A307**, 51–66.

Srivatsan, T.S., and E.J. Lavernia (1992), *J. Mater. Sci.*, **27**, 5965.

Stefanescu, D.M., B.K. Dhindaw, A.S. Kakar, and A. Mitra (1988), *Metall. Trans.*, **19A**, 2847–2855.

Thadhani, N.N. (1988), *Adv. Mater. Manuf. Proc.*, **3**, 493–549.

Thadhani, N.N., N. Chawla, and W. Kibbe (1991), *J. Mater. Sci.*, **26**, 232–240.

Tham, L.M., M. Gupta, and L. Cheng (2002), *Mater. Sci. Eng.*, **326**, 355–363.

Thomas, D.G. (1965), *J. Colloid. Sci.*, **20**, 267.

Trivedi, R., S.H. Han, and J.A. Shekhar (1990), in *Solidification of Metal Matrix Composites*, P. Rohatgi, ed., TMS, p. 23.

Uhlmann, D.R., B. Chalmers, and K.A. Jackson (1964), *J. Appl. Phys.*, **35**, 2986–2993.

Williams, J.J., G. Piotrowski, R. Saha, and N. Chawla (2002), *Metall. Mater. Trans.*, **33A**, 3861–3869.

Yang, N., J. Boselli, and I. Sinclair (2001), *J. Micros.*, **201**, 189–200.

Chapter 5
Interface

Interface is a very general term used in different fields of science and technology to denote the location where two entities meet. The term in composites refers to a bounding surface between the reinforcement and matrix across which there occurs a discontinuity in a parameter such as chemical composition, elastic modulus, coefficient of thermal expansion (CTE), and thermodynamic properties such as chemical potential. Interface (fiber/matrix or particle/matrix) is very important in all kinds of composites. This is because in most all composites, the interfacial area per unit volume is very large. Also, in most metal matrix composite (MMC) systems, the reinforcement and the matrix will not be in thermodynamic equilibrium, i.e., there will be a thermodynamic driving force for an interfacial reaction that will reduce the energy of the system. All these items make the interface to have very important influence on the properties of the composite.

Mathematically, an interface is a bidimensional boundary. In practice, we have an interfacial zone with a finite thickness and possibly consisting of multiple layers. The multilayer boundary zone will be in equilibrium at the high temperature at which the components are originally brought together. At any other temperature, there exists a complex stress field in the boundary zone because of the mismatch in the CTE of the various layers. These stresses will be proportional to the difference in the elastic moduli, difference in the coefficients of thermal expansion, and of course the amplitude of temperature difference between the equilibrium (or initial) temperature and the final temperature. Thermodynamically speaking, the phases in the boundary zone will tend to change such that the free energy of the system is minimized. This may involve generation of dislocations, grain boundary migration, crack nucleation, and/or propagation. An ideal interface in a MMC should promote wetting and bond the reinforcement and the matrix to a desirable degree. The interface should protect the ceramic reinforcement and allow load transfer from the soft metallic matrix to the strong reinforcement.

Besides the compositional parameter, we also need to take into account some other parameters that characterize the interfacial zone, for example, geometry and dimensions; microstructure and morphology; and mechanical, physical, chemical,

N. Chawla and K.K. Chawla, *Metal Matrix Composites*,
DOI 10.1007/978-1-4614-9548-2_5, © Springer Science+Business Media New York 2013

and thermal characteristics of different phases that might be present in the interfacial zone. Initially the components of a composite system are chosen on the basis of their mechanical and physical characteristics in isolation. When one puts together two components to make a composite, the composite will rarely be a system in thermodynamic equilibrium. More often than not, there will be present a driving force for some kind of interfacial reaction(s) between the two components leading to a state of thermodynamic equilibrium for the composite system. Of course, thermodynamic information such as phase diagrams can help predict the final equilibrium state of the composite. Data regarding reaction kinetics, for example, diffusivities of one constituent in another can provide information about the rate at which the system would tend to attain the equilibrium state. In the absence of thermodynamic and kinetic data, experimental studies would have to be done to determine the compatibility of the components.

In this chapter, we first describe some important concepts related to interfaces in MMCs, types of bonding in MMCs with examples from various systems, followed by a description of some tests to determine the mechanical properties of interfaces.

5.1 Crystallographic Nature of the Interface

In crystallographic terms, one can describe an interface between two crystalline phases as coherent, semi-coherent, or incoherent. A coherent interface implies a one-to-one correspondence between lattice planes on the two sides of the interface. The lattice constants of any two phases are not likely to be exactly the same. Thus, in order to provide continuity of lattice planes across an interface, i.e., a coherent interface, there will be some coherency strains associated with the interface because of the straining of the lattice planes in the two phases. Commonly, such coherent interfaces are observed between some precipitates and the metallic matrix where the mismatch in the lattice parameter of the two phases is quite small. For example, in the Al–Li system, Al_3Li precipitate is coherent with aluminum matrix. An incoherent interface, on the other hand, consists of such severe atomic disorder that no matching of lattice planes occurs across the boundary, i.e., no continuity of lattice planes is maintained across the interface. Thus, an incoherent boundary or interface will have no coherency strains, but the energy associated with the interfacial boundary is high because of severe atomic disorder associated with such an interface. A situation that is intermediate between coherent and incoherent can exist, i.e., we can have a semi-coherent interface. A semi-coherent interface has some lattice mismatch between the phases which can be accommodated by the introduction of dislocations at the interface. Crystallographically, most of the interfaces that one encounters in fiber-, whisker-, or particle-reinforced MMCs are incoherent and high-energy interfaces. Accordingly, they can act as efficient vacancy sinks and provide rapid diffusion paths, segregation sites, sites of heterogeneous precipitation, as well as sites for precipitate-free zones. Among the

possible exceptions to this are the eutectic composites and the XD-type particulate composites wherein particles are dispersed exothermically into a metal matrix, in which the interfaces can be semi-coherent.

5.2 Wettability

Wettability is defined as the ability of a liquid to spread on a solid surface. Figure 5.1 shows two conditions of a liquid drop resting on a solid substrate. There are three specific energy (energy per unit area) terms: γ_{SV}, the energy of the solid–vapor interface; γ_{LS}, the energy of the liquid–solid interface; and γ_{LV}, the energy of the liquid–vapor interface. It should be mentioned here that the term surface tension is also used to denote surface energy, although rigorously speaking, surface energy is more appropriate term for solids. When we put a liquid drop on a solid substrate, we replace a portion of the solid–vapor interface by a liquid–solid and a liquid–vapor interface. Thermodynamically, spreading of the liquid will occur if this results in a decrease in the free energy of the system, i.e.,

$$\gamma_{SL} + \gamma_{LV} < \gamma_{SV}$$

Figure 5.1 serves to define these terms. An important parameter in regard to wettability is the contact angle, θ, which is a measure of wettability for a system. From the equilibrium of forces in the horizontal direction, we can write

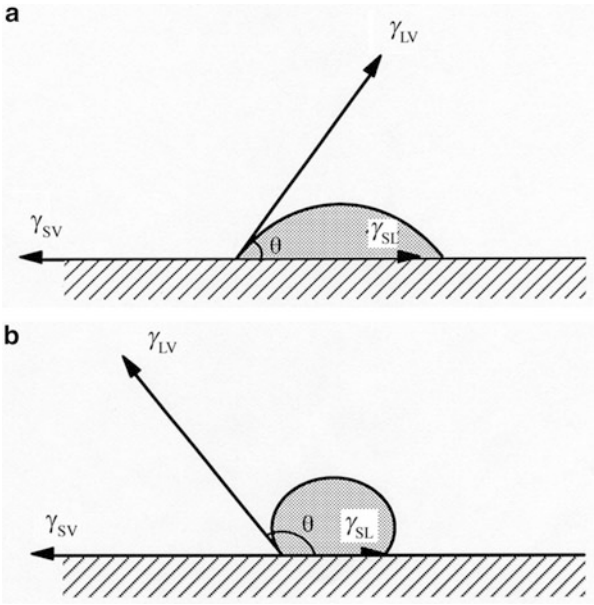

Fig. 5.1 Contact angle, θ, a measure of wettability for a system, is defined by interaction among three surface energies: γ_{SL} solid–liquid surface energy, γ_{SI} solid–vapor surface energy, γ_{LV} liquid–vapor surface energy

$$\gamma_{SL} + \gamma_{LV}\, cos\theta = \gamma_{SV}$$
$$\theta = \cos^{-1}(\gamma_{SV} - \gamma_{SL})/\gamma_{LV}$$

From this equation, we see that for $\theta = 0^\circ$, we have perfect wetting, while for $\theta = 180^\circ$, we have no wetting. For $0^\circ < \theta < 180^\circ$, there will be partial wetting. It should be pointed out that the contact angle for a given system can vary with temperature, stoichiometry, hold time, interfacial reactions, presence of any adsorbed gases, roughness and geometry of the substrate, etc.

It is worth emphasizing that wettability only describes the extent of intimate contact between a liquid and a solid. It does not necessarily mean a strong bond at the interface. One can have excellent wettability but only a weak physical, low energy bond. A low contact angle, implying good wettability, is a necessary but not sufficient condition for strong bonding. Wettability of ceramic reinforcement by molten metal is very important for liquid-state processing of MMCs. One can modify the contact angle by changing the composition of the liquid matrix, which changes the value of its surface energy. The effect of roughness of the solid substrate can be evaluated in terms of a ratio, r, defined as

$$r = \frac{\text{true surface area}}{\text{mean plane surface area}}$$

In general, if $\theta < 90^\circ$, wettability is enhanced by roughness while if $\theta > 90^\circ$, wettability is reduced by roughness.

5.3 Types of Bonding

There are two important types of bonding at an interface in a MMC:

- Mechanical bonding
- Chemical bonding

A brief description of mechanical and chemical bonding is given below with examples from various MMC systems.

5.3.1 Mechanical Bonding

Most fibers have a characteristic surface roughness or texture resulting from the fabrication process used. This, in turn, imparts a roughness to the interface when the fibers are incorporated in a matrix to make a composite. Mechanical keying of the matrix into the hills and valleys of the surface (due to roughness) of the reinforcement is an important but generally neglected aspect of the interface in all composites. It turns out that interface roughness-induced mechanical bonding is

quite important in all kinds of composites. What is important to realize is that this surface roughness of the reinforcement can contribute to bonding only if the liquid matrix wets the reinforcement surface. If the liquid matrix (polymer, metal, or ceramic) is unable to penetrate the asperities on the fiber surface, then the matrix will leave interfacial voids on solidification. In a mechanical bond, the degree of interfacial roughness is a very important parameter, which, in turn, is controlled by the fiber surface roughness. We digress a bit to point out some key differences among the three types of composites. In polymer matrix composites (PMCs) and MMCs, one would like to have mechanical bonding in addition to chemical bonding. In ceramic matrix composites (CMCs), one would like to have mechanical bonding than chemical bonding. It should be mentioned that in fiber-reinforced composites, mechanical bonding will be effective mostly in the longitudinal or fiber direction. Transverse to the fiber, it will provide only a minor effect.

Mechanical keying between two surfaces can lead to bonding between them and can be quite important in MMCs. An ideal, smooth interface is only an idealization. Interfaces in real composites are invariably rough, which allows for interlocking. The degree of interfacial roughness can be controlled to some extent, but there is always some mechanical bonding present. Consider the situation of a likely MMC made of a ceramic reinforcement and a metallic matrix. Metals generally have a higher CTE than ceramics. Consider the events in the radial direction of the fiber during cool down from the processing temperature. The metallic matrix in a composite will shrink radially more than the ceramic fiber on cooling from a high temperature. This would lead to a mechanical gripping of the fiber by the matrix even in the absence of any chemical bonding. The matrix penetrating the crevices on the fiber surface, by liquid flow or high-temperature diffusion, can contribute to mechanical bonding. The radial gripping stress, σ_r, can be related to the interfacial shear strength, τ_i, by the following expression:

$$\tau_i = \mu\sigma_r$$

where μ is the coefficient of friction, generally, between 0.1 and 0.6. In general, mechanical bond is a low energy bond vis-à-vis a chemical bond.

Mechanical keying of the matrix into the pores and surface roughness of the reinforcement is what gives us the mechanical bond. Thus, the surface roughness is an important contributor to mechanical bonding. However, roughness-induced mechanical bonding will come into play only if the liquid matrix wets the reinforcement surface. If the molten metal matrix is unable to penetrate the asperities on the fiber surface, then the matrix will solidify and leave interfacial voids! Examples of mechanical bonding include carbon fibers in a variety of metals and Al_2O_3 fiber in aluminum. Mechanical bonding with carbon fibers is improved by chemically treating the surface with nitric acid. This is called oxidation and it results in increased specific surface area of the fibers.

We cite two examples showing the importance of mechanical gripping effects in MMCs. Hill et al. (1969) confirmed this experimentally for tungsten filaments in an aluminum matrix while Chawla and Metzger (1978) observed mechanical gripping

effects at Al_2O_3/Al interfaces. Hill et al. etched tungsten wires along a portion of their length to produce a rough interface. The tungsten filaments were then incorporated into an aluminum matrix by the liquid metal infiltration technique in vacuum. They evaluated three interface conditions by longitudinal tensile tests of composites. In the first case, they used unetched fibers, a smooth interface resulted, and a chemical bond formed between the aluminum matrix and tungsten fiber, which resulted in a high-strength composite. In the second case, they coated the fibers with a graphite layer; the graphite barrier layer prevented the reaction from taking place, that is, there was no chemical bonding, and because the interface was smooth, there was also very little mechanical bonding. The resultant strength of the composite was, therefore, very low. In the third case, they etched the tungsten filaments and applied a graphite layer. In this case, there was no reaction bonding, but there was a mechanical keying effect because of the rough surface produced by etching. The result was that the mechanical bonding restored the strength of the composite to the level achieved with chemical reaction at the interface. Chawla and Metzger (1978) compared the load transfer from aluminum to alumina as a function of interfacial roughness. They used a polished aluminum surface and roughened aluminum surface. They introduced roughness by etch-pitting. Alumina was formed by electrolytically anodizing the aluminum. When this composite was loaded in tension, the cracks appeared in alumina perpendicular to the loading direction. Figure 5.2 shows these results in the form of linear crack density (number of cracks per unit length) in alumina as a function of strain in an alumina/aluminum composite for different degrees of interface roughness. Solid circles represent the polished substrate or smooth interface while filled squares represent steep-sided pits (10^6 pits/cm^2) or rough interface. Cracks in alumina first appeared at about the same strain and initially the crack density rose at about the same rate for the rough and smooth interfaces. However, for a smooth interface, the crack density remained constant above 8 % strain in the matrix while for a rough interface, the crack density continued to increase beyond this value, i.e., in the case of a rough interface, the load transfer from aluminum to alumina continued to higher strain values than in the case of a smooth interface. Thus, mechanical bonding at the rough interface was responsible for the load transfer from the soft aluminum matrix to hard alumina.

5.3.2 Chemical Bonding

Ceramic/metal interfaces in MMCs are generally formed at high temperatures. Diffusion and chemical reaction kinetics are faster at elevated temperatures. Knowledge of the chemical reaction products and, if possible, their properties are needed. It is therefore imperative to understand the thermodynamics and kinetics of reactions such that processing can be controlled and optimum properties obtained.

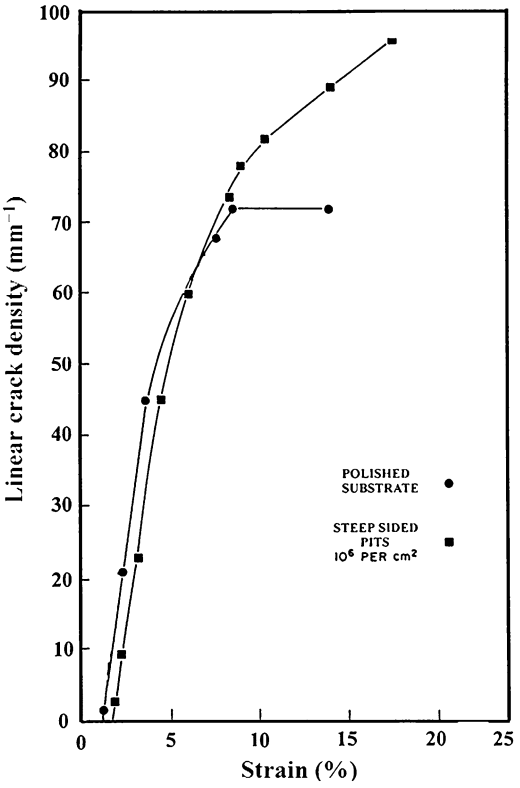

Fig. 5.2 Load transfer from aluminum to alumina as a function of interfacial roughness (After Chawla and Metzger 1978). For a smooth interface, the crack density remained constant above 8 % strain in the matrix, while for a rough interface, the crack density continued to increase beyond this value, i.e., the load transfer from aluminum to alumina continued to higher strain values in the case of a rough interface

Techniques for Measuring Roughness

Most fibers have surface markings or *striations* that originate from the edges of the surface of the spinneret or the edges of die in the case of wire drawing. Thus, the origin of surface roughness lies in the processing of fibers. Such roughness is characterized by rather close and irregular changes in the surface height, resulting in peaks and valleys about an imaginary mean surface line. There is a whole range of techniques available for measuring surface roughness. In a mechanical profilometer, a diamond stylus is run over the surface, and the up and down movement of the stylus is recorded. Atomic force microscopy (AFM) can offer a greater spatial resolution than any of the conventional techniques. Best mechanical profilometer can resolve variations in surface heights down to 0.1 μm, while AFM can resolve as small as 1 nm. Scanning tunneling microscope (STM) can be used to characterize an electrically conducting surface. STM detects changes in the quantum-mechanical tunneling current of electrons between the surface and an electrode (W or Pt)

(continued)

(continued)

as the electrode scans the surface in a raster mode. The magnitude of tunneling current decreases with distance between the electrode and the surface, which can be used to provide information about the topography of the surface. AFM can characterize most any material, including an electrically insulating material such as a glass or a ceramic. Commonly a silicon or silicon nitride tip is used at the end of a microcantilevered arm. Atomic forces (van der Waals or electrostatic) between the tip and the surface deflect the arm, with the deflection falling off with distance from the surface.

The deflection is higher where the peaks are and it is lower where the valleys are. A laser beam from a laser diode is reflected off the back of the cantilever with an optical lever detection system. Conventionally, a stylus-based profilometer provides height information in one direction. In this regard, AFM can be regarded as a high-magnification profilometer that has a superior vertical and lateral resolution. AFM is controlled by a microprocessor that provides a variety of computer-based topographical images of the surface. For example, a grayscale image can be obtained, in which x and y data from the horizontal and vertical axes, while the z data are used to give the gray scale. The gray scale is a linear scale in which the brightness of a point is in proportion to its height. A brighter point corresponds to a higher height, while a darker point corresponds to a lower height on the surface. One can then draw a line across the grayscale image and display the surface topographical profile corresponding to the line. The figure below shows an AFM picture of the surface of a Nicalon fiber and the roughness profile corresponding to the line between the arrows in the AFM picture.

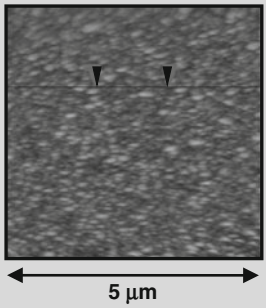

(continued)

(continued)

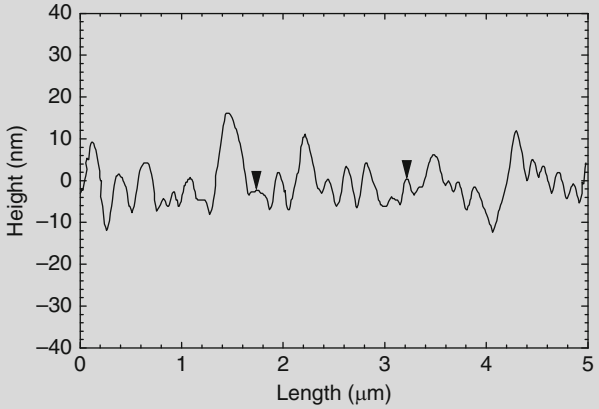

Another possibility is a three-dimensional representation of the surface wherein the height is indicated by superimposing the gray scale along the perpendicular axis and rotating the display to a convenient viewing angle. A three-dimensional picture of the surface of Nicalon fiber is shown in the figure below. It is possible to further enhance the three-dimensional aspect by adding a computer-generated light source to cast shadows. This is called illumination mode, not shown here.

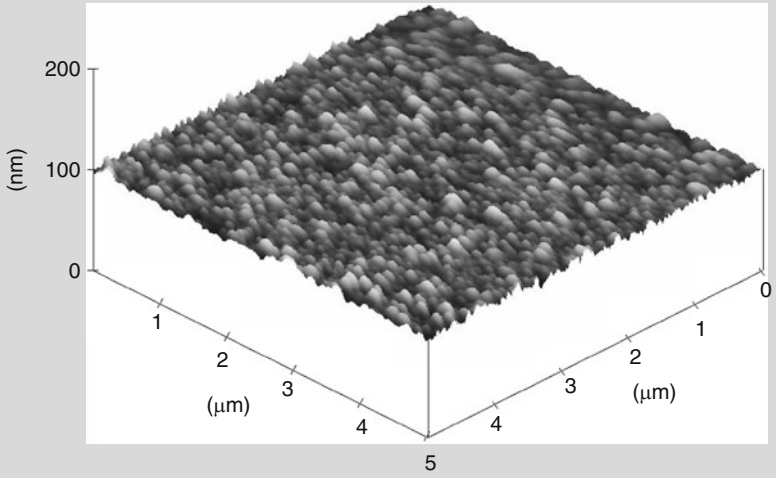

Chemical bonding in MMCs involves atomic transport by diffusion. Thus, chemical bonding includes solid solution and/or chemical compound formation at the interface. It may lead to the formation of an interfacial zone containing a solid solution and/or a reinforcement/matrix interfacial reaction zone with a certain thickness.

For diffusion-controlled growth in an infinite diffusion couple with planar interface, we have the following important relationship:

$$x^2 \approx Dt$$

where x is the thickness of the reaction zone, D is the diffusivity, and t is the time. The diffusivity, D, depends on the temperature in an exponential manner:

$$D = D_o \exp(-\Delta Q/kT)$$

where D_o is a pre-exponential constant, ΔQ is the activation energy for the rate controlling process, k is the Boltzmann's constant, and T is the temperature in kelvin. Strictly speaking, for a composite containing small diameter cylindrical fibers, the assumption of an infinite diffusion couple is not valid, i.e., the diffusion distances are quite small. However, to a first approximation, we can write:

$$x^2 \approx Bt$$

where B is a pseudo-diffusivity constant and has the dimensions of diffusivity, i.e., m^2s^{-1}. One may use this approximate relationship for composites where the thickness of reaction zone is small compared to the interfiber spacing. Under these conditions, one can use an Arrhenius-type relationship:

$$B = A \exp(-\Delta Q/kT)$$

where A is a pre-exponential constant. A plot of ln B vs. 1/T can then be used to obtain the activation energy, ΔQ, for a fiber/matrix reaction in a given temperature range. The dependence of the reaction zone thickness on the square root of time indicates the operation of volumetric diffusion. Figure 5.3 shows in a schematic manner the effect of temperature on the reaction zone thickness vs. √time. With increasing temperature, the slope of the line increases.

Most MMC systems are nonequilibrium systems in the thermodynamic sense; that is, there exists a chemical potential gradient across the fiber/matrix interface. This means that given favorable kinetic conditions, which in practice means a high enough temperature or long enough time, diffusion and/or chemical reactions occur between the components. Prolonged contact between liquid metal and reinforcement can lead to a significant chemical reaction, which may adversely affect the behavior of composite. For example, molten aluminum can react with carbon fiber to form Al_4C_3 and Si as per following reaction:

$$4Al + 3SiC \leftrightarrow Al_4C_3 + 3Si$$

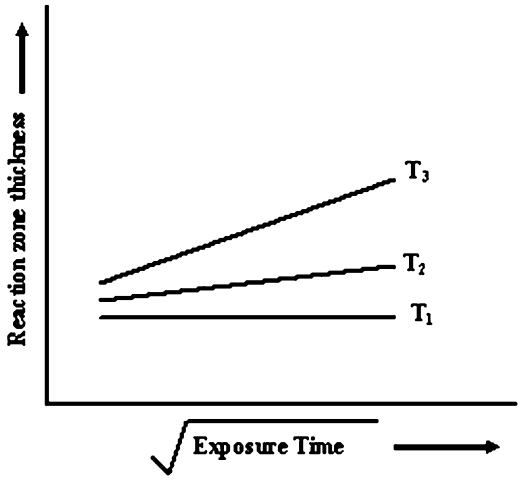

Fig. 5.3 Schematic representation of thickness of reaction zone between fiber and matrix as a function of square root of exposure time for three different temperatures, $T_3 > T_2 > T_1$

This reaction, as indicated by the two arrows, can go leftward or rightward. When it goes rightward, it injects silicon in the molten aluminum, which can have important consequences. Change of matrix alloy composition is one. Addition of silicon in aluminum also results in lowering of the melting point of the alloy; in fact it will result in a mushy range. Kinetics, i.e., time and temperature, will control the Si level required to prevent the reaction. This reaction can be prevented from going rightward by using high levels of Si in the matrix, say ~10 % Si. It is for this reason that only high silicon aluminum alloys are suitable for SiC particles for making composites by casting route. Al_2O_3 is stable in pure molten aluminum. It does, however, react with magnesium, a common alloying element in aluminum. The following reactions can occur between Mg and Al_2O_3:

$$3\,Mg + Al_2O_3 \leftrightarrow 3\,MgO + 2Al$$

$$3\,Mg + 4\,Al_2O_3 \leftrightarrow 3\,MgAl_2O_4 + 2Al$$

In alumina-reinforced composites with a high level of Mg in the matrix, MgO is expected to form at the interface, while spinel ($MgAl_2O_4$) forms at low level of Mg (Pfeifer et al. 1990).

Figure 5.4 shows a transmission electron micrograph of the reaction zone between alumina fiber and magnesium matrix made by liquid metal infiltration process. The interface layer(s) formed because of such a reaction generally has characteristics different from those of either one of the components. However, at times some controlled amount of reaction at the interface may be desirable for obtaining strong bonding between the fiber and the matrix; too thick an interaction zone adversely affects the composite properties.

The importance of matrix alloy composition cannot be overemphasized. For example, in pure Mg matrix, SiC particle would be stable, and no reaction is observed at the interface. In Mg alloys containing Al and Si as the main alloying

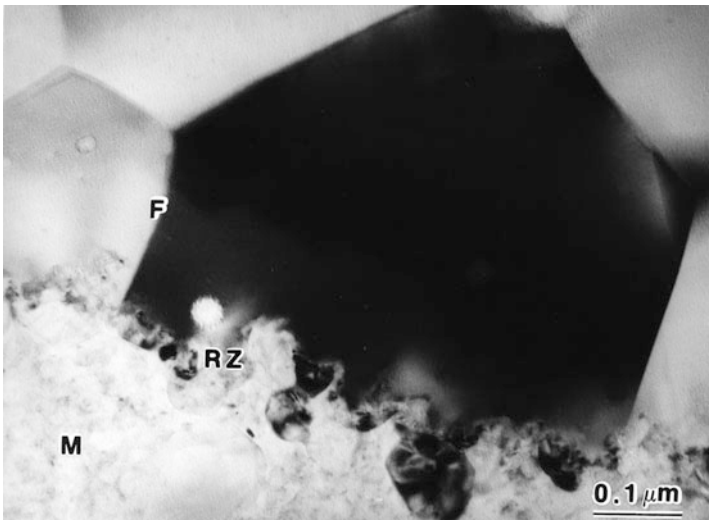

Fig. 5.4 Bright field (BF) transmission electron micrograph showing interface in a continuous fiber (F) α-Al_2O_3/Mg alloy (ZE41A) matrix (M). RZ indicates the interfacial reaction zone

Table 5.1 Interfacial reaction products in some important MMCs

Reinforcement	Matrix	Reaction product(s)
SiC	Ti alloy	TiC, Ti_5Si_3
	Al alloy	Al_4C_3
Al_2O_3	Mg alloy	MgO, $MgAl_2O_4$ (spinel)
Al_2O_3	Al alloy	None
B	Al alloy	AlB_2
ZrO_2	Al alloy	$ZrAl_3$
C	Al alloy	Al_4C_3
C	Cu	None
W	Cu	None
NbTi	Cu	None
Nb_3Sn		
Various oxides	Ag	None

elements, interfacial reaction can occur between Al and SiC as described above. Such a reaction will form the undesirable Al_4C_3 and inject Si into the matrix, which can react with Mg to form Mg_2Si. Another important composite system involves SCS-6-type silicon carbide fiber and a titanium alloy (Ti-6Al-4V) matrix. Interfacial reaction products in this case include TiC and Ti_xSi_y (Gabryel and McLeod 1991).

We provide a summary of interfacial reaction products in some important MMCs in Table 5.1. It is important to have an understanding of the structure and properties of the reaction products that form in a given system because they will be

a key element in determining the final properties of the composite. For example, in carbon fiber reinforced aluminum, processed at around 700 °C, a very brittle intermetallic Al_4C_3 forms. It is also very sensitive to ambient moisture. It would be very desirable to avoid formation of such brittle phases at the interface because they lead to a catastrophic failure of the composite.

5.3.3 Interactions at the Interface due to Thermal Mismatch

Thermal stresses arise in composite materials because of the mismatch between the coefficients of thermal expansion of the components making up the composite. Mismatch in the elastic constants of the components exacerbates the problem. It is easy to see that in a fiber reinforced composite, if the matrix thermal expansion coefficient is higher than that of the fiber, then on cooling from high temperature, radial compression will result, i.e., the matrix will grip the fiber. Such a radial gripping of the fiber by the matrix will increase the strength of the interface, thus, increasing the tendency toward brittleness in the composite. This will make phenomena such as fiber debonding and pullout, desirable for enhanced toughness, difficult to operate.

Quite frequently, the very process of fabrication of a composite can involve interfacial interactions that can cause changes in the constituent properties and/or interface structure. For example, if the fabrication process involves cooling from high temperatures to ambient temperature, then the difference in the expansion coefficients of the two components can give rise to thermal stresses of such a magnitude that the softer component (generally the matrix) will deform plastically. Chawla and Metzger (1972) observed in a tungsten reinforced single crystal copper matrix (nonreacting components) that liquid copper infiltration of tungsten fibers at about 1,100 °C followed by cooling to room temperature resulted in a dislocation density in the copper matrix that was much higher in the vicinity of the interface than away from the interface. The high dislocation density in the matrix near the interface resulted from the plastic deformation of the matrix caused by high thermal stresses near the interface. Other researchers observed similar results in the system SiC whiskers in an aluminum matrix (Arsenault and Fisher 1983) and in a composite consisting of short alumina fibers in aluminum matrix (Dlouhy et al. 1998). If powder metallurgy fabrication techniques are used, the nature of the powder surface will influence the interfacial interactions. For example, an oxide film on the powder surface affects its chemical nature. Topographic characteristics of the components can also affect the degree of atomic contact obtainable between the components. This can result in geometrical irregularities (e.g., asperities and voids) at the interface, which can be a source of stress concentrations.

5.4 Measurement of Interfacial Bond Strength

Once the matrix and the reinforcement of a composite are chosen, the set of characteristics of the interface region become very important in determining the final properties of the composite. In this regard a thorough microstructural and mechanical characterization of the interface region assumes a great deal of importance. A variety of sophisticated techniques is available for this purpose. A quantitative measure of the strength of the interfacial bond between the matrix and reinforcement is of great importance. We describe below some of the important techniques to measure interfacial bond strength.

5.4.1 Bend Tests

Bend tests are easy to perform, but they do not give a true measure of the interfacial strength. We describe below some variants of bend tests.

(a) *Transverse Bend Test*
A three-point bend test configuration with fibers aligned perpendicular to the specimen length is called a transverse bend test. There are two possible arrangements of fibers, one with fibers parallel to the width of the specimen and the other with fibers perpendicular to the width of fibers. Under either one of these configurations, the fracture will occur on the outermost surface of the specimen which is under a tensile stress and thus will put the fiber/matrix interface under tension, which gives us a measure of tensile strength of the fiber/matrix interface. The transverse strength is given by

$$\sigma = \frac{3PS}{2bh^2} \tag{5.1}$$

where P is the applied load, S is the load span, b is the specimen width, and h is the specimen height.

(b) *Longitudinal Bend Test or Short Beam Shear Test*
This test is also known as the interlaminar shear strength (ILSS) test. In this test, the fibers are aligned parallel to the length of the three-point bend bar. In such a test, the maximum shear stress, τ, occurs at the midplane and is given by

$$\tau = \frac{3P}{4bh} \tag{5.2}$$

The maximum tensile stress occurs at the outermost surface and is given by (5.1). Dividing (5.2) by (5.1), we get

$$\frac{\tau}{\sigma} = \frac{h}{2S} \tag{5.3}$$

According to (5.3), we can maximize the shear stress by making the load span, S, arbitrarily small and thus ensure that the specimen fails under shear with a crack running along the midplane. The test becomes invalid if the fibers fail in tension before shear-induced failure occurs. The test will also be invalid if shear and tensile failure occur simultaneously. It is advisable to make an examination of the fracture surface after the test and make sure that the crack is along the interface and not through the matrix.

5.4.2 *Fiber Pullout and Pushout Tests*

Single fiber pullout and pushout tests have been devised to measure interfacial characteristics. Such tests give load vs. displacement curves, with a peak load corresponding to fiber/matrix debonding and a frictional load corresponding to the fiber pullout from the matrix. The main simplification that is frequently made in the analysis of such tests involves averaging the load values over the entire interfacial surface area to get the interface debond strength and/or frictional strength. Analytical and finite element analyses show that the shear stress is a maximum close to the fiber end and falls rapidly within a distance of a few fiber diameters. Thus, one would expect the interface debonding to start near the fiber end and progressively propagate along the embedded length. We describe the salient features of these tests.

(a) *Single Fiber Pullout Tests*

Single fiber pullout tests can provide useful information about the interface strength in *model* composite systems. They are not very helpful in the case of commercially available composites. One must also carefully avoid any fiber misalignment and introduction of bending moments. The mechanics of the single fiber pullout test is complicated (see, e.g., Penn and Lee 1989; Marshall et al. 1992; Kerans and Parthasarthy 1991). In all variants of such test, the fiber is pulled out of the matrix in a tensile testing machine, and a load vs. displacement record is obtained.

Figure 5.5 shows the experimental setup for such a test. A portion of fiber, length ℓ, is embedded in a matrix. We apply a pulling tensile force, as shown, and measure the stress required to pull the fiber out of the matrix as a function of the embedded fiber length. The stress required to pull the fiber out without breaking it increases linearly with the embedded fiber length, up to a critical length, ℓ_c. This critical fiber length is the length of fiber that is used in load transfer from the matrix to fiber. We discuss the concept of critical fiber length in Chap. 6. For an embedded fiber length, $\ell > \ell_c$, the fiber will fracture under the action of the tensile stress, σ, acting on the fiber. When we apply a tensile force

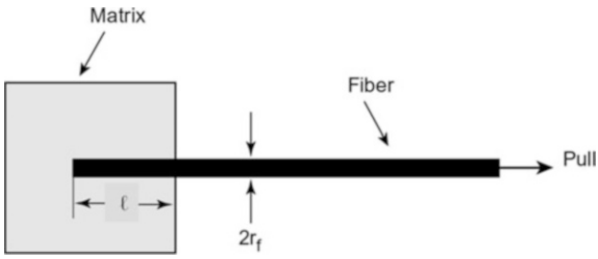

Fig. 5.5 A fiber of radius r embedded in a matrix and being pulled out. The longitudinal tensile force on the fiber generates shear at the fiber/matrix interface

on the fiber, there will result a shear force at the fiber/matrix interface. A simple force balance along the embedded fiber length, ℓ, and radius, r_f, gives

$$\sigma \pi r^2 = \tau 2\pi \ell r_f$$

For $\ell < \ell_c$, the fiber is pulled out and the interfacial shear strength is given by

$$\tau = \frac{\sigma r_f}{2\ell}$$

One measures the load, P, required to debond the interface as a function of the embedded fiber length. Then, we can write

$$P = \tau 2\pi r_f \ell$$

and the interfacial shear strength, τ, can be calculated from the slope of P vs. ℓ plot. For $\ell > \ell_c$, fiber failure rather than pullout occurs. The interfacial shear strength is a function of the coefficient of friction, μ, and any normal compressive stress at the interface, σ_r, i.e., $\tau_i = \mu\sigma_r$. A common source of radial compressive stress is the shrinkage of the matrix during cooling from the processing temperature. The most doubtful assumption in this analysis is that the shear stress acting along the fiber/matrix interface is a constant.

The fabrication of the single fiber pullout test sample is often the most difficult part; it entails embedding a part of the single fiber in the matrix. The peak load corresponds to the initial debonding of the interface. This is followed by frictional sliding at the interface and finally by the fiber pullout from the matrix, during which a steady decrease in the load with displacement is observed. The steady decrease in the load is attributed to the decreasing area of the interface as the fiber is pulled out. Thus, the test simulates the fiber pullout that may occur in the actual composite and, more importantly, provides the bond strength and frictional stress values.

The effect of different Poisson's contractions of fiber and matrix can lead to a radial tensile stress at the interface. The radial tensile stress will no doubt aid the fiber/matrix debonding process. The effect of Poisson's contraction together with the problem that the imposed shear stress is not constant along the interface complicates the analysis of fiber pullout test. Fiber pullout tests have been used

to determine the interfacial shear strength in a variety of fiber reinforced ceramic or glass matrix composites.

(b) *Pushout or Indentation Tests*
Interfacial frictional sliding is an important parameter. Many researchers (e.g., Marshall 1984; Doerner and Nix 1986; Eldridge and Brindley 1989; Ferber et al. 1993; Mandell et al. 1986, 1987; Marshall and Oliver 1987; Cranmer 1991; Chawla et al. 2001) have used the technique of pressing an indenter on a fiber cross section in a composite to measure the interfacial bond strength in a fiber-reinforced composite. An instrumented indentation system, the apparatus for which is sometimes called a *nanoindenter*, is available commercially. Such an instrument allows extremely small forces and displacements to be measured. A nanoindenter is essentially a computer-controlled depth-sensing indentation system. Indentation instruments have been in use for hardness measurement for more than a century, but "depth-sensing" instruments having high resolution became available in the 1980s (Doerner and Nix 1986; Weihs and Nix 1991). Consequently, very small volumes of a material can be studied and a very local characterization of microstructural variations is possible by mechanical means. Both pointed and rounded indenters can be used to displace a fiber aligned perpendicular to the composite surface. By measuring the applied force and the displacement, interfacial stress can be obtained. One generally loads several fibers in a polished cross section of composite system. Most commercially available nanoindenter instruments are capable of accurately applying very small loads (mN) via a Berkovich pyramidal diamond indenter having the same depth–area ratio as a Vickers diamond tip indenter. A nanoindenter records the total penetration of an indenter into the sample. The Berkovich indenter is a triangular pyramid and its position is determined by a sensitive capacitance displacement gage. The capacitance gage can detect displacement changes less than one nm while the applied force can be detected to less that 1 μN. The indenter can be moved toward the sample or away from the sample by means of a magnetic coil assembly.

In the pushout test, one pushes a fiber out, by means of an indenter, in a thin sample with the fibers aligned perpendicular to the viewing surface. Such a fiber pushout test can give the frictional shear stress, τ, acting at the fiber/matrix interface. In a valid pushout test, a three-region curve is obtained, see Fig. 5.6. In the first region, the indenter is in contact with the fiber and the fiber sliding is less than the specimen thickness t. This is followed by a horizontal region in which fiber sliding length is greater than or equal to the sample thickness. In the third region, the indenter comes in contact with the matrix. From the second region, we can determine the interfacial shear stress. The specimen thickness should be much greater than the fiber diameter for this relationship to be valid. In the horizontal region (region two), the interfacial shear stress is given by

$$\tau_i = \frac{P}{2\pi r_f t}$$

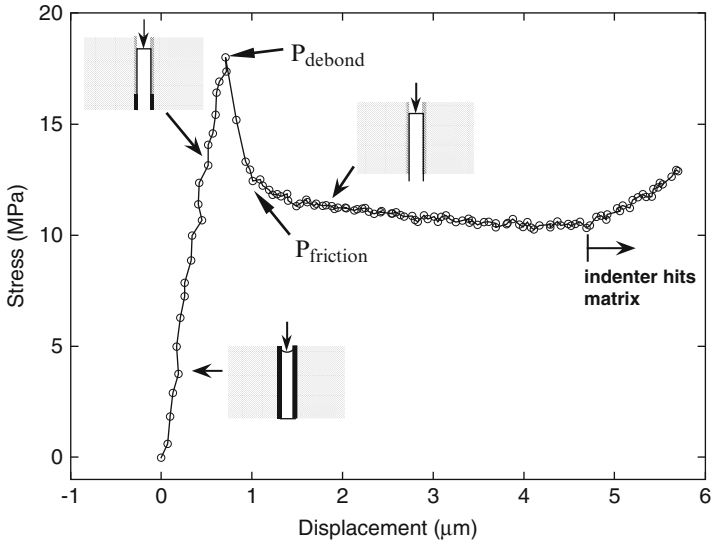

Fig. 5.6 Stress–displacement curve during fiber pushout. After elastic loading, progressive fiber debonding takes place, followed by interfacial sliding (Chawla et al. 2001)

where t is the specimen thickness. In the third region of Fig. 5.6b, the value of the interfacial shear stress cannot be determined because the indenter comes in contact with the matrix.

If the fiber is strongly bonded to the matrix, the energy at the crack tip at the interface will be high enough to fracture the fiber. In this case, the crack propagates straight through the interface, into the fiber, and the composite fails in a catastrophic manner. If the fiber/matrix interface is tailored, such that bonding between fiber and matrix is weak, a crack propagating normal to the interface will be deflected at the interface, causing it to lose energy. In this manner, debonding and sliding of the fiber with respect to the matrix act as an energy-absorbing mechanism.

Several important factors control the fiber/matrix behavior such as thermal residual stresses from processing that can induce radial clamping stresses and axial stresses from the matrix to the fiber. Thermal mismatch in CTE between fiber and matrix is responsible for residual stresses in all types of composites. If the matrix shrinks more than the fiber, then a compressive clamping stress is applied on the fiber, and an opposite tensile stress acts on the matrix. Therefore, when a cyclic load is applied to the composite, for example, the fibers are subjected to tension–tension loading while the matrix is under tension–compression or compression–compression.

Fiber surface roughness can also contribute significantly to the radial clamping stresses, because the matrix becomes mechanically keyed to the fiber. A roughness-induced strain arises because of this mechanical keying, and it can be estimated by the roughness amplitude between fiber and matrix.

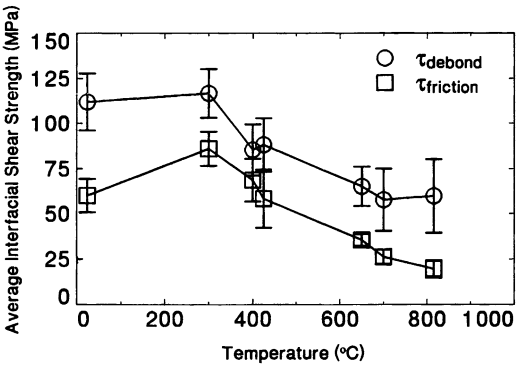

Fig. 5.7 Effect of temperature on fiber debond stress and frictional sliding stress in SCS-6/Ti-24Al-11Nb (Eldridge and Ebihara 1994)

To relieve radial clamping stresses from CTE mismatch as well as from fiber roughness, a compliant fiber coating can be applied to the fiber. The effect of interfacial clamping stress, temperature, and environment on the debonding and sliding of the pushed fibers was examined by Eldridge and Ebihara 1994. They tested the system SCS-6/Ti-24Al-11Nb (at. %), from ambient temperature to 1,100 °C. The fiber debond stress and frictional sliding stress decreased continuously at temperatures higher than 300 °C, Fig. 5.7. The decrease in interfacial shear strength was attributed to the relief of the residual compressive stresses on the fiber and oxidation of the carbon coating at higher temperatures. Figure 5.8 shows the pushed out fiber at low and high temperatures, showing a relatively rough and smooth surface, respectively.

Eldridge and Ebihara (1994) postulate that the sensitivity of the degree of wear to the environment can be attributed to the well-documented (Savage 1948; Lancaster and Pritchard 1981) dependence of adsorbed species for the lubricative properties of graphite, which exists on the outer shell of the SCS-6 fiber, and thus, acts as a weak interface between the fiber and the matrix. The low friction and wear at room temperature of graphite is attributed to water in the form of moisture, and secondarily oxygen adsorption (Savage 1948). In the absence of adsorbed species, sliding graphite surfaces exhibit "dusting" wear, producing extremely fine debris. At room temperature in air, once the interface in SCS-6 fiber/matrix debonds, the gap created at the failed interface exposes both sides of the interface to the environment and the two surfaces could slide smoothly.

Incorporating an interfacial coating with easy debonding and sliding characteristics is an important interface engineering technique (Chawla 2003). Materials with layered structure such as graphite or hexagonal boron nitride (hBN) are candidates for such coatings. Zhong et al. (2008) studied the effect of applying an interfacial coating in alumina fiber/NiAl composite. They did fiber pushout testing at room temperature and 900 °C on alumina fiber/NiAl matrix composites with and without a hBN interfacial coating. The hBN interfacial coating, because of its layered structure, led to a decrease in the average interfacial stress at room temperature and at 900 °C.

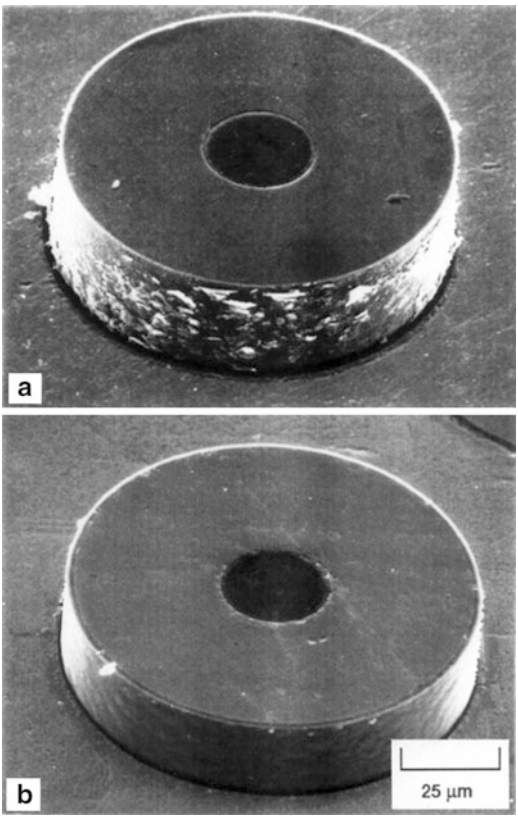

Fig. 5.8 SEM micrographs of pushed out fibers at (**a**) low temperature and (**b**) high temperature, showing a relatively rough and smooth surface, respectively (Courtesy of J.I. Eldridge)

References

Arsenault, R.J. and R.M. Fisher (1983) Scripta Met., **17**, 43.
Chawla, K.K. (2003) *Ceramic Matrix Composites*, 2nd edition, Kluwer Academic Publishers, Boston.
Chawla, K.K. and M. Metzger (1972) *J. Mater. Sci*., **7**, 34.
Chawla, K.K. and M. Metzger (1978) in *Advances in Research on Strength and Fracture of Materials*, Vol. 3, Pergaman Press, New York, p. 1039.
Chawla, N., K.K. Chawla, M. Koopman, B. Patel, C. Coffin, and J.I. Eldridge (2001) *Composite Sci. & Tech*., **61**, 1923.
Cranmer, D.C. (1991) in *Ceramic and Metal Matrix Composites*, Pergamon Press, New York, p. 157.
Dlouhy, A., N. Merk, and G. Eggeler (1998) *Acta Metall. Mater*, **41**, 3245.
Doerner, M.F. and W.D. Nix (1986) *J. Mater. Res*., **1**, 601.
Eldridge, J.I. and P.K. Brindley (1989) *J. Mater. Sci. Lett*., **8**, 1451.
Eldridge, J.I. and B.T. Ebihara (1994) *J. Mater. Res*., **9** 1035.
Ferber, M.K., A.A. Wereszczsak, L. Riester, R.A. Lowden, and K.K. Chawla (1993) *Ceram. Eng. Sci. Proc*., **13**, 168.
Gabryel, C.M. and A.D. McLeod (1991) Met. Trans, **23A**, 1279.

Hill, R.G, R.P. Nelson, and C.L. Hellerich, in *Proc. of the 16th Refractory Working Group Meeting*, Seattle, WA, October, 1969.
Iosipescu, N. (1967) *J. Mater.*, **2**, 537.
Kerans, R. J. and T. A. Parthasarathy (1991) *J. Amer. ceram. Soc.*, **74**, 1585.
Lancaster, J.K. and J.R. Pritchard (1981) *J. Phys. D: Appl. Phys.*, 14 747.
Mandell, J.F., D.H. Grande, T.H. Tsiang, and F.J. McGarry (1986) in *Composite Materials: Testing & Design*, ASTM STP 327, ASTM, Philadelphia, 87.
Mandell, J.F., K.C.C. Hong, and D.H. Grande (1987) *Ceram. Eng. Sci. Proc.* **8**, 937.
Marshall, D.B. (1984) *J. Amer. Ceram. Soc.*, **67**, C259.
Marshall, D.B. and W.C. Oliver (1987) *J. Amer. Ceram. Soc.*, **70**, 542.
Marshall, D.B., M.C. Shaw, and W.L. Morris (1992) *Acta Met.*, **40**, 443.
Penn, L.S. and S.M. Lee (1989) *J. Comp. Tech. & Res.*, **11**, 23.
Pfeifer, M., J.M. Rigsbee, and K.K. Chawla (1990) *J. Mater. Sci.*, **25**, 1563.
Savage, R.H. (1948) *J. Appl. Phys.*, 19 1.
Weihs, T.P. and W.D. Nix (1991) *J. Amer. Ceram. Soc.*, **74**, 524.
Zhong, Y., W. Hu, J. I. Eldridge, H. Chen, J. Song, and G. Gottstein (2008) *Mater. Sci. Eng. A*, 488, 372.

Chapter 6
Micromechanics

In this chapter, we examine a variety of means of calculating elastic and physical constants of metal matrix composites, given the same constants for the individual components and the arrangement of components in the composite, and thermal stresses generated because of mismatch in the coefficient of thermal expansion (CTE) of the components. In fact, most of the material discussed in this chapter is applicable to all kind of composites. Specifically, we provide a micromechanical description of physical properties such as density, thermal expansion coefficients, thermal and electrical conductivity, and various elastic constants. Of particular interest are methods or expressions that predict elastic constants of composites because of the generally high anisotropy found in composites. A description of conventional and microstructure-based finite element techniques to predict the elastic and thermal constants is also provided.

We first briefly review the theory of elasticity and the concept of the number of independent elastic constants required for a fiber reinforced composite. We then provide expressions for the elastic constants as per different schemes available. This is followed by a description of physical properties and thermal stresses in composites.

6.1 Elastic Constants of a Fiber Reinforced Composite

Hooke's law relates the second-rank *stress* tensor, σ_{ij}, and the second-rank *strain* tensor, $\varepsilon_{k\ell}$, and can be written as

$$\sigma_{ij} = C_{ijkl}\,\varepsilon_{k\ell} \tag{6.1}$$

where C_{ijkl} is a fourth-rank tensor called the elastic stiffness tensor and the indices i, j, k, and ℓ have values of 1, 2, and 3. The stress and strain tensors, being second rank, have $3^2 = 9$ components each. The stiffness tensor is a fourth-rank tensor; it has $3^4 = 81$ components. Stress, strain, and stiffness are symmetric tensors,

N. Chawla and K.K. Chawla, *Metal Matrix Composites*,
DOI 10.1007/978-1-4614-9548-2_6, © Springer Science+Business Media New York 2013

Table 6.1 Independent elastic constants for systems of different symmetry

Symmetry	Number of independent constants	Constants
Orthorhombic	9	C_{11}, C_{12}, C_{13}, C_{22}, C_{23}, C_{33}, C_{44}, C_{55}, C_{66}
Trigonal	6	C_{11}, C_{12}, C_{13}, C_{14}, C_{33}, C_{44}
Tetragonal	6	C_{11}, C_{12}, C_{13}, C_{33}, C_{44}, C_{66}
Hexagonal	5	C_{11}, C_{12}, C_{13}, C_{33}, C_{44}
Cubic	3	C_{11}, C_{12}, C_{44}
Isotropic	2	C_{11}, C_{12}

i.e., $\sigma_{ij} = \sigma_{ji}$, $\varepsilon_{k\ell} = \varepsilon_{\ell k}$, and $C_{ijk\ell} = C_{k\ell ji} = C_{ji\ell k} = C_{jik\ell}$. These symmetry relationships reduce the maximum number of independent elastic constants to 21. Hooke's law in (6.1) can then be simplified and rewritten in a contracted notation more appropriate for matrix operations as follows:

$$\sigma_i = C_{ij}\varepsilon_j \tag{6.2}$$

In a similar manner, we can write Hooke's law in terms of the elastic compliance matrix, S_{ij}, as

$$\varepsilon_i = S_{ij}\sigma_j \tag{6.3}$$

Both C_{ij} and S_{ij} are 6×6 symmetric matrices, i.e., $C_{ij} = C_{ji}$ and $S_{ij} = S_{ji}$. Also, the stiffness and the compliance matrices are inverse of each other, i.e.,

$$[C][S] = [I]$$

where [I] is the identity matrix. The total number of independent constants required to describe the elastic behavior of a material completely decreases with increasing symmetry elements present. Table 6.1 presents a summary.

For an isotropic material, there are only two independent elastic constants. For a material with cubic symmetry, we need three independent elastic constants. The most general situation is that of the triclinic system (not shown in Table 6.1) in which there are no symmetry elements present; it requires 21 independent elastic constants. For a material with cubic symmetry, we can write Hooke's law in an extended form as follows (The off-diagonal constants are omitted; the matrix is symmetric):

$$\begin{bmatrix} \sigma_1 \\ \sigma_2 \\ \sigma_3 \\ \sigma_4 \\ \sigma_5 \\ \sigma_6 \end{bmatrix} = \begin{bmatrix} C_{11} & C_{12} & C_{12} & 0 & 0 & 0 \\ & C_{11} & C_{12} & 0 & 0 & 0 \\ & & C_{11} & 0 & 0 & 0 \\ & & & C_{44} & 0 & 0 \\ & & & & C_{44} & 0 \\ & & & & & C_{44} \end{bmatrix} \begin{bmatrix} \varepsilon_1 \\ \varepsilon_2 \\ \varepsilon_3 \\ \varepsilon_4 \\ \varepsilon_5 \\ \varepsilon_6 \end{bmatrix}$$

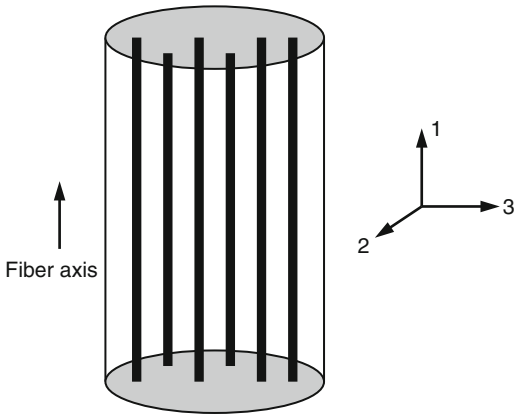

Fig. 6.1 A unidirectionally reinforced fiber-reinforced composite with fibers arranged in a random in the transverse (2–3) plane. Such a composite is called transversely isotropic

Note that there are only three independent constants. For an isotropic material, the number of independent constants is reduced from 3 to 2 because of the following relationship:

$$C_{11} - C_{22} = 2C_{44}$$

In engineering usage, for an isotropic material, any two of the following four constants will suffice: Young's modulus (E), Poisson's ratio (ν), shear modulus (G), and bulk modulus (K). This is because of the following relationships among the four constants:

$$E = 3K(1 - 2\nu)$$

$$G = \frac{E}{2(1+\nu)}$$

$$K = \frac{E}{3(1-2\nu)}$$

$$\text{and} \quad \nu = \frac{E}{2G} - 1$$

Thus, only two of the four constants for an isotropic material are independent.

A unidirectionally reinforced fiber reinforced composite with fibers arranged in a random manner in the transverse section is said to be transversely isotropic, i.e., there is no preferred direction in the 2–3 plane; see Fig. 6.1. Such an arrangement of fibers gives us the same elements as the hexagonal crystal, i.e., five independent elastic constants are needed to fully describe the elastic behavior of such a composite. Note that this follows from the disposition of long fibers in a matrix, even though the two components, fiber and matrix, may individually be isotropic in nature. On the other hand, a particle or whisker/short fiber reinforced composite, with no preferential alignment of reinforcement, can be treated as an isotropic material. We describe a variety of approaches to obtain the elastic constants of the composite below, knowing the elastic constants of the individual components.

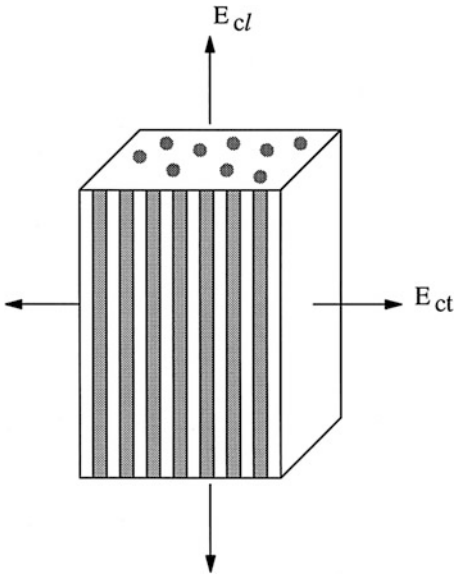

Fig. 6.2 Longitudinal ($E_{c\ell}$) and transverse (E_{ct}) Young's moduli for a unidirectionally reinforced fiber reinforced composite

6.1.1 Strength of Materials Approach

We can get some quick estimates of elastic constants of a composite by using the strength of materials approach. Here we make simplifying assumptions of uniform strain or uniform stress in the constituents of the composite. The results are satisfactory for E_{11} and ν_{12}, but underestimate E_{22} and G_{12}. We use $E_{c\ell}$ and E_{11} interchangeably to indicate longitudinal Young's modulus in the fiber direction. Similarly, E_{ct} and E_{22} indicate Young's modulus in the direction transverse to the fiber axis. Two simple cases are *isostrain* and *isostress* models for Young's modulus of a unidirectionally aligned, fiber reinforced composite; see Fig. 6.2. We shall also derive expressions for the principal shear modulus and principal Poisson's ratio.

Longitudinal Young's Modulus

If we apply the *isostrain* condition to a unidirectional, fiber-reinforced composite loaded along the fiber direction, we get the longitudinal Young's modulus, $E_{c\ell}$ or E_{11}, of the composite. The isostrain condition says that the strains in the fiber, matrix, and composite are identical (see Fig. 6.2), i.e.,

$$\varepsilon_f = \varepsilon_m = \varepsilon_{c\ell} = \frac{\Delta \ell}{\ell_o} \tag{6.4}$$

where ε is the strain, $\Delta\ell$ is the change in length, ℓ_o is the original length, and the subscripts f, m, and cℓ indicate fiber, matrix, and composite in the longitudinal direction, respectively.

For components behaving elastically, we can use Hooke's law for a uniaxial stress acting on the fiber and the matrix:

$$\sigma_f = E_f \varepsilon_{c\ell} \quad \text{and} \quad \sigma_m = E_m \varepsilon_{c\ell}$$

where σ is the stress, E is the Young's modulus, and the subscripts have the meanings given above.

The applied load on the composite, P_c, is partitioned between the fiber and the matrix, i.e.,

$$P_c = P_f + P_m$$

where P_f and P_m indicate the load on the fiber and matrix, respectively. Converting loads into stresses, we can write

$$\begin{aligned} \sigma_{c\ell} A_c &= \sigma_f A_f + \sigma_m A_m \\ &= E_f A_f \varepsilon_{c\ell} + E_m A_m \varepsilon_{c\ell} \\ &= (E_f A_f + E_m A_m)\, \varepsilon_{c\ell} \\ \sigma_{c\ell} = E_{c\ell} \varepsilon_{c\ell} &= (E_f A_f / A_c + E_m A_m / A_c)\, \varepsilon_{c\ell} \end{aligned} \tag{6.5}$$

From this we get the following expression:

$$E_{c\ell} = E_f V_f + E_m V_m \tag{6.6}$$

It turns out that the longitudinal modulus predicted by (6.6) is quite reasonable. As an example, Fig. 6.3 shows the linear dependence of longitudinal Young's modulus of a tungsten fiber reinforced copper as a function of fiber volume fraction (McDanels et al. 1965).

Transverse Young's Modulus

The transverse modulus, E_{ct} or E_{22}, can be estimated by applying an *isostress* condition, i.e., the fiber, matrix, and composite experience the same stress; see Fig. 6.2. Thus,

$$\sigma_f = \sigma_m = \sigma_{ct} \tag{6.7}$$

where the subscript ct denotes the composite in the transverse direction and the other subscripts have the significance given earlier.

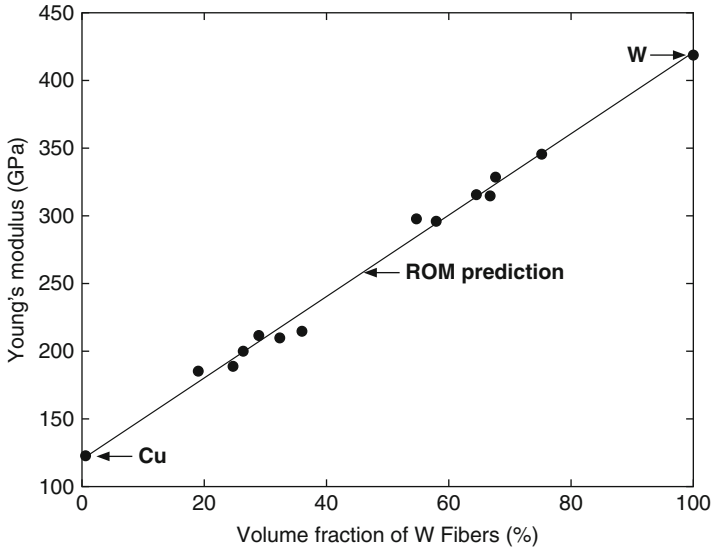

Fig. 6.3 Linear dependence of longitudinal Young's modulus of tungsten fiber-reinforced copper as a function of fiber volume fraction (after McDanels et al. 1965)

The total displacement of the composite in the thickness direction, Δt_c, is the sum of the displacement in the fiber, Δt_f, and that in the matrix, Δt_m. We can then write the following relationship for the displacement in the thickness direction:

$$\Delta t_c = \Delta t_m + \Delta t_f$$

Let the original thickness of the composite be t_c. Dividing throughout by t_c, the gage length, we get the strain in the transverse direction:

$$\varepsilon_{ct} = \frac{\Delta t_c}{t_c} = \frac{\Delta t_m}{t_m}\frac{t_m}{t_c} + \frac{\Delta t_f}{t_f}\frac{t_f}{t_c}$$

$$\varepsilon_{ct} = \varepsilon_m \frac{t_m}{t_c} + \varepsilon_f \frac{t_f}{t_c} \tag{6.8}$$

Also, we can write the volume fractions of fiber and matrix as

$$V_m = \frac{t_m}{t_c} \quad \text{and} \quad V_f = \frac{t_f}{t_c}$$

Using Hooke's Law, we can rewrite (6.8) as

$$\frac{\sigma_{ct}}{E_{ct}} = \frac{\sigma_{ct} V_m}{E_m} + \frac{\sigma_{ct} V_f}{E_{ft}}$$

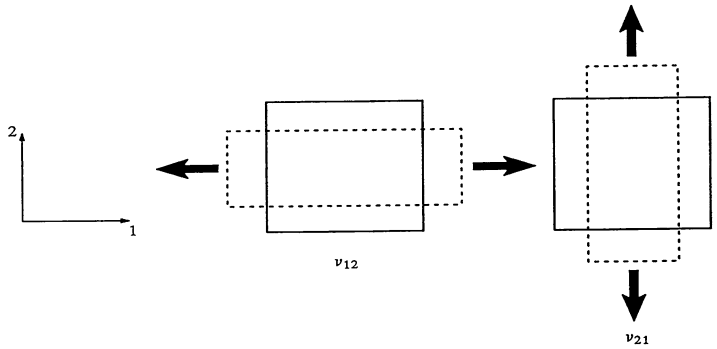

Fig. 6.4 The two Poisson's ratios in an anisotropic material. The principal Poisson's ratio (ν_{12}) gives the transverse strain caused by an axial stress. The secondary Poisson's ratio (ν_{21}) gives the axial strain caused by a transversely applied stress

or

$$\frac{1}{E_{ct}} = \frac{V_m}{E_m} + \frac{V_f}{E_{ft}} \tag{6.9}$$

We should point out that when computing Young's modulus in the transverse direction, we have chosen the transverse modulus of the fiber, E_{ft}. This is especially important when the fiber is anisotropic, for example, carbon fiber.

Poisson's Ratio

Consider a composite containing unidirectionally aligned fibers loaded in tension parallel to the fibers; see Fig. 6.4. The composite will extend longitudinally by ε_1 (direction 1) and contract transversely by ε_2 (direction 2). The contraction in direction 2 due to all the fibers will be $-\varepsilon_1 V_f \nu_f$, where V_f is the fiber volume fraction and ν_f is the Poisson's ratio of the fiber. The contraction due to the matrix will be $-\varepsilon_1 V_m \nu_m$, where V_m is the matrix volume fraction and ν_m is the Poisson's ratio of the matrix.

The total contraction of the composite in direction 2 is then given by

$$\begin{aligned}\varepsilon_2 &= -\varepsilon_1 V_f \nu_f - \varepsilon_1 V_m \nu_m \\ &= -\varepsilon_1 (V_f \nu_f + \varepsilon_1 V_m \nu_m)\end{aligned}$$

Defining the principal Poisson's ratio of the composite as $\nu_{12} = -\varepsilon_2/\varepsilon_1$, we get

$$\nu_{12} = V_f \nu_f + V_m \nu_m$$

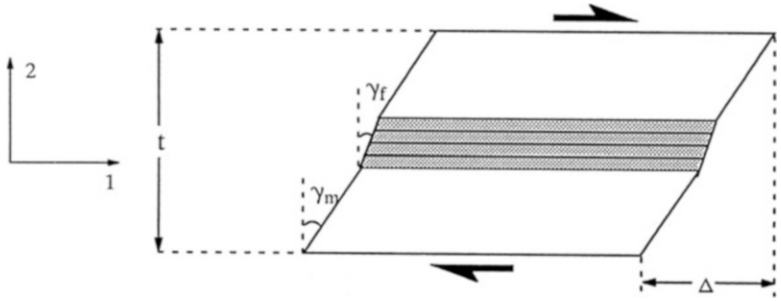

Fig. 6.5 A unidirectional fiber-reinforced composite loaded in shear parallel to the fibers

Shear Modulus

In the case of longitudinal or principal shear modulus, both the fiber and matrix are subjected to the same shear stress as shown in Fig. 6.5. Note that the fibers have been bundled together to show total shear in all the fibers. We can write the shear strain in the matrix and fiber as follows:

$$\gamma_m = \frac{\tau_m}{G_m}$$

and

$$\gamma_f = \frac{\tau_f}{G_f}$$

The total shear displacement in the composite, Δ, is given by

$$\Delta = \gamma t$$

where γ is the average shear strain in the composite and t is the thickness of the composite. We can then write the total shear displacement as the sum of the shear displacements of the components:

$$\Delta = \Delta_f + \Delta_m$$

$$\text{or,} \quad \Delta = \gamma_f t_f + \gamma_m t_m$$

$$\gamma = \frac{\Delta}{t} = \gamma_f V_f + \gamma_m V_m$$

Shear strain, γ, is nothing but shear stress divided by shear modulus, G_{12}, i.e.,

$$\tau/G_{12} = V_m\tau/G_m + V_f\tau/G_f$$
$$\text{or} \quad 1/G_{12} = V_m/G_m + V_f/G_f$$

6.1.2 Micromechanical Approaches

In this section we include the following important techniques:

- Self-consistent field methods
- Variational calculus methods
- Numerical methods

Brief descriptions of these as well as some key results are presented below.

Self-Consistent Field Methods: The strength of materials approach described above involves gross simplification of uniform stress (isostress) or uniform strain (isostrain). Self-consistent (SC) models improve on the internal stress and strain fields by introducing a simplified geometry of the phases. It should be pointed out, though, that in these techniques one still makes approximations of microstructure, i.e., the actual microstructure is not used. In one version, the phase geometry is represented by one single fiber embedded in a cylinder made of an average matrix material. This outer cylinder is embedded in an infinite, homogeneous material whose properties are taken to be the average properties of the composite. In the second version, a three-cylinder model is used. The intermediate cylinder surrounding the fiber has the properties of the matrix. The outermost cylinder has average properties of the composite. The radii of the cylinders are dictated by the fiber volume fraction. A uniform load, applied at infinity, introduces a uniform strain field in the fiber. Elastic constants are then obtained from this strain field. The results obtained are independent of fiber arrangements in the matrix and, in general, are reliable at low fiber volume fractions (V_f), reasonable at intermediate V_f, and unreliable at high V_f (Hill 1964).

Variational Calculus or Energy Methods: Energy methods involving variational calculus can be used to obtain bounds on a property of the composite. These techniques are also called bounding methods. Effective elastic constants (or compliances) of a composite (a heterogeneous system) are obtained from those of a homogeneous system with the same free energy. In simple terms, we can describe the rationale behind these methods as follows. Consider a linear elastic solid under deformation. We can express the strain energy stored in this solid in terms of a stress field

$$U_s = \frac{1}{2} S_{ij}\,\sigma_j$$

and in terms of strain field

$$U_c = \frac{1}{2} C_{ij}\, \varepsilon_j$$

These two expressions are equivalent for a homogeneous material but not for a heterogeneous material. The difference between these two expressions for a heterogeneous material (i.e., a composite) can be exploited to obtain the upper and lower bounds. Specifically, the theorem of least work gives the lower bound while the theorem of minimum potential energy provides the upper bound. There is a considerable amount of literature available on the subject; see, for example, Paul (1960), Hermans (1967), Hashin and Rosen (1964), and Whitney and Riley (1966).

These bounding methods do not predict properties exactly, but give upper and lower bounds on elastic constants. The property is determined exactly only if the upper and lower bounds coincide. More often than not, the upper and lower bounds are not very close. Only when these bounds are close enough can we safely use them as indicators of the material behavior. It turns out that this is the case for longitudinal properties of a unidirectionally aligned fiber reinforced composite such as longitudinal constants (E_{11}, ν_{12}), but they can be far apart in case of transverse and shear properties (E_{22} and G_{12}).

Hill (1965) derived bounds for the elastic constants of a fiber-reinforced composite. In particular, he put rigorous bounds on the longitudinal Young's modulus, E, in terms of bulk modulus in plane strain (k_p), Poisson's ratio (ν), and the shear modulus (G) of the two phases. No restrictions were made on fiber form or packing geometry. The bulk modulus in plane strain, k_p, is the modulus for lateral dilation with zero longitudinal strain and is given by

$$k_p = \frac{E}{2(1-2\nu)(1+\nu)}$$

The bounds on the longitudinal modulus, $E_{c\ell}$, are

$$\begin{aligned} &4V_f V_m(\nu_f - \nu_m)^2 / \left(V_f/k_{pm} + V_m/k_{pf} + 1/G_m\right) \\ &\leq E_{c\ell} - E_f V_f - E_m V_m \leq \\ &4V_f V_m(\nu_f - \nu_m)^2 / \left(V_f/k_{pm} + V_m/k_{pf} + 1/G_f\right) \end{aligned} \tag{6.10}$$

We can readily verify, from (6.10), that deviations from the rule of mixtures (ROM) for $E_{c\ell}$ are quite small. If we substitute some values of practical composites, such as silicon carbide fibers in an aluminum matrix, we find that the deviations in $E_{c\ell}$ from the ROM are <2 %. Note that the deviation from the rule-of-mixtures value comes in from the $(\nu_f - \nu_m)^2$ factor. For $\nu_f = \nu_m$, we have $E_{c\ell}$ given precisely by the rule-of-mixtures expression. Numerical simulations confirm that Hill's bounds are the best possible general bounds for linear elastic behavior of unidirectionally aligned fiber reinforced composites under axial loading (Rossoll et al. 2005).

For Poisson's ratio of a unidirectionally aligned fiber composite, Hill also showed that

$$\begin{aligned} &\nu_{12} > \nu_f V_f + \nu_m V_m \quad \text{for} \quad (\nu_f - \nu_m)\left(k_{pf} - k_{pm}\right) > 0 \\ &\text{and} \quad \nu_{12} < \nu_f V_f + \nu_m V_m \quad \text{for} \quad (\nu_f - \nu_m)\left(k_{pf} - k_{pm}\right) < 0 \end{aligned} \tag{6.11}$$

If $\nu_f < \nu_m$ and $E_f >> E_m$, then, ν_{12} will be less than that predicted by the ROM ($= \nu_f V_f + \nu_m V_m$). It is easy to see that the bounds on ν_{12} are not as close as the ones on $E_{c\ell}$. This is because $(\nu_f - \nu_m)$ appears in the case of ν_{12} (6.11), while $(\nu_f - \nu_m)^2$ appears in the case of $E_{c\ell}$ (6.10). If $(\nu_f - \nu_m)$ is very small, the bounds will be close enough to allow us to write

$$\nu_{12} \approx \nu_f V_f + \nu_m V_m \tag{6.12}$$

We can summarize the results of Hashin and Rosen (1964) and Hill (1965) as follows. For a transversely isotropic composite, with fibers along direction 1 and the 2–3 plane being the transverse (isotropic) plane, the equations for five independent moduli are given below.

Plane-strain bulk modulus, k_{23}:

$$k_{23} = \frac{k_f k_m + G_m(\nu_f k_f + \nu_m k_m)}{G_f + \nu_m k_f + \nu_f k_m}$$

where k_m and k_f are the plane-strain bulk moduli of the matrix and fiber, respectively. The plane-strain bulk modulus is defined as

$$k = K + \frac{1}{3}G$$

In-plane shear modulus, G_{12}:

$$G_{12} = G_m \frac{G_f(1 + V_f) + G_m V_m}{G_f V_m + G_m(1 + V_f)}$$

Longitudinal Young's modulus, E_{11}:

$$E_{11} = E_f V_f + E_m V_m + \left[4 V_f V_m (\nu_m - \nu_f)^2\right] \Big/ \left[(V_f/k_m) + (V_m/k_f) + 1/G_m\right]$$

For most practical purposes, the last term is negligible in the above expression.

Longitudinal Poisson's ratio, ν_{12}:

$$\begin{aligned} &\nu_{12} = \nu_f V_f + \nu_m V_m + \\ &[V_f V_m (\nu_f - \nu_m)] \ \left[(1/k_m) - (1/k_f)/(V_f/k_m) + (V_m/k_f) + 1/G_m\right] \end{aligned}$$

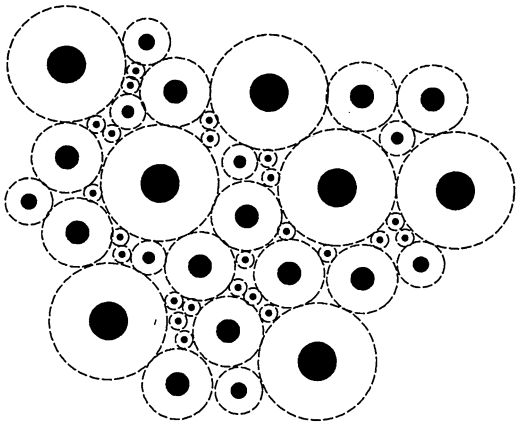

Fig. 6.6 A composite made up of an assemblage of spherical particles surrounded by their respective matrix shells. The volume fractions of phases are maintained constant in each unit; individual units can be of any size

Transverse plane shear modulus, G_{23}:

In this case, the upper and lower bounds are not coincident. The *lower* bound is

$$G_{23L} = G_m + \frac{V_f}{\frac{1}{G_f - G_m} + (K_m + 2G_m)\frac{V_m}{2G_m(k_m + G_m)}}$$

The *upper* bound is

$$G_{23U} = G_m + \frac{(\alpha + \beta_m V_f)\left(1 + \rho\nu_f^3\right) - 3\nu_f\nu_m^2\beta_m^2}{(\alpha - \nu_f)\left(1 + \rho\nu_f^3\right) - 3\nu_f\nu_m^2\beta_m^2}$$

where

$$\alpha = \frac{\gamma + \beta_m}{\gamma - 1} \qquad \rho = \frac{\beta_m - \gamma\beta_f}{1 + \gamma\beta_f}$$

$$\gamma = \frac{G_f}{G_m} \qquad \beta_m = \frac{1}{3 - 4V_m} \qquad \beta_f = \frac{1}{3 - 4V_f}$$

For particulate composites, Hashin (1962) proposed a composite sphere assembly model wherein the composite is made up of units consisting of a spherical particle and its surrounding matrix shell. In each spherical unit, the volume fractions of the particle and matrix are the same, but the spherical units can be of any size. Figure 6.6 shows such an assembly. Hashin analyzed this model by variational calculus methods and obtained a closed-form solution for the bulk modulus and upper and lower bounds for the effective shear modulus. The bulk modulus, K, is given by

$$K = \frac{K_p K_m + \frac{4}{3}G_m\left(V_p K_p + V_m K_m\right)}{V_p K_m + V_m K_p + \frac{4}{3}G_m}$$

where K, G, and V indicate the bulk modulus, shear modulus, and volume fraction, respectively, and the subscripts p and m refer to the particle and the matrix, respectively. Hashin and Shtrikman (1963) and Rosen (1973) have also analyzed macroscopically isotropic, particulate composite with an arbitrary internal phase geometry and only phase volume fractions being specified. The bounds of Hashin and Shtrikman on the bulk modulus, K, and shear modulus, G, are given below:

$$K_{upper} = K_p + (1 - V_p)\left[\frac{1}{K_m - K_p} + \frac{3V_p}{3K_p + 4G_p}\right]^{-1}$$

$$K_{lower} = K_m + V_p\left[\frac{1}{K_p - K_m} + \frac{3(1 - V_p)}{3K_m + 4G_m}\right]^{-1}$$

$$G_{upper} = G_p + (1 - V_p)\left[\frac{1}{G_m - G_p} + \frac{6V_p(K_p + 2G_p)}{5G_p\left(3K_{p}+{}^{p}4G_p\right)}\right]^{-1}$$

$$G_{lower} = G_m + V_p\left[\frac{1}{G_p - G_m} + \frac{6(1 - V_p)(K_m + 2G_m)}{5G_m(3K_m + 4G_m)}\right]^{-1}$$

where $K_m < K_p$ and $G_p < G_m$. For $K_m > K_p$ and $G_p > G_m$, the inequalities will be reversed. Treating the particulate composite as an isotropic material, we can obtain the bounds on the Young's modulus of the composite, E_c, by using the following relationship:

$$E = \frac{9K}{1 + 3K/G}$$

We can easily use this relationship to obtain the bounds on Young's modulus. For $0.5 < E_p/E_m < 3$, the bounds are close enough to give us a value within ~10 % of the true modulus.

6.1.3 Semiempirical Expressions

Halpin and Tsai (1967) and Halpin and Kardos (1976) used an empirical approach to obtain some generalized equations which give quite satisfactory results for unidirectional composites compared to the complicated micromechanical equations. These equations contain adjustable fitting parameters and work quite well at low fiber volume fractions. They can also provide useful estimates of properties

of composites containing oriented short fibers or whiskers. The adjustable parameters must be obtained from experimental data or must conform to some analytical solution. One uses a single equation of the form

$$\frac{p}{p_m} = \frac{1 + \xi\eta V_f}{1 - \eta V_f}$$
$$\eta = \frac{\frac{p_f}{p_m} - 1}{\frac{p_f}{p_m} + \xi} \tag{6.13}$$

where p represents one of the various moduli of the composite, e.g., E_{11}, E_{22}, $G_{12,}$ or G_{23}; p_f and p_m are the corresponding matrix and fiber moduli, respectively; V_f is the fiber volume fraction; and η is a measure of reinforcement which depends on the boundary conditions (fiber geometry, fiber distribution, and loading conditions). The term ξ is a fitting parameter that is used to make (6.13) conform to the experimental data. The function ξ in (6.13) is constructed in such a way that we get the two extreme values of property corresponding to $V_f = 0$ and 1, i.e., when $V_f = 0$, we have $p = p_{m,}$ and when $V_f = 1$, we get $p = p_f$. Furthermore, the form of η is such that

$$p = p_f V_f + p_m V_m \quad \text{for} \quad \xi \to \infty$$
$$1/p = V_m/p_m + V_f/p_f \quad \text{for} \quad \xi \to 0$$

These two extremes provide the bounds, although not necessarily tight bounds, on the properties of the composite. For example, for the transverse modulus of the composite E_{ct} or E_{22}, we can write

$$\frac{E_{ct}}{E_m} = \frac{1 + \xi\eta V_f}{1 - \eta V_f}$$
$$\eta = \frac{\frac{E_f}{E_m} - 1}{\frac{E_f}{E_m} + \xi}$$

Comparing these expressions with the exact elasticity solutions, one can obtain a value of ξ. Note that, in principle, ξ can range from 0 to ∞. ξ can be thought of as a measure of the "effectiveness" of fiber reinforcement. For small values of ξ, fibers are less effective than for large values of ξ. For computing E_{ct}, $\xi = 1$ or 2 works for hexagonal or square array of fibers, respectively. One can also point out some limiting values of η. The term ηV_f is akin to reduced fiber volume fraction. For a homogeneous material, $\eta = 0$. For very stiff fibers, $\eta = 1$ while for very compliant

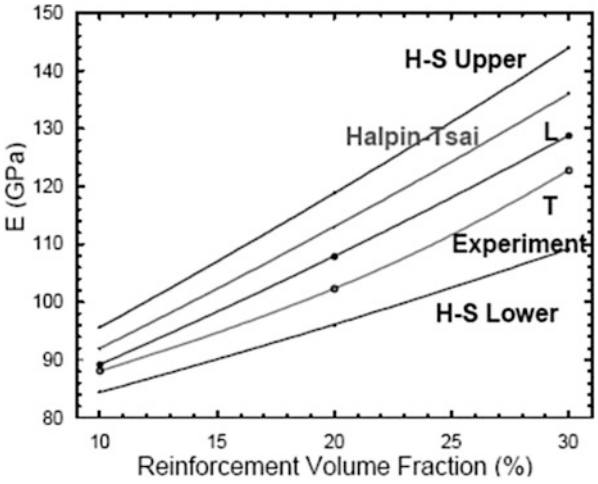

Fig. 6.7 Young's modulus, E, as a function of SiC particle reinforcement showing lower and upper bounds of Hashin–Shtrikman, Halpin–Tsai expression, and the experimental values measured in the longitudinal (L) and transverse (T) directions (after Ganesh and Chawla 2005). The experimental results show difference between longitudinal and transverse directions because of particle alignment caused by extrusion. Hashin–Shtrikman and Halpin–Tsai expressions treat the composite to be isotropic which is not quite true in this case

inclusions (e.g., voids) $\eta = -1/\xi$. Figure 6.7 shows plots of Young's modulus, E, as function of volume fraction of SiC particles in 2080 Al matrix, as per lower and upper bounds of Hashin–Shtrikman expressions, Halpin–Tsai expression, and the experimental values measured in the longitudinal and transverse directions (Ganesh and Chawla 2005). Note that Hashin–Shtrikman and Halpin–Tsai expressions treat the composite to be an isotropic material. The experimental results show that because of particle alignment caused by extrusion, the longitudinal values of modulus are higher than the transverse values. The experimental values fall somewhere between the Hashin–Shtrikman upper and lower bounds. Figure 6.8 shows similar plots for a composite where the particles are distributed in a homogeneous manner, a WC/Co composite (Koopman et al. 2002).

6.1.4 Eshelby Method or Equivalent Homogeneous Inclusion Technique

Eshelby (1957) formulated the problem of an elastic ellipsoidal inclusion embedded in an elastic matrix subjected to a displacement, with uniform strain field, an infinite distance away from the inclusion. The Eshelby technique provides the solution to a general problem of an infinite medium containing an inclusion. It involves replacing the real inclusion by an inclusion made of matrix (hence the use of expression

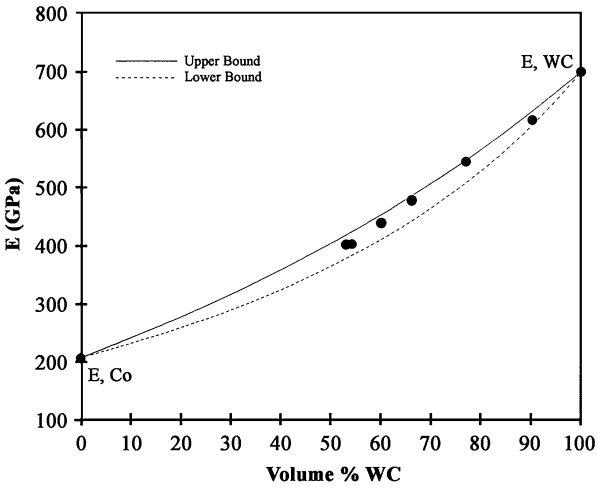

Fig. 6.8 Young's modulus, E, as a function of volume fraction of WC in a WC–Co composite (after Koopman et al. 2002)

equivalent homogeneous inclusion) but with a proper misfit strain, called *equivalent transformation strain*. The resultant stress field is the same as that for the real inclusions. In very simple terms, we can outline the technique as follows:

- Cut a piece of material from the unstressed, homogeneous matrix, leaving a hole.
- Allow the cut piece of material to undergo a shape change that corresponds to a transformation strain, ε^t.
- Insert the transformed inclusion back into the original hole, preventing interfacial sliding and then releasing the tractions. This requires the application of surface tractions so that the transformed shape of the inclusion can be fit back into the original hole.

A constrained strain, ε^c, is developed in the inclusion relative to the initial shape. The Eshelby tensor, S, relates the constrained strain, ε^c, to the transformation strain, ε^t, by the following expression:

$$\varepsilon^c = S\varepsilon^t$$

The Eshelby tensor is a function of the aspect ratio of the inclusion (or reinforcement) and the Poisson's ratio of the matrix. The reinforcement (short fibers, whiskers, or particles) is represented as prolate spheroid. The equation for such an inclusion in terms of Cartesian coordinates is

$$\frac{x^2 + y^2}{a^2} + \frac{z^2}{c^2} = 1$$

where c/a represents the aspect ratio of the inclusion and $c/a > 1$.

The important general result of the Eshelby analysis is that for an ellipsoidal inclusion the resulting stress and strain in the inclusion are homogeneous. The strains in the matrix and in the inclusion are therefore related algebraically. We can

write for the stress in the inclusion, σ_i, in terms of stiffness of the material, C_m, and the elastic strain in the inclusion as

$$\sigma_i = C_m(\varepsilon^c - \varepsilon^t)$$

In a composite, the ellipsoid inclusion or reinforcement will generally be stiffer than the matrix, i.e., the reinforcement has elastic constants, C_i. The inclusion being a different material than the matrix, we need to replace ε^t with an equivalent strain. With appropriate rearrangement, the resulting stress in the inclusion is

$$\sigma_i = C_i\left(\varepsilon^c - \varepsilon^t{}_{eq}\right)$$

Now, $\varepsilon^c \neq S\varepsilon^t{}_{eq}$, since $C_i \neq C_m$. However, we can find an equivalent homogeneous transformation strain, ε^t, such that the equivalent inclusion resembles the inhomogeneity, i.e.,

$$\begin{aligned} C_i\left(\varepsilon^c - \varepsilon^t{}_{eq}\right) &= C_m\left(\varepsilon^c - \varepsilon^t\right) \\ \text{or} \quad C_i\left(S\varepsilon^t - \varepsilon^t{}_{eq}\right) &= C_m(S - I)\varepsilon^t \end{aligned} \tag{6.14}$$

From (6.14), we can obtain the transformation strain for any shape change, $\varepsilon^t{}_{eq}$, and stiffness mismatch ($C_i - C_m$) as

$$\varepsilon^t = [(C_i - C_m)S + C_m]^{-1}C_i\varepsilon^t$$

This then gives the stress in the reinforcement as

$$\sigma_i = C_m(S - I)[(C_i - C_m)S + C_m]^{-1}C_i\varepsilon^t \tag{6.15}$$

This expression allows us to calculate the internal stresses in the inclusion. It is valid when the concentration of the inclusion phase is small. If this is not so, the interaction of the fields from the other inclusions would affect the average fields in the matrix and the reinforcement. The main advantage of the Eshelby tensor is that it allows us to determine the stress and strain in the inclusion without worrying about the complex stress field in the matrix. Determining the full field values can be an extremely difficult proposition depending on the geometry and the selected load case.

The Eshelby method would work nicely if the composite had ellipsoidal inclusions of arbitrary aspect ratios. The reinforcements, however, are generally of any shape causing singularities and problems in the local fields. The averaging schemes, in general, break down for some reinforcement shapes and if there occurs a clustering of particles or fibers. Last but not least, the effect of shape and spatial distribution of particles can become quite marked when constrained plastic deformation occurs in one of the phases, for example, in a WC/Co composite.

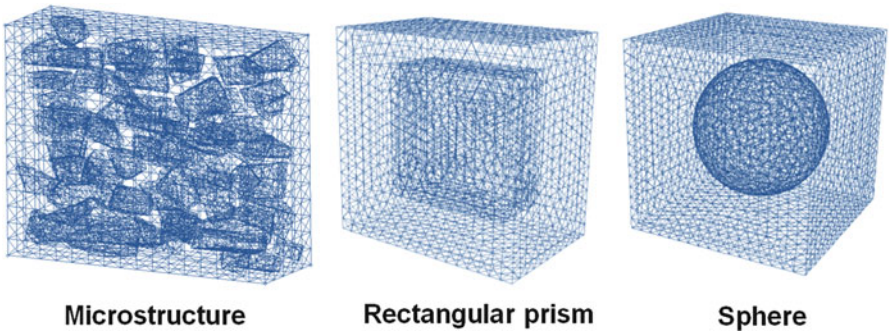

Fig. 6.9 Comparison of different types of numerical models: microstructure-based, unit cell rectangular prism, and unit cell sphere (after Chawla et al. 2004)

6.1.5 Numerical Methods

As an alternative to analytical analysis, numerical techniques such as finite element method (FEM) have become very popular, especially when the geometry of the component and thermomechanical history of the composite can be incorporated into the simulation of the properties. One common approach is to use a unit-cell model, where one or more reinforcement, fibers or particles, are embedded within the matrix, to simulate a composite material with a periodic array of reinforcement. It should be noted that in actual composites the particles commonly contain sharp corners, so spherical particles are not necessarily a realistic choice for simulation. Microstructure-based finite element techniques have been employed that are able to incorporate the "true" microstructures that take into consideration particle morphology and clustering of particles, as a basis for analysis using finite element techniques (Chawla et al. 2003, 2004). Figure 6.9 shows a microstructure-based model and two unit-cell models.

Chawla et al. (2003) applied an object-oriented finite element technique to particle reinforced metal matrix composites from images (micrographs) of real systems. In particular, the effect of reinforcement particle volume fraction and alignment (with respect to the loading axis) on the anisotropy of elastic properties was investigated. Chawla et al. (2004) obtained numerical predictions of the effective Young's modulus for an Al/SiC_p composite, which are shown in Table 6.2. The unit-cylinder particle has a greater stiffening effect than the spherical particle. Clearly, load transfer by a shear-lag type of mechanism (see Chap. 7) is more effective across a planar interface than a spherical interface.

The advantage of using a three-dimensional (3D) microstructure-based model is shown by a comparison of the predicted Young's modulus of the composite versus typical prismatic (rectangular) and spherical unit-cell models, Table 6.2. The highest and lowest simulated moduli and strength were obtained by the prismatic rectangle unit cell and sphere unit cell, respectively. This can be attributed to the

Table 6.2 Young's modulus predicted by various finite element models and comparison to experiment (Chawla et al. 2004)

Method	Young's modulus (GPa)
Unit cell, rectangular prism	113
Unit cell, sphere	100
3D microstructure	107.4 ± 0.4
Experiment (Ganesh and Chawla 2004)	107.9 ± 0.7

higher degree of load transfer for the prismatic, rectangular particle than for the spherical particles. The 3D microstructural models, from two different regions of the material, exhibited a higher degree of strengthening, since the actual microstructure incorporated the inherent aspect ratio and alignment of the SiC particles along the loading direction. A comparison of all predicted moduli with experimental tensile data on the same composite, from Chawla et al. (2004), shows that the result from the 3D microstructure model correlates very well with the experimentally determined Young's modulus value of 108 GPa (Ganesh and Chawla 2004). The shape of the particles also has an important effect. The angular particles result in better load transfer but also stress concentrations at the sharp corners, compared to ellipsoidal particles (Williams et al. 2012).

6.2 Physical Properties

In this section we provide expressions for some important physical properties such as density, coefficients of thermal expansion, and electrical and thermal conductivity.

6.2.1 Density

Density of a material is mass per unit volume. Density is one property for which the ROM works for any composite irrespective of the distribution of the constituents. The mass of a composite is the sum of the masses of the constituents. Thus,

$$m_c = m_m + m_r \tag{6.16}$$

where m represents the mass and the subscripts c, m, and r indicate composite, matrix, and reinforcement, respectively. The above equation is valid even in the presence of voids in the composite. For the volume of the composite, we can write

$$v_c = v_m + v_r + v_v \tag{6.17}$$

where v denotes the volume of a component, while the subscripts c, m, r, and v indicate composite, matrix, reinforcement, and void, respectively. We can then write in terms of mass fractions and volume fractions of the composite the following two expressions:

$$M_m + M_r = 1$$
$$V_m + V_r + V_v = 1$$

For the density of the composite, we can write

$$\rho_c = \frac{m_c}{v_c} = \frac{m_r + m_m}{v_c} = \frac{\rho_r v_r + \rho_m v_m}{v_c} = \rho_r V_r + \rho_m V_m \tag{6.18}$$

An experimental measurement of density of a composite is frequently used to test for the presence of any porosity in the composite. It is worth pointing out that should there be any interfacial reaction between the components of a composite, the reaction product(s) should be treated as additional component(s) of the composite.

6.2.2 Coefficient of Thermal Expansion (CTE)

Most materials, with very few exceptions, expand when heated, i.e., their volume increases. This of course stems from the atomic or molecular vibrations that materials undergo at all temperatures. The amplitude of these vibrations increases with temperature. We first review the basic expression for CTE of materials. We can characterize this in terms of a *volumetric* CTE, β, defined as

$$\beta_{ij} = \frac{1}{V}\left(\frac{\delta V}{\delta T}\right)$$

where V is the volume of the material, T is its temperature, and the two indices of the volumetric CTE indicate that it is a second-rank tensor.

We can also define a *linear* CTE, α, as

$$\alpha_{ij} = \frac{\delta \varepsilon_{ij}}{\delta T}$$

where ε is the strain and α is another second-rank symmetric tensor. The CTE, α, does not have a constant value over a very large range of temperature. Over a small temperature range, ΔT, we write

$$\varepsilon_{ij} = \alpha_{ij} \Delta T$$

It is instructive to recall that the sum of the diagonal terms of the strain tensor represents the volume change, i.e.,

$$\beta = \varepsilon_{11} + \varepsilon_{22} + \varepsilon_{33} = 3\alpha$$

$$\alpha = \frac{1}{3}[\varepsilon_{11} + \varepsilon_{22} + \varepsilon_{33}]$$

For small strains,

$$\beta_{ij} = 3\alpha_{ij}$$

In matrix notation, we can write (omitting the off-diagonal terms)

$$\begin{vmatrix} \varepsilon_{11} & \varepsilon_{12} & \varepsilon_{13} \\ & \varepsilon_{22} & \varepsilon_{23} \\ & & \varepsilon_{33} \end{vmatrix} = \begin{vmatrix} \alpha_{11} & \alpha_{12} & \alpha_{13} \\ & \alpha_{22} & \alpha_{23} \\ & & \alpha_{33} \end{vmatrix} \Delta T$$

In contracted notation, the above expression takes the following form:

$$\begin{vmatrix} \varepsilon_1 \\ \varepsilon_2 \\ \varepsilon_3 \\ \varepsilon_4 \\ \varepsilon_5 \\ \varepsilon_6 \end{vmatrix} = \begin{vmatrix} \alpha_1 \\ \alpha_2 \\ \alpha_3 \\ \alpha_4 \\ \alpha_5 \\ \alpha_6 \end{vmatrix} \Delta T$$

Expressions for CTE of Composites

In general, the CTE of a composite is different from that given by a simple ROM ($\alpha_f V_f + \alpha_m V_m$). This is because the presence of reinforcement, with an expansion coefficient different from that of the matrix, introduces a mechanical constraint on the matrix. The degree of constraint is also dependent on the nature of the reinforcement, e.g., a fiber will cause a greater constraint on the matrix than a particle.

Many models have been proposed to predict the coefficients of thermal expansion (CTE) of fibrous and particulate composites. Experimental determination of these coefficients and analysis of the general thermal expansion characteristics of a variety of composites are available in the literature; see, for example, Turner (1946), Kerner (1956), Rosen and Hashin (1970), Schapery (1968), Marom and Weinberg (1975), and Vaidya and Chawla (1994).

Unidirectionally Aligned Fibrous Composites

In fiber reinforced composites, two thermal expansion coefficients are needed: α_{cl} in the longitudinal direction and α_{ct} in the transverse direction. Fibers generally have a lower expansion coefficient than that of the matrix. Thus, the fibers mechanically constrain the matrix resulting in $\alpha_{c\ell}$ being generally smaller than α_{ct} for the

composite. At low V_f, it is possible that the transverse expansion coefficient of a fibrous composite, α_{ct}, may be greater than the CTE of the matrix by itself. Long, stiff fibers prevent the matrix from expanding in the longitudinal direction, which forces the matrix to expand more than usual in the transverse direction. Schapery (1968) put bounds on the CTE of a unidirectional fiber reinforced composite. These bounds are quite narrow in the longitudinal direction. The following assumptions are made in this analysis:

(a) The bonding between the fiber and matrix is perfect and mechanical in nature, i.e., no chemical interaction is allowed.
(b) The fibers are continuous and perfectly aligned.
(c) The properties of the constituents do not change with temperature.
(d) Poisson's ratios of the components are not very different.

Expressions for expansion coefficient of a fibrous composite are as follows. The longitudinal expansion coefficient for the composite is

$$\alpha_{c\ell} = \frac{\alpha_m E_m V_m + \alpha_f E_f V_f}{E_m V_m + E_f V_f} \tag{6.19}$$

The transverse expansion coefficient is

$$\alpha_{ct} \cong (1+\nu_m)\alpha_m V_m + (1+\nu_f)\alpha_f V_f - \alpha_{c\ell}\overline{\nu} \tag{6.20}$$
$$\overline{\nu} = \nu_f V_f + \nu_m V_m$$

For low fiber volume fractions, $V_f < 0.2$ or 0.3, α_{ct} can be approximated by

$$\alpha_{ct} \cong (1+V_m)\alpha_m V_m + \alpha_f V_f$$

Anisotropy in expansion can be reduced if the composite contains randomly oriented short fibers or whiskers in three dimensions. For such a composite, the isotropic thermal expansion coefficient is given by

$$\alpha \cong \frac{\alpha_{c\ell} + 2\alpha_{ct}}{3}$$

Particle Reinforced Composites

One can regard a particulate composite as a homogeneous material in a statistical sense, i.e., assuming a uniform distribution of the particles in the matrix; see Fig. 6.10. Volume fractions of the two phases are

$$V_1 \quad \text{and} \quad V_2 (= 1 - V_1)$$

Volumetric CTE of a composite consisting of spherical particles dispersed in a matrix (Kerner 1956) is given by

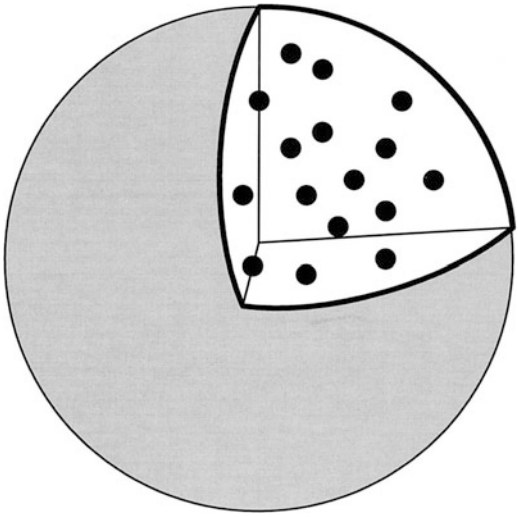

Fig. 6.10 Schematic of a particulate composite

$$\beta_c = \beta_m V_p + \beta_p V_p - \left(\beta_m - \beta_p\right) V_p \left[\frac{\frac{1}{K_m} - \frac{1}{K_p}}{\frac{V_m}{K_p} + \frac{V_p}{K_m} + \frac{0.75}{G_m}}\right]$$

Kerner's expression does not differ significantly from the ROM because the particle constrains the matrix a lot less than fibers. The solution due to Schapery (Schapery 1968) gives upper and lower bounds for the thermal expansion coefficient. The upper bound is given by

$$\alpha_c = V_p \alpha_p + V_m \alpha_m + \left[\frac{4G_m}{K_c}\right]\left[\frac{\left(K_c - K_p\right)\left(\alpha_m - \alpha_p\right)V_p}{4G_m + 3K_p}\right]$$

and the lower bound is

$$\alpha_c = V_p \alpha_p + V_m \alpha_m + \left[\frac{4G_p}{K_c}\right]\left[\frac{\left(K_c - K_m\right)\left(\alpha_p - \alpha_m\right)V_m}{4G_p + 3K_m}\right]$$

where K_c is the bulk modulus of the composite and is obtained from the Hashin–Shtrikman analytical model (Hashin and Shtrikman 1963) described above.

The expression of the linear CTE of a particulate composite has also been given by Turner (1946):

$$\alpha_c = \frac{\alpha_m V_m K_m + \alpha_p V_p K_p}{V_p K_p + V_m K_m}$$

Turner's expression, generally, gives an expansion coefficient much lower than the rule-of-mixtures value.

The models described above have been used extensively to predict the experimental behavior of particle reinforced MMCs. Elomari et al. (1997) studied the CTE behavior of SiC particle-reinforced pure Al matrix composites, in the volume fraction range of 47–55 % particles. The SiC particles were oxidized prior to matrix infiltration to minimize interfacial reaction. In their study the ROM predicted the highest CTE, followed by the predictions of Kerner, Schapery, and Turner, which was the lowest. The experimental data were in between the broad range between Kerner and Schapery predictions. Similar trends were observed by Sadanandam et al. (1992) for composites of 2124 Al reinforced with SiC (10, 20 %), Al_2O_3 (20 %), and TiC (20 %). Vaidya and Chawla (1994) measured CTE in several particle reinforced composites, 2014/SiC/17_p, 2014/Al_2O_3/17_p, 8090 (Al–Li)/SiC/15_p, 6061/SiC/15_p, and 6061/B_4C/15_p. Kerner's model was closest to experiment, although the Turner model predictions were much lower than the experiment. They attributed this to the fact that the Kerner's model is close to the rule-of-mixtures approximation when the constraint term is small, i.e., since the reinforcement is in particulate form, the constraint is not as large as that from fiber reinforcement.

Chawla et al. (2006) studied the thermal expansion behavior of extruded SiC particle reinforced Al matrix composites, using 2D microstructures as the basis for the models, Fig. 6.11a. The stress state in the composite was very much influenced by the morphology and distribution of the SiC particles, Fig. 6.11b. The stress was highest at the particle/matrix interface, while the matrix between closely spaced particles was also under high thermal stress. "Networks" of high-stress regions, linking particles in the composite, were also observed. The CTE of the composites was measured in three different orientations: longitudinal (parallel to the extrusion axis), transverse (normal to the extrusion axis but in the extrusion plane), and short transverse (normal to the extrusion axis and out of the plane). They also showed that the Turner prediction was below the experimental values, while the Schapery bounds were somewhat higher than the experiments, Fig. 6.12a. Using the microstructure-based models, better agreement was obtained with experiments than with the analytical models above. Because of the 2D nature of the model, however, the predictions were slightly higher than the experimental values, Fig. 6.12b.

Effect of Interface on CTE of a Composite

As we have described above, most models predict a value of thermal expansion coefficient of a composite that is less than that given by a simple ROM. The CTE of the composite is generally less than the ROM value because the presence of ceramic particles (usually of low α) introduces a constraint on the expansion of the metallic matrix (usually of high α). In this regard, it is important to point out that interface can exert some influence on the value of CTE, especially for very small particle size.

Xu et al. (1994) examined the effect of particle size on the thermal expansion of A1/TiC_p composites, in which the TiC particle size was varied. In this system, the

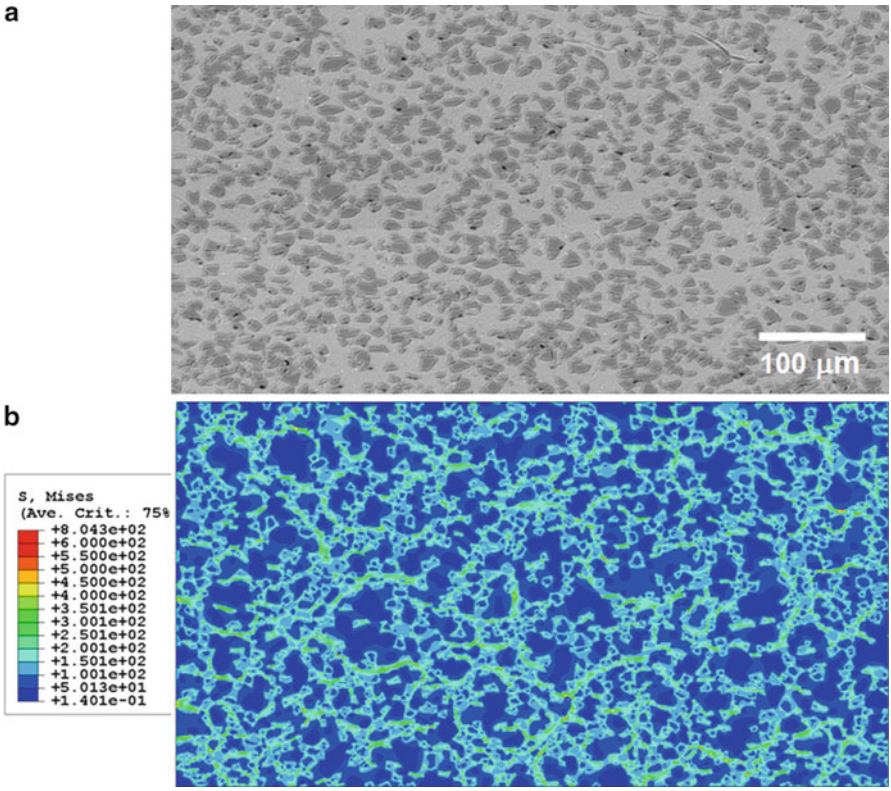

Fig. 6.11 (**a**) 2D microstructure used as the basis for finite element modeling of thermal expansion behavior in extruded SiC particle-reinforced Al matrix composites and (**b**) von Mises stress distribution after thermal expansion. The stress state in the composite was very much influenced by the morphology and distribution of the SiC particles (after Chawla et al. 2006)

interface is semi-coherent (Mitra et al. 1993). The particle volume fraction was maintained constant at about 15 % while two particle sizes were used, 0.7 and 4 µm. Figure 6.13 shows the values of CTE for the two composites (circles and squares). Also plotted in Fig. 6.13 are the CTE values for pure aluminum and titanium carbide. The 4-µm particle composite showed, consistently, a higher CTE than the 0.7-µm particle composite. Note that the CTE of the 4-µm particle composite is very close to the rule-of-mixtures (ROM) value, while that of the 0.7-µm particle composite is not, implying that more constraint on the aluminum matrix is caused by the 0.7-µm particle than by the 4.0-µm particle. A very good interfacial bond between the TiC particle and matrix exists. Although no chemical compound formation was observed in the interfacial area, lattice distortion in the interfacial area was observed. The thickness of this region of strain localization varied between 10 and 50 nm (Mitra et al. 1993). Such a lattice distortion at the interface will affect the CTE value of the composites. Since the interfacial area is related to the particle size, the volume of such a lattice distortion layer will depend on the

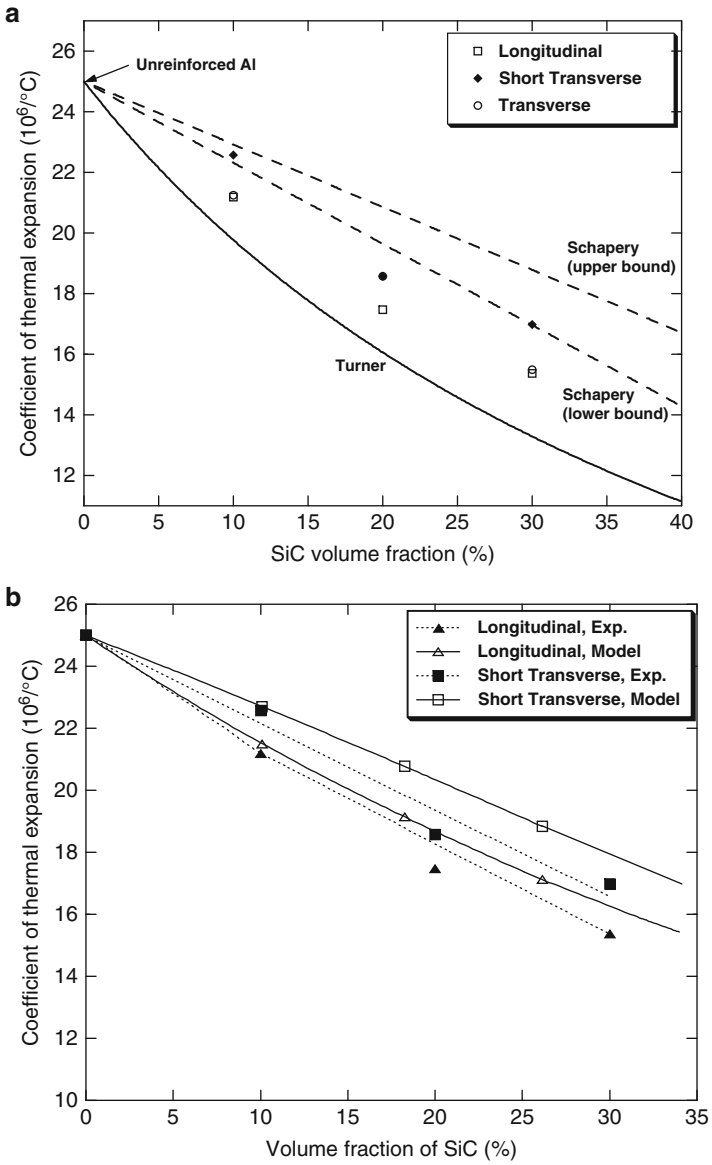

Fig. 6.12 (**a**) Comparison of experimentally determined CTE in extruded 2080 Al/SiC_p matrix composites, along with analytical predictions by Schapery and Turner, and (**b**) 2D microstructure-based FEM predictions. The effect of CTE anisotropy is more adequately captured by the microstructure-based model (after Chawla et al. 2006)

particle size, and, accordingly, the effect of the particle size on the CTE of the composites will vary with the particle size as well as shape. For a given particle volume fraction, the smaller particle size, the greater the volume fraction of interfacial zone. Figure 6.14a illustrates the effect of particle size on the interfacial

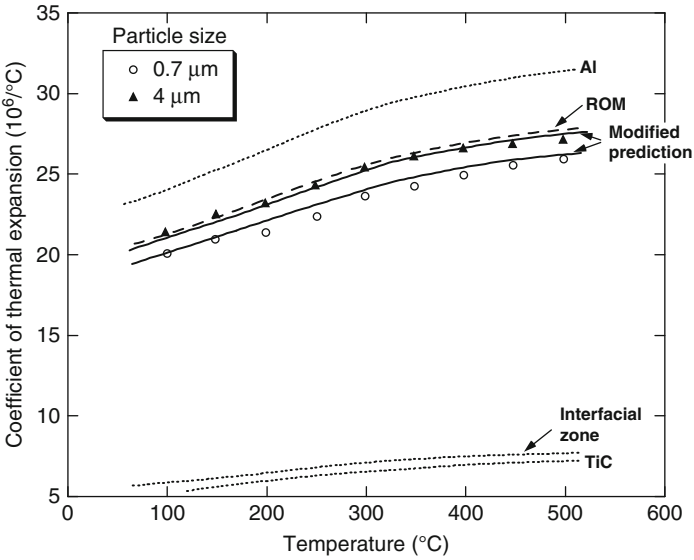

Fig. 6.13 CTE versus temperature for TiC particle-reinforced Al composites with different particle size (after Xu et al. 1994). The 4-μm particle composite showed, consistently, a higher CTE than the 0.7-μm particle composite. The modified rule-of-mixtures (ROM) prediction, which includes the CTE of the interface, predicted the experimental behavior very well

zone size for a given volume fraction of particle. A quantitative comparison of volume fraction of interfacial zone, V_i, between two particle size composites is shown in Fig. 6.14b. If the thickness of the distortion layer is assumed to be 25 nm, V_i can be 3 %, which is quite significant. This interfacial zone will be constrained to expand or contract with the particle, and thus, CTE of this zone will be closer to that of the particle than that of the metal matrix. In order to explain the effect of the particle size on the CTE of the particle reinforced metal matrix composite, consider that the composite consists of a matrix phase, a particulate reinforcement, and an interfacial zone to which a CTE different from that of the matrix can be ascribed. In this approximation, the constraint on the matrix expansion is thus embedded in the interfacial zone term. We can then write for the CTE of a three-component composite as follows:

$$\alpha_c = \alpha_p V_p + \alpha_m V_m + \alpha_i V_i \tag{6.21}$$

where the subscripts, c, p, m, and i, denote the composite, particle, matrix, and interfacial zone, respectively. The interfacial zone volume fraction, V_i, was calculated by the interfacial area and the thickness of the lattice distortion layer. The best fit CTE curves using (6.21) for the 4.0 and 0.7-μm particle composites are obtained for the same assumed value α_i but different V_i; see the solid lines with data points in Fig. 6.13. The apparent CTE values for the interfacial zone are also shown in

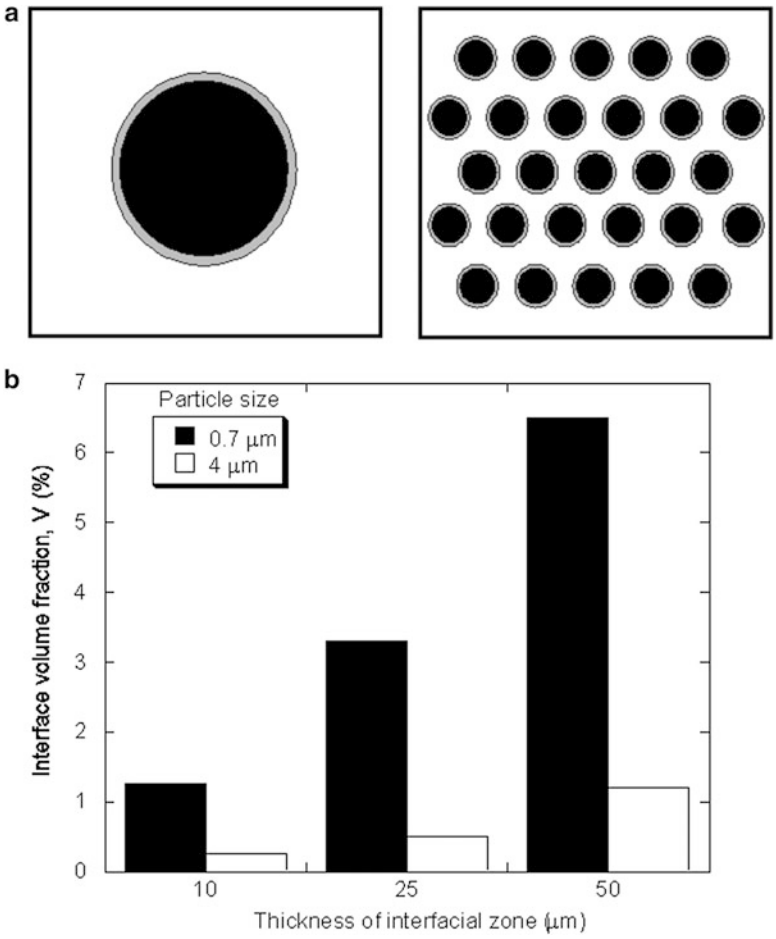

Fig. 6.14 (**a**) Schematic of the effect of particle size on fraction of interfacial zone. A smaller particle size results in a larger interfacial area. (**b**) Quantitative measurements of interfacial zone in Al–TiC_p composites. A larger interfacial zone will have a stronger effect on the CTE of the composite (after Xu et al. 1994)

Fig. 6.13. The agreement between the prediction (6.21) and the experimental results confirms the effect of particle size on the CTE of this particle reinforced composite.

A lower CTE may also result from an interfacial phase between particle and matrix. Elomari et al. (1997) studied the CTE behavior of SiC particle reinforced pure Al matrix composites. The SiC particles were oxidized prior to matrix infiltration to minimize interfacial reaction. A thin SiO_2 coating formed on the particles resulted in a lower CTE than that of unoxidized materials. Furthermore, a decrease in particles size (i.e., more surface area for oxides to form) also resulted in reduced CTE.

Other Factors Influencing CTE of Composites

In addition to the interface, the CTE of particle reinforced MMCs is affected by several other factors. These include plasticity due to CTE mismatch between reinforcement and matrix, during heating or cooling; reinforcement fracture; residual stress; and local stresses at points of contact between reinforcements. Lee et al. (1991), for example, noted that the experimentally measured CTE in Al alloy/SiC_p composites was lower than that of model predictions by Paul (1960). They postulated that the irregular shape of the SiC particles may cause different thermal stress fields relative to perfectly spherical particles. Furthermore, an incompressible plastic layer may form at the particle/matrix interface and result in lower expansion of the matrix and, thus, the overall composite.

The CTE may also be affected by the particle fracture. Elomari et al. (1996) examined the CTE in particle reinforced MMCs, $6061/Al_2O_3/10_p$ and 20_p, with increasing particle fracture. An increase in particle fracture resulted in increased CTE, presumably due to the increased compliance and easier expansion of the material with cracked surfaces. Residual stress also has an important effect on CTE. Chang et al. (2000) studied the CTE behavior of 40 vol.% Al_2O_3 particle reinforced Al matrix composites. Water-quenched samples had a lower CTE than furnace-cooled samples. This was attributed to thermal residual stresses present in the water-quenched samples. At temperatures above 100 °C, the CTE increased and was closer to the prediction by Kerner. This was attributed to a relief in the residual stresses with increasing temperature. Shen et al. (1994) used a unit cell FEM approach to model the thermal expansion behavior of SiC particle reinforced Al matrix composites. They showed that residual stress increased the apparent CTE of the composite, since the residual stress in the metal matrix has a tensile component. Shen et al. (1994) also showed that the CTE is much less sensitive to particle distribution (clustering) than tensile stiffness. This was attributed to the fact that for an elastically deforming, isotropic composite, the effective CTE is given as (e.g., per Hashin–Shtrikman and Schapery)

$$\alpha = \alpha_2 + (\alpha_1 - \alpha_2)\frac{1/K - 1/K_2}{1/K_1 - 1/K_2}$$

where K is the bulk modulus and the subscripts 1 and 2 refer to ductile and brittle phases. From this equation one can see that the CTE is highly dependent on K, which is relatively insensitive to the distribution of particles in the matrix of the composite. Interestingly, the contiguity of a phase had a significant effect on CTE. For example, when the brittle phase is continuous, an additional constraint is placed on the expansion of the ductile phase. Microvoid nucleation and propagation at points where particles touch or at preexisting processing-induced voids may also cause a deviation in strain versus temperature, with slight increase in CTE taking place (Balch et al. 1996).

6.2.3 Thermal Conductivity

Thermal conductivity is another thermal property of great importance. Some general background on thermal conductivity is given in the inset. A composite consisting of unidirectionally aligned carbon fibers in an aluminum matrix can show extremely high thermal conductivity along the fiber direction, especially if pitch-based carbon fibers are used. This is because pitch-based carbon fibers have very high thermal conductivity along the fiber axis. Thus, depending on the volume fraction of carbon fiber used, the thermal conductivity of a C/Al/ composite along the fiber direction can be greater than that of even copper. The thermal conductivity transverse to the fibers in such a composite will be about two-thirds that of aluminum. Such a C/Al/ composite can find applications in heat transfer applications where weight reduction is an important consideration. Examples of such applications might include high-density, high-speed integrated-circuit packages for computers and base plates for electronic equipment (see the chapter on applications, Chap. 11). Another possibility is to use this composite to dissipate heat from the leading edges of wings in high-speed airplanes. Tungsten carbide/cobalt composites are used extensively in operations such as metal cutting or rock drilling where they experience very high temperatures. The ability to dissipate heat away from the wear surface, and thus avoid any localized temperature-induced softening, depends on the thermal conductivity of the composite. In WC/Co composite, both phonons (quanta of lattice waves) and electrons contribute to thermal conductivity. In ceramics, only phonon (lattice) thermal conductivity contributes to the total thermal conductivity.

The heat flow in a material is proportional to the temperature gradient, and the constant of proportionality is called the thermal conductivity. In indicial notation, the equation for heat transfer is

$$q_i = -k_{ij} dT/dx_j$$

where q_i is the heat flux along x_i axis, dT/dx_j is the temperature gradient across a surface that is perpendicular to the x_j axis, and the coefficient k_{ij} is called thermal conductivity. Thermal conductivity is also a second-rank tensor; note the two indices. Similar to thermal expansion coefficient, the second-rank, symmetric thermal conductivity tensor, k_{ij}, in an isotropic material reduces to a scalar number, k. In an orthotropic material, we need three constants along the three principal axes: k_{11}, k_{22}, and k_{33}. In a transversely isotropic material such as a unidirectionally reinforced fibrous composite, there will be two constants: k_{cl} in the axial direction and k_{ct} in the transverse direction. The thermal conductivity in the axial direction, k_{cl}, can be predicted by a rule-of-mixtures type expression (Behrens 1968):

$$k_{c1} = k_{c\ell} = k_{f\ell} V_f + k_m V_m$$

where $k_{f\ell}$ is the thermal conductivity of the fiber in the axial direction and k_m is the thermal conductivity of the isotropic matrix. This relationship is similar to the ROM in the longitudinal direction for the Young's modulus obtained by action in parallel.

Thermal conductivity of a unidirectionally aligned fiber composite (i.e., transversely isotropic) in the transverse direction can be approximated by the action-in-series model. This would give

$$k_{ct} = k_2 = k_{f2}\,k_m/(k_{f2}\,V_f + k_m\,V_m)$$

Halpin–Tsai–Kardos equations can be used to obtain the following expression for the transverse thermal conductivity of a composite containing unidirectionally aligned fibers:

$$k_{c2} = k_{c3} = k = (1 + \eta V_f)/(1 - \eta V_f)k_m$$
$$\text{and } \eta = [(k_{f2}/k_m) - 1]/[(k_{f2}/k_{fm}) + 1]$$

Transport Properties

Electrical and thermal conductivities represent two very important transport properties. Electrical resistivity, ρ, is the inverse of electrical conductivity, σ. Electrical resistance of a piece of metal of length, L, and cross-sectional area, A, is given by

$$R = \frac{L\rho}{A}$$

Ohm's law relates the voltage drop, V, and current, I, as V = IR. Another form of Ohm's laws is as follows:

$$J_i = \sigma_{ij}\,E_j \qquad (A)$$

where J is the current density (current per unit area) I/A (Am^{-2}), E is the electric field (Vm^{-1}), and σ is the electrical conductivity ($\Omega^{-1}\,m^{-1}$), which is equal to 1/ρ. Electrical conductivity is also second-rank tensor as indicated by the two indices. Metals are generally good conductors with σ on the order of $10^7\ \Omega^{-1}\ m^{-1}$. In general, impurities, solid solution alloying, and plastic deformation reduce the electrical conductivity of metals.

The heat flow in a material is proportional to the temperature gradient, and the constant of proportionality is called the thermal conductivity. The basic equation has the form

$$q_i = -k_{ij}dT/dx_j$$

where q_i is the heat flux along x_i axis, dT/dx_j is the temperature gradient across a surface that is perpendicular to the x_j axis, and k_{ij} is the thermal

(continued)

(continued)

conductivity. The two indices indicate that thermal conductivity is also second-rank tensor. Another form of heat transfer equation is

$$q_i = -k_{ij} \Lambda T \tag{B}$$

where q_i is the heat flux, ΛT is the temperature gradient, and k_{ij} is the thermal conductivity tensor (W/mK). Equations A and B are mathematically similar. In these equations, the quantity on the left-hand side is the response to the stimulus on the right-hand side. The two are related via a constant of proportionality (σ and k) which is a tensor of rank two. For cubic symmetry, the tensor reduces to a scalar.

where we have taken ξ equal to 1.

6.2.4 Electrical Conductivity

In terms of electrical conductivity, most metal matrix composites are mixtures of good electrical conductors (e.g., Cu, Al, Ti) and insulators (e.g., B, C, SiC, Al_2O_3). There are exceptions such as W/Cu composites. Some general background on electrical conductivity is given in the inset. The conductivity (thermal or electrical) of a composite will depend on the conductivity characteristics of the matrix, reinforcement, volume fraction and aspect ratio and shape of the reinforcement, and, of course, the interfacial characteristics (Weber et al. 2003a, b; Weber 2005). In particular, interfacial resistance will vary with the form and size of reinforcement and the connectivity of the phases. Weber (2005) analyzed the influence of reinforcement size on the electrical conductivity of a metal matrix composite. He explained the observed size effect in terms of additional scattering of the conduction electrons at the metal/ceramic particle interface. The scattering effect of dislocations, generated by plastic deformation in the metal matrix during cooling from the processing temperature, on electrical conductivity was not significant.

For the simple case of a fiber-reinforced composite, assuming no significant interfacial effect, we can write for the resistivity of the composite in the axial direction, in a manner similar to other rule-of-mixtures type relationships:

$$\rho_{c\ell} = \rho_1 V_1 + \rho_2 V_2$$

where ρ is the electrical resistivity, V is volume fraction of a phase, and the subscripts $c\ell$, 1, and 2 designate the composite in the longitudinal direction and

the two components of the composite, respectively. Or in terms of electrical conductivity, σ (unfortunately, it is customary to use the same symbol as that for strength), we can write

$$\sigma_{c\ell} = \sigma_1 V_1 + \sigma_2 V_2$$

In the transverse direction, we have

$$\frac{1}{\sigma_{ct}} = \frac{V_1}{\sigma_1} + \frac{V_2}{\sigma_2}$$

where the symbols have the significance given earlier. There is a logarithmic expression also:

$$\log \sigma_c = V_1 \log \sigma_1 + V_2 \log \sigma_2$$

Of course, one can generalize these expressions to more than two composites in the composite, should that be the case. One can also use self-consistent models to obtain the electrical conductivity of a composite; see, for example, Hale (1976).

An important point that needs to be emphasized here is that the electrical resistivity (and therefore electrical conductivity) of the metal matrix in a composite is likely to be different from that of the unreinforced metal. This is because of possible plastic deformation during processing which will introduce dislocations due to thermal mismatch between the matrix and the reinforcement. The dislocations in turn will increase the resistivity of the matrix. Unlike the unreinforced metal, one cannot recover electrical conductivity by resorting to an annealing treatment because the annealing treatment will again cause plastic deformation of the matrix because of the thermal mismatch between the components.

6.3 Thermal Stresses in Composites

Thermal stresses are internal stresses that arise when a constraint on free dimensional change of a body exists (Chawla 1973a, b). In the absence of this constraint, the body can experience free thermal strains without any accompanying thermal stresses. In a composite material, this constraint comes from the fact that it is made of dissimilar materials, i.e., materials having different coefficients of thermal expansion. Thermal stresses result in a composite because of the ever present mismatch in the coefficients of thermal expansion of the reinforcement and the matrix ($\Delta\alpha = \alpha_m - \alpha_r$). Thermal strain, in the absence of any temperature gradients, is given by $\Delta\alpha\Delta T$, where ΔT is the amplitude of temperature change. During cooling from the processing temperatures, a large magnitude of thermal stresses can

result because of the thermal mismatch between the reinforcement (particle, short fiber or long fiber) and the matrix. Thermal stresses generated will depend on the reinforcement volume fraction, reinforcement geometry, thermal mismatch, temperature interval ($T_{final} - T_{initial}$), and modulus ratio, E_r/E_m, where the subscript r denotes the reinforcement. Generally, $\alpha_m > \alpha_r$, i.e., on cooling from $T_{initial}$ to T_{final} ($T_{initial} > T_{final}$), the matrix would tend to contract more than the reinforcement, putting the reinforcement in compression and the matrix in tension. That is the explanation in simple terms. In reality, it is a complex three-dimensional situation. We derive below the analytical expressions for (three-dimensional) thermal stress components in two types of composites: a central particle surrounded by its associated spherical matrix shell and a central fiber surrounded by its cylindrical shell of matrix. The following assumptions are made in this analysis:

- Matrix and reinforcement obey Hooke's law.
- Elastic reinforcement is embedded in an elastic continuum of matrix.
- No chemical reactions between reinforcement and matrix.

In what follows, we need to use the following sets of relationships to solve problems in elasticity involving a complex state of stress:

- Equations of equilibrium of forces
- Equations of compatibility
- Constitutive equations (stress–strain relations)
- Boundary conditions

6.3.1 Thermal Stresses in Particulate Composites

Consider a particulate composite consisting of small ceramic particles distributed in a metal matrix. If we regard this composite as an assembly of elastic spheres of uniform size, embedded in an infinite elastic continuum, then it can be shown from the theory of elasticity (Timoshenko and Goodier 1951; Brooksbank and Andrews 1970) that an axially symmetrical stress distribution will result around each particle. Figure 6.15 shows a schematic of such a particle reinforced composite. Let us say that each particle has a radius, a, while the surrounding matrix sphere has the outer radius, b. This spherical symmetry problem calls for the use of spherical coordinates, r, θ, and φ as indicated in Fig. 6.15. We have the following stress, strain, and displacement components:

$$\sigma_r, \sigma_\theta = \sigma_\varphi$$

$$\varepsilon_r, \varepsilon_\theta = \varepsilon_\varphi$$

$u_r = u$, radial displacement, independent of θ or φ

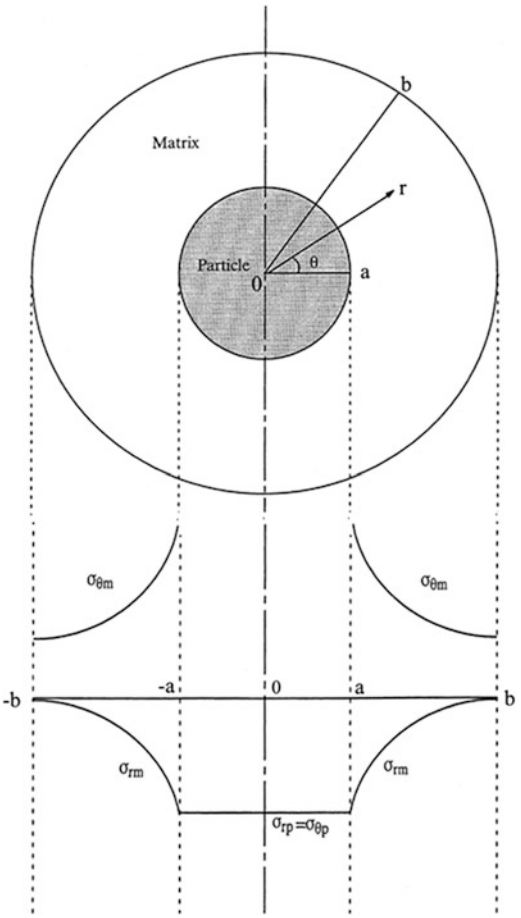

Fig. 6.15 Thermal stress distribution, on cooling, in a particulate composite that has CTE of matrix, $\alpha_m >$ particle CTE, α_p. The particle is under a uniform pressure, P, while the matrix has radial and tangential stress components; radial and tangential components in the matrix vary with distance as $1/r^3$

The stress–strain and strain–displacement relationships are

$$\begin{aligned} \varepsilon_\theta &= \frac{u}{r} = \frac{1}{E}[\sigma_\theta(1-\nu) - \nu\sigma_r] + \alpha\Delta T = \varepsilon_\phi \\ \varepsilon_r &= \frac{du}{dr} = \frac{1}{E}[\sigma_r(1-\nu) - \nu\sigma_\theta] + \alpha\Delta T \end{aligned} \tag{6.22}$$

The equilibrium equation for this spherical problem is

$$\frac{d\sigma_r}{dr} + \frac{2(\sigma_r - \sigma_\theta)}{r} = 0 \tag{6.23}$$

From (6.22) and (6.23), we get the following governing differential equation:

$$\frac{d^2u}{dr^2}+\frac{2}{r}\frac{du}{dr}-\frac{2}{r^2}u=0 \tag{6.24}$$

The solution to this differential equation is

$$u=Ar+\frac{C}{r^2} \tag{6.25}$$

This is the general solution that gives the displacement as a function of radial distance. We can obtain our stress components by applying the following boundary conditions relevant to our problem:

(a) Stress vanishes at the free surface (i.e., at r = b).
(b) The radial stress at the interface (r = a) is the interfacial pressure, P, i.e., $\sigma_r(a) = -P$.

When we apply these boundary conditions, we find that the stresses in the particle are

$$\sigma_{rp}=\sigma_{\theta p}=-P$$

while the stresses in the matrix are

$$\sigma_{rm}=\frac{P}{1-V_r}\left[\frac{a^3}{r^3}-V_r\right] \quad \text{and} \quad \sigma_{\theta m}=-\frac{P}{1-V_r}\left[\frac{1}{2}\frac{a^3}{r^3}+V_r\right]$$

The expression for P becomes

$$P=\frac{(\alpha_m-\alpha_r)\Delta T}{\left[\frac{0.5(1+\nu_m)+(1-2\nu_m)V_r}{E_m(1-V_r)}+\frac{1-2\nu_r}{E_r}\right]} \tag{6.26}$$

$$V_r=\left(\frac{a}{b}\right)^3$$

In the above expressions, V_r is the particle volume fraction, a is the particle radius, b is the matrix outer radius, and other symbols have the significance given earlier. A schematic of the stress distribution in the particulate composite is shown in the bottom half of Fig. 6.15 for case of cooling for a particulate composite that has CTE of matrix, $\alpha_m >$ particle CTE, α_r. We can summarize the main results for a particulate composite as follows:

- The particle is under a uniform pressure, P.
- The matrix has radial and tangential stress components that vary as $1/r^3$.
- The radial component goes to zero at the free surface, r = b, as per our boundary conditions. The tangential component has a nonzero value at the free surface.

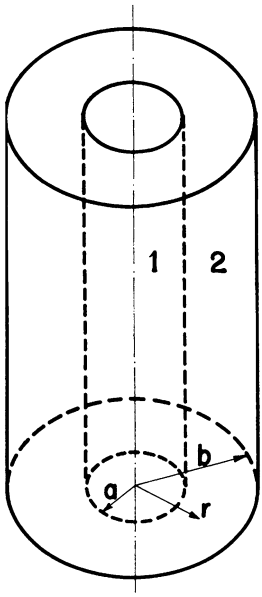

Fig. 6.16 Unit composite cylinder consisting of a fiber and its associated matrix sleeve. *1* and *2* indicate fiber and matrix, respectively

6.3.2 Thermal Stresses in Fiber Reinforced Composites

This important problem has been analyzed by a number of researchers (Poritsky 1934; Hull and Burger 1934; Chawla and Metzger 1972; Scherer 1986; Herrman and Wang 1991; Hsueh et al. 1988). In the case of a unidirectionally reinforced fibrous composite, it is convenient to use polar coordinates because of the inherent cylindrical symmetry. Figure 6.16 shows the basic fiber/matrix unit consisting of a central fiber (radius, a) surrounded by its sleeve of matrix (outer radius, b). The matrix outer radius, b, will depend on the volume fraction of the matrix. Such a simple axisymmetric model can be used to obtain the three-dimensional state of thermal stress up to a moderate fiber volume fraction.

The axial symmetry means that we can treat the problem in terms of the principal stresses that are independent of θ. We derive expressions for the thermal stresses in the two-element cylindrical composite shown in Fig. 6.16. For the axial symmetric case under consideration, the generalized Hooke's law can be written as follows (Poritsky 1934; Hull and Burger 1934; Chawla and Metzger 1972):

$$\varepsilon_r = \frac{\partial u}{\partial r} = \frac{1}{E}[\sigma_r - \nu(\sigma_\theta + \sigma_z)] + \alpha \Delta T$$
$$\varepsilon_\theta = \frac{u}{r} = \frac{1}{E}[\sigma_\theta(1-\nu) - \nu(\sigma_r + \sigma_z)] + \alpha \Delta T \qquad (6.27)$$

$$\varepsilon_z = \frac{\partial w}{\partial z} = \frac{1}{E}[\sigma_z - \nu(\sigma_r - \sigma_\theta)] + \alpha \Delta T$$

In (6.27) ε is strain, u is the radial displacement, σ is stress, α is the CTE, ΔT is the temperature change, and r, θ, and z are the cylindrical coordinates.

The only equilibrium equation for this rotationally symmetric problem is

$$\frac{d\sigma_r}{dr} + \frac{(\sigma_r - \sigma_\theta)}{r} = 0 \tag{6.28}$$

From (6.27) and (6.28), we get the following governing differential equation for our problem:

$$\frac{d^2u}{dr^2} + \frac{1}{r}\frac{du}{dr} - \frac{u}{r^2} = 0 \tag{6.29}$$

The general solution to this differential equation is

$$u = Ar + \frac{C}{r} \tag{6.30}$$

where A and C are constants of integration.

This relationship between displacement, u, and radial distance, r, needs to be solved for each component, central fiber, and outer matrix sleeve by applying boundary conditions. Thus, in component 1 or fiber, we have the radial displacement given by

$$u_1 = A_1 r + \frac{C_1}{r} \tag{6.31}$$

and in component 2 or matrix, we have

$$u_2 = A_2 r + \frac{C_2}{r} \tag{6.32}$$

The constants of integration in these expressions need to be obtained by applying our boundary conditions. The boundary conditions are:

(a) Stress vanishes at the free surface, i.e., $\sigma_{r2} = 0$ at $r = b$.
(b) Continuity of displacement at the fiber/matrix interface, i.e., $u_1 = u_2$ at $r = a$.
(c) Continuity of radial stress at the fiber/matrix interface, i.e., $\sigma_{r1} = \sigma_{r2}$ at $r = a$.
(d) The radial displacement, u, must vanish at the axis of symmetry, i.e., $u_1 = 0$ at $r = 0$.

By using these boundary conditions, we can determine the constant of integration in (6.31) and (6.32). The last condition gives C_2 to be identically zero because if that were not so, u_1 will become infinity at $r = 0$. That leaves us with three

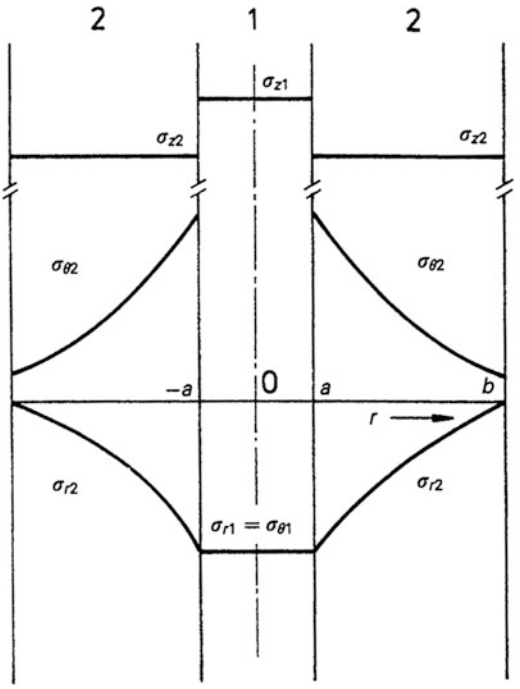

Fig. 6.17 Schematic of three-dimensional stress distribution in a fiber-reinforced composite. *1* and *2* indicate fiber and matrix, respectively

equations and three unknowns. Since ceramic fibers used to reinforce metals remain elastic until fracture but the metal can undergo plastic deformation in response to the thermal stresses generated, we give below full expressions for the three stress components in the matrix. These are

$$\sigma_r = A\left(1 - \frac{b^2}{r^2}\right) \quad \sigma_\theta = A\left(1 + \frac{b^2}{r^2}\right) \quad \sigma_z = B \tag{6.33}$$

where we have omitted the subscript m, and the constants A and B have the following expressions:

$$A = -\left(\frac{E_m(\alpha_m - \alpha_f)\Delta T(a/b)^2}{1 + (a/b)^2(1-2)\left[(b/a)^2 - 1\right](E_m/E_f)}\right)$$

$$B = \frac{A}{(a/b)^2}\left(2\nu\left(\frac{a}{b}\right)^2 \frac{1 + (a/b)^2(1-2\nu) + (a/b)^2(1-2\nu)\left[(b/a)^2 - 1\right](E_m/E_f)}{1 + \left[(b/a)^2 - 1\right](E_m/E_f)}\right)$$

$$\text{and} \quad \nu_m = \nu_f = \nu$$

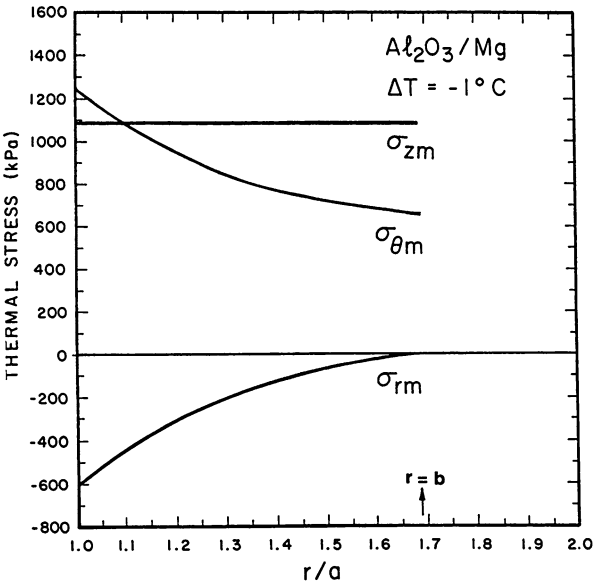

Fig. 6.18 Thermal stress distribution in magnesium matrix in an alumina fiber/magnesium matrix composite as a function of radial distance from the interface. The stress values correspond a cooling of −1 °C. Normalized radial distance is used, i.e., r/a = 1 corresponds to the interface

Figure 6.17 shows a schematic plot of three-dimensional stress distribution in a fiber reinforced composite. We use subscripts 1 and 2 in Fig. 6.17 to indicate fiber and matrix, respectively.

This thermoelastic solution can provide information about the magnitude of the elastic stresses involved and if the elastic limit will be exceeded or not. In the case of a metallic matrix, it is likely to deform plastically in response to these thermal stresses (Chawla 1973a, b; Arsenault and Fisher 1983; Christman and Suresh 1988).

We can draw some important conclusions from Fig. 6.17:

(a) Axial stress is uniform in fiber and matrix, although its magnitude is different in the two and depends on the respective elastic constants.
(b) In the fiber, i.e., the central component 1, σ_{rf} and $\sigma_{\theta f}$ are equal in magnitude and sense. In the matrix, i.e., the sleeve 2, σ_{rm} and $\sigma_{\theta m}$ vary as $[1 - (b^2/r^2)]$ and $[1 + (b^2/r^2)]$, respectively.
(c) When either the temperature difference or the expansion coefficient difference goes to zero, the thermal stresses vanish, as expected.

As an illustration, we plot in Fig. 6.18 the variation of thermal stresses generated in the magnesium matrix in an alumina fiber/magnesium matrix as a function of radial distance from the interface. The stress values shown correspond to a cooling of −1 °C. Normalized radial distance is used, i.e., r/a = 1 corresponds to the interface. Note the constant value of the axial stress. Also to be noted is the compressive radial stress, which is highest at the fiber/matrix interface and goes to zero at the free surface. The tangential stress is tensile in nature and highest at the interface and drops to a positive value at the surface.

References

Arsenault, R.J., and R.M. Fisher (1983) *Scripta Metall.*, **17,** 67.

Balch, D.K., T.J. Fitzgerald, V.J. Michaud, A. Mortensen, Y.-L. Shen, and S. Suresh (1996) *Metall. Mater. Trans.*, **27A**, 3700–3717.

Behrens, E. (1968) *J. Composite Mater.*, **2**, 2.

Brooksbank, D., and K.W. Andrews (1970) *J. Iron and Steel Inst.*, **208,** 582.

Chang, S.-Y., S.-J. Lin, and M.C. Flemings (2000) *Metall. Mater. Trans.*, **31A**, 291–298.

Chawla, K.K. (1973a) *Phil. Mag.*, **28**, 401.

Chawla, K.K. (1973b) *Metallography*, **6**, 55.

Chawla, K.K., and M. Metzger (1972) *J. Mater. Sci.*, **7,** 34.

Chawla, N., B.V. Patel, M. Koopman, K.K. Chawla, R. Saha, B.R. Patterson, E.R. Fuller, and S.A. Langer (2003) *Mater. Charac.*, **49,** 395–407.

Chawla, N., V.V. Ganesh, and B. Wunsch (2004) *Scripta Mater.*, **51,** 161–165.

Chawla, N., X. Deng, and D.R.M. Schnell (2006) *Mater. Sci. Eng.*, **426A**, 314–322.

Christman, T., and S. Suresh (1988) *Acta Metall.*, **36**, 1691.

Elomari, S., R. Boukhili, and D.J. Lloyd (1996) *Acta Mater.*, **44**, 1873–1882.

Elomari, S., R. Boukhili, C. San Marchi, A. Mortensen, and D.J. Lloyd (1997) *J. Mater. Sci.*, **32**, 2131–2140.

Eshelby, J. D. (1957) *Proc. Royal Soc.*, **A241**, 376–396.

Ganesh, V.V., and N. Chawla (2004) *Metall. Mater. Trans.*, **35A**, 53–62.

Ganesh, V.V., and N. Chawla (2005) *Mater. Sci. Eng.*, **A391**, 342–353.

Hale, D. K. (1976) *J. Mater. Sci.*, **11**, 2105.

Halpin, J.C., and J.L. Kardos (1976) *Polymer Eng. Sci.*, **16**, 344.

Halpin, J.C., and S.W. Tsai (1967) "Environmental Factors Estimation in Composite Materials Design," AFML TR 67–423.

Hermans, J.J. (1967) *Proc. K. Ned.Akad. Wet.*, **B70** (1), 1.

Herrman, K.P., and Y.Q. Wang (1991) in *Inelastic Deformation of Composite Materials*, Springer-Verlag, New York, p. 445.

Hashin, Z. (1962) *J. Appl. Mech.*, **29**, 143–53.

Hashin Z., and B.W. Rosen (1964) *J. Appl. Mech.*, **31**, 233.

Hashin, Z., and S. Shtrikman (1963) *J. Mech. Phys. Solids*, **11**, 127–140.

Hill, R. (1964) *J. Mech. Phys. Solids*, **12**, 199.

Hill, R. (1965) *J. Mech. Phys. Solids*, **13**, 189.

Hsueh, C.-H., P.F. Becker, and P. Angelini (1988) *J. Am. Ceram. Soc.*, **71**, 929–933.

Hull, A.W., and E.E. Burger (1934) *Physics*, **5**, 384.

Kerner, E.H. (1956) *Proc. Phys. Soc.*, **B69**, 808.

Koopman, M., K.K. Chawla, C. Coffin, B.R. Patterson, X. Deng, B.V. Patel, Z. Fang, and G. Lockwood (2002) *Adv. Eng. Mater.*, **4**, 37.

Lee, Y.S., M.N. Gungor, T.J. Batt, and P.K. Liaw (1991) *Mater. Sci. Eng.*, **A145**, 37–46.

Marom, G.D., and A. Weinberg (1975) *J. Mater. Sci.*, **10**, 1005.

Mitra, R., W.A. Chiou, M.E. Fine, and J.R. Weertman (1993) *J. Mater. Res.*, **8**, 2300.

McDanels, D.L., R.W. Jech, and J.W. Weeton (1965) *Trans. TMS-AIME*, **233**, 636.

Paul, B. (1960) *Trans. AIME*, **218**, 36.

Poritsky, H. (1934) *Physics*, **5**, 406.

Rosen, B.W. (1973) *Composites*, **4**, 16.

Rosen, B.W., and Z. Hashin (1970) *Int. J. Eng. Sci.*, **8,** 15.

Rossoll, A., B. Moser, and A. Mortensen (2005) *Mech. Mater.*, **37**, 1.

Sadanandam, J., G. Bhikshamaiah, B. Gopalakrishna, S.V. Suryanarayana, Y.R. Mahajan, and M.K. Jain (1992) *J. Mater. Sci. Lett.*, **11**, 1518–1520.

Schapery, R.A. (1968) *J. Comp. Mater.*, **2**, 380.

Scherer, G. (1986) *Relaxation in Glass and Composites*, Wiley, New York.

Shen, Y.-L., A. Needleman, and S. Suresh (1994) *Metall. Mater. Trans.*, **25A**, 839–850.

Timoshenko, S., and J.N. Goodier (1951) *Theory of Elasticity*, McGraw-Hill, New York, p. 416.
Turner, P.S. (1946) *J. Res. Natl. Bur. Stand.*, **37**, 239.
Vaidya, R.U., and K.K. Chawla (1994) *Composites Sci. Tech.*, **50**, 13.
Weber, L. (2005) *Acta Mater,* **53**, 1945.
Weber, L., J. Dorn, and A. Mortensen (2003a) *Acta Mater.*, **51**, 3199
Weber, L., C. Fischer, and A. Mortensen (2003b) *Acta Mater.*, **51**, 495.
Williams, J.J., J. Segurado, J. LLorca, and N. Chawla (2012) *Mater. Sci. Eng. A*, **557**, 113–118.
Xu, Z.R., K.K. Chawla, R. Mitra, and M.E. Fine (1994) *Scripta Metall. Mater.*, **31**, 1525.
Whitney, J.M., and M.B. Riley (1966) *AIAA Journal*, **4**, 1537.

Chapter 7
Monotonic Behavior

In this chapter we discuss the monotonic strengthening and fracture mechanisms of continuous fiber and discontinuously reinforced (short fiber and particle) metal matrix composites. Cyclic fatigue and creep of MMCs are discussed in Chaps. 8 and 9, respectively.

7.1 Strengthening Mechanisms

The monotonic strength and stiffness of MMCs are usually much higher than those of the unreinforced metal. Figure 7.1 shows a general schematic of the evolution of damage in an MMC during monotonic loading. Since the reinforcing phase typically is much stiffer than the matrix, a significant fraction of the stress is initially borne by the reinforcement. Microplasticity then takes place, at a fairly low stress, which corresponds to the original deviation from linearity in the stress–strain curve. This point is termed the proportional limit stress. Microplasticity in the composites has been attributed to stress concentrations in the matrix at the sharp ends of fibers, whiskers, and particles or at the poles of the reinforcement (Goodier 1933; Corbin and Wilkinson 1994; Chawla et al. 1998b, 2003). With increasing strain, microplasticity increases in magnitude to global plasticity in the matrix. The incorporation of reinforcement results in an increase in work-hardening rate of the material, relative to the unreinforced matrix. The higher observed work-hardening rate, relative to the unreinforced material, is a simple function of lower matrix volume (by incorporation of the reinforcement) and not necessarily due to a change in work-hardening mechanisms. When the matrix is significantly work hardened, the matrix is placed under great constraint (i.e., a triaxial tensile stress develops) with an inability for strain relaxation to take place. This causes the onset of void nucleation and growth, which take place at a lower far-field applied strain than that observed in the unreinforced material. With the onset of void growth in the matrix, the stress in the reinforcement approaches its fracture stress, followed by fracture of the composite. It should be pointed out that the damage evolution will

N. Chawla and K.K. Chawla, *Metal Matrix Composites*,
DOI 10.1007/978-1-4614-9548-2_7, © Springer Science+Business Media New York 2013

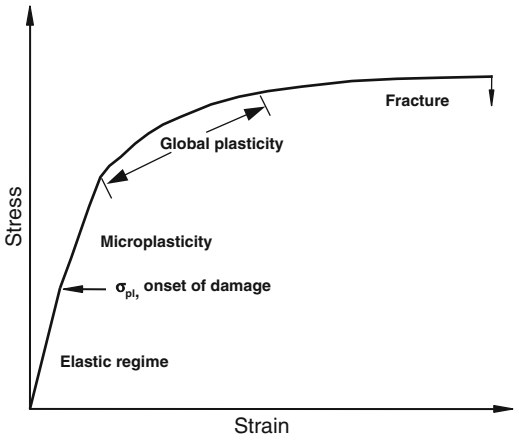

Fig. 7.1 Schematic of damage evolution in MMCs under tensile loading

also be very much influenced by the strength and nature of the reinforcement/matrix interface, as discussed in Sects. 7.2 and 7.3 below.

7.1.1 Direct Strengthening

The strengthening mechanisms observed in MMCs may be divided into two broad categories, direct and indirect strengthening. Direct strengthening takes place primarily in continuous fiber-reinforced composites but also takes place in discontinuously reinforced composites. Under an applied load, the load is transferred from the weak matrix, across the matrix/reinforcement interface, to the typically high-stiffness reinforcement (Cox 1952; Kelly and Lilholt 1969; Cheskis and Heckel 1970; Kelly 1973; Chawla 1998; Chawla and Shen 2001). In this manner, strengthening takes place by the reinforcement "carrying" much of the applied load. This is shown schematically in Fig. 7.2. Let us assume a single high-stiffness fiber embedded in a lower-modulus matrix. The composite is loaded without direct loading of the fiber itself. If a set of parallel imaginary lines are drawn on the composite, after loading the lines will become distorted because of the shear stresses generated by differing axial displacements in the fiber and matrix. Thus, load transfer to the fiber occurs by means of shear strains in the matrix.

Let us consider the case of a purely elastic fiber in an elastic matrix mathematically, Fig. 7.3. Let u be the displacement in the matrix in the presence of the fiber, at a distance x from one end, and let v be the displacement at x in the absence of the fiber. If P_f is the normal load on the fiber, then we can write the following expression for load transfer from the matrix to the fiber:

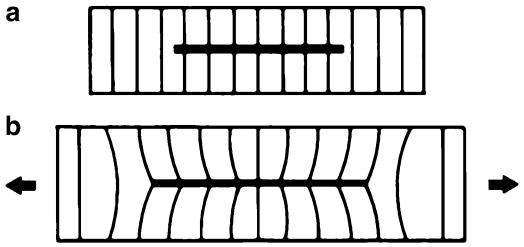

Fig. 7.2 A single fiber embedded in a matrix with lower modulus: (**a**) unstressed state and (**b**) stressed state. The imaginary *vertical lines* become distorted, indicating shear strains at the interface and load transfer to the fiber

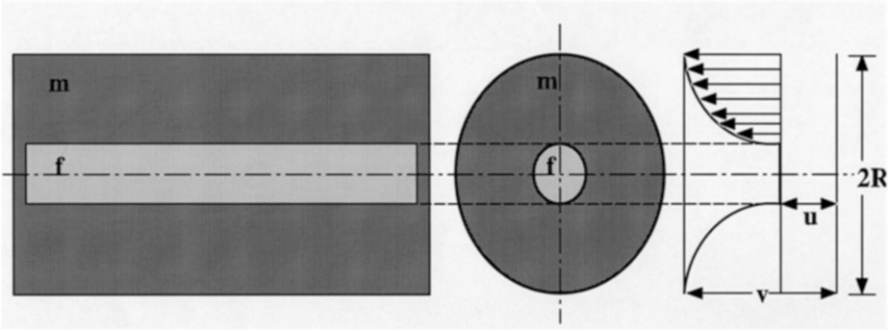

Fig. 7.3 A single fiber embedded in a cylindrical matrix shell subjected to an axial strain, e, which causes displacements in the fiber (u) and in the matrix (v)

$$\frac{dP_f}{dx} = B(u - v) \tag{7.1}$$

where B is a constant that is a function of fiber arrangement and matrix and fiber properties. The exact expression for B is described later in this section. Differentiating (7.1), we get

$$\frac{d^2P_f}{dx^2} = B\left(\frac{du}{dx} - \frac{dv}{dx}\right) \tag{7.2}$$

where $\frac{du}{dx}$ is the strain in fiber $= \frac{P_f}{E_f A_f}$ and $\frac{dv}{dx}$ is the strain in the matrix away from the fiber = e, imposed strain.

Equation 7.2 can be rewritten as

$$\frac{d^2P_f}{dx^2} = B\left[\frac{P_f}{A_f E_f} - e\right]$$

This second-order differential equation has the following solution:

$$P_f = E_f A_f e + S\sinh\beta x + T\cosh\beta x$$

where $\beta = \sqrt{\frac{B}{A_f E_f}}$.

In order to evaluate the integration constants, S and T, we apply the boundary conditions, $P_f = 0$ at $x = 0$ and $x = \ell$. Using half-angle trigonometric relations, we obtain the following result:

$$P_f = E_f A_f e\left[1 - \frac{\cosh\beta\left(\frac{\ell}{2} - x\right)}{\cosh\frac{\beta\ell}{2}}\right] \text{ for } 0 < x < \ell/2 \tag{7.3a}$$

or

$$\sigma_f = \frac{P_f}{A_f} = \frac{E_f e}{\ell}\left[1 - \frac{\cosh\beta\left(\frac{\ell}{2} - x\right)}{\cosh\frac{\beta\ell}{2}}\right] \text{ for } 0 < x < \ell/2 \tag{7.3b}$$

The maximum possible value of strain in the fiber is the imposed strain, e, so the maximum stress in the fiber is eE_f. The parameter β is a measure of how fast the load is transferred from the matrix to the fiber from the two ends. A value of $\beta = 0.5$ indicates a linear dependence of load transfer. If we have a long enough fiber, Fig. 7.4, the stress in the fiber will increase from both ends to a maximum value of the ultimate tensile strength of the fiber, i.e., $\sigma_{fu} = E_f e$. Only a portion of the fiber (in the center) will be under the maximum stress. The *average* stress in the fiber, then, can be written as

$$\overline{\sigma}_f = \frac{E_f e}{\ell}\int_0^{\ell}\left[1 - \frac{\cosh\beta\left(\frac{\ell}{2} - x\right)}{\cosh\frac{\beta\ell}{2}}\right] dx = E_f e\left[1 - \frac{\tanh\frac{\beta\ell}{2}}{\frac{\beta\ell}{2}}\right]$$

We can obtain the variation of shear stress, τ, along the fiber/matrix interface by considering the equilibrium of forces acting over an element of fiber (radius r_f). Thus, we can write, from Fig. 7.4,

$$\frac{dP_f}{dx}dx = 2\pi r_f dx\tau \tag{7.4}$$

Let us now consider the variation of shear stress, τ, along the fiber/matrix interface. We can obtain an expression for the interfacial shear stress by considering the equilibrium of forces over an element of fiber. The tensile load on the fiber, P_f, is equal to $P_f = \sigma_f \pi r_f^2$. Substituting this into (7.4), we get

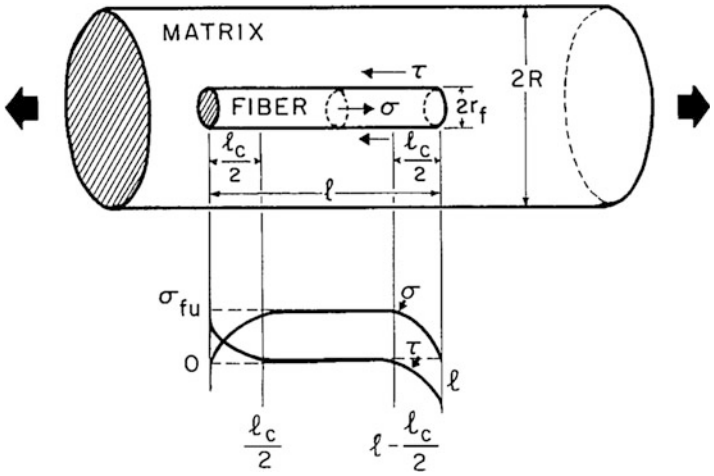

Fig. 7.4 Tensile stress (σ) and shear stress (τ) distribution in a single fiber embedded in a cylindrical matrix shell

$$\tau = \frac{1}{2\pi r_f}\frac{dP_f}{d\ell} = \frac{r_f}{2}\frac{d\sigma_f}{dx} \tag{7.5}$$

From (7.3b) and (7.5), we obtain

$$\tau = \frac{E_f r_f e\beta}{2}\frac{\sinh\beta\,(\ell/2 - x)}{\cosh\beta\,\ell/2}$$

Figure 7.4 shows the variation of τ and σ with distance x. At the ends of the fiber, the axial stress is zero. It increases until it reaches σ_{fu} in the center of the fiber (assuming a sufficiently long fiber that will enable the stress to build to σ_{fu}). The shear stress is a maximum at the fiber ends and a minimum in the center of the fiber. Such a stress distribution has also been confirmed by finite difference technique (Termonia 1987) and by micro-Raman spectroscopy for polymer matrix composites (Young 1994).

We now return to the expression for the constant B, which is a function of fiber packing geometry. In Fig. 7.4 we note that 2R is the average center-to-center fiber spacing. Let τ(r) represent the shear stress at a distance r from the fiber axis. Then at the fiber surface ($r = r_f$), we can write

$$\frac{dP_f}{dx} = -2\pi r_f \tau(r_f) = B(u - v)$$

or

$$B = -\frac{2\pi r_f \tau(r_f)}{(u - v)} \tag{7.6}$$

Consider now the equilibrium of forces on volume of matrix material between r_f and R. We can write

$$2\pi r\tau(r) = \text{constant} = 2\pi r_f \tau(r_f)$$
$$\tau(r) = \frac{r_f \tau(r_f)}{r}$$

The shear strain in The shear strain in the matrix by

$$\tau(r) = G_m \gamma$$

where G_m is the shear modulus of the matrix and γ is the shear strain in the matrix. The shear strain in the matrix is given by

$$\gamma = \frac{dw}{dr} = \frac{\tau(r)}{G_m} = \frac{\tau(r_f) r_f}{G_m r}$$

where w is the real displacement in the matrix at any distance r. Integrating the above expression between the surface of the fiber, r_f, and the outer radius of the matrix, R, gives us the total displacement in the matrix:

$$\int_0^R dw = \Delta w = \frac{\tau(r_f) r_f}{G_m} \int_0^R \frac{1}{r}\, dr = \frac{\tau(r_f) r_f}{G_m} \ell n \left(\frac{R}{r_f}\right) \tag{7.7}$$

We can also write for the total displacement as

$$\Delta w = v - u = -(u - v) \tag{7.8}$$

From (7.7) and (7.8), we obtain the following relationship:

$$\frac{\tau(r_f) r_f}{u - v} = -\frac{G_m}{\ln(R/r_f)} \tag{7.9}$$

From (7.6) and (7.9), we get

$$B = \frac{2\pi G_m}{\ln(R/r_f)} \tag{7.10}$$

B is related to load transfer parameter β as follows:

$$\beta = \left(\frac{B}{E_f A_f}\right)^{\frac{1}{2}} = \left[\frac{2\pi G_m}{E_f A_f \ln(R/r_f)}\right]^{\frac{1}{2}} \tag{7.11}$$

The ratio R/r_f is a function fiber packing. For a square array and hexagonal array of fibers, we can write the following two expressions:

$$\ln\left(\frac{R}{r_f}\right) = \frac{1}{2}\ln\left(\frac{\pi}{V_f}\right) \quad \text{(square array)}$$

$$\ln\left(\frac{R}{r_f}\right) = \frac{1}{2}\ln\left(\frac{2\pi}{\sqrt{3}V_f}\right) \quad \text{(hexagonal array)}$$

A more general, maximum fiber packing factor, ϕ_{max}, can also be introduced into the above equation:

$$\ln\left(\frac{R}{r_f}\right) = \frac{1}{2}\ln\left(\frac{\phi_{max}}{V_f}\right)$$

Substituting into (7.11), we get

$$\beta = \left[\frac{4\pi G_m}{E_f A_f \ln(\phi_{max}/V_f)}\right]^{\frac{1}{2}}$$

From the discussion above, it can be seen that in order to load the fibers to their ultimate tensile strength, the matrix shear strength must be relatively high. The maximum shear stress will be the smaller of the following two stresses: (a) yield stress of the matrix in shear and (b) shear strength of the fiber/matrix interface. In MMCs, the interface shear strength is quite high, so plastic yielding of the matrix will take place first. If we assume that the matrix does not work-harden, the matrix shear yield strength, τ_y, will control the load transfer. Then, the equilibrium of forces over a fiber length $\ell/2$ (since the fiber is loaded from both ends) gives us the following relation:

$$\sigma_f \frac{\pi d^2}{4}\ell = \tau_y \pi d \frac{\ell}{2} \quad \text{or} \quad \frac{\ell}{d} = \frac{\sigma_f}{2\tau_y} \tag{7.12}$$

The term ℓ/d is called the aspect ratio of the fiber. Given a sufficiently long fiber, it should be possible to load the fiber to its ultimate tensile strength, σ_{fu}, by means of load transfer through the plastically deforming matrix. Thus, in order to load the fiber to σ_{fu}, a critical aspect ratio of fiber is required, $(\ell/d)_c$, which is obtained by rewriting (7.12):

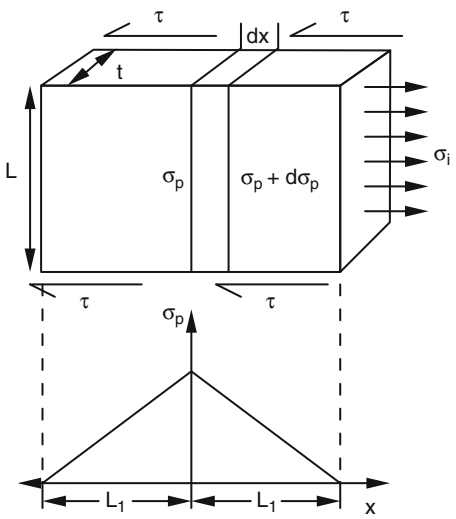

Fig. 7.5 Schematic of modified shear-lag analysis used to quantify load transfer in low-aspect-ratio particles (after Nardone and Prewo 1986)

$$\left(\frac{\ell}{d}\right)_c = \frac{\sigma_{fu}}{2\tau_y} \tag{7.13}$$

Thus, in order to load the fiber to σ_{fu} at a single point, ℓ must be equal to ℓ_c. In order to load a larger fraction of the fiber to σ_{fu}, ℓ should be much larger than ℓ_c. Thus, load transfer is more efficient in composites with large aspect ratio reinforcement, such as continuous fibers or whiskers. Due to the lower aspect ratio of particulate materials, load transfer is not as efficient as in the case of continuous fiber reinforcement, but is still significant in providing strengthening (Nardone and Prewo 1986; Davis and Allison 1993; Chawla et al. 1998a, 2000).

Nardone and Prewo (1986) proposed a modified shear-lag model for load transfer in particulate materials, Fig. 7.5. The model incorporates load transfer from the particle ends, which is neglected in fiber-reinforced composites because of the large aspect ratio. The yield strength of the particulate composite, σ_{cy}, is increased over the matrix yield strength, σ_{my}:

$$\sigma_{cy} = \sigma_{my}\left[V_p\left(\frac{S+4}{4}\right) + V_m\right]$$

where S is the aspect ratio of the particle (equal to the particle length, L, divided by the particle thickness, t, for a rectangular particle), V_p is the volume fraction of particles, and V_m is the volume fraction of matrix. Note that this relation does not account for the effect of particle size directly or matrix microstructure on load transfer.

7.1.2 Indirect Strengthening

Indirect strengthening arises from a change in matrix microstructure and properties due to the addition of reinforcement. In this section we describe some possible sources of indirect strengthening. Thermal expansion mismatch between reinforcement and matrix can result in internal stresses whenever there is a temperature change (e.g., during cooldown from processing or during service). Such a mismatch is generally present in all kinds of composites. It is a very important feature of MMCs comprised as they are of a high coefficient of thermal expansion (CTE) metallic matrix and a low CTE ceramic reinforcement. If the thermal mismatch-induced stress is greater than the yield stress of the matrix, upon cooling, dislocations form at the reinforcement/matrix interface because plastic deformation in common metals occurs via dislocations. In this manner, thermally induced dislocation punching results in "indirect strengthening" of the matrix (Chawla and Metzger 1972; Chawla 1973a, b; Vogelsang et al. 1986; Arsenault and Shi 1986; Dunand and Mortensen 1991). Chawla and Metzger (1972) showed this effect in W fiber-reinforced Cu single crystal matrix composites. The density of dislocations in the matrix was measured (by an etch-pitting technique) as a function of distance from the fiber/matrix interface, for composites with various volume fractions of W fiber, Fig. 7.6a. With increasing volume fraction, the dislocation density in the matrix increased. The dislocation density was also highest in the interface region because the thermal stresses between the fiber and matrix in the interface region are the highest. The three-dimensional thermal stress model described in Chap. 6 can be used to explain the distribution of dislocation density in the matrix. Figure 7.6b shows thermally induced slip lines in the polycrystalline Cu matrix in a W/Cu composite that was thermally cycled between room temperature and 450 °C. Dunand and Mortensen (1991) used a model system of glass fiber-reinforced AgCl to study dislocation punching due to thermal mismatch. The AgCl matrix is optically transparent, and the dislocations can be seen emanating from the fiber, Fig. 7.7. The degree of thermally induced dislocations can also be exacerbated by the degree of fiber roughness (Isaacs and Mortensen 1992).

Arsenault and Shi (1986) developed a model to quantify the degree of dislocation punching that takes place due to CTE mismatch between a particle and matrix, Fig. 7.8. The dislocation density generated due to the mismatch is given by

$$\rho_{\mathrm{CTE}} = \frac{A\varepsilon V_{\mathrm{p}}}{\mathrm{b}(1 - \mathrm{V_p})\mathrm{d}} \tag{7.14}$$

where A is a geometric constant, b is the Burgers vector, d is the diameter of the particle, V_p is the particle volume fraction, and ε is the thermal misfit strain equal to $\Delta\alpha\Delta T$. The incremental increase in strength due to dislocation punching, then, can be written as

$$\Delta\sigma = BGb\rho_{\mathrm{CTE}}^{1/2}$$

where B is a constant and G is the shear modulus of the matrix. Substituting in (7.14), we can write $\Delta\sigma$ as

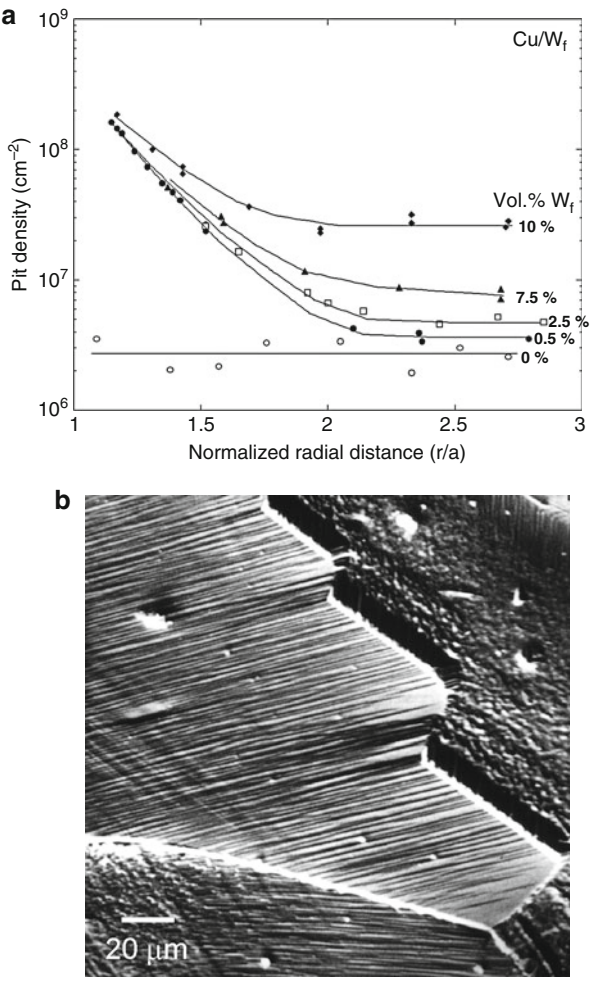

Fig. 7.6 (**a**) Dislocation density in W fiber-reinforced Cu matrix composites, as a function of distance from the fiber/matrix interface. With increasing volume fraction of fiber, the thermal stress mismatch at the interface increased, resulting in a higher dislocation density (after Chawla and Metzger 1972). (**b**) Thermally induced slip lines in the Cu matrix

$$\Delta\sigma = \mathrm{BGb}\left[\frac{A\varepsilon V_\mathrm{p}}{\mathrm{b}(1-\mathrm{V_p})}\frac{\mathrm{S}}{\mathrm{d}}\right]^{\frac{1}{2}} \tag{7.15}$$

where S is the aspect ratio of the particle and the other symbols have the significance given above. Inspection of (7.15) shows that the degree of indirect strengthening is directly proportional to volume fraction and inversely proportional to particle size. Thus, a larger degree of interfacial area (i.e., smaller particle size) will result in enhanced dislocation punching. This is shown schematically in Fig. 7.9. Note that for a constant volume fraction of 0.3, a significant enhancement in indirect strengthening is observed for particles of 3-μm diameter, vis-à-vis particles of 100-μm diameter.

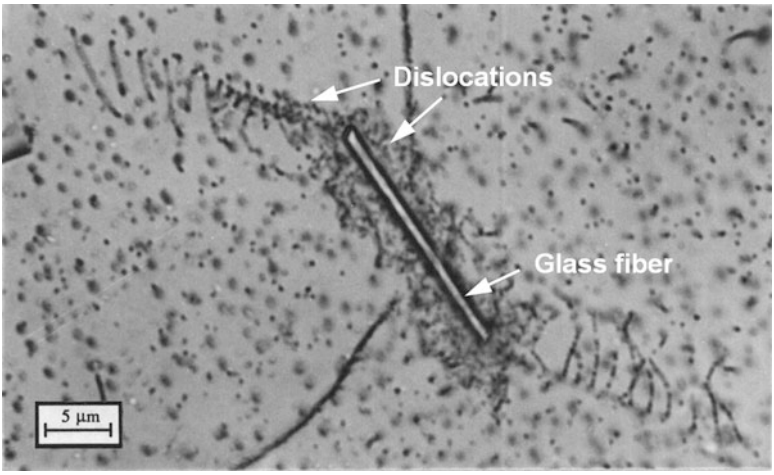

Fig. 7.7 Thermally induced dislocation punching in a model glass fiber/AgCl system (Dunand and Mortensen 1991). Note the high density of dislocations at the interface and the punching of dislocation loops from the fiber ends (courtesy of A. Mortensen and reprinted with permission of Elsevier Ltd.)

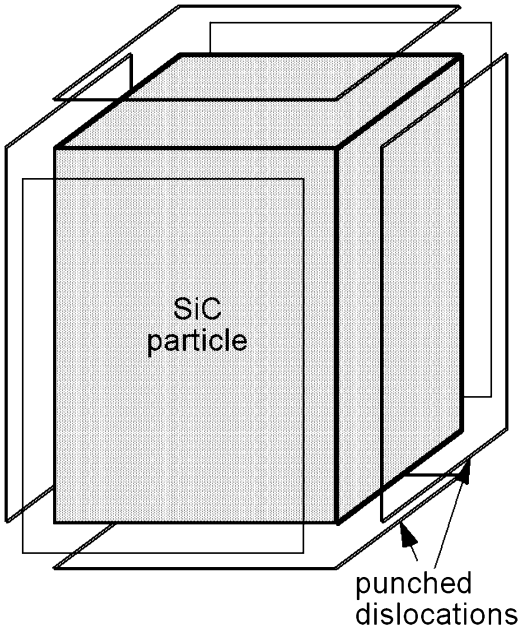

Fig. 7.8 Schematic of model used to quantify the degree of dislocation punching that takes place due to CTE mismatch between particle and matrix (after Arsenault and Shi 1986)

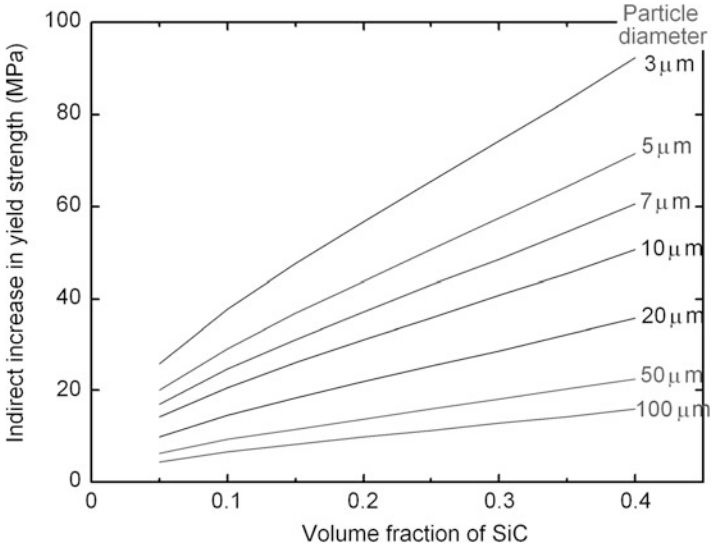

Fig. 7.9 Increase in yield strength due to dislocation punching, as predicted by the model of Arsenault and Shi (1986). The degree of strengthening is significantly influenced by particle size, for a given volume fraction

In age-hardenable matrix materials, the thermally induced dislocations (formed upon quenching from the solution treatment) serve as heterogeneous nucleation sites for precipitate formation during the aging treatment (Suresh and Chawla 1993). Not only is there a preferential distribution of precipitates in the particle/matrix interface region, but the higher density of dislocations also causes an acceleration in the time to peak age compared to the unreinforced alloy of the same composition.

In composites processed by liquid-phase routes, the matrix grain size can be much finer than that of the unreinforced alloy, due to pinning of grain boundaries by the particles or Zener pinning (Humphreys 1977, 1991). Differences in matrix texture may also result by the incorporation of reinforcement, for example, in deformation-processed materials (see Chap. 4).

Separating and quantifying the contributions of direct and indirect strengthening, to the overall composite strength, is a challenge. The extent of indirect strengthening is more difficult to quantify than the contribution from direct strengthening. One way to separate the two types of strengthening is to process composites such that the matrix microstructure is similar to that of the unreinforced alloy. Krajewski et al. (1993) used a thermomechanical treatment in Al 2080/SiC_p, consisting of solution treating and rolling, followed by aging (T8 treatment), to provide a homogeneous distribution of dislocations (and subsequently precipitates) in both the matrix of the composite and the unreinforced alloy. In such a situation,

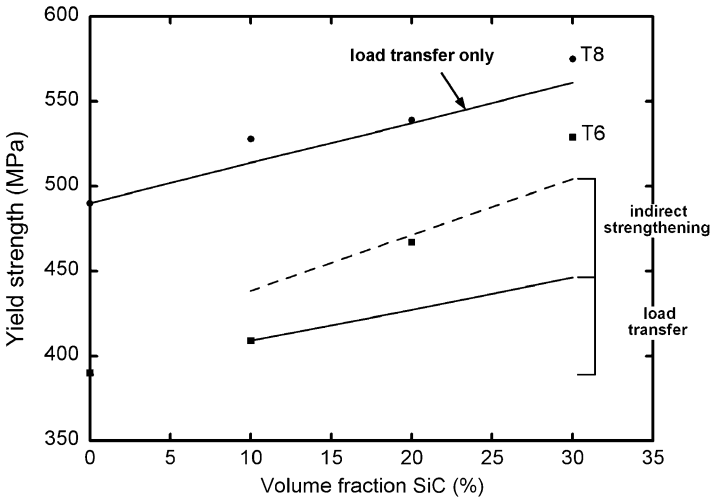

Fig. 7.10 Yield strength versus volume fraction of SiC particles in 2080/SiC_p composite (after Chawla et al. 1998a). The rolled and aged materials (T8 matrix composites) have similar microstructure to the unreinforced T8 alloy. T6 matrix composites are aged only, so their microstructure is different from 2080–T6. The experimental increase in yield strength in T8 materials correlated well with predictions from the modified shear-lag model. In T6 matrix composites, the strength of the composite consisted of contributions of both indirect and direct strengthening

the difference in strengthening between unreinforced alloy and composite was attributed primarily to load transfer to the reinforcement (Chawla et al. 1998a). This is shown in Fig. 7.10. Chawla et al. (1998a) showed that in T8 matrix composites, the experimental increase in yield strength correlated well with predictions from the modified shear-lag model. In composites that were solution treated, quenched, and aged (T6 heat treatment), the strength of the composite consisted of contributions of both indirect and direct strengthening; see Fig. 7.10.

7.2 Monotonic Behavior of Continuous Fiber Reinforced MMCs

The monotonic strength and damage evolution in continuous fiber-reinforced MMCs are dependent on several factors:

1. *Fiber characteristics*. The volume fraction, strength, and relative orientation of the fibers, with respect to the loading axis.
2. *Strength and nature of the interface*. Interfacial strength has a significant effect on the strengthening and damage tolerance of continuous fiber-reinforced MMCs. Interfacial reactions between fiber and matrix, and fiber dissolution,

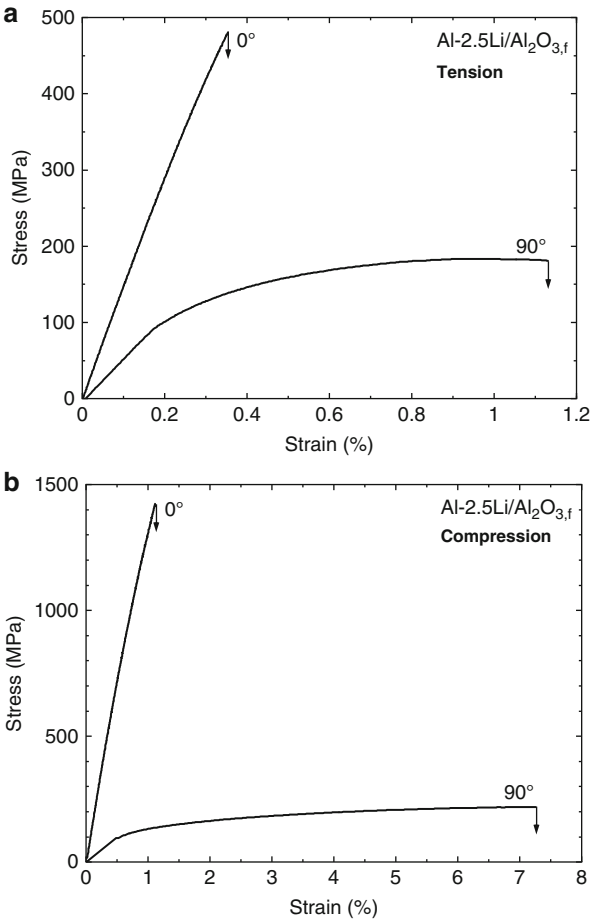

Fig. 7.11 Anisotropy in strength of Al–2.5Li/$Al_2O_{3,f}$ composites, parallel to the fibers (0°) and perpendicular to the fiber direction (90°), in (**a**) tension and (**b**) compression (after Schulte and Minoshima 1993)

may be detrimental to the strength of the composite. Preferential precipitation at the interface, in age-hardenable systems, can have mixed effects on strength.

3. *Matrix work-hardening and strength characteristics*. Of particular importance are the changes in matrix microstructure, during processing, due to the incorporation of the reinforcement (i.e., indirect strengthening, described above).

We now examine each of the three main factors described above. Continuous fiber-reinforced MMCs exhibit very high strength in the direction parallel to the fibers but comparatively low strength perpendicular to the fiber direction. Figure 7.11 shows the anisotropy in strength of Al–2.5Li/$Al_2O_{3,f}$ composites, parallel to the fibers (0°) and perpendicular to the fiber direction (90°), in both tension and compression (Schulte and Minoshima 1993). Clearly, along the axis of the fibers, the degree of strengthening from the fibers will be much higher than that perpendicular to the fiber direction. The mechanical properties of fiber-reinforced metal

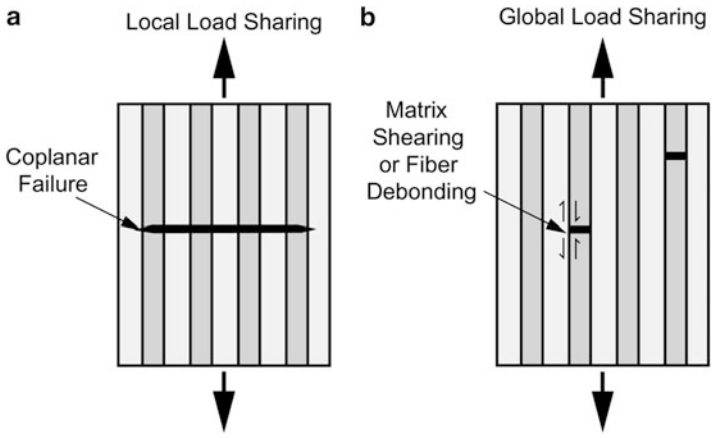

Fig. 7.12 Schematic of damage for the case of (**a**) relatively strong fiber/matrix interface, resulting in local load sharing and coplanar failure, and (**b**) relatively weak interface, where global load sharing is observed and fiber debonding and matrix shear are predominant

matrix composites are also very much dependent on the strength of the fiber/matrix interface. Figure 7.12 shows a schematic of damage for the case of a relatively weak fiber/matrix interface and that of a relatively strong interface. When a fiber fractures in the composite with a weak interface, fiber debonding and crack deflection take place. These local energy-absorbing mechanisms allow for uniform redistribution of the load, originally borne by the fiber before fracture, to the surrounding fibers. This condition is called *global load sharing* (Curtin 1993). When the interface strength is very large, fiber fracture will not result in debonding and crack deflection. Rather, the load cannot be redistributed homogeneously, so the single fiber fracture will result in precipitous fracture of adjacent fibers. As the neighboring fibers fracture, more and more fibers will continue to fracture until the composite fails. This series of successive fiber failures due to localization of strain around a single fiber results in *local load sharing* (Gonzalez and LLorca 2001). It should be noted that a very weak interface is also not desirable in MMCs. Such an interface would not allow efficient load transfer from the matrix to the fiber.

Whether a composite exhibits global or local load sharing, behavior may also be influenced by the work-hardening characteristics of the matrix. A matrix with high strain hardening rate would be less conducive to plastic relaxation of the stress concentration around the fractured fiber. Thus, more brittle matrix materials are more conducive to local load sharing and a lower ductility. Figure 7.13 shows a comparison of $Al/Al_2O_3/60_f$ and $6061/Al_2O_3/60_f$ fiber-reinforced composites (Devé and McCullough 1995).

Because of the combined effects of high interfacial shear strength and higher matrix work-hardening rate of the Al 6061 matrix, this composite has a much lower ductility and strength than the composite with the pure Al matrix. Voleti et al. (1998) used a finite element model of a composite consisting of a broken

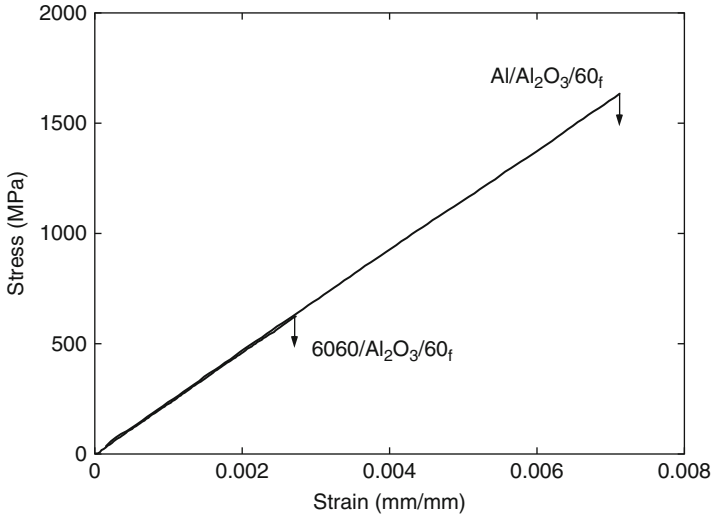

Fig. 7.13 Tensile stress–strain comparison of $Al/Al_2O_3/60_f$ and Al6061/ $Al_2O_3/60_f$ fiber-reinforced composites (after Devé and McCullough 1995). The high interfacial shear strength and higher matrix work hardening rate of the Al6061 matrix resulted in a much lower ductility and strength than the composite with pure Al matrix

fiber surrounded by the matrix and an intact fiber. They showed that the stress concentration in the intact fiber was influenced by both interfacial debonding and matrix plasticity surrounding the broken fiber. If fiber fracture takes place at very low strains (much below the onset of global plasticity), then the matrix plasticity "propagates" toward the intact fiber resulting in a large degree of stress elevation. Interfacial debonding, on the other hand, reduces the stress concentration around the fractured fiber and the intact fiber.

The degree of global load sharing is also a function of strain rate. Galvez et al. (2001) tested large-diameter SiC fiber-reinforced Ti-6Al-4V matrix composites at strain rates ranging between 2×10^{-5} and 500 s^{-1}. It was shown that at very high strain rates local load sharing conditions were predominant, and a lower ductility of the composite was observed. Lower strain rates were more conducive to allowing a gradual redistribution of the load, so global load sharing was observed. Microstructural observations showed that at low strain rates, the carbon coating on the SiC fiber resulted in crack deflection at the interface, while at very high strain rates, the cracks penetrated the coating. These authors did not, however, observe a strain rate dependence of strength of the composite.

Guden and Hall (2000) noticed significant increases in compressive flow stress and strength with increasing strain rate in $Al/Al_2O_{3,f}$ composites. The strain rate sensitivity was observed in both longitudinal and transverse orientations. The strain rate sensitivity of transverse strength was attributed to the matrix strain rate sensitivity, while that in the longitudinal direction was due to strain rate-dependent fiber buckling. In static compression, significant kinking and buckling of the fibers

also take place (Devé 1997). Unfortunately, while relatively weak interfaces are conducive to global load sharing and, thus, high tensile strength and ductility, they are quite detrimental to the transverse properties of the composite (Jansson et al. 1991; McCullough et al. 1994; Bushby 1998). This can be explained by the fact that, under transverse loading, the weak interfaces are perpendicular to the applied load. Similar observations have been made for Al_2O_3 fiber/Mg matrix composites under off-axis loading (Hack et al. 1984).

7.2.1 *Criteria for Debonding and Crack Deflection at an Interface*

In MMCs, as well as in other types of composites, interfacial bonding affects the fracture behavior of the composite. In very general terms, a strong interfacial bond will allow an oncoming crack to go unimpeded through the interface and the composite will fail, more or less, in one plane and in a brittle manner. The interaction of a crack with a weak interface, on the other hand, is likely to lead to debonding at the interface, followed by crack deflection, crack bridging, fiber fracture, and finally fiber pullout. These are all energy-absorbing phenomena that contribute to enhanced fracture toughness and a non-catastrophic failure mode.

A strength-based model for crack deflection or the formation of secondary crack at a weak interface was first proposed by Cook and Gordon (1964). They analyzed the problem of crack deflection at an interface between materials of identical elastic constants, i.e., the same material joined at an interface. Consider a crack advancing perpendicular to the fiber/matrix interface. Cook and Gordon (1964) estimated the strength of the interface necessary to cause a diversion of the crack from its original direction. At the tip of a crack, there exists a triaxial state of stress (plane strain) or a biaxial stress (plane stress); see Fig. 7.14. The principal stress component, σ_y, has a very high value at the crack tip and decreases sharply with distance from the crack tip. The stress component acting normal to the interface, σ_x, is zero at the crack tip. It rises to a maximum value at a small distance from the crack tip and then falls off in a manner similar to σ_y. If the tensile strength of the interface is less than the maximum value of σ_x, then the interface will fail in front of the crack tip. According to the estimates of Cook and Gordon, an interface with strength equal to or less than one-fifth of σ_x will result in the opening of the interface in front of the crack tip.

One can also analyze the interaction between a crack and an interface in terms of a fracture energy parameter instead of strength (He and Hutchinson 1989). Two materials meeting at an interface are more than likely to have *different* elastic constants. The modulus mismatch leads to shearing of the crack surfaces. This results in a mixed-mode stress state in the vicinity of an interface crack tip involving both the tensile and shear components. This, in turn, results in mixed-mode fracture, which can occur at the crack tip or in the wake of the crack. Figure 7.15 shows this crack front and crack wake debonding in a fiber-reinforced composite. What this

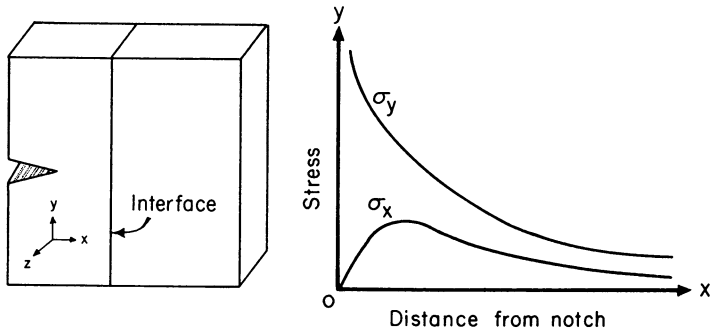

Fig. 7.14 Stress distribution at a crack tip under a uniaxial applied stress in the y-direction (after Cook and Gordon 1964). σ_y has a very high value at the crack tip and decreases sharply with distance from the crack tip. The stress component acting normal to the interface, σ_x, is zero at the crack tip; it rises to a maximum value at a small distance from the crack tip and then falls off in a manner similar to σ_y

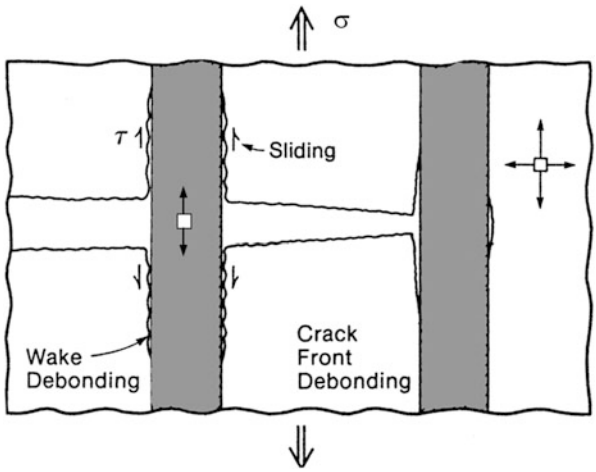

Fig. 7.15 Crack front and crack wake debonding in a fiber-reinforced composite under a far-field, uniaxial stress, σ. Note the interfacial shear stress, τ, causing sliding and triaxial state of stress at the crack tip

means in practical terms is that instead of a simple, one parameter description by the critical stress intensity factor K_{Ic}, one needs a more complex formalism of fracture mechanics to describe the situation in the composite. The parameter K under such a situation becomes scale sensitive, but the critical strain energy release rate, G_{Ic}, is not a scale-sensitive parameter. The strain energy release rate, G, is a function of the phase angle, ψ, which is a function of normal and shear loading.

One needs to specify G and ψ to analyze the debonding at the interface. G and ψ are related, through the so-called Dundurs parameters, α and β as defined below:

$$\alpha = \frac{G_1(1-\nu_2) - G_2(1-\nu_1)}{G_1(1-\nu_2) + G_2(1-\nu_1)}$$

$$\beta = \frac{1}{2}\frac{G_1(1-2\nu_2) - G_2(1-2\nu_1)}{G_1(1-\nu_2) + G_2(1-\nu_1)}$$

The parameter α can also be defined as

$$\alpha = \frac{\overline{E}_1 - \overline{E}_2}{\overline{E}_1 + \overline{E}_2}$$

$$\overline{E}_1 = \frac{E}{1-\nu^2}$$

In the above expressions, ν is the Poisson's ratio, E is Young's modulus, and the subscripts 1 and 2 refer to the interface and fiber, respectively. The expression for the phase angle, ψ, in terms of the elastic coefficients of the two media, radius r from the crack tip and the displacements, u and v, at the crack tip, is as follows:

$$\phi = \tan^{-1}\left(\frac{\nu}{u}\right)$$

$$\psi = \phi - \left(\frac{\ln r}{2\pi}\right)\ln\frac{(1-\beta)}{(1+\beta)}$$

These expressions have been used by several researchers (Ruhle and Evans 1988; He and Hutchinson 1989; Evans and Marshall 1989; Gupta et al. 1993; Chan 1993) to analyze the conditions for fiber/matrix debonding in terms of the energy requirements. Without going into the details of the model, the main message of such a plot is to display the conditions under which the crack will deflect along the interface or penetrate through the interface into the fiber. The chart of G_i/G_f versus α is shown in Fig. 7.16. G_i is the mixed-mode interfacial fracture energy of the interface, G_f is the mode I fracture energy of the fiber, and α is a measure of elastic anisotropy as defined above. For opening mode or mode I, $\psi = 0^\circ$, while for mode II, $\psi = 90^\circ$. For all values of G_i/G_f below the line, interfacial debonding is predicted. For the special condition of $\alpha = 0$, i.e., zero elastic mismatch, the model predicts debonding at the fiber/matrix interface for G_i/G_f less than about 0.25. Conversely, for G_i/G_f greater than 0.25, the crack will propagate across the fiber. In general, for the elastic mismatch, α, greater than zero, the minimum interfacial toughness required for interface debonding increases, i.e., high-modulus fiber tends to favor debonding.

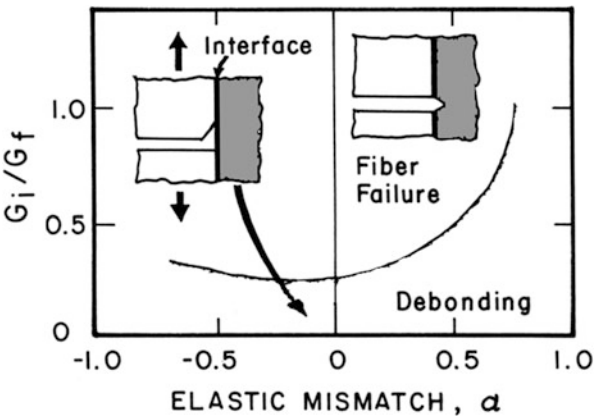

Fig. 7.16 A chart of relative energies, G_i/G_f versus elastic mismatch, α (after Evans and Marshall 1989)

Gupta et al. (1993) have also derived strength and energy criteria for crack deflection at a fiber/matrix interface for several composite systems. They took due account of the anisotropic nature of the fiber as well as the fact that a crack can deflect along the interface in one direction (singly) or two directions (doubly). Their experimental technique involved laser spallation of a film from a substrate and the measurement of displacement by a sophisticated laser Doppler displacement interferometer. This technique allows the measurement of the tensile strength of the planar interface between the film and the substrate. The strength determined in the laser spallation experiment is thought to be independent of any inelastic processes because the interface separation takes place at a very high strain rate, about $10^6\ s^{-1}$. The tensile strength determined in this fashion is then related to the *intrinsic* interface toughness. According to the analysis of Gupta et al., for most pairs of materials, the energy release rate is higher for the doubly deflected crack than that for the singly deflected case. In this formulation, a generalized interface delamination chart based on the energy criterion cannot be made. However, the authors did provide the ratio of energies of crack deflection and crack penetration for a few chosen interface systems (Gupta 1991; Gupta et al. 1993).

7.2.2 Work Done in Fiber Pullout

Fiber pullout can be an important feature of the failure process in fiber-reinforced composites. We now derive an expression for the work done in the pullout process. Consider the situation depicted in Fig. 7.17. Let us say that the fiber, of diameter d, fractures at some distance k below the main crack plane, such that $0 < k < \ell_c/2$, where ℓ_c is the critical length for load transfer. Locally, debonding of the fiber/matrix interface occurs. When the fiber is pulled out of the matrix, an interfacial frictional shear stress, τ_i, will be generated. In our simple analysis here, we assume

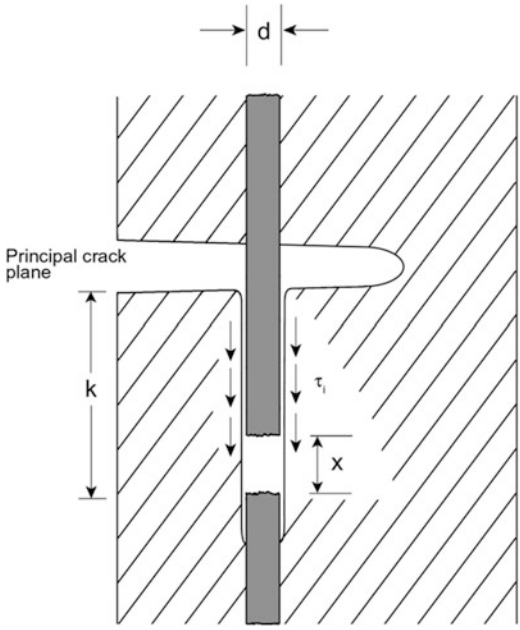

Fig. 7.17 Fiber pulled out through a distance x after fiber fracture. A shear stress, τ_i, comes into play at the interface during pullout

that this shear stress, τ_i, resisting fiber sliding is a constant. More complex treatments involving a Coulomb friction law governing fiber sliding resistance (Shetty 1988; Gao et al. 1988) and treatments taking into account residual stresses are available in the literature (Cox 1990; Hutchinson and Jensen 1990; Kerans and Parthasarathy 1991).

Let us assume that the fiber be pulled out through a distance x. The interfacial shear force opposing this motion of fiber is $\tau_i \pi d\,(k - x)$, where $\pi d\,(k - x)$ is the cylindrical surface area over which the shear stress is acting. Let the fiber be pulled out through a small distance dx. Then the work done by the interfacial shear force is $\tau_i \pi d\,(k - x)\,dx$. The total work done in the fiber pullout process over the length k is obtained by integration:

$$\int_0^k \tau_i \pi d(k - x)\,dx = \frac{\tau_i \pi d k^2}{2}$$

The length of the fiber pulled out will vary between 0 and $\ell_c/2$, where ℓ_c is the critical length for load transfer. Therefore, the average work done in the fiber pullout process is

$$W_{fp} = \frac{1}{\ell_c/2} \int_0^{\ell_c/2} \frac{\tau_i \pi d k^2 \, dk}{2} = \frac{\tau_i \pi d {\ell_c}^2}{24}$$

This expression assumes that all of the broken fibers are pulled out. Experimental observations, however, show that only fibers with broken ends within a distance $\ell_c/2$ from the principal fracture plane undergo pullout. Thus, we should expect a fraction (ℓ_c/ℓ) of fibers to pullout, and the average work done per fiber in fiber pullout can be written as

$$W_{fp} = \frac{\ell_c}{\ell} \frac{\tau_i \pi d {\ell_c}^2}{24}$$

7.2.3 *Effect of Interfacial Reactions on Monotonic Behavior*

In Chap. 4, we described the general features of the interface and provided some examples of interfacial reactions in MMCs. Here we explore the effects of interfacial reactions on the monotonic properties of MMCs. Interfacial reactions can play an important role in damage of continuous fiber-reinforced MMCs (Page et al. 1984). In Ti matrix composites reinforced with SCS-6 fibers, the C-rich fiber coating reacts with the Ti matrix to form layers of brittle TiC and Ti_5Si_3 (Konitzer and Loretto 1989; Leyens et al. 2003). In B fiber-reinforced Al, AlB_2 is formed at the interface at temperatures as low as 500 °C (Grimes et al. 1977). Tensile loading in the longitudinal axis results in circumferential cracks in the reaction layer, which severely impair the strength of the composite (Grimes et al. 1977; Mikata and Taya 1985; Kyono et al. 1986). Figure 7.18a shows that the longitudinal strength decreases with increasing exposure time at 500 °C (Kyono et al. 1986). In the transverse orientation, however, Fig. 7.18b, there was a slight increase in strength. This is because the damage mechanisms in transversely loaded composites were quite different. Here, the fracture surfaces of as-fabricated samples showed significant interfacial debonding. With increasing exposure time and an increase in the reaction layer thickness, the interface strength increased, so microcracks formed in the reaction layer and propagated through the boron fiber, resulting in fiber splitting.

Transverse strength may also be affected by binders used to densify the matrix of the composite. Eldridge et al. (1997) fabricated sapphire fiber-reinforced NiAl matrix composites with and without a polymethyl methacrylate (PMMA) organic binder. Transverse fracture surfaces showed that the composites with the binder exhibited a large amount of carbon residue at the fiber/matrix interface, which prevented a strong interfacial mechanical bond and led to low interfacial strength, Fig. 7.19a. Composites processed without binder had a much "cleaner" fracture surface, Fig. 7.19b, and stronger bond strength.

The extent of interfacial reaction can be reduced by the application of a thin fiber coating. In SiC fiber-reinforced W composites, for example, a reaction zone of

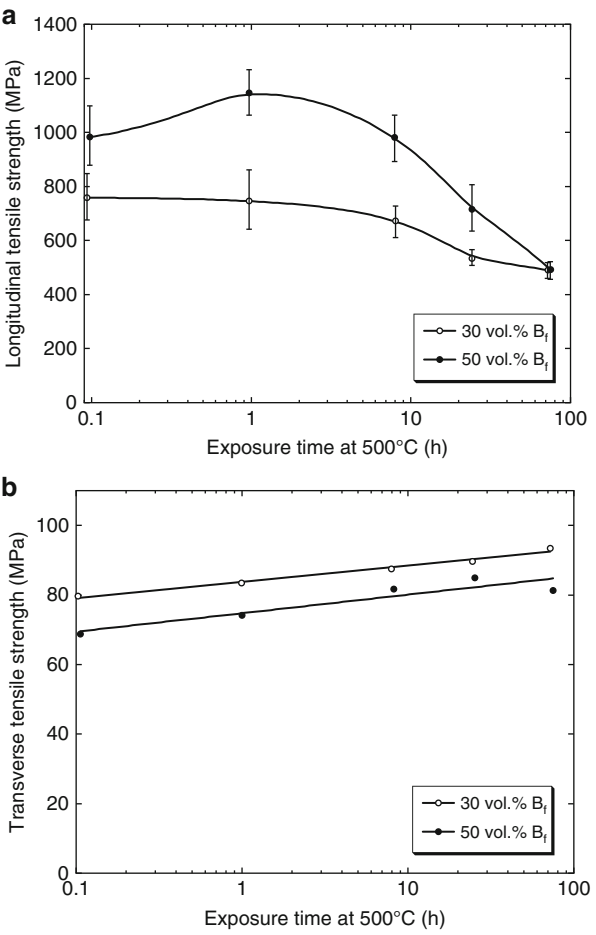

Fig. 7.18 Effect of exposure time at 500 °C on the tensile behavior of Al/B_f composites in (**a**) longitudinal orientation and (**b**) transverse orientation (after Kyono et al. 1986). AlB_2 is formed at the interface, and its thickness increases with exposure time. Circumferential cracks in the brittle interface form during tensile loading along the longitudinal direction. In the transverse orientation, the interface strength increases slightly with exposure time

tungsten silicide is formed, which embrittles the interface and reduces the strength of the composite. Deposition of a TiC coating significantly limited the reduction in strength (Faucon et al. 2001). It should be noted that while the incorporation of a fiber coating may hinder interfacial reaction, it may also contribute to a lower degree of wetting by the matrix and poorer densification of the composite.

As mentioned above, in composites with a precipitation-hardenable matrix, the interface may be affected by precipitates in the matrix which typically nucleate heterogeneously at the fiber/matrix interface (see Chap. 3). Cornie et al. (1993) tailored heat treatments to control the precipitate size and spacing at the interface. They found that a minimum in precipitate spacing (which corresponds to a minimum in precipitate size) resulted in a maximum in longitudinal strength and a minimum in transverse strength. This was caused by the decrease in interfacial strength due to precipitation at the interface. With increasing annealing time, coarsening of the precipitates took place, increasing the precipitate spacing and

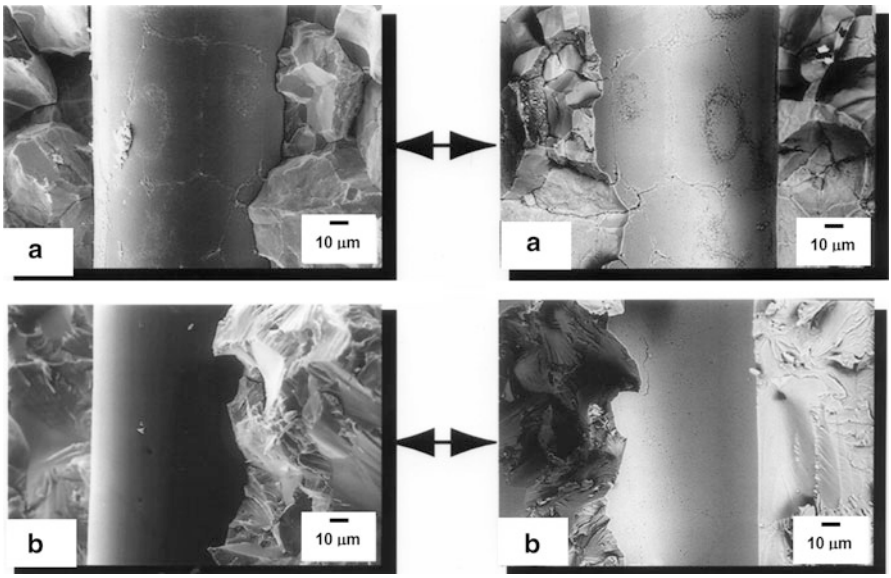

Fig. 7.19 Matching transverse fracture surfaces of sapphire fiber-reinforced NiAl matrix composites (after Eldridge et al. 1997; courtesy of J.I. Eldridge): (**a**) with polymethyl methacrylate (PMMA) binder and (**b**) without binder (after Eldridge et al. 1997). Composites with the binder exhibited a large amount of carbon residue at the fiber/matrix interface, which prevented a strong interfacial mechanical bond and led to lower interfacial strength

increasing the interfacial bond strength. In this case, the transverse strength was maximized, although the longitudinal strength degraded by a small amount. The increase in transverse strength was explained by the increase in the interfacial area fraction of fiber/pure matrix (precipitate-free) bond.

The preceding discussion points to the difficulty in obtaining a combination of longitudinal *and* transverse strengthening in continuous fiber reinforced MMCs. The longitudinal properties are controlled primarily by the strength and volume fraction of the fibers, while the transverse properties are dictated primarily by the matrix (Rao et al. 1993) and fiber/matrix interface strength (Warrier and Majumdar 1997). An increase in fiber volume fraction, however, increases the residual stresses during cooling from processing while also decreases the transverse strength (Rosenberger et al. 1999). Thus, increasing the fiber strength would be a logical step toward increasing the longitudinal strength and simultaneously retaining the transverse properties of the composite. Rosenberger et al. (1999) compared the strength of composites with a high-strength ultra-SCS fiber in a Ti alloy matrix, to those with conventional SCS fibers, and showed an increase in longitudinal strength with no corresponding decrease in transverse strength.

Slight changes in composite modulus may also be achieved by controlling the matrix microstructure through heat treatments (Miller and Lagoudas 2000). This is confined to matrix materials, such as Ti alloys, where a change in crystal structure

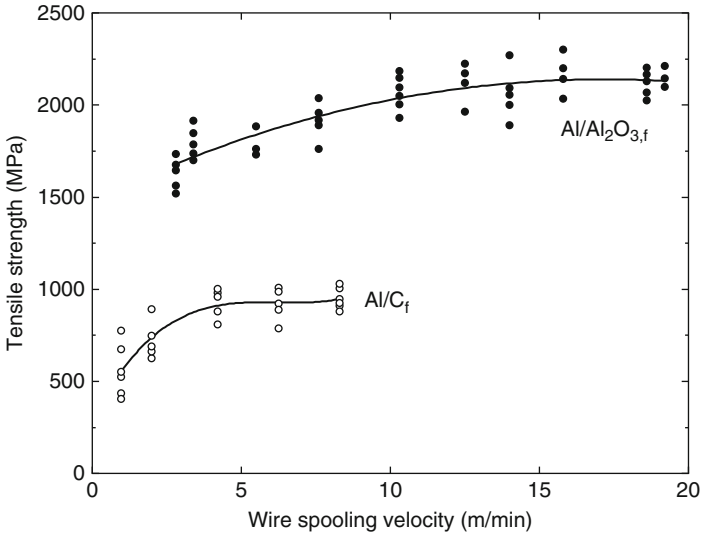

Fig. 7.20 Effect of wire spooling velocity on the tensile strength of $Al/Al_2O_{3,f}$ and Al/C_f composites (after Blucher et al. 2001). Increasing drawing velocity results in faster solidification rate and finer microstructure. In the case of Al/C_f, it also reduces the time for interfacial reaction

morphology of second phases takes place during heat treatment. Such manipulation of the matrix microstructure and crystal structure can also be used to tailor composite strength and ductility (Boehlert et al. 1997). In addition, other processing parameters may be used to tailor the matrix microstructure. Blucher et al. (2001), for example, studied the tensile behavior of composite wires of $Al/Al_2O_{3,f}$ (Nextel 610), $6061/Al_2O_{3,f}$, and Al/C_f. With increasing wire drawing velocity, an increase in strength was observed, Fig. 7.20. This was attributed to the refinement in the microstructure, due to higher solidification rate, at higher drawing velocity. In the Al/C_f composites, a reduction in interfacial reaction with increasing drawing velocity may have also contributed to the observed behavior.

7.2.4 Modeling of Monotonic Behavior of Continuous Fiber Reinforced MMCs

The tensile behavior of continuous fiber reinforced MMCs has been modeled extensively by finite element modeling (Brockenbrough et al. 1991; Gonzalez and LLorca 2001; Rossoll et al. 2005). Gonzalez and LLorca (2001) studied the tensile behavior of SCS-6 fiber reinforced Ti-6Al-4V matrix composites at ambient and elevated temperatures. The fibers are modeled using an axisymmetric model shown in Fig. 7.21a. The fibers are embedded in a "homogeneous composite" with average composite properties. A comparison of the stress–strain behavior predicted by the

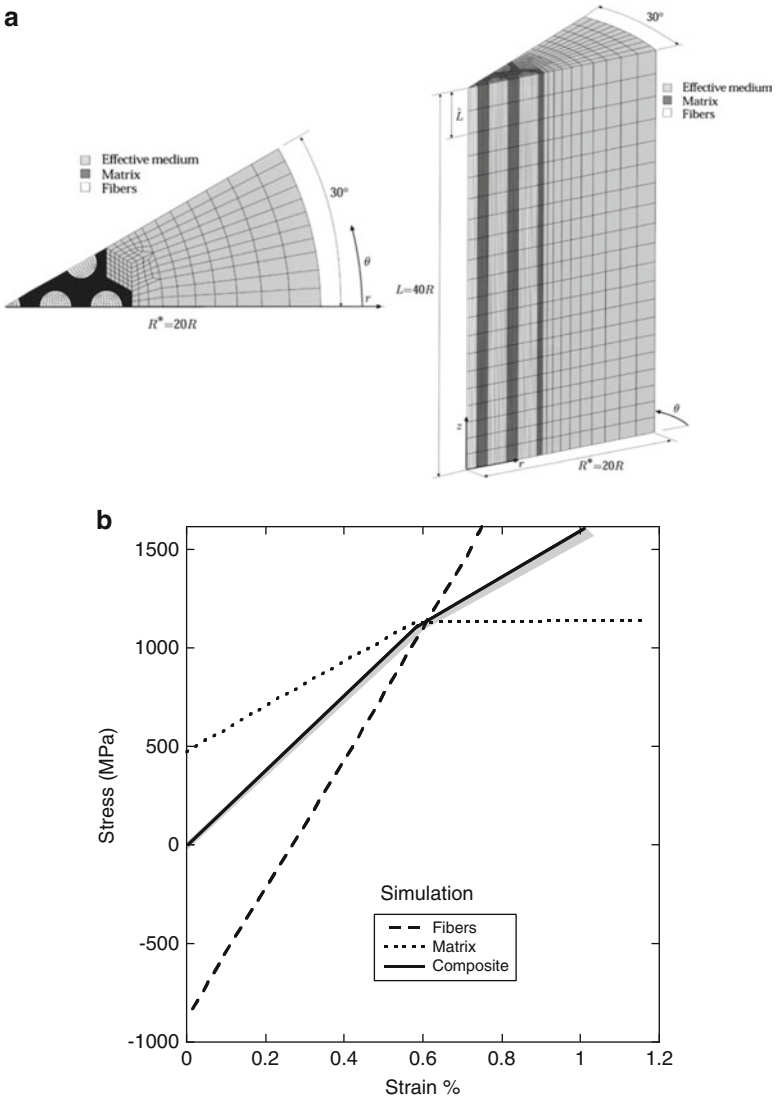

Fig. 7.21 Finite element modeling of tensile behavior of fiber-reinforced Ti-6Al-4V matrix composites (after Gonzalez and LLorca 2001; courtesy of J. LLorca): (**a**) finite element model and (**b**) simulated composite, fiber, and matrix response. The simulated response correlates well with the experiment

model with the experiment is shown in Fig. 7.21b. The experimental behavior is shown as the gray-shaded region (due to slight scatter in the data), while the model prediction is shown in the solid black line. The composite exhibited an initial linear portion followed by a pronounced deviation from linearity and fracture of the composite. Note that due to the processing-induced residual stress, at zero applied

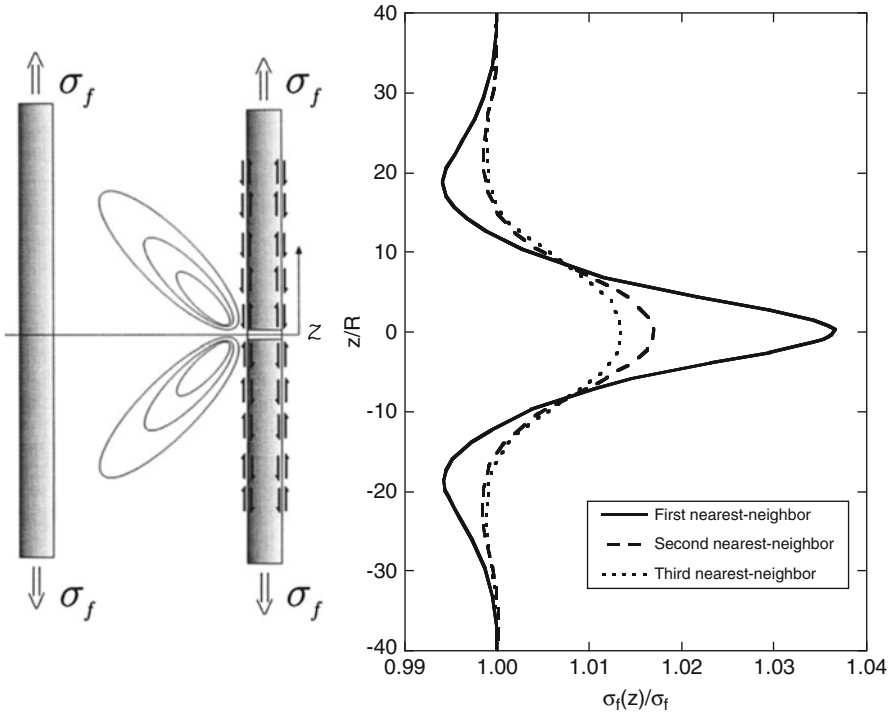

Fig. 7.22 Effect of single fiber fracture on stress state in neighboring fibers, predicted by finite element modeling (after Gonzalez and LLorca 2001; courtesy of J. LLorca). The stress is highest in the first nearest-neighbor

stress, the matrix is in a state of residual tension while the fiber is in compression. With increasing applied stress, the load on both the fiber and matrix increases, although the rate of loading in the fiber is higher because of load transfer from the matrix. When the matrix yields, the stress in the matrix reaches a plateau. This stress corresponds to the deviation from linear stress–strain behavior of the composite. The stress in the fiber, on the other hand, continuously increases until fracture of the composite takes place.

When a fiber fractures, the stress on neighboring fibers is also affected, since more load is carried by the surviving fibers. The stress state in neighboring fibers is shown in Fig. 7.22. The stress in the neighboring fibers is highest in the plane of fracture of the original fiber. The first nearest-neighbor fiber has the highest stress, followed by the second and third nearest neighbor, respectively.

As shown above, during longitudinal loading, the load is carried primarily by the fibers, although plastic deformation of the matrix between the fibers also takes place. Under transverse loading, however, significant plastic deformation between the fibers takes place. Thus, under transverse loading, the distribution of the fibers plays an important role in the composite response. Brockenbrough et al. (1991)

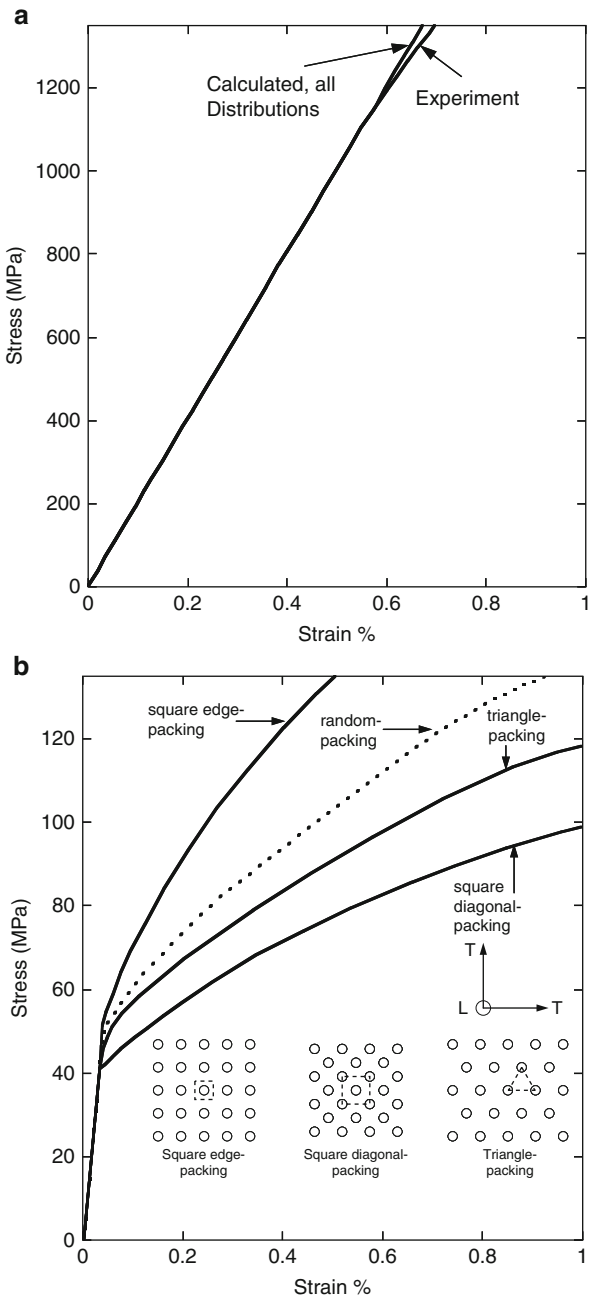

Fig. 7.23 Finite element model predictions of tensile behavior of continuous fiber-reinforced composites with varying fiber arrangement (after Brockenbrough et al. 1991): (**a**) longitudinal and (**b**) transverse

modeled the longitudinal and transverse response of a 6061/B/46$_f$ composite with varying fiber distributions. As one would expect, under longitudinal loading, fiber distribution did not have a significant influence on the modeled behavior, Fig. 7.23a, since the composite behavior was dominated by the response of the fibers. The experimental behavior compared well with the model prediction. Under transverse loading, the fiber distribution was modeled as square, square-diagonal, and triangle-packed, Fig. 7.23b. The elastic regime was somewhat unaffected by the fiber distribution. Once the matrix yielded, the effect of fiber distribution became more apparent. The distribution of square packing exhibited the highest work-hardening rate, followed by triangle and square-diagonal packing, respectively.

Rossoll et al. (2005) used finite element analyses (FEA) for varying fiber distributions, ranging from single fiber unit cells to complex cells to study the damage evolution during a tensile test. The in situ flow stress of the matrix in the composite was found to be different from that of the unreinforced alloy. This is the result of constrained deformation of the metal matrix in the composite, especially in the presence of clustering of fibers. This results in a deviation from the rule of mixtures, based on isostrain, because of a stiffening effect of matrix confinement when surrounded by touching fibers.

7.3 Monotonic Behavior of Discontinuously Reinforced MMCs

The monotonic behavior of discontinuously reinforced MMCs is dependent on several factors, such as reinforcement volume fraction, particle size, shape, and matrix microstructure. Chawla et al. (1998a) examined the effect of particle volume fraction (at a constant SiC particle size) on monotonic tensile behavior. Figure 7.24 shows the tensile behavior of an Al–Cu–Mg (2080)/SiC$_p$–T8 composite with varying volume fraction (at a constant particle size of 5 μm). With an increase in particle volume fraction, higher elastic modulus, macroscopic yield and tensile strengths, and lower ductility were observed. A comparison of the measured increase in yield strength, with increasing reinforcement volume fraction, compared very well with predictions from a simple modified shear-lag analysis by Nardone and Prewo (1986) (see Sect. 7.1.1).

As mentioned in Sect. 7.1, microplasticity takes place at a fairly low stress, which corresponds to the proportional limit stress in the stress–strain curve. This microplasticity originates from stress concentrations at the poles and sharp corners of the particle, Fig. 7.25 (Chawla et al. 1998b). The initial microyielding stress decreases with increasing volume fraction of reinforcement, as the number of stress concentration points increases. The work-hardening rate increases with increasing volume fraction of reinforcement (and decreasing matrix volume). The lower ductility can be attributed to the earlier onset of void nucleation with increasing reinforcement.

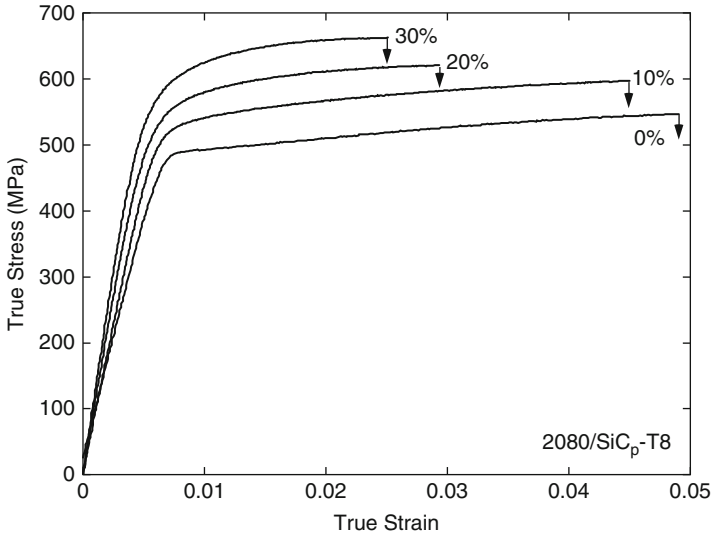

Fig. 7.24 Tensile behavior of an Al–Cu–Mg (2080)/SiC_p–T8 composite with varying volume fraction, at a constant particle size of 5 μm (after Chawla et al. 1998a). With an increase in volume fraction, higher elastic modulus, macroscopic yield, and tensile strengths result, coupled with lower ductility

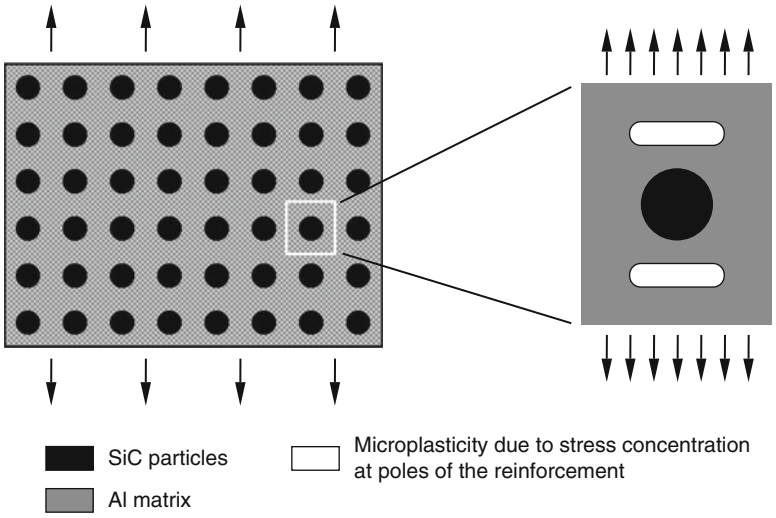

Fig. 7.25 Microplasticity in the matrix of particle-reinforced MMCs due to stress concentrations at the poles of the reinforcement and/or at sharp corners of the reinforcing particles (after Chawla et al. 1998b)

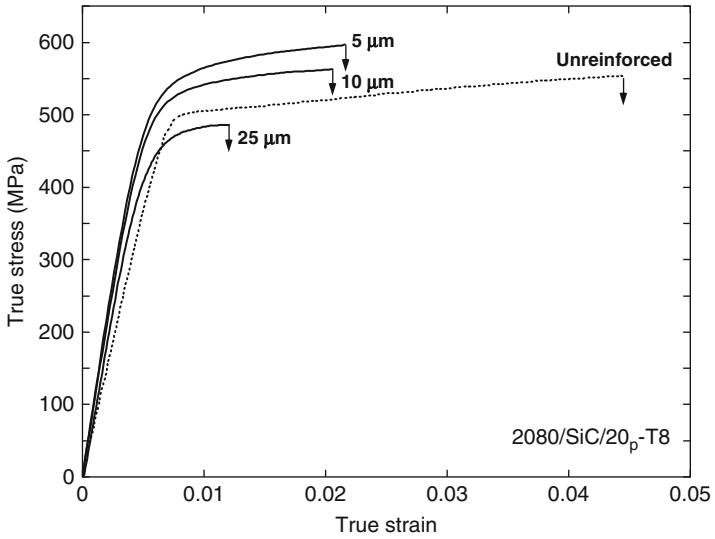

Fig. 7.26 Effect of reinforcement particle size on tensile behavior of an Al–Cu–Mg (2080)/SiC_p–T8 composite, at a constant volume fraction of 20 % (after Chawla et al. 1998a). Very large particles are detrimental to strength because of processing-induced fracture, prior to testing. Above about 20 μm or so, strength and ductility both increased with decreasing particle size

The high-stress concentration at the tips of the cracked particles could also contribute to a lower ductility in the composite, compared to the unreinforced alloy.

The effect of particle size on tensile behavior has been documented by several investigators (Mummery et al. 1991; Manoharan and Lewandowski 1992; Chawla et al. 1998a). Figure 7.26 shows the general trend of increase in strength and ductility with a decrease in particle size. This may be attributed to an increase in the SiC particle strength with a decrease in particle size. This inverse relationship between particle size and particle strength can be explained as follows. As the volume of the particle increases, the probability of a strength-limiting flaw existing in the volume of the material also increases. At relatively large particle sizes of this material, a significant amount of particle cracking takes place during extrusion prior to testing. Chawla et al. (1998a) showed that in Al 2080/SiC_p composites, with volume fractions ranging from 10 to 30 vol.%, particle cracking was observed above an average particle size of 20 μm. Cracked particles do not carry any load, so the strength of the composite is lower than that of the unreinforced material, Fig. 7.26.

A smaller particle size also means a smaller interparticle spacing (for a given volume fraction of particles) so that nucleated voids in the matrix are unable to coalesce as easily (Mummery et al. 1991). A higher work-hardening rate has also been observed with decreasing particle size (Lewandowski et al. 1991; Manoharan and Lewandowski 1992). This is attributed to the formation of dislocation tangles

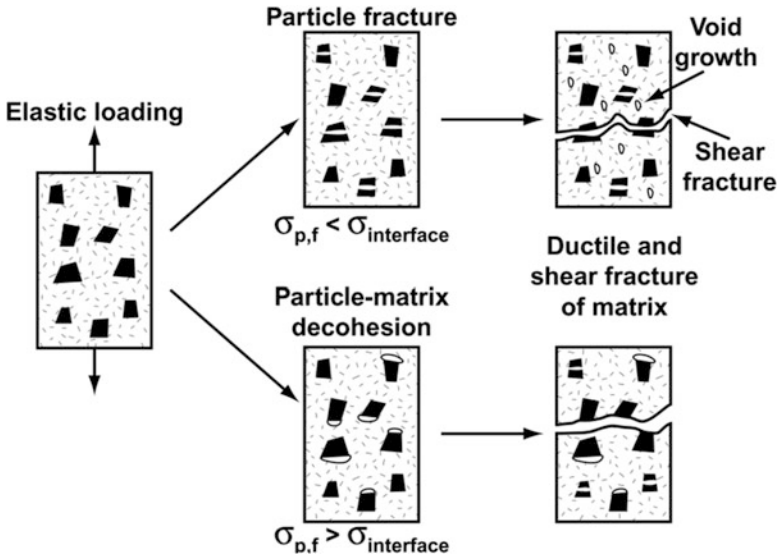

Fig. 7.27 Schematic of the two possible types of tensile damage evolution in particle-reinforced MMCs: (**a**) interface strength greater than particle strength and (**b**) interface strength less than particle strength

around the particles and the formation of a dislocation cell structure with a cell size directly proportional to the interparticle spacing (Kamat et al. 1989).

The fracture of particle-reinforced MMCs is very much dependent on particle strength and particle/matrix interface strength. A schematic of the two possible types of damage evolution is shown in Fig. 7.27. If the strength of the interface is greater than the particle strength (often observed in peak-aged composites), then the particles fracture before the interface. Matrix void growth takes place, and shear localization between fractured particles results in failure of the composite. In order to quantify the extent of particle fracture and particle pullout during tensile loading, both mating fracture surfaces need to be examined. An example of mating fracture surfaces is shown in Fig. 7.28. A particle found on both mating fracture surfaces has fractured. The nature of fracture of the brittle SiC particles is quite interesting. Figure 7.29 shows the fractured surface of a SiC particle after tensile loading. Note the spherical flaws or voids on the fracture surface, which presumably were responsible for crack initiation in the particles. The flaws arise during processing of the particles.

Williams et al. (2010) conducted X-ray tomography on a SiC particle-reinforced 2080 Al alloy under tensile loading. Close inspection of damage in the composite shows that there are three major types of damage, Fig. 7.30: (a) SiC particle fracture, (b) interfacial debonding close to the SiC/Al alloy matrix interface, and (c) matrix void growth which appears primarily within regions of SiC particle clustering. The latter can be attributed to a lack of plasticity (shear) within the

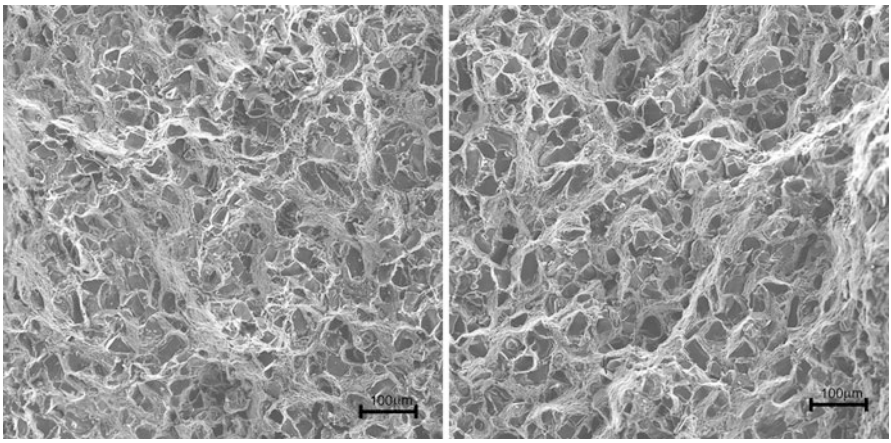

Fig. 7.28 Mating tensile fracture surfaces of a 2080/SiC/20p composite showing significant amount of particle fracture (after Chawla et al. 2002a)

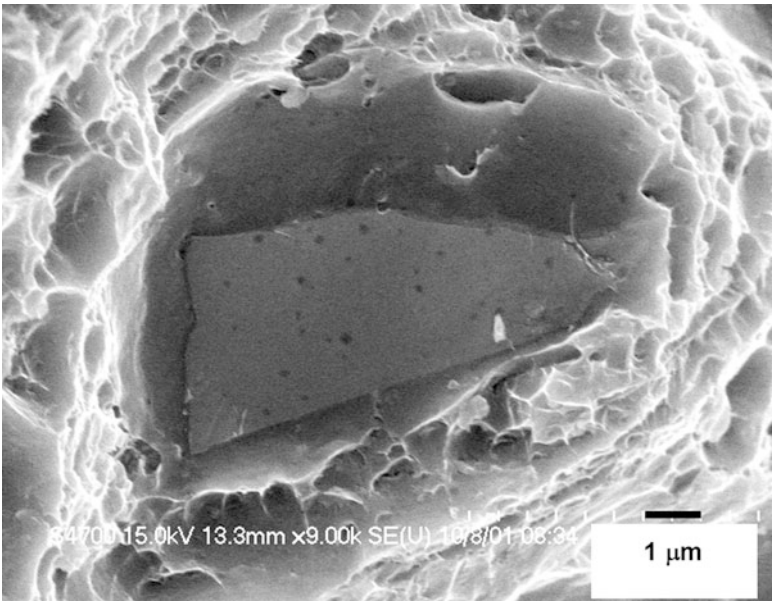

Fig. 7.29 Fracture surface of a SiC particle after tensile loading (after Chawla et al. 2002b). Note the spherical flaws or voids on the fractured particle surface, which presumably are responsible for crack initiation. The flaws arise during processing of the particles

highly constrained region of matrix within the SiC particle cluster and the high degree of tensile stress triaxiality. There are also very small voids at the tips of the sharp, angular SiC particles. These are natural locations for stress concentration which result in voids, although it appears that some of these voids are present even

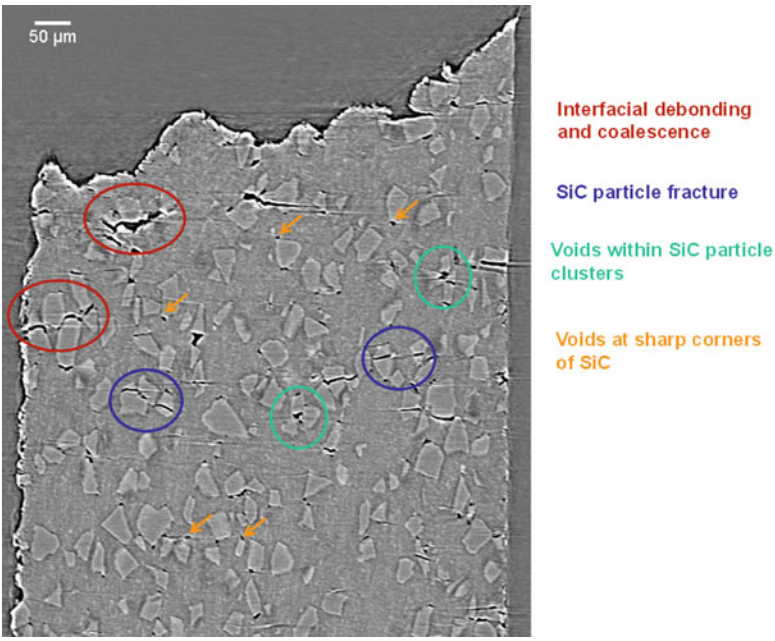

Fig. 7.30 "Virtual section" through the thickness of the composite after tensile damage by X-ray tomography (Williams et al. 2010). Three major types of damage are observed: SiC particle fracture, interfacial debonding close to the SiC/Al alloy matrix interface, and matrix void growth which appears primarily within regions of SiC particle clustering or at sharp corners of SiC particles

in the as-processed condition. It is possible that even during extrusion high stresses are developed at the sharp corners of the SiC particles. Links between debonding and cracks in particles are also present.

Quantitative analysis of particle and inclusion fracture was also conducted from the 3D datasets. Between 1,500 and 2,000 SiC particles were analyzed in the as-processed sample and after tensile fracture. For each sample, the location of cracked and uncracked particles was recorded through inspection of four uniformly spaced 2D slices of the 3D tomography data. Figure 7.31 shows the location of the fractured particles in the as-processed condition, Fig. 7.31a, and after tensile fracture, Fig. 7.31b. After tensile fracture, the high density of fractured particles close to the fracture plane can be observed. In fact, the damage zone extends to about 1 mm from the fracture plane.

Williams et al. (2011) also showed the evolution of damage using in situ testing inside a synchrotron source. Figure 7.32 shows the evolution of tensile damage at three different strains. The onset of damage appears to begin very close to the ultimate strength, at about 440 MPa. This damage is primarily dominated by particle fracture, which begins around 1 % strain. Figure 7.32a shows the onset of particle fracture through the center of the particle, likely at a flaw within the

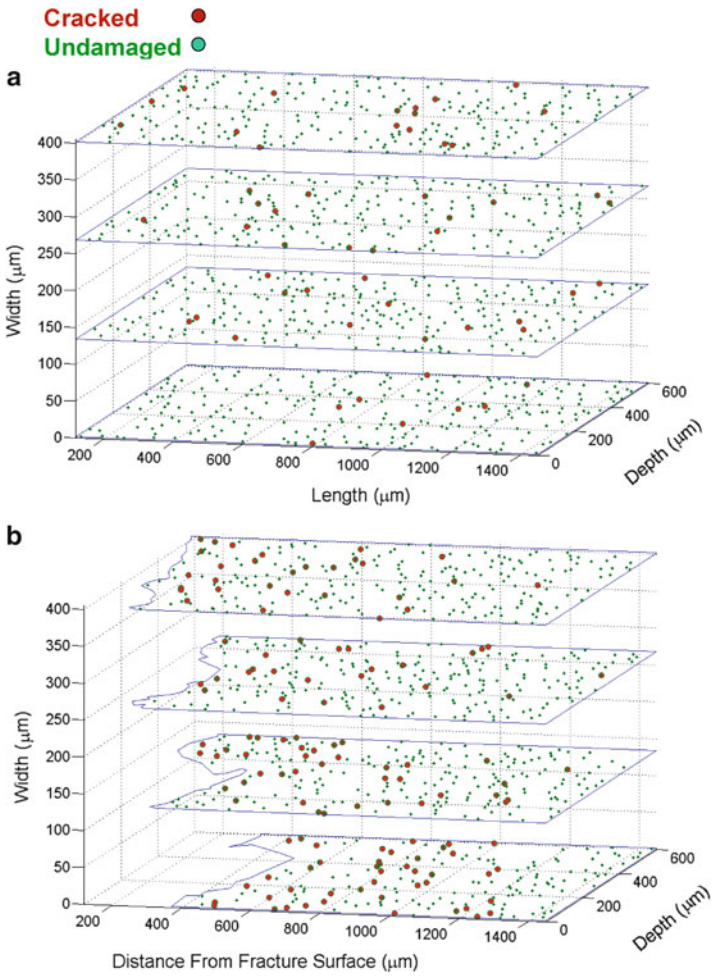

Fig. 7.31 2D sections through the thickness of the composite illustrating cracked and undamaged particles (Williams et al. 2010): (**a**) as-processed and (**b**) after tensile fracture. The damage zone extends to over a 1 mm from the fracture plane

particle, and propagates out to the matrix. Figure 7.32c shows that most of the particle fracture is observed very close to the fracture stress. Some instances of localized void growth are also observed, particularly at the sharp corners of the SiC particles, but also in regions where particles are very closely spaced. Here, the thin layer of matrix is highly constrained and under a triaxial state of stress which promote void growth. The degree of void growth was quite limited, however, and seemed to take place primarily at preexisting voids from processing.

Through analysis of particle fracture statistics obtained from X-ray synchrotron tomography, the probability of particle fracture was shown to be controlled by

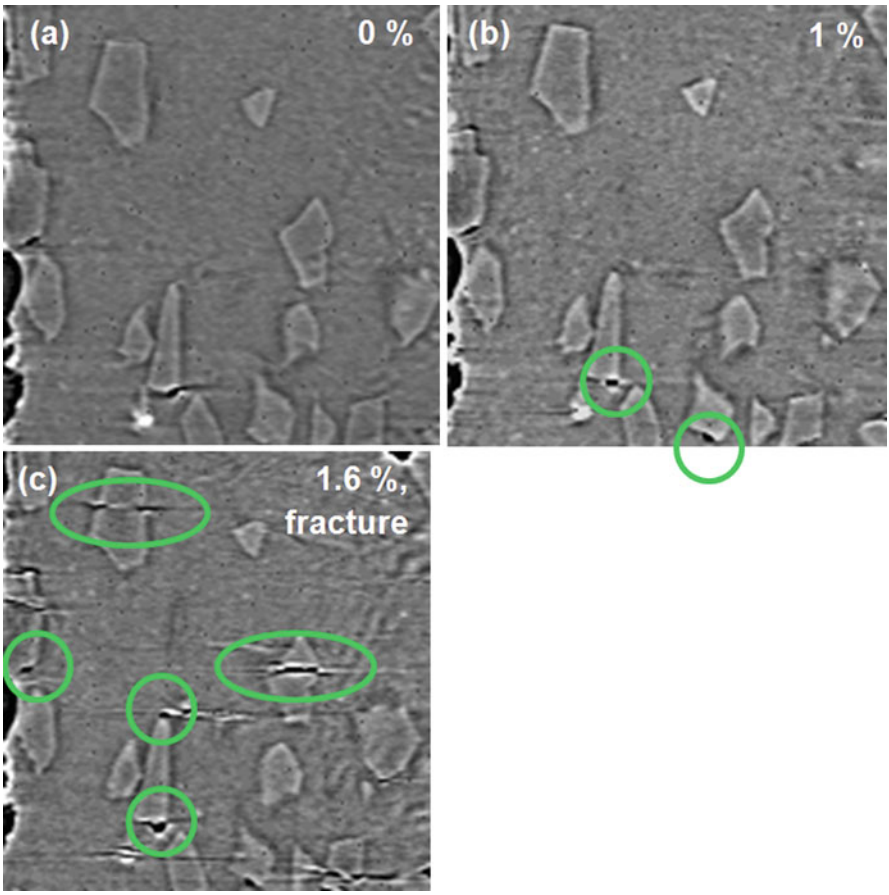

Fig. 7.32 Evolution of damage as a function of applied stress by in situ X-ray tomography (Williams et al. 2011): (**a**) 0 % strain, (**b**) 1 % strain, and (**c**) 1.6 % strain. At 0–0.4 % strain, no damage is observed. At 1 %, void growth begins at sharp corners and regions of high constraint and triaxiality. At fracture (1.6 %), particle fracture is quite predominant

particle size and aspect ratio (Williams et al. 2010), as shown in Fig. 7.33. It is a stronger function of aspect ratio than of particle size. It was shown that, using the statistics from the 3D tomography, aspect ratio and particle size are important parameters in determining the probability of fracture in the SiC particles. More specifically, higher aspect ratio particles (due to better load transfer) and larger particles (which have a larger probability of a strength-limiting flaw) are more prone to fracture.

The second scenario for damage in particle-reinforced MMCs is when the interface strength is much lower than the particle strength. Here, void nucleation and growth will take place at the interface, due to decohesion of the matrix from the particle. This will be followed by ductile shear fracture through the matrix alone.

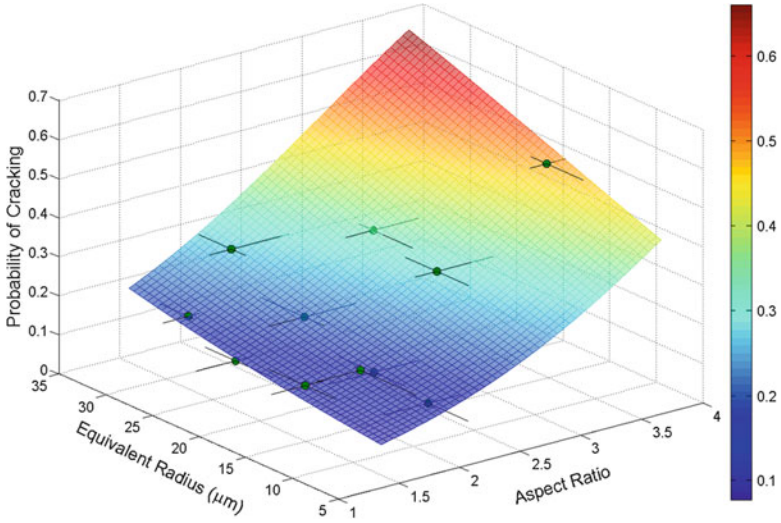

Fig. 7.33 Quantitative analysis of particle radius and aspect ratio of fracture characteristics of the SiC particles (Williams et al 2010). Higher aspect ratio and higher equivalent radius result in a greater probability of fracture. Higher-aspect-ratio particles enable more load transfer, while higher radius results in a higher probability of a strength-limiting flaw in the SiC particle

An example of this is shown in Figure 7.34, for a composite with an overaged matrix, with relatively weak interface strength. Note that a thin matrix layer has been left on the SiC particle surface.

Particle-reinforced composites, especially those subjected to extrusion, exhibit a fair amount of anisotropy due to preferential particle orientation along the extrusion axis. Logsdon and Liaw (1986) studied the tensile strength anisotropy behavior in SiC particle and whisker-reinforced aluminum alloys and noted that the strength was higher parallel to the extrusion axis than perpendicular to the extrusion axis. Jeong et al. (1994) also noted a higher Young's modulus of the composite along the extrusion axis. Ganesh and Chawla (2004, 2005) noted that the extent of orientation was highest for lowest volume fraction composites, since with increasing volume fraction the mean free path for rotation and alignment of a given particle decreased. The Young's modulus and tensile strength of the composites, independent of orientation, increased with increasing volume fraction of reinforcement, Fig. 7.35. Thus, although the degree of microstructural anisotropy was greatest for 2080/SiC/10_p, the greatest anisotropy in mechanical behavior was observed in 2080/SiC/30_p.

The mechanical properties of lower-cost processing techniques, such as sinter-forging, have been compared to existing hot-pressed and extruded materials. Chawla et al. (2002a) examined the strength of composites fabricated by a low-cost sinter-forging approach. The SiC particle size was relatively coarse, e.g., 25 μm. Materials processed by the sinter-forged approach exhibited similar tensile properties to those of the extruded material of similar composition, reinforcement

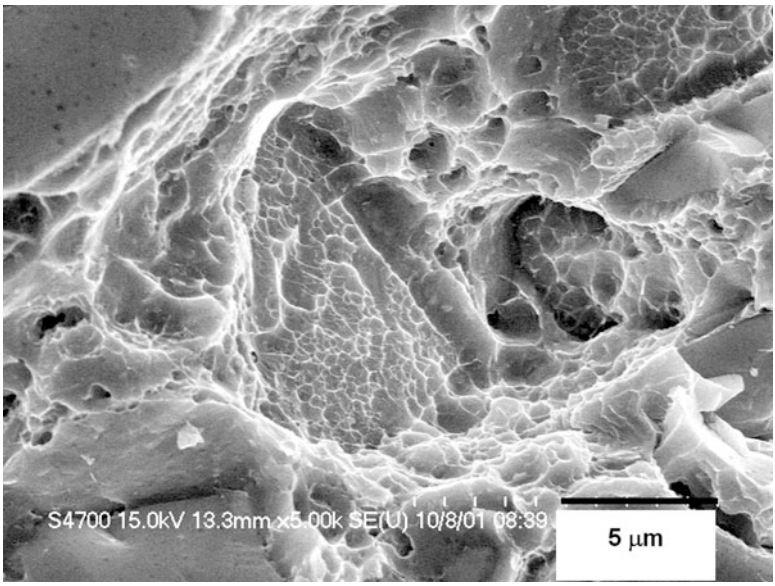

Fig. 7.34 Void nucleation and growth at the particle/matrix interface, due to relatively weak interface strength (overaged condition). Ductile shear fracture is also observed in the matrix of the composite (after Chawla et al. 2002b)

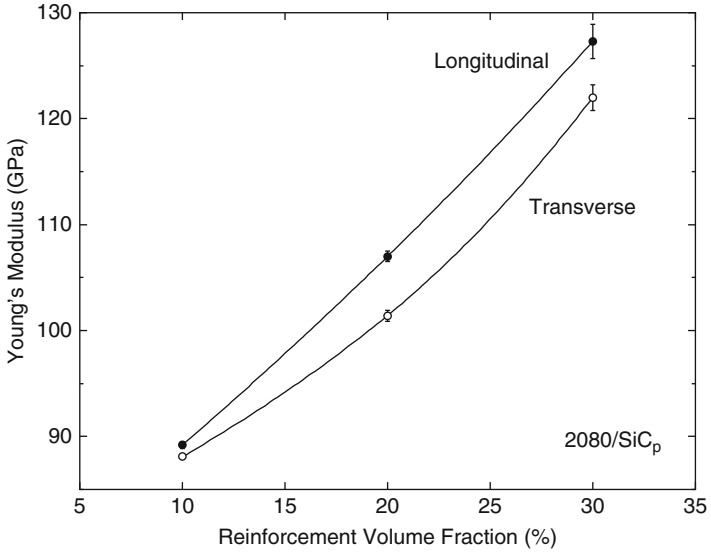

Fig. 7.35 Anisotropy in Young's modulus in a 2080/SiC_p composite (after Ganesh and Chawla 2005). The longitudinal orientation is parallel to the extrusion axis, while transverse is perpendicular

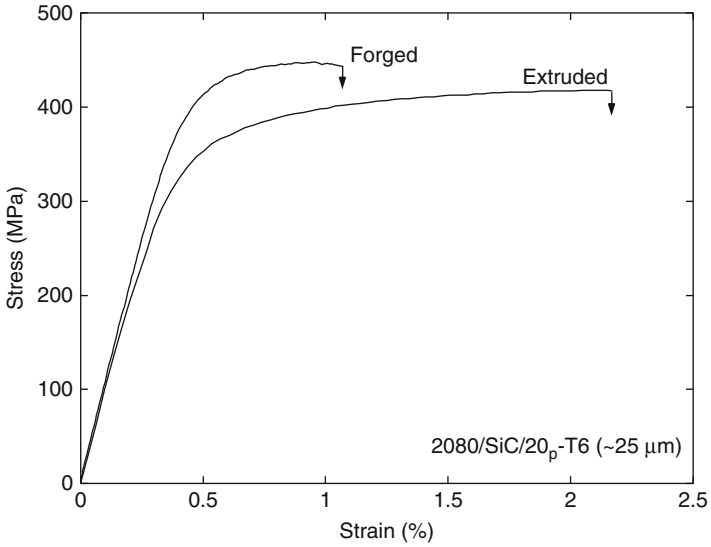

Fig. 7.36 Tensile strength of 2080/SiC/20_p–T6 fabricated by low-cost sinter-forging and extrusion approach (after Chawla et al. 2002a). The sinter-forged material exhibited similar tensile properties, with slightly lower ductility, than the extruded material

volume fraction, and particle size, Fig. 7.36. The microstructure of the sinter-forged composites exhibited relatively uniform distribution of SiC particles, which appeared to be somewhat aligned perpendicular to the forging direction. The degree of particle alignment and interparticle bond strength was not as high as that observed for the extruded composite. The sinter-forged composite exhibited higher Young's modulus and ultimate tensile strength than the extruded material, but lower strain-to-failure. The higher modulus and strength were attributed to the absence of any significant processing-induced particle fracture, while the lower strain-to-failure was caused by poorer matrix interparticle bonding compared to the extruded material. Indeed, secondary working of the composite, such as extrusion after initial casting, can significantly improve the ductility of the composite, Fig. 7.37 (Lloyd 1997). The ductility of the composite is also very much a function of the degree of particle clustering. Murphy et al. (1998) controlled the degree of particle

Quantifying Reinforcement Clustering

During processing of continuous fiber or particle-reinforced MMCs, clustering of the reinforcement is likely to take place (see Chap. 4). While individual fibers can be distributed relatively homogeneously (e.g., when woven in a fiber fabric), controlling particle distribution can be more challenging. As

(continued)

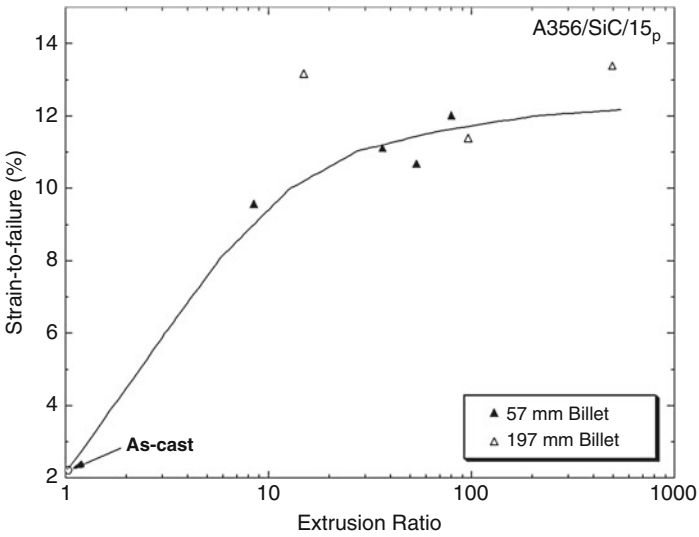

Fig. 7.37 Effect of degree of secondary working (i.e., extrusion ratio) on ductility of Al–SiC/15$_p$ (after Lloyd 1997). Extrusion significantly improved the ductility of the composite

Quantifying Reinforcement Clustering (continued)

shown in this chapter, reinforcement clusters have a profound effect on mechanical properties, because the clusters act as stress concentrations. Many techniques have been used to quantify the degree of reinforcement clustering. Here we describe two techniques that can be used to obtain some quantitative measure of reinforcement clustering: (a) Dirichlet and finite-body tessellation and (b) digital image dilation.

The technique is named after the mathematician Dirichlet (1850) who proposed a tessellation scheme to quantify the arrangement of geometric objects in space. Consider a hypothetical two-dimensional microstructure consisting of elliptical particles in space (see figure below). Let us mark the centroid of each ellipse. We can now construct cells around the particles, such that each cell wall is equidistant between two centroids (part (b) in the figure below). This construction is called a tessellation. The tessellation is very useful because it yields information about the cell size, nearest-neighbor spacing distributions between particles, etc. Inspection of the Dirichlet tessellation, however, shows that when the objects are not perfect spheres (in this case ellipses), the particles are not always fully contained within the cell boundaries. This is because the centroid of the ellipse is used to construct the tessellation. Thus, for the case of nonspherical reinforcement, a conventional tessellation is not quite adequate for quantifying the microstructure.

(continued)

Quantifying Reinforcement Clustering (continued)

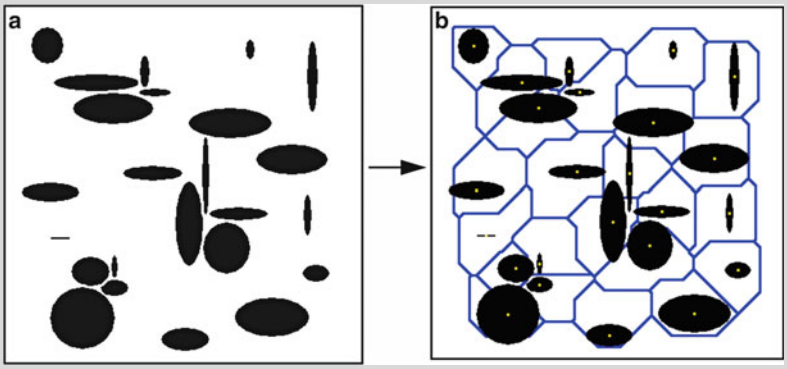

The conventional tessellation scheme can be enhanced by employing a finite-body tessellation (Chawla et al. 2002a). The steps involved in this process are shown in the panel below. An optical or scanning electron micrograph, (a), is segmented into a black and white image, (b). A watershed image operation is then conducted, (c), which analyzes distances between particles based on the centroid and perimeter of each particle. A tessellation is then constructed, (d), whereby each of the irregular particles resides within the boundaries of the cell. Similar statistics can be obtained from the finite-body tessellation as those from the conventional tessellation.

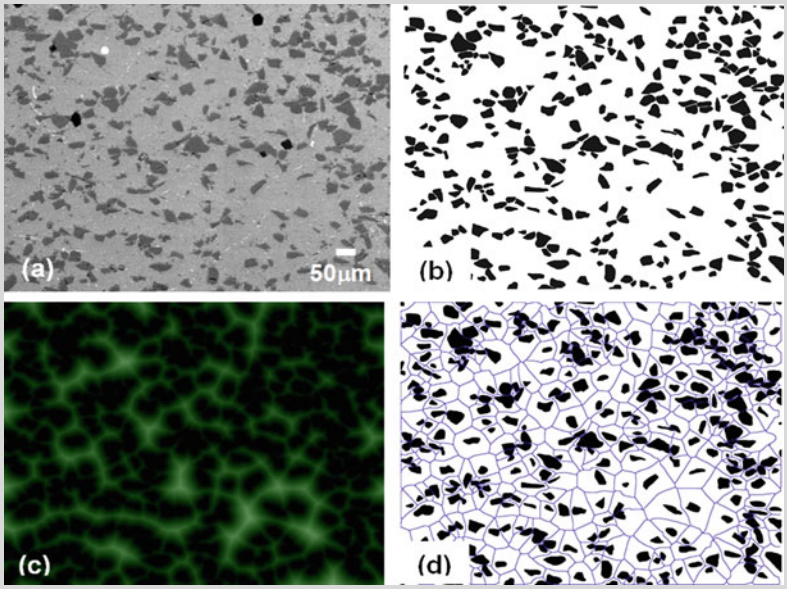

(continued)

Quantifying Reinforcement Clustering (continued)

An alternative method for quantifying the degree of clustering in a composite is to use a digital image dilation technique (Chawla et al. 2002a). This technique consists of, again, analyzing a segmented microstructure (part (a) below). The perimeter of each particle is "dilated" by a certain increment, part (b). The dilation increment can be calculated by analytical expressions for the average interparticle spacing for a random distribution of particles of single (Meyers and Chawla 1999) or multiple sizes (Torquato 2002). If the particles are touching after the dilation, then this set of particles is identified as a cluster (shaded region in part (b)). The cluster may be quantified by the number of particles in the cluster or by the area fraction of the cluster, relative to the whole microstructure. Ayyar and Chawla (2006) used this technique to show the relative degree of clustering between two microstructures (also shown below). The microstructure on the left is relatively homogeneous, and the one on the right is highly clustered. Part (c) shows a histogram of the cluster size distribution for the two microstructures. Note that the clustered microstructure has a much higher fraction of larger clusters. This information is particularly useful from a cyclic fatigue design perspective, since the fatigue life is controlled by the largest defect (cluster) size.

(continued)

Quantifying Reinforcement Clustering (continued)

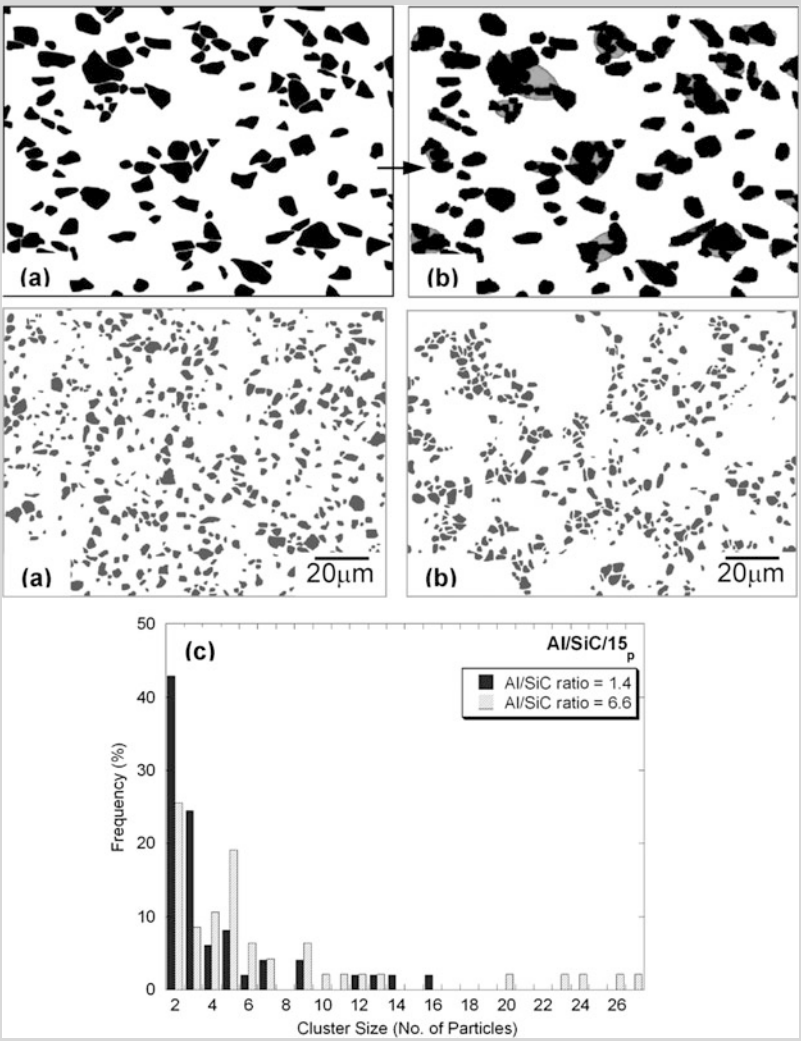

clustering by controlling the cooling rate of the composite. The degree of particle clustering was measured by tessellation techniques (see inset), to determine a clustering severity parameter, P. The ductility of the composite was found to significantly decrease with increasing P.

Matrix microstructure also plays an important role on the strength of the composite. Overaging heat treatments modify the matrix microstructure, resulting

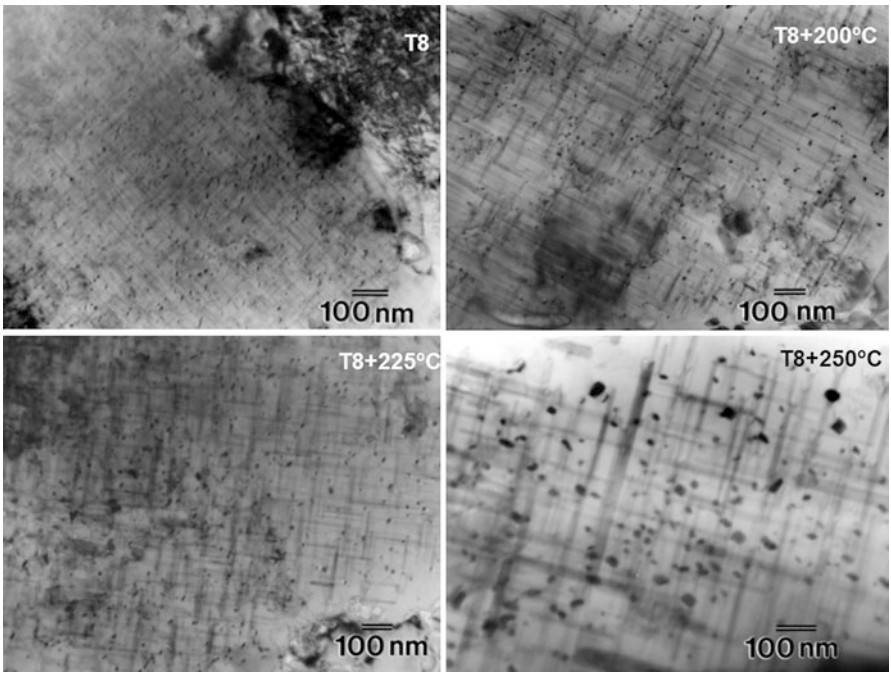

Fig. 7.38 Coarsening and increase in precipitate spacing in the matrix of 2080/SiC/20_p–T8 overaged at various temperatures for 24 h (after Chawla et al. 2000)

in coarsening of the precipitate structure, while retaining a homogeneous precipitate distribution, which directly influences the strength of the composite (Chawla et al. 2000). Figure 7.38 shows the coarsening and increase in precipitate spacing in the matrix of MMCs overaged at various temperatures for 24 h. Increasing precipitate spacing decreases tensile strength, Fig. 7.39. This is to be expected since coarser precipitates result in a larger interprecipitate spacing and easier bypass of dislocations. For the composites subjected to higher overaging temperatures, the yield strength also decreased with an increase in precipitate spacing.

7.3.1 Modeling of Monotonic Behavior of Particle-Reinforced MMCs

Similar to modeling of continuous fiber-reinforced MMCs, FEM modeling has also been used to model the behavior of discontinuously reinforced MMCs. Figure 7.40a shows several single particle unit-cell models, in which the left vertical boundary represents the axially symmetric axis and mirror symmetry exists about the horizontal boundary. A periodic arrangement of particles with the shape of a "unit

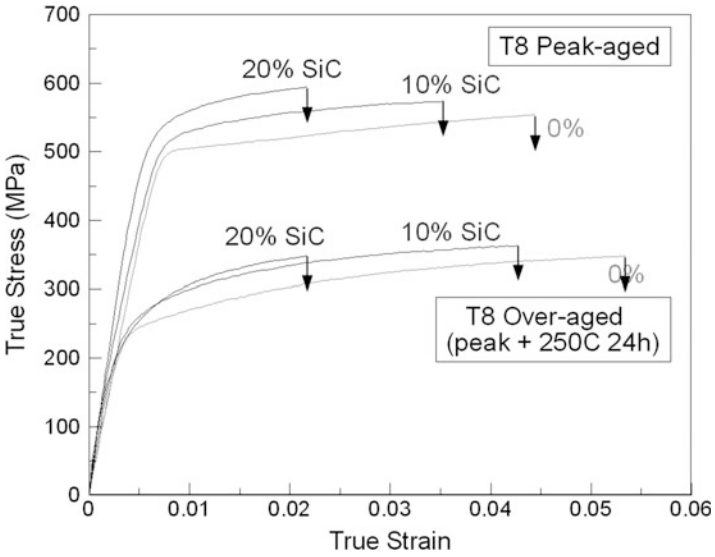

Fig. 7.39 Decrease in strength due to overaging of 2080–T8 and 2080/SiC_p–T8 composites (after Shen and Chawla 2001). The reduction in strength is similar for all materials. Coarser precipitates result in a larger interprecipitate spacing and easier bypass by dislocations

cylinder," "truncated cylinder," "double cone," and "sphere" may be simulated using the appropriate boundary conditions (Shen et al. 1994). The matrix is modeled as an isotropically hardening elastoplastic solid (following the experimental stress–strain curve of a peak-aged Al–3.5Cu alloy) and the SiC particles as an elastic solid. The calculated tensile stress–strain response of Al–$SiC/20_p$ composites, having the four particle shapes described above, is shown in Fig. 7.40b. Clearly, particle shape has a significant influence on the overall tensile behavior of the composite. The unit-cylinder particles clearly strengthen the composite more than the other three shapes for a given reinforcement fraction. This, however, does not imply that particles with sharp corners have a more pronounced strengthening effect, as shown by the case of "double-cone" particles, possessing the "sharpest" type of corners. A detailed analysis (Shen et al. 1995) showed that the unit-cylinder and double-cone particles result in the highest and lowest degrees of "disturbance" of the local plastic flow paths in the matrix, respectively. This directly reflects the different extents of constrained plastic flow and hence the strengthening behavior in the composite. The reader is referred to other simple unit-cell approaches focusing on various aspects of elastoplastic behavior of short fiber and particle-reinforced composites, such as reinforcement particle fracture (LLorca 1995; Steglich et al. 1999), reinforcement clustering (Christman et al. 1989; Toda et al. 1998), matrix void growth (LLorca et al. 1991), and residual stress from thermal treatments and processing (Levy and Papazian 1991; Dutta et al. 1993).

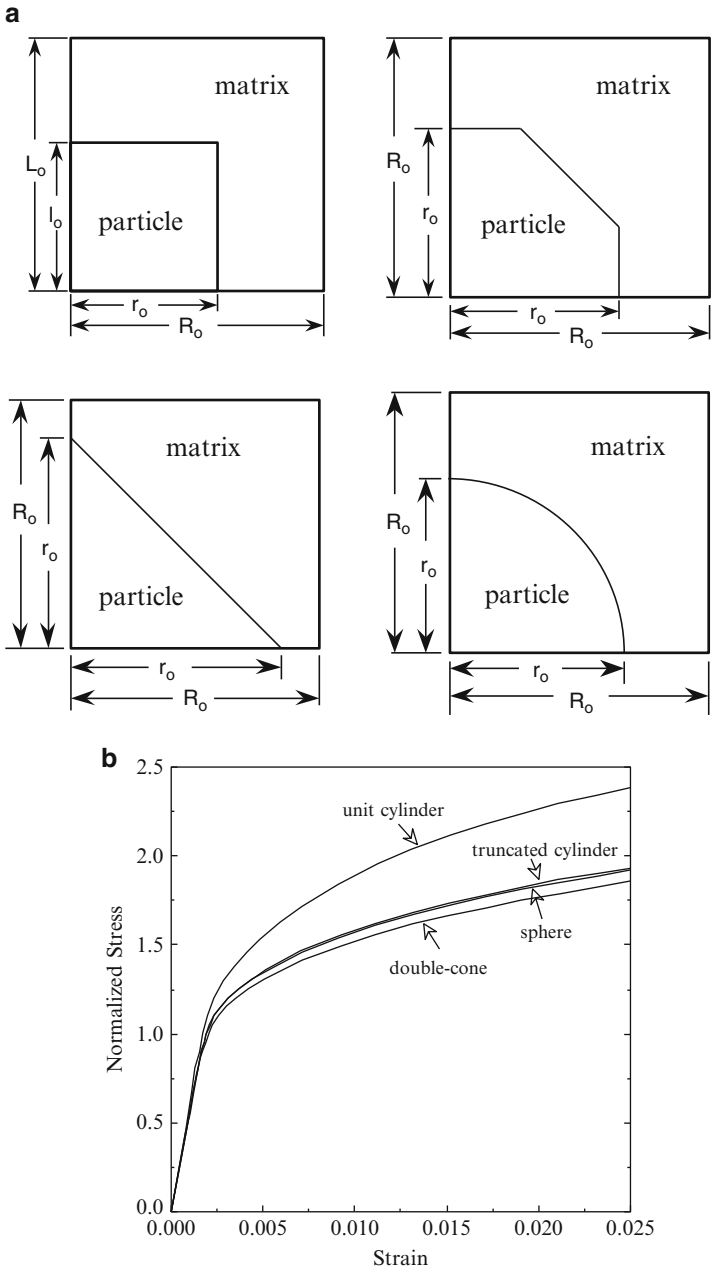

Fig. 7.40 (**a**) Unit-cell finite element models used to illustrate the effect of particle shape and (**b**) predicted stress–strain behavior (after Shen et al. 1994)

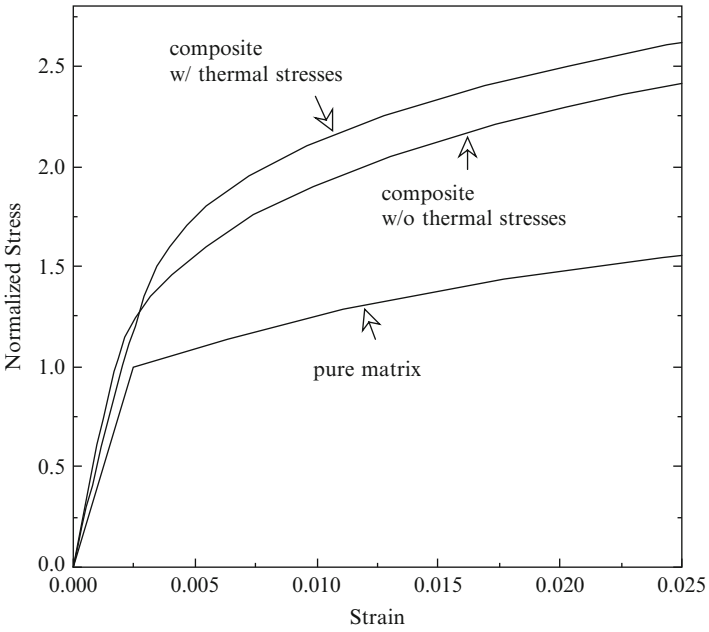

Fig. 7.41 Tensile stress–strain curves for Al–SiC/20$_p$ utilizing the unit-cylinder particles with and without thermal residual stress (after Shen et al. 1994). Hardening caused by cooling-induced plasticity leads to higher strength for the composite

The thermal expansion mismatch between the reinforcement and the matrix results in thermal stresses within the composite upon cooling from the processing temperature to ambient temperature. As mentioned above, in actual composites, thermal residual stresses are relieved by plastic deformation in the matrix, resulting in indirect strengthening. Figure 7.41 shows the calculated tensile stress–strain curves for 20 % SiC-reinforced Al alloy utilizing the unit-cylinder particles (Fig. 7.40a), with and without the presence of thermal residual stress. As before, the matrix was taken to be anisotropically hardening elastoplastic material in the model. The thermal residual stresses were calculated for a composite cooled from the solutionizing temperature of 500 °C, where the composite is in a relatively stress-free state, to room temperature, 20 °C. Also included in the figure is the stress–strain response used for the pure matrix. During cooling the matrix near the particle/matrix interface undergoes yielding. This has direct bearing on subsequent loading of the material. It can be seen in Fig. 7.41 that in the presence of thermal stresses, a smaller slope is observed at the early stage of deformation, due to the slightly smaller apparent modulus arising from prior plastic deformation. When compared with the material free of residual stresses, higher values of the average axial stress were observed. This means that the existence of residual stresses enhanced the initial strain hardening rate in the material. Comparing the curves for the pure matrix and for the composite without thermal residual stresses, direct

strengthening effects are observed. The higher flow stress for the composite is a direct consequence of load transfer from the matrix to the reinforcement, which is also related to the constrained plastic flow within the matrix. A comparison of the two curves of the composite reveals the indirect strengthening effect. In the model, strain hardening caused by cooling-induced plasticity leads to subsequent higher strength for the composite with thermal stresses incorporated (after the crossover point). In actual materials, thermal mismatch-induced dislocation punching renders higher matrix strength due to strain hardening. Thus, when appropriate constitutive models are chosen (e.g., hardening plasticity rather than perfect plasticity in the present case), continuum-based numerical modeling can provide insights into the deformation mechanisms.

Models involving simple, shaped single particle and multiparticles can provide useful insight into deformation. Microstructure-based models, however, more accurately predict the deformation behavior of the composites (Chawla et al. 2003, 2004; Ganesh and Chawla 2004). This is because in actual composites, the particles are highly irregular in shape and commonly contain sharp corners, so spherical particles are not necessarily a realistic choice for simulation. Thus, while simplifications in unit-cell models may aid in computation, they fail to capture the complex morphology, size, and spatial distribution of the reinforcement. It follows that an accurate simulation of the mechanical behavior of material can only be obtained by incorporating actual three-dimensional (3D) microstructural morphologies as a basis for the model.

A comparison of the modeled 3D response using the actual microstructure versus a simplified representation of spherical particles is shown in Fig. 7.42. The spatial distribution of the particles in both models is about the same. Note that the angular particles are under a much larger stress than the spherical particles, indicating more load transfer to the angular particles. The stress in the spherical particles is quite uniform, while that in the angular particles is not. The plastic strain contours in the matrix are also quite different. More localization of strain is observed in the model with angular particles. This simple comparison shows that, indeed, the microstructure-based model predictions are quite different from those of simplified spherical particles. Thus, modeling of the material using the actual microstructure is extremely important.

A comparison of Young's modulus predicted by unit-cell models versus the microstructure-based model was shown in Chap. 6. The microstructure-based model was closest to the experiment (Chawla et al. 2004). A comparison of the overall stress–strain curve (elastic and plastic parts) of the 3D microstructure simulation to the experiment is shown in Fig. 7.43. These simulations incorporate a cooling step in the model, from the solution treating temperature of 493–25 °C. The prismatic rectangle and microstructure-based models both predict the experimental behavior quite well. Nevertheless, the microstructure-based models more faithfully represent the experimental behavior. More importantly, the localized plasticity that results from the sharp and angular nature of SiC particles can only be captured in the microstructure-based model. Thus, other models that

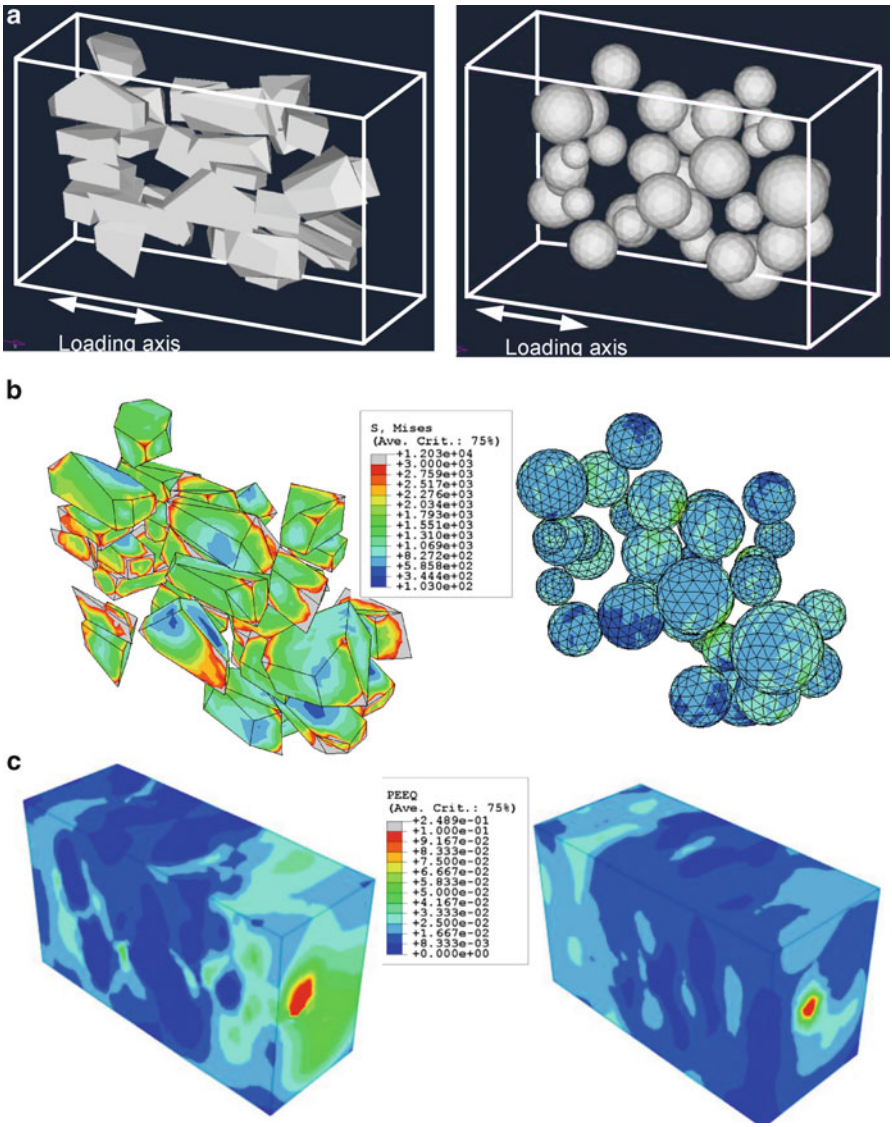

Fig. 7.42 Comparison between 3D finite element models incorporating (1) actual microstructure and (2) approximation to spherical particles: (**a**) FEM models, (**b**) stress distribution in particles, and (**c**) plastic strain in matrix. Note that the microstructure model exhibits much higher stress in the particles and larger and more inhomogeneous plastic strain than the simplified spherical particle model

approximate the shape of the particles to ellipsoids underestimate the extent of strengthening.

The effect of particle clustering has also been modeled using FEM. Segurado et al. (2003) conducted 3D finite element simulations of clustered composites. They

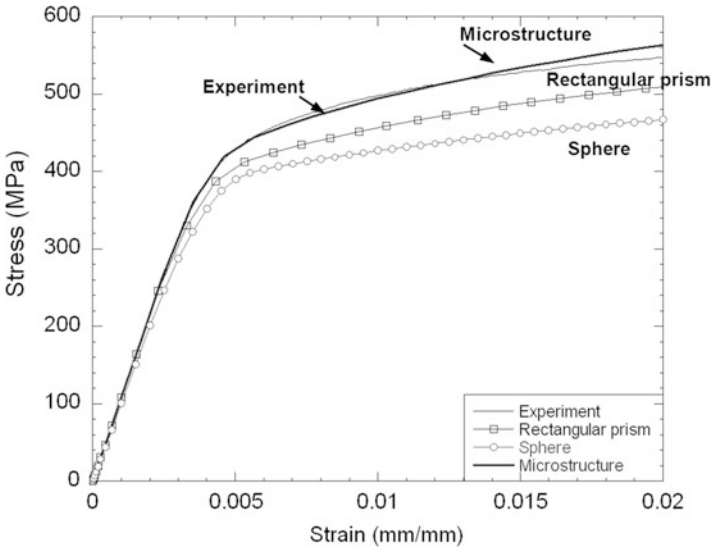

Fig. 7.43 Comparison of stress–strain predictions from various FEM models after cooling (after Chawla et al. 2004). The 3D microstructure model (from two random regions in the microstructure) is most accurate in predicting the experimentally observed behavior

showed that within a particle cluster, the stresses in the particles are much higher than the average particle stress, Fig. 7.44a. With an increase in particle clustering, the standard deviation of the particle stress increased significantly, Fig. 7.44b. In a practical sense, this would cause particle fracture at a much lower far-field applied stress (Fig. 7.44c) compared to a composite with homogeneous distribution.

Chawla and Deng (2005) developed model microstructures, consisting of circular reinforcement particles in a metallic matrix. The microstructures had varying degrees of particle clustering, as quantified by the coefficient of variance in particle spacing (see inset). The tensile behavior of the microstructure was modeled using two-dimensional (2D) finite element analysis. Matrix plasticity and particle fracture were explicitly modeled. All the particles had a homogeneous strength of 1 GPa. The plastic strain distribution in the matrix is much more homogeneous in the homogeneous particle arrangement, Fig. 7.45a, although the plastic strain is intensified in the region of particle fracture. In the clustered particle microstructure, larger stresses develop which results in particle fracture within the cluster, Fig.7.45b. A lower degree of plastic strain is observed. The modeled stress–strain response shows that the clustered microstructure has a lower "ductility," although matrix fracture was not modeled. This model verifies the experimental results of Murphy et al. (1998), described above.

Shen and Chawla (2001) and Shen et al. (2001) explored the correlation between macro-hardness and tensile properties of particle-reinforced metal matrix composites. It was shown that, unlike most monolithic metals and alloys, hardness does not necessarily scale with the overall strength of particle-reinforced

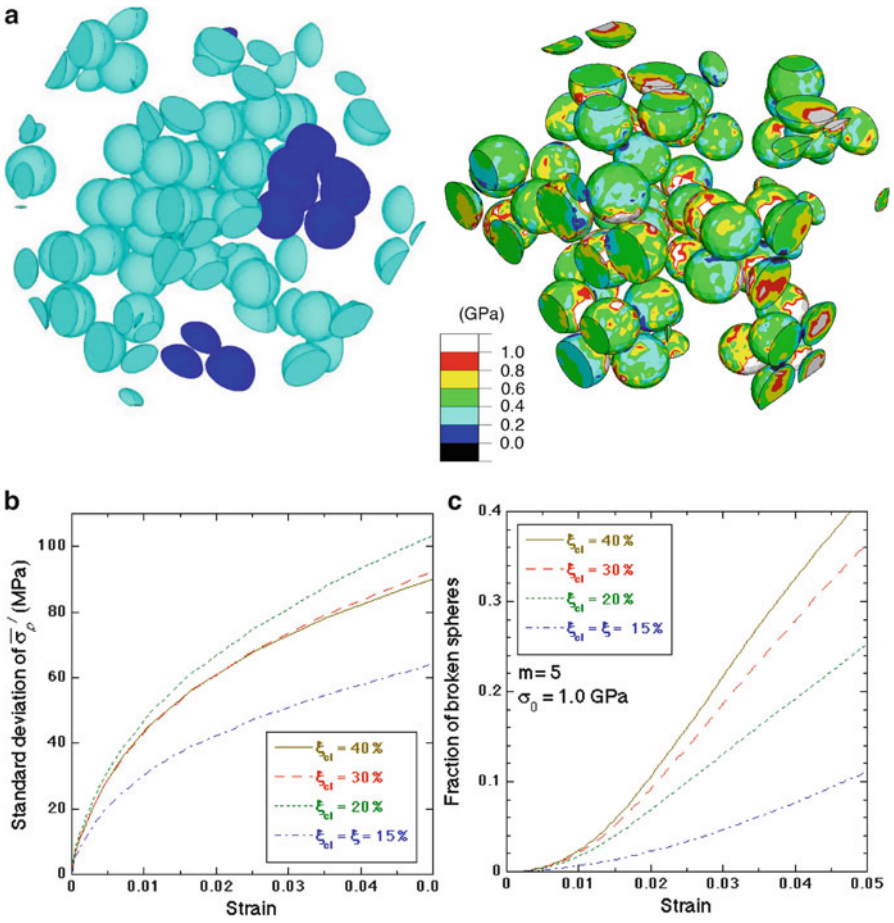

Fig 7.44 (**a**) 3D finite element model consisting of perfectly spherical SiC particles in an Al matrix (after Segurado et al. 2003; courtesy of J. LLorca). The model consists of 49 particles and 7 "clusters." The stress within the cluster is higher than the average stress. (**b**) Standard deviation of stress in particles with increasing clustering, for a given strain, and (**c**) fraction of broken particles predicted. ξ and ξ_{cl} are the volume fraction of particles (15 %) in the composite and within the cluster, respectively

metal matrix composites, Fig. 7.46. The hardness test may significantly overestimate the overall tensile and yield strengths of composites containing large reinforcement particles, which are prone to fracture during deformation processing and/or tensile loading. The predominant local compressive stress state in a hardness test prevents the preexisting fractured particles from weakening the material during indentation. For composites having relatively small reinforcement particles, a unique relationship between hardness and tensile/yield strength did not exist, even when the material was essentially free of

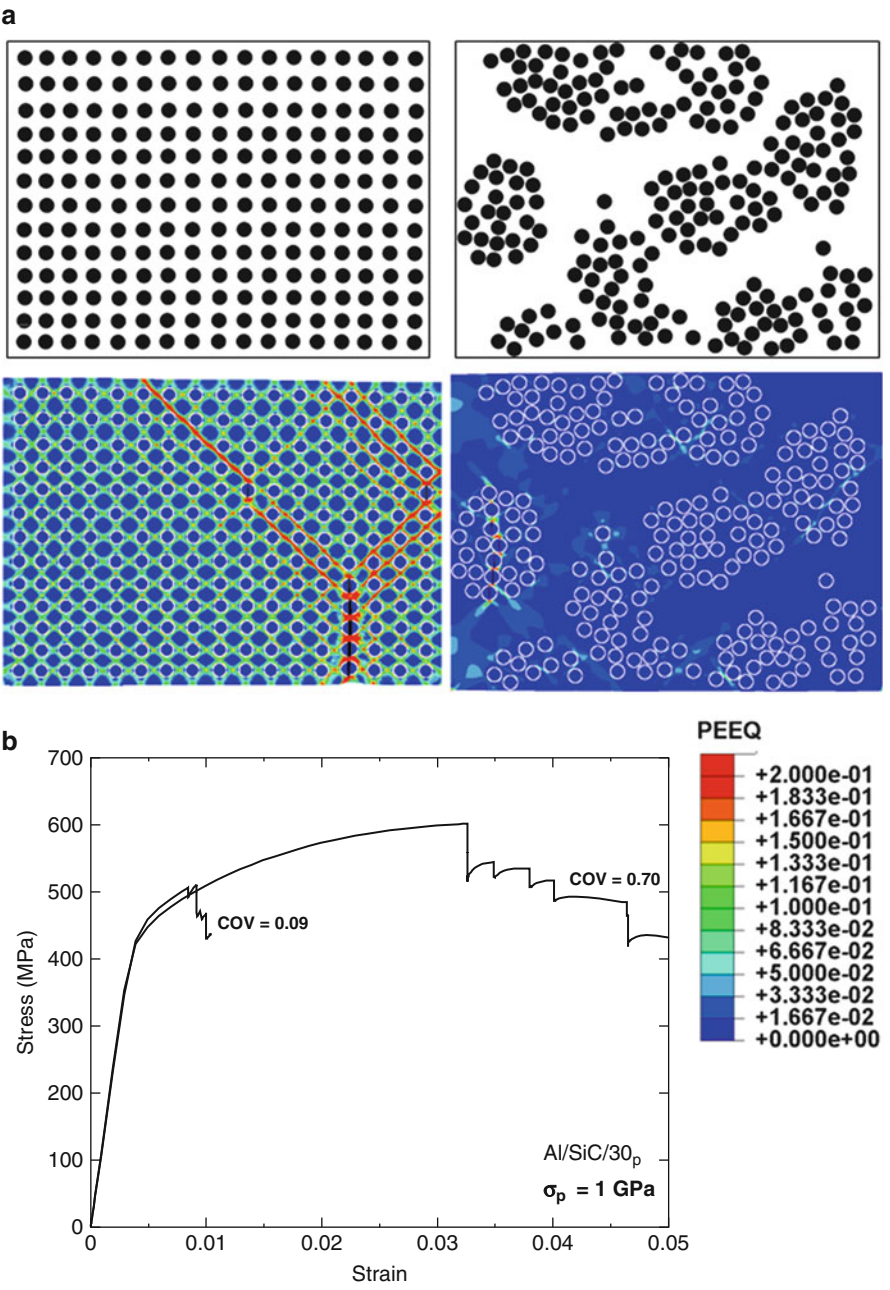

Fig 7.45 Two-dimensional (2D) finite element analysis of the effect of particle clustering (after Chawla and Deng 2005): (**a**) model microstructures consisting of circular SiC particles in Al, showing particle fracture within the cluster and (**b**) predicted tensile stress–strain behavior; all particles were assumed to have a strength of 1 GPa. The clustered microstructure has a lower "ductility"

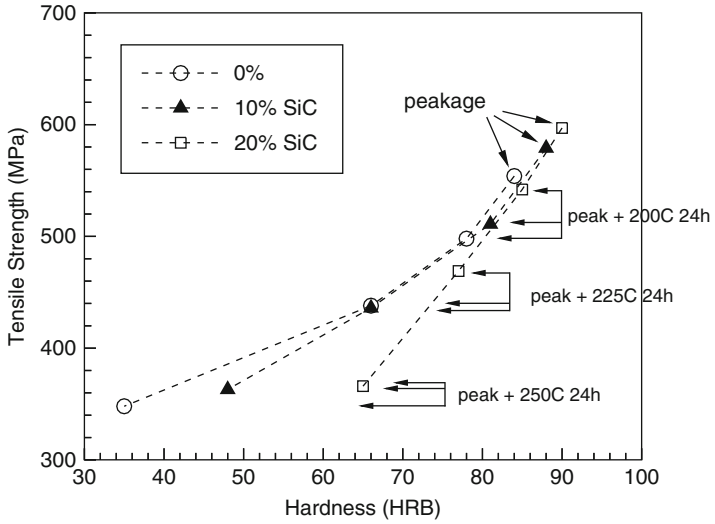

Fig. 7.46 Correlation between macro-hardness and tensile properties of particle-reinforced MMCs (after Shen et al. 2001). Unlike most monolithic metals and alloys, hardness does not necessarily scale with strength of MMCs

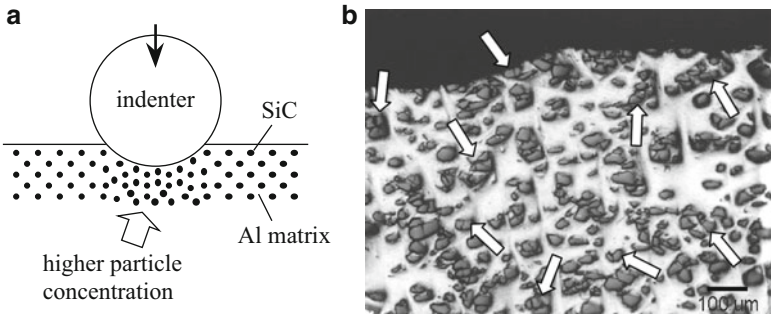

Fig. 7.47 Deformation behavior of particle-reinforced MMCs during microindentation (after Shen and Chawla 2001): (**a**) localized increase in particle concentration due to plastic flow of the matrix and (**b**) localized particle fracture, indicated by the arrows

preexisting fractured particles. This was especially true in cases where the strength of the Al matrix was relatively low. The tendency of higher hardness for particle-reinforced composites can be attributed to the localized increase in particle concentration directly underneath the indenter during hardness testing, Fig. 7.47. This was illustrated by micromechanical modeling using the finite element method. Under indentation, the material system with discrete particles exhibits a higher resistance to deformation than the homogenized system having exactly the same overall stress–strain behavior, Fig. 7.48 (Shen et al. 2001).

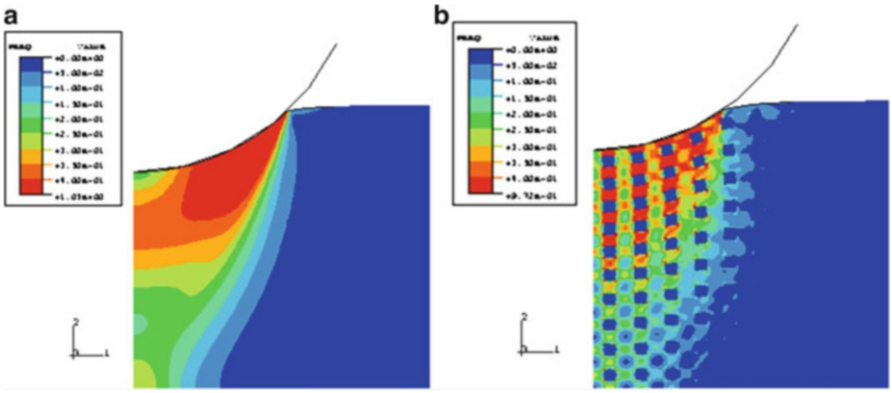

Fig. 7.48 Finite element model of indentation in (**a**) homogeneous material and (**b**) particle-reinforced composite. In the model, both materials had the same macroscopic tensile constitutive behavior (after Shen et al. 2001). Under indentation, the material system with discrete particles exhibited a higher resistance to deformation

7.4 *In Situ* Metal Matrix Composites

Some interesting work on in situ MMCs has involved using appropriate heat treatments to obtain a hard phase (at fairly high volume fractions) distributed in a ductile matrix. Examples include dual-phase steels where a hard martensitic phase is distributed in a soft ferrite matrix (Speich and Miller 1979; Tamura et al. 1973; Rios, et al. 1981; Stewart et al. 2012) and an ultrahigh-carbon steel (UHCS) heat treated to give a composite consisting of hard cementite particles distributed in a ferritic matrix (Young et al. 2007). These kinds of materials are nothing but particle-reinforced MMCs as shown in Fig. 7.49. Typically, the microstructure of the so-called dual-phase steels consists of 5–20 vol.% of hard martensite dispersed in a ductile ferrite matrix. Such a material can be treated as a metal matrix composite; as such we can use some concepts from the field of composites to model the stress–strain behavior of a dual-phase steel. Rios et al. (1981) used a phenomenological model involving partitioning of stress and strain between ferrite and martensite. The linear partitioning of the applied stress between ferrite and martensite gave a good agreement with the experimental result.

Stewart et al. (2012) used micropillar compression to obtain the constitutive behavior of ferrite and martensite. Micropillars of ferrite and martensite were fabricated by focused ion beam (FIB) milling of dual-phase steel, Fig. 7.50. The stress–strain curves, in compression, of ferrite and martensite were obtained by means of a nanoindenter, Fig. 7.51. By using a rule-of-mixtures approach, the mechanical properties of the individual constituents were combined to predict the mechanical behavior of the bulk steel.

Young et al. (2007) studied load partitioning between ferrite and cementite in UHCS (34 % by volume) by synchrotron X-ray diffraction under uniaxial tensile

Fig. 7.49 Microstructure of dual-phase steel, an in situ composite with ferrite and martensite constituents (Rios et al. 1981). *White* phase is martensite, while the *dark* phase is ferrite

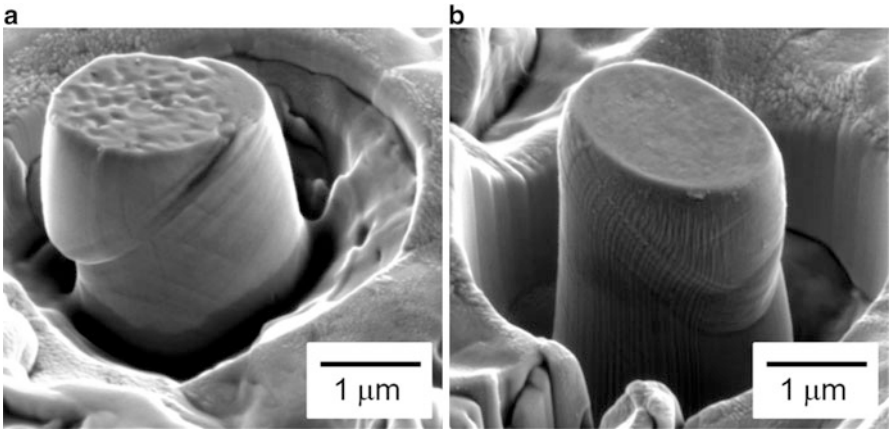

Fig. 7.50 Scanning electron microscope images of (**a**) ferrite and (**b**) martensite pillar post deformation (Stewart et al. 2012). Note pillar deformation occurs by crystallographic slip

stress. In the elastic range, the two components (α-Fe and Fe_3C) have almost the same properties. After the ductile ferrite goes plastic, there occurs load transfer from the soft α-Fe to the hard, elastic Fe_3C particles. No thermal residual stresses occur in this case because the strain due to mismatch in CTE is balanced by that due to phase transformation. The two phases have nearly the same elastic constants. So there is no load transfer in the elastic range. In the stage where the ferrite is deforming plastically while cementite is deforming elastically, there occurs a

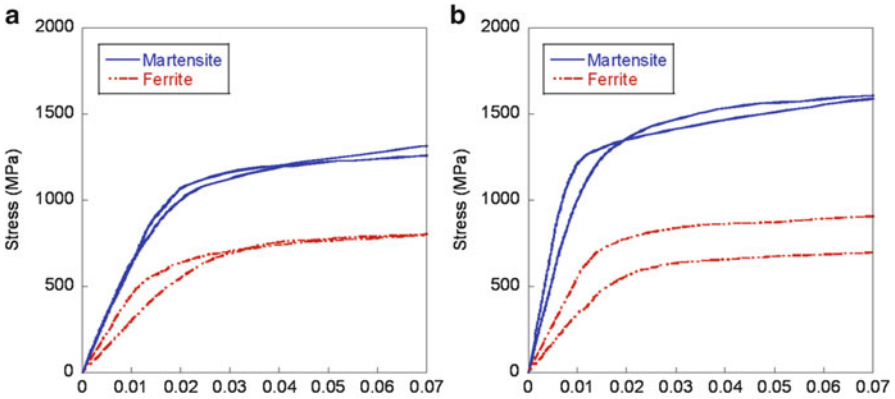

Fig. 7.51 Stress–strain curves from ferrite and martensite micropillar compression of (**a**) as sintered and (**b**) aged at 538 °C specimens. Note increased martensite strength with aging

load transfer from ferrite to cementite. Young et al. (2007) used a two-parameter power law hardening equation for the ferrite matrix in the finite element modeling to obtain the macroscopic stress–strain curve. Experimentally determined diffraction strain data in the axial and transverse directions matched reasonably well with predictions of the mold.

7.5 Fracture Toughness

The fracture toughness of particle-reinforced MMCs is controlled by several factors. These include (a) volume fraction of reinforcement, (b) interparticle spacing and strength of particles, (c) spatial distribution of particles (i.e., particle clustering), and (d) microstructure of matrix and interface region (as controlled by heat treatment in age-hardenable alloys). Figure 7.52 is a compilation of toughness in several composite systems, as a function of reinforcement volume fraction (Manoharan et al. 1993; Hunt et al. 1993, and Beck Tan et al. 1994). Note that all the composites show a decrease in toughness with increasing volume fraction of reinforcement. The toughness appears to reach a "plateau" at volume fractions of 20 % and above. The decrease in toughness, shown in Fig. 7.52, can be explained by an increase in stress triaxiality with increasing volume fraction of particles (similar to what takes place during tensile loading of the composite).

The effect of particle size is less clear-cut. This is because decreasing particle size results in a smaller interparticle spacing. In addition, it also results in an increase in strength of ceramic particle, because of a lower probability of encountering a strength-limiting flaw. It has been shown that the degree of clustering increases with decreasing particle size (Hunt et al. 1993) and that the degree of indirect strengthening increases with decreasing particle size (Arsenault and Shi

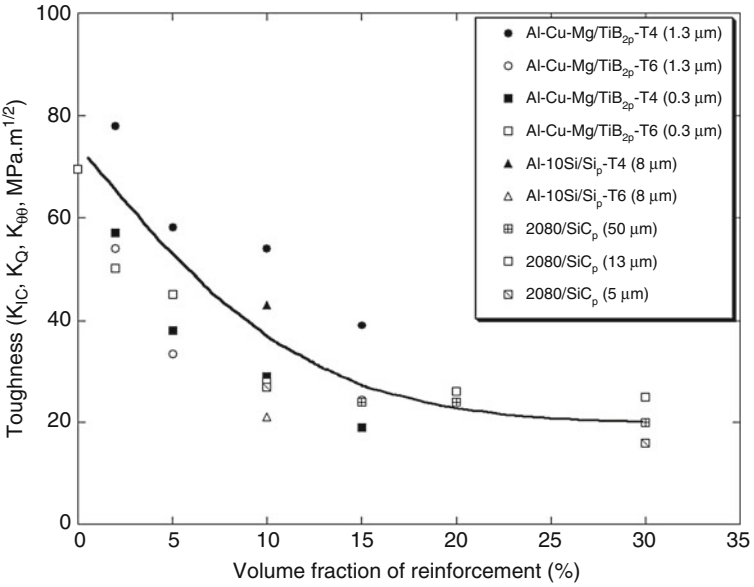

Fig. 7.52 Toughness of several particle-reinforced MMCs as a function of reinforcement volume fraction (after Manoharan et al. 1993; Hunt et al. 1993, and Beck Tan et al. 1994). All the composites show a decrease in toughness with increasing volume fraction, reaching a "plateau" at volume fraction of about 20 % and above

1986). Figure 7.53 shows the decrease in toughness of a 2080/SiC_p composite with increasing strength, at three volume fractions and as a function of particle size. The curve for the largest particle size is farthest left, because of the decrease in the strength of the composite with increasing particle size. It is interesting to note that, for a given volume fraction, the toughness of the composite decreases slightly with decreasing particle size. The effect of particle size on toughness was also investigated by Kamat et al. (1989). They studied the fracture toughness behavior of Al_2O_3 particle-reinforced Al matrix composites at volume fractions of 10 and 20 % Al_2O_3 and several particle sizes ranging between 5 and 50 μm. At large particle sizes (>15 μm), particle fracture was hypothesized to cause unstable crack growth and much lower crack growth toughness. At smaller particle diameter, interfacial decohesion took place. In this smaller particle size (and smaller interparticle spacing) regime, the behavior of the composites was found to follow the model of Rice and Johnson, where particle/matrix decohesion is assumed to take place at the interface ahead of the main crack. The coalescence of voids arising from particle/matrix decohesion is facilitated by a decrease in interparticle spacing. Their model showed the ratio of toughness-to-fracture strength, J_{Ic}/σ_f, to be directly proportional to the interparticle diameter, λ:

$$\frac{J_{Ic}}{\sigma_f} \propto \lambda$$

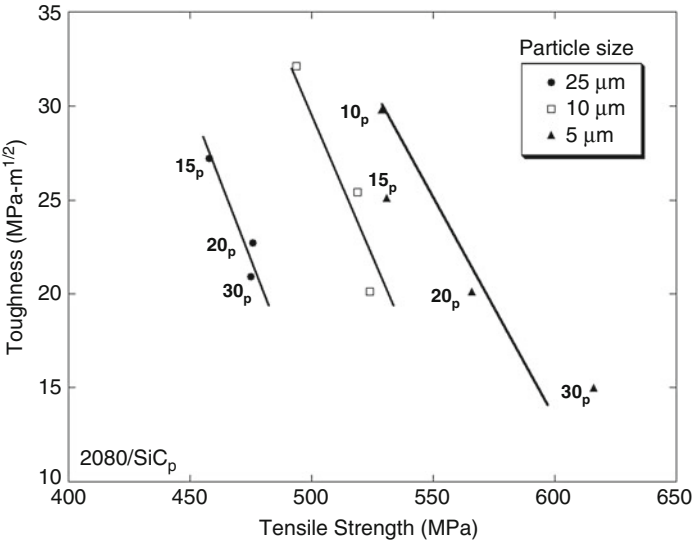

Fig. 7.53 Effect of particle size on toughness of a 2080/SiC_p composite, at three volume fractions (after Hunt et al. 1993). For a given volume fraction, the toughness of the composite decreases slightly with decreasing particle size

The fracture toughness is also influenced by the degree of clustering of particles. Lloyd (1995) obtained varying degrees of clustering by varying the cooling rate of a cast A356/SiC/15_p composite, Fig. 7.54. As mentioned in Chap. 4, faster cooling rates result in less time for particle pushing from dendrites, resulting in a more homogeneous distribution of particles. This work clearly shows that with increasing clustering (quantified by an increase in minimum edge-to-edge spacing of particles), the toughness decreases. This stems from an increase in stress triaxiality caused by particle clusters. The toughness is also very much affected by matrix microstructure. Manoharan and Lewandowski (1990) studied the fracture toughness behavior of SiC particle-reinforced Al matrix composites, Fig. 7.55. The materials were heat treated to the underaged (UA) and overaged (OA) conditions and had the same nominal tensile strength. The fracture toughness in the two heat-treated conditions was quite different. In the UA condition, the toughness was twice as large as that of the OA material. This was attributed to a transition in fracture mode from particle fracture controlled (UA) to interfacial decohesion (OA). The ease of interfacial decohesion was explained by coarsening of precipitates and weakening at the particle/matrix interface. In the unreinforced alloy, the toughness in both UA and OA conditions was similar.

The toughness of particle-reinforced MMCs has also been shown to be a function of loading velocity. Wang and Kobayashi (1997) examined the effect of loading velocity on the fracture toughness of a 6061/SiC/22_w, Fig. 7.56. At a loading velocity above 10 m/s, the fracture toughness increased significantly. Fractographic analysis showed that matrix dimples were deeper and the damage

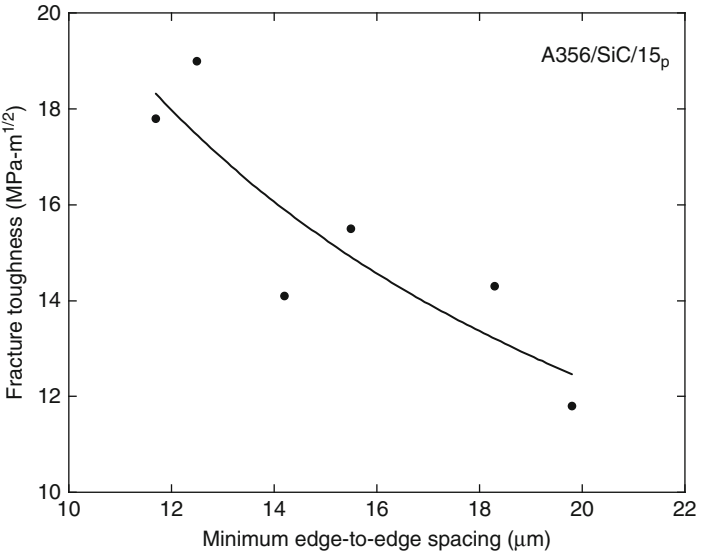

Fig. 7.54 Effect of particle clustering on toughness of a cast A356/SiC/15_p composite (after Lloyd 1995). With increasing clustering (quantified by minimum edge-to-edge spacing of the particles), the toughness decreases

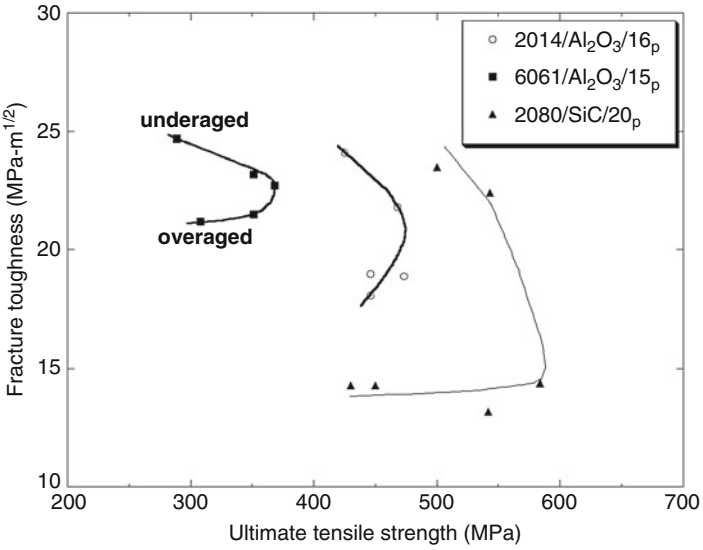

Fig. 7.55 Effect of matrix microstructure on the fracture toughness–tensile strength relationship in particle-reinforced MMCs (after Lewandowski 2000; Hunt et al.; 1993; Kamat et al. 1989). For a given tensile strength, the toughness is higher in the underaged condition vis-à-vis the overaged condition

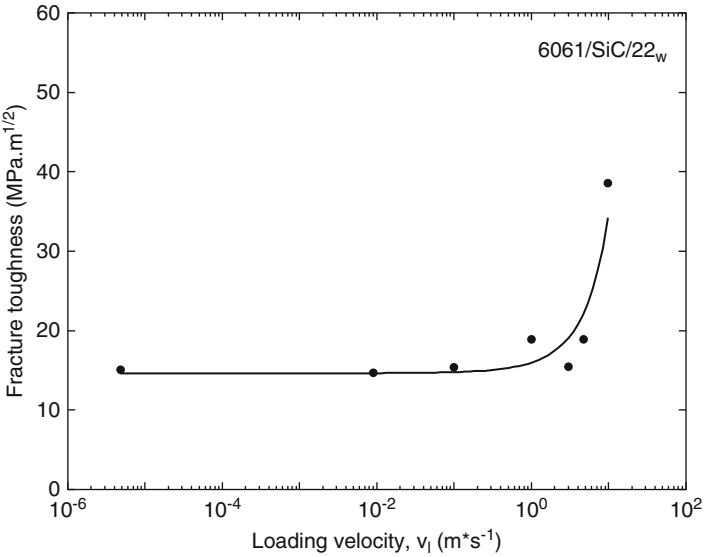

Fig. 7.56 Effect of loading velocity on the fracture toughness of a 6061/SiC/22_w (after Wang and Kobayashi 1997). Above a loading velocity of 10 m/s, the fracture toughness increased significantly

zone extended to a longer distance at the faster loading rate. It was postulated that the very fast loading rate did not allow enough time for interaction and coalescence between cracks and voids.

References

Arsenault, R.J., and N. Shi (1986) *Mater. Sci. Eng.*, **81**, 175.
Ayyar, A. and N. Chawla (2006) *Comp. Sci. Tech.*, **66** 1980–1994..
Beck Tan, N.C., R.M. Aikin, Jr., and R.M. Briber (1994) *Metall. Mater. Trans.*, **25A**, 2461–2468.
Blucher, J.T., U. Narusawa, M. Katsumata, and A. Nemeth (2001) *Composites*, **32**, 1759–1766.
Boehlert, C.J., B.S. Majumdar, S. Krishnamurty, and D.B. Miracle (1997) *Metall. Mater. Trans.*, **28A**, 309–323.
Brockenbrough, J.R., S. Suresh, and H.A. Wienecke (1991) *Acta Metall. Mater.*, **39**, 735–752.
Bushby, R.S. (1998) *Mater. Sci. Tech.*, **14**, 877–886.
Chan, K.S. (1993) *Metall. Trans.*, **24A**, 1531–1542.
Chawla, K.K. (1973a) *Phil. Mag.*, **28**, 401.
Chawla, K.K. (1973b) *Metallography*, **6**, 155–169.
Chawla, K.K. (1998) *Composite Materials - Science and Engineering*, 2nd Ed., Springer-Verlag, New York, p. 102.
Chawla, K.K., and M. Metzger (1972) *J. Mater. Sci.*, **7**, 34.
Chawla, N., C. Andres, J.W. Jones, and J.E. Allison (1998a) *Metall. Mater. Trans.*, **29A**, 2843.
Chawla, N., C. Andres, J.W. Jones, and J.E. Allison (1998b) *Scripta Mater.*, **38**, 1596.

Chawla, N., U. Habel, Y.-L. Shen, C. Andres, J.W. Jones, and J.E. Allison (2000) *Metall. Mater. Trans*., **31A**, 531–540.
Chawla**,** N., and Y.-L. Shen (2001) *Adv. Eng. Mater*., **3**, 357–370.
Chawla, N., J.J. Williams, and R. Saha (2002a) *J. Light Metals*, **2**, 215–227.
Chawla, N., J.J. Williams, and R. Saha (2002b) *Metall. Trans*., **33A**, 3861–3869.
Chawla, N., B.V. Patel, M. Koopman, K.K. Chawla, E.R. Fuller, B.R. Patterson, and S. Langer (2003) *Mater. Charac*., **49**, 395–407.
Chawla, N., V.V. Ganesh, and B. Wunsch (2004) *Scripta Mater*., **51,** 161–165.
Chawla, N., and X. Deng (2005) *Mater. Sci. Eng*., **A390**, 98–112.
Cheskis, H.P., and R.W. Heckel (1970) *Metall. Trans*., **1**, 1931–1942.
Christman, T., A. Needleman and S. Suresh (1989) *Acta Metall. Mater*., **37**, 3029.
Cook, J., and J.E. Gordon (1964) *Proc. Roy. Soc. London*, **A228**, 508.
Corbin, S.F. and D.S. Wilkinson (1994) *Acta Metall. Mater*., **42**, 1319.
Cornie, J.A., M.L. Seleznev, M. Ralph, and F.A. Armatis (1993) *Mater. Sci. Eng*., **A162**, 135–142.
Cox, B.N. (1990) *Acta Metall. Mater*., **38**, 2411.
Cox, H.L. (1952) *Brit. J. App. Phys*., **3**, 122.
Curtin, W.A. (1993) *Composites*, **24** 98–102.
Davis, L.C., and J.E. Allison (1993) *Metall. Trans*., **24A**, 2487.
Devé, H.E. (1997) *Acta Mater*., **45**, 5041–5046.
Devé, H.E., and C. McCullough (1995) *JOM*, **7,** 33–37.
Dirichlet, G.L. (1850) *J. Reine Angew. Math*., **40**, 209–227.
Dunand, D.C., and A. Mortensen (1991) *Acta Metall. Mater*., **39**, 1417–1429.
Dutta, I., J.D. Sims and D.M. Seigenthaler (1993) *Acta Metall. Mater*., **41**, 885.
Eldridge, J.I., D.R. Wheeler, R.R. Bowman, and A. Korenyi-Both (1997) *J. Mater. Res*., **12**, 2191–2197.
Evans, A.G., and D.B. Marshall (1989) *Acta Metall*., **37**, 2567.
Faucon, A., T. Lorriot, E. Martin, S. Auvray, Y. Lepetitcorps, K. Dyos, and R.A. Shatwell (2001) *Comp. Sci. Tech*., **61**, 347–354.
Galvez, F., C. Gonzalez, P. Poza, and J. LLorca (2001) *Scripta Mater*., **44**, 2667–2671.
Ganesh, V.V., and N. Chawla (2004) *Metall. Mater. Trans*., **35A**, 53–62.
Ganesh, V.V., and N. Chawla (2005) *Mater. Sci. Eng*., **A391**,342–353.
Gao, Y.C., Y.W. Mai, and B. Cotterell (1988) *SAMPE*, **39**, 550.
Gonzalez, C., and J. LLorca (2001) *Acta Mater*., **49**, 3505–3519.
Goodier, J.N. (1933) *J. Appl. Mech*., **55–7**, 39.
Grimes, H.H., R.A. Lad, and J.E. Maisel (1977) *Metall. Trans*., **8**, 1999–2005.
Guden, M., and I.W. Hall (2000) *Computers and Struc*., **76**, 139–144.
Gupta, V. (1991) *MRS Bull*., **16**(No. 4), 39.
Gupta, V., J. Yuan, and D. Martinez (1993) *J. Amer. Ceram. Soc*., **76**, 305.
Hack, J.E., R.A. Page, and G.R. Leverant (1984) *Metall. Trans*., **15A**, 1389–1396.
He, M.Y., and J.W. Hutchinson (1989) *J. App. Mech*., **56**, 270.
Humphreys, F.J. (1977) *Acta Metall*., **25** 1323–1344.
Humphreys, F.J. (1991) *Mater. Sci. Eng*., **135A,** 267–273.
Hunt, W.H., T.M. Osman, and J.J. Lewandowski (1993) *JOM*, **45**, 30–35.
Hutchinson, J.W., and H.M. Jensen (1990) *Mech. Matls*., **9**, 139–163.
Isaacs, J.A., and A. Mortensen (1992) *Metall. Trans*., **23A**, 1207–1219.
Jansson, S., H.E. Deve, and A.G. Evans (1991) *Metall. Mater. Trans*., **22A**, 2975.
Jeong, H., D.K. Hsu, R.E. Shannon, P.K. Liaw (1994) *Metall. Mater. Trans*., **25A**, 799–809.
Kamat, S., J.P. Hirth, and R. Mehrabian (1989) *Acta Metall*., **37**, 2395.
Kelly, A. (1973) *Strong Solids*, Clarendon Press, Oxford, p. 157.
Kelly, A., and H. Lilholt (1969) *Phil. Mag*., **20**, 311–328.
Kerans, R.J., and T.A. Parthasarathy (1991) *J. Am. Ceram. Soc*., **74**, 1585–1596.
Krajewski, P.E., J.E. Allison, and J.W. Jones (1993) *Metall. Mater. Trans*., **24**, 2731.
Konitzer, D.G., and M.H. Loretto (1989) *Mater. Sci. Eng*., **A107**, 217–223.

Kyono, T., I.W. Hall, and M. Taya (1986) *J. Mater. Sci.*, **21**, 4269–4280.
Levy, A., and J. M. Papazian (1991) *Acta Metall. Mater.*, **39**, 2255.
Lewandowski, J.J. (2000) in *Comprehensive Composite Materials*, T.W. Clyne, A. Kelly, and C. Zweben (eds.), Elsevier, vol. 3, pp. 151–187.
Lewandowski, J.J., D.S. Liu, and C. Liu (1991) *Scripta Metall.*, **25**, 21.
Leyens, C., J. Hausmann, and J. Kumpfert (2003) *Adv. Eng. Mater.*, **5**, 399–410.
LLorca, J. (1995) *Acta Metall. Mater.*, **43**, 181–192.
LLorca, J., A. Needleman and S. Suresh (1991) *Acta Metall. Mater*, **39**, 2317.
Lloyd, D.J. (1995) in *Intrinsic and Extrinsic Fracture Mechanisms in Inorganic Composite Systems*, J.J. Lewandowski and W.H. Hunt (eds.), TMS-AIME, Warrendale, PA, pp. 39–47.
Lloyd, D.J. (1997) in *Composites Engineering Handbook* (P.K. Mallick, ed.), Marcel Dekker, New York, pp. 631–669.
Logsdon, W.A., and P.K. Liaw (1986) *Eng. Frac. Mech.*, **24**, 737–751.
Manoharan, M., and J.J. Lewandowski (1990) *Acta Metall. Mater.*, **38**, 489–496.
Manoharan, M., and J.J. Lewandowski (1992) *Mater. Sci. Eng.*, **A150**, 179–186.
Manoharan, M., J.J. Lewandowski, and W.H. Hunt (1993) *Mater. Sci. Eng.*, **A172**, 63–69.
Meyers, M.A., and K.K. Chawla (1999) *Mechanical Behavior of Materials*, Prentice-Hall, Upper Saddle River, NJ, p. 493.
Miller, D.A., and D.C. Lagoudas (2000) *J. Eng. Mater. Tech.*, **122**, 74–79.
Mikata, Y., and M. Taya (1985) *J. Compos. Mater.*, **19**, 554.
McCullough, C., H.E. Devé, and T.E. Channel (1994) *Mater. Sci. Eng.*, **A189**, 147–154.
Mummery, P.M., B. Derby, D.J. Buttle, and C.B. Scruby (1991) in *Proc. of Euromat 91*, T.W. Clyne and P.J. Withers (eds.), vol. 2, Cambridge, UK, pp. 441–447.
Murphy, A.M., S.J. Howard, and T.W. Clyne (1998) *Mater. Sci. Tech.*, **14**, 959–968.
Nardone, V.C., and K.M. Prewo (1986) *Scripta Metall.*, **23**, 291.
Page, R.A., J.E. Hack, R. Sherman, and G.R. Leverant (1984) *Metall. Trans.*, **15A**, 1397–1405.
Rao, K.T. Venkateshwara, S.C.Siu, and R.O. Ritchie (1993) *Metall. Trans.*, **24A**, 721–734
Rosenberger, A.H., P.R. Smith, and S.M. Russ (1999) *J. Comp. Tech. Res.*, **21**, 164–172.
Rossoll, A., B. Moser, and A. Mortensen (2005) *Mech. Mater.*, **37**, 1.
Ruhle, M., and A.G. Evans (1988) *Mater. Sci. Eng.*, **A107**, 187.
Segurado, J., C. Gonzalez, and J. LLorca (2003) *Acta Mater.*, **51**, 2355–2369.
Shen, Y.-L., and N. Chawla (2001) *Mater. Sci. Eng.*, **A297**, 44–47.
Shen, Y.-L., M. Finot, A. Needleman, and S. Suresh (1994) *Acta Metall. Mater.*,**42**, 77.
Shen, Y.-L., M. Finot, A. Needleman, and S. Suresh (1995) *Acta Metall. Mater.*,**43**, 1701.
Shen, Y.-L., J.J. Williams, G. Piotrowski, N. Chawla**,** and Y.L. Guo (2001) *Acta Mater.*, **49**, 3219–3229.
Schulte, K., and K. Minoshima (1993) *Composites*, **24**, 197–208.
Shetty, D.K. (1988) *J. Amer. Ceram. Soc.*, **71**, C-107.
Steglich, D., T. Siegmund, and W. Brocks (1999) *Comput. Mater. Sci.*, **16**, 404–413.
Suresh, S., and K.K. Chawla (1993) in *Fundamentals of Metal Matrix Composites*, Suresh, S., A. Mortensen, and A. Needleman, eds., Butterworth-Heinemann, Stoneham, MA, p. 119.
Termonia, Y. (1987) *J. Mater. Sci.*, **22**, 504–508.
Toda, H., T. Gouda, and T. Kobayashi (1998) *Mater. Sci. Tech.*, **14**, 925–932.
Torquato, S. (2002) *Random Heterogeneous Materials: Microstructure and Macroscopic Properties*, Springer-Verlag, New York, pp. 160–176.
Vogelsang, M., R.J. Arsenault, and R.M. Fisher (1986) *Metall. Trans.*, **17A**,379.
Voleti, S.R., C.R. Ananth, and N. Chandra (1998) *J. Comp. Tech. Res.*, **29**, 203–209.
Wang, L., and T. Kobayashi (1997) *Mater. Trans. JIM.*, **38**, 615–621.
Warrier, S.G., and B.S. Majumdar (1997) *Mater. Sci. Eng.*, **237**, 256–257.
Williams, J.J., Z. Flom, A.A. Amell, N. Chawla, X. Xiao, and F. De Carlo (2010) *Acta Mater.*, **58**, 6194–6205.
Williams, J.J., N.C. Chapman, V. Jakkali, V.A. Tanna, N. Chawla, X. Xiao, and F. De Carlo (2011) *Metall. Mater. Trans.*, **42A** 2999–3005.

Young, R.J. (1994) in *High Performance Composites: Commonalty of Phenomena*, K.K. Chawla, P.K. Liaw, and S.G. Fishman, eds., TMS, Warrendale, PA, p. 263.

Speich, G.R., R.L. Miller (1979) in *Structure and Properties of Dual-Phase Steels*, American Institute of Mining, Metallurgical, and Petroleum Engineers, p. 145.

Tamura, I., Y. Tomota, M. Ozawa (1973) in *Proceedings 3rd Intl. Conf. on the Strength of Metals and Alloys,* Cambridge, Vol. 1, p. 611.

Rios, P.R., J.R.C. Guimarães, K.K. Chawla (1981) *Scripta Metall.*, **15**, 899.

Stewart, J.L., L. Jiang, J.J. Williams, and N. Chawla (2012) *Mater. and Metall. Trans.,* **43A**, 124.

Young, M. L., J. D. Almer, M. R. Daymond, D.R. Haeffner, and D. C. Dunand (2007) *Acta Mater.*, **55,** 1999.

Chapter 8
Cyclic Fatigue

Fatigue is the phenomenon of mechanical property degradation under cyclic loading. The cyclic loads may be mechanical, thermal, or a combination of the two. Many high-volume applications of composite materials involve cyclic-loading situations, e.g., automobile components and aircraft structures. Below we provide a brief description of the two main approaches that have been used to quantify fatigue behavior of materials. For a more complete description, the reader may consult the texts by Meyers and Chawla (2009) and Suresh (1998).

Stress versus cycles (S–N): This approach involves cyclic fatigue testing to develop *S–N* curves, where S is the stress amplitude and *N* is the number of cycles to failure. In general, for ferrous metals, a clear fatigue limit or endurance limit is observed. For stress levels below this endurance limit, theoretically, the material can be cycled infinitely without failure. In nonferrous materials, such as aluminum, a true endurance limit does not exist. Here one can arbitrarily define a certain number of cycles, say 10^7, as the point of "fatigue runout," at which point the experiment is stopped. With the advent of ultrasonic fatigue testing techniques, where frequencies of 20–30 kHz can be applied, fatigue tests out to 10^8 or 10^9 can be routinely carried out. The fatigue behavior of structural materials can be conveniently divided into two stages: crack initiation and propagation. In high cycle fatigue (HCF) of metals, most of the fatigue life is spent initiating a fatigue crack, and a very small fraction of the life is spent in propagation. In low cycle fatigue (LCF), a much larger fraction of the fatigue life is spent in crack propagation. The phenomena of work hardening and work softening also play an important role in LCF. One major drawback of the *S–N* approach is that no distinction can be made between the crack initiation phase and the crack propagation phase.

Fatigue crack growth: This approach is based on fracture mechanics, and it enables the study of fatigue crack propagation. Fatigue crack propagation experiments are generally conducted on notched samples. The crack length, a, is measured as a function of fatigue cycles, N, over a range of cyclic stress intensity factors, ΔK. The applied cyclic stress intensity range is given by

N. Chawla and K.K. Chawla, *Metal Matrix Composites*,
DOI 10.1007/978-1-4614-9548-2_8, © Springer Science+Business Media New York 2013

$$\Delta K = Y\Delta\sigma\sqrt{\pi a}$$

where Y is a geometric parameter that depends on the nature of the notch and specimen configuration, $\Delta\sigma$ is the cyclic stress range, and a is the crack length. The results are then presented as log da/dN (crack growth per cycle) versus log ΔK. Crack growth rate, da/dN, is related to ΔK according to the power-law relationship first formulated by Paris et al. (1961) and Paris and Erdogan (1963):

$$\frac{da}{dN} = C(\Delta K)^m$$

where C and m are constants that depend on the material and test conditions.

The application of a fracture mechanics based approach to composites is not straightforward. The main reason for this is the inherent heterogeneity and anisotropic nature of the composites. These attributes of composites result in damage mechanisms that are very different from those encountered in conventional, homogeneous materials. Despite these limitations, conventional approaches have been used and modified to quantify the fatigue behavior of composites. As in previous chapters, we divide our discussion of fatigue into two major types of MMCs: continuous fiber-reinforced and discontinuously reinforced (primarily particle-reinforced) MMCs.

8.1 Stress Versus Cycles (S–N) Fatigue

Several material variables play an important role in fatigue of MMCs. These include modulus, strength, ductility, and work-hardening characteristics of the constituents (reinforcement and matrix) as well as the characteristics of the interface. As mentioned above, conventional approaches to fatigue involve *S–N* curves and fatigue crack propagation studies. Another approach involves the monitoring of damage accumulation. Specifically, measurement of modulus loss as a function of cycles has been used extensively in polymer matrix and ceramic matrix composites (Chawla 2012). In the following, we describe the fatigue behavior of continuous fiber-reinforced MMCs.

8.1.1 Continuous Fiber-Reinforced MMCs

Incorporation of fibers generally improves the fatigue resistance in the fiber direction. In general, in composites containing fibers aligned along the stress axis and in large volume fractions, high monotonic strength and modulus translate into high fatigue strength. This can be explained by the fact that with increasing stiffness and strength, an increasing fraction of the load is borne by the fibers. High-strength,

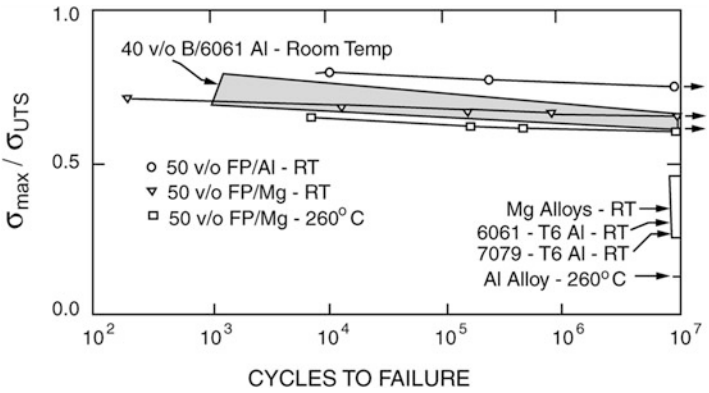

Fig. 8.1 Stress versus cycles (*S–N*) curves for unidirectionally reinforced 6061/B/40_f, Al/Al_2O_3(FP)/50_f, and Mg/Al_2O_3(FP)/50_f under tension–tension fatigue (after Champion et al. 1978). The fatigue strength of the composites is significantly enhanced over that of the monolithic alloys. FP is the DuPont's trade name for alumina fibers

brittle fibers such as carbon or boron do not fatigue as readily as metals, although ceramic fibers have been shown to be susceptible to cyclic fatigue (Chawla et al. 2005; Kerr et al. 2005).

Typically, the *S–N* curves of fiber-reinforced MMCs are close to horizontal. Figure 8.1 shows the *S–N* curves for unidirectionally reinforced 6061/B/40_f, Al/Al_2O_3(FP)/50_f, and Mg/Al_2O_3(FP)/50_f under tension–tension fatigue (Champion et al. 1978). The cyclic stress is normalized with respect to the ultimate tensile strength. The unidirectional MMCs show better fatigue properties than the matrix, when loaded parallel to the fibers. Note the rather flat *S–N* curves for all the composites. In unidirectional composites, the fatigue strength will be a maximum along the fiber direction, and the greatest efficiency will be achieved if the fibers have uniform properties, are as defect-free as possible, and are much stronger and stiffer than the matrix. McGuire and Harris (1974) observed that increasing the fiber volume fraction from 0 to 24 % resulted in increased fatigue resistance of tungsten fiber-reinforced Al–4Cu alloy under tension–compression cycling ($R = \sigma_{min}/\sigma_{max} = -1$). This was a direct result of increased monotonic strength and stiffness of the composite as a function of the fiber volume fraction. The enhancements in fatigue life due to increased stiffness of the composite are most pronounced in the HCF regime. Thus, in stress-controlled fatigue, for a given applied stress, the matrix in the composite will undergo a much lower strain than that of the unreinforced alloy.

Some work has been done to understand the fatigue damage mechanisms in continuous fiber-reinforced MMCs. Baker et al. (1972) conducted one of the earliest studies on fatigue of continuous fiber-reinforced MMCs. The *S–N* fatigue behavior of Al/B_f (125 μm fiber diameter) and Al/C_f (8 μm fiber diameter) composites was studied. The carbon fiber-reinforced composites exhibited poor fatigue resistance, because of processing-induced fracture of the fibers and poor interfacial bonding. The following mechanisms were observed during fatigue: (a) fiber fracture dominated

damage, where the rate of fiber fracture was much higher than cyclic plasticity in the matrix, and (b) matrix shear and plasticity induced localized and progressive fiber fracture. Mechanism (a) was shown to be predominant in LCF, where the applied stresses were much closer to the ultimate strength of the fibers (and the composite). In high cycle fatigue, the fatigue damage in the composite is more likely to be controlled by matrix plasticity, followed by fiber fracture, or mechanism (b). Gouda et al. (1981) also observed crack initiation early in the fatigue life at defects in boron fibers in unidirectionally reinforced Al/B_f composites. These cracks then grew along the fiber/matrix interface and accounted for a major portion of the fatigue life, as would be the case in a composite with high fiber-to-matrix strength ratio. In composites with low fiber-to-matrix strength ratio, crack propagation may be a major portion of fatigue life, but the fatigue cracks grow through the fibers, resulting in poor fatigue resistance. Uniform spacing of fibers is also crucial, because clustered or touching fibers will result in enhanced stress concentration and easier crack nucleation.

The reader should note that because of the highly anisotropic nature of the fiber-reinforced composites in general, the fatigue strength of off-axis MMCs, as in any fibrous composite, will be expected to decrease with increasing angle between the fiber axis and the applied stress axis. This has been confirmed by studies involving *S–N* behavior of alumina fiber-reinforced magnesium composites (Hack et al. 1987; Page et al. 1987). It was found that the fatigue strength mirrored the tensile strength of the composites. Increased fiber volume fractions resulted in enhanced fatigue lifetimes in the axial direction, but little or no improvement was observed in the off-axis directions. Fatigue crack initiation and propagation occurred primarily through the magnesium matrix. Thus, alloy additions to increase the strength of the matrix and fiber/matrix interface were incorporated. The alloy additions did improve the off-axis properties but decreased the axial properties. The reason for this was that while the alloy additions resulted in strengthening of the matrix and interface, they decreased the fiber strength.

Few direct microstructural observations of fatigue damage in continuous fiber-reinforced MMCs have been conducted. One such study involved a single crystal copper matrix containing tungsten fibers (Chawla 1975). Tungsten/copper is an unusual metal matrix composite system. The two metals are mutually insoluble, yet molten copper wets tungsten. This allows for a strong mechanical bond between the tungsten fiber and the copper matrix, without any attendant chemical complications at the interface. The composites were made by liquid metal infiltration of fibers in vacuum. It was observed that the process of fabrication involving cooling from a temperature >1,080 °C (melting point of copper) to room temperature resulted in thermal stresses large enough to deform the copper matrix plastically (Chawla and Metzger 1972). Dislocation etch-pitting technique was used to characterize the dislocation density in the single crystal copper matrix. The dislocation density in the matrix was higher ($>10^8$ cm^{-2}) near the fiber/matrix interface than away from the interface. The dislocation distribution had a cellular structure, with the cell structure being better defined and smaller near the fiber than away from the fiber. This very heterogeneous distribution became homogeneous on cycling stress. The copper matrix structure after cycling had a high dislocation density distributed in a more or less uniform cellular structure.

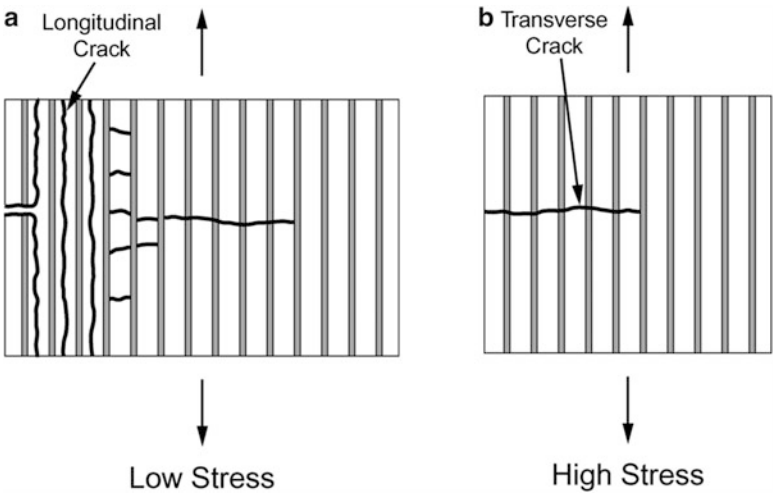

Fig. 8.2 Fatigue damage mechanisms in $Al/Al_2O_{3,f}$ composites: (**a**) low stress (high cycle fatigue), longitudinal splitting between fibers is the dominant failure mechanism, and (**b**) high stress (low cycle fatigue), a single dominant crack propagates (after Zhang et al. 2003)

Zhang et al. (2003) studied the *S–N* fatigue behavior of a 45 vol.% Nextel 610 alumina fiber-reinforced pure Al matrix composite. The composite exhibited a tensile stress–strain behavior that was linear to failure, with about 0.7 % strain-to-failure. In fatigue, the *S–N* curve was linear, with a fatigue strength (fatigue runout taken at 10^7 cycles) around 700 MPa. A clear and definitive fatigue strength was not apparent. The damage mechanisms varied considerably with applied stress. At very low stress (HCF regime), longitudinal cracking between fibers was the dominant failure mechanism, Fig. 8.2a. It was suggested that these cracks initiated at fractured fibers and then grew parallel to the fiber direction. With increasing cyclic stress amplitude, in the intermediate regime between HCF and LCF, longitudinal matrix cracking was accompanied by transverse matrix cracks between fibers. Finally, at very high stresses (LCF regime), a single crack propagated in a catastrophic fashion perpendicular to the fibers, with no significant toughening, Fig. 8.2b. Persistent slip band (PSB) formation in the matrix has also been shown to contribute to the development of fatigue cracks in the fibers, leading to fiber fracture (Majumdar and Newaz 1995).

The fracture morphology is directly related to the fatigue regime of the material, i.e., crack velocity. Figure 8.3 shows the fracture surface of a SiC fiber-reinforced Ti alloy matrix composite in the power-law regime (also called the Paris regime) and in the fast fracture regime. In the Paris-law regime, the localized fatigue striations are observed in the matrix of the composite. In the fast fracture region, the fracture is similar to that observed under monotonic tension, because of the very high crack velocities. Here, void nucleation and growth in the matrix are predominant, along with debonding at the fiber/matrix interface.

Finally, in composite systems where the interfacial bond strength is relatively weak, interfacial wear may contribute to fiber fracture. Interestingly, this behavior

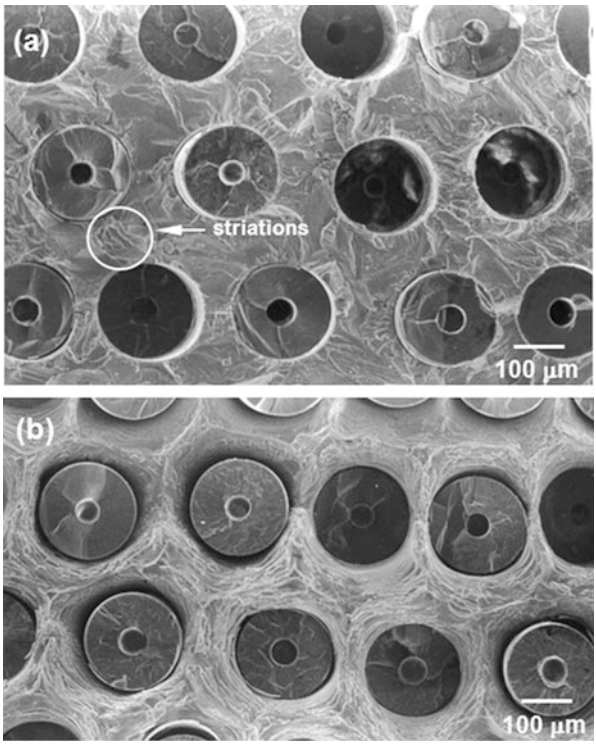

Fig. 8.3 Fatigue fracture in a Ti-β-21s/SiC_f(SCS-6) composite: (**a**) Paris-law regime, showing localized striations in the matrix, and (**b**) fast fracture regime, where the matrix morphology is characteristic of void nucleation and growth (courtesy of J. Liu)

has been shown in ceramic matrix composites and can result in significant temperature rise in the ceramic matrix composite at high frequencies (>100 Hz), due to frictional heating (Chawla et al. 1996; Chawla 1997). Walls and Zok (1994) quantified the extent of interfacial wear during fatigue in a fiber pushout test (see Chap. 4). The interfacial strength in the composite after increasing fatigue cycles was significantly lower than that in the as-received material, with a continuously increasing fiber displacement, Fig. 8.4. This indicates that significant wear processes were taking place during fatigue (Walls et al. 1993). Figure 8.5 shows quantitative microstructural evidence of the interfacial wear process during fatigue of a Ti-β-21s (Ti-15Mo-2.7Nb-3Al-0.2Si)/SiC_f(SCS-6) composite obtained in an in situ SEM test (Liu and Bowen 2003).

In addition to the mechanisms described above, elevated temperature also exacerbates fatigue damage. The mechanisms of fatigue damage are very much dependent on the composite system. In large-diameter SiC fibers (such as SCS-6), the surface of the fiber is C-rich. The fibers also contain a central carbon core. Thus, at elevated temperatures, the carbon will react with the matrix, such as Ti, to form hard and brittle carbides at the interface. The brittle carbides can act as fatigue crack initiation sites and catastrophic crack propagation can result. Foulk et al. (1998) also noted that oxygen dissolution of the interface combined with mechanical wear at the interface also degraded fatigue life. It was found that the stress on the fiber

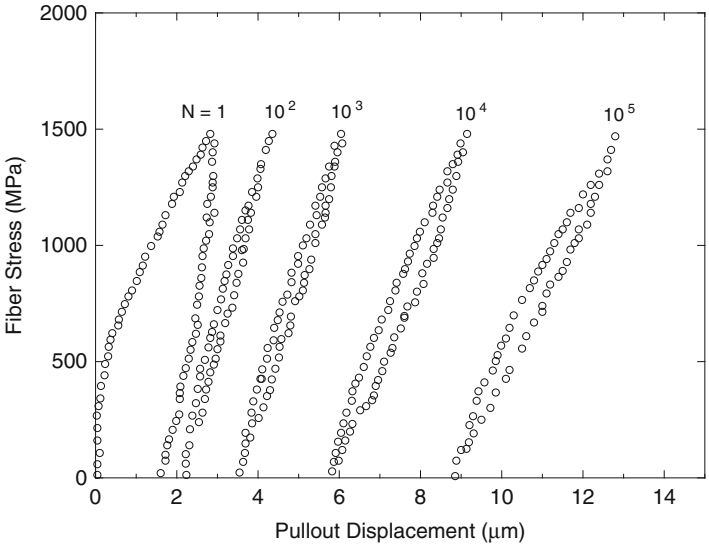

Fig. 8.4 Stress–strain hysteresis of a single fiber SiC fiber (SCS-6) in a Ti alloy matrix during fatigue. The hysteresis loops become wider with increasing cycles, indicating inelastic deformation in the form of wear at the fiber/matrix interface (after Walls and Zok 1994)

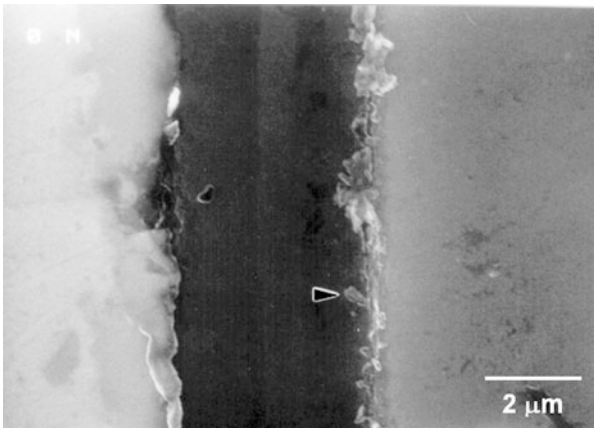

Fig. 8.5 In situ SEM micrograph of interfacial wear process during fatigue (indicated by *arrow*) of a Ti–β–21s/SiC_f(SCS-6) composite (courtesy of J. Liu)

increased with increasing degradation of the interface. Significant degradation in interfacial shear strength, as measured by fiber pushout, due to interfacial wear and degradation due to elevated temperature fatigue has also been observed (Blatt et al. 1995). The fatigue damage is also controlled by cycling frequency. Lower frequencies allow more time for interfacial reaction to take place, leading to lower

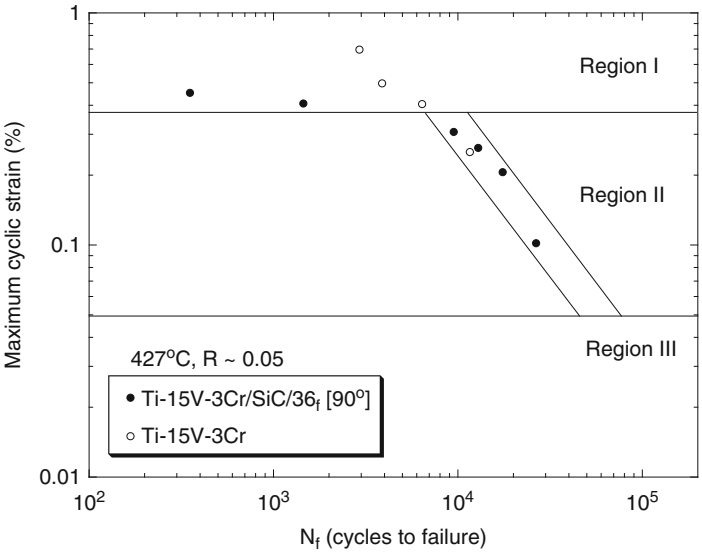

Fig. 8.6 Elevated temperature fatigue response (in strain control) of a Ti-15V-3Cr/SiC(SCS-6)/36_f in the transverse orientation. At relatively high strains, termed Region I, the composite has lower fatigue resistance than the matrix material. With decreasing applied strain, Region II, the composite has equivalent transverse fatigue strength as the unreinforced alloy (after Sanders and Mall 1996)

fatigue lives (in cycles) in LCF, although in the HCF regime, the fatigue strength is about the same (Mall and Portner 1992).

Sanders and Mall (1996) investigated the elevated temperature fatigue response (in strain control) of a Ti-15V-3Cr/SiC(SCS-6)/36_f in the transverse orientation. At relatively high strains, termed Region I, the composite had lower fatigue resistance than the matrix material, Fig. 8.6. This was attributed to matrix cracks, originating at the fiber/matrix interface, which resulted in premature failure of the composite, relative to the unreinforced alloy. With decreasing applied strain, Region II, the composite had equivalent transverse fatigue strength as the unreinforced alloy, although the damage mechanisms were quite different. In the monolithic alloy, creep–fatigue mechanisms took place. In the composite, however, the interfacial damage took place which gradually progressed into matrix cracking. The matrix cracks, assisted by matrix creep, resulted in failure of the composite.

In nonstructural composites, such as filamentary superconductor-reinforced MMCs, the degradation of other functional properties is important. Salazar et al. (2004) studied the degradation in critical current density of a $Bi_2Sr_2Ca_2Cu_3O_x$(BSCCO)/Ag–Mg composite superconductor as a function of fatigue cycles at 77 K. Figure 8.7 shows the microstructure of the composite,

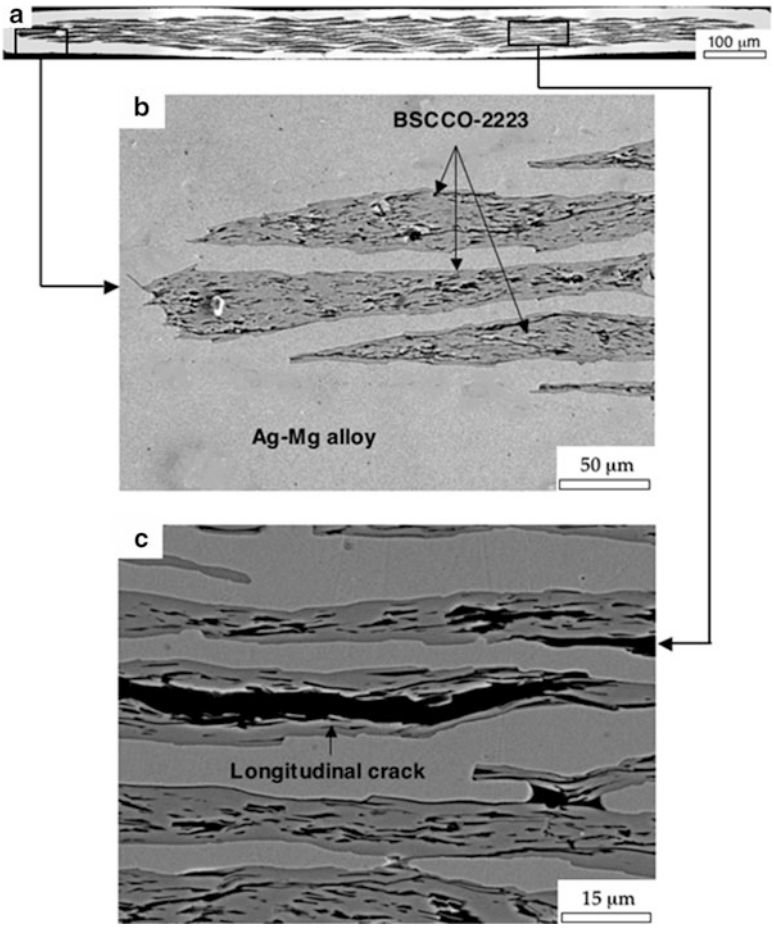

Fig. 8.7 Microstructure of $Bi_2Sr_2Ca_2Cu_3O_x$(BSCCO)/Ag–Mg composite superconductor (courtesy of J. LLorca). (**a**) is a low magnification image of the microstructure. The BSSCO filaments contain some processing-induced longitudinal cracks shown in parts (**b**) and (**c**)

which contains some processing-induced longitudinal cracks in the BSSCO filaments. An electric fatigue limit was defined, analogous to the mechanical fatigue limit, which corresponds to the stress below which degradation in electrical properties is negligible. In the BSSCO/Ag–Mg system, this corresponded to between 80 and 90 % of the yield strength of the composites. Fracture of the ceramic superconductor filaments also took place during fatigue, eventually resulting in fatigue failure of the composite. Figure 8.8 shows fatigue microcracks that nucleated in the superconductor sheaths, which are not fully dense. These cracks propagated until the superconductor/matrix interface was reached. Necking of the matrix between filaments occurred followed by fracture of the composite.

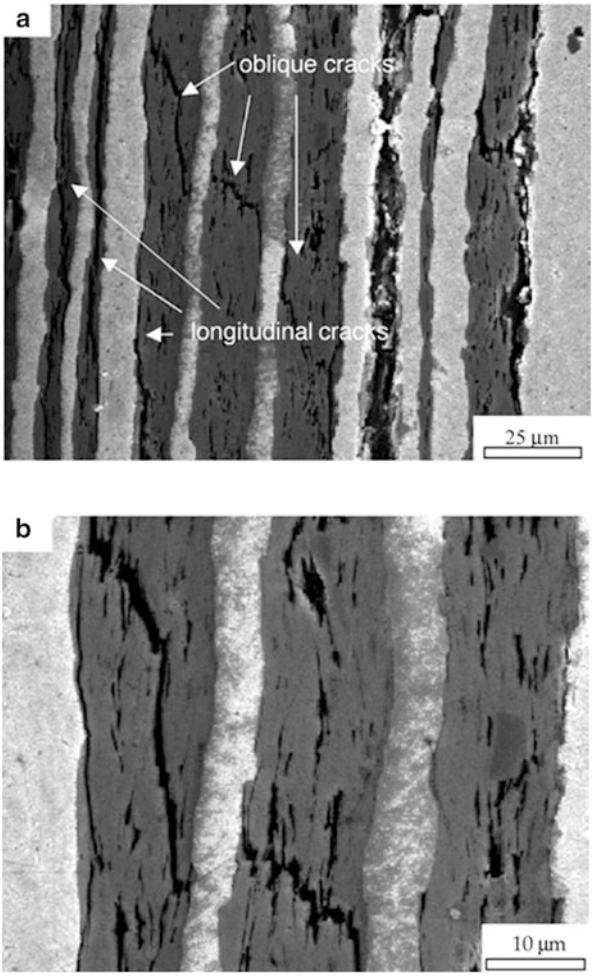

Fig. 8.8 Fatigue microcracks in $Bi_2Sr_2Ca_2Cu_3O_x$(BSCCO)/Ag–Mg composite superconductor: (**a**) lower magnification and (**b**) higher magnification (courtesy of J. LLorca). The cracks nucleate in the superconductor sheaths, which are not fully dense. These cracks propagate until the superconductor/matrix interface is reached

8.1.2 Stiffness Loss

The major problem in quantifying the stress intensity range during fatigue crack growth of fiber-reinforced MMCs is the absence of *one and only* one dominant crack that is propagating. This lack of *self-similar* crack growth, i.e., when the crack propagates in the same plane and direction as the initial crack, is caused by the many modes of damage in MMCs, such as matrix cracking, fiber fracture, interfacial delamination and debonding, void growth, and multidirectional cracking. These modes appear rather early in the fatigue life of composites. One manifestation of such damage is the stiffness loss as a function of cycles. In general, one would expect the scatter in fatigue data of composites to be much greater than that in fatigue of monolithic, homogeneous materials. This is because

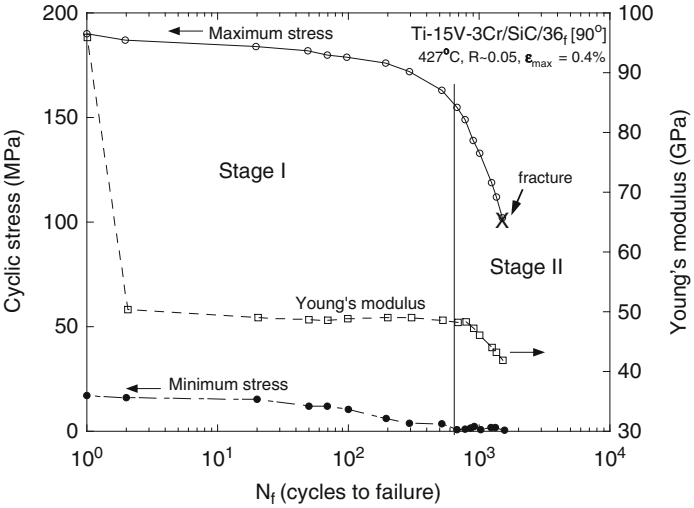

Fig. 8.9 Decrease in Young's modulus and maximum stress in strain-controlled fatigue of Ti-15V-3Cr/SiC(SCS-6)36_f, under transverse loading (after Sanders and Mall 1996). In stage I, the damage in modulus and stress is relatively stable. In stage II, however, significant damage, likely due to interfacial fracture, resulted in a significant decrease in the stress carried by the composite and the Young's modulus

of the existence of a variety of damage mechanisms in composites. Thus, with continued cycling, there occurs an accumulation of damage. This accumulated damage results in a reduction of the overall stiffness of the composite. Measurement of stiffness loss as a function of cycling has been shown to be quite a useful technique of assessing the fatigue damage in polymer matrix composites (Chawla 2012). In MMCs, the fatigue behavior of boron fiber- and silicon carbide fiber-reinforced aluminum and titanium alloy matrix composite laminates having different stacking sequences has been examined using the stiffness-loss measurement technique (Johnson 1982, 1988; Johnson and Wallis 1986). It was observed that on cycling below the fatigue limit but above a distinct stress range, $\Delta\sigma$, the plastic deformation and cracking (internal damage) in the matrix led to a reduced modulus. Johnson (1988) has proposed a model that envisioned the specimen reaching a "saturation damage state" (SDS) during constant amplitude fatigue testing.

Gomez and Wawner (1988) observed stiffness loss in silicon carbide (SCS)/aluminum composites subjected to tension–tension fatigue ($R = 0.1$) at 10 Hz. The Young's modulus was measured at periodic intervals between cycles. The coating on the SCS fiber fractured at high cycles, and the fracture surface showed the coating clinging to the matrix. Sanders and Mall (1996) also observed a distinct decrease in Young's modulus and maximum stress under strain-controlled fatigue of Ti-15V-3Cr/SiC(SCS-6)36_f, under transverse loading, Fig. 8.9. Two distinct stages of damage were observed. In stage I, the damage in modulus and stress was relatively stable. In stage II, however, significant damage, likely due to interfacial fracture, resulted in a significant decrease in the Young's modulus and the stress carried by the composite.

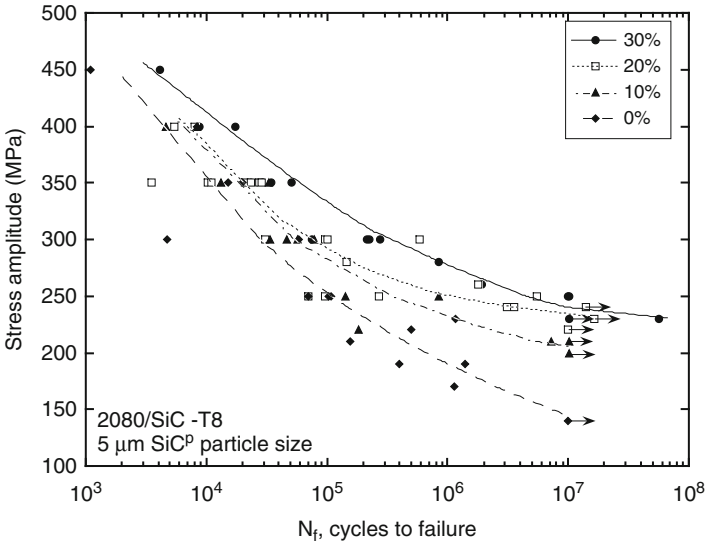

Fig. 8.10 Effect of SiC volume fraction on the stress versus cycles fatigue behavior of 2080 Al/SiC_p composites. Increasing volume fraction results in higher fatigue life (after Chawla et al. 1998a)

8.1.3 Particle-Reinforced MMCs

The use of a high-stiffness ceramic reinforcement in particulate form can result in a substantial increase in fatigue resistance while maintaining cost at an acceptable level. The fatigue resistance of particulate MMCs depends on a variety of factors, including reinforcement particle volume fraction, particle size, matrix and interfacial microstructure, the presence of inclusions or defects that arise from processing, and testing environment (Chawla and Shen 2001; Chawla and Allison 2001; Lewandowski 2000; LLorca 2002; Ganesh and Chawla 2004). The effect of these factors on the fatigue behavior of particle-reinforced MMCs is summarized in this section.

Several studies have shown that increasing volume fraction and decreasing particle size both result in enhanced fatigue resistance (Hall et al. 1994; Poza and LLorca 1999; Chawla et al. 1998a, 2000a, b). In the composite, most of the load is carried by the high-modulus, high-strength reinforcement, so for a given stress, the composite undergoes a lower average strain than the unreinforced alloy. Thus, the fatigue lives of particle-reinforced metal matrix composites are generally superior to those of unreinforced metals as shown in Fig. 8.10. These improvements are most pronounced at low cyclic stresses, i.e., in the high cycle fatigue regime, while at higher cyclic stresses the differences between reinforced and unreinforced materials are reduced. This has been called “ductility exhaustion” of the composites,

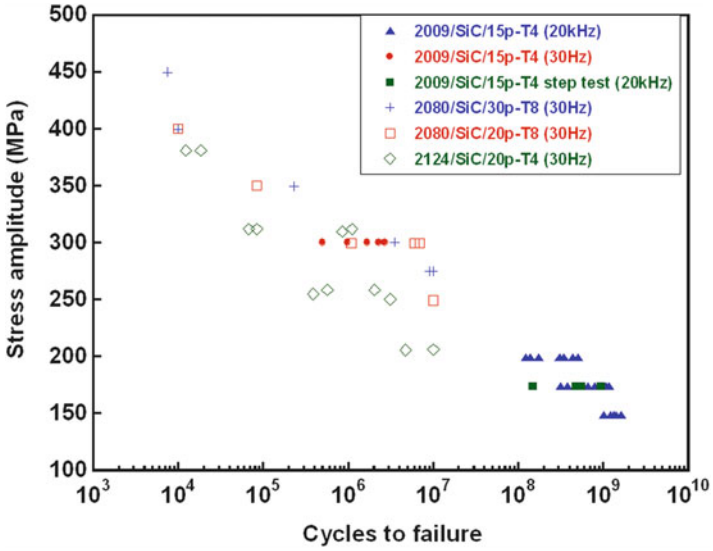

Fig. 8.11 Effect of SiC volume fraction on the stress versus cycles fatigue behavior of 2XXX Al/SiC_p composites at 30 Hz and 20–30 kHz. Note that the ultrahigh cycle fatigue data follows the data at lower frequencies (Huang et al. 2006)

which takes place in the LCF regime. The higher ductility of the unreinforced alloy in this regime contributes to higher fatigue life than that of the composite. With decreasing particle size, for a given reinforcement volume fraction, the reinforcement interparticle spacing decreases, resulting in more barriers to the reversible slip motion that takes place during fatigue, and a decrease in strain localization by cyclic slip refinement. Above a critical particle size, reinforcement fracture is predominant and contributes to a low fatigue life, because of the increased propensity for particle cracking as the particle size increases (Chawla et al. 1998a). Narrowing of the particle size range distribution also results in higher fatigue life, particularly when eliminating larger particles that are more prone to cracking (Couper and Xia 1991).

Huang et al. (2006) studied the fatigue behavior of SiC particle-reinforced Al alloy matrix composites in the ultrahigh cycle (UHC) fatigue regime, as shown in Fig. 8.11. Using ultrasonic techniques, they were able to achieve frequencies in the 20–30 kHz range and fatigue failures between 10^8 and 10^9 cycles. It is interesting to note that the trend in stress versus fatigue life for the UHC (and, thus, high-frequency data) is consistent with the data at lower frequencies.

The cyclic stress–strain behavior of the composite is also affected by the onset of microplasticity at relatively low stress (see Chap. 7). Chawla et al. (1998b) compared the cyclic stress–strain behavior of a 2080/$SiC/30_p$ composite with that of the unreinforced alloy. The composite exhibited microplasticity at relatively low stresses, presumably due to stress concentrations at SiC particles and localized

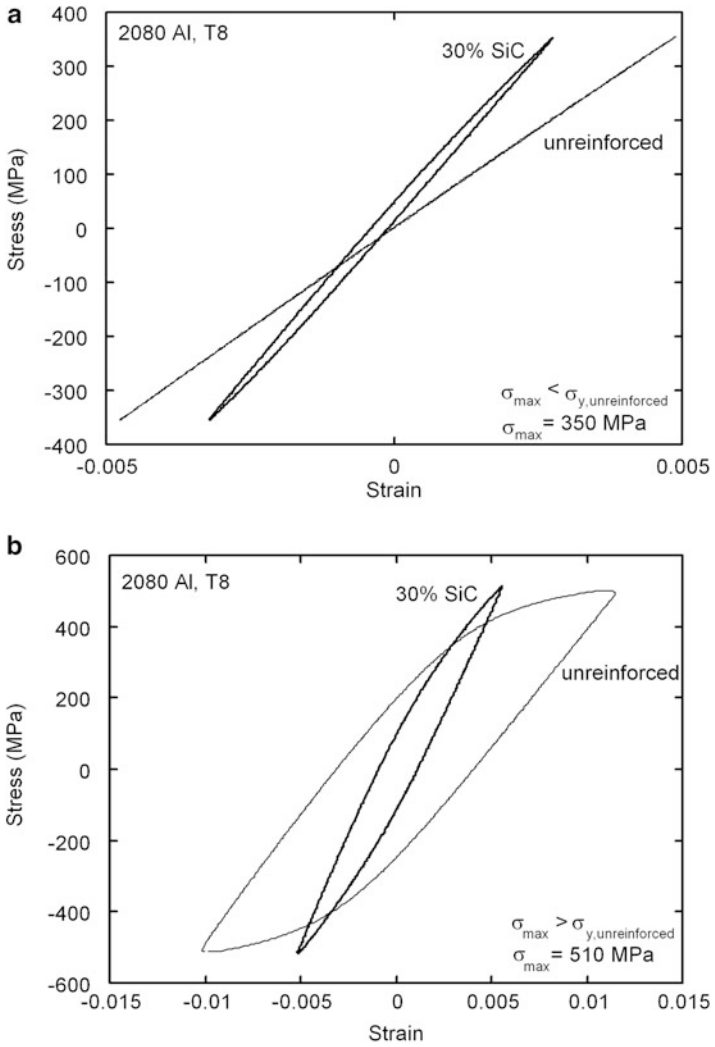

Fig. 8.12 Comparison of cyclic stress strain behavior of a 2080/SiC/30p composite and 2080 Al-unreinforced alloy (Chawla et al. 1998b): (**a**) low cyclic stress ($\sigma_{max} < \sigma_{y,unreinforced}$) and (**b**) high cyclic stress ($\sigma_{max} > \sigma_{y,unreinforced}$). The composite exhibits microplasticity at very low stress, due to localized plasticity at the poles of the SiC reinforcement and at sharp particle corners

plasticity at the poles of the reinforcement, Fig. 8.12a. The cyclic stress–strain curve of the 2080 Al alloy at the same stress was elastic in nature, although it was more compliant than the composite. At an applied stress higher than the yield strength of the unreinforced alloy, the hysteresis loop for the unreinforced alloy was much larger than that of the composite, Fig. 8.12b. It should be noted that the onset of cyclic microplasticity in the composite at low stress did not appear to affect

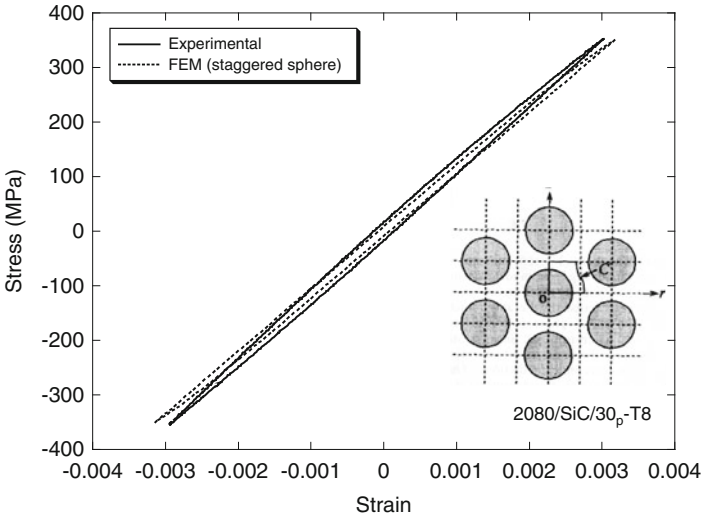

Fig. 8.13 Cyclic stress–strain hysteresis behavior of a 2080/SiC/30_p composite (after Chawla and Shen 2001). A finite element model consisting of spherical, staggered SiC particles in Al predicts the experimental behavior very well

the fatigue life of the composite in a detrimental fashion. Rather, the composites had higher fatigue life than the unreinforced alloy. Chawla and Shen (2001) used a unit-cell finite element model, consisting of spherical particles arranged in a staggered arrangement, shown in the inset of Fig. 8.13. The cyclic stress–strain hysteresis obtained from this simple model yielded surprisingly good agreement with the experimental behavior; see Fig. 8.13. The effects of reinforcement aspect ratio, shape, and matrix hardening characteristics on cyclic fatigue have also been elucidated (LLorca et al. 1992; LLorca 1994).

The cyclic stress–strain behavior of MMCs is also affected by a phenomenon called the Bauschinger effect. The Bauschinger effect is defined as a decrease in flow stress that occurs when we reverse the loading direction, e.g., from a tensile to compressive stress or vice versa (Bauschinger 1886). Thus, an understanding of the Bauschinger effect is essential to understanding of work hardening and cyclic loading.

One of the origins of the Bauschinger effect in monolithic materials has been attributed to dislocation pileup. Pileup of dislocations, in the forward loading direction, creates a "back stress" which aids deformation upon reversal in loading, resulting in a lower flow stress (Mott 1952; Seeger et al. 1958). In precipitation-hardened materials, Orowan loops associated with the precipitate particles also induce a back stress (Orowan 1959). The phenomenon has also been observed in particle-reinforced MMCs (Arsenault and Wu 1987; LLorca et al. 1990). Here, the back stress is enhanced by tensile residual stresses that are generated upon cooling from the processing temperature as well as constrained deformation of the matrix

by the rigid particles. This results in a loading asymmetry (Arsenault and Wu 1987; Arsenault and Pillai 1996) where a more significant Bauschinger effect was observed under compression–tension sequence than for a tension–compression sequence.

Indeed, finite element modeling shows that even when the matrix is assumed to exhibit isotropic hardening behavior (i.e., no Bauschinger effect exists), the composite shows a distinct Bauschinger effect upon reversed loading (LLorca et al. 1990), as was observed experimentally. An examination of the evolution of local stress field showed an apparent early reversed yielding for the composite, due to nonuniformity of deformation in the matrix caused by the constraint imposed by the brittle reinforcement (Shen et al. 1995). Thus, high *local* effective stresses trigger early *local* yielding after the load is reversed, which is reflected in the macroscopic stress–strain behavior.

In addition to particle reinforcement, the matrix microstructure also significantly influences the fatigue behavior of the composite. Factors affecting the matrix microstructure include size, shape, and spacing of precipitates, grain size, and non-reinforcement dispersoids or inclusions (such as Fe-rich inclusions in aluminum that are commonly formed during processing). It would appear that with regard to grain size, composites follow the same trend as monolithic materials, i.e., for a given matrix alloy composition and volume fraction of reinforcement, finer grain sizes generally result in improved properties. Contrary to conventional wisdom for monolithic materials, in MMCs, high matrix yield and ultimate tensile strength do not necessarily reflect high fatigue strength (defined here as fatigue runout at 10^7 cycles). Vyletel et al. (1991) showed that there was no significant difference in fatigue behavior between naturally aged and artificially aged MMC, even though the naturally aged material had a much lower yield and ultimate strength. Chawla et al. (2000b) compared two materials with constant reinforcement volume fraction and particle size, but very different microstructures. A thermomechanical treatment (T8) of the Al–Cu–Mg alloy produced a fine and homogeneous distribution of S′ precipitates, while a thermal treatment only (T6) resulted in coarser and inhomogeneously distributed S′ precipitates. Because of finer and more closely spaced precipitates, the composite that underwent a T8 treatment exhibited higher yield strength than the T6 material. Despite its lower yield strength, however, the T6 matrix composites exhibited higher fatigue resistance than the T8 matrix composites. This contrasting behavior between monotonic and cyclic loading can be attributed to the strong influence of the presence, stability, and morphology of the S′ precipitates in the matrix of the composite (Calabrese and Laird 1974a, b; Starke and Luetjering 1979). In fatigue, failure processes are affected by a variety of microstructural factors, which include resistance to dislocation motion and possible dislocation pileup at precipitates and/or reinforcement particles and cracking along slip bands. In aluminum alloys, small precipitates with a coherent interface are easily sheared (Calabrese and Laird 1974a, b). Coarser precipitates, which have a semicoherent or incoherent interface with the matrix, cause the dislocation to loop around the precipitate. In the T8 materials, the precipitates are fine enough that it is believed that the precipitates are cut by dislocations and PSBs are formed during fatigue,

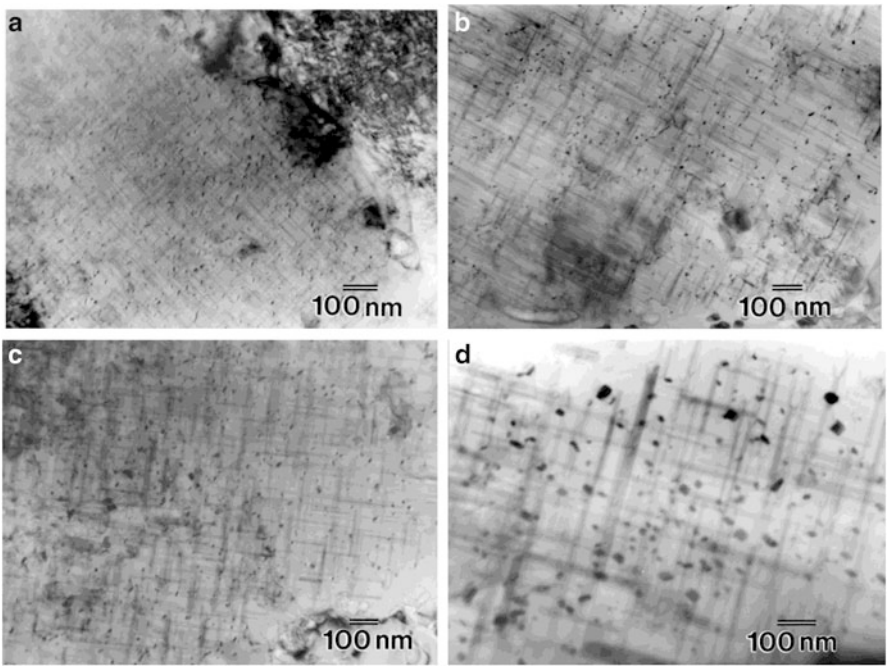

Fig. 8.14 Coarsening of S′ precipitates due to overaging: (**a**) solution treated, rolled, and aged (T8), (**b**) T8 + 24 h at 200 °C, (**c**) T8 + 24 h at 225 °C, and (**d**) T8 + 24 h at 250 °C (Chawla et al. 2000a)

which reduces the strengthening effect of precipitates, thereby impairing the fatigue strength. In the T6 materials, the larger precipitate size allows them to retain their precipitates structure and strength during fatigue.

Overaging heat treatments also modify the matrix microstructure, resulting in coarsening of the precipitate structure while retaining a homogeneous precipitate distribution, which directly influences fatigue life (Chawla et al. 2000b). Figure 8.14 shows the precipitate coarsening and increase in precipitate spacing in the matrix of MMCs overaged at various temperatures for 24 h. Increasing precipitate spacing decreases both fatigue strength and fatigue lifetime, Fig. 8.15. This is to be expected since coarser precipitates result in a larger interprecipitate spacing and easier bypass of dislocations. For the composites subjected to higher overaging temperatures, the yield strength and fatigue strength also decrease with increasing precipitate spacing. It is important to realize that precipitate size alone should not be taken as the determining factor for fatigue resistance. Rather, the precipitates should be of sufficient size not to be susceptible to precipitate shearing, but should be semi- or completely coherent with the matrix to impede dislocation motion.

Processing-related defects in the form of intermetallic inclusions or particle clusters are also part of the matrix microstructure and can play a role in fatigue strength,

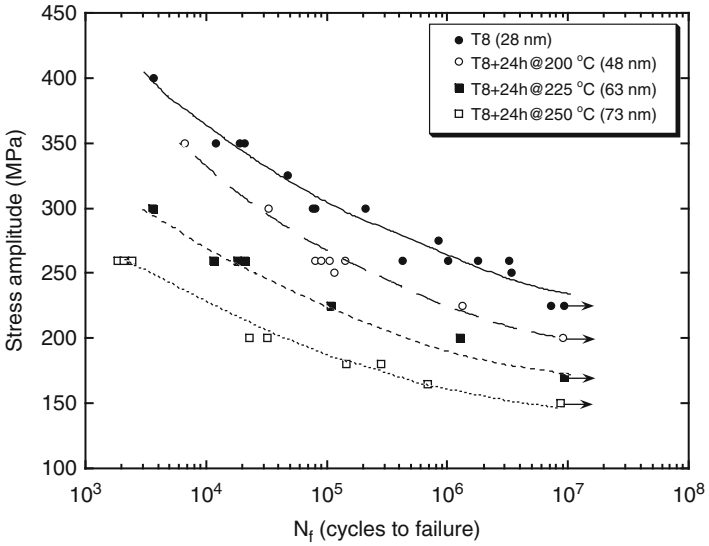

Fig. 8.15 Influence of matrix precipitate spacing on fatigue life of 2080/SiC/20_p–T6 composite. Increase in precipitate spacing results in a reduction in fatigue life (after Chawla et al. 2000a)

particularly in powder metallurgy processed materials (Chawla et al. 1998a, 2000a; Li and Ellyin 1996). Figure 8.16 shows a fracture surface of a 2080/SiC/20_p composite (Chawla et al. 1998a). The crack initiates at an Fe-rich inclusion. This is followed by a region of stable crack propagation, followed by fast fracture. The last stage is characterized by a large amount of particle fracture, due to the high crack velocity. The defects (e.g., inclusions, particle clusters) act as stress concentrators and increase the local stress intensity in the material, promoting easy crack nucleation. For a given inclusion size, the stress concentration in a composite, where the inclusion is surrounded by high-stiffness reinforcement particles, is lower than in the unreinforced alloy. Since more of the load is being "shared" by the high-stiffness SiC particles in the composite, an inclusion in the composite will be subjected to lower stress than a similar inclusion in the unreinforced alloy.

In extruded composites, the overall size of inclusions is also lower since the ceramic reinforcement particles break the brittle inclusions into smaller sizes during extrusion, Fig. 8.17 (Chawla et al. 2000a). It is interesting to note that in the low cycle regime, cracks seem to originate relatively early in fatigue life (around 10 % of total life) (Chawla et al. 1998a; Lukasak and Koss 1993). In the high cycle regime, on the other hand, crack initiation can occur quite late (after about 70–90 % of the life of the specimen). While crack growth is relatively unimpeded in unreinforced materials, crack growth is hindered by mechanisms such as crack deflection and crack trapping in the composite. A more detailed discussion of crack growth in these materials is given in the next section.

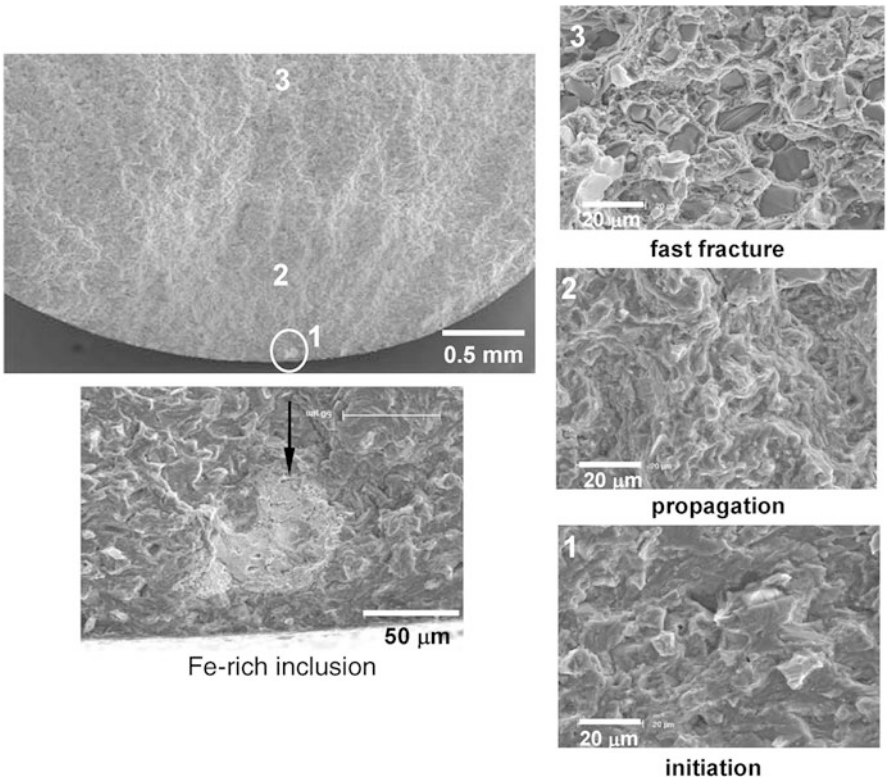

Fig. 8.16 Fatigue fracture morphology in a 2080/SiC/20_p–T6 composite consisting of initiation, propagation, and fast fracture regions (after Chawla et al. 1998a)

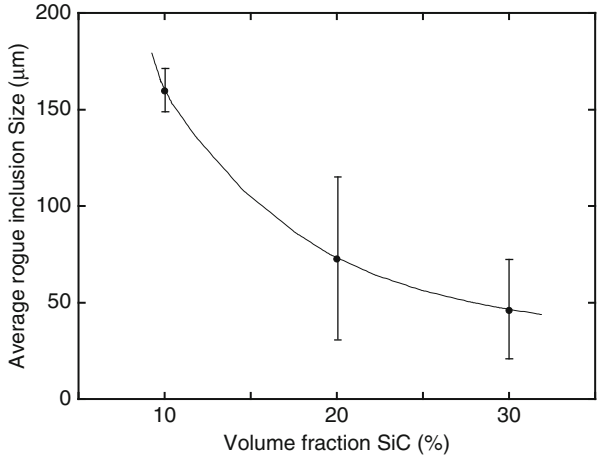

Fig. 8.17 Average "rogue inclusion" size as a function of SiC particle volume fraction. The hard particles contribute to the beneficial fracture and comminution of the Fe-rich inclusions during processing (after Chawla et al. 2000b)

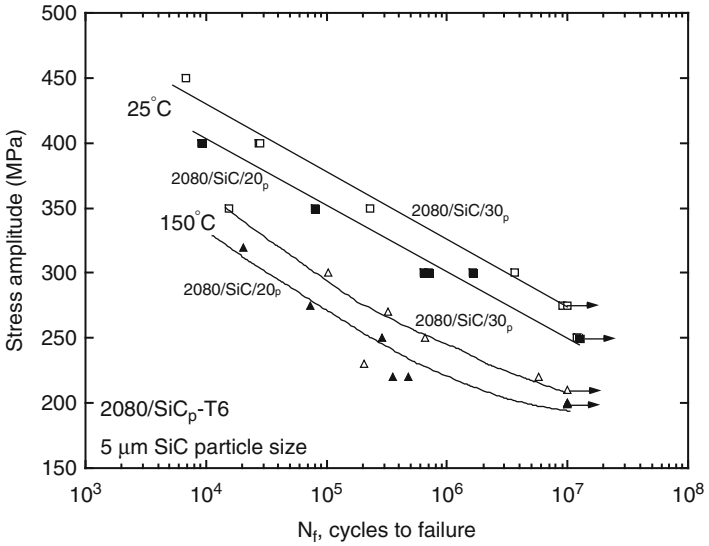

Fig. 8.18 Elevated temperature fatigue of 2080/SiC_p composites. A slight decrease in fatigue resistance is observed at elevated temperature (after Chawla et al. 1999)

Several MMC applications require fatigue resistance at elevated temperatures (on the order of 150–175 °C). Figure 8.18 shows the elevated temperature fatigue performance of MMCs in comparison with the room temperature data shown in Fig. 8.10 (Chawla et al. 1999). The most significant debit in fatigue strength occurred between 25 and 150 °C. The incremental increase in temperature to 170 °C resulted in a modest decrease in fatigue strength. In applications where elevated temperature fatigue resistance is a criterion, the temperature at which the composite is aged also becomes very important. At temperatures slightly higher than the aging temperature, a severe decrease in fatigue strength may take place because of significant matrix overaging. The fatigue strength in the composites seems to be directly proportional to the strength of the matrix, although the decrease in fatigue strength due to temperature is significantly higher than the decrease in yield strength. This may be caused by changes in matrix microstructure and decrease in matrix strength from a combination of long-term exposure and cyclic stress. The fatigue fracture morphology after elevated temperature fatigue is quite different from that at room temperature. At elevated temperature, while crack initiation takes place at the inclusions, fractography also indicates evidence of interfacial decohesion and void growth at the particle/matrix interface and particle corners, as well as in the matrix of the composite, Fig. 8.19. It appears that microvoid nucleation and coalescence in the matrix have also taken place prior at fracture.

Temperatures during metal cutting can rise to as much 1,200 °C (Kindermann et al. 1999). Tungsten carbide/cobalt composites, commonly referred to as

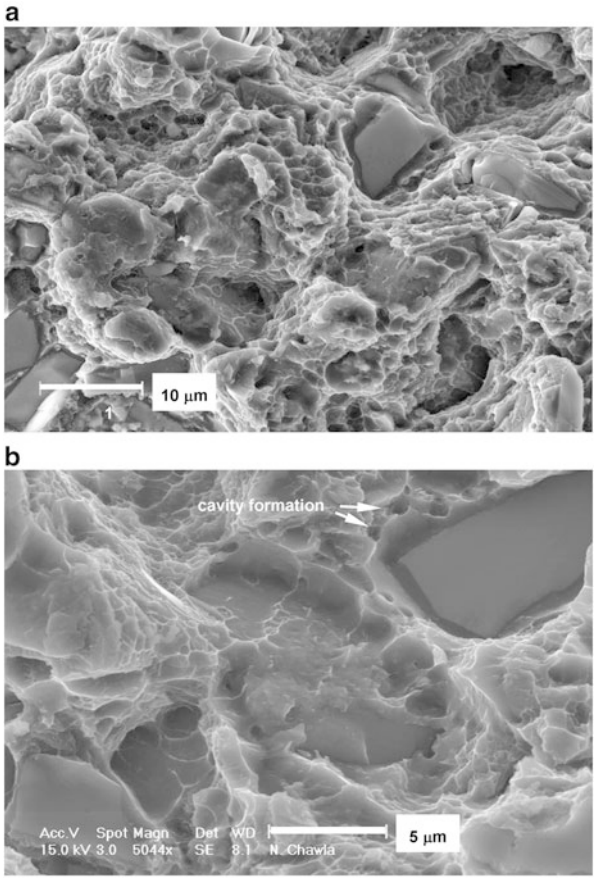

Fig. 8.19 Elevated temperature fatigue fracture morphology, showing (**a**) dimpled fracture and interfacial decohesion and (**b**) cavity formation in the matrix (Chawla et al. 1999)

cemented carbides or hard metal, are used for cutting a range of materials under environments involving aggressive chemicals, high temperatures, lubricants, and water-based coolants. Cyclic fatigue behavior of such materials is of importance because cyclic loading in these materials occurs during the alternating slip and stick of the metal chips during machining, vibrations of the machines, and the interrupted cutting process (Almond and Roebuck 1980; Roebuck et al. 1984; Kindermann et al. 1999; Pugsley and Sockel 2004). An example of an S–N curve for WC/6 wt% Co composite in air and tannic acid (to simulate wood cutting) is shown in Fig. 8.20a. The evidence of corrosion fatigue effect at low stress amplitudes is clear. Figure 8.20b shows a strong decrease in fatigue behavior at 700 °C vis-à-vis room temperature. Also shown in the figure are the inert strength values of these composites, which are significantly higher than the cyclic strength values at all cycles. This indicates the loss of strength is not due to surface oxidation of WC at high temperatures but a true high-temperature cyclic fatigue phenomenon.

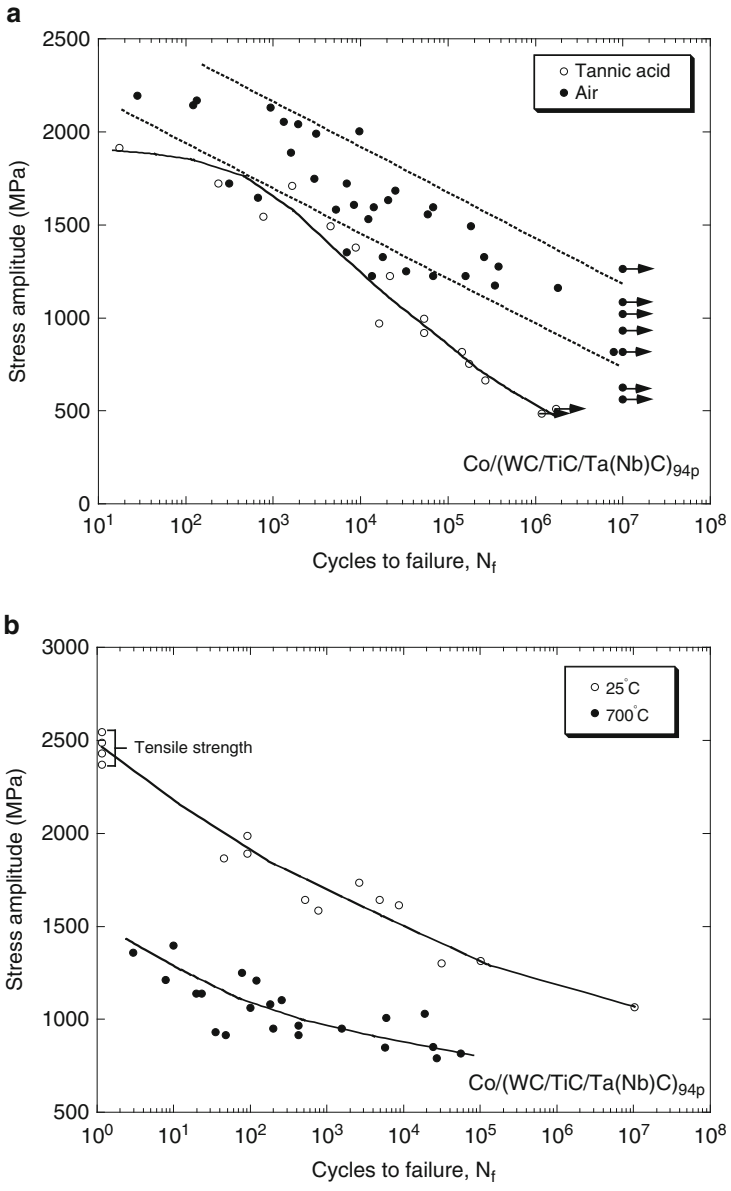

Fig. 8.20 (**a**) S–N curve for WC/Co composites in air and in tannic acid at 4 Hz (after Pugsley and Sockel 2004). The effect of corrosion fatigue effect, at low stress amplitudes, is clear. (**b**) S–N curves for WC–Co composites at room temperatures and at 700 °C (after Kindermann et al. 1999)

8.2 Fatigue Crack Growth

In this section, we describe the fatigue crack growth behavior of MMCs. A brief summary of the salient features of fatigue crack growth in engineering materials, including a description of fatigue crack closure and the two-parameter approach to fatigue, is given in an inset.

8.2.1 Continuous Fiber-Reinforced MMCs

In general, the fibers provide a crack-impeding effect, but the nature (morphology, stiffness, and fracture strain) of the fiber, the fiber/matrix interface, and/or any reaction zone phases at the interface can have a great influence on fatigue crack growth processes (Chawla 1991). In composites with a relatively high interface strength, the fatigue crack propagates straight through the fibers, as shown in Fig. 8.21a. With a weak interface, fiber/matrix debonding, crack deflection, fiber bridging, and fiber pullout take place; see Figs. 8.21b and 8.22. This leads to a significant amount of energy dissipation during crack growth which results in macroscopic toughening of the composite.

In general, fiber-reinforced MMCs exhibit superior fatigue crack growth resistance to monolithic alloys. An example is the comparison of boron fiber (coated with B_4C)-reinforced Ti-6Al-4V composite and the parent matrix alloy, shown in Fig. 8.23 (Harmon et al. 1987). Note that the MMC has a higher fatigue threshold and a much lower rate of crack growth through most of the fatigue life. Soumelidis et al. (1986) observed lower fatigue crack growth

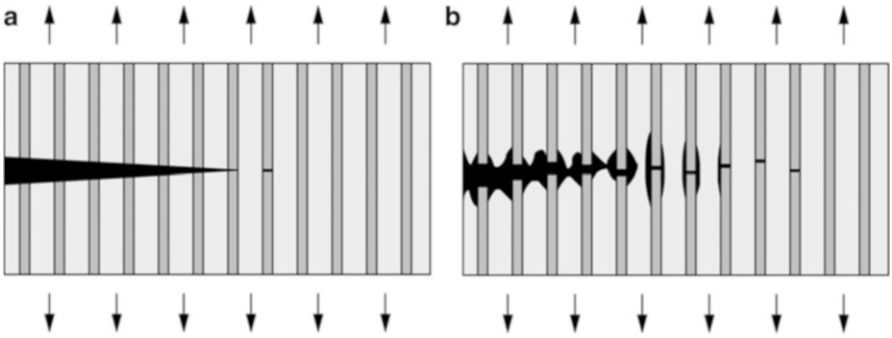

Fig. 8.21 Schematic of damage mechanisms in continuous fiber-reinforced MMCs: (**a**) strong interface (fatigue crack propagates straight through the fibers) and (**b**) weak interface (fiber/matrix debonding, crack deflection, fiber bridging, and fiber pullout take place)

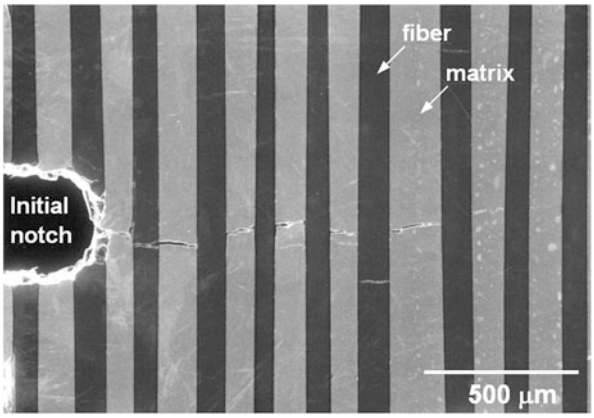

Fig. 8.22 Fatigue crack growth in a Ti-β-21s/SiC_f(SCS-6) composite exhibiting interfacial debonding, crack deflection, and fiber bridging (courtesy of J. Liu)

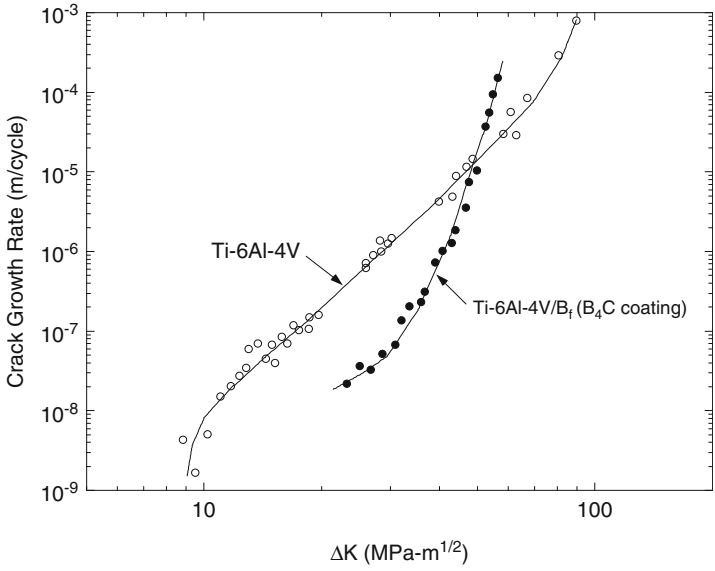

Fig. 8.23 Fatigue crack growth behavior of a boron fiber (coated with B_4C)-reinforced Ti-6Al-4V composite and the parent matrix alloy (after Harmon et al. 1987). The fiber-reinforced MMC has superior fatigue crack growth resistance to the monolithic alloy

Fatigue Crack Growth in Engineering Materials.

As described in the beginning of the chapter, the fatigue crack growth behavior of engineering materials is characterized by a plot of log da/dN versus log ΔK; see figure below. A three-region curve is obtained. Regime 1 is often denoted as the threshold regime, to indicate a threshold stress intensity factor, ΔK_{th} (typically corresponding to ~10^{-10} m/cycle), for crack growth. With increasing ΔK, a linear portion on the log–log plot is observed, which is called the Paris regime. At even higher ΔK, the crack growth rate increases rapidly, resulting in fracture of the material.

In order to fully understand the crack growth behavior, let us define some important parameters. The nominal cyclic stress intensity factor range, ΔK, is equal to

$$\Delta K = K_{max} - K_{min}$$

where K_{max} and K_{min} are the maximum and minimum stress intensity factors, respectively, obtained from the maximum and minimum applied stress, σ_{max} and σ_{min} and the corresponding crack lengths.

Fatigue Crack Closure

During the cyclic process, premature "closure" of the crack may take place, at a stress intensity value before reaching K_{min}. Crack closure during fatigue has been attributed to many origins, including plasticity at the crack tip, oxidation, crack surface roughness, and by wedging of asperities in the crack mouth. These are shown in the figure on the following page.

(continued)

Fatigue Crack Growth in Engineering Materials (continued)

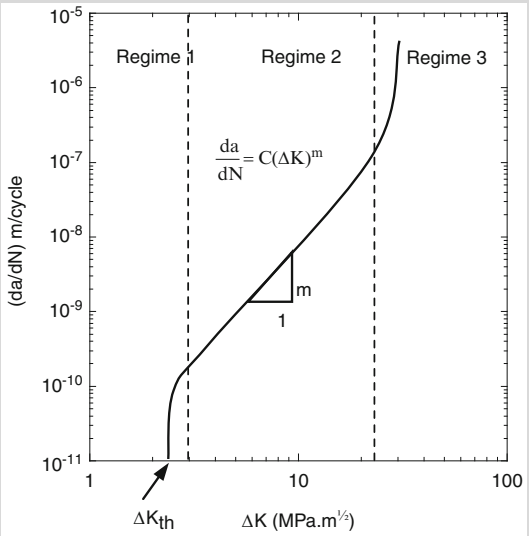

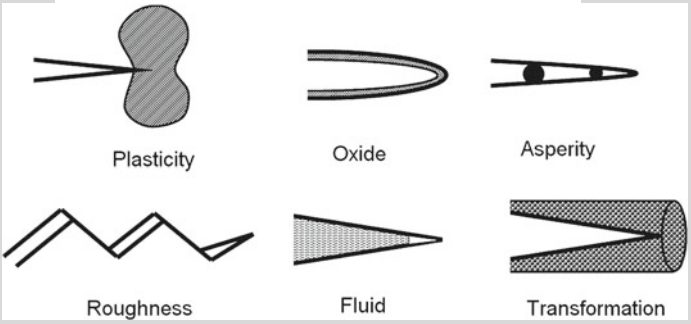

Because of premature closure of the crack faces, the driving force for crack growth is smaller than ΔK. Thus, we define an additional parameter, which corresponds to the stress intensity factor required to open the crack or K_{cl}. Now, the *effective* stress intensity factor, ΔK_{eff} (as shown schematically below), is given by

$$\Delta K_{eff} = K_{max} - K_{cl}$$

(continued)

Fatigue Crack Growth in Engineering Materials (continued)

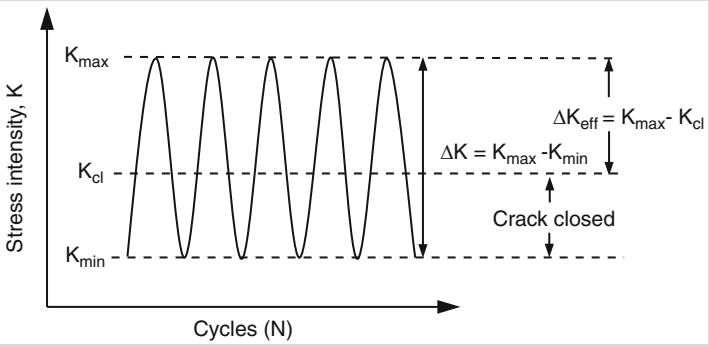

Two-Parameter Approach to Fatigue

Fatigue crack growth behavior can also be analyzed using a two-parameter approach (Doker and Marci 1983; Vasudevan et al. 1994). The basis of this analysis is that there are two driving forces for fatigue crack growth: (a) static parameter or K_{max} and (b) cyclic parameter or ΔK. By conducting experiments at several R-ratios (K_{min}/K_{max} or $\sigma_{min}/\sigma_{max}$), the ΔK_{th} is obtained for a range of K_{max}. By plotting ΔK_{th} versus K_{max}, an "L"-shaped curve is obtained. The vertical and horizontal asymptotes of the curve correspond to ΔK^*_{th} and K^*_{max}. The physical meaning of these two parameters is that critical values of both the static and cyclic driving forces must be met *simultaneously* for fatigue crack growth to take place. This is shown by the shaded region in the curve.

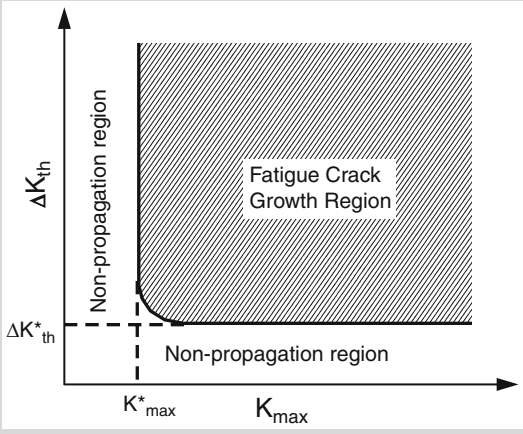

(continued)

Fatigue Crack Growth in Engineering Materials (continued)

Using the two-parameter analysis, several important materials can be subdivided into different classes (Vasudevan and Sadananda 1995). It is shown that environmental effects also play an important role on fatigue crack growth behavior.

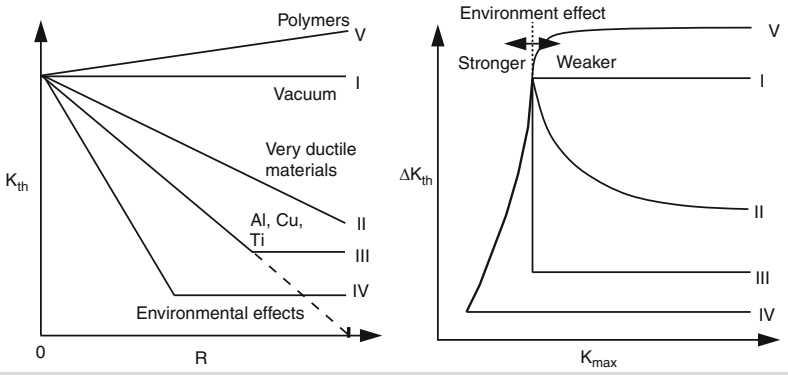

rates in fiber-reinforced Ti-6Al-4V compared with that in the unreinforced alloy. Long isothermal exposures at 850 °C, however, resulted in reduced crack growth resistance of the MMC. This was due to fiber degradation, fiber/matrix debonding, and an increase in matrix brittleness. Short-time isothermal exposures (up to about 10 h for Ti-6Al-4V/B_f, 30 h for Ti-6Al-4V/B_f (B_4C), and 60 h for Ti-6Al-4V/SiC_f(SCS-6)) improved the fatigue crack resistance. This was attributed to an energy-dissipating mechanism of fiber microcracking in the vicinity of the crack tip.

Cotterill and Bowen (1993) studied the fatigue crack growth behavior of SCS-6 fiber-reinforced Ti-15V-3Al-3Sn-3Cr (Ti-15-3) composites. In general, the crack growth rates decreased with increasing crack length. This was attributed to crack tip "shielding" from the bridging fibers, which are stronger and stiffer than the matrix. When a single fiber fracture took place, however, the crack growth rate increased by two orders of magnitude. This was also accomplished by a single cycle overload or by increasing the R-ratio (e.g., an increase in K_{min}). Cotterill and Bowen (1996) examined the effects of ΔK and K_{max}, the cyclic and static stress intensity components for fatigue crack growth, respectively. It was also shown that K_{max} controlled fiber fracture, but ΔK controlled the matrix crack growth rate. Thus, if fiber fracture takes place, K_{max} is the parameter that controls the crack growth rate. The crack growth rate was also shown to be dependent on ΔK. Below a critical value of ΔK, the crack was arrested, but above that value, fiber fracture took place and the crack was able to propagate, Fig. 8.24. The transition from crack arrest to catastrophic failure is also affected by fiber strength distribution and specimen geometry

(Liu and Bowen 2002). Figure 8.25 shows fractographic analysis of an SCS-6/Ti alloy matrix composite subjected to LCF at room temperature (Bettge et al. 2007). A distinct transition between stable fatigue crack growth and fast fracture is observed.

At very high temperatures in S–N fatigue, frequency plays a role in fatigue crack growth behavior. At lower frequencies, aging of the matrix and weakening of grain boundaries contribute to fracture in the composite (Cotterill and Bowen 1993). Stress relaxation of the matrix during creep or due to hold times (or lower cyclic frequency) may also result in crack closure and aid in crack bridging (Zhang and Ghonem 1995).

Rao et al. (1993) examined the fatigue crack growth behavior of 6061/SiC/40_f (SCS-8) composites in longitudinal and transverse orientations. Their results, shown in Fig. 8.26, indicate that the crack growth resistance of the composite was higher than that of the unreinforced alloy in the longitudinal orientation, but lower in the transverse orientation. Fiber debonding and crack deflection mechanisms toughened the composites in the L–T orientation, due to the relatively weak bonding between fiber and matrix provided by the C-rich coating on the SCS-8 fibers. These authors also proposed a mechanistic model for fatigue crack growth in the transverse orientation, whereby fiber debonds grew until a critical point where individual debonds were linked, resulting in fracture, Fig. 8.27. These authors also attempted to quantify the extent of bridging by the *ductile phase*, during transverse loading. The contribution from bridging, ΔK_b, was given by

$$\Delta K_b = \frac{2}{\sqrt{\pi a}} \int_0^{\ell} \sigma(x) F\left(\frac{x}{a}, \frac{a}{W}\right) dx$$

where a is the crack length, ℓ is the bridging zone length, W is the specimen width, $\sigma(x)$ is the stress distribution over the bridging zone, and x is the distance behind the crack tip. The total toughness, then, is given as

$$K = K_o + \Delta K_b$$

where K_o is the intrinsic toughness of the composite. Assuming that $\sigma(x) = f\sigma_o$, where f is the fraction of ductile phase and σ_o is the flow stress of the matrix,

$$\Delta K_b = 2f\sigma_o \sqrt{\frac{2\ell}{\pi}}$$

Using this relation the steady-state toughness of the composite was predicted to be around 12.4 MPa $\sqrt{m}$, which was slightly lower than that measured experimentally. The authors attributed the difference to an additional contribution from thermally induced dislocation punching at the interface, which strengthened the matrix, as well as residual strains from plasticity.

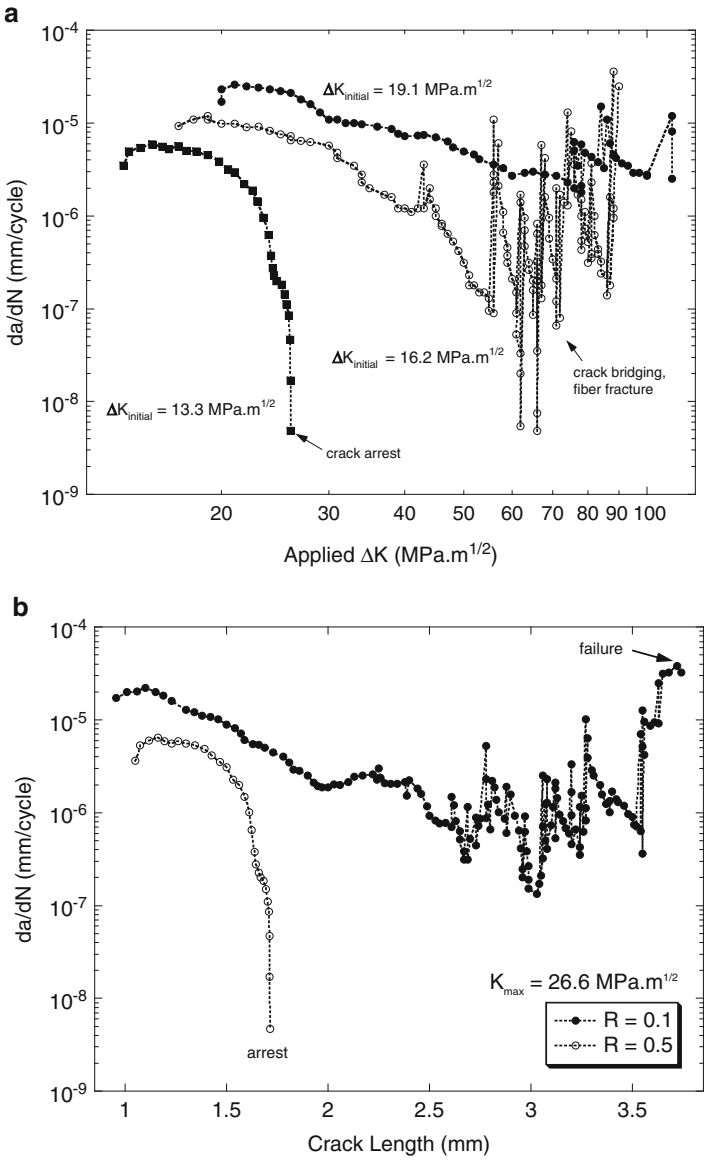

Fig. 8.24 Fatigue crack growth behavior of a SiC fiber-reinforced Ti alloy composite: (**a**) influence of increasing ΔK and (**b**) influence of R-ratio. Critical values of K_{max} and ΔK are required to propagate the crack (after Cotterill and Bowen 1996)

Davidson et al. (1989) examined the fatigue crack growth behavior of an Al_2O_3 fiber-reinforced Mg alloy composite (made by liquid infiltration). A simple model was developed to predict the crack growth rate as a function of ΔK. The cyclic crack opening displacement (COD), δ_c, is given by

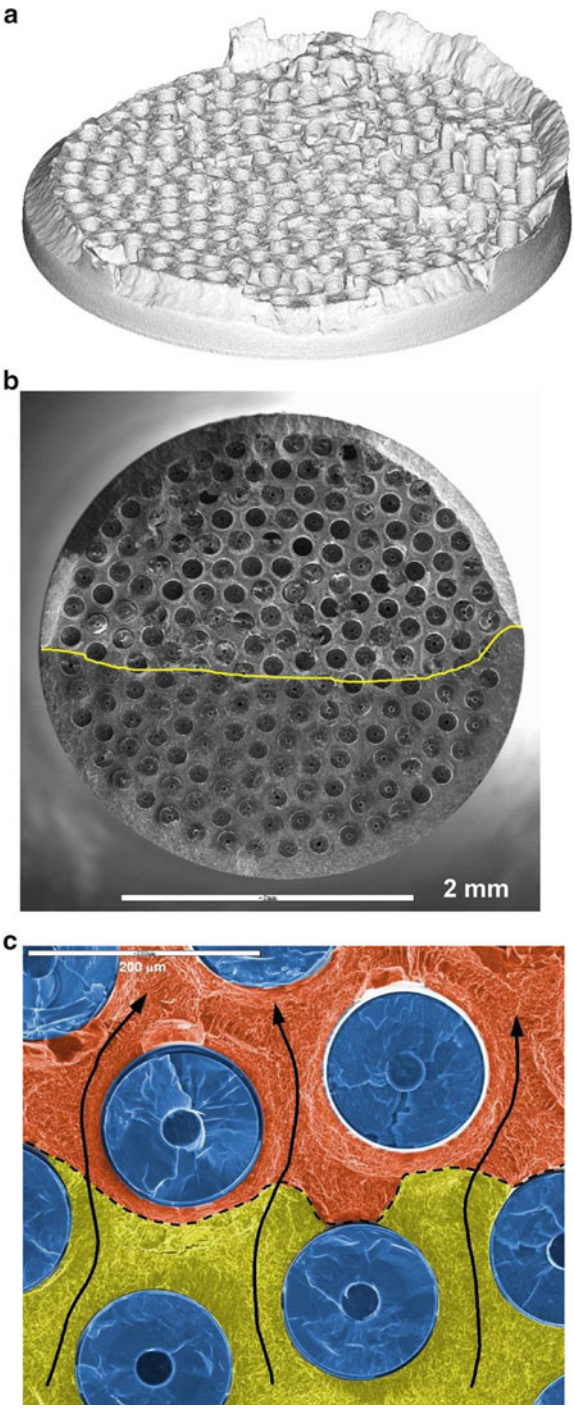

Fig. 8.25 Fatigue crack growth behavior of a SCS-6 fiber-reinforced Ti alloy matrix composite, in the low cycle fatigue regime at room temperature (after Bettge et al. 2007): (**a**) confocal microscopy image of the fatigue fracture surface, (**b**) low-magnification image of transition from stable fatigue crack growth to fast fracture, and (**c**) higher-magnification image of (**b**). (Images courtesy of P. Portella)

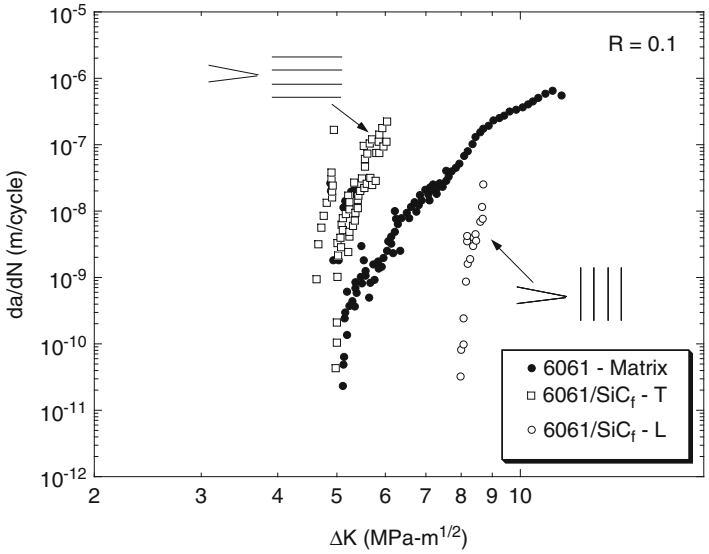

Fig. 8.26 Fatigue crack growth response of a SiC fiber-reinforced Al 6061 matrix composite. The fatigue threshold in the longitudinal orientation is superior to that in the transverse orientation and that of the unreinforced alloy (after Rao et al. 1993)

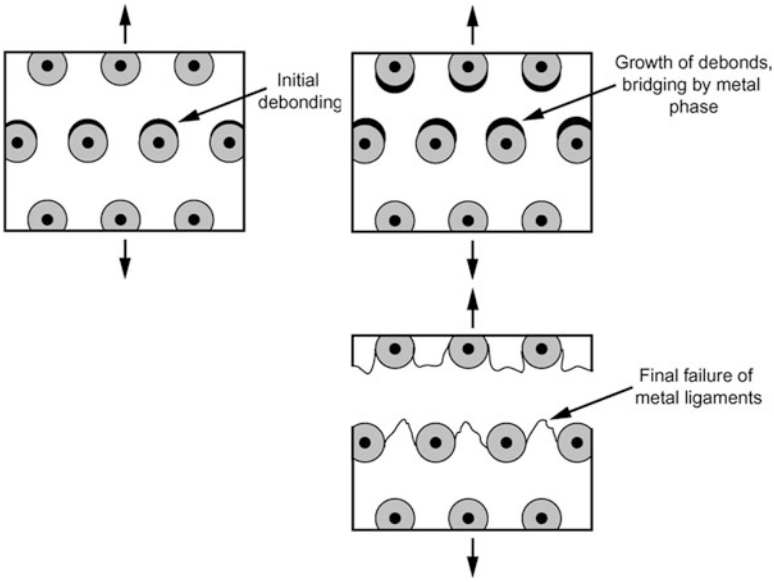

Fig. 8.27 Schematic of mechanisms for fatigue crack growth under transverse loading. Fiber debonds grow until a critical point where individual debonds are linked, resulting in fracture (after Rao et al. 1993)

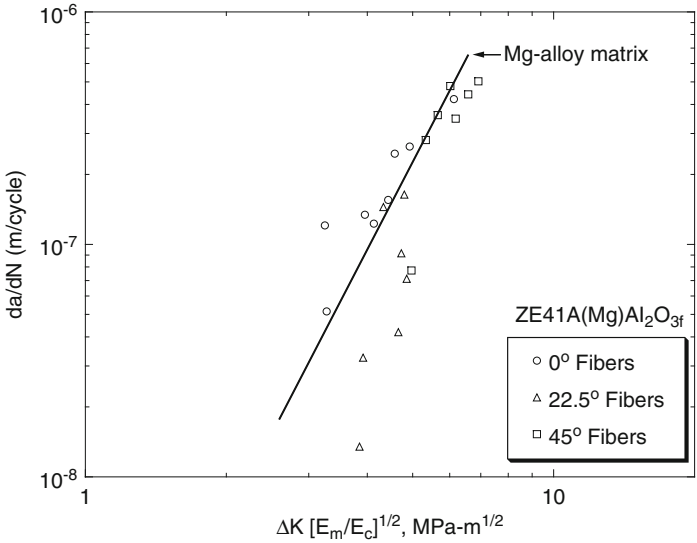

Fig. 8.28 Fatigue crack growth behavior of Mg(ZE41A)/$Al_2O_{3,f}$ composite, normalized by the Young's moduli of matrix and composite. Good agreement was obtained for composites with varying fiber orientation, as well as with the unreinforced Mg alloy (after Davidson et al. 1989)

$$\delta_c = \frac{c_o \Delta K^2}{E_i}$$

where c_o is a constant, ΔK is the cyclic stress intensity, and E_i is the elastic modulus of the matrix (E_m) or the composite (E_c). If the crack growth rate is assumed to be proportional to COD, then the Paris law can be written as

$$\frac{da}{dN} = C\left[\left(\frac{E_m}{E_c}\right)^{\frac{1}{2}} \Delta K\right]^n$$

By incorporating shielding from the fibers, a lower bound was obtained, while an upper bound was obtained by incorporating the interaction between the main crack and microcracks. By normalizing the crack growth data with respect to the modulus of the composite, good agreement was obtained for composites with varying fiber orientation, with respect to the loading axis, as well as with the unreinforced Mg alloy, Fig. 8.28.

Fatigue crack propagation studies have also been conducted on aligned eutectic or in situ composites. Since many of these in situ composites are meant for high-temperature applications in turbines, their fatigue behavior has been studied at temperatures ranging from room temperature to 1,100 °C. The general consensus

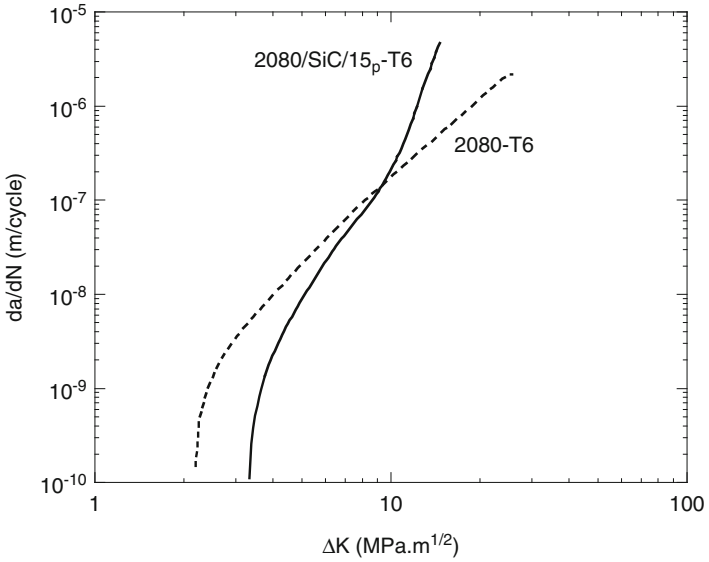

Fig. 8.29 Fatigue crack growth behavior of 2080–T6 alloy versus 2080/SiC/15_p–T6 composite. The composite exhibits a higher fatigue threshold and slightly higher Paris-law slope (after Lukasak and Bucci 1992)

is that the mechanical behavior of in situ composites, i.e., static and cyclic strengths, is superior to that of the conventional cast superalloys (Stoloff 1978).

8.2.2 Particle-Reinforced MMCs

The crack growth behavior in particle-reinforced MMCs is also very much dependent on reinforcement characteristics (Shang et al. 1988; Lukasak and Bucci 1992; Allison and Jones 1993; LLorca et al. 1994; Vasudevan and Sadananda 1995) and on matrix microstructure (Bonnen et al. 1990; Sugimura and Suresh 1992). In general, higher threshold values, ΔK_{th}, are observed for composites than for monolithic materials, Fig. 8.29. In addition, increasing volume fraction of particles results in an increase in ΔK_{th}, Fig. 8.30. This can be attributed to the higher modulus of the composite, which results in a lower COD for a given applied stress intensity factor. The Paris-law slope of da/dN versus ΔK curve for the composites is generally comparable to that of unreinforced alloys, although, at very high ΔK, the crack propagation in the composites is much higher. This is due to lower fracture toughness of the composite, relative to the unreinforced alloy.

It is very important to note, however, that these trends are only true for composites with a constant matrix microstructure. Sugimura and Suresh (1992), for example, examined the effect of SiC volume fraction on fatigue crack growth of

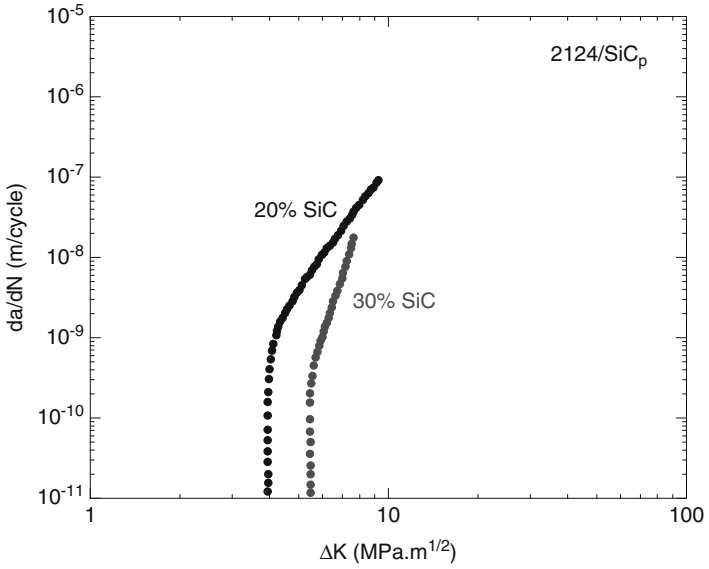

Fig. 8.30 Effect of volume fraction on fatigue crack growth of 2124/SiC_p composites (after Bonnen et al. 1990). Increasing volume fraction results in an increase in fatigue threshold (the matrix microstructure of this powder metallurgy-processed composite was relatively constant)

cast MMCs. Because of the casting process, the grain size in the matrix was inversely dependent on the volume fraction of particles (see Chap. 4), i.e., the matrix microstructure changed with increasing volume fraction. This was because a higher volume fraction of particles resulted in a larger number of possible grain nucleation sites and a finer overall grain size in the matrix of the composite. Thus, in their study, an increase in volume fraction of particles (i.e., a decrease in matrix grain size) contributed to a decrease in fatigue crack growth resistance, Fig. 8.31.

It is interesting to note that coarser particles provide better fatigue crack growth resistance than finer particles, because of a large extent of roughness-induced crack closure (Shang et al. 1988), Fig. 8.32. Furthermore, experiments on overaged and underaged composites showed little difference in fatigue crack growth resistance (Bonnen et al. 1990), indicating that the controlling deformation mechanisms are related to the particle characteristics and spatial distribution, Fig. 8.33. The fatigue crack growth behavior is also very much affected by the load ratio R ($K_{min}/K_{max} = \sigma_{min}/\sigma_{max}$). Figure 8.34a shows the fatigue crack growth behavior for a 2080/SiC/20_p composite at various R-ratios, ranging from -2 to 0.8. With increasing R-ratio, the fatigue threshold decreases and the Paris-law slope increases. These data can be further represented by using the two-parameter approach of ΔK versus K_{max}, by Vasudevan et al. (1994), shown in Fig. 8.34b. This approach can be understood simply by the fact that critical values of both ΔK and K_{max} must be met for the crack to propagate. Thus, with increasing crack growth rate, at higher

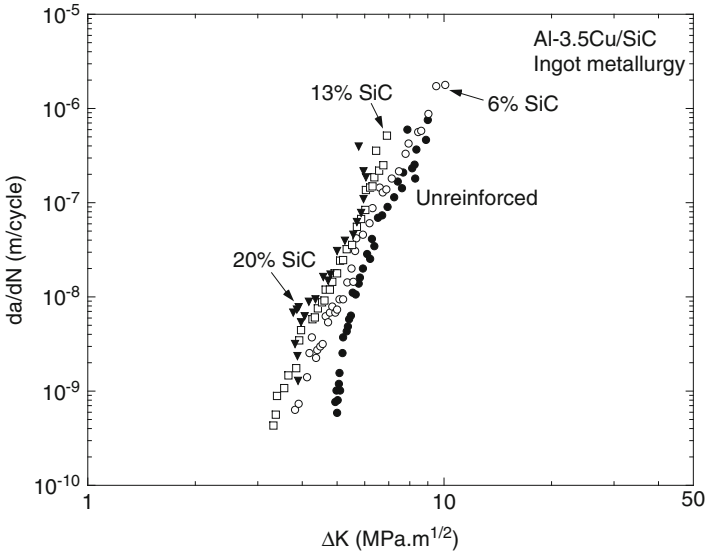

Fig. 8.31 Decrease in fatigue crack growth resistance with increasing volume fraction of SiC particles (cast composite). Because of the casting processing route, the matrix grain size at higher volume particle fractions decreased significantly, yielding lower fatigue resistance (after Sugimura and Suresh 1992)

R-ratios, for a given value of ΔK, a much smaller value of K_{max} needs to be applied for the crack to propagate.

The effects of ΔK and K_{max} can be explained in terms of the damage zone size at the crack tip and reinforcement/crack interactions (Shang et al. 1988; Chawla and Chawla 2004). This is shown by in situ 3D X-ray tomography of a fatigue crack in 2080 Al alloy reinforced with 20 vol.% SiC particles (Hruby et al. 2013). Specimens were pre-cracked and fatigued in the synchrotron at R-ratios of 0.1 and 0.65. At the lower R-ratio, crack deflection was observed, as shown in Fig. 8.35 with minimal particle fracture. At the higher R-ratio, the particles were cracked ahead of the crack tip (green particles), and then the crack propagated through the particles (dark blue), Fig. 8.36. Quantitative measurements of particle fracture illustrating this behavior are shown in Fig. 8.37. Note that an "overload" or spike in load for one cycle is sufficient to introduce significant damage ahead of the crack tip. Figure 8.38 shows a schematic of this observed behavior during fatigue crack growth (Chawla and Chawla 2004). At low K_{max} and/or ΔK, the fatigue crack propagates around the particles, while at high K_{max} and/or ΔK particle fracture takes place ahead of the crack tip, resulting in relatively planar crack growth.

The mechanisms responsible for this behavior can be explained by the size of the damage zone, relative to the size and fracture strength of the particles. At low K_{max} and/or ΔK, the plastic zone at the crack tip is on the order of the particle size. Ayyar and Chawla (2006) modeled the crack growth behavior in a SiC particle-reinforced composite, by using the two-dimensional microstructure of the material as a basis

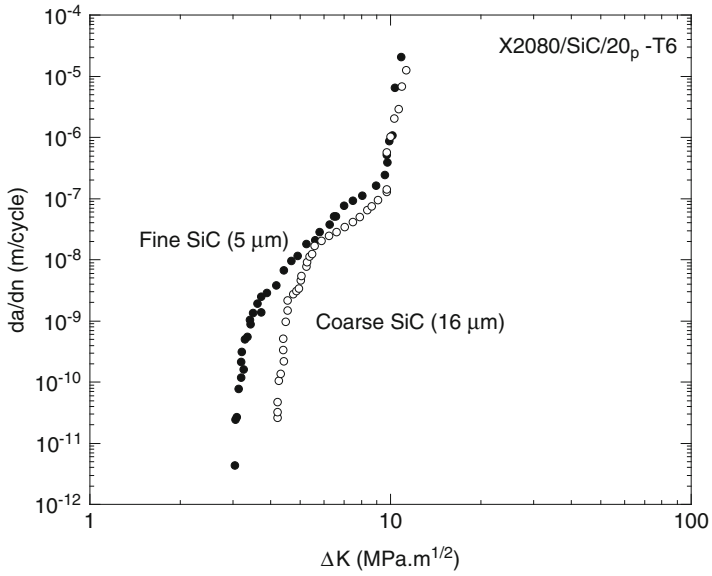

Fig. 8.32 Effect of particle size on fatigue crack growth behavior in a 2080/SiC/20p–T6 composite. The larger particles results in a larger degree of roughness-induced closure, thus increasing the fatigue threshold (after Shang et al. 1988)

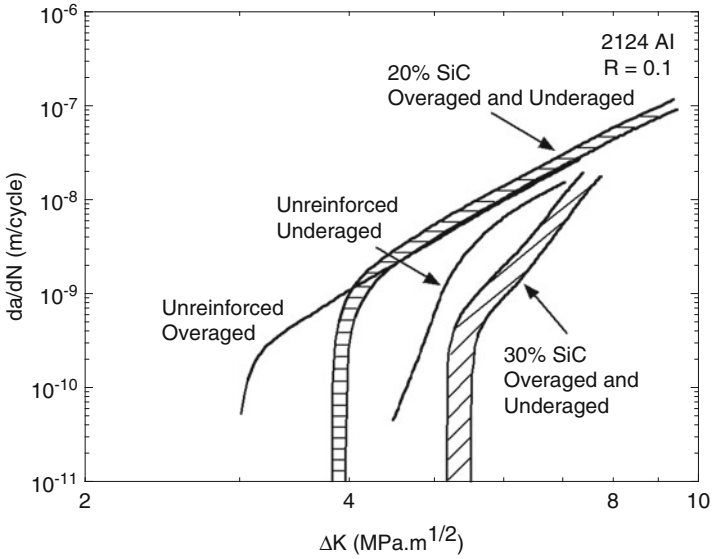

Fig. 8.33 Fatigue crack behavior for 2124 alloy and its composites in underaged and overaged conditions. While the unreinforced alloy is sensitive to aging, the composites are not, indicating that the particles control fatigue crack growth behavior (after Bonnen et al. 1990)

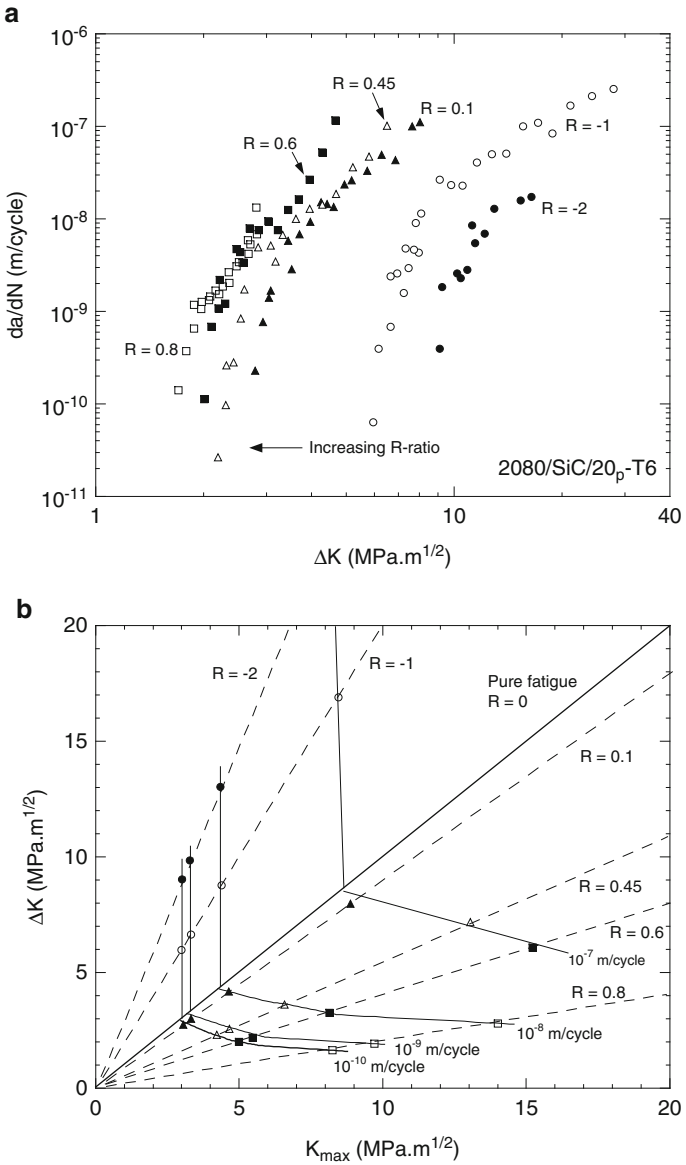

Fig. 8.34 Effect of R-ratio on fatigue crack growth of 2080/SiC/20_p: (**a**) da/dN versus ΔK behavior, showing decreasing fatigue threshold and increasing Paris-law slope with increasing R, and (**b**) same data plotted using ΔK versus K_{max} approach, showing decreasing resistance to fatigue crack growth with increasing K_{max} (after Ganesh and Chawla 2004)

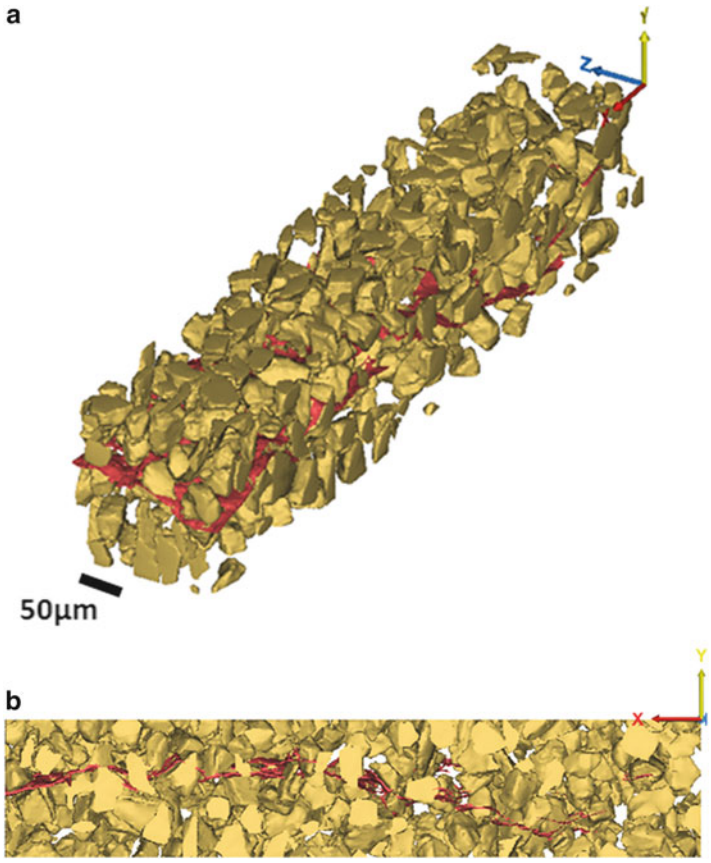

Fig. 8.35 In situ X-ray synchrotron tomography of fatigue crack growth in a SiC particle reinforced 2080 Al alloy composite, at low R-ratio (R = 0.1) (Hruby et al. 2013): (**a**) tilted 3D model and (**b**) side view of 3D model. Note that the crack (in *red*) propagates around the particles with very little particle fracture and significant amount of crack deflection

for the finite element model. A modified crack closure criterion was used to calculate the stress intensity at the crack tip, while the maximum circumferential tensile stress criterion was used to determine the direction of crack propagation. The predicted response qualitatively shows the same behavior as that observed in the experiment, i.e., the cracks grow around the SiC particles in a somewhat tortuous fashion, Fig. 8.39. Similar models have been developed by Boselli et al. (2001), for perfectly circular particles of single size.

At high K_{max} and/or ΔK, the plastic zone is large enough to engulf several particles, so particle fracture ahead of the crack tip takes place, and the crack growth is relatively linear. This behavior is confirmed by the degree of experimentally measured particle fracture at R-ratios of 0.1 and 0.8, respectively, Fig. 8.40.

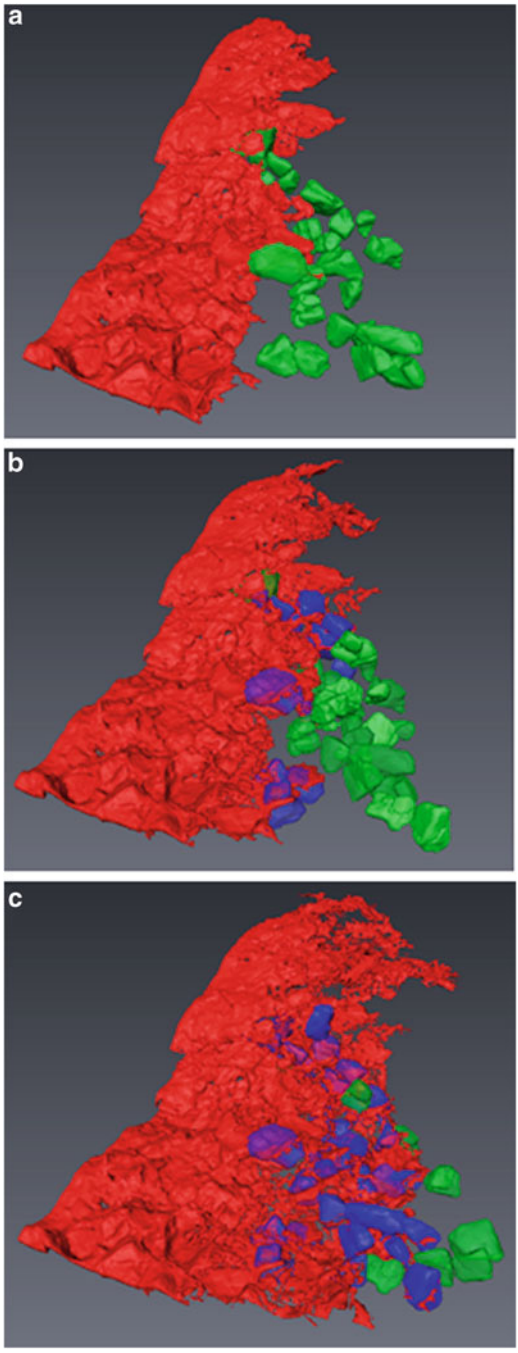

Fig. 8.36 In situ X-ray synchrotron tomography of fatigue crack growth in a SiC particle-reinforced 2080 Al alloy composite, at high R-ratio (R = 0.65) (Hruby et al. 2013): (**a**) 0 cycles, (**b**) 6,000 cycles, and (**c**) 17,000. The *green* particles crack ahead of the crack (*red*). *Blue* particles correspond to particles in which the crack has travelled through the particle. Note that the particles crack ahead of the crack tip and that the crack then propagates through the particles

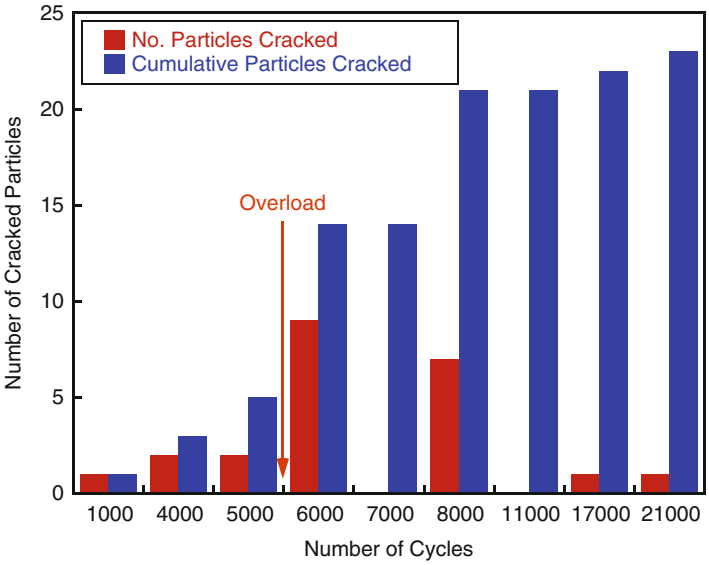

Fig. 8.37 Quantitative measurements of particle fracture at R-ratio of 0.65. The number of fracture particles in the volume analyzed increases with increasing fatigue cycles (Hruby et al. 2013). Note that an "overload" or spike in load for one cycle is sufficient to introduce significant damage ahead of the crack tip

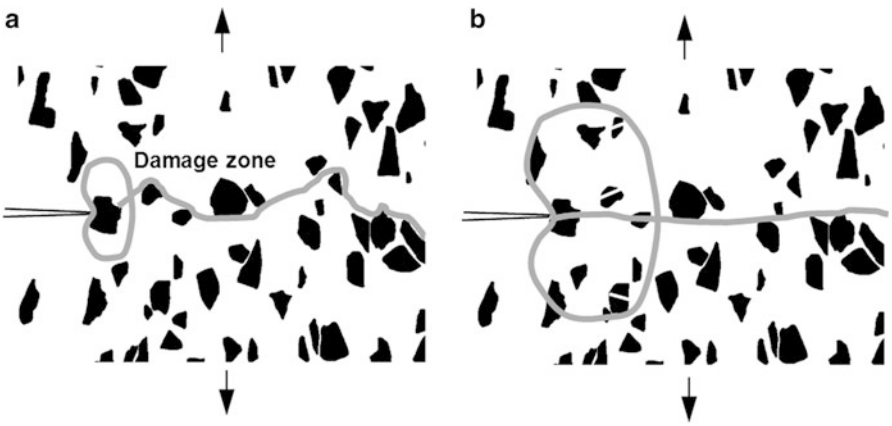

Fig. 8.38 Schematic of fatigue damage in particle-reinforced MMCs: (**a**) low R-ratio, damage zone is on the order of the particle size, and crack growth is tortuous, and (**b**) high R-ratio, damage zone is much larger than the particle size resulting in particle fracture ahead of the crack tip, and planar crack growth (after Chawla and Chawla 2004)

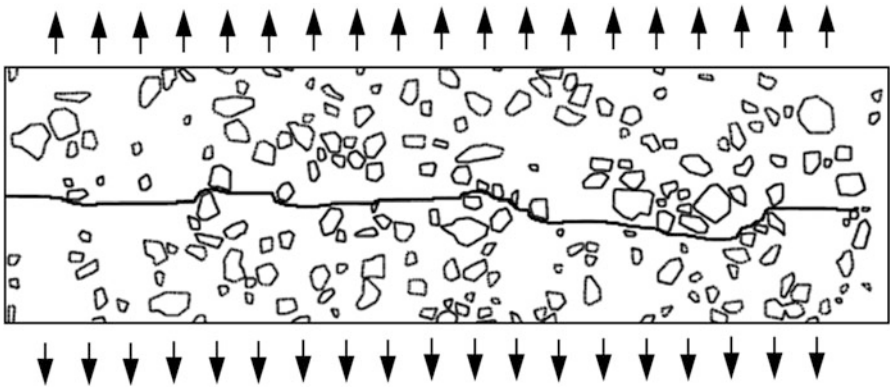

Fig. 8.39 Microstructure-based finite element model prediction of crack growth in a SiC particle-reinforced Al matrix composite, showing tortuous crack growth around the reinforcement particles (after Ayyar and Chawla 2006)

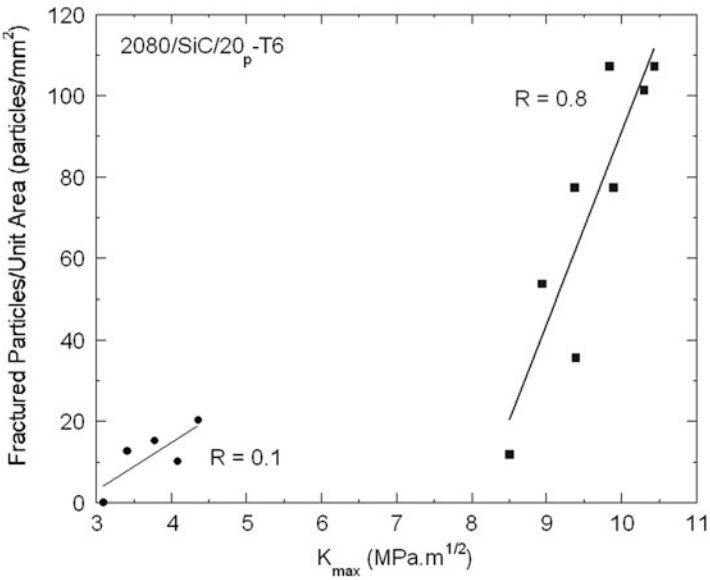

Fig. 8.40 Degree of particle fracture in 2080/SiC/20_p versus applied K_{max}, at R-ratios of 0.1 and 0.8. Higher K_{max} results in a significantly larger degree of particle fracture

Note that the degree of particle fracture is much higher at the higher R-ratio, i.e., it is driven by K_{max}.

We end this section by discussing the fatigue damage mechanisms in compression–compression fatigue. Here, the nature of damage is quite different from that observed in tension–tension fatigue. Figure 8.41 shows the fracture surface of a 2080/SiC/20_p composite after fatigue growth for an R-ratio of −2.

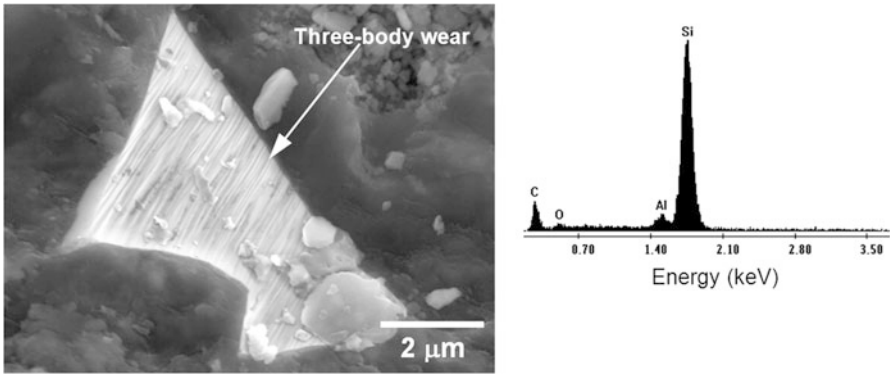

Fig. 8.41 Fatigue fracture surface after compression fatigue (R = −2) (Chawla and Ganesh 2010). Debris from the fatigue process (Al_2O_3, from EDS spectra on the right) is embedded into the SiC particles resulting in three-body wear

Observe the wear markings on the SiC particle surface, and that spherical particles are present on the surface. Energy-dispersive spectroscopy (EDS) analysis showed these particles to be Al_2O_3, indicating that matrix particles likely oxidized were wedged into the SiC particle. A similar behavior has been observed in steels containing carbide particles (Aswath et al. 1988).

8.2.3 Hybrid and Laminated Composites

Composites containing more than one type of reinforcement are called hybrid composites. Such composites made by using two or more type of reinforcements extend the idea of tailor-making a composite material to meet specific property requirements. Partial replacement of expensive fibers by cheaper but adequate fiber types is another attractive feature of hybrid composites.

Metallic sheet laminated composites have been shown to have improved fatigue resistance over their monolithic counterparts (Chawla and Liaw 1979). There are two possible crack geometries: crack arrester and crack divider geometries. In the crack arrest geometry, with the crack growing perpendicular to the thickness of the composite, the mechanism proposed by Cook and Gordon (1964) would appear to work (see also Chap. 5). According to this model, if the interface is weak, then the crack bifurcates and changes its direction when it reaches the interface, and thus the failure of the composite is delayed. The improved fatigue crack propagation resistance in crack divider geometry has been verified by a number of researchers (McCartney et al. 1967; Taylor and Ryder 1976, and Pfeiffer and Alic 1978). This improved performance has been attributed either to interfacial separation, which removes the triaxial state of stress, or to a holding back of crack at the interface in the faster crack-propagating component by the slower crack-propagating component.

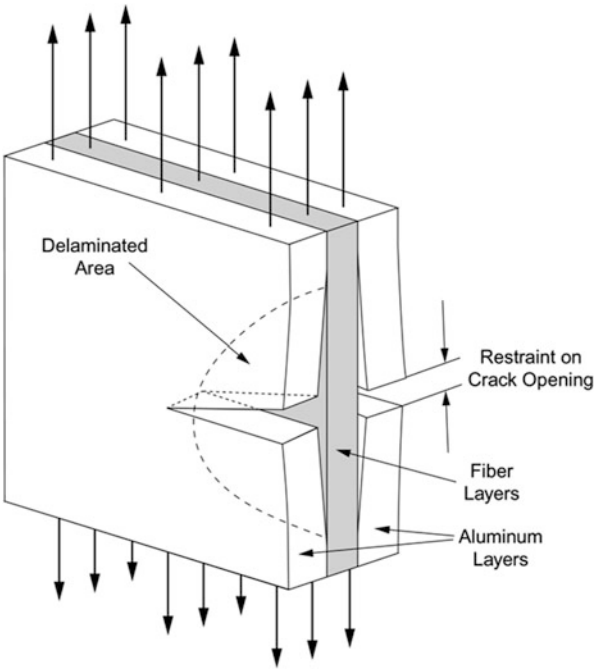

Fig. 8.42 Schematic of fatigue damage in GLARE. Cracks can grow only a short distance before being blocked by the glass fiber/epoxy composite spanning the crack tip (after Wu and Yang 2005)

An interesting type of hybrid composite consists of alternating layers of high-strength aluminum alloy sheets and layers of unidirectional aramid or glass fibers in an epoxy matrix. Many such laminates are possible; the one that has received notable commercial success is GLAss-REinforced aluminum (GLARE) laminate. Improved fatigue resistance of GLARE over that of monolithic aluminum structures is the main attractive feature. Cracks in aluminum can grow only a short distance before being blocked by the glass fibers spanning the crack tip, Fig. 8.42 (Wu and Yang 2005). Figure 8.43 shows the slow fatigue crack growth characteristics of aramid fiber/epoxy aluminum (ARALLs) compared with two monolithic aluminum alloys (Mueller and Gregory 1988). ARALL has been used in tension-dominated fatigue structures in some small military aircraft fuselage, lower-wing, and tail skins. The use of ARALL resulted in 15–30 % weight savings over conventional construction. GLARE has been used in the fuselage of the twin-deck, 550-seat, Airbus A380 aircraft. Besides having superior fatigue behavior, GLARE is also lighter than aluminum, cutting the weight of the Airbus A380 by 1,000 kg. Another version of hybrid laminated MMCs is a family of layered composites consisting of metallic outer skins with a viscoelastic core material (e.g., polyethylene, nylon, polypropylene, paper, or cork). Such composites are useful where sound and vibration dampening are required. The viscoelastic layer provides a high loss factor, i.e., a high capacity to convert vibrational energy to heat.

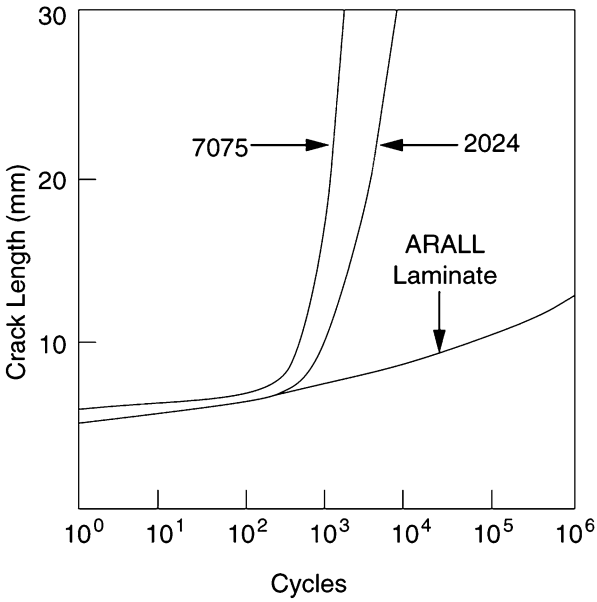

Fig. 8.43 Fatigue crack growth behavior of ARamid ALuminum Laminate (ARALL) compared to conventional 7075 and 2024 aluminum alloys (after Mueller and Gregory 1988). The ARALL has significantly better crack growth resistance

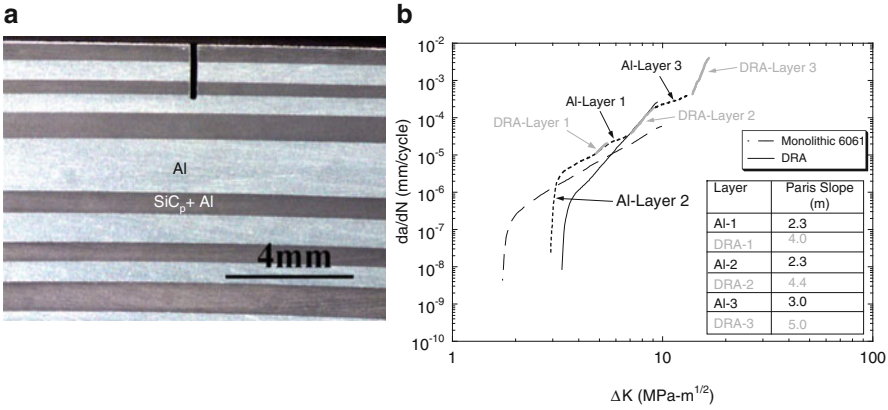

Fig. 8.44 (**a**) Notched hybrid composite of pure Al and SiC particle-reinforced Al composite (courtesy of J. Lewandowski) and (**b**) fatigue crack growth behavior, showing enhanced crack growth resistance in the Paris-law regime (after Hassan et al. 2004)

Other innovative approaches to engineering hybrid composites include laminated composites of SiC particle-reinforced Al layers diffusion bonded to pure Al alloy layers, Fig. 8.44a (Hassan et al. 2004). It was shown that incorporation of the ductile metallic layers resulted in lower crack growth rate in the Paris-law regime, higher fracture toughness, and slightly lower fatigue crack threshold compared to conventional particle-reinforced MMCs, Fig. 8.44b. The authors attributed the

resistance to crack growth to the higher Young's modulus of the laminate, which resulted in a lower COD, for a given applied stress intensity factor. The elastic mismatch also resulted in a crack tip shielding effect at the interface between the layers.

8.3 Thermal Fatigue

The problem of thermal expansion mismatch between the components of a composite is a very general and serious one (Chawla 2012). Thermal stresses arise in composite materials because of the large differences in the thermal expansion coefficients (α) of the reinforcement and the matrix. It should be emphasized that thermal stresses in composites will arise even if the temperature change is uniform throughout the volume of the composite. Such thermal stresses can be introduced in composites during cooling from high temperature of fabrication, annealing, or during any temperature excursions (inadvertent or by design) during service. Turbine blades, for example, are very much susceptible to thermal fatigue.

We described the origin and analysis of thermal stresses in Chap. 6. To recapitulate, the magnitude of thermal stresses in composites is proportional to the thermal strain, $\Delta\alpha\Delta T$, where $\Delta\alpha$ is the difference in the expansion coefficients of the two components and ΔT is the amplitude of the thermal cycle. In MMCs, the metal matrix generally has a much higher coefficient of thermal expansion than the ceramic reinforcement. Rather large internal stresses can result when fiber-reinforced composites are heated or cooled through a temperature range. When this happens in a repeated manner, we have *thermal fatigue*, because the cyclic stress is thermal in origin. Thermal fatigue can cause plastic deformation in a ductile metallic matrix (Chawla 1973a, b). Cavitation in the matrix and fiber/matrix debonding are the other forms of damage observed due to thermal fatigue in composites (Kwei and Chawla 1992; Xu et al. 1995). Figure 8.45 shows a scanning electron micrograph of an alumina fiber (35 % by vol.)-reinforced magnesium alloy (ZE41A) matrix that was subjected to different thermal cycles between room temperature and 300 °C. Note increasing cavitation damage with increasing number of cycles.

Xu et al. (1995) quantified the damage during thermal cycling by measuring the change in Young's modulus and density as a function of thermal cycles. The damage during thermal cycle may also be quantified by a change in damping behavior of the composite (Carreno-Morelli et al. 2001). A damage parameter was defined, where the damage in Young's modulus, for example, is given by

$$D_E = 1 - \left(\frac{E_n}{E_o}\right)$$

where E_n is the Young's modulus after n cycles and E_o is the initial Young's modulus prior to cycling. A similar approach was used to monitor damage in

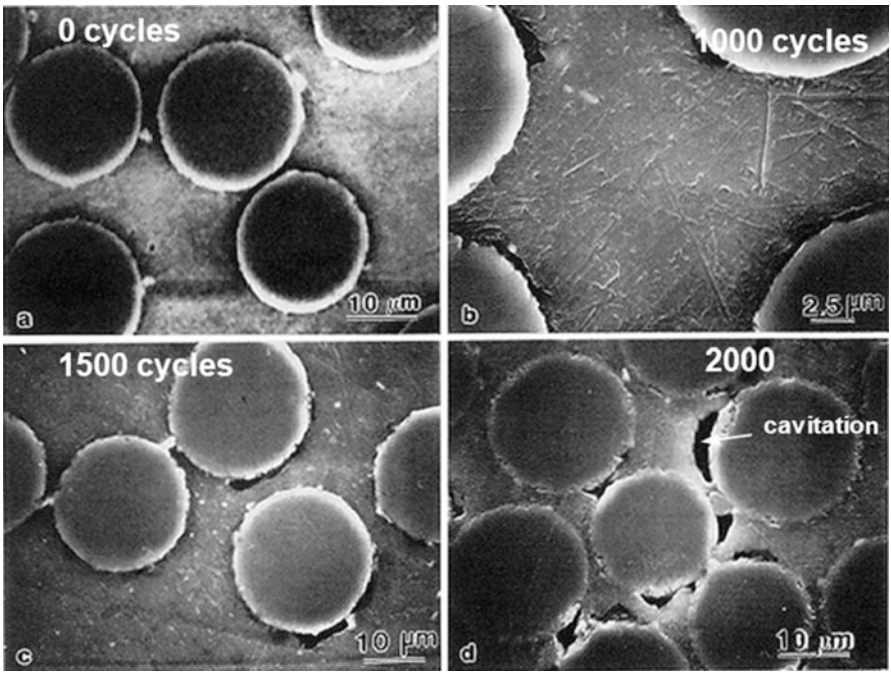

Fig. 8.45 Evolution of thermal fatigue damage in an Mg/Al_2O_{3f} composite. With increasing cycles, interfacial cavitation takes place due to internal stress mismatch between fiber and matrix (after Xu et al. 1995)

density, ρ. In order to correlate D_E and D_ρ, Mackenzie's equation was invoked (Mackenzie 1950):

$$E_n = E_o\left(1 - aV_v - bV_v^2\right)$$

where V_v is the volume fraction of voids and *a* and *b* are constants of a fully dense material. For materials with Poisson's ratio of 0.3, a = 1.91 and b = −0.91. By incorporating these equations and using the rule of mixtures for the density of the composite, $\rho_c = \rho_f V_f + \rho_m V_m$, the following relation is obtained:

$$D_E = b\left(\frac{\rho_o}{\rho_m}\right)D_n + b_1\left[\left(\frac{\rho_o}{\rho_m}\right)D_\rho\right]^2$$

where ρ_m is the density of the matrix. Figure 8.46 shows a plot of experimental and predicted values of D_E versus D_ρ, showing very good agreement. In general, one can reduce the damage in the matrix by choosing a matrix material that has a high yield strength and a large strain-to-failure (i.e., ductility). The eventual fiber/matrix debonding can only be avoided by choosing the components such that the difference in the thermal expansion characteristics of the fiber and the matrix is low.

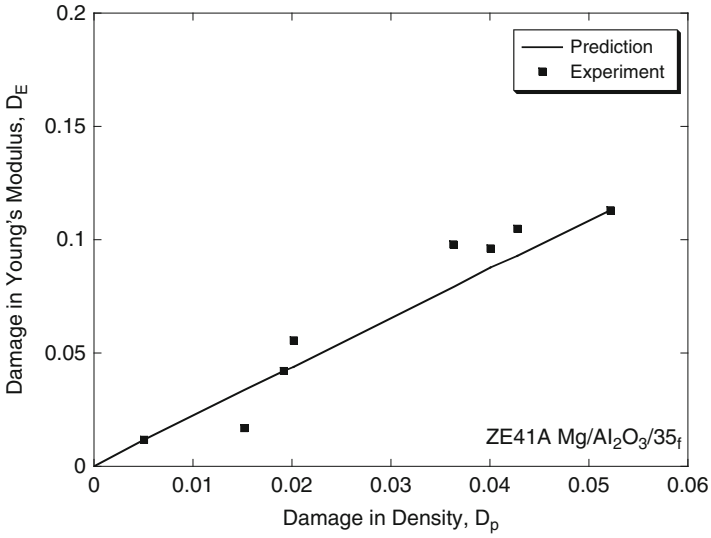

Fig. 8.46 Damage in Young's modulus versus damage in density for a $Mg/Al_2O_3/35_f$ composite showing good correlation between predicted and experimental results (Xu et al. 1995)

We should point out that surface observation of damage may not always be sufficient. As an example, consider the evolution of void growth in a SiC particle-reinforced 2080 Al alloy, as observed by in situ thermal cycling in a X-ray synchrotron source, as shown in Fig. 8.47 (Chapman et al. 2013). An in situ furnace was used to thermally cycle the specimen, and X-ray tomography was conducted at various numbers of cycles. The voids are prevalent at sharp corners of the SiC particles, where there is a stress concentration, or within particle clusters where there is a high triaxial state of stress. The volume fraction of voids goes up almost five times over the period of 1,200 cycles, Fig. 8.48a. It is also interesting that preexisting very small pores coalesce and become larger with increasing number of thermal cycles, as shown in Fig. 8.48b.

One type of thermal fatigue test involves cycling temperature of the sample while its gage length is kept constant. This constraint results in an internal stress on the sample. Thus, measurement of the internal stresses generated when subjecting a composite to thermal cycling can be used to study thermal fatigue. Figure 8.49 shows the results of cycling between 300 and 500 °C for alumina fiber/Al–Li composite (Kwei and Chawla 1992). The alumina fibers were unidirectionally aligned parallel to the stress axis, and the fiber volume fraction was 35 %. The plot shows the variation of the maximum stress in tension and compression as a function of number of cycles. The initial rise in the maximum tensile stress curve is due to the work hardening of the aluminum alloy matrix caused by the thermal stresses. With continued cycling, the microstructural damage sets in, and a plateau in the maximum tensile stress versus cycles curve is obtained as long as the strength increase due to work hardening of the matrix is balanced by the strength decrease

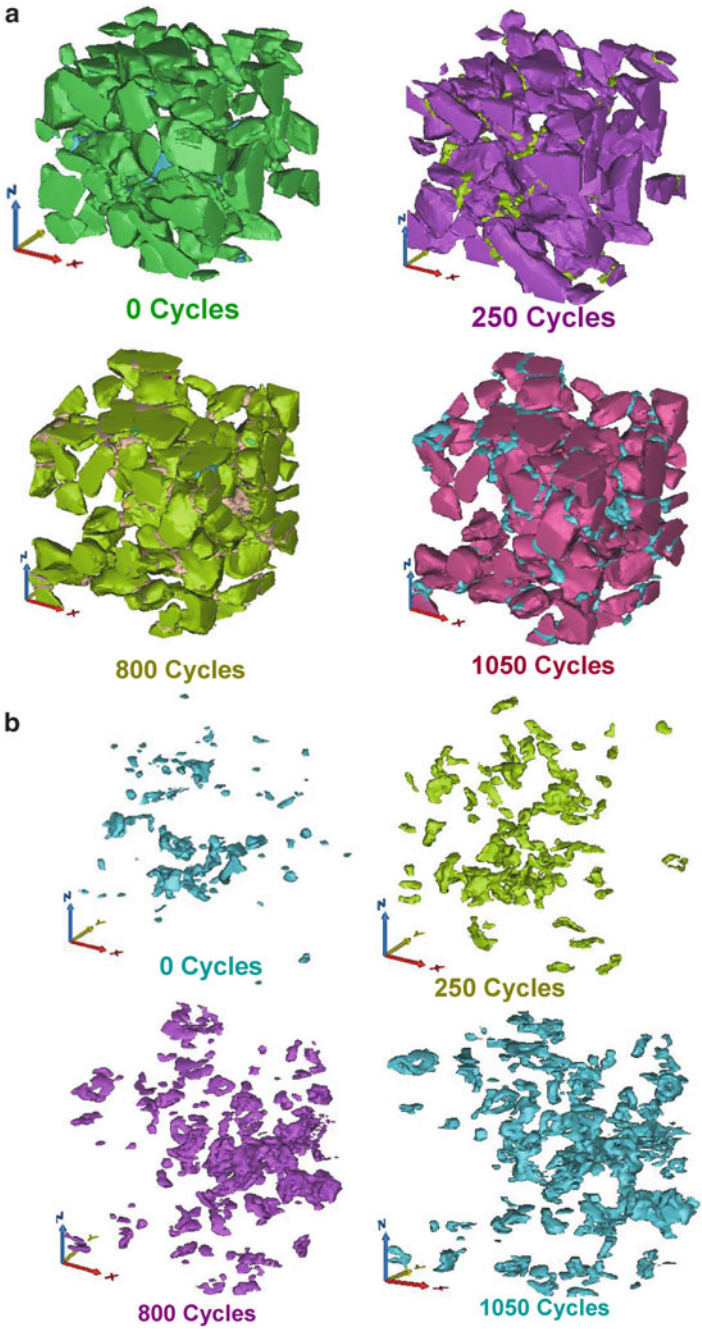

Fig. 8.47 Damage evolution during thermal cycling in a SiC particle-reinforced aluminum alloy composite by X-ray synchrotron tomography (Chapman et al. 2013): (**a**) particles and voids and (**b**) voids only. The primary damage mechanism is void initiation and growth at particle corners and within particle clusters

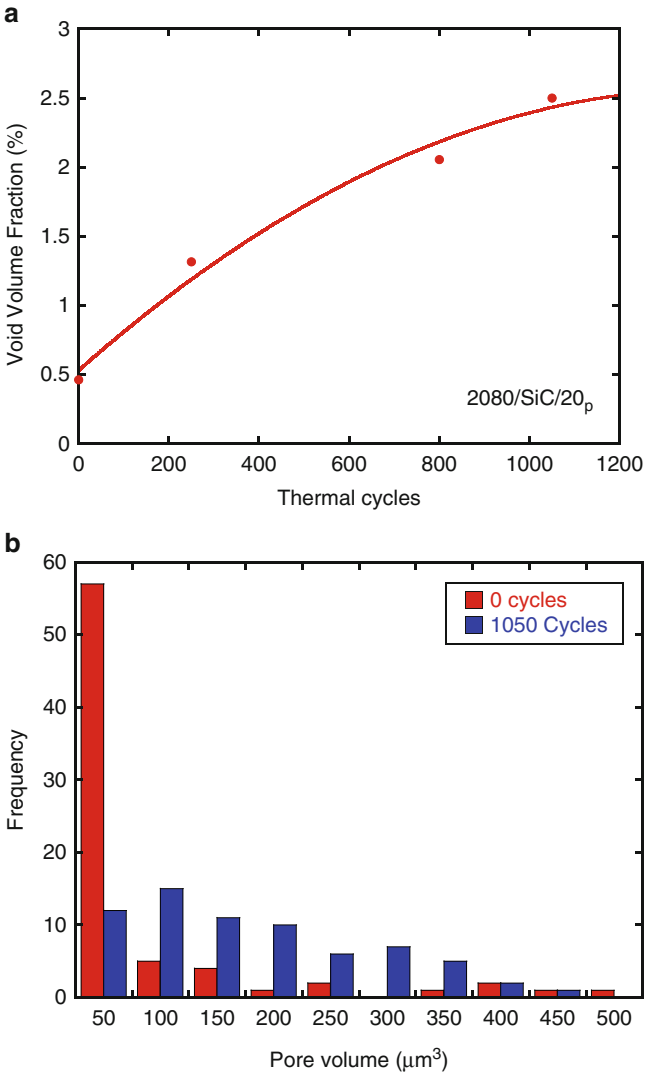

Fig. 8.48 Damage evolution during thermal cycling in a SiC particle-reinforced aluminum alloy composite by X-ray synchrotron tomography(Chapman et al. 2013): (**a**) void volume fraction as a function of cycles and (**b**) distribution of void size with cycling. Void fraction increases with cycling. Part (**b**) shows the coalescence of smaller voids into larger voids

due to microstructural damage, e.g., voiding at the interface. The maximum compressive stress, however, decreases with cycling to a plateau value. This may be due to the Bauschinger effect, i.e., a higher strength in tension results in a concomitant lowering of the strength in compression. Eventually, the alumina fibers suffer fracture, which causes the tensile stress curve in Fig. 8.49 to decrease.

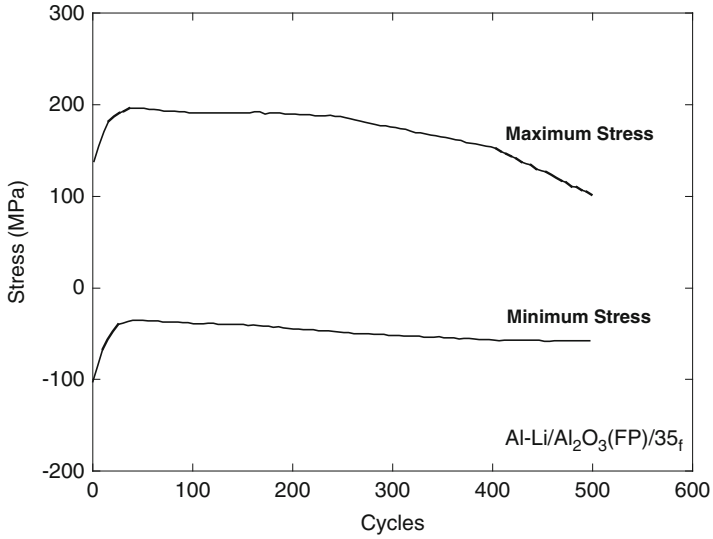

Fig. 8.49 Evolution of stess during strain-controlled thermal cycling of Al–Li/Al_2O_3/35_f composite (after Kwei and Chawla 1992). With increasing thermal cycles, relaxation processes such as interfacial cavitation result in stress relaxation

Superimposed effects of mechanical and thermal loading are important in a variety of applications such as in an automotive engine or gas turbine. Two types of thermomechanical loading may be applied: (a) in-phase loading, where the maximum and minimum stress take place at maximum and minimum temperature, respectively; and (b) out-of-phase loading, where the maximum stress and minimum stress are opposite to the maxima and minima in temperature. The nature of thermomechanical loading has a direct influence on the internal stress in the fiber and matrix. Consider the case of out-of-phase loading. During cooling, the ceramic fiber is in a state of residual compression, and the metal matrix is in tension. Thus, at the minimum temperature, where the applied stress is a maximum, the total stress on the matrix will be enhanced, while that in the fiber will be lowered. In in-phase loading, at the maximum temperature, the fiber is in tension while the matrix is in compression. Since the maximum temperature corresponds to the point of maximum stress, the stress on the fiber is maximized.

The effects of the internal stress during out-of-phase and in-phase TMF for a Ti-6242/SiC_f composite are shown in Fig. 8.50a (Bettge et al. 2004, 2007; Peters et al. 2004). In general, the fatigue life under TMF loading is significantly lower than in pure mechanical LCF. In-phase loading results in lower overall fatigue resistance, while out-of-phase loading exhibits an abrupt decrease in fatigue life at about 10^3 cycles. Due to the different internal stress states, the mechanisms for fracture in TMF are also quite different. Under in-phase loading, matrix relaxation takes place which results in a gradual increase in the stress in the fiber. Thus, fatigue

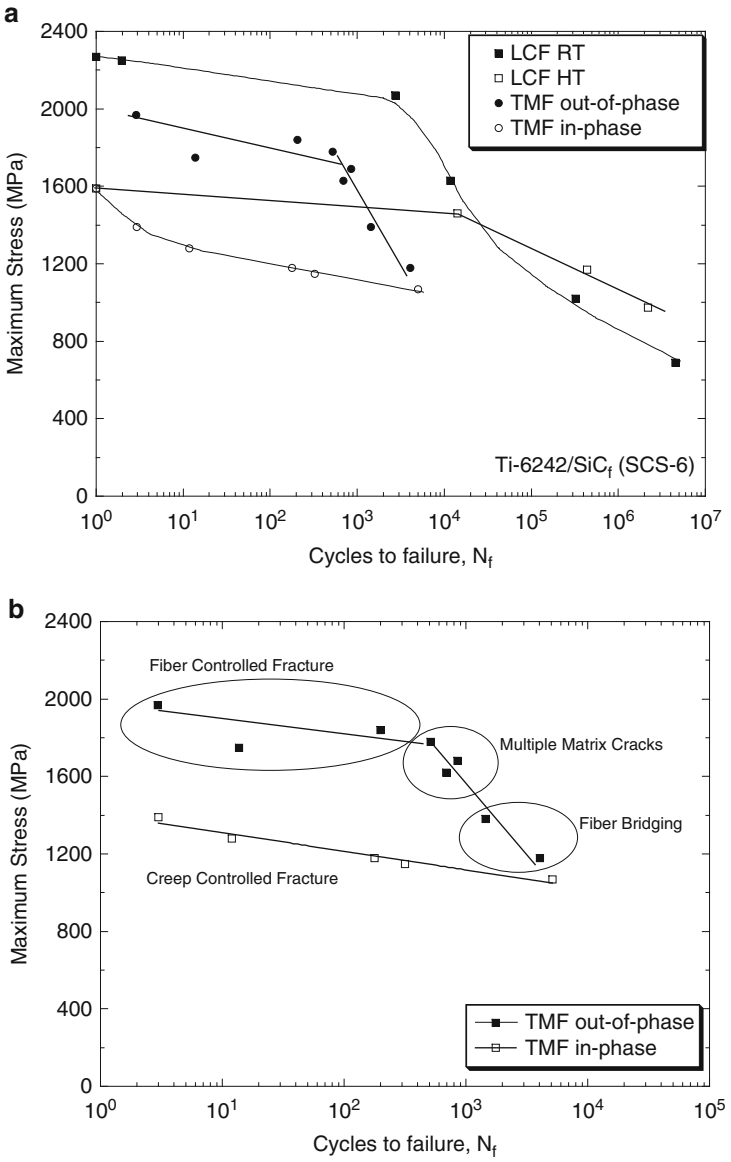

Fig. 8.50 Comparison of thermomechanical fatigue and low cycle fatigue of a Ti/SiC_f composite: (**a**) stress versus cycles behavior, showing the more damaging effect of thermal fatigue, and (**b**) damage mechanisms (after Bettge et al. 2004)

life is creep-controlled, Fig. 8.50. In out-of-phase loading, the strain range in the matrix is very large, so the damage is primarily matrix-controlled. With matrix cracking, oxygen ingression takes place, and when the cracks reach the fiber/matrix interface, oxidation and fracture of the fiber take place, Fig. 8.50b. Thus, at higher

stress, the fracture is fiber-controlled, with decreasing stress multiple matrix cracks and fiber bridging observed. Thermal cycling damage in discontinuously reinforced MMCs is somewhat lower than that of continuous fiber-reinforced MMCs, because diffusional relaxation of the matrix is easier (the constraint on the matrix is lower for discontinuous reinforcement). Very large plastic strains (on the order of 150 % for Al composites with 20 and 30 % SiC) have been observed during thermal cycling (Pickard and Derby 1990). In addition, a significant increase in surface roughness of the composite has been observed. Rezai-Aria et al. (1993) studied the thermal cycling behavior of an $Al/Al_2O_3/15_{sf}$ (Saffil) composite. The increase in surface roughness was attributed to the higher mobility of dislocations near the free surface. Within the bulk of the material, a cellular dislocation structure evolved during thermal cycling.

References

Allison, J.E., and J.W. Jones (1993) in *Fundamentals of Metal Matrix Composites*, S. Suresh, A. Mortensen, and A. Needleman, eds., Butterworth-Heinemann, Stoneham, MA, p. 269.

Almond, E.A., and B. Roebuck (1980) *Metals Technology*, **7**, 83–85.

Arsenault, R.J., and U.T.S. Pillai (1996) *Metall. Mater. Trans.*, **27A,** 995–1001.

Arsenault, R.J., and S.B. Wu (1987) *Mater. Sci. Eng.*, **96,** 77–88.

Aswath, P.B., S. Suresh, D.K. Holm, and A.F. Blom (1988) *J. Eng. Mater. Tech.*, **110** 278–85.

Ayyar, A., and N. Chawla (2006) *Comp. Sci. Tech.*, **66**, 1980–1994.

Baker, A.A., D.M. Braddick, and P.W. Jackson (1972) *J. Mater. Sci.*, **7**, 747–762.

Bauschinger, J. (1886) *Mitt: Mech-Tech Lab.*, XIII Munchen.

Bettge, D., B. Gunther, W. Wedell, P.D. Portella, J. Hemptenmacher, and P.W.M. Peters (2004) in *Low Cycle Fatigue 5*, (P. D. Portella, H. Sehitoglu, K. Hatanaka, eds.), DVM, Berline, pp. 81–86.

Bettge, D., B. Gunther, W. Wedell, P.D. Portella, J. Hemptenmacher, P.W.M. Peters, and B. Skrotzki (2007) *Mater. Sci. Eng.*, **A452–453**, 536–544

Blatt, D., J.R. Jira, and J.M. Larsen (1995) *Scripta Metall. Mater.*, **33**, 939–944.

Bonnen, J.J., C.P. You, J.E. Allison, and J.W. Jones (1990) in *Proceedings of the International Conference on Fatigue,* Pergamon Press, New York, pp. 887 – 892.

Boselli, J., P.D. Pitcher, P.J. Gregson, and I. Sinclair (2001) *Mater. Sci. Eng.*, **A300**, 113–124.

Calabrese, C., and C. Laird (1974a) *Mater. Sci. Eng.,* **13**, 141–157.

Calabrese, C., and C. Laird (1974b) *Mater. Sci. Eng.,* **13**, 159–174.

Carreno-Morelli, E., N. Chawla, and R. Schaller (2001) *J. Mater. Sci. Lett.*, **20**, 163–165.

Champion, A.R., W.H. Krueger, H.S. Hartman, and A.K. Dhingra (1978), in *Proc. 1978 Intl. Conf. Composite Materials* (ICCM/2), TMS-AIME, New York, p. 883.

Chapman, N.C., S.S. Singh, J.J. Williams, X. Xiao, F. De Carlo, and N. Chawla, *Mater. Sci. Eng.* (2013) in preparation.

Chawla, K.K. (1973a) *Metallography*, **6**, 155.

Chawla, K.K. (1973b) *Phil. Mag.*, **28**, 401.

Chawla, K.K. (2012) *Composite Materials: Science & Engineering*, 3rd ed., Springer-Verlag, New York.

Chawla, K.K. (1975) *Fiber Sci. Tech.,* **8**, 49.

Chawla, K.K. (1991) in *Metal Matrix Composites: Mechanisms and Properties*, R.K. Everett and R.J. Arsenault, eds., Academic press, pp. 235–253.

Chawla, K.K. and N. Chawla (2004) in *Kirk-Othmer Encyclopedia*, John-Wiley and Sons, New York.
Chawla, K.K., and P.K. Liaw (1979) *J. Mater. Sci.*, **14,** 2143.
Chawla, K.K., and M. Metzger (1972) *J. Mater. Sci.,* **7**, 34.
Chawla, N. (1997) *Metall. Mater. Trans.*, **28A**, 2423.
Chawla, N. and J.E. Allison (2001) in *Encyclopedia of Materials: Science and Technology***,** vol. 3**,** (B. Ilschner and P. Lukas, eds.), Elsevier Science, pp. 2969–2974.
Chawla, N., C. Andres, J.W. Jones, and J.E. Allison (1998a) *Metall. Mater. Trans.*, **29A**, 2843.
Chawla, N., C. Andres, J.W. Jones, and J.E. Allison (1998b) *Scripta Mater.*, **38**, 1596.
Chawla, N., L.C. Davis, C. Andres, J.E. Allison, J.W. Jones (2000a) *Metall. Mater. Trans.*, **31A**, 951–957.
Chawla, N., and V.V. Ganesh, *Int. J. Fatigue* (2010) **32**, 856–863.
Chawla, N., U. Habel, Y.-L. Shen, C. Andres, J.W. Jones, and J.E. Allison (2000b) *Metall. Mater. Trans.*, **31A**, 531–540.
Chawla, N., J.W. Holmes, and R.A. Lowden (1996) *Scripta Mater.*, **35**, 1411.
Chawla, N., J.W. Jones, and J.E. Allison (1999) in *Fatigue '99* (X.R. Wu and Z.G. Wang, eds.), EMAS/HEP.
Chawla, N., M. Kerr, and K.K. Chawla (2005) *J. Am. Ceram. Soc.*, **88**, 101–108.
Chawla, N. and Y.-L. Shen (2001) *Adv. Eng. Mater.*, **3**, 357–370.
Cook, J., and J.E. Gordon (1964) *Proc. Roy. Soc. Lond.*, **A282**, 508.
Cotterill, P.J., and P. Bowen (1993) *Composites*, **24**, 214–221.
Cotterill, P.J., and P. Bowen (1996) *Mater. Sci. Tech.*, **12,** 523–529.
Couper, M.J., and K. Xia (1991) in *Metal Matrix Composites–Processing, Microstructure and Properties*, (N. Hansen et al., eds.), Riso National Laboratory, Roskilde, Denmark, p. 291.
Davidson, D.L., K.S. Chan, A. McMinn, and G.R. Leverant (1989) *Metall. Trans.*, **20A**, 2369–2378.
Doker, H., and G. Marci (1983) *Int. J. Fatigue*, **5**, 187–191.
Foulk III, J.W., D.H. Allen, and K.L.E. Helms (1998) *Mech. Mater.*, **29**, 53–68.
Ganesh, V.V., and N. Chawla (2004) *Metall. Mater. Trans.*, **35A**, 53–62.
Gomez, J.P., and F.E. Wawner (1988) personal communication.
Gouda, M., K.M. Prewo, and A.J. McEvily (1981) in *Fatigue of Fibrous Composite Materials*, p. 101, ASTM STP, 723, Amer. Soc. Testing and Materials, Philadelphia.
Hack, J.E., R.A. Page, and G.R. Leverant (1987) *Metall. Trans.,* **15A**, 1389.
Hall, J., J.W. Jones, and A. Sachdev (1994) *Mater. Sci. Eng.,* **A183**, 69.
Harmon, D.M., C.R. Saff, and C.T. Sun (1987) AFW AL- TR-87–3060. Air Force Wright Aeronautical Labs., Dayton, Ohio.
Hassan, H.A., J.J. Lewandowski, and M.H. Abd El-latif, (2004) *Metall. Mater. Trans.*, **35A**, 45–52.
Hruby, P., S.S. Singh, J. Silva, J.J. Williams, X. Xiao, F. De Carlo, and N. Chawla, *Comp. Sci. Tech.*, (2013) submitted.
Huang, J., J.E. Spowart, and J.W. Jones (2006) *Fatigue Fract. Engng. Mater. Struct.*, **29**, 507–517
Johnson, W.S. (1982) in *Damage in Composite Materials*, *ASTM STP 775*, American Society for Testing and Materials, Philadelphia, p. 83.
Johnson, W.S. (1988) in *Mechanical and Physical Behavior of Metallic and Ceramic Composites*, 9th Risø Intl. Symp. on Metallurgy and Materials Science, Rise Nat. Lab., Roskilde, Denmark.
Johnson, W.S., and R.R. Wallis (1986) in *Composite Materials: Fatigue and Fracture*, *ASTM STP 907*, American Society for Testing and Materials, Philadelphia, p. 161.
Kerr, M., N. Chawla, and K.K. Chawla (Feb.,2005) *JOM*, **2**, 67–70.
Kindermann, P., P. Schlund, H.-G. Sockel, M. Herr, W. Heinrich, K. Görtring, and U. Schleinkofer (1999) *Int. J. Refractory & Hard Materials*, **17**, 55
Kwei, L.K., and K.K. Chawla (1992) *J. Mater. Sci.*, **27**, 1101–1106.

Lewandowski, J.J. (2000) in *Comprehensive Composite Materials*, vol. 3, (A. Kelly and C. Zweben, eds.), Elsevier Press, pp. 151–187.
Li, C., and F. Ellyin (1996) *Mater. Sci. Eng.*, **A214**, 115.
Liu, J., and P. Bowen (2002) *Acta Mater.*, **50**, 4205–4218.
Liu, J., and P. Bowen (2003) *Metall. Mater. Trans.*, **34A**, 1193–1202.
LLorca, J. (1994) *Acta Metall. Mater.*, **42**, 151–162.
LLorca, J. (2002) *Prog. Mater. Sci.*, **47**, 283–353.
LLorca, J., A. Needleman, and S. Suresh (1990) *Scripta Metall. Mater.*, **24**, 1203.
LLorca, J., J. Ruiz, J.C. Healy, M. Elices, and C.J. Beevers (1994) *Mater. Sci. Eng.*, **A185**, 1–15.
LLorca, J., S. Suresh, and A. Needleman (1992) *Metall. Mater. Trans.*, **23A,** 919–933.
Lukasak, D.A., and R.J. Bucci (1992) Alloy Technology Div. Rep. No. KF-34, Alcoa Technical Center, Alcoa, PA.
Lukasak, D.A., and D.A. Koss (1993) *Composites*, **24**, 262.
Mackenzie, J.K. (1950) *Proc. Phys. Soc.*, **B63**, 2.
Mall, S., and B. Portner (1992) *J. Eng. Mater., Tech.*, **114**, 409–415.
McCartney, R.F., R.C. Richard, and P.S. Trozzo (1967) *Trans. ASM*, **60**, 384.
McGuire, M.A., and B. Harris (1974) *J. Phys., Appl. Phys.,* **7**, 1788.
Majumdar, B.S., and G.M. Newaz (1995) *Mater. Sci. Eng.*, **A200**, 114–129.
Meyers, M.A., and K.K. Chawla (2009) *Mechanical Behavior of Materials*, 2nd ed., Cambridge University Press, Cambridge .
Mott, N.F. (1952) *Phil. Mag.*, **43**, 1151.
Mueller, L.R., and M. Gregory (1988) paper presented at First Annual Metals and Metals Processing Conf., SAMPE, Cherry Hill, NJ.
Orowan, E. (1959) in *Internal Stresses and Fatigue in Metals*, (G.M. Rassweiler and W.L. Grube, eds.), Elsevier Press, New York.
Page, R.A., J.E. Hack, R. Sherman, and G.R. Leverant (1987) *Metall. Trans.,* **15A**, 1397.
Paris, P.C., M.P. Gomez, and W.P. Anderson (1961) *The Trend in Engineering*, **13**, 9.
Paris, P.C., and F. Erdogan (1963) *J. Basic. Eng. Trans. ASME*, **85**, 528.
Pfeiffer, N.J., and J.A. Alic. (1978) *J. Eng. Mater. Tech.*, **100**, 32.
Peters, P.W.M., J. Hemptenmacher, B. Gunther, D. Bettge, and P.D. Portella (2004) in *Proc. ECCM-11*.
Pickard, S.M., and B. Derby (1990) *Acta Metall. Mater.* **38**, 2537–2552.
Poza, P., and J. LLorca (1999) *Metall. Mater. Trans.*, **30A**, 857.
Pugsley, V.A., and H.-G. Sockel (2004) *Mater. Sci. Eng.*, A**366**, 87.
Rao, K.T. Venkateshwara, S.C. Siu, and R.O. Ritchie (1993) *Metall. Trans.*, **24A**, 721–734.
Rezai-Aria, F., T. Liechti, and G. Gagnon (1993) *Scripta Metall. Mater.*, **28**, 587–592.
Roebuck, B., E.A. Almond, and A.M. Cottenden (1984) *Mater. Sci. Eng*, **66**, 179.
Salazar, A., J.Y. Pastor, and J. LLorca (2004) *IEEE Trans. Appl. Supercon.*, **14**, 1941–1947.
Sanders, B.P., and S. Mall (1996) *J. Comp. Tech. Res.*, **18**, 15–21.
Seeger, A., J. Diehl, S. Mader, and H. Rebstock (1958) *Phil. Mag.*, **2**, 323.
Shang, J.K., W.K. Yu, and R.O. Ritchie (1988) *Mater. Sci. Eng.* **A102,** 181 − 192.
Shen, Y.-L., M. Finot, A. Needleman and S. Suresh (1995) *Acta Metall. Mater.*, **43**, 1701.
Soumelidis, P., J.M. Quenisset, R. Naslain, and N.S. Stoloff (1986) *J. Mater. Sci.*, **21**, 895–903.
Starke, E.A., and G. Luetjering (1979) in *Fatigue and Microstructure,* J.T. Stayley and E.A. Starke, eds., American Society for Metals, pp 205–243.
Stoloff, N.S. (1978) in *Advances in Composite Materials*, p. 247. Applied Sci. Pub., London.
Sugimura, Y., and S. Suresh (1992) *Metall. Trans.*, **23A**, 2231–2242.
Suresh, S. (1998) *Fatigue of Materials*, 2nd Ed., Cambridge University Press, Cambridge, UK.
Taylor, L.G., and D.A. Ryder (1976) *Composites*, **1**, 27.
Vasudevan, A.K., K. Sadananda, and N. Louat (1994) *Mater. Sci. Eng.*, **A188**, 1–22.
Vasudevan, A.K., and K. Sadananda (1995) *Metall. Mater. Trans.*, **26**, 1221–1234.
Vyletel, G.M., D.C. Van Aken, and J.E. Allison (1991) *Scripta Metall. Mater.*, **25**, 2405–2410.
Walls, D.P., G. Bao, and F.W. Zok (1993) *Acta Metall. Mater.*, **41**, 2061–2071.

Walls, D.P., and F.W. Zok (1994) *Acta Metall. Mater.*, **42**, 2675–2681.
Wu, G., and J.-M. Yang (2005) *JOM*, **57**, 72–79.
Xu, Z.R., K.K. Chawla, A. Wolfenden, A. Neuman, G.M. Liggett, and N. Chawla (1995) *Mater. Sci. Eng.*, **A203**, 75.
Zhang, T., and H. Ghonem (1995) *Fatigue. Fract. Eng. Mater. Struc.*, **18**, 1249–1262.
Zhang, W., M. Gu, J. Chen, Z. Wu, F. Zhang, H.E. Devé (2003) *Mater. Sci. Eng.*, **A341**, 9–17.

Chapter 9
Creep

The creep behavior of MMCs is of great significance, since in many structural and nonstructural applications, these materials will be subjected to constant stress (or strain) for long periods of time, at temperature above half of the homologous temperature (homologous temperature is the temperature of interest divided by melting point, both in K; i.e., T/T_m). Most materials exhibit three distinct stages of creep: (1) primary creep, (2) secondary or steady-state creep, and (3) tertiary creep. In primary creep, the strains are relatively small. In the secondary or steady-state regime, a linear relationship exists between the strain and time (constant strain rate). This is believed to be a result of the combination of hardening and recovery mechanisms during creep. Finally, in the tertiary regime, the material undergoes cavitation and void growth, which is manifested in terms of a very rapid increase in strain with time.

In general, the steady creep rate, $\dot{\varepsilon}_s$, is described by the following general expression called the Mukherjee–Bird–Dorn relation (Mukherjee et al. 1964):

$$\dot{\varepsilon}_s = \frac{AGbD}{kT}\left(\frac{b}{d}\right)^p\left(\frac{\sigma}{G}\right)^n$$

where σ is the applied stress, T is the temperature in kelvin, G is the shear modulus, b is the Burgers vector, d is the average grain size, p is the inverse grain size exponent, n is the stress exponent, D is the diffusion coefficient of the material, k is the Boltzmann's constant, and A is a dimensionless constant. The value of the stress exponent can usually be correlated with a particular creep mechanism (e.g., $n \sim 4$–5 corresponds to dislocation climb). The diffusion coefficient, D, is given by

$$D = D_o \exp\left(\frac{-Q_D}{RT}\right)$$

N. Chawla and K.K. Chawla, *Metal Matrix Composites*,
DOI 10.1007/978-1-4614-9548-2_9, © Springer Science+Business Media New York 2013

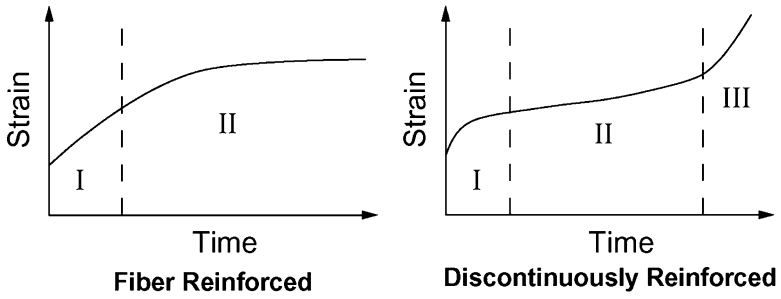

Fig. 9.1 Schematic of creep strain versus time for fiber reinforced and discontinuously reinforced MMCs (after Lilholt 1991). The three stages of creep are (*I*) primary creep, (*II*) steady-state creep, and (*III*) fast fracture

where D_o is the pre-exponential constant, R is the universal gas constant, and Q_D is the activation energy for creep, which is often equal to the activation energy for diffusion. For a detailed discussion on the fundamentals of creep, the reader is referred to texts such as Evans and Wilshire (1993) and Meyers and Chawla (2009).

In general, the addition of high-stiffness reinforcement greatly increases the creep resistance over that of unreinforced alloys. The addition of the reinforcement also changes the creep deformation mechanisms, relative to the creep mechanisms in pure matrix. A schematic of typical creep curves (strain versus time) for MMCs with continuous and discontinuous reinforcement is shown in Fig. 9.1 (Lilholt 1991). Composites with continuous fibers exhibit a short primary creep regime, followed by a long steady-state regime, see Fig. 9.1. This behavior can be predicted by simple viscoelastic models, such as an isostrain model, where the matrix is modeled as the viscous component and the fiber is elastic. In the case of discontinuous reinforcement (short fibers or particles), a more typical creep curve is observed, with three distinct creep regimes, see Fig. 9.1, since the degree of load transfer is not as high as that for continuous fibers.

9.1 Continuous Fiber Reinforced MMCs

The creep strength of continuous fiber reinforced MMCs in the longitudinal direction is usually significantly higher than that of the unreinforced alloy. Figure 9.2a shows creep strain versus time for Ti–6Al–4V–/SiC_f composite at temperatures ranging between 430 and 650 °C (Leyens et al. 2003). As mentioned above, the creep curves exhibit two stages during creep. At the highest temperature, 650 °C, the creep strain increases exponentially with time. A plot of creep strain rate, $\dot{\varepsilon}$, versus stress, σ, see Fig. 9.2b, shows that a much higher stress is required to induce a given creep strain in the composite, relative to the unreinforced alloy. The stress exponent, for the composite, however, is much larger (n ~ 20 for the composite,

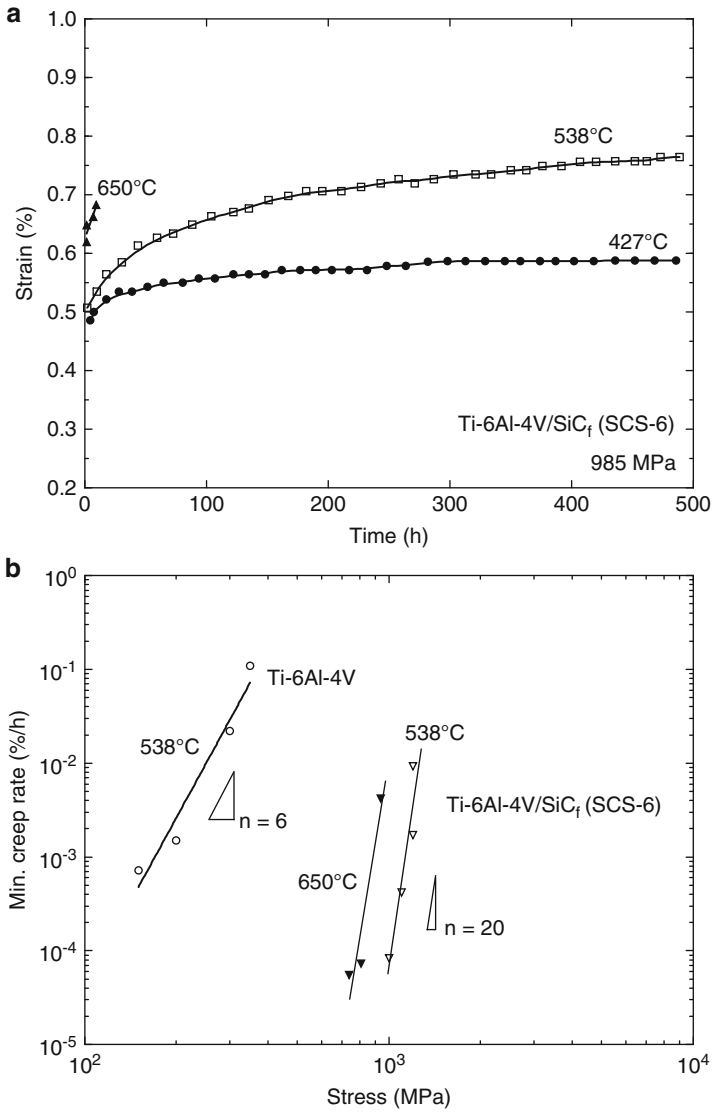

Fig. 9.2 Creep behavior of Ti-6Al-4V/SiC_f composite versus the unreinforced alloy: (**a**) creep strain versus time plots for temperatures ranging between 430 and 650 °C and (**b**) steady-state creep rate versus stress. The MMC exhibits significantly higher creep resistance, but much higher creep stress exponent, n (after Leyens et al. 2003)

vis-à-vis n ~ 6 for the unreinforced alloy). The reasons for the anomalously high values of the stress exponent in the composite are explained later in this chapter. In general, off-axis creep results in poorer creep resistance (Ohno et al. 1994). At 45° large-scale shear deformation takes place in the matrix, while at 90° (transverse loading) interfacial debonding results in creep fracture.

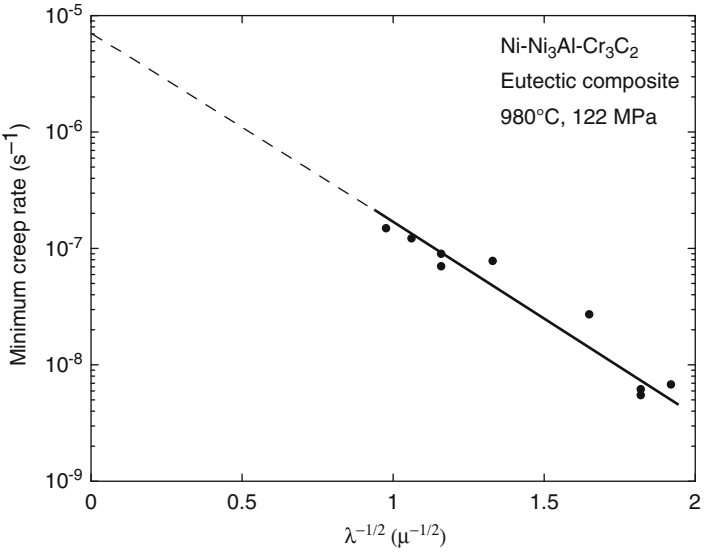

Fig. 9.3 Minimum creep rate versus inverse square root of fiber radius of directionally solidified in situ composites of Ni-Ni_3Al-Cr_3C_2 (after Bullock et al. 1977). The creep rate follows a modified Hall-Petch relationship

Bullock et al. (1977) studied the behavior of directionally solidified in situ composites of Ni–Ni_3Al–Cr_3C_2. The creep rate was found to be inversely proportional to the scale of the eutectic microstructure, i.e., the mean fiber radius, λ. The Hall–Petch relation was modified for creep rate and written as

$$\log \dot{\varepsilon} = \log \dot{\varepsilon}_{\infty} + K\lambda^{-\frac{1}{2}}$$

where $\dot{\varepsilon}$ is the creep rate, $\dot{\varepsilon}_{\infty}$ is the creep rate for $\lambda = \infty$, and K is a constant. A comparison of the experimentally determined creep rates and the model prediction is presented in Fig. 9.3, showing reasonable agreement.

The evolution of load transfer during creep, from the creeping matrix to the rigid reinforcement (most fibers do not creep at temperatures at which the metal matrix creeps), has an important influence on the creep of the composite. As the matrix creeps, an increasing fraction of the load is transferred to the fibers, see Fig. 9.4a. Upon unloading, the loads on the fiber and matrix decrease. The stress in the matrix, however, dips below zero and then increases slightly. This phenomenon is termed creep recovery. A 3D finite element model of a fiber reinforced MMC ($E_m = 60$ GPa, $E_f = 470$ GPa, 15 vol.% of fibers, with a matrix deforming by power-law creep) illustrates this behavior very nicely, see Fig. 9.4b (Sørensen et al. 1992).

The gradual transfer of load from the matrix to the fibers can be modeled by assuming that the fiber behaves elastically and that the matrix follows power-law creep ($\dot{\varepsilon} = A\sigma^n$). Then the creep rate of the composite is given by:

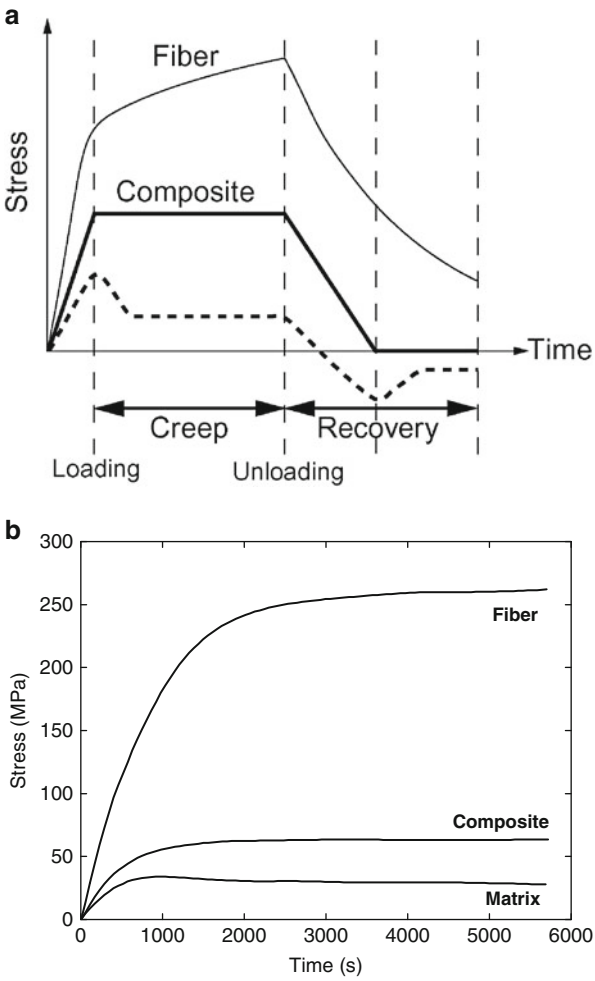

Fig. 9.4 Evolution of load transfer during creep, from the creeping matrix to the rigid reinforcement: (**a**) schematic of experimental behavior and (**b**) 3D finite element model (after Sørensen et al. 1992). As the matrix creeps, an increasing fraction of the load is transferred to the fibers. Upon unloading, slight creep recovery in the matrix takes place

$$\dot{\varepsilon}_c = \frac{A\sigma^n \left[1 - \frac{\dot{\varepsilon}}{\dot{\varepsilon}_\infty}\right]^n}{\left[1 + \frac{V_f E_f}{V_m E_m}\right] V_m^n}$$

where $\dot{\varepsilon}_\infty$ is the asymptotic creep strain, which is achieved when all of the load has been transferred to the fibers. It is given by

$$\dot{\varepsilon}_\infty = \frac{\sigma_c}{V_f E_f}$$

The creep behavior of the composite is also dependent on whether the matrix creeps faster than the fiber, $\dot{\varepsilon}_m > \dot{\varepsilon}_f$, or vice versa, see Fig. 9.5. In the case of matrix creeping

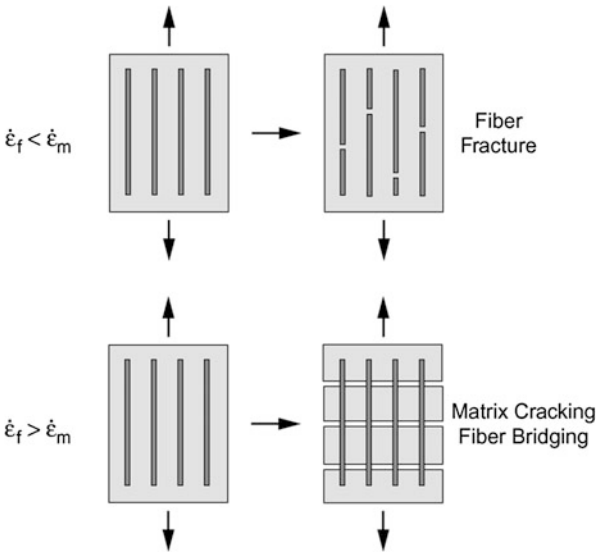

Fig. 9.5 Creep behavior of fiber reinforced MMC. When the matrix creeps faster than the matrix, $\dot{\varepsilon}_m > \dot{\varepsilon}_f$, the fibers fracture first. For $\dot{\varepsilon}_f > \dot{\varepsilon}_m$, the matrix cracks first, allowing the fibers to bridge the crack

faster, one may expect the fibers to fracture first. In the reverse scenario, $\dot{\varepsilon}_f > \dot{\varepsilon}_m$, the matrix should crack first, allowing the fibers to bridge the crack.

Lilholt (1985) proposed analytical models for predicting the creep behavior of fiber reinforced MMCs. He considered two cases: (a) fiber elastic and matrix creeping and (b) both and fiber and matrix creeping. Load transfer to the fibers was modeled using a modified shear-lag theory, with the matrix between the fibers deforming by shear and matrix at the fiber ends deforming in tension. While pure metals undergo power-law creep, the local stress in the matrix of the composite is significantly higher, so an exponential law describing matrix creep was deemed to be more appropriate (at these stresses the power law breaks down). The exponential law for matrix creep strain is given by

$$\dot{\varepsilon} = \dot{\varepsilon}_o \exp\left[-\frac{Q}{RT}\left(1 - \frac{\sigma}{\sigma_o}\right)\right]$$

where σ is the applied stress, $\dot{\varepsilon}$ is the creep rate, $\dot{\varepsilon}_o$ is a constant, Q is the activation energy for creep (taken here as the activation energy for dislocation glide), and σ_o is the strength of the glide obstacles at 0 K. The total composite strength was modeled as a sum of the following components:

$$\sigma_c = \sigma_m + \sigma_{th} + < \sigma >$$

where σ_m is the creep strength of the matrix, σ_{th} is a threshold stress for Orowan bowing of dislocations, and $< \sigma >$ is a mean stress that is directly proportional to the applied strain. Good agreement was obtained with experimental results on model composites, such as Ni/W_f and $Ni/NiAl_f$, Cr_3C_{2f}.

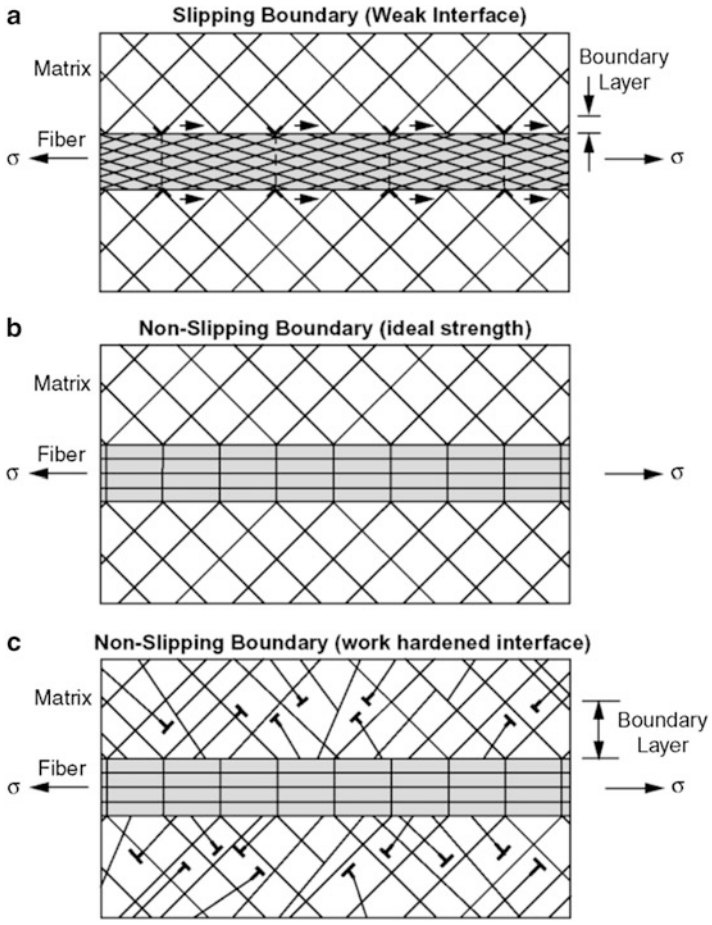

Fig. 9.6 Types of fiber/matrix interface used in modeling creep behavior (after Goto and McLean 1989, 1991): (**a**) weak interface, (**b**) ideal strength interface, and (**c**) work hardened interface

Goto and McLean (1989, 1991) modeled the creep behavior of continuous and short fiber reinforced MMCs, based on the nature of the fiber/matrix interface, see Fig. 9.6. If the fiber/matrix interface is completely incoherent, Orowan loops will stop at the interface and climb parallel to the fiber length. This results in extensive recovery and very little hardening at the interface. It also results in extensive strain relaxation at the interface and contributes to slipping of the boundary. For the case of the completely coherent boundary, two cases exist. If the modulus of the matrix is greater than that of the fiber, i.e., $E_m > E_f$, the dislocations are attracted to the boundary and the coherency is retained, although some slippage may take place. For the case of $E_m < E_f$, the dislocation loops are repelled from the fiber and a work-hardened zone (WHZ) is created that is not conducive to interface slipping. The results of their model showed that the work-hardened boundary temporarily

carries a large fraction of the load, prior to transferring it to the fibers. This results in an enhancement of creep life. The case for a weak interface did not appear to have a significant effect on creep behavior in continuous fibers, although it did affect the short fiber behavior.

Aspects of fiber fracture and interfacial debonding were also analyzed by Lee et al. (1995). These authors conducted a parametric analysis of the creep behavior of SCS-6 fiber reinforced Ti matrix composites. They used an iterative computer simulation to determine the stress in the fiber and matrix at a given time. Models with single and multiple fibers were considered. Figure 9.7 shows two examples of predictions of numerical models. Figure 9.7a shows the case of composites with (1) no fiber fracture, (2) fiber fracture but no interfacial debonding, and (3) fiber fracture with interfacial debonding. As expected, the material with fiber fracture and interfacial debonding exhibits the highest creep strain, for a given time, while the composite with no fiber fracture is the most creep resistant. The effect of interfacial strength is illustrated in Fig. 9.7b. Note that with increasing interfacial strength, creep of the matrix is more constrained, so the overall composite creep rate is lower.

9.2 Discontinuously Reinforced MMCs

Dlouhy et al. (1993, 1995) examined the creep behavior of Al_2O_3 short fiber-reinforced Al7Si3Cu alloy matrix composites, processed by squeeze casting. Three major mechanisms for creep damage were proposed as follows: (1) load transfer to the fibers through a WHZ some distance from the fiber/matrix interface; (2) diffusional/recovery mechanisms that result in a decrease in dislocation density in the WHZ; and (3) multiple fiber fracture. The WHZ develops in the primary creep regime, which contributes to significant load transfer to the fibers. The recovery process results from dislocations moving to the fiber ends by combined climb and glide processes, see Fig. 9.8. Figure 9.9 shows a comparison of the dislocation structure, in the matrix of the composite, in the as-processed condition, and after-creep deformation at 623 K, stress of 40 MPa, and rupture at 1.7 % total strain. Note the much higher dislocation density at the fiber/matrix interface after creep. The addition of Mg to the alloy resulted in the formation of intermetallic particles at the fiber/matrix interface (Dlouhy et al. 1993). The proposed effect of the particles at the interface was a longer effective path for recovery and thus, an increase in creep strength. Eventually, the stress concentration caused by dislocation pileup at the fiber/matrix interface results in fiber fracture, see Figs. 9.10 and 9.11. This also aids in recovery because of matrix diffusion at the fiber cracks. Fiber fracture and the increase in recovery contribute to the onset of tertiary creep. By using springs (elastic behavior) and dashpots (viscoelastic behavior) to represent individual components of the material behavior, excellent correlation with the experiment was obtained. 3D X-ray synchrotron tomography shows that areas between fibers are also more prone to having a higher density of pores, due to the

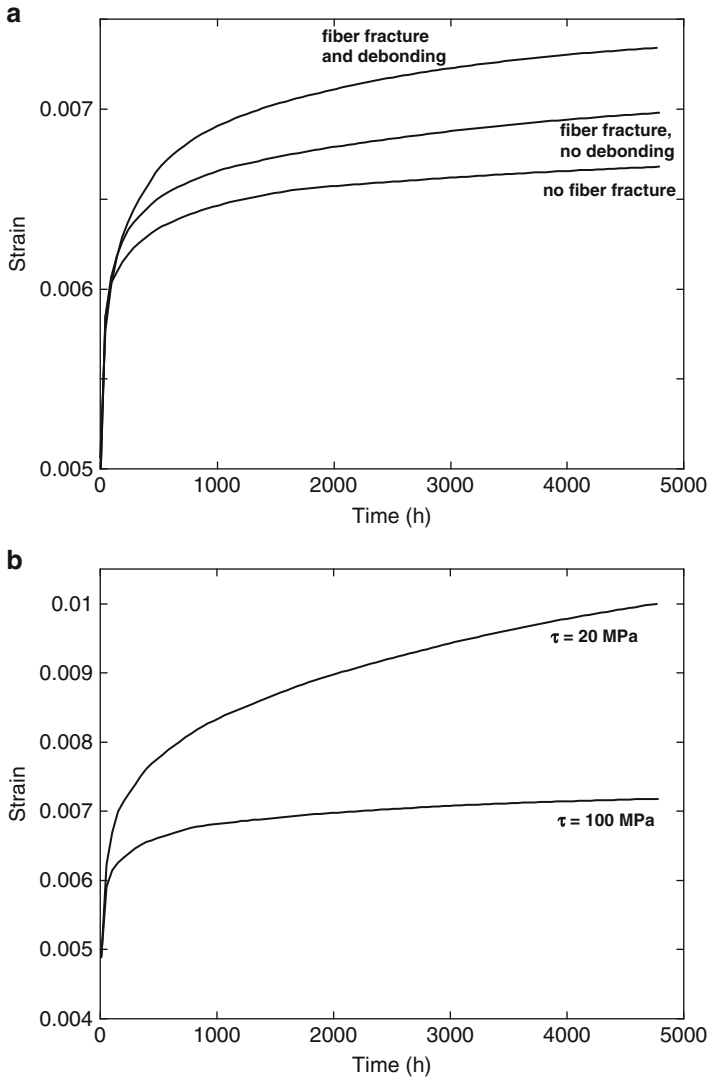

Fig. 9.7 Numerical analysis of creep behavior of SCS-6 fiber reinforced Ti matrix composite (after Lee et al. 1995): (**a**) effect of fiber fracture and debonding—fracture and debonding increase the creep rate of the composite; and (**b**) effect of interfacial shear strength, τ—increasing interface strength increases the constraint on the matrix, which lowers the creep rate of the composite

difficulty of obtaining matrix from squeeze casting between the interstices of the fibers (Kurumlu et al. 2012), see Fig. 9.12. Thus, during the creep, the preexisting voids between fibers can also affect fiber fracture.

While short fibers or whiskers provide significant creep strengthening, particulate reinforcement has also been used to improve creep resistance. Nieh (1984)

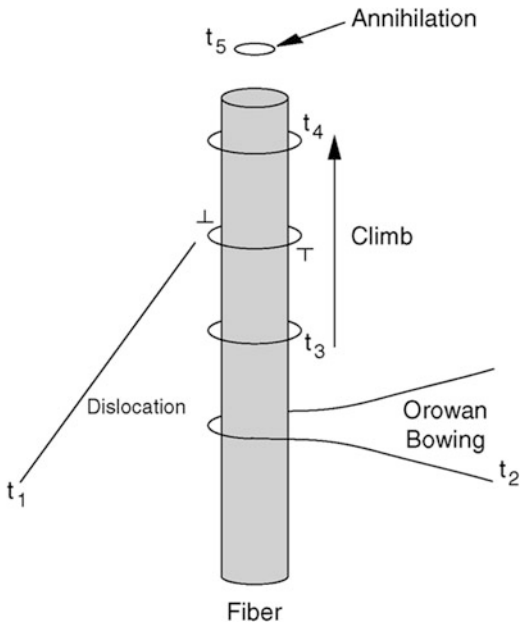

Fig. 9.8 Proposed mechanism for creep deformation in a fiber reinforced MMC (after Dlouhy et al. 1993, 1995). A dislocation bows around the fiber. The dislocation segment at the interface climbs parallel to the fiber axis and is annihilated at the fiber ends

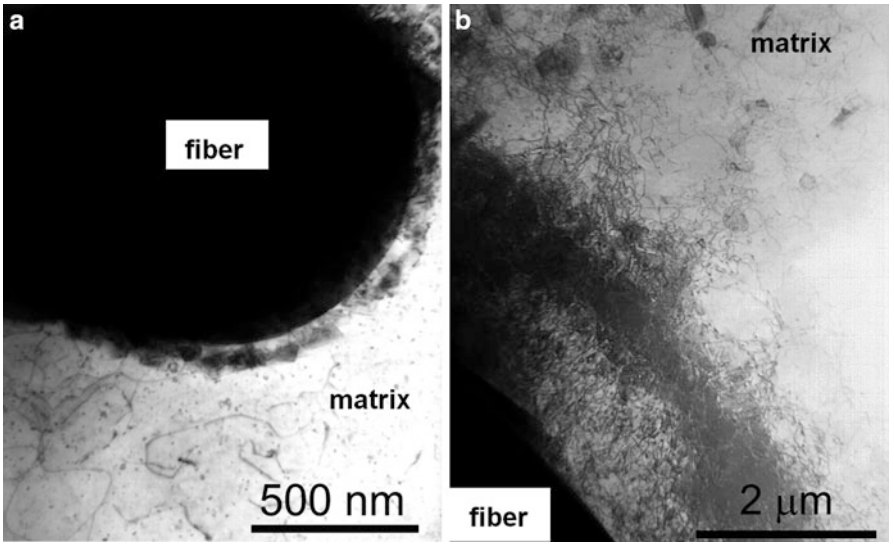

Fig. 9.9 Comparison of dislocation in the matrix of the composite in (**a**) the as-processed condition and (**b**) after creep deformation at 623 K, 40 MPa, and rupture at 1.7 % total strain (courtesy of A. Dlouhy and G. Eggeler). Note the enhanced dislocation density at the fiber/matrix interface after creep

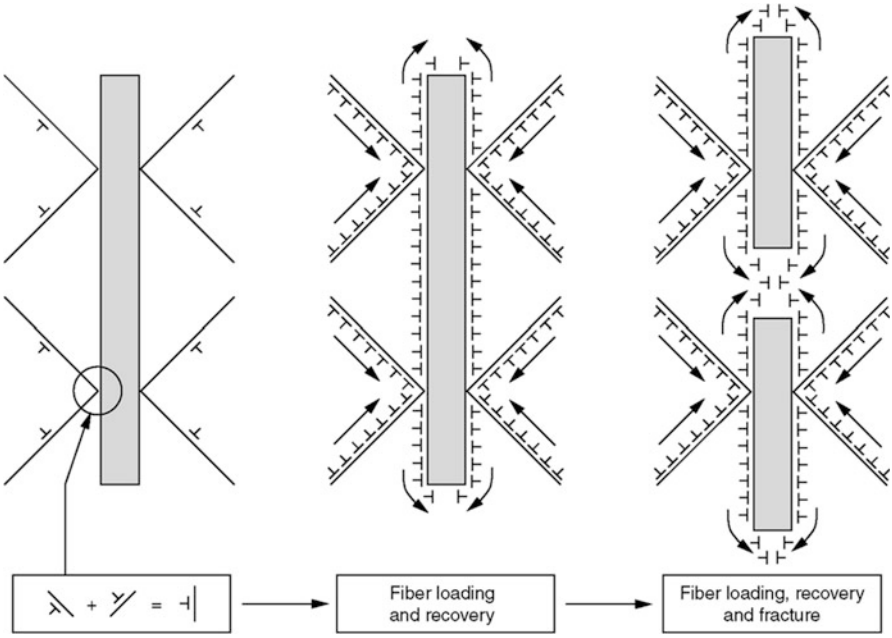

Fig. 9.10 Effect of dislocation pile-up at the fiber/matrix interface during creep (after Dlouhy et al. 1993). The stress concentration caused by dislocation pile-up results in fiber fracture, aiding in recovery because of diffusion at the fiber cracks

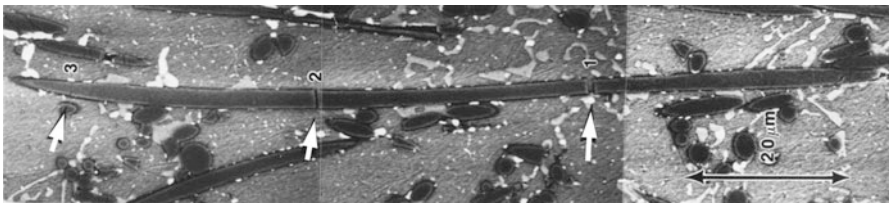

Fig. 9.11 Fiber fracture (indicated by *arrows*) in Al_2O_3 short fiber reinforced Al7Si3Cu alloy matrix composite during creep (courtesy of A. Dlouhy and G. Eggeler). The loading axis is horizontal

studied the creep behavior of 6061/SiC/20_p and 6061/SiC/20_w and compared it to that of the unreinforced 6061 alloy, see Fig. 9.13. He noted a much higher creep resistance in the composite with an accompanying higher sensitivity to applied stress (much higher stress exponent n). Enhanced creep resistance was also obtained with the higher aspect ratio whiskers than with particles, presumably due to more effective load transfer from the matrix to the whisker of high stiffness and large aspect ratio. Webster (1982) also characterized the creep behavior of the matrix alloy and its whisker-reinforced composite with increasing temperature. At intermediate temperatures (500–720 K), the strength was controlled by the

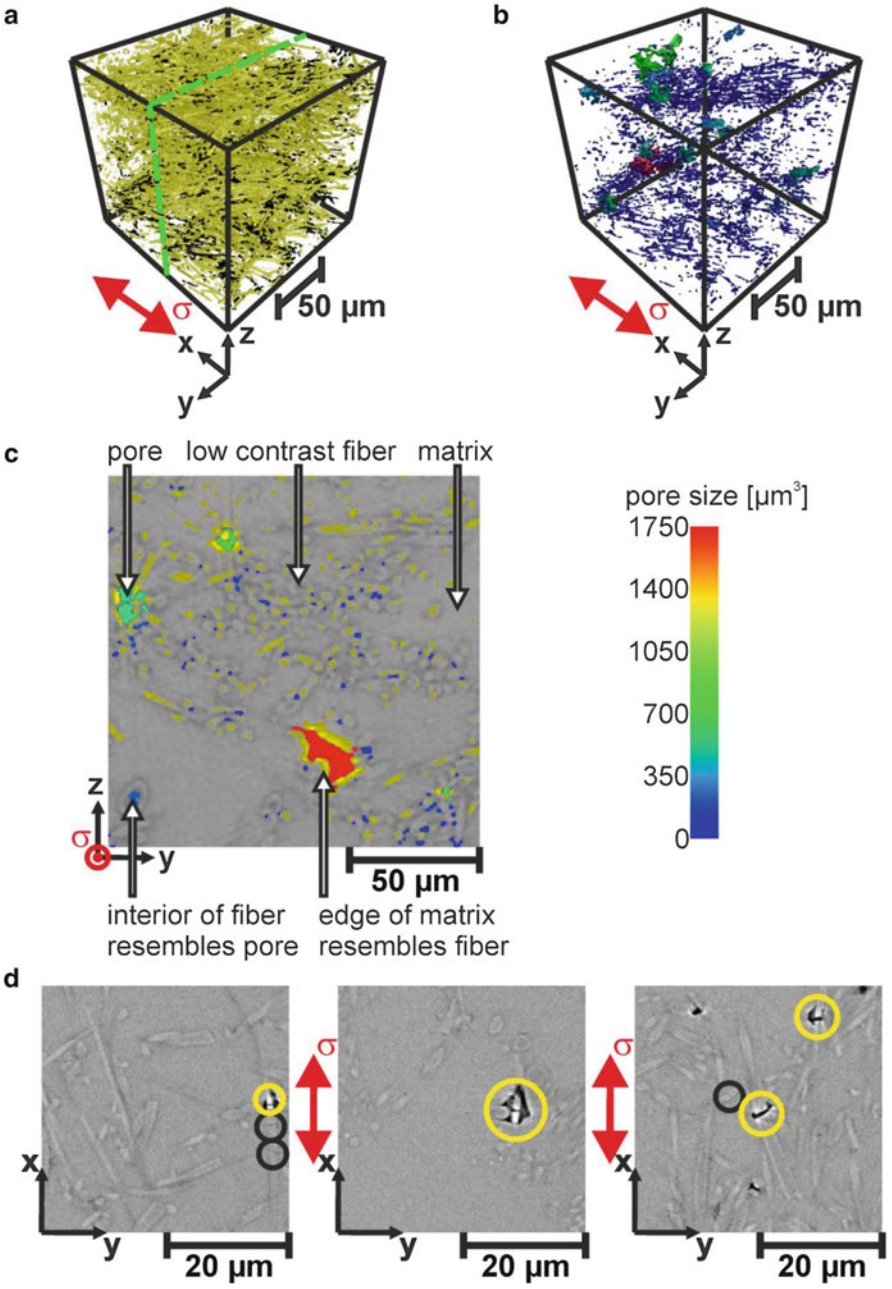

Fig. 9.12 X-ray microtomography images of Al_2O_3 short fiber reinforced Al–11Zn–0.2 Mg matrix alloy matrix composite: (**a**) fibers, (**b**) voids, (**c**) pore size map, and (**d**) fiber fracture and voiding during creep (courtesy of G. Eggeler)

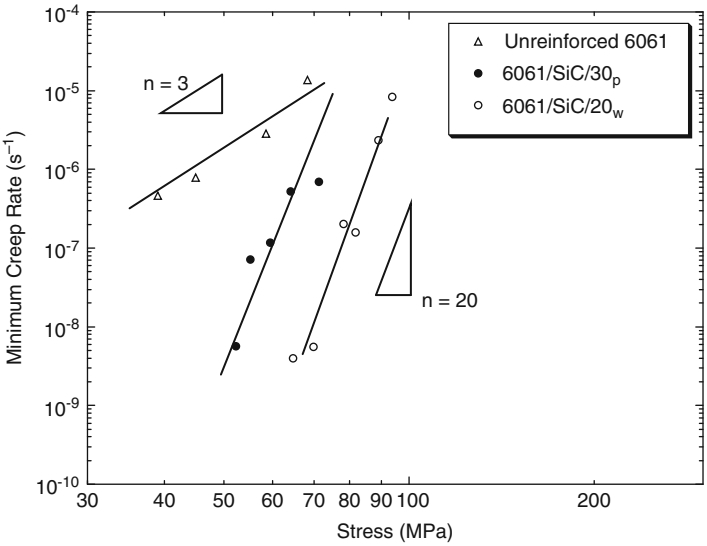

Fig. 9.13 Creep behavior of 6061/SiC particle and whisker reinforced composites (after Webster 1982). Notice the higher creep resistance of the whisker reinforced material, due to more effective load transfer to the reinforcement

whiskers, as the load was transferred to the high-modulus and high-aspect ratio reinforcement. The strength becomes matrix controlled at very high temperatures (720–900 K), perhaps due to increasingly lower interfacial shear strength and lower efficiency in load transfer to the whisker reinforcement. Evidence of creep cavitation, predominantly at reinforcement particle clusters, has also been observed (Whitehouse et al. 1998).

Krajewski et al. (1993, 1995) studied the creep behavior of 2219/TiC/15$_p$–T6 composites and compared it to that of the unreinforced alloy. They found that the precipitate structure in the matrix of the composite had a dominant effect on controlling creep rate. The composite had a finer interprecipitate spacing than that of the unreinforced alloy, due to indirect strengthening (see Chap. 7). Figure 9.14a shows the unreinforced precipitate structure in the matrix of the composite. The precipitates exhibit characteristic needle-like morphology observed in Al–Cu and Al–Cu–Mg alloys. After-creep deformation at 250 °C and 75 MPa, the precipitates serve as barriers for dislocation motion, see Fig. 9.14b.

In unreinforced aluminum alloys, Sherby et al. (1977) showed that the creep behavior was proportional to the substructure grain size, λ, to the third power, i.e., λ^3. They also concluded that in materials where a subgrain size during creep was relatively constant, the steady-state creep rate was better described by a stress exponent of 8, rather than the conventional value of 5 for dislocation creep. Thus, the following equation was used to describe the steady-state creep rate in pure aluminum:

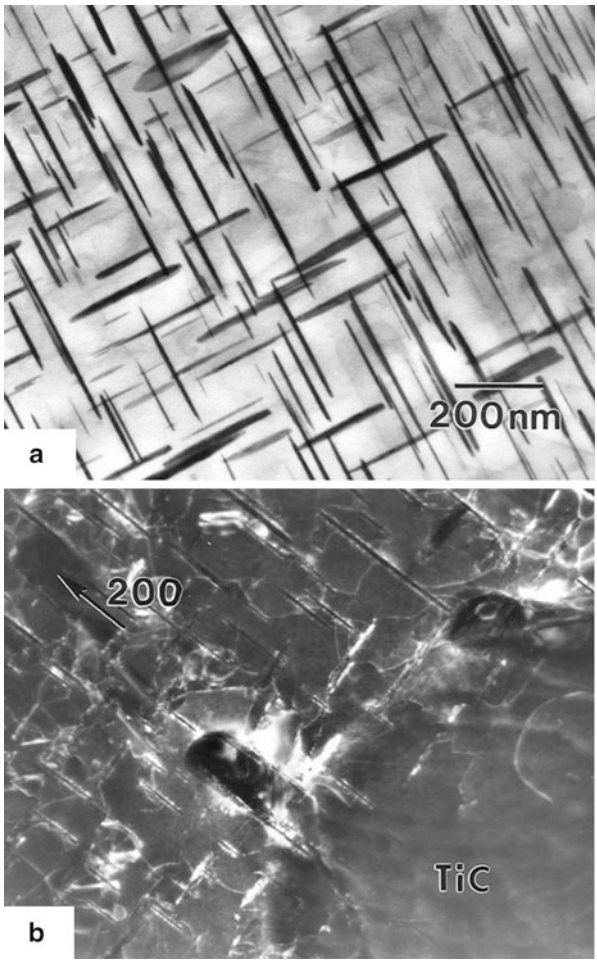

Fig. 9.14 Precipitate structure in the matrix of a 2219/TiC/15$_p$-T6 composite (after Krajewski et al. 1993): (**a**) as-processed and (**b**) after creep deformation at 250 °C and 75 MPa. Note the interactions between dislocations and precipitates (courtesy of P. Krajewski)

$$\dot{\varepsilon} = S\left(\frac{D_{eff}}{b^2}\right)\left(\frac{\lambda}{b}\right)^3\left(\frac{\sigma}{E}\right)^8$$

where S is a constant, E is the Young's modulus of the materials, and D_{eff} is the effective diffusivity for creep. Krajewski et al. (1993, 1995) also found that the creep rate in 2219/TiC/15$_p$ composites was proportional to the interprecipitate spacing, in the matrix, to the third power. They rationalized this behavior by postulating that a substructure is formed due to the presence of the reinforcement, and the size of the substructure may be controlled by the interprecipitate spacing.

The anomalously high values of the stress exponent, n, and activation energy, Q, can be rationalized by using the concept of a threshold stress (Webster 1982;

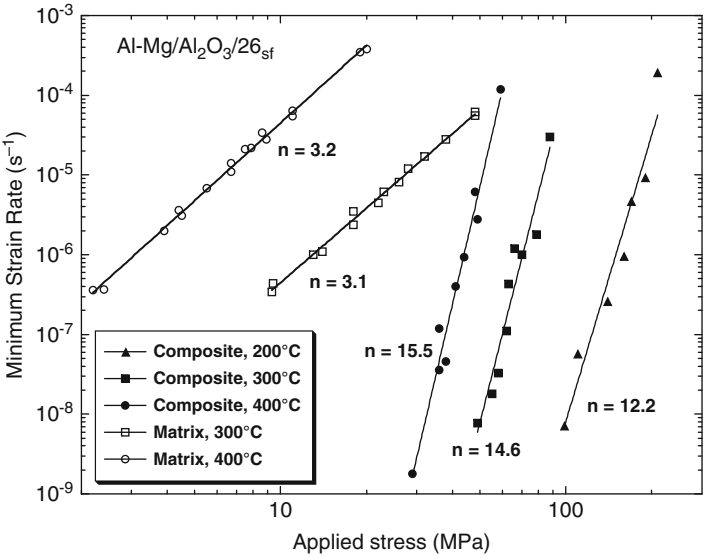

Fig. 9.15 Comparison of creep behavior of Al-5 $Mg/Al_2O_3/26_{sf}$ versus the unreinforced alloy (after Dragone and Nix 1992). Anomalously high values of the stress exponent, n, were observed in the composite

Nieh 1984; Nardone and Strife 1987). Nardone and Strife (1987) used the concept of a threshold stress, σ_R, for creep deformation in composites. This theory was originally used to explain the high values for Q and n in dispersion-strengthened alloys (Davies et al. 1973; Parker and Wilshire 1975; Nardone and Tien 1986; Kerr and Chawla 2004). By introducing the threshold stress, the general steady-state creep rate is modified to

$$\dot{\varepsilon}_{ss} = A\left(\frac{\sigma - \sigma_R}{E}\right)^n \exp\left(\frac{-Q}{RT}\right)$$

where A is a constant, E is the elastic modulus of the composite, and Q is the activation energy. A methodology for determining the threshold stress from experiments is shown in an inset.

The physical explanation for the threshold stress in discontinuously reinforced composites can be attributed to a variety of reasons (Dunand and Derby 1993; Pandey et al. 1992): (1) Orowan bowing between particles, (2) back stress associated with dislocation climb, and (3) attractive force between dislocations and particles, resulting from relaxation of the strain field of dislocations at the particle/matrix interface (Arzt and Wilkinson 1986). Due to the higher work-hardening rate of the matrix, i.e., the addition of particle results in a smaller volume of matrix material, increasing the work-hardening rate relatively to the unreinforced alloy,

the enhancement of dislocation/dislocation interactions can contribute to σ_R, although this mechanism is more plausible at ambient temperature.

A threshold stress approach cannot always be used to explain the high stress exponents observed in MMCs. Load transfer to the reinforcement, despite the lower aspect ratios of particles and whiskers, is significant. With increasing load transfer to the reinforcement, the resolved shear stress on dislocations in the matrix may be lowered significantly below that required for Orowan bowing. Dragone and Nix (1992) studied the creep behavior of Al_2O_3 short fiber reinforced Al-5 % Mg alloy between 200 and 400 °C. They also observed anomalously high values of stress exponent (n ~ 12–15) in the composites, while the unreinforced alloy exhibited much lower, typical values (n ~ 3), see Fig. 9.15. The measured activation energy (225 kJ/mol) for the composites was also anomalously high. A threshold stress analysis showed that the contribution from Orowan bowing was very small. Using a model consisting of randomly oriented short fibers in the Al alloy matrix, and considering the progressive damage to the fibers during creep, they were able to predict the experimentally observed high values of stress exponent and activation energy. Dragone and Nix (1990) also noted that the arrangement of fibers had a significant effect on the degree of matrix constraint. A decrease in effective stress (increase in matrix constraint) was observed with increasing volume fraction, fiber aspect ratio, and degree of overlap between fibers. Figure 9.16 shows a decrease in the von Mises stress in the matrix with increasing volume fraction and aspect ratio of the short fibers. The stress and strain distributions in fiber and matrix with increasing time are shown in Fig. 9.17. The stress in the fiber increases steadily with creep, indicating load transfer from the matrix to the fiber. Localization of plastic stain begins at the sharp corner of the fiber and progresses at the fiber/matrix interface normal to the loading axis. The normal and shear stresses at the fiber/matrix interface are also quite large, indicating that void growth or debonding may take place during the creep process.

Threshold Stress Analysis in Creep

The threshold stress analysis can be illustrated as follows. The figure in part (a) (after Li and Langdon 1998a) below shows the experimental creep data for an Al 7005/Al_2O_3/20_p composite, in terms of shear strain rate, $\dot{\gamma}$, versus shear stress, τ, between 573 and 773 K. As described above, the composite exhibits an increasing stress exponent with decreasing applied stress.

The next step is to find the "true" stress exponent. This is obtained by plotting the data in terms of $\dot{\gamma}^{1/n}$ for several values of n. The plot with the best linear fit is usually a good indication of the true stress exponent. In the current case, a stress exponent of ~4 was obtained, part (b) (after Li and Langdon 1998a). The exponent calculated from linear regression should be similar to that of the unreinforced alloy, where pure metallic behavior applies (unless the matrix itself has some oxide dispersions and behaves as a dispersion-

(continued)

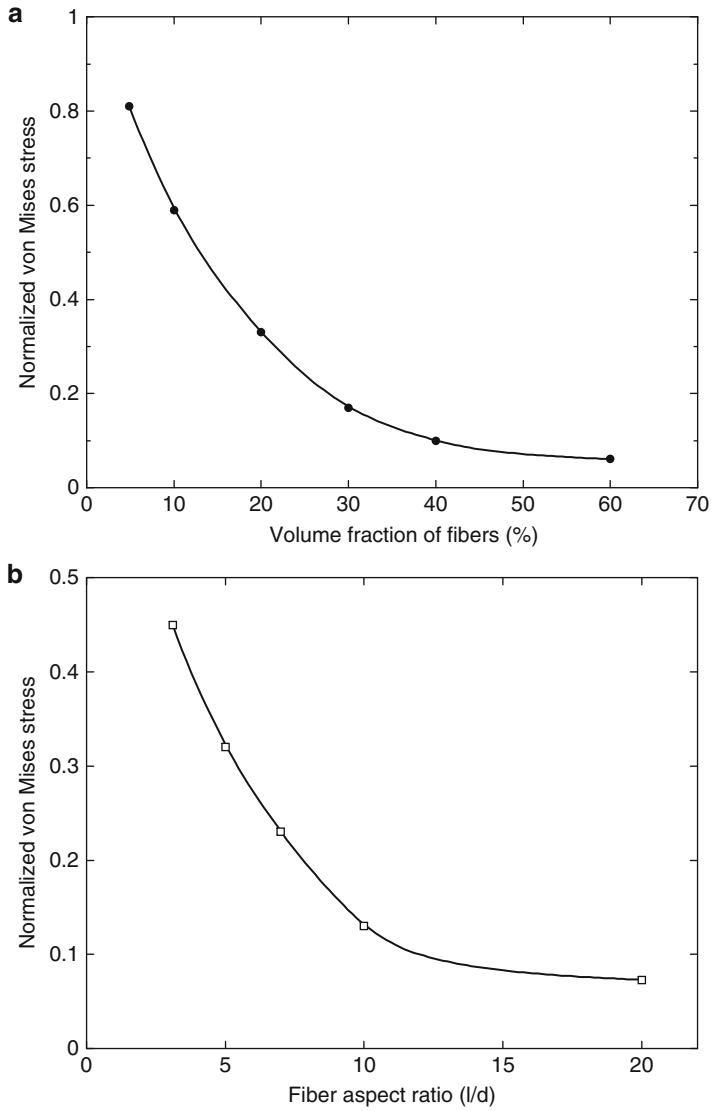

Fig. 9.16 Finite element model of creep in an Al_2O_3 short fiber reinforced Al alloy matrix composite (after Dragone and Nix 1990). The von Mises stress in the matrix decreases with: (**a**) increasing volume fraction and (**b**) aspect ratio of the short fibers

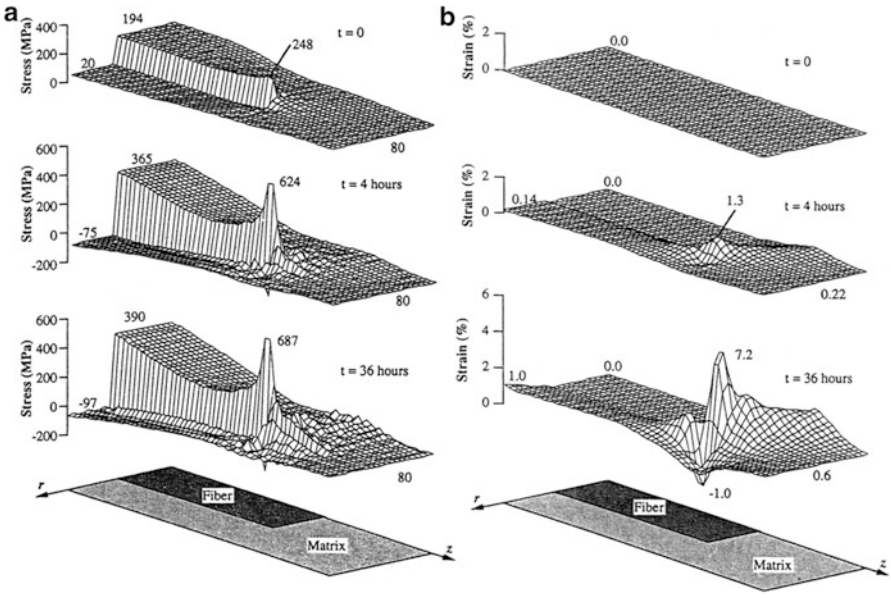

Fig. 9.17 Finite element model of creep in an Al_2O_3 short fiber reinforced Al alloy matrix composite: (**a**) stress distribution and (**b**) strain distribution during, with increasing time (after Dragone and Nix 1990; courtesy of W.D. Nix). The stress in the fiber increases steadily with creep, indicating load transfer from the matrix to the fiber. Localization of plastic stain begins at the sharp corner of the fiber and progresses at the fiber/matrix interface normal to the loading axis

Threshold Stress Analysis in Creep (continued)

strengthened material). Linear extrapolation of the linear fits to the x-axis yields the threshold stress of the material at a given temperature, τ_o.

In order to complete the analysis, the normalized creep rate is plotted versus the effective stress, part (c) (after Li and Langdon 1998a). The normalized creep rate, from the Mukherjee–Bird–Dorn equation, is given by

$$\frac{\dot{\gamma} kT}{D_c Gb}$$

The effective stress is the applied stress minus the threshold stress, normalized by the temperature dependence of the shear modulus:

$$\frac{(\tau - \tau_o)}{G}$$

If the threshold stress values are correct, the above plot should "collapse" the data for all temperatures onto a single line with a slope equal to the true stress exponent.

Other continuum-based unit-cell approaches have also been used to model creep of discontinuously reinforced metal matrix composites (Bao et al. 1991; Davis and Allison 1995; Atkins and Gibeling 1995; Biner 1996). Assuming a spherical particle and the power-law creep formulation for the metal matrix, Davis and Allison (1995) showed that the ratio of composite to matrix steady-state creep rates depended primarily on the volume fraction and geometry of the reinforcing phase, with the stress exponent of the composite and that of the matrix remaining relatively constant. The higher resistance to creep in the composite is largely attributed to the constrained matrix flow, leading to a reduced creep rate in the composite. Changes in modulus ratio of reinforcement to matrix affected the initial stress distribution and creep rates, but did not really affect the final creep rates. Higher modulus mismatch between reinforcement and matrix resulted in higher initial creep rates. Residual stresses due to thermal expansion mismatch also resulted in higher initial creep rates in the composite.

Other aspects of creep deformation, such as grain boundary sliding, have also been included (Biner 1996). It was shown that when the grains in the matrix were allowed to slide, incorporation of the reinforcement resulted in an enhancement in stress in the matrix (described above) which can result in inhomogeneous grain boundary sliding. Figure 9.18a shows the evolution of grain boundary cavitation and sliding in a short fiber reinforced metal matrix composite. As described above, the strain concentration takes place at the pole of the reinforcement, which coincides with the onset of matrix grain cavitation. With increasing time, grain boundary sliding takes place at the cavities or facet cracks. This effect is accentuated with an increase in reinforcement aspect ratio, see Fig. 9.18b, as the local strain concentration in the matrix, immediately above the reinforcement, increases. Figure 9.19 shows a comparison of predicted creep rates for (1) matrix exhibiting cavitation and sliding, (2) composite exhibiting matrix cavitation and sliding, and (3) composite exhibiting matrix cavitation without sliding. The unreinforced alloy has a higher creep rate than the composite. The composite with matrix sliding but no cavitation exhibits slower creep rates at lower stress, but the creep rates approach that of the matrix at relatively large stress.

It has also been observed that below a critical strain rate, diffusional relaxation around the SiC particles is the rate-controlling mechanism, while above this point, a greater degree of load is carried by the high-stiffness particles (Zong and Derby 1997). In addition to the threshold stress, additional proposed mechanisms for the anomalously high values of Q and n include power-law breakdown for the matrix (Zong and Derby 1997; Lilholt 1985) and interfacial decohesion at the particle/matrix interface (Taya and Lilholt 1986). The reinforcement may contribute to changes in the matrix during creep by localized recrystallization at corners or interfaces and precipitate coarsening at the particle/matrix interface, where the density of precipitates is the highest (because of the greatest thermal mismatch stress upon cooling being at the interface).

It is interesting to note that in powder-processed composite materials, oxide dispersions (not present in the unreinforced alloy) may also contribute to extremely high "anomalous" values of n and Q (Park et al. 1990; Li and Langdon 1998b). Park

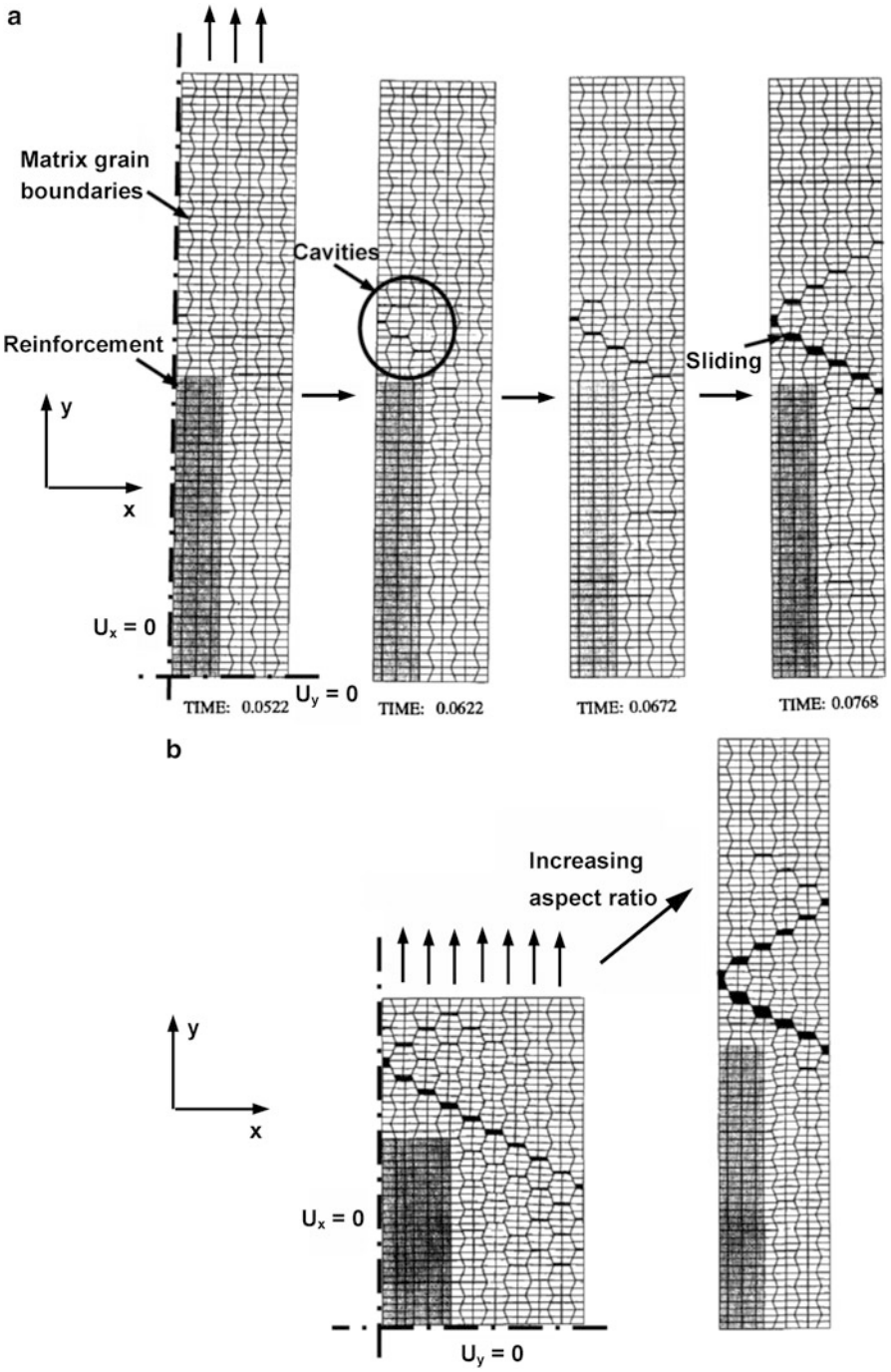

Fig. 9.18 (**a**) Finite element modeling of grain boundary cavitation and sliding in a short fiber reinforced metal matrix composite (after Biner 1996; courtesy of S. Biner). Strain concentration takes place at the pole of the reinforcement, which coincides with the onset of matrix grain cavitation. With increasing time, sliding takes place at the cavities or facet cracks. (**b**) Increase in reinforcement aspect ratio accentuates local strain concentration in the matrix

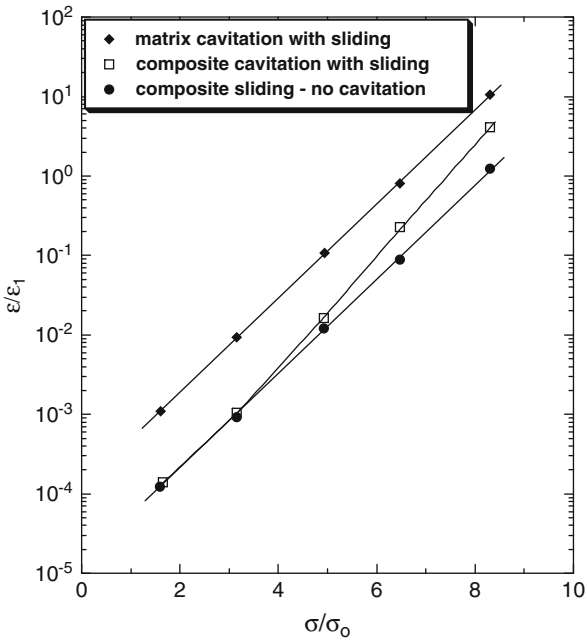

Fig. 9.19 Finite element model comparison of predicted creep rates for (1) matrix exhibiting cavitation and sliding, (2) composite exhibiting matrix cavitation and sliding, and (3) composite exhibiting matrix cavitation without sliding (after Biner 1996). The unreinforced alloy has a higher creep rate than the composite. The composite with matrix sliding but no cavitation exhibits slower creep rates at lower stress, but the creep rates approach that of the matrix at relatively large stress

et al. (1990) suggested that the presence of fine oxide particles, incoherent with the matrix, arising from the powder metallurgy process used to fabricate the composite, served as effective barriers for dislocation motion and gave rise to a threshold creep stress. The high creep stress exponent and increase in exponent with decreasing applied stress were attributed to the oxide particles in the matrix. The work of Li and Langdon (1998a) supports this conclusion. They add that in composites processed via ingot metallurgy, compared to powder metallurgy-processed composites of the same composition, viscous glide is the rate-controlling mechanism because of the absence of oxide particles.

Li and Langdon (1998a) also proposed two separate classes of creep behavior in metal matrix composites. In class M (pure metal type), materials dislocation climb is the rate-controlling mechanism, with a stress exponent of around 5 and activation energy similar to the value for self-diffusion in the matrix. In class A (alloy type) metals, viscous dislocation glide is the rate-controlling mechanism, with a stress exponent of around 3 and an activation energy associated with the viscous drag of the solute atmospheres. Exceptionally high creep rates were observed at the highest stress levels, perhaps due to dislocations breaking away from solute atom atmospheres (Li and Langdon 1998b). It should be noted that in unreinforced solid solution alloys, a transition occurs between class M behavior at low stresses and class A behavior at higher stresses (Yavari et al. 1981).

Li and Langdon (1998a) derived an expression which can be used to determine the transition in material behavior from class M to class A:

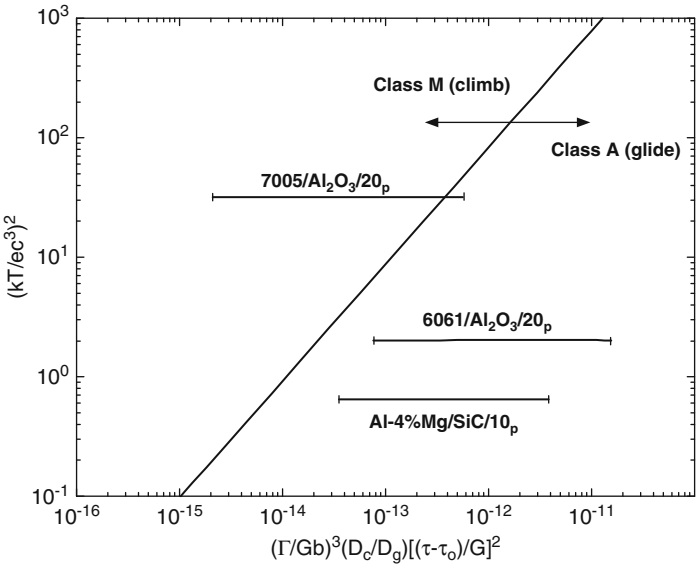

Fig. 9.20 Graphical representation of the transition from class M (pure metal type) behavior class A (alloy type) behavior (after Li and Langdon 1998a)

$$\alpha\left(\frac{kT}{ec^{1/2}Gb^3}\right)^2 = B\left(\frac{\Gamma}{Gb}\right)^3\left(\frac{D_c}{D_g}\right)\left(\frac{\sigma_e}{G}\right)^2$$

where σ_e is the effective stress, β is a constant associated with the relative contributions from various viscous glide processes, e is the solute–solvent size mismatch, Γ is the stacking fault energy of the matrix, B is a constant, and D_c and D_g are the diffusion coefficients for dislocation climb and glide, respectively. A graphical representation of this equation, for several material systems, is shown in Fig. 9.20.

9.3 Superplasticity

Superplasticity can be defined as the ability of a material to undergo very large plastic strains in a uniform manner (>100 % strain), i.e., without necking (Meyers and Chawla 2009). The stress (σ)–strain-rate ($\dot{\varepsilon}$) behavior of most materials can be described by the following equation:

$$\sigma = K\dot{\varepsilon}^m$$

where K and m are constants, and m is termed the strain-rate sensitivity parameter. For a Newtonian viscous solid, $m = 1$. Thus, any enhancement in m will contribute to an enhancement in superplasticity. In most alloys, the microstructural

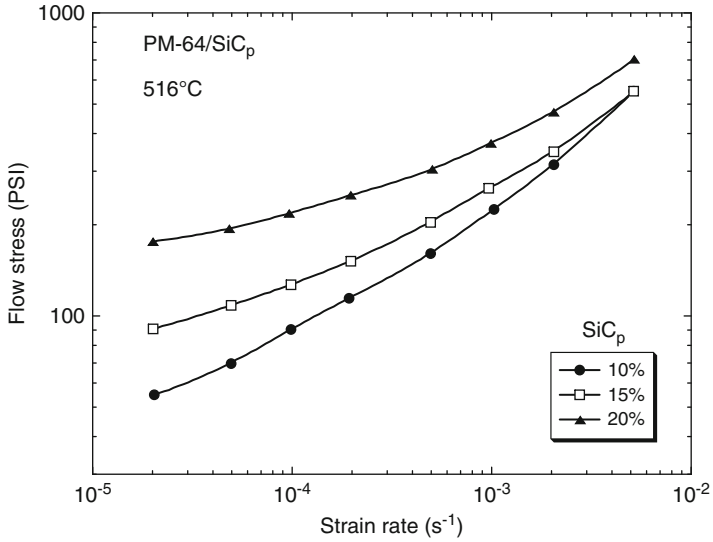

Fig. 9.21 Slow stress versus strain rate during superplasticity at 516 °C of an Al alloy matrix composites reinforced with SiC particles (after Mahoney and Ghosh 1987). An increase in SiC volume fraction resulted in an increase in the flow stress necessary for superplasticity

requirement for a high value of m is a very fine grain size. This is because the large plastic strains attained in superplasticity are accommodated by grain boundary sliding (Ahmed and Langdon 1977; Mohamed et al. 1977).

Superplasticity has been demonstrated in particle-reinforced metal matrix composites, such as SiC particle or whisker-reinforced Al. Because of the lower ductility and higher strain-hardening rates in these materials, conventional superplasticity by reduction in grain size is not feasible. Wu and Sherby (1984) used thermal cycling to generate internal stresses in the composite, due to thermal expansion mismatch between reinforcement and matrix. The internal stresses assisted plastic flow and increased the m exponent. Nieh et al. (1984) conducted isothermal forming in the solid–liquid region of the material and were able to obtain 300 % strain at relatively high strain rates (~3×10^{-1}/s). Mahoney and Ghosh (1987) studied the superplastic behavior of an Al–Zn–Mg–Cu matrix composite with SiC particles (about 5 μm in diameter). They were able to achieve superplastic strains of 500 % in the composite, compared to 800 % in the unreinforced alloy. Figure 9.21 shows a plot of flow stress versus strain rate during superplasticity at 516 °C. An increase in SiC volume fraction resulted in an increase in the flow stress necessary for superplasticity. The flow stress versus strain-rate behavior was divided into three regions, see Fig. 9.22. The expected behavior of the composite is given by the dashed line. The measured flow stress, however, particularly in Region I, is much higher than the expected behavior. This was attributed to a threshold stress due to pinning of grain boundaries by the SiC particles. In Region

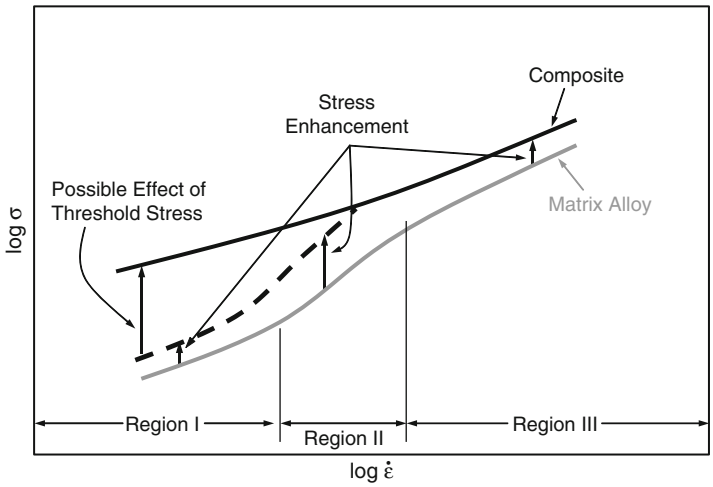

Fig. 9.22 Schematic of flow stress versus strain rate behavior for MMCs and unreinforced alloy (after Mahoney and Ghosh 1987). The expected behavior of the composite is given by the *dashed line*. The measured flow stress, particularly in Region I, is much higher than the expected behavior. In Region II, the strain rate sensitivity is the highest (highest value of m), while in Region III, superplasticity is controlled by dislocation creep in the matrix

II, the strain rate sensitivity is the highest (highest value of m), while in Region III, superplasticity is controlled by dislocation creep in the matrix.

The measured activation energies during superplasticity are often higher than for lattice diffusion or grain boundary diffusion. Li and Langdon (1998c) showed that by incorporating the contribution of load transfer to the particles (through a threshold stress approach), the true activation energy was similar to that for grain boundary diffusion. Mishra et al. (1997) studied the mechanisms for superplasticity in Si_3N_4 particle-reinforced 2124Al matrix composites. In single phase materials, slip accommodation is provided by grain boundary sliding. In dispersion-strengthened systems, where fine second-phase particles are present, they pin the grain boundaries, so local diffusional relaxation around the particles must take place. In particle-reinforced MMCs, however, the particles are larger than those in dispersion-strengthened systems, so sliding is controlled by diffusional accommodation at the particle/matrix interface. If strain accommodation does not take place, then cavitation will occur. Mahoney and Ghosh (1987) showed that for a given applied strain, an increase in reinforcement fraction led to an increase in the fraction of voids, see Fig. 9.23a. This can be explained by the increase in triaxiality of stress in the matrix due to the presence of rigid, nondeforming particles (see Chap. 7).

The onset of cavitation can be delayed by the superposition of a compressive hydrostatic pressure, which counteracts the triaxial tensile stress (Vasudevan et al. 1989; Lewandowski and Lowhaphandu 1998). Figure 9.22b shows the delay

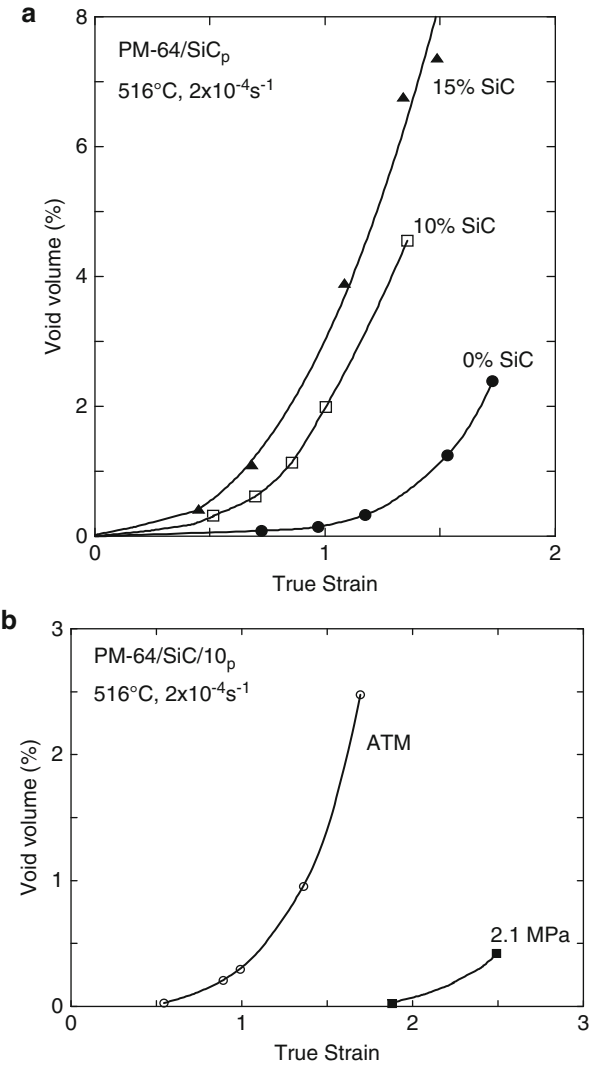

Fig. 9.23 (**a**) Increase in degree of cavitation (void volume) with increase in SiC particles in an Al alloy matrix composite (after Mahoney and Ghosh 1987). If strain accommodation does not take place, then cavitation will occur. The increase in traixiality of stress in the matrix due to the presence of rigid, non-deforming particles results in cavitation. (**b**) Delay in the onset of cavitation results when a compressive hydrostatic pressure is superimposed, which counteracts the triaxial tensile stress

in the onset of void growth, during superplasticity, by the superposition of a hydrostatic pressure. Mabuchi and Higashi (1999) suggested that a liquid phase during superplasticity may also decrease local stress concentrations and delay the onset of superplasticity. A large fraction of liquid phase is not desirable, however, since it will form a brittle intermetallic between the particle and matrix (see Chap. 5), and cavitation will take place (Mishra et al. 1997).

References

Ahmed, M.M.I., and T.G. Langdon (1977) *Metall. Trans.*, **8**, 1832.
Arzt, E., and D.S. Wilkinson (1986) *Acta Metall Mater.*, **34**, 1893–1898.
Atkins, S.L., and J.C. Gibeling (1995) *Metall. Mater. Trans.*, **26A**, 3067–3079.
Bao, G., J.W. Hutchinson, and R.M. McMeeking (1991) *Acta Metall. Mater.*, **39**, 1871–1882.
Biner, S.B. (1996) *Acta Mater.*, **44**, 1813–1829.
Bullock, E., M. McLean, and D.E. Miles (1977) *Acta Metall.*, **25**, 333–344.
Davies, P.W., G. Nelmes, K.R. Williams, and B. Wilshire (1973) *Metal Sci. J.*, **7**, 87–92.
Davis, L.C., and J.E. Allison (1995) *Metall. Mater. Trans.*, **26A**, 3081–3089.
Dlouhy, A., N. Merk, and G. Eggeler (1993) *Acta Metall. Mater.*, **41**, 3245–3256.
Dlouhy, A., G. Eggeler, and N. Merk (1995) *Acta Metall. Mater.*, **43**, 535–550.
Dragone, T.L., and W. D. Nix (1990) *Acta Metall. Mater.*, **38**, 1941.
Dragone, T.L., and W. D. Nix (1992) *Acta Metall. Mater.*, **40**, 2781.
Dunand, D.C., and B. Derby (1993) in *Fundamentals of Metal Matrix Composites*, (S. Suresh, A. Mortensen, and A. Needleman, eds.), Butterworth-Heinneman, Boston, pp. 191–214.
Evans, R.W., and B. Wilshire (1993) *Introduction to Creep*, The Institute of Materials, London.
Goto, S., and M. McLean (1989) *Scripta Mater.*, **23**, 2073–2078.
Goto, S., and M. McLean (1991) *Acta Metall. Mater.*, **39**, 153–164.
Kerr, M., and N. Chawla (2004) *Acta Mater.*, **52**, 4527–4535.
Krajewski, P.E., J.E. Allison, and J.W. Jones (1993) *Metall. Trans.*, **24A**, 2731–2741.
Krajewski, P.E., J.E. Allison, and J.W. Jones (1995) *Metall. Mater. Trans.*, **26A**, 3107–3118.
Kurumlu, D., E.J. Payton, M.L. Young, M. Schöbel, G. Requena, G. Eggeler (2012) *Acta Materialia*, **60**, 67–78.
Lee, S., S.M. Jeng, and J.-M. Yang (1995) *Mech. Mater.*, **21**, 303–312.
Lewandowski, J.J., and P. Lowhaphandu (1998) *Int. Mater. Rev.*, **43**, 145–187.
Leyens, C., J. Hausmann, and J. Kumpfert (2003) *Adv. Eng. Mater.*, **5**, 399–410.
Li, Y., and T.G. Langdon (1998a) *Acta Mater.*, **46**, 1143–1155.
Li, Y., and T.G. Langdon (1998b) *Mater. Sci. Eng.*, **A245**,1–9.
Li, Y., and T.G. Langdon (1998c) *Acta Mater.*, **46**, 3937–3948.
Lilholt, H. (1985) *Comp. Sci. Tech.*, **22**, 277–294.
Lilholt, H. (1991) *Mater. Sci. Eng.*, **A135**, 161-171.
Mabuchi, M., and K. Higashi (1999) *Acta Mater.*, **47**, 1915–1922.
Mahoney, M., and A.K. Ghosh (1987) *Metall. Trans.*, **18A**, 653–661.
Meyers, M.A., and K.K. Chawla (2009) *Mechanical Behavior of Materials*, 2nd ed., Cambridge University Press, Cambridge, UK, pp. 653–705.
Mishra, R.S., T.R. Bieler, and A.K. Mukherjee (1997) *Acta Mater.*, **45**, 561–568.
Mohamed, F.A., M.M.I. Ahmed, and T.G. Langdon (1977) *Metall. Trans.*, **8**, 933.
Mukherjee, A.K., J.E. Bird, and J.E. Dorn (1964) *Trans. ASM*, **62**, 155.
Nardone, V.C., and J.R. Strife (1987) *Metall. Trans.*, **18A**, 109–114.
Nardone, V.C., and J.K. Tien (1986) *Scripta Mater.*, **20**, 797–802.
Nieh, T.G. (1984) *Metall. Trans.*, **15A**, 139–146.
Nieh, T.G., C.A. Henshall, and J. Wadsworth (1984) *Scripta Metall.*, **18**, 1405–1408.
Ohno, N., K. Toyoda, N. Okamoto, T. Miyake, and S. Nishide (1994) *Trans. ASME*, **116**, 208–214.
Pandey, A.B., R.S. Mishra, and Y.R. Mahajan (1992) *Acta Metall. Mater.*, **40**, 2045–2052.
Park, K.-T., E.J. Lavernia, and F.A. Mohamed (1990) *Acta Metall. Mater.*, **38**, 2149–2159.
Parker, J.D., and B. Wilshire (1975) *Metal Sci. J.*, **9**, 248–252.
Sherby, O.D., R.H. Klundt, and A.K. Miller (1977) *Metall. Trans.*, **8A**, 843–850.
Sørensen, N, A. Needleman, and V. Tvergaard (1992) *Mater. Sci. Eng.*, **A158**, 129–137.
Taya, M., and H. Lilholt (1986) in *Advances in Composite Materials and Structures* (S.S. Wang and Y.D.S. Rajapakse, eds.), ASME, New York, 21–27.

Vasudevan, A.K., O Richmond, F. Zok, and J.D. Embury (1989) *Mater. Sci. Eng*., **A107**, 63–69.
Webster, D. (1982) *Metall. Mater. Trans*., **13A**, 1511–1519.
Whitehouse, A.F., H.M.A. Winand, and T.W. Clyne (1998) *Mater. Sci. Eng*., **A242**, 57–69.
Wu, M.Y., and O.D. Sherby (1984) *Scripta Metall*., **18**, 773–776.
Yavari, P., F.A. Mohamed, and T.G. Langdon (1981) *Acta Metall*., **29**, 1495.
Zong, B.Y., and B. Derby (1997) *Acta Mater*., **45**, 41–49.

Chapter 10
Wear and Corrosion

10.1 Introduction

Wear can be defined as the loss of material that occurs when two surfaces rub against each other. Two common forms of wear are:

- Adhesive wear
- Abrasive wear

Adhesive wear is also known as scouring, galling, or seizing. Deformation in shear is the main mechanism in adhesive wear. Generally, high contact stresses are involved which lead to local plastic deformation, resulting in the formation of adhesive bonds between the two surfaces; see Fig. 10.1. Continuing the sliding motion increases the shear stress in the bonded region until the yield strength of the softer material is significantly exceeded.

Abrasive wear occurs when hard ceramic particles such as WC or SiC get trapped between the sliding surfaces as shown in Fig. 10.2a. This is called two-body abrasive wear. The degree of material loss (volume or mass) is a function of the relative hardness of the ceramic particles and the sliding surface area. Environment can be an additional factor in wear. It can lead to fretting, cavitation, erosion, etc. During abrasive wear, the surface asperities are worn down and the contact surfaces become mated. This reduces the local contact stress because of the increase in contact area. After this initial abrasive wear, the removal of oxidized particles occurs along the surface. This is generally a steady-state process inasmuch as it requires reoxidation of the denuded surface in order to continue removing oxidized particles. The final stage of wear occurs in adhesive mode and occurs if the contact pressure increases to the point of shearing the particles. The result of shear is the formation of thin plate-like sheets of wear debris. Depending upon the applied load, the sheets can result in significant material loss.

It is important to remember that, more often than not, wear is a system property. Consider the different types of variables involved: the matrix, reinforcement fibers or particles, orientation of fibers with respect to the wear direction, reinforcement/

N. Chawla and K.K. Chawla, *Metal Matrix Composites*,
DOI 10.1007/978-1-4614-9548-2_10,

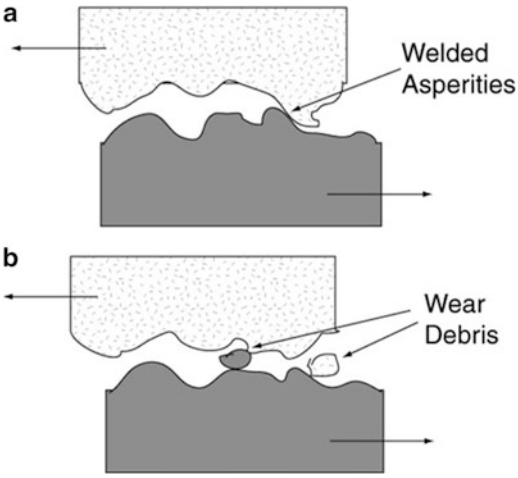

Fig. 10.1 Adhesive wear due to high contact stresses which lead to local plastic deformation and (**a**) welded asperities and (**b**) wear debris between the two surfaces

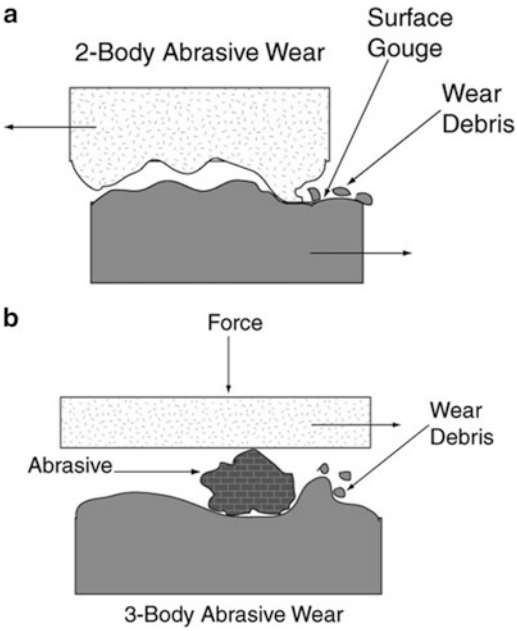

Fig. 10.2 Abrasive wear involving ceramic particles such as WC or SiC leading to debris trapped between the sliding surfaces: (**a**) two-body wear and (**b**) three-body wear

matrix interface, and morphology, size, and volume fraction of the phases in the composite. These are *intrinsic* microstructural variables. Testing or operational conditions can also affect the wear behavior. These include the type of counter surface or abrasive, force, speed, contact area, geometry, and environment (lubrication or dry). These are *extrinsic* variables. Two important wear testing techniques are described in the inset.

Under appropriate conditions, the addition of ceramic particles to a metal matrix can lead to improved wear resistance. It should be recognized, however, that if the conditions are not suitable, the addition of ceramic particles may decrease wear resistance. For example, the ceramic particles may be removed from the matrix and lead to a wear process by three-body abrasive wear as shown in Fig. 10.2b. Another point to keep in mind is that as the volume fraction or size of the reinforcement becomes large, the fracture toughness of the composite will be reduced significantly. If the fracture toughness is inadequate, the reinforcement particles will fracture and contribute to the wear process. Increasing wear resistance without a penalty in toughness is a challenge.

Most of the work in the area of wear of MMCs has been on particle-reinforced composites. Thus, in this chapter we focus mainly on the wear behavior of two important systems: silicon carbide/aluminum composites and tungsten carbide/cobalt. In the end we devote a short section on wear aspects in braking materials. A more comprehensive treatment on the applications of braking materials is given in Chap. 11.

Wear Testing

Pin-on-Disk Wear Testing (*ASTM G99-95a*)

In this test, a normal load is applied via a pin onto a rotating disc. The sliding motion may be in one direction or reciprocating. The tests may be conducted in dry or under lubrication. The coefficient of friction, μ, can be obtained from this test at any point in the test. Typically one measures the mass before and after the wear test by means of a sensitive microbalance. The wear rate is given by

$$\text{wear rate} = \frac{\text{mass loss}}{\text{sliding distance}}$$

The wear rate may also be reported as

$$\text{wear rate} = \frac{\text{volume loss}}{\text{sliding distance}}$$

High-Stress and Low-Stress Wear Testing

In the high-stress wear test (ASTM B611), a coarse alumina particle slurry (~590 μm) is used as an abrasive. A steel wheel is rotated at 100 rpm through the slurry bath. The test sample is pressed against the steel wheel with a known force. One measures the mass loss, after 1,000 revolutions of the steel wheel, and obtains the wear number as

(continued)

(continued)

$$\text{Wear number} = \frac{\text{Density}}{\text{Mass loss}}$$

Physically, the wear number gives the number of revolutions to remove a unit volume of the sample. The higher the wear number, the better the wear resistance.

In the low-stress wear test (ASTM G65), dry quartz sand (particle size, 200–300 μm) is used as the abrasive. It is softer than the alumina slurry used in the high-stress wear test. Instead of a steel wheel, a rubber wheel is used. After 0.5 h at 200 rpm, we obtain the volume loss as

$$\text{Volume loss} = \frac{\text{Mass loss}}{\text{Density}}$$

The lower the volume loss, the higher the wear resistance.

10.2 Particle Reinforced Aluminum Matrix Composites

In the abrasive stage of wear of MMCs, the degree of abrasion is a function of the applied load, speed, size and volume fraction of reinforcement, and interfacial bond strength between the reinforcement and matrix. Several researchers have examined the abrasive wear resistance of several Al alloys containing a range of ceramic particles and volume (Hosking et al. 1982; Wang and Rack 1991; Chung and Hiang 1994; Zhang et al. 1995; Garcia-Cordovilla et al. 1996). The addition of ceramic particles, such as alumina, to aluminum alloys results in substantial reduction of the wear rate (Hosking et al. 1982), i.e., the wear performance is improved. The reduction in wear rate is influenced by the size of the reinforcement particle and the volume fraction of reinforcement. The greatest wear resistance is typically achieved with the alloy containing the largest volume fraction and the largest particle size, as shown in Fig. 10.3. Figure 10.4 shows an example of the effect of SiC particles on wear resistance (Venkataraman and Sundarajan 1996a, b). The improvement of the composite over the unreinforced alloy is greatest at higher loads.

After wear, the worn surface of the unreinforced aluminum alloys typically consists of long, continuous grooves, which are the result of abrasive particles plowing the surface. The surface of composites, on the other hand, exhibits substantially reduced surface plowing (Garcia-Cordovilla et al. 1996). The wear rate of the composites decreases as the volume fraction of reinforcement increases. This may be attributed to the particle strength being higher than the interface strength, for smaller particles. Thus, the smaller particles are pulled out before fracturing.

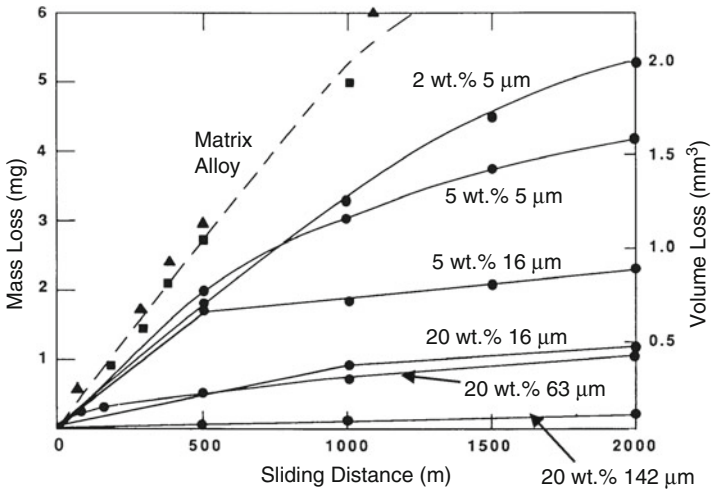

Fig. 10.3 Improved wear resistance of aluminum 2024 alloy matrix composites with increasing volume fraction and size of the alumina particles (After Hosking et al. 1982)

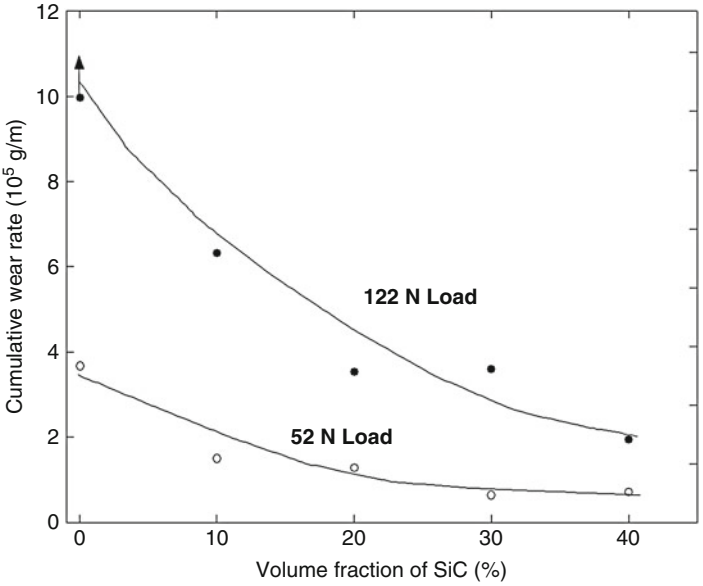

Fig. 10.4 Increase in wear resistance with increased volume fraction of SiC (After Venkataraman and Sundarajan 1996a)

The larger particles remain in the matrix longer and are able to carry the surface load until they fracture into smaller particles.

One should remember that, besides hardness, the fracture toughness of the reinforcement also has an important role to play. As the stress is increased, the fracture toughness of the reinforcement becomes an important parameter. The fracture toughness determines the extent of fracture of the reinforcement. Thus, the governing factor for wear with increased stress is the fracture toughness of the reinforcement particles.

Oxidation of surface debris during wear process is another phenomenon during wear of MMCs. Abrasion transforms to oxidative wear after a certain sliding distance. With increasing load, the wear behavior changes from mild, oxidative wear to severe wear by adhesion. Examination of the worn surface and debris indicates that debris formation is more influential on wear rate, within the abrasive regime, than deformation of the material (Ludema 1996). After a certain sliding distance, the surface asperities wear down, which reduces the contact stress because of the increase in contact area for the same load. As a result, the wear rate and coefficient of friction also decrease during this period.

Suh (1973) proposed a delamination wear mechanism wherein voids and cracks nucleate at second-phase particles in the subsurface region, i.e., below the contact surface. This was attributed to the large hydrostatic pressure acting near the asperity contact. Cracks during wear typically propagate parallel to the contact surface (Suh 1973; Jahanmir and Suh 1977). During sliding wear the surface is plastically deformed, which introduces dislocations in the subsurface region of the contacting materials. These dislocations lead to eventual formation of cracks and/or voids in the subsurface region. Fragmentation of the particles can also lead to decohesion of the particle/matrix interface, resulting in more void formation. With continued sliding, the cracks and void eventually coalesce and result in longer cracks. When the crack reaches a critical length, the material between the crack and the surface is removed from the surface in the form of wear debris. The severe wear by adhesion can occur by such a delamination process initiated by subsurface cracking. Three factors influence this phenomenon: particle size, volume fraction, and type of reinforcement. Larger particles require larger loads to initiate subsurface cracking and eventual delamination. The work of Zhang and Alpas (1993) and Chung and Hiang (1994) supports Suh's delamination theory. They examined cross sections of worn surfaces of aluminum alloys reinforced with SiC particles, which showed evidence of wear debris in the form of flakes. These flakes of debris were produced by subsurface delamination. Microscopic analysis showed cracks, which formed at the particle/matrix interface and propagated parallel to the surface. The cracks and resultant voids coalesced with eventual delamination of material from the surface. Depending upon the rate of wear debris formation, delamination may result in a reduction of wear by the formation of a debris layer between the contacting surfaces. This layer, also termed a mechanically mixed layer (MML), comprises the reinforcement, matrix material, and material from the counter surface (Venkataraman and Sundarajan 1996a, b).

Venkataraman and Sundarajan (1996b) found the hardness of the MML to be approximately six times that of the bulk composite. They hypothesized that as the deformation increased, the reinforcement particles at the wearing surface

fragmented and the number of voids began to increase. Once a critical void density was reached, shear instability was initiated at selected locations within the subsurface. The shear instability promoted turbulent plastic flow, which resulted in a mixture of material from both surfaces. The mixture of the material led to the formation of the MML, which appeared to have a direct influence on the wear rate. The rate of formation of the MML controlled the wear rate and was directly related to delamination wear.

Frequently, improved wear performance can also be obtained by adding a lubricant or by adding a reinforcement that provides lubricating characteristics. Rohatgi et al. (1992) observed that carbon, in the form of graphite particles, in aluminum can decrease the coefficient of friction against dry steel. Carbon in microcrystalline form, on the other hand, had practically no effect. This is understandable inasmuch as graphite flakes cleave easily and serve as lubricants. One should be cautioned that in addition to the parameters described above, the environment can also play a decisive role in the ultimate wear performance.

10.3 Tungsten Carbide/Cobalt Composites

Tungsten carbide/cobalt (WC/Co) composites, commonly known as cemented carbides, are one of the most important metal matrix composites used for their excellent wear resistance (Upadhyaya 1998). They were originally developed for making dies to draw tungsten incandescent filament; wear resistance is clearly very important in such drawing operations. They are also widely used for cutting, machining, and drilling purposes. Cemented carbides consist mainly of fine tungsten carbide particles and the binder metal cobalt.

The wear behavior of conventional WC/Co composites is characterized by plasticity of cobalt matrix and the high strength and hardness of the WC particles. In high-speed machining, the temperature at the cutting edge can exceed 1,000 °C leading to phenomena such as diffusion and oxidation of the cutting tool, abrasion, and adhesion (the chip can adhere to the flank face.) In general, the wear behavior is directly related to hardness, which in turn is a function of volume fraction and size of tungsten carbide particles.

10.3.1 Hardness and Strength of Cemented Carbides

Hardness is a critical property in determining the wear resistance of a material. WC/Co composites have been studied extensively and some useful correlations have been obtained. Lee and Gurland (1978) proposed the following expression for the hardness of WC/Co composites:

$$H = H_{WC}CV_{WC} + H_{Co}(1 - CV_{WC})$$

where H is the hardness of the composite; H_{WC} and H_{Co} are the hardness of WC and Co, respectively; C is the contiguity of the WC particles, and V_{WC} is the volume fraction of WC in the composite. The parameter contiguity is defined as

$$C = \frac{2S_{cc}}{2S_{cc} + S_{cm}}$$

where S_{cc} is the area between the carbide particles and S_{cm} is the area between the carbide particles and the matrix in a unit volume. The hardness of cobalt is related to the mean free path (λ) of the cobalt matrix in the composite by the following empirical relation:

$$H_{Co} = 304 + 12.7\lambda^{-0.5}$$

The important result in this case is that the hardness of cobalt matrix goes as the inverse square of the mean free path.

The homogeneous distribution of a high volume fraction of fine WC particles in a cobalt matrix, in conventional cemented carbides, enhances strength, wear resistance, thermal conductivity, etc. of the composite, but at the expense of toughness. This has led to the development of a new type of composite which we describe in the next section.

10.3.2 Double Cemented Carbide

A novel particulate composite metal matrix composite called double cemented carbide (DCC) has been developed (Fang and Albert 1999; Fang et al. 1999; Deng et al. 2001). This material consists of granules of WC/Co composite embedded within Co or another metal matrix as shown in Fig. 10.5. Thus, it is a kind of "dual" composite with a "composite-within-a-composite" structure. This concept provides microstructural design variables not available in conventional particulate metal matrix composites. We describe some interesting relationships among the processing, microstructure, and properties of this novel composite material. These additional degrees of freedom enable remarkably enhanced *combinations* of properties, such as high toughness and wear resistance.

Figure 10.5a, b shows composites containing 75 vol.% WC particles in a cobalt matrix but with the two different types of structure: (a) conventional particulate composite structure with homogeneously distributed particles and (b) DCC structure. The DCC material has granules of WC/Co in a Co matrix. It has twice the toughness and six times the high-stress abrasive wear resistance than the conventional material, at the same total particle volume fraction. These improvements in properties result from the partitioning of the matrix to produce particle-free matrix

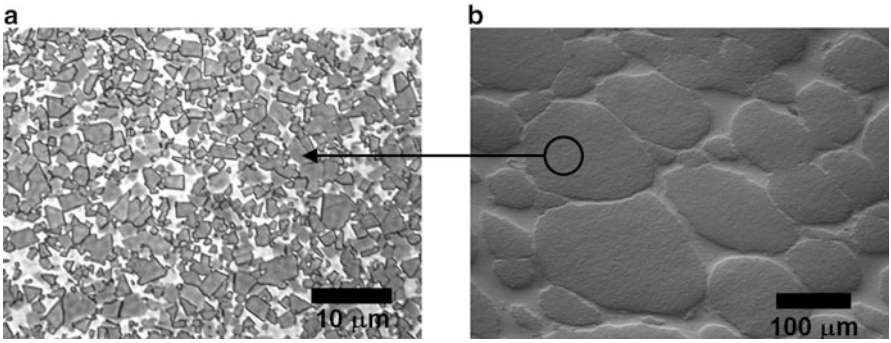

Fig. 10.5 Microstructures of cemented carbide (WC/Co) with (**a**) conventional and (**b**) DCC structure, containing the same *total* cobalt contents, 25 vol.%. The coarse granules in (**b**) have a fine dispersed microstructure similar to that of (**a**)

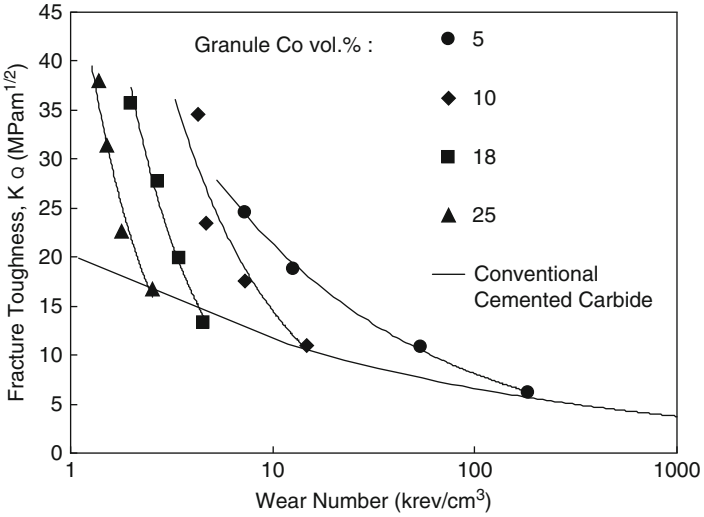

Fig. 10.6 Superior combination of toughness and wear resistance of DC carbide versus conventional cemented carbide (After Deng et al. 2001)

regions separating the granular regions, which have higher particle volume fractions than the overall average. These ductile intergranular regions of Co enhance fracture resistance with little detriment to abrasive wear resistance. Wide ranges of combinations are achievable by fine-tuning of granule composition and properties, granule size, matrix composition, and heat treatment.

Figure10.6 shows a plot of fracture toughness versus wear number in terms of revolutions per unit volume, more specifically, kilo revolutions per unit cm^3. It illustrates the difference in toughness/wear resistance behavior between conventional and DCC composites. Recall that the higher the number of revolutions, the

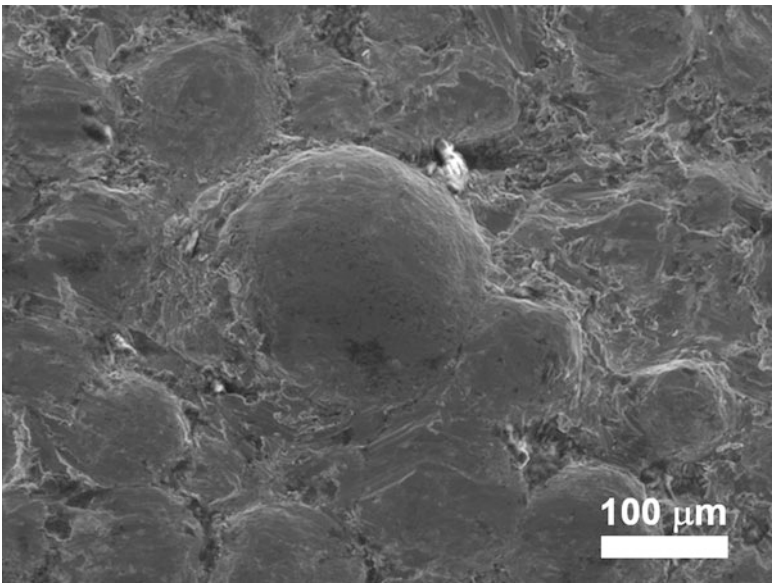

Fig. 10.7 Wear surface of DC carbide after high-stress abrasive wear testing, showing protrusions (After Deng et al. 2001)

better the wear resistance. The thicker line represents the relationship for essentially all grades of conventional cemented carbide, i.e., with wide variations in cobalt matrix fraction and WC particle size. As with most conventional particulate composites, improvement in either property comes at the expense of the other. Thus, enhanced toughness means poor wear resistance and vice versa. This restricted relationship results from the limited degrees of freedom in microstructural design and restricts the balance of properties in essentially all particulate MMCs. The curves for different DCCs with different granule properties (decreased cobalt yields harder granules with increased wear resistance and decreased toughness) and different volume fractions of intergranular matrix show that at comparable wear resistance the DC structure has higher toughness than the conventional structure and at comparable toughness DC has higher wear resistance (Deng et al. 2001).

The improved toughness of the DCC composite is a function of the increased mean free path through the intergranular matrix (~20 μm versus <1 μm in conventional cemented carbide). The improved abrasive wear resistance of the double composite is due to a different wear resistance mechanism than with conventional particulate MMCs. Protrusion of the large, hard composite granules from the wear surface can be seen after wear as shown in Fig. 10.7. The best wear resistance/toughness combination results from a high volume fraction of relatively large, hard granules, since increased granule size increases the intergranular mean free path, which enhances toughness. Larger granules exhibit the greatest protrusion for wear resistance and are the most difficult to remove via matrix erosion.

10.4 Wear in Braking Materials

Wear and frictional characteristics are very important in materials used for braking applications. In addition, one must consider physical properties such as thermal conductivity. Every time we apply a brake to stop a moving vehicle, the kinetic energy of the rotating elements of the vehicle must be absorbed by the brake. This energy is dissipated in the form of heat within the brake. The rise in temperature because of energy dissipated as heat can be simply written as

$$\mathrm{E} = mC\Delta T$$

where m is the mass of the device, C is the specific heat, and ΔT is the temperature rise. Conventionally, we use steel, cast iron (trains), and asbestos as braking materials. Asbestos has been mostly replaced because of its carcinogenic nature. A material used in a braking system must be able to generate the torque sufficient for stopping the vehicle, must absorb and dissipate the heat produced during the stopping process, and must withstand the high temperatures reached during stopping. It should also have superior structural properties for transferring the torque to the tires, without adding extra weight to the vehicle (Chawla 2012). MMCs with appropriate frictional characteristics such as wear, durability, and ability to withstand higher temperatures are excellent candidates for braking materials. Heat-resistance capability of aluminum alloys can be increased substantially by adding 30 % by volume of SiC particles. Such a composite was used to make a brake rotor (Nakanishi et al. 2002). The composite brake rotor had a higher heat resistance than a conventional cast iron rotor, especially a more stable coefficient of friction.

Zeuner et al. (1998) developed an MMC disc brake for high-speed trains that resulted to be not only mechanically superior to conventional cast irons but also cost-effective in terms of manufacturing. A braking system of a train is composed of four brake discs and the necessary calipers, hand brake, and electromagnetic track brakes. The higher thermal conductivity and lower modulus of elasticity of aluminum result in relatively low thermal stresses during the braking operation, which is a great advantage for Al–MMC discs over cast iron. For a given braking load, the cast iron discs showed higher thermal stresses and nonuniform temperature distribution than the Al–MMC disc, resulting in cracks due to thermal stresses in cast iron brakes but not in composite; see Chap. 11.

In summary, metal matrix composites, especially the particulate variety, can provide significant improvements in applications involving friction and wear. The ability to tailor their properties such as stiffness, hardness, and toughness is the main key to such improvements. The material properties, reinforcement size, and volume fraction have a profound influence on wear resistance. Increased volume fraction increases the stiffness but generally lowers the fracture toughness. Thus, increased volume fraction of ceramic particles will result in greater wear resistance at lower loads, but the fracture toughness becomes an important issue with increased load. For a given volume fraction, increased particle size provides the

best wear resistance, but larger particles are also more susceptible to fracture. Fine particles are less likely to experience fracture, but are more likely to be buried in matrix and removed by delamination. The loading conditions, matrix and reinforcement properties, and reinforcement size and volume fraction influence the creation of a MML between the contacting surfaces, which will help to protect the surfaces and slow the wear rate. Thus, in designing for wear resistance, it is important to select the proper combinations of matrix, reinforcement, and reinforcement size and volume fraction.

10.5 Corrosion of MMCs

Much work has been done on corrosion, stress corrosion, and corrosion fatigue behavior of metal matrix composites (Lucas and Clarke 1993; Hihara and Latanision 1994). Metzger and Fishman (1983) pointed out that the main potential corrosion problems in MMCs are (a) galvanic coupling between the reinforcement and matrix, (b) preferential corrosion at the reinforcement/matrix interface, and (c) corrosion at defects such as voids, pores, or microcracks.

Early work centered on carbon fiber-reinforced Al matrix composites. The work on this system showed the combination of a carbon fiber and aluminum matrix formed a galvanic couple. However, the high cathodic current in this system is due to oxygen reduction of carbon fibers. So, if the fibers can be isolated from the inert environment, by coating the fibers or ensuring that the fibers themselves are not exposed to the environment, then the galvanic current does not come into play (see Chap. 4 for the processing of carbon fiber/aluminum composites).

It is important to avoid the formation of Al_4C_3, in both carbon- and SiC-reinforced MMCs. The reason is that Al_4C_3 reacts with water as per the following reaction (Crowe 1985):

$$Al_4C_3 + 12H_2O \rightarrow 4Al(OH)_3 + 3CH_4 \uparrow$$

Thus, $Al(OH)_3$ is formed which results in local volume expansion, gas evolution by CH_4, and cracking. In cast Al–SiC, the formation of Al_4C_3 can be minimized by the addition of Si (see Chap. 4).

Finally, under corrosion fatigue loading, both composite and unreinforced alloy suffer reductions in fatigue life (Crowe and Hasson 1982). Figure 10.8 shows alternating stress versus cycles to failure for silicon carbide whisker-reinforced aluminum 6061 alloy in air and in moist salt air. Both show a drop in moist salt condition, but since the composite has a better fatigue resistance in air, it also has better performance than the aluminum alloy in salt environment.

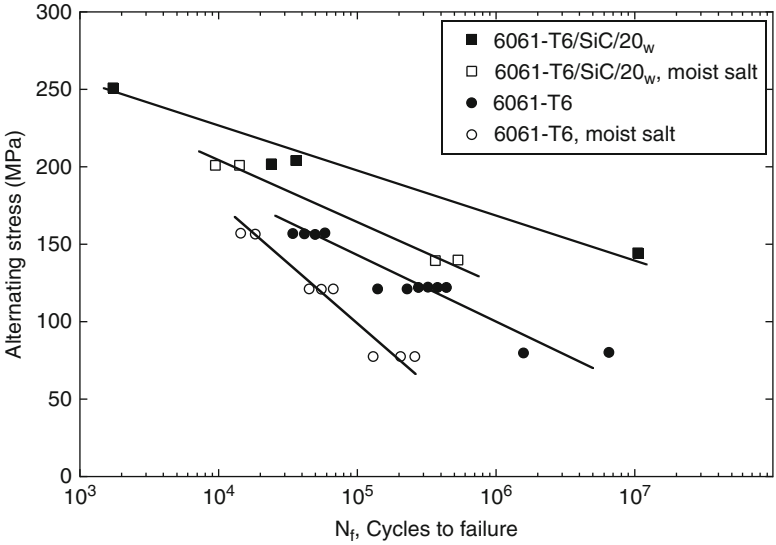

Fig. 10.8 Alternating stress versus cycles to failure for silicon carbide whisker-reinforced aluminum 6061 alloy in air and in moist salt air. Both show a drop in moist salt condition, but since the composite has a better fatigue resistance in air, it also has better performance than the aluminum alloy in salt environment (after Lucas and Clarke 1993)

References

Chawla, K.K. (2012) *Composite Materials: Science and Engineering*, 3rd ed., Springer, New York, p. 304.

Chung, S., and B. Hiang (1994) *Tribol. Inter.*, **27**, 307–314.

Crowe, C.R., U.S. Naval Research Laboratory, Report No. MR-5415, (1985).

Crowe, C.R., and D.F. Hasson, *Proc. Strength of Metals and Alloys* (1982) Oxford: Pergamon Press, **2**, pp. 859–865.

Deng, X., B.R. Patterson, K.K. Chawla, M.C. Koopman, Z. Fang, G. Lockwood and A. Griffo (2001) *J. Refractory Metals and Hard Materials*, **19**, 547.

Fang, Z. and S.J. Albert (1999) U.S. Patent **5**,880,382.

Fang, Z., G. Lockwood, and A. Griffo (1999) *Metall. Mater. Trans.*, **30A**, 3231

Garcia-Cordovilla, C., J. Narciso, and E. Louis (1996) *Wear*, **192**, 170.

Hihara, L. H. and R. M. Latanision (1994) *Inter. Mater. Rev.*, **39**, 245.

Hosking, F. M., F. Folgar-Portillo, R. Wundnerlin, and R. Mehrabian (1982) *J. Mater. Sci.*, **17**, 477.

Jahanmir, S., and N.P. Suh (1977) *Wear*, **44**, 17–38.

Lee H.C. and J. Gurland (1978) *Mater. Sci. Eng.*, **33**, 125.

Ludema, K.C. (1996) *Friction*, *Wear*, *Lubrication*: *A Textbook in Tribology*, CRC Press: Boca Raton, FL, p. 139.

Lucas, K.A., and H. Clarke, Corrosion of Aluminium-Based Metal Matrix Composites (1993), Wiley, pp. 49, 65, 79, 97, 117–120.

Metzger, M., and S.G. Fishman (1983) *Ind. Eng. Chem. Prod. Res. Dev.*, **22**, 296–302.

Nakanishi, H., K. Kakihara, A. Nakayama, and T. Murayama (2002) *Japan Soc. Auto. Eng. Rev.*, **23**, 365–370.

Rohatgi, P.K., S. Ray, Y. Liu (1992) *Inter. Mater. Rev.*, **37**, 192.
Suh, N.P. (1973) *Wear*, **25**, 111–124.
Upadhyaya, G.S. (1998) *Cemented Tungsten Carbides*, Noyes Pub., Westwood, NJ.
Venkataraman, B., and G. Sundarajan (1996a) *Acta Mater.*, **44**, 451–460.
Venkataraman, B., and G. Sundarajan (1996b) *Acta Mater.*, **44**, 461–473.
Wang A., and H.J. Rack (1991) *Wear*, **146**, 337.
Zeuner, T., P. Stojanov, P.R. Sahm, H. Ruppert, and A. Engels (1998) *Mater. Sci. Tech.*, **14**, 857–863.
Zhang, J., and A.T. Alpas (1993) *Mater. Sci. Eng.*, **A160**, 25–35.
Zhang, Z.F., L.C. Zhang, and Y.W. Mai (1995) *J. Mater. Sci.*, **30**, 1961–1966.

Chapter 11
Applications

Metal matrix composites are used in a myriad of applications. The high strength-to-weight ratio, enhanced mechanical and thermal properties over conventional materials, and tailorability of properties make them very attractive in a variety of applications. Increasingly MMCs have been used in several areas including (Evans et al. 2003):

- Aerospace
- Transportation (automotive and railway)
- Electronics and thermal management
- Filamentary superconducting magnets
- Electric power transmission
- Recreational products and sporting goods
- Wear-resistant materials

In this chapter, we review some important applications of MMCs and point out the advantages of using MMCs.

11.1 Aerospace

In aerospace applications, low density, tailored thermal expansion and conductivity, and high stiffness and strength are the primary drivers. In this industry, performance often outweighs cost considerations in materials development.

11.1.1 Aircraft Structures

MMCs have been used in several applications in aerospace components. This stems in large part to the fact that materials with increased specific stiffness and strength can significantly enhance the performance of the aircraft. A simple example is

N. Chawla and K.K. Chawla, *Metal Matrix Composites*,
DOI 10.1007/978-1-4614-9548-2_11, © Springer Science+Business Media New York 2013

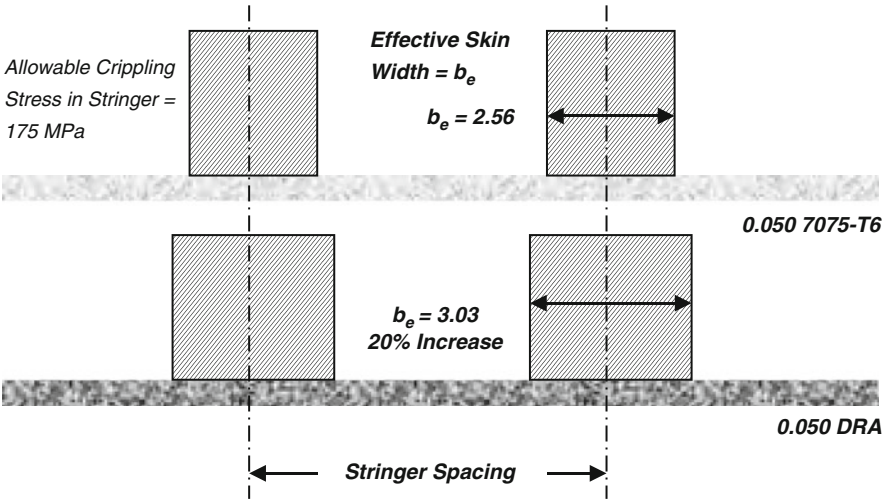

Fig. 11.1 Schematic of stringers on aircraft skin. By using a particle reinforced MMC skin, the effective allowable stringer size increases, resulting in enhanced stiffness of the skin (Courtesy of D. Bowden). DRA stands for discontinuously reenforced aluminum

shown in Fig. 11.1. Stringers are often used to stabilize the skin in the fuselage. Increased skin stiffness means that there is less chance of the skin buckling. Furthermore, a large stringer can be used to stabilize the skin. Using a SiC particle reinforced Al matrix composite skin, the effective allowable aluminum alloy stringer size increased resulting in enhanced stability of the skin.

In military aircraft, MMCs have found a large number of applications (Miracle 2001). In the F-16 aircraft, aluminum access doors were increasingly susceptible to fatigue cracking. The aluminum doors were replaced with particle reinforced MMC (Al/SiC_p) as a weight-neutral solution. MMC was also used as a replacement for unreinforced aluminum in the ventral fins of the F-16, see Fig. 11.2a, b. Figure 11.2c shows the deflection of the ventral fin as a function of number of missions. The MMC material exhibited much lower deflection because of the higher stiffness. The incorporation of the MMC resulted in fourfold increase in life of the component and $26 million life cycle cost savings. Similar improvements were obtained by incorporation of the MMC in the F-16 fuel access door covers. Continuous fiber-reinforced MMCs have also been used in military aircraft applications, due to their high specific strength, stiffness, and fatigue resistance. SiC monofilament-reinforced Ti matrix composites have been used as nozzle actuator controls for the F119 engine in F-16. The MMC replaced a heavier Inconel 718 in the actuator links and stainless steel in the piston rods.

MMCs have also been used in commercial aircraft. Figure 11.3 shows an application of MMC in the fan-exit guide vane of a Pratt & Whitney engine on a Boeing 777. The MMC replaced a carbon/epoxy composite that had problems with foreign object damage (FOD). The increased specific stiffness characteristics of

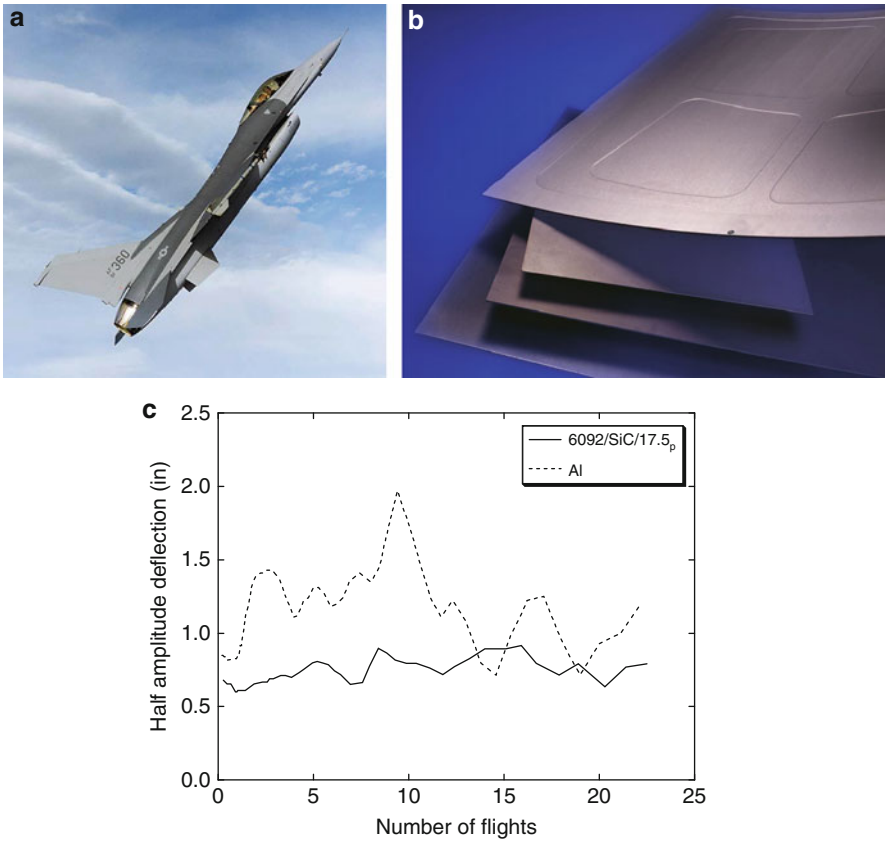

Fig. 11.2 SiC particle-reinforced Al alloy MMC used as a replacement for unreinforced aluminum in the ventral fins of the F16 (Courtesy of D. Miracle): (**a**) F16 aircraft, (**b**) composite ventral fin (Courtesy of DWA aluminum composites), and (**c**) deflection of the ventral fin as a function of number of missions. The MMC material exhibited much lower deflection because of the higher stiffness. 1 in = 25 mm

MMCs were also exploited in a fuselage strut application considered by Airbus. The MMC replaced a carbon fiber reinforced polymer for the strut, in order to reduce cost and increase damage tolerance.

In general, the cost of particle-reinforced MMCs is significantly lower than that of carbon/epoxy counterparts. The distribution of costs for each type of material is also quite different. A comparison of the cost breakdown for polymer matrix composites and the MMC is shown in Fig. 11.4. In polymer matrix composites, a large fraction of the cost goes into primary and secondary processing. In the MMC, the processing cost is a very small fraction of the total cost. Rather, the raw material cost of the matrix and reinforcement makes up most of the cost.

Another important application in aerospace is blade sleeves in helicopters, see Fig. 11.5. The blade sleeve must be able to tolerate centrifugal loads from the blades

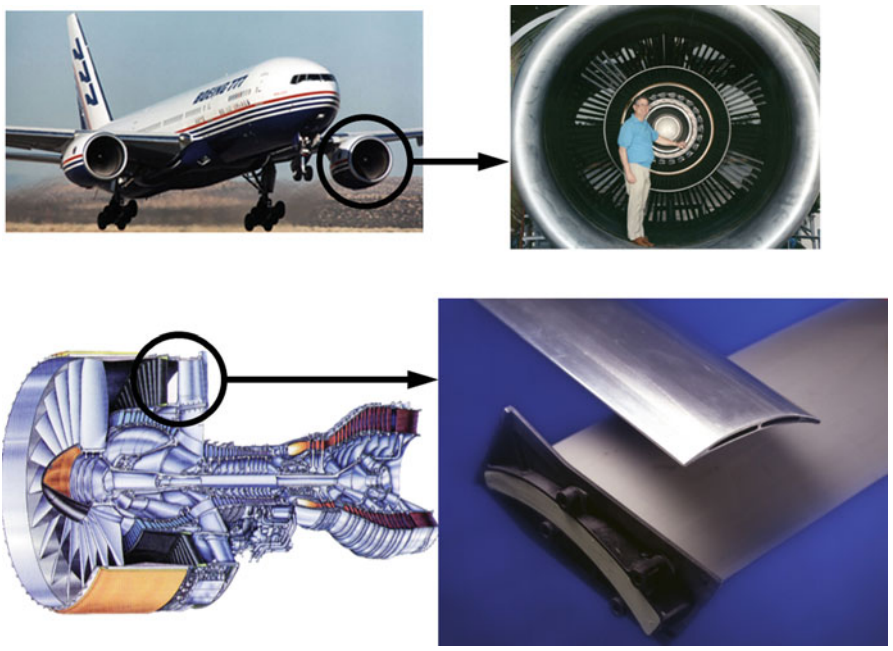

Fig. 11.3 Application of a SiC particle reinforced Al MMC in the fan-exit guide vane of a Pratt & Whitney engine on a Boeing 777 (Courtesy of D. Miracle). The MMC replaced a carbon/epoxy composite that had problems with foreign object damage (FOD) and at a lower cost

to the rotor. Thus, fatigue life, fretting resistance, toughness, and high specific strength are required. The composite consisted of SiC particles in an Al alloy matrix. Powder metallurgy-processed billets were extruded, cut, and forged. The final component yielded only 1 % in waste. The fatigue strength of the composite was around 270 MPa (assuming a fatigue runout at 10^7 cycles), which was a 50–70 % increase over the fatigue strength of unreinforced Al. The fracture toughness was reasonable, at 25 MPa $\sqrt{m}$, and the specific strength and cost were lower than those of the initial Ti alloy used in this application.

11.1.2 Fiber Metal Laminates

Fiber metal laminates (FMLs) consist of alternately stacked thin (about a millimeter or less in thickness) sheets of metal (commonly aluminum) and fiber-reinforced polymer (commonly epoxy) (Vlot and Gunnick 2001; Vogelesang et al. 1995). The first commercial FML was *AR*amid *AL*uminum *L*aminate, ARALL. ARALL was used in a few select aircraft components, but it had structural limitations that prevented wider use. GLARE or *GLA*ss-*RE*inforced laminate, a glass–aluminum FML, was developed in part to overcome these limitations. GLARE consists of

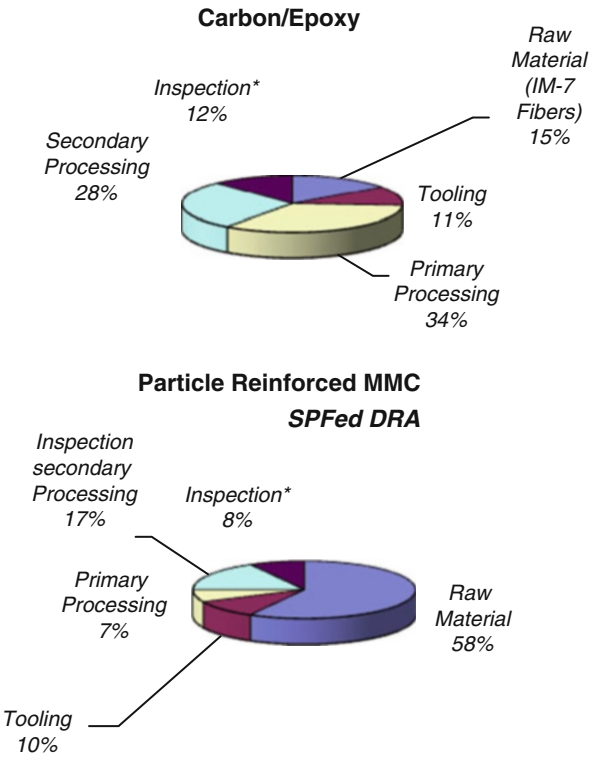

Fig. 11.4 Cost comparison between the polymer matrix composite and the particle reinforced MMC for the fan-exit guide vane (Courtesy of D. Bowden). In the polymer matrix composite, a large fraction of the cost goes into primary and secondary processing. In the MMC, the processing cost is a very small fraction of the total cost. Raw material cost (matrix and reinforcement) makes up most of the cost

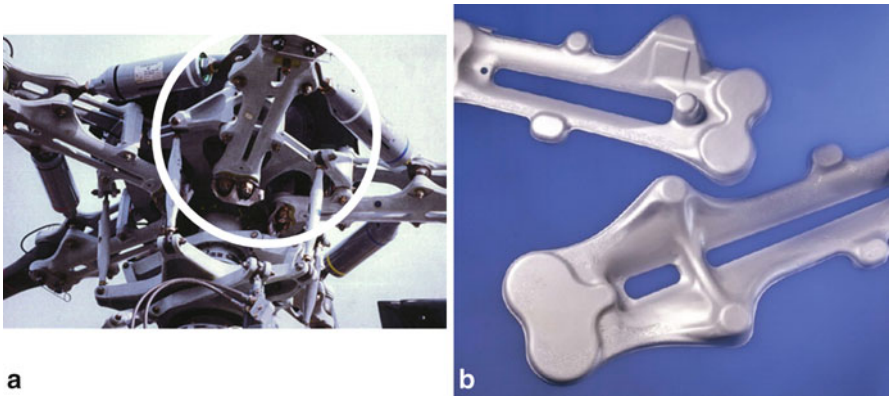

Fig. 11.5 (**a**) MMC blade sleeves in helicopters and (**b**) forged components (Courtesy of D. Miracle and DWA aluminum composites). The blade sleeve must be able to tolerate centrifugal loads from the blades to the rotor. Thus, fatigue life, fretting resistance, toughness, and high specific strength are required. The specific strength equivalent and cost were lower than those of the monolithic Ti alloy used in this application

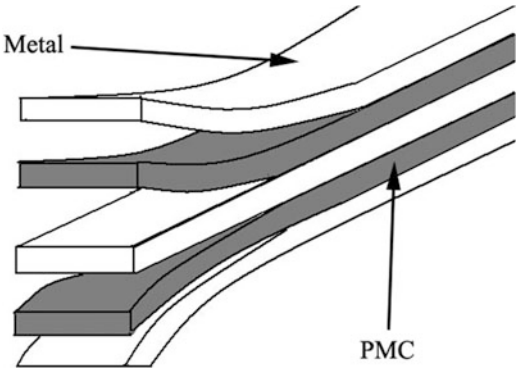

Fig. 11.6 Schematic of fiber metal laminate consisting of alternating sheets of metal and fiber reinforced polymer matrix composite

alternating layers of aluminum and glass fiber/epoxy layers. Such a laminate is produced in an autoclave for the curing of the polymer matrix. The different layers of the laminate are stacked before curing, manually or by automated machines. There is a high degree of tailorability in these composites because both the number of layers as well as the direction of the fibers in the PMC layers can be varied depending on the application of the structural part. The main characteristics of GLARE are extremely good fatigue properties, high damage tolerance capabilities, and optimal impact properties. Many structural parts (primary and secondary) can be identified where these properties play an important role. In particular, GLARE is used in the fuselage of the twin-deck, 550-seat, Airbus A380 aircraft.

Figure 11.6 shows schematically the configuration of metallic sheets and sheets of polymer matrix composite. Besides having superior fatigue behavior, GLARE is also lighter than aluminum, cutting the weight of the Airbus A380 by 1,000 kg. It was discovered that bonded and laminated aluminum had favorable resistance to crack growth because cracks would grow in a single layer at a time, and the remaining layers would effectively bridge the crack. This discovery was made use of in the development of the F-27 aircraft wings, which is a very highly fatigue sensitive structure.

Fuselage construction with ARALL revealed that under loading conditions encountered in an aircraft fuselage, the aramid fibers around a fatigue crack would fracture. Once the fibers fractured, the crack was no longer inhibited and would grow. As the crack grows, delamination occurs and a compressive stress is placed on the aramid fibers, causing buckling. Low compressive stress of aramid fibers is well known (see, for example, Chawla 1998). It was observed that aramid fibers would fracture under rather low compressive loads, and it also became evident that ARALL was also sensitive to strength reductions caused by any holes that might be drilled in it. Such holes are unavoidable in a large structure such as a fuselage; they would lead to premature fatigue cracks to develop. Although use of ARALL was not suitable for fuselage construction, the weight savings by using this material were very attractive. The first commercial application of ARALL was on the C-17 military transport plane. Because of heavy weight problems toward the rear of the plane, the large aluminum cargo door was replaced with ARALL.

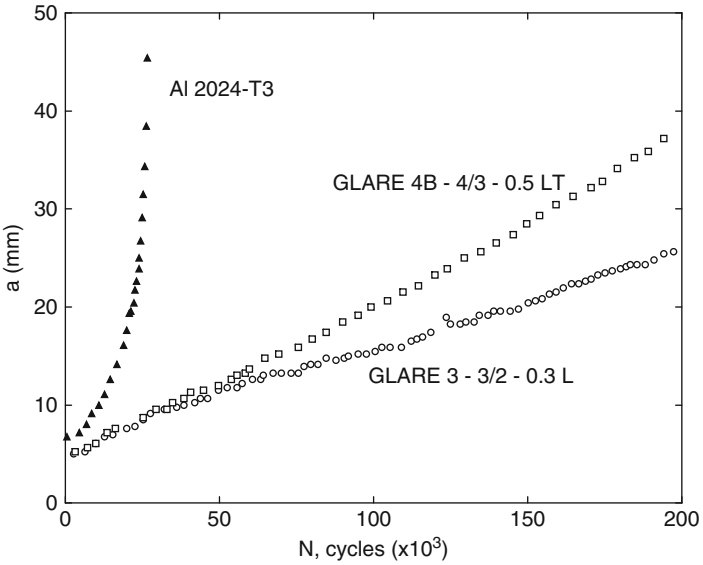

Fig. 11.7 Comparison of fatigue crack growth resistance of GLARE composites and 2024 Al. GLARE has significantly better fatigue resistance (After Vlot and Gunnick 2001)

Glass fibers were used to replace aramid fibers in the new GLARE FML, which has superior blunt notch strength and the ability to handle greater compressive stresses than ARALL (Vlot and Gunnick 2001). GLARE is also more resistant to impact than ARALL and for this reason the first commercial application of GLARE was in the cargo floor of Boeing's 777 where the excellent impact properties of GLARE were put to use. The next area big use of GLARE was in the form of panels for the fuselage of Airbus A380 aircraft.

The main consideration that underlies the design of fiber metal laminates is their superior fatigue strength. This is shown schematically in Fig. 11.7 where a plot of crack length as function of number of cycles shows GLARE to be superior to aluminum under cyclic loading. Flammability is another important consideration for any aircraft material. Damage from sources such as fire has troubled early aircraft design because of the low melting point of aluminum. For example, an accident at Manchester airport resulted in loss of life from an external fire that entered the passenger cabin by burning through and melting the fuselage (Vlot and Gunnick 2001). Introduction of GLARE to fuselage design improved the fire resistance of aircraft because of the nature of the composite. After burn-through of the outer aluminum layer, Fig. 11.8, the glass fiber/epoxy layer is exposed to the flames. Since the softening temperature of the glass fibers is high and the epoxy layer becomes carbonized, the prepreg effectively creates an insulation barrier, which prevents damage to the remaining aluminum layers. No flame penetration was observed for GLARE after 10 min, whereas the 2024-T3 aluminum samples showed burn-through within 100 s at approximately 1,150 °C. The fire retardant

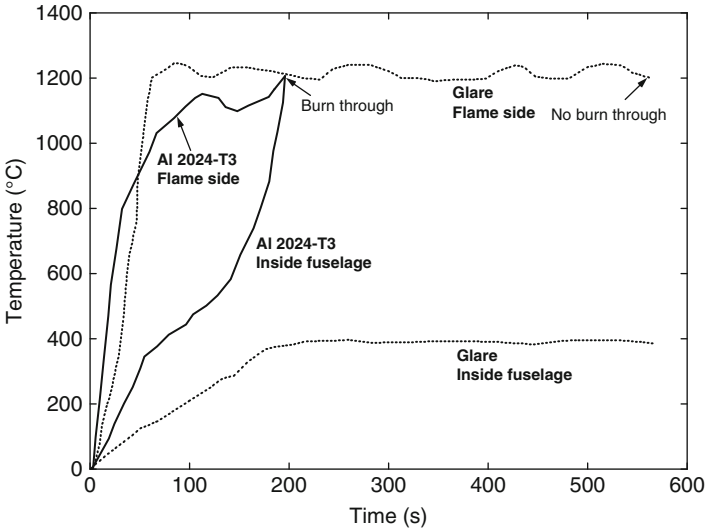

Fig. 11.8 Temperature of 2024 Al and GLARE inside of fuselage and on flame side (After Vlot and Gunnick 2001). The introduction of GLARE to fuselage design improved the fire resistance of aircraft because of the nature of the composite

character of GLARE allows much of its strength and fatigue properties, after burn-through of the outer aluminum layer, to remain although repair may be necessary (Vogelesang et al. 1995).

Fiber metal laminates have a large degree of tailorability built into them. It is easy to see that, depending on the final application, one can choose the fiber/polymer composite, the metallic alloy type, the layer thickness and stacking sequence, fiber orientation in the PMC layer, etc. The density of the GLARE laminates depends on the relative thickness of aluminum sheet and glass fiber/epoxy layers, the number of layers in the laminate, and the fiber volume fraction. In general, the density of GLARE laminates is at least 8 % lower than that of the monolithic aluminum alloy.

11.1.3 Missiles

An important application for MMCs is in missiles (Shakesheff and Purdue 1998). With increasing performance demands for missiles, conventional aluminum alloys do not have the required strength and temperature resistance. Steel and titanium are not acceptable from a weight point of view. MMCs offer enhanced strength and stiffness with no penalty in weight. In addition the elevated temperature exposure of the missile is for a very short duration (from the time it is launched to where it meets its target). Thus, MMCs are candidates for missile wings and fins, Fig. 11.9.

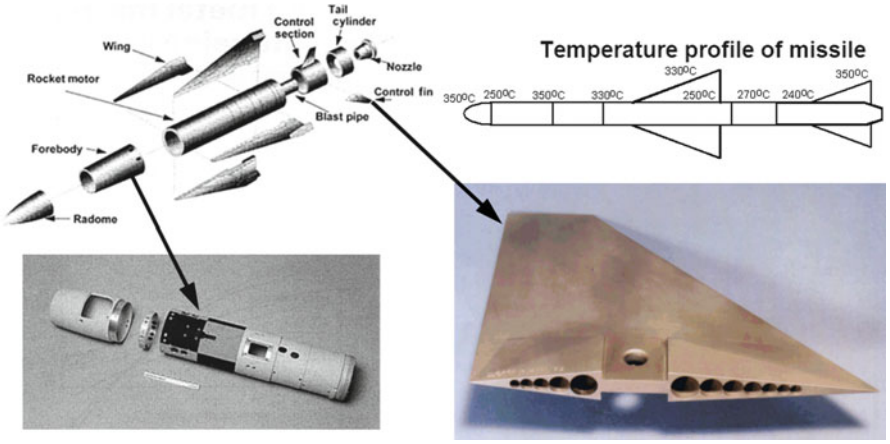

Fig. 11.9 MMC applications in missiles (After Shakesheff and Purdue 1998; Reprinted with permission from Maney Publishing). The elevated temperature exposure of the missile is for a very short duration

Fig. 11.10 Al/B_f tubular struts in the frame and rib truss members of the mid fuselage section of the space shuttle (Courtesy of S. Rawal, reprinted with permission from The Minerals, Metals, and Materials Society). The struts provide a weight savings of 45 % over unreinforced aluminum

11.1.4 Space Structures

Reduction in the weight of a component is a significant driving force for any application in aerospace. The first successful application of continuous fiber-reinforced MMCs was boron fiber-reinforced tubular struts in the frame and rib truss members of the mid-fuselage section of the space shuttle, Fig. 11.10 (Rawal 2001). The struts provided a weight savings of 45 % over unreinforced aluminum.

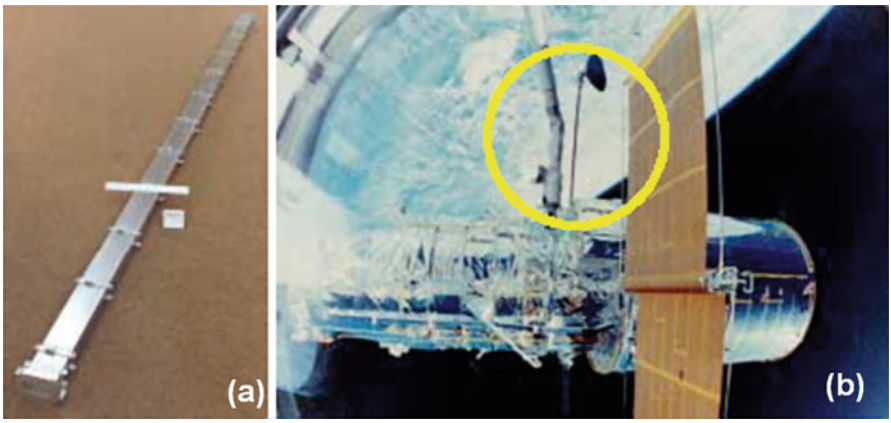

Fig. 11.11 Carbon fiber reinforced 6061 Al matrix composite used as antenna waveguide/boom on the Hubble space telescope (Courtesy of S. Rawal, reprinted with permission from The Minerals, Metals, and Materials Society): (**a**) before integration on the telescope and (**b**) deployed in space

Table 11.1 Properties of unidirectional fiber reinforced metal matrix composites used in space applications (After Rawal 2001)

	P100/6061 Al	P100/AZ91C Mg	Boron–Al
Reinforcement volume fraction (%)	42.2	43	50
Density (g/cm^3)	2.5	2.0	2.7
Poisson ratio	0.3	0.3	0.2
Specific heat (J/kg K)	812	795	801
Longitudinal			
Young's modulus (GPa)	343	324	235
Ultimate tensile strength (MPa)	905	710	1,100
Thermal conductivity (W/mK)	320	189	–
Coefficient of thermal expansion (10^{-6}/K)	−0.49	0.54	5.8
Transverse			
Young's modulus (GPa)	35	21	138
Ultimate tensile strength (MPa)	25	22	110
Thermal conductivity (W/m K)	72	32	–

P100 is a pitch-based carbon fiber

In the Hubble telescope, pitch-based continuous carbon fiber reinforced aluminum was used for waveguide booms because of its light weight, high elastic modulus, and low coefficient of thermal expansion, Fig. 11.11. The material is made of diffusion bonded sheet material and is 3.6 m in length. The boom requires good stiffness and low coefficient of expansion to maintain the position of the antenna during space maneuvers. The boom also functions as a waveguide due to its excellent electrical conductivity. Table 11.1 shows selected properties of unidirectional fiber-reinforced MMCs used in space applications.

In addition to Al-based composites, copper-based composites containing Nb, Ta, or Cr as the second phase in a discontinuous form are also of interest for certain applications requiring high thermal conductivity and high strength, e.g., in high heat flux applications in rocket engine thrust chambers.

11.2 Transportation (Automotive and Railway)

MMCs have been used in a variety of automotive applications. An early and successful engine application was selectively reinforced aluminum pistons in the Toyota diesel engine (Donomoto et al. 1983). In this application, an alumina–silica chopped fiber preform was incorporated into the ring groove area of the piston during pressure casting of the aluminum. The conventional diesel engine piston has an Al−Si casting alloy with a crown made of a nickel cast iron. The main property requirement was increased wear resistance in this area. The previous approach used a Ni-resist ring that increased weight and differed in coefficient of thermal expansion from the aluminum alloy piston material. Aluminum matrix materials reinforced with SiC particles have also been used in piston applications, primarily in drag racing cars. In this case, the lower coefficient of thermal expansion of the MMC compared to conventional aluminum allowed reduced clearances between the piston and cylinder wall with improved performance.

Another early MMC application in an automotive engine was a hybrid particulate-reinforced Al matrix composite used as a cylinder liner in the Honda Prelude, Fig. 11.12. The composite consisted of an Al–Si matrix with 12 % Al_2O_3 for wear resistance and 9 % carbon for lubricity. The composite was integrally cast with the engine block, had improved cooling efficiency, and exhibited improved wear and a 50 % weight savings over cast iron, without increasing the engine package size. While this concept was initially implemented in the Honda Prelude 2.3L engine, it has also been used in the Honda S2000, Toyota Celica, and Porsche Boxster engines (Hunt and Miracle 2001).

An important application of MMCs in the automotive sector is as a driveshaft. The key limitation in this case arises from the critical rotational speed at which the material becomes dynamically unstable. The critical rotational speed (N_c) is given by Hoover (1991)

$$N_c = \frac{15\pi}{L^2}\left[\frac{E}{\rho}(R_o + R_i)^2\right]^{\frac{1}{2}}$$

where L is the length of the driveshaft, E is the Young's modulus, ρ is the density, and R_o and R_i are the outer and inner radii of the shaft, respectively.

The important point to be made from this equation is that the material parameter that controls critical speed is the specific modulus, E/ρ. One of the requirements of the driveshaft is that it be welded to a yoke. Thus, SiC reinforcement is precluded

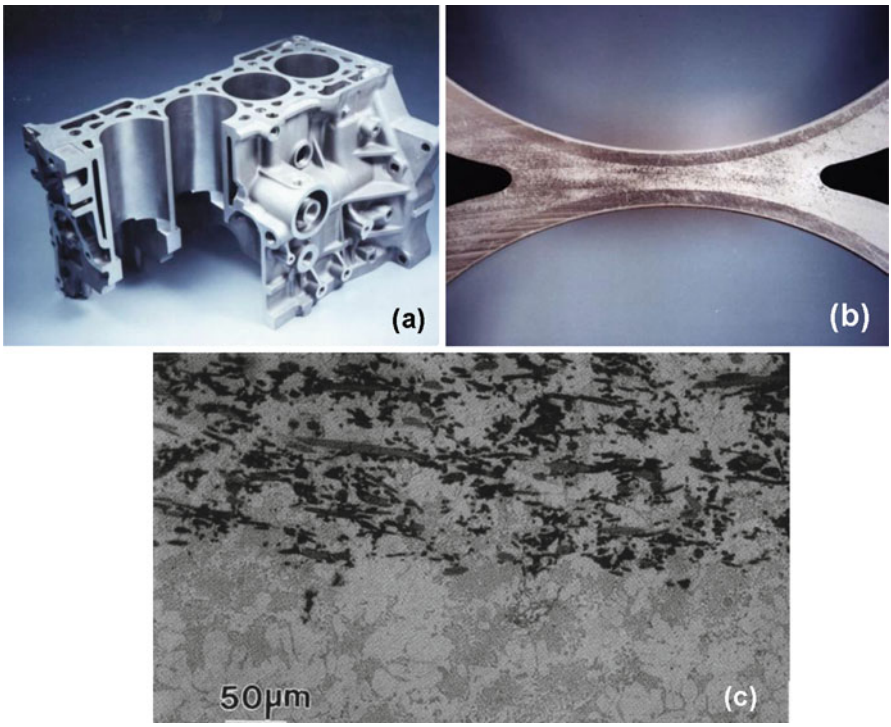

Fig. 11.12 Hybrid particulate reinforced Al matrix composite used as a cylinder liner in the Honda Prelude (parts (**a**) and (**b**) Courtesy of D. Miracle). The composite consisted of an Al–Si matrix with 12 % Al_2O_3 for wear resistance, and 9 % carbon for lubricity. (**a**) Prelude engine block, (**b**) magnified view of cylinder liner, and (**c**) microstructure of composite showing carbon short fibers (*black*) and Al_2O_3 fibers (*dark gray*)

from material selection, because of the harmful reaction products formed between Al and SiC in liquid-phase processes (see Chap. 4). Duralcan has used a 6061/$Al_2O_3/20_p$ composite, which exhibits a 36 % increase in specific modulus over steel, Fig. 11.13 (Koczak et al. 1993).

Another important potential replacement of steel by SiC particle-reinforced Al matrix composite is in the connecting rod, Fig. 11.14. The connecting rod requires high fatigue resistance at temperatures as high as 150 °C. A lighter connecting rod would result in the following: (a) 12–20 % reduction in secondary shaking force, (b) 0.5–1 % improvement in fuel economy (with lightweight piston and pin), (c) 15–20 % increase in peak RPM, (d) decreased bearing width (package improvement), and (e) increased bearing and crankshaft durability. Initial attempts at developing an MMC connecting rod used hot pressing followed by extrusion, commonly used to fabricate aerospace components. This technique proved to be too costly in the automotive sector (where production volume is much larger than in the aerospace industry) because of the large amount of wasted material. Near-net-shape sinter-forging (see Chap. 3) was used to fabricate MMC connecting rods with

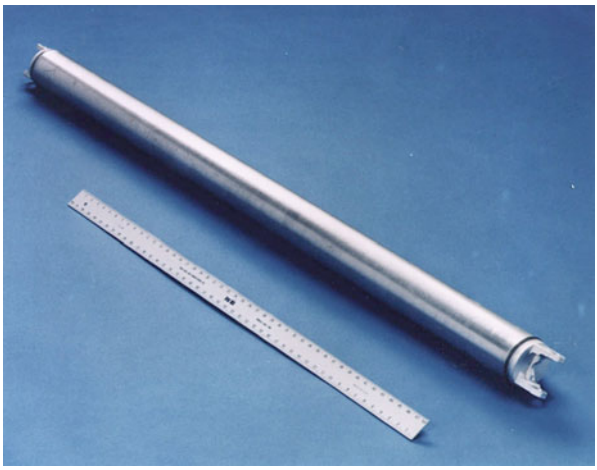

Fig. 11.13 6061/Al_2O_3/20_p composite used as driveshaft in the Corvette (Courtesy of D. Miracle). The composite exhibits a 36 % increase in specific modulus over steel

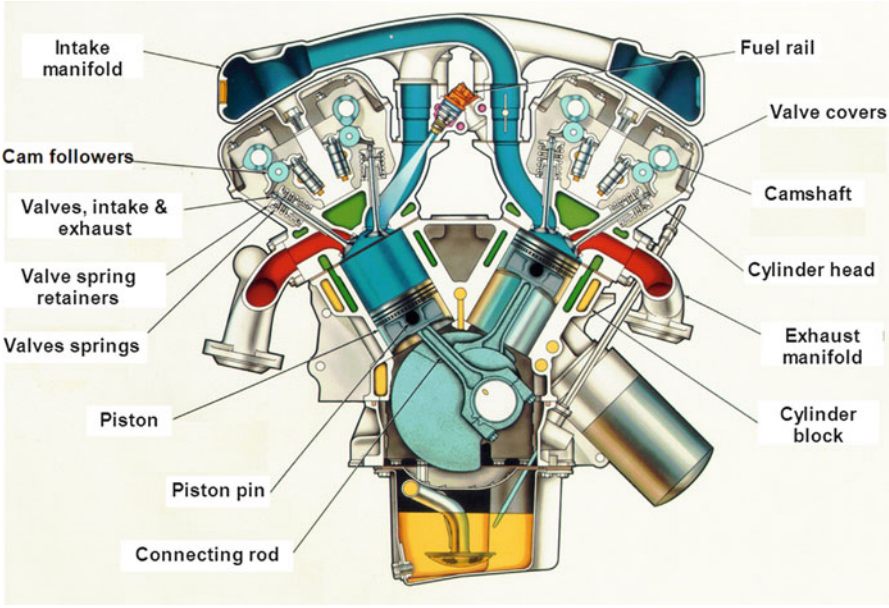

Fig. 11.14 Cross-section of a passenger car engine showing the location of the connecting rod (Courtesy of J. Allison)

tensile and fatigue properties comparable to those of extruded materials (Chawla et al. 2002). A prototype model of this rod is shown in Fig. 11.15.

In Table 11.2 we compare the weight of the MMC rod vis-à-vis that of the steel rod (Chawla and Chawla 2004). A 57 % weight savings was achieved with the MMC

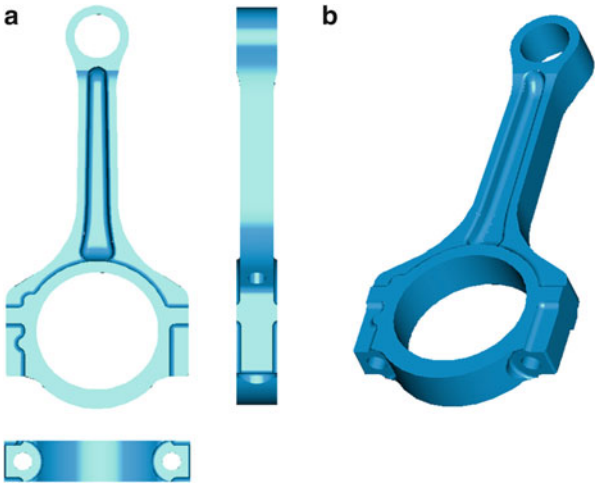

Fig. 11.15 Models of sinter-forged MMC connecting rods: (**a**) 2D view and (**b**) 3D view (Courtesy of F. Liu)

Table 11.2 Weight comparison of MMC and steel connecting rods

	2080/SiC/20_p	Steel
Pin weight (g)	65.2	144.7
Crank weight (g)	184.0	437.7
Total weight (g)	249.2	582.4

rod, with a moderate increase in cost. In addition, it is estimated that for every 1 kg of weight removed from connecting rods, 7 kg of supporting and counterbalancing structure can be eliminated (Hunt and Miracle 2001). Other demanding power train applications are intake and exhaust valves. These components must have good high cycle fatigue performance at elevated temperature, good sliding wear resistance, and creep resistance. Austenitic stainless steel was replaced by a TiB_2-reinforced Ti matrix composite in the Toyota Altezza (Hunt and Miracle 2001).

The use of particulate MMCs, particularly Al-based MMCs, has been made in brake drums and brake rotors as a replacement for cast iron, Fig. 11.16. The high wear resistance and thermal conductivity coupled with 50–60 % weight savings make MMCs quite attractive for this application. An intensive development effort was carried out using cast 359Al/SiC/20_p composite. While the costs for this rotor were somewhat higher than those made of cast iron, the benefits were justified in a number of specialty vehicles, such as the Plymouth Prowler and Lotus Elise (Hunt and Miracle 2001). The concept of "selective reinforcement" whereby the hard SiC particles are used where high strength and wear resistance are required would appear to be quite attractive. This also minimizes the machining costs since the SiC-free regions are easier to machine.

Metal matrix composite foams have also been developed for damping/energy-absorbing applications in automobiles (Leitlmeier et al. 2002). A 6061Al/Al_2O_3/22_p composite foam has been used in Ferrari cars. Figure 11.17a shows the 3D

Fig. 11.16 Particulate MMCs for use in brake drums and brake rotors, as a replacement for cast iron (Courtesy of D. Miracle). The high wear resistance and thermal conductivity coupled with 50–60 % weight savings, make MMCs quite attractive for this application

microstructure of the foam obtained by computed X-ray tomography. The pores are a few millimeters in diameter and are homogeneously distributed. Figure 11.17b shows the microstructure of the composite (Babcsan et al. 2004). The SiC particles stabilize the wall thickness, Fig. 11.17b, and segregate to the cell wall, Fig. 11.17c. The cell walls are about twice the SiC particle diameter.

11.2.1 Railroad Brakes

The driving force for lightweight railway vehicles has also prompted the use of high-performance MMCs (Zeuner et al. 1998). A conventional brake system for a railway vehicle, shown in Fig. 11.18, consists of four brake disks, calipers, hand brake, and electromagnetic track brake. This makes up about 20 % of the total weight of the bogey. Zeuner et al. (1998) used a selectively cast Al matrix composite with SiC particles for this application. The composites were fabricated by a multipouring process, where alternating layers of the unreinforced alloy and MMC were cast in successive layers. This contributed to reduced cost by using less MMC and placing the composite in the strategically important region (i.e., in contact with the wearing surface). In this particular application, the weight was

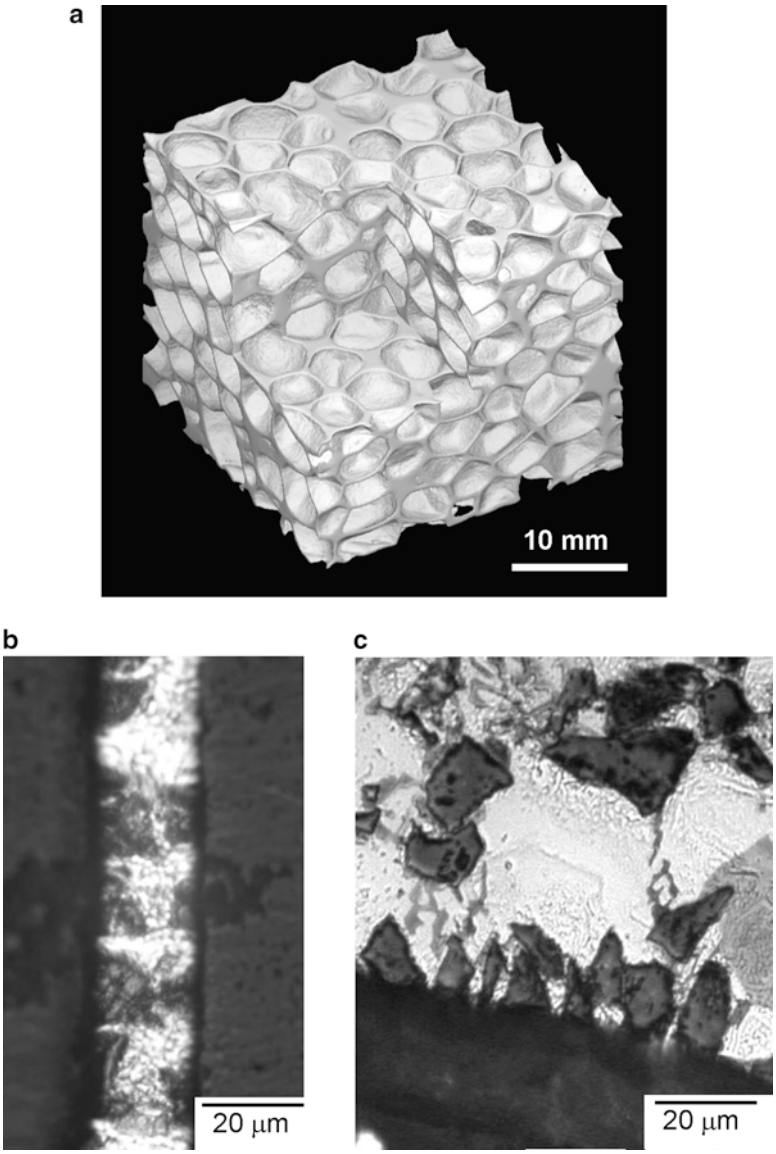

Fig. 11.17 6061/Al_2O_3/22_p composite foam used in Ferrari cars (Courtesy of H.P. Deigischer): (**a**) 3D microstructure obtained by computed X-ray tomography, (**b**) microstructure in the cell wall, which is about twice the SiC particle diameter, and (**c**) segregation of SiC particles to the cell wall

reduced from 115 kg for a spheroidal graphite iron disk to 65 kg for the MMC disk, a weight savings of 43 %. Figure 11.19 shows photographs of MMC and steel brakes after wear testing. One can see that the steel brake shows a significant amount of cracking, while the MMC brake is in relatively good condition.

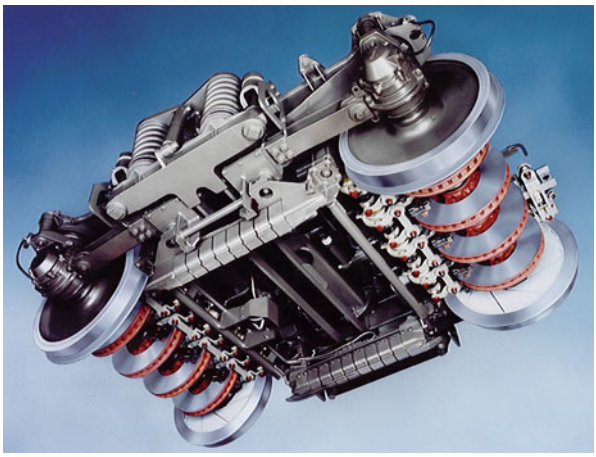

Fig. 11.18 High speedway railroad coach bogey with four brake disks produced by SAB Wabco (Courtesy of H. Ruppert)

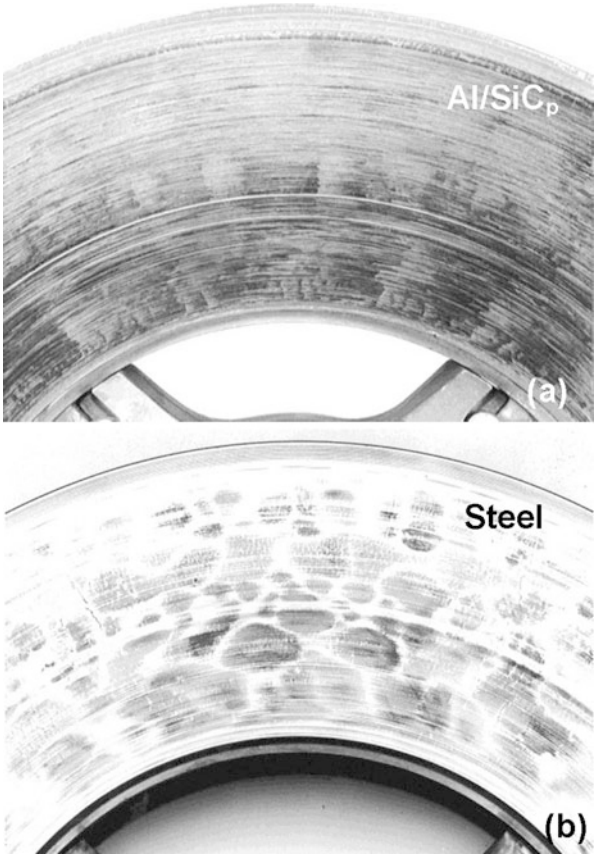

Fig. 11.19 Thermal cracking behavior in (**a**) Al/SiC_p and (**b**) steel after wear testing (Courtesy of H. Ruppert). The steel brake shows significant amount of cracking (*white lines*) while the MMC is in relatively good condition

11.3 Electronics and Thermal Management

A very important market area for aluminum and to a lesser degree copper matrix MMCs is in electronic packaging and thermal management. Metal matrix composites can be tailored to have optimal thermal and physical properties to meet requirements of electronic packaging systems, e.g., cores, substrates, carriers, and housings. The main attraction of MMCs for these applications is controlled thermal expansion with a negligible penalty in thermal conductivity. Figure 11.20 shows the decrease in coefficient of thermal expansion with increasing volume fraction of SiC in a 2080/SiC_p composite (Deng et al. 2006).

In a multilayered package, a solder joint bonds the substrate (such as AlN) to the baseplate, usually made of Cu. The thermal expansion mismatch between Cu and AlN results in thermal stresses in the solder that may lead to failure of the package. By making the baseplate of an MMC instead of copper, the CTE may be tailored to that of AlN (or any other suitable substrate). From a heat dissipation point of view, a metallic matrix (such as Cu or Al) reinforced with SiC will not lose much in the way of thermal conductivity, because the conductivity of SiC is similar to that of Al. In order to attain the necessary requirements in thermal expansion and thermal conductivity, composite with 55–65 % reinforcement particles are typically used. Such high volume fraction of reinforcement is obtained by innovative techniques for enhancing the degree of packing of particles. In particular, a bimodal

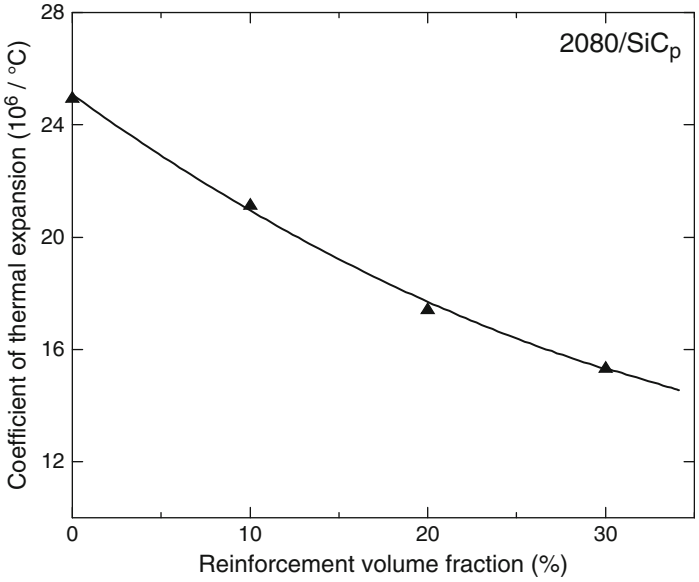

Fig. 11.20 Coefficient of thermal expansion (CTE) of a SiC particle reinforced Al 2080 matrix composite (After Deng et al. 2006). With increasing volume fraction of the low expansion ceramic particle reinforcement, the composite CTE decreases

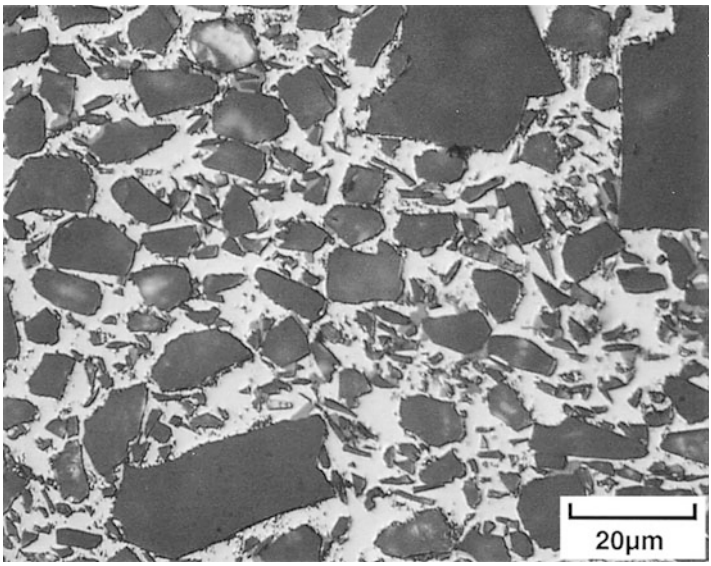

Fig. 11.21 Microstructure of SiC particle reinforced Al matrix composite used for thermal applications (Courtesy of M. Occhionero, Ceramic Process Systems). The bimodal particle size distribution enables a large volume fraction of particles (>50 %) to be used

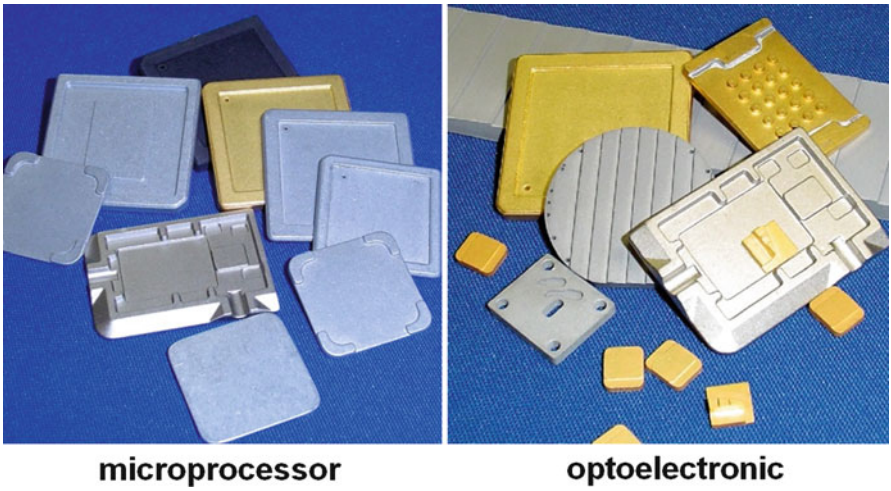

Fig. 11.22 Examples of SiC particle reinforced Al matrix composites used in microprocessor and optoelectronic packaging applications (Courtesy of M. Occhionero, Ceramic Process Systems)

distribution of particles has been used to obtain the desired packing because very small particles can fit in the space between large reinforcement particles, see Fig. 11.21. Examples of SiC particle-reinforced aluminum used in microprocessor and optoelectronic packaging applications are shown in Fig. 11.22.

An early application was in microwave packaging where a 40 vol% SiC particle-reinforced aluminum MMC replaced Kovar, a heavier Ni–Co–Fe alloy. The major drivers here were weight savings, with a 65 % cost reduction realized, along with improved thermal conductivity over the baseline alloy. Increased thermal conductivity and lightweight in a CTE-matched material are also the features being exploited in the use of both Al–SiC and Al–carbon MMCs in insulated gate bipolar transistors (IGBT) power module baseplates. Printed wiring board cores have also been made of Al–SiC materials in replacement of conventional copper or aluminum cores. In addition to the CTE matching, the increased specific stiffness of these MMCs reduces the thermal cycling and vibration-induced fatigue. Yet another application in which the thermophysical properties of Al–SiC are important is in carriers for hybrid circuits for power amplifiers in cellular phone base stations. Continuous boron fiber-reinforced aluminum composites made by diffusion bonding have also been used as heat sinks in chip carrier multilayer boards.

Unidirectionally aligned, pitch-based carbon fibers in an aluminum matrix can have high thermal conductivity along the fiber direction. The conductivity transverse to the fibers is about two-thirds that of aluminum. Such a C/Al composite is useful in heat transfer applications where weight reduction is an important consideration, e.g., in high-density, high-speed integrated circuit packages for computers and in baseplates for electronic equipment. Another possible use of this composite is to dissipate heat from the leading edges of wings in high-speed airplanes.

An interesting application involved MMCs for covers of inertial guidance system for a missile system. The requirement here was that the MMC should match the coefficient of thermal expansion of beryllium covers. The ability to tailor the CTE through reinforcement content and matrix selection proved invaluable, and a 6061/SiC/40_p material was used. It should be noted that beryllium, used in this application, is very expensive to machine and has significant toxicity problems. In contrast, the MMC covers were precision forged to near net shape, with some minimal final machining required.

11.4 Filamentary Superconducting Magnets

Filamentary superconducting composites have some very important applications. Examples of applications of metal matrix composite superconducting coils include (Cyrot and Pavuna 1992):

- High-field magnets for research in high energy and in condensed matter physics.
- Magnetic resonance imaging (MRI), which requires extremely uniform magnetic fields of ~1–2 T.
- Coils for windings in motors and generators.
- Magnetic levitating (MAGLEV) coils for high-speed trains.
- Magnetohydrodynamic and electromagnetic thrust systems for propulsion in ships and submarines.

Since the discovery of the so-called high-T_c superconductors, much emphasis has been placed on the high T_c of these superconductors. As pointed out in Chap. 3, one should be mindful of not only just T_c but also J_c (critical current density) and H_c (critical magnetic field). As a rule of thumb for most superconductor applications, the critical temperature, T_c, of a technological superconductor should be about twice the use temperature (Cyrot and Pavuna 1992). This implies that superconductors that are used with liquid helium (4.2 K) as a coolant should have a $T_c > 8$ K. In fact, due to heating of the magnet, the actual operational temperature is closer to ~7 K, so one needs a T_c ~15 K. Thus, to use the oxide high-temperature superconductors (HTS) in applications at 77 K, one needs a superconductor with a T_c ~150 K. Such a material has not yet been synthesized; the thallium-compound with T_c ~125 K is the best candidate for the "true" technological material at liquid nitrogen temperature.

Nb_3Sn/Cu superconducting composites are used for magnetic fields greater than 12 T. Such high fields are encountered in thermonuclear fusion reactors, and superconducting composite magnets would represent a sizable fraction of the capital cost of such a fusion power plant. The main difference between the magnets used in a fusion reactor and in power transmission is that the former use superconductors at very high magnetic fields while the latter use them at low fields.

A large-scale application of Nb–Ti/Cu superconducting magnets is in magnetically levitated trains. Japan National Railways has tested such trains over a small stretch at speeds over 500 km/h. Figure 11.23a shows a Nb–Ti/Cu superconductor cable with 15 strands. A higher magnification micrograph of an individual strand, Fig. 11.23b, shows 1,060 superconducting filaments. Nb–Ti/Cu superconductor composites are also employed in pulsed magnets for particle accelerators in high-energy physics.

Some use of superconductors in power generation has been made by companies such as GE and Siemens. In some cases, by using superconducting materials, the designers could make a generator that developed a much stronger magnetic field than a conventional generator, permitting a significant reduction in the size of the generator for the same power output. Superconducting magnets do require cryogenic temperatures to operate, but the cost of this refrigeration is more than compensated by the energy savings. One has only to remember that in a superconducting machine working with almost zero resistance, the normal losses associated with the flow of electricity in rotor windings of a conventional machine are absent, resulting in a higher efficiency and reduced operating costs. It is worth pointing out that a big problem in one such project by GE was to prevent the movement of rotor windings under the intense centrifugal and magnetic forces exerted on them. The rotor spins at a speed of 360 rpm. Thus, even an infinitesimally small movement of these components would generate enough heat by friction to quench the superconductors. The GE researchers used a special vacuum epoxy impregnation process to bond the Nb–Ti superconductors into rock solid modules and strong aluminum supports to hold the windings rigidly.

An important landmark in the development of high-temperature oxide superconductors occurred in 1997, when Geneva's electric utility, SIG, put an electrical

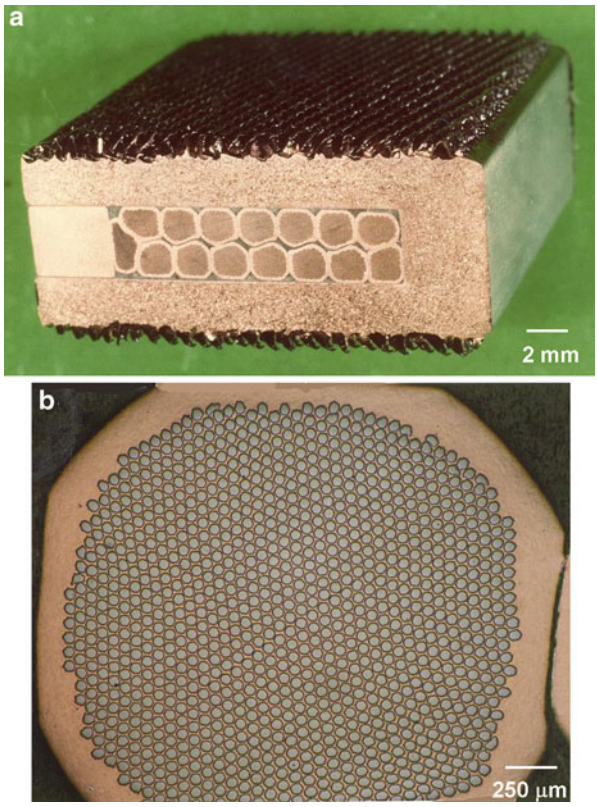

Fig. 11.23 (**a**) Compacted strand superconducting cable made of 15 multifilamentary strands and (**b**) magnified view of one of the strands containing 1,060 filaments (Courtesy of Hitachi Cable Co.)

transformer using HTS wires into operation. This transformer was built by ABB; it used the flexible HTS wires made by American Superconductor by the process involving packing of the raw material into hollow silver tubes, drawing into fine filaments, grouping the multifilaments in another metal jacket, further drawing and heat treating to convert the raw material into the oxide superconductor (see Chap. 4). This transformer loses only about one-fifth of the AC power losses of the conventional ones. Because HTS wires can carry a higher current density, this new transformer is more compact and lighter than a conventional transformer. Liquid nitrogen used as a coolant in the HTS transformer is safer than oils used as insulators in conventional transformers. These superconductors are termed "first-generation" superconductors, Fig. 11.24a. Newer, second-generation coated superconductors, made by the RABiTS process (see Chap. 4), consist of a superconductor layer, coated with a noble metal on an alloy substrate, Fig. 11.24b. Figure 11.25 shows the second-generation superconductors in tape form.

We now describe a very important application of Nb-based superconducting composites that has become quite commonplace—magnetic resonance imaging. The phenomenon of nuclear magnetic resonance (NMR) is exploited in the technique of magnetic resonance imaging (MRI). This technique has a major advantage

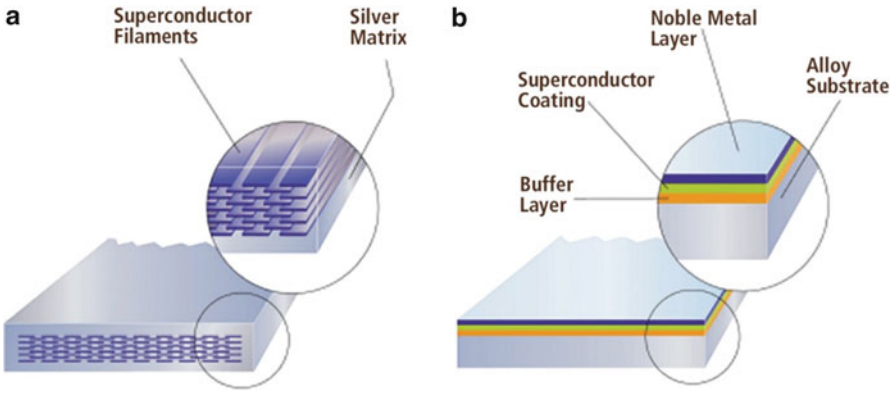

Fig. 11.24 Superconducting metal matrix composites: (**a**) first generation high temperature superconductor (HTS) filaments in a silver matrix (in commercial production), (**b**) second generation coated conductor composite, consisting of a superconductor layer, coated with a noble metal, on an alloy substrate (Courtesy of J. Jackson, American Superconductor)

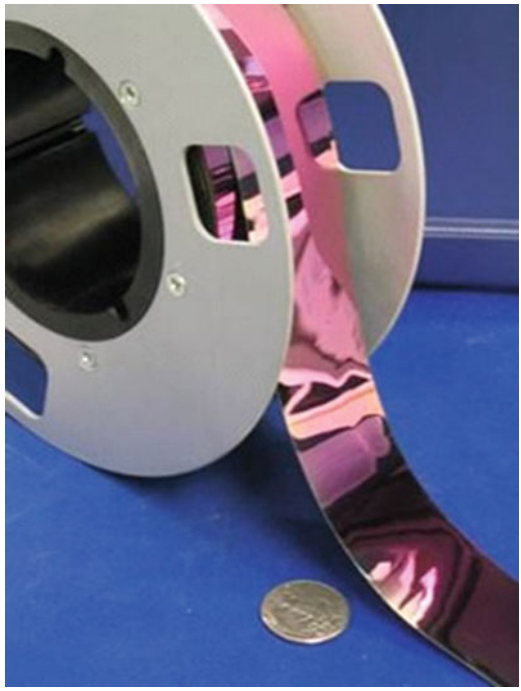

Fig. 11.25 Second generation superconductors, processed by RABiTS process, in tape form (Courtesy of J. Jackson, American Superconductor)

over X-ray radiography in that it is a noninvasive diagnostic technique, and thus the human body is not exposed to an ionizing radiation. Use is made of the electromagnetic characteristics of the nuclei of elements such as hydrogen, carbon, and phosphorus that are present in the human body. The nuclei of these elements act as

bar magnets when placed in a strong magnetic field. The patient is placed in the center of a very powerful magnet. When the magnetic field is turned on, the nuclei of the elements in the patient's body part under examination realign along the magnetic field direction. If we apply a radio frequency field, the nuclei will reorient. And if we repeat this process over and over again, the nuclei will resonate. The resonance frequency is picked up by a sensitive antenna, amplified, and processed by a computer into an image. The MRI images, obtained from the resonance patterns are more detailed and have a higher resolution than traditional techniques of visualization of soft tissues. And best of all, these images are obtained without exposing the patient to a radiation or performing biopsy.

The superconducting solenoid, made from Nb–Ti/Cu composite wire, is immersed in a liquid helium cryogenic Dewar. The liquid helium is consumed at about 4 mL/h, and each refill of the Dewar lasts about 3 months. Commercially manufactured NMR (nuclear magnetic resonance) spectrometer systems, also called magnetic resonance imaging systems, for medical diagnostics became available in the 1980s. As mentioned above, the big advantage of magnetic resonance imaging in clinical diagnostics is that it does not expose the patient to ionizing radiation and its possible harmful side effects. Of course, MRI techniques do not have to use superconducting magnets but certain advantages exist with superconductors, for example, better homogeneity and resolution and higher-field strengths than are available with conventional magnets. The disadvantage is that higher fields with superconductors lead to greater shielding problems.

11.5 Power Conductors

A relatively new application of MMCs is in the field of power transmission cable (3M Aluminum Conductor Composite Reinforced Technical Notebook 2003). The cable consists of a composite core, consisting of Al_2O_3 continuous fibers (Nextel 610) in an Al matrix, and is wrapped with Al–Zr wires. Figure 11.26a shows a power line with composite conductors installed in Buckeye, Arizona. The composite core bears most of the load, due to its much higher stiffness and strength. The maximum allowable temperature of the core (300 °C) is also higher than that of the surrounding wires (240 °C). The properties of the composite core and surrounding Al–Zr strands are shown in Table 11.3 (Kawakami et al. 1991).

Several tests were conducted on the actual conductor, including sag-tension behavior, vibration fatigue, thermal expansion, lightning resistance, and electrical resistance. These were conducted on a 235-m span installed in Les Renardieres, France. Lightning resistance was conducted by applying lightning arcs to the wires and monitoring damage, see Fig. 11.27. The level of damage between the aluminum conductor composite reinforced (ACCR) and the conventional aluminum conductor steel reinforced (ACSR) was similar. Damage was typically restricted to the outer aluminum layers and consisted of individual strand fracture, "splattering," and/or localized melting of the strand (3M).

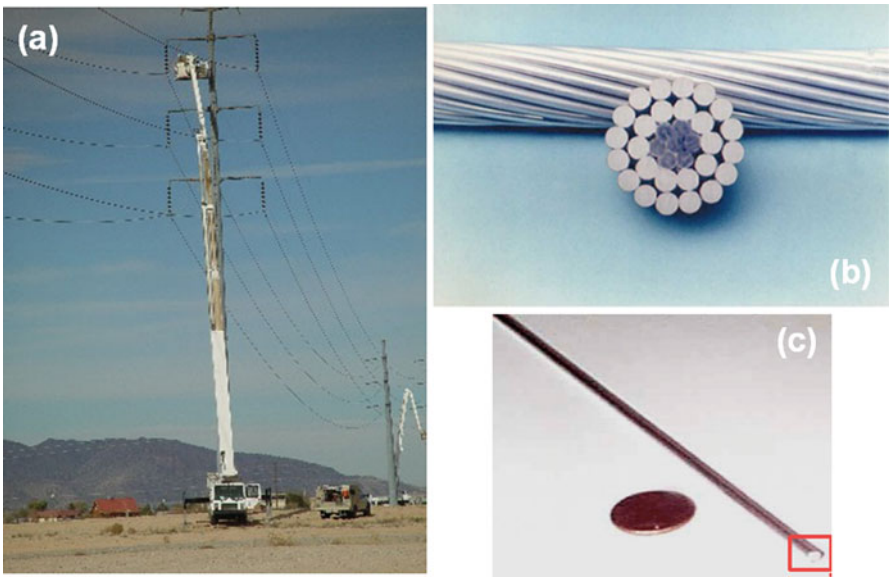

Fig. 11.26 Continuous fiber aluminum composite conductors: (**a**) 230 kV power line in Buckeye, AZ, (**b**) stranded composite conductor with aluminum alloy cables surrounding the composite core, and (**c**) individual composite filament (Courtesy of H. Devé, 3M Co.)

Table 11.3 Properties Al/Al_2O_{3f} composite core and Al–Zr wire (Kawakami et al. 1991)

Property	Composite core	Al–Zr wire
Tensile strength	1,380 MPa	162 MPa
Density	3.3 g/cm^3	2.7 g/cm^3
Young's modulus	215–230 GPa	–
Conductivity	24 % IACS[a]	>60 % IACS
Maximum allowable temperature	300 °C	240 °C
Fatigue endurance limit (10^7 cycles)	690 MPa	–

[a]IACS stands for International Annealed Copper Standard. Commonly, the electrical conductivity in power industry is expressed in terms of a percentage of this standard

Another important aspect of the testing of the conductors was vibration fatigue resistance. Long conductors were tested with a 7 m long gage length; see Fig. 11.28a. The applied peak-to-peak amplitude was varied between 0.7 and 1.4 mm, resulting in stresses approximately 25 % of the fracture strength and a turning angle of 5º. An endurance limit (taken here as 100 million cycles) was observed at an amplitude of 0.75 mm (0.03 in.). Figure 11.28b shows the onset of aluminum strand failures as a function of amplitude and vibration cycles. The aluminum wires always failed before the composite wires, since the composite core wires had a higher fatigue resistance.

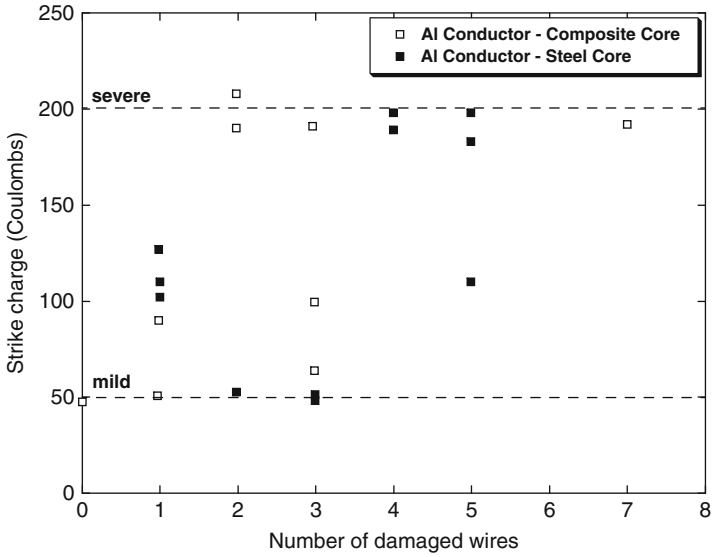

Fig. 11.27 25 C charge versus number of damaged wires (After 3M Aluminum Conductor Composite Reinforced Technical Notebook 2003). The number of damaged wires increases with charge level, with little difference between conductor types

11.6 Recreational and Sporting Goods

Particulate metal matrix composites, especially with light metal matrix composites such as aluminum and magnesium, also find applications in automotive and sporting goods. In this regard, the price per kg becomes the driving force for application. An excellent example involves the use of Duralcan particulate MMCs to make mountain bicycles. The Specialized Bicycle Co. in the USA sells these bicycles with the frame made from extruded tubes of 6061 aluminum containing about 10 % alumina particles. The primary advantage is the gain in stiffness.

The search for improved performance in recreational products often leads to new and exciting materials options. Metal matrix composites have been applied in both prototype and production applications of recreational products. The primary property advantage that has been utilized is the higher specific stiffness, especially in the golf club and bike frame applications.

An interesting recreational application of MMCs is in track shoe spikes (Grant 1999), shown in Fig. 11.29. The composite consists of an aluminum alloy matrix reinforced with particulate reinforcement of aluminum oxide, silicon carbide, boron carbide, or titanium carbide. The volume fraction of particles can range between 5 and 30 %. The composites are processed using a technique called "progressive cold forging," where about 300 parts/min can be produced. The unique shapes of the spikes are designed to compress the track without providing unwanted impact and stress to the athlete's feet and legs.

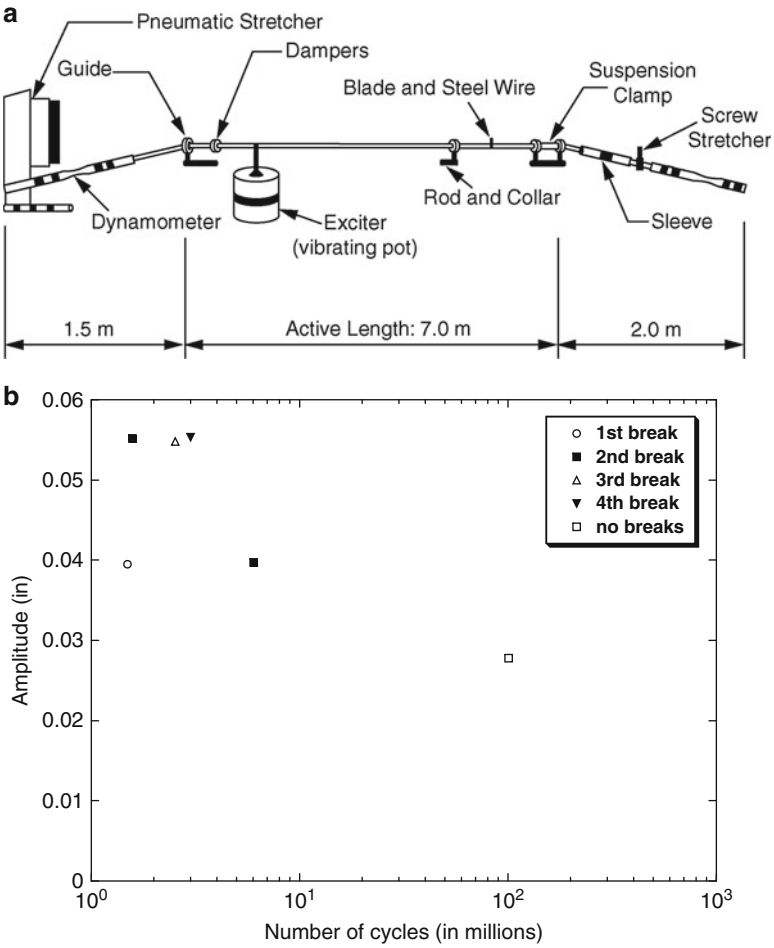

Fig. 11.28 (**a**) Schematic of set-up for vibration fatigue tests conducted on a 284-kcmil conductor and (**b**) displacement amplitude versus fatigue cycles curve. Below an amplitude of 0.03 in., the conductor did not fail (After 3M Aluminum Conductor Composite Reinforced Technical Notebook 2003). 1 in = 25 mm

An interesting example of particulate MMC involves a watch casing (Discovery News 2011). The composite used consisted of nanosized B_4C particles in an 18-karat gold matrix was developed by Hublot and the researchers at the Swiss Federal Institute in Lausanne, Fig. 11.30a. The composite contains 70 vol% reinforcement and 30 % matrix. By weight the composite is still about 75 % gold, so the composite can still be termed 18-carat gold, even though it is really a composite and not a metallic alloy. The reinforcement preform is heated to almost 2,000 °C to form a 3D porous network that is then infiltrated with liquid gold, resulting in a

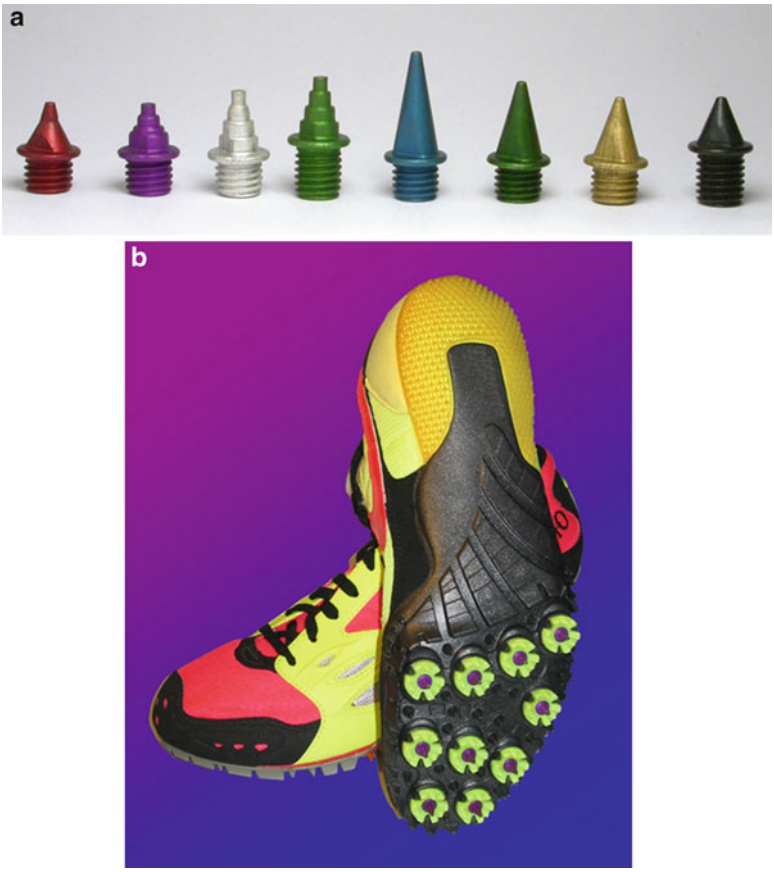

Fig. 11.29 (**a**) Particle reinforced MMCs used in track shoe spikes and (**b**) track shoe with MMC spikes (Courtesy of T. Wang, Omni-Lite Corp.)

microstructure shown in Fig. 11.30b. The composite is extremely scratch resistant, compared to pure gold, but retains the luster and aesthetic appeal of the pure metal. The material has a Vickers hardness of about 1,000 HV.

11.7 Wear-Resistant Materials

Extensive use is made of metal matrix composites in applications requiring wear resistance. Carbides, in general, and tungsten carbide, in particular, are very hard materials. Combined with a suitable ductile metal matrix, we can get a composite that is very useful for cutting, grinding, drilling, roll surfaces for rolling mills, and nibs of dies for wire drawing and such operations. One can get, by suitable

Fig. 11.30 (**a**) B_4C particle reinforced gold matrix composite watch casing and (**b**) 3D network microstructure of the composite, where *bright* is gold matrix and *dark* is B_4C. The volume fraction of reinforcement is 70 % (Courtesy of S. Hasanovic, Hublot)

microstructural design techniques, a wide range of hardness (which relates to wear resistance) and toughness combinations (Deng et al. 2001, 2002). Commonly, the volume fraction of WC particles varies between 0.70 and 0.90. The particle size typically ranges between 0.2 and 15 µm. Besides, the straight tungsten carbide/cobalt composite, one may incorporate different amounts of other carbides such as titanium carbide (TiC), tantalum carbide (TaC), and niobium carbide (NbC).

Microstructurally, tungsten carbide-based composites are isotropic and quite homogeneous. They have provided a technically very effective and reliable and economically very reasonable product. Figure 11.31 shows a roller-cone bit used for oil well drilling; the rock cutting inserts, made of WC/Co composites, are used on the cones.

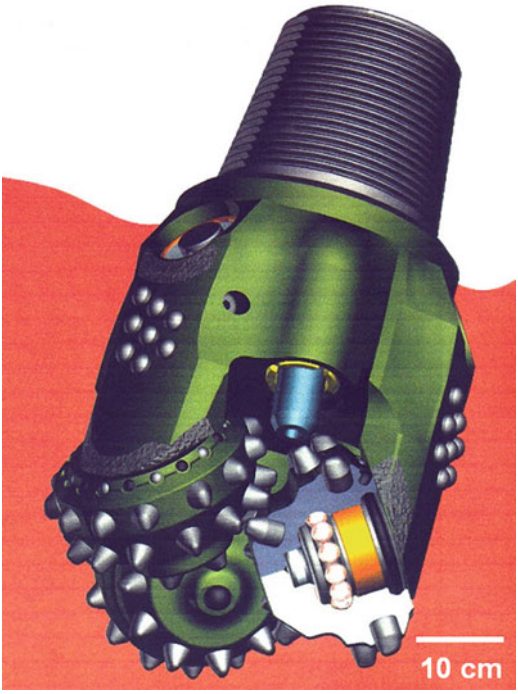

Fig. 11.31 Roller cone bit used for oil well drilling. The rock cutting inserts are made of WC/Co metal matrix composites (Courtesy of A. Griffo, Smith International, Inc.)

References

3M Aluminum Conductor Composite Reinforced Technical Notebook (2003) 3M, Minneapolis, MN, pp. 1–28.

Babcsan, N., D. Leitlmeier, H.P. Degischer, J. Banhart (2004) *Adv. Eng. Mater.*, **6**, 421–428.

Chawla, K.K. (1998) *Fibrous Materials*, Cambridge University Press.

Chawla, K.K., and N. Chawla (2004) in *Kirk-Othmer Encyclopedia*, John-Wiley and Sons.

Chawla, N., J.J. Williams, and R. Saha (2002) *J. Light Metals*, **2**, 215–227.

Cyrot M., and D. Pavuna (1992) Introduction to Superconductivity and High-Tc Materials, World Scientific Publishers.

Deng, X., B.R. Patterson, K.K. Chawla, M.C. Koopmnan, C. Mackin, Z. Fang, G. Lockwood, and A. Griffo (2001) *Int. J. Refrac. Met. Hard Mater.*, **19**, 547–552.

Deng, X., B.R. Patterson, K.K. Chawla, M.C. Koopmnan, C. Mackin, Z. Fang, G. Lockwood, and A. Griffo (2002) *J. Mater. Sci. Lett.*, **21**, 707–709.

Deng, X., D.R.M. Schnell, and N. Chawla (2006) *Mater. Sci. Eng.*, **426A**, 314–322.

Discovery News, http://news.discovery.com/tech/unscratchable-gold-111227.htm, December 2011.

Donomoto, T., N. Miura, K. Funatani, and N. Miyake (1983) *SAE Tech. Paper no. 83052*.

Evans, A.,C.S. Marchi, and A. Mortensen (2003) *Metal Matrix Composites in Industry*, Kluwer Academic Publishers, Dordrecht.

Grant, D. (1999) *United States Patent*, # 5,979,084.

Hoover, W. (1991) in *12th Risø International Symposium*, (N. Hansen et al. eds.), Roskilde, Denmark, Risø National Laboratory, pp. 387–392.

Hunt, W.H., and D.B. Miracle (2001) in *ASM Handbook – Composites*, vol. 21, 1029–1032, Materials Park, OH.

Koczak, M.J., S.C. Khatri, J.E. Allison, and M. Bader (1993) in *Fundamentals of Metal Matrix Composites*, (S. Suresh, A. Mortensen, and A. Needleman, eds.), Butterworth-Heinemann, Stoneham, MA.

Kawakami, K., M. Okuno, K. Ogawa, M. Miyauchi, and K. Yoshida (1991) *Furukawa Rev*., **9**, 81–85.

Leitlmeier, D., H.P. Degischer, H. Flankl (2002) *Adv. Eng. Mater*., **4**, 735- 740.

Miracle, D.B. (2001) in *ASM Handbook – Composites*, vol.21, 1043–1049, Materials Park, OH.

Rawal, S.P., (April 2001) *JOM*, **53**, 14.

Shakesheff, A.J., and G. Purdue (1998) *Mater. Sci. Tech*., **14**, 851.

Vlot, A., and J.W. Gunnick. (2001) *Fibre Metal Laminates*: *An Introduction*. Kluwer Academic Publishers, Netherlands.

Vogelesang, L.B., J. Schijve, and R. Fredell, "Fiber Metal Laminates: Damage Tolerant Aerospace Materials," *Case Studies in Manufacturing with Advanced Materials*, vol. 2, (1995) (A. Demaid and J.H.W. de Wit, eds.), Amsterdam: Elsevier, pp. 253–271.

Zeuner, T., P. Stojanov, P.R. Sahm, H. Ruppert, and A. Engels (1998) *Mater. Sci. Tech*., **14**, 857–863.

Author Index

A
Abd El-latif, M.H., 270, 272
Aghajanian, M.K., 59
Ahmed, M.M.I., 304
Ahuja, S., 74
Aikin, R.M., 218, 219
Akimitsu, J., 50
Albert, S.J., 318
Alic, J.A., 270
Allen, D.H., 233
Allison, J.E., 75, 79, 81, 163, 170, 174, 175, 191–193, 206, 237–239, 241–248, 260–263, 295, 296, 301, 336
Almer, J.D., 215, 217
Almond, E.A., 245
Alpas, A.T., 92, 316
Amell, A.A., 194, 196, 197, 199
Ananth, C.R., 176
Anderson, C.H., 57
Anderson, D.P., 15, 16
Anderson, I.E., 76
Anderson, W.P., 228
Andres, C., 75, 79, 81, 163, 170, 175, 191–193, 206, 237–239, 241–246
Andrews, K.W., 155
Angelini, P., 157
Armatis, F.A., 185
Arsenault, R.J., 111, 160, 170, 171, 173, 174, 218, 240
Arzt, E., 297
Aswath, P.B., 268
Atkins, S.L., 301
Auvray, S., 184
Ayers, J.D., 62
Ayyar, A., 204, 265–266, 268

B
Babcsan, N., 337
Bachler, E., 50
Bader, M., 336
Baker, A.A., 229
Balch, D.K., 150
Balooch, M., 25
Banhart, J., 337
Bao, G., 231, 301
Batt, T.J., 148
Bauschinger, J., 240
Beach, D.S., 87
Beck Tan, N.C., 218, 219
Becker, P.F., 157
Beevers, C.J., 260
Behrens, E., 151
Bettge, D., 255, 257, 278, 279
Bhikshamaiah, G., 144
Bieler, T.R., 306, 308
Biner, S.B., 301–303
Birchall, J.D., 22
Bird, J.E., 283
Blatt, D., 233
Blom, A.F., 268
Blucher, J.T., 186, 187
Boehlert, C.J., 186
Bolling, G.F., 69, 74
Bonnen, J.J., 260–263
Boselli, J., 76, 268
Boukhili, R., 144, 147, 148
Bowen, P., 231, 255, 256
Bowman, R.R., 184, 186
Bradbury, J.A.A., 22
Braddick, D.M., 229
Briber, R.M., 218, 219

N. Chawla and K.K. Chawla, *Metal Matrix Composites*,
DOI 10.1007/978-1-4614-9548-2,

Brindley, P.K., 115
Brockenbrough, J.R., 187, 189, 190
Brocks, W., 207
Brooksbank, D., 155
Brown, W.S., 29
Bucci, R.J., 260, 261
Budai, J.D., 87
Bullock, E., 284, 287
Bunsell, A.R., 28
Burger, E.E., 157
Burke, J.T., 59
Bushby, R.S., 179
Buttle, D.J., 191, 193

C
Calabrese, C., 242
Calvert, L.D., 48
Carreño-Morelli, E., 273
Carter, W.L., 86, 87
Chalmers, B., 72, 74
Champion, A.R., 229, 230
Chan, K.S., 181, 259, 260
Chandra, N., 176
Chang, S.-Y., 148
Channel, T.E., 179
Chapman, N.C., 196, 198, 274, 275, 276
Chawla, K.K., 5, 22, 34, 35, 41, 63, 85, 87, 92, 95, 104, 105, 109, 115–117, 135, 136, 138, 142, 144, 145, 148, 149, 154, 157, 160, 163, 164, 170, 172, 174, 204, 209, 215–217, 227–230, 237, 247, 262, 265, 267, 269, 272–274, 277, 284, 304, 318–321, 330, 337, 352
Chawla, N., 34, 35, 43, 45, 61, 62, 75, 76, 79, 81, 82, 84, 85, 90, 92, 94, 95, 115, 116, 135, 138, 139, 144–146, 163, 164, 170, 175, 191–201, 203, 204, 206, 207, 209, 210, 212, 214–217, 229, 231, 237–248, 262, 264–266–269, 272–276, 297, 337, 342
Chen, H., 117
Chen, J., 231, 232
Cheng, L., 79
Cheskis, H.P., 164
Chiou, W.A., 146, 147
Chirayil, T.G., 87
Cho, B., 24
Chou, T.C., 92
Christen, D.K., 87
Christman, T., 160, 207
Christodolou, L., 63
Chung, S., 314, 316
Cisse, J., 74
Clarke, H., 322
Cleveland, C., 92, 95
Clyne, T.W., 201, 212, 295
Cockayne, B., 23
Coffin, C., 115, 116, 135, 136
Cole, G.S., 69
Cook, J., 179, 180, 270
Corbin, S.F., 163
Cornie, J.A., 185
Cottenden, A.M., 245
Cotterell, B., 182
Cotterill, P.J., 255, 256
Couper, M.J., 238
Cox, B.N., 182
Cox, H.L., 164
Cranmer, D.C., 115
Crasto, A.S., 15, 16
Crowe, C.R., 63, 322
Cui, X., 87
Curtin, W.A., 176
Cutler, I.B., 29

D
Davidson, D.L., 259, 260
Davies, P.W., 297
Davis, L.C., 170, 237, 243–245, 301
Daymond, M.R., 215, 217
De Carlo, F., 194, 196, 197, 198, 199, 262, 265, 266, 274, 275, 276
DeBolt, H.E., 24
Degischer, H.P., 337
Deng, X., 85, 86, 92, 95, 135, 136, 144–146, 212, 214, 318–321, 342, 352
Derby, B., 89, 191, 193, 278, 297, 303
Deurbergue, A., 15
Deve, H.E., 179
Devé, H.E., 176, 178, 231, 232
Dhindaw, B.K., 74
Dhingra, A.K., 229, 230
DiCarlo, J.A., 28
Dickerson, P.O., 23
Diefendorf, R.J., 10, 13
Diehl, J., 240
Ding, Y., 92
Dinwoodie, J., 22
Dirichlet, G.L., 76, 202
Divecha, A.P., 58
Djazeb, M.R., 81
Dlouhy, A., 111, 289, 290, 292, 293
Doerner, M.F., 115
Doker, H., 253

Donomoto, T., 334
Dorn, J., 153
Dorn, J.E., 283
Dragone, T.L., 297–300
Dresher, W.H., 6
Dunand, D.C., 170, 171, 173, 215, 217, 297
Duszczyk, J., 76
Dutta, I., 209
Dyos, K., 184

E
Ebihara, B.T., 117
Eggeler, G., 289–293
Einstein, A., 57
Eldridge, J.I., 115–117, 184, 186
Elices, M., 260
Ellis, L., 85
Ellyin, F., 243
Elomari, S., 144, 147, 148
Embury, J.D., 92, 308
Engels, A., 321, 338, 339
Erdogan, F., 228
Eshelby, J.D., 135
Estrada, J.L., 76
Evans, A., 325
Evans, A.G., 179, 181, 182
Evans, R.W., 284
Ezekiel, H.N., 10

F
Fang, Z., 85, 135, 136, 318–321, 352
Farmer, S.C., 23
Faucon, A., 184
Feenstra, R., 87
Felten, J.J., 24
Ferber, M.K., 92, 115
Fine, M.E., 145–149
Finot, M., 207, 208, 210, 240
Fischer, C., 153
Fisher, R.M., 111, 160, 170
Fishman, S.G., 322
Fitzgerald, T.J., 150
Flank, A.M., 28
Flankl, H., 337
Flemings, M.C., 56, 148
Flom, Z., 194, 196, 197, 199
Foley, J.C., 76
Folgar-Portillo, M.F., 314, 315
Foulk, J.W. III., 233
Fredell, R., 328, 331
Froes, F.H., 76
Fuller, E.R., 138, 163, 209
Funatani, K., 334

G
Gabryel, C.M., 110
Gac, F.D., 30
Gagnon, G., 278
Galvez, F., 177
Ganesh, V.V., 43, 79, 81, 82, 135, 138, 139, 200, 209, 210, 212, 237, 264, 269
Gao, Y.C., 182
Garcia-Cordovilla, C., 314
Gasson, D.G., 23
Ghonem, H., 255
Ghosh, A.K., 75, 78, 305–307
Gibeling, J.C., 301
Godefroid, L.B., 85
Gomez, J.P., 237
Gomez, M.P., 228
Gonzalez, C., 176, 177, 187–189, 212, 213
Goodier, J.N., 155, 163
Gopalakrishna, B., 144
Gordon, J.E., 179, 180, 270
Görtring, K., 245, 249
Goto, S., 287, 290
Gottstein, G., 117
Gouda, M., 229
Gouda, T., 207
Goyal, A., 87
Grande, D.H., 115
Grant, D., 350
Gregory, M., 270, 271
Gregson, P.J., 268
Griffith, W.M., 76
Griffo, A., 85, 318–321, 352
Grimes, H.H., 184
Grube, W.L., 240
Gu, M., 231, 232
Guden, M., 177
Gungor, M.N., 148
Gunnick., J.W., 328, 330–332
Gunther, B., 255, 257, 278, 279
Guo, Y.L., 212, 215, 216
Guo, Z.X., 89
Gupta, M., 79
Gupta, V., 181, 182
Guth, E., 57
Gurland, J., 317

H
Habel, U., 170, 206, 237, 242, 243, 246
Hack, J.E., 179, 184, 230
Haeffner, D.R., 215, 217
Haggerty, J.S., 23
Hale, D.K., 153
Hall, I.W., 177, 184, 185
Hall, J., 237
Halpin, J.C., 133
Han, S.H., 70, 72
Hansen, N., 81
Harmon, D.M., 248, 251
Harris, B., 229
Hartman, H.S., 229, 230
Hashin, Z., 130–132, 142, 144
Hassan, H.A., 270, 272
Hasson, D.F., 322
Hatanaka, K., 255, 257, 278
Hatfield, E., 87
Hausmann, J., 184, 284, 286
Hayashi, J., 25
Haynes, J.A., 92
He, J.L., 92
He, M.Y., 179, 181
He, Q., 87
Healy, J.C., 260
Heckel, R.W., 164
Heinrich, W., 245, 249
Helinski, E.J., 82
Hellerich, C.L., 104
Helms, K.L.E., 233
Hemptenmacher, J., 255, 257, 278, 279
Henshall, C.A., 305
Hermans, J.J., 130
Herr, M., 245, 249
Herrman, K.P., 157
Hiang, B., 314, 316
Hiasyuki, T., 29
Higashi, K., 308
Hill, R., 129–131
Hill, R.G., 104
Hillmann, H., 53
Hirth, J.P., 193, 219, 221
Hoffman, R.W., 92
Holm, D.K., 268
Holmes, J.W., 231
Hong, K.C.C., 115
Hoover, W., 335
Hosking, F.M., 314, 315
Howard, S.J., 201, 212
Hruby, P., 262, 265, 266
Hsu, D.K., 200
Hsu, F.S.L., 50
Hsueh, C.-H., 157
Hu, W., 117
Huang, J., 238, 239
Hull, A.W., 157
Humphreys, F.J., 81, 174
Hunt, W.H., 76, 78, 85, 218–221, 335, 337
Hurley, G.F., 23
Hutchinson, J.W., 179, 181, 182, 301
Hwang, H.J., 23

I
Isaacs, J.A., 171
Ichikawa, H., 28, 29
Ishirkawa, T., 29

J
Jackson, K.A., 72, 74
Jackson, P.W., 229
Jahanmir, S., 316
Jain, M.K., 144
James, W.B., 83
Jansson, S., 179
Jech, R.W., 126
Jeng, S.M., 288, 291
Jensen, D.J., 81
Jensen, H.M., 182
Jeong, H., 200
Ji, Z., 92
Jiang, L., 215, 216, 217
Jin, I., 68, 69, 72
Jira, J.R., 233
Johnson, D.J., 10
Johnson, W., 10
Johnson, W.S., 237
Jones, J.W., 75, 79, 81, 163, 170, 174, 175, 191–193, 206, 237–239, 241–248, 260–263, 295, 296

K
Kakar, A.S., 74
Kakihara, K., 321
Kamat, S., 193, 219, 221
Karcher, T., 92, 95
Kardos, J.L., 133
Karmarkar, S.D., 58
Kataoka, T., 58
Katsumata, M., 186, 187
Katsura, M., 57
Kaufmann, A.R., 54
Kawakami, K., 348, 349

Kelly, A., 164
Kerans, R.J., 113, 182
Kerchner, H.R., 87
Kerner, E.H., 142, 143
Kerr, M., 34, 35, 229, 297
Khatri, S.C., 336
Kibbe, W., 90, 94
Kim, J.K., 74, 75
Kim, Y.W., 76
Kindermann, P., 245, 249
Kinney, J.H., 25
Kitano, T., 58
Klundt, R.H., 295
Kobayashi, T., 207, 220, 222
Koczak, M.J., 75, 336
Komarneni, S., 21
Konitzer, D.G., 184
Koopman, M.C., 85, 92, 95, 115, 116, 135, 136, 138, 163, 209, 318–321, 352
Korenyi-Both, A., 184, 186
Korevaar, B.M., 76
Koss, D.A., 243
Kowalski, L., 76
Krajewski, P.E., 174, 295, 296
Krishnamurty, S., 186
Kroeger, J.D., 87
Krueger, W.H., 229, 230
Krukonis, V.J., 24
Kumagai, M., 21
Kumar, S., 15, 16
Kumpfert, J., 184, 284, 286
Kung, H., 92
Kunzler, J.E., 50
Kurumlu, D., 291
Kwei, L.K., 272, 277
Kyono, T., 184, 185

L

LaBelle, H.E., 23
Lad, R.A., 184
Laffon, C., 28
Lagarde, P., 28
Lagoudas, D.C., 186
Laird, C., 242
Lancaster, J.K., 117
Langdon, T.G., 298, 300, 303–305
Langer, S., 163, 209
Langer, S.A., 138
Lara-Curzio, E., 25
Larsen, J.M., 233
Latanision, R.M., 322
Lavernia, E.J., 62, 303
Lee, D.F., 87
Lee, H.C., 317
Lee, J.-G., 29
Lee, S., 288, 291
Lee, S.M., 113
Lee, Y.S., 148
Leitlmeier, D., 337
Lepetitcorps, Y., 184
Leverant, G.R., 179, 184, 230, 259, 260
Levy, A., 209
Lewandowski, J.J., 76, 82, 85, 191, 193, 218–221, 237, 270, 272, 308
Leyens, C., 184, 284, 286
Li, C., 243
Li, H.D., 92
Li, W.Z., 92
Li, Y., 298, 300, 303–305
Liaw, P.K., 79, 104, 148, 198, 200, 269
Liechti, T., 278
Liggett, G.M., 272–274
Lilholt, H., 164, 284, 285, 303
Lin, S.-J., 148
Lindemanis, A., 30
List, F.A., 87
Liu, C., 76, 193
Liu, C.H., 92
Liu, D.S., 193
Liu, J., 231, 255
Liu, Y., 317
Liu, Y.L., 81
LLorca, J., 139, 176, 177, 187–189, 207, 208, 212, 213, 234, 237, 240, 260
Lloyd, D.J., 57, 59, 63, 69, 70, 72, 75–76, 78, 144, 147, 148, 201, 202, 220, 221
Loang, F.L., 61
Lockwood, G., 85, 135, 136, 318–321, 352
Logsdon, W.A., 79, 198
Loretto, M.H., 184
Lorriot, T., 184
Louat, N., 253, 262
Louis, E., 314
Lowden, R.A., 115, 231
Lowhaphandu, P., 308
Lu, Y.C., 92
Lucas, K.A., 322
Ludema, K.C., 316
Luetjering, G., 242
Lukasak, D.A., 243, 260, 261

M

Mabuchi, M., 308
Mackenzie, J.K., 273

Mackin, C., 352
Mader, S., 240
Mahajan, Y.R., 144, 297
Mahoney, M., 305–307
Mai, Y.W., 182, 314
Maisel, J.E., 184
Majumdar, B.S., 186, 231
Mall, S., 234, 237, 238
Mandell, J.F., 115
Mann, A.B., 25
Manoharan, M., 85, 191, 193, 218–220
Marchi, C.S., 325
Marci, G., 253
Margolin, H., 61
Marom, G.D., 142
Marshall, D.B., 113, 115, 181, 182
Martin, E., 184
Martin, P.M., 87
Martinez, D., 181, 182
Maruyama, B., 76
Mater, J., 92
Mathis, J., 87
McCartney, R.F., 270
McCullough, C., 176, 178, 179
McDanels, D.L., 126
McEvily, A.J., 229
McGarry, F.J., 115
McGuire, M.A., 229
McLean, M., 64, 284, 287, 290
McLeod, A.D., 110
McMeeking, R.M., 301
McMinn, A., 259, 260
Meartini, G.T., 92
Mehrabian, R., 56, 193, 219, 221, 314, 315
Merk, N., 289, 290, 292, 293
Messing, G.L., 21
Metzger, M., 104, 105, 157, 170, 172, 230, 322
Meyers, M.A., 41, 204, 227, 284, 304
Michaud, V.C., 65, 67, 75
Mikata, Y., 184
Miles, D.E., 284, 287
Milewski, J.V., 29, 30
Miller, A.K., 295
Miller, D.A., 186
Miller, R.L., 215
Miller, W.S., 81
Minoshima, K., 176, 177
Miracle, D.B., 76, 186, 326, 335, 337
Mishra, R.S., 297, 306, 308
Misra, A., 92
Mitchell, T.E., 92
Mitra, A., 74
Mitra, R., 145–149
Miura, N., 334
Miyake, N., 334
Miyake, T., 284
Miyauchi, M., 348, 349
Mlavsky, A.I., 23
Mohamed, F.A., 303, 304
Morell, J.S., 87
Morris, E., 61, 62
Morris, W.L., 113
Mortensen, A., 68, 69, 72, 130, 144, 147, 150, 153, 170, 171, 173, 187, 191, 325
Moser, B., 130, 187, 191
Mott, N.F., 240
Mueller, L.R., 270, 271
Mukherjee, A.K., 283, 306, 308
Mummery, P.M., 191, 193
Muranaka, T., 50
Murayama, T., 321
Murphy, A.M., 201, 212

N

Nagamatsu, J., 50
Nagelberg, A.S., 59
Nakagawa, N., 50
Nakanishi, H., 321
Nakayama, A., 321
Narciso, C.J., 314
Nardone, V.C., 170, 171, 191, 297
Narusawa, U., 186, 187
Nastasi, M., 92
Needleman, A., 149, 207, 208, 210, 240, 285, 288
Nelmes, G., 297
Nelson, R.P., 104
Nemeth, A., 186, 187
Neuman, A., 272–274
Newaz, G.M., 231
Nieh, T.G., 92, 293, 297, 305
Niihara, K., 23
Nishide, S., 284
Nix, W.D., 115, 297–300
Nordine, P.C., 24
Northwood, D.O., 92
Norton, D.P., 87
Nourbakhsh, S., 61

O

Oberlin, A., 15
Ogawa, K., 348, 349
Ohno, N., 284
Okamoto, N., 284

Okamura, K., 25, 29
O'Keefe, M.J., 92
Okuno, M., 348, 349
Oliver, W.C., 92, 115
Omori, M., 25
Orowan, E., 240
Osman, T.M., 85, 218–221
Ozawa, M., 215

P
Page, R.A., 179, 184, 230
Pandey, A.B., 297
Papazian, J.M., 209
Paranthaman, M., 87
Paris, P.C., 228
Park, C., 87
Park, K.-T., 303
Parker, J.D., 297
Parrish, P.A., 63
Parthasarathy, T.A., 113, 182
Partridge, P.G., 89
Pastor, J.Y., 234
Patel, B., 115, 116
Patel, B.V., 135, 136, 138, 163, 209
Patterson, B.R., 85, 135, 136, 138, 163, 209, 318–321, 352
Paul, B., 130, 148
Payton, M.L., 291
Peebles, L.H., 15
Penn, L.S., 113
Pennander, L., 57
Peters, P.W.M., 255, 257, 278, 279
Petrovic, J.J., 30
Pfeifer, M., 109
Pfeiffer, N.J., 270
Pharr, G.M., 92
Pickard, S.M., 61, 62, 278
Pickett, J.J., 54
Pillai, U.T.S., 240
Piotrowski, G., 81, 212, 215, 216
Pitcher, P.D., 268
Pollack, J.T.A., 23
Poritsky, H., 157
Portella, P.D., 255, 257, 278, 279
Portner, B., 234
Potschke, J., 72
Poza, P., 177, 237
Prewo, K.M., 170, 171, 191, 229
Pritchard, J.R., 117
Pugsley, V.A., 245, 249
Purdue, G., 331, 333

R
Rack, H.J., 314
Ralph, M., 185
Rao, Venkateshwara T., 186, 255, 258
Rassweiler, G.M., 240
Rawal, S.P., 333, 335
Ray, S., 317
Rebstock, H., 240
Requena, G., 291
Rezai-Aria, F., 278
Richard, R.C., 270
Richmond, O ., 308
Riek, R.G., 56
Riester, L., 115
Riggs, J.P., 14
Rigsbee, J.M., 92, 109
Riley, G.N., Jr., 86, 87
Riley, M.B., 130
Rios, P.R., 215–217
Ritchie, R.O., 186, 255, 258, 260, 262, 263
Rodjom, T.J., 82
Roebuck, B., 245
Rogge, V., 72
Rohatgi, P.K., 74, 75, 317
Rohr, D.L., 30
Rosen, B.W., 130–132, 142
Rosenberger, A.H., 186
Rossoll, A., 130, 187, 191
Roy, R., 21
Ruhle, M., 181
Ruiz, J., 260
Ruppert, H., 321, 338, 339
Russ, S.M., 186
Ryder, D.A., 270

S
Sachdev, A., 237
Sadananda, K., 253, 254, 260, 262
Sadanandam, J., 144
Saff, C.R., 248, 251
Saha, R., 45, 61, 62, 76, 81, 82, 84, 85, 138, 195, 199–201, 203, 204, 337
Sahm, P.R., 321, 338, 339
Sahoo, P., 75
Salazar, A., 234
San Marchi, C., 144, 147
Sanders, B.P., 234, 237, 238
Sandhage, K.H., 86, 87
Sando, M., 23
Sandstrom, J.L., 29
Sauthoff, G., 48

Savage, R.H., 117
Sayir, A., 23
Schaller, R., 273
Schapery, R.A., 142, 143
Scherer, G., 157
Schijve, J., 328, 331
Schleinkofer, U., 245, 249
Schlund, P., 245, 249
Schnell, D.R.M., 144–146, 342
Schöbel, M., 291
Schulte, K., 176, 177
Scruby, C.B., 191, 193
Seeger, A., 240
Segurado, J., 139, 212, 213
Sehitoglu, H., 255, 257, 278
Seigenthaler, D.M., 209
Seleznev, M.L., 185
Shakesheff, A.J., 331, 333
Shang, J.K., 260, 262, 263
Shangguan, D., 74
Shannon, R.E., 200
Shatwell, R.A., 184
Shaw, M.C., 113
Shekhar, J.A., 70, 72
Shen, Y.-L., 92, 95, 149, 150, 164, 170, 206–208, 210, 212, 215, 216, 237, 240, 242, 243, 246
Sherby, O.D., 295, 305
Sherman, R., 184, 230
Shetty, D.K., 182
Shi, N., 170, 171, 173, 174, 218
Shibuya, M., 29
Shirota, T., 58
Shtrikman, S., 132, 144
Siegmund, T., 207
Silva, J., 262, 265, 266
Simha, R., 57
Simon, G., 28
Sims, J.D., 209
Sinclair, I., 76, 268
Singer, L., 10, 13, 14
Singh, D.R.P., 92
Singh, S.S., 262, 265, 266, 274, 275, 276
Siu, S.C., 186, 255, 258
Skaggs, S.R., 30
Skrotzki, B., 255, 257, 278
Smith, P.R., 186
Sockel, H.-G., 245, 249
Song, J., 117
Sørensen, N., 285, 288
Spain, R.G., 10
Specht, E.D., 87
Speich, G.R., 215
Spowart, J.E., 76, 238, 239
Srivatsan, T.S., 62
Starke, E.A., 242
Stayley, J.T., 242
Stefanescu, D.M., 74
Steglich, D., 207
Sternstein, S., 25
Stewart, J.L., 215, 216, 217
Stojanov, P., 321, 338, 339
Stoloff, N.S., 259
Strife, J.R., 297
Sugimura, Y., 260, 262
Suh, N.P., 316
Sun, C.T., 248, 251
Sundarajan, G., 314–316
Suresh, S., 149, 150, 160, 174, 187, 189, 190, 207, 208, 210, 227, 240, 260, 262, 268
Suryanarayana, S.V., 144
Suwa, Y., 21

T

Tachikawa, K., 54
Tamura, I., 215
Tang, G., 92
Taya, M., 184, 185, 303
Taylor, L.G., 270
Termonia, Y., 167
Thadhani, N.N., 90, 94
Tham, L.M., 79
Thomas, D.G., 57
Tien, J.K., 297
Timoshenko, S., 155
Toda, H., 207
Tokarsky, E., 10, 13
Tomota, Y., 215
Torquato, S., 204
Towata, A., 23
Toyoda, K., 284
Trivedi, R., 70, 72
Trozzo, P.S., 270
Tsai, S.W., 133
Tsiang, T.H., 115
Tsui, T.Y., 92
Turner, P.S., 142, 144
Tvergaard, V., 285, 288
Tyson, C.N., 10

U

Uhlmann, D.R., 72, 74
Upadhyaya, G.S., 317

V
Vaidya, R.U., 142, 144
Van Aken, D.C., 242
Vasudevan, A.K., 253, 254, 260, 262, 308
Venkataraman, B., 314–316
Verdier, M., 92
Verebelyi, D.T., 87
Villers, P., 48
Visser, L.R., 21
Vlot, A., 328, 330–332
Vogelesang, L.B., 328, 331
Vogelsang, M., 170
Voleti, S.R., 176
Vyletel, G.M., 242

W
Wadsworth, J., 305
Wallis, R.R., 237
Walls, D.P., 231, 233
Wang A., 314
Wang, L., 220, 222
Wang, P.T., 82
Wang, Y.Q., 157
Ward-Close, C.M., 89
Warrier, S.G., 186
Watt, W., 10, 15
Wawner, F.E., 24, 237
Wax, S.G., 26
Weber, J.K.R., 24
Weber, L., 153
Webster, D., 293, 295, 297
Wedell, W., 255, 257, 278, 279
Weertman, J.R., 146, 147
Weeton, J.W., 126
Weibull, W., 33
Weihs, T.P., 25, 115
Weinberg, A., 142
Wereszczsak, A.A., 115
Wernick, J.E., 50
Wheeler, D.R., 184, 186
White, D.R., 59
Whitehouse, A.F., 295
Whitney, J.M., 130
Wienecke, H.A., 187, 189, 190
Wilkinson, D.S., 163, 297
Williams, J.J., 45, 76, 81, 82, 84, 85, 139, 194–201, 203, 204, 212, 215–217, 262, 265–266, 268, 274–276, 337
Williams, K.R., 297
Wilshire, B., 284, 297
Wilson, D.M., 21
Winand, H.M.A., 295
Wolfenden, A., 272–274
Wu, G., 270, 271
Wu, M.Y., 305
Wu, S.B., 240
Wu, Z., 231, 232
Wundnerlin, R., 314, 315
Wunsch, B., 138, 139, 209, 210, 212

X
Xia, K., 238
Xiao, X., 194, 196, 197, 198, 199, 262, 265, 266, 274, 275, 276
Xu, Z.R., 145, 148, 149, 272–274

Y
Yajima, S., 25
Yamamura, T., 29
Yang, J.-M., 270, 271, 288, 291
Yang, N., 76
Yasuoka, M., 23
Yavari, P., 304
Yoshida, K., 348, 349
You, C.P., 260–263
Young, M.L., 217
Young, R.J., 167
Yu, W.K., 260, 262, 263
Yuan, J., 181, 182
Yun, H.M., 23

Z
Zenitani, Y., 50
Zeuner, T., 321, 338, 339
Zhang, F., 231, 232
Zhang, J., 316
Zhang, L.C., 314
Zhang, T., 255
Zhang, W., 231, 232
Zhang, Z.F., 314
Zhong, Y., 117
Zok, F.W., 231, 233, 308
Zong, B.Y., 303

Subject Index

A
AFM. *See* Atomic force microscopy (AFM)
Age hardening. *See also* Precipitation strengthening
  accelerated aging, 174
Alumina, 1, 20–24, 32, 104, 105, 109, 111, 117, 160, 161, 230, 231, 272, 276, 277, 313–315, 334, 350
Alumina/Mg
  interface, 55, 59, 109, 297
Aluminum, 1, 18, 20, 21, 23, 42–46, 49, 100, 103–105, 108–111, 130, 147, 150, 227, 237, 270, 296, 317, 321, 322, 326, 328, 330, 331, 333, 334, 339, 343, 344, 348–350
Aluminum alloys
  precipitation strengthening, 42
Angle of contact, 84, 101, 102
Applications
  aerospace, 46, 325–334
  electronics and thermal management, 339–344
  fiber metal laminates, 328–331
  power conductors, 348–349
  recreational and sporting goods, 349–353
  superconducting magnets, 344–348
  transportation, 334–339
  wear-resistant materials, 352–354
Aspect ratio, 5, 29, 30, 136–138, 153, 169–172, 197, 199, 293, 297, 299, 301
Atomic force microscopy (AFM), 105, 106

B
Bauschinger effect, 240, 277
Bonding
  chemical, 102–110
  crystalline structure, 37–38
  mechanical, 81, 102–104, 184, 186
Bulk modulus, 122, 130–132, 144, 150
Burgers vector, 39–41, 44, 171, 283

C
Carbon fibers
  fabrication, 10
  PAN-based, 10–12, 14–16
  pitch-based, 12–13
  structure, 14–16
Casting
  centrifugal, 55, 58–60
Cobalt (Co), 1, 47, 84, 150, 245, 313, 317–319, 352
Coefficient of thermal expansion (CTE)
  effect of interface, 145–148
Copper, 1, 41, 47, 49–52, 85, 88, 111, 126, 150, 230, 231, 342, 343
Crack deflection criteria, 179–182
Crack growth. *See* Fatigue
Creep
  activation energy, 283, 287, 297, 304, 305
  continuous fiber, 284–289
  discontinuously reinforced, 285, 289–304
  dislocation climb, 283, 297, 304
  dispersion strengthening, 297, 300, 307
  grain boundary sliding, 301, 304, 307
  load transfer, 285, 288, 289, 293, 295, 297, 298, 300, 305
  recovery, 283, 285, 287–290, 293

N. Chawla and K.K. Chawla, *Metal Matrix Composites*,
DOI 10.1007/978-1-4614-9548-2, © Springer Science+Business Media New York 2013

Creep (*cont.*)
stress exponent, 283, 284, 286, 293, 297, 298, 301, 303, 304
threshold stress, 287, 297–301, 303, 305
Critical fiber length, 113
CTE. *See* Coefficient of thermal expansion (CTE)

D
Damage evolution, 163–164, 175, 191, 193, 194, 275
Density, 6, 8, 14, 17, 21, 22, 26, 28, 29, 32, 40, 41, 45–51, 56, 66–68, 75, 82, 84–87, 89, 104, 105, 111, 121, 139–140, 150, 152, 170–174, 196, 230, 231, 234, 273, 274, 289–292, 303, 314, 317, 325, 331, 335, 344, 345, 349
Diffusion bonding
foil-fiber-foil, 90, 91
Diffusivity
activation energy for creep, 108, 283–284, 287, 297, 304, 305
Dislocation
climb, 283, 289, 292, 297, 304
fiber reinforced composites, 121–161
punching, 170, 171, 173, 174, 209, 259
strengthening, 41, 42, 170, 174, 193, 209, 230, 242, 293
W/Cu, 171
Dispersion strengthening, 42, 297, 308
Dual phase steel, 216, 217

E
Elastic constants
strength of materials approach, 123–129
Electrical conductivity, 1, 47, 67, 121, 151–154, 333, 349
Energy methods, 129–130
Eshelby method, 135–138
Explosive shock consolidation, 90–91
Extrusion
co-extrusion, 85–89

F
Fatigue
crack closure, 247, 250, 251, 255, 267–268
crack growth
continuous fiber, 247–260
particle reinforced, 260–269
threshold stress intensity factor, 248
crack initiation, 227, 229, 230, 243
damage mechanisms, 229, 231, 232, 234, 236–237, 250, 268, 279
elevated temperature, 231, 233, 234, 243–244, 247, 248, 337
hybrid and laminated composites, 268–272
Paris law, 231, 232, 259–262, 264, 270, 272
stiffness loss
Mackenzie's equation, 273
stress *versus* cycles (S-N)
continuous fiber, 228–236
particle reinforced, 237–249
thermal, 227, 230, 242, 259, 272–279
two parameter approach, 247, 253, 254, 262
ultrasonic fatigue testing, 227
FEM. *See* Finite element method (FEM)
Fiber(s)
alumina, 1, 20–24, 109, 111, 117, 160, 161, 230, 231, 272, 276–277
alumina + silica, 20–24
boron, 17–20, 25, 184, 229, 237, 247, 251, 333, 344
carbon, 8–18, 25–29, 103, 108, 110, 117, 127, 150, 177, 184, 186, 229, 231, 322, 327, 331, 333–336, 344
comparison, 28, 32, 176, 178, 247–248
flexibility, 6–7, 32, 90
mullite, 20, 22, 23
silicon carbide
Nicalon, 8, 29, 106, 107
strength, 15, 17, 29, 32–35, 90, 111, 176, 186, 230
surface roughness, 102, 103, 105, 116–117
Weibull, 33, 34
Fiber pullout
work of pullout, 111, 113–118, 179, 182–184, 247, 250
Fiber pushout, 113–118, 231, 233
Finite element method (FEM)
cyclic fatigue, 242
microstructure based, 138, 146, 211, 212
three dimensional (3D), 138, 212
Flexibility. *See* Fiber
Forging, 3, 75, 76, 82–85, 200, 350
Fracture toughness
effect of particle clustering, 218

G
Grain boundary
sliding, 23, 301, 302, 304, 307
strengthening, 41–42, 307

H
Hall-Petch relation, 284, 287
Halpin-Tsai-Kardos, 151
Hardness
relation to tensile strength, 169
relation to wear, 231, 233, 240, 311, 316–319, 321, 337, 352
High temperature superconductor (HTS). *See also* Superconductor
oxide powder in tube (OPIT), 86, 89
RABiTS™, 87, 88, 346, 347
Yttrium-Barium-Copper-Oxide (YBCO), 23, 49, 87
HTS. *See* High temperature superconductor (HTS)

I
ILSS. *See* Interlaminar shear strength (ILSS)
Indentation, 115–118, 213, 216
In situ, 55, 66, 191, 196, 198, 215–218, 233, 259, 262, 265, 274, 284, 287
In situ processing, 55, 63–66
Interface
bend tests, 112–113
bond strength, 112–118, 184, 185, 200, 231
crystallographic nature, 100–101
reaction products, 18, 59, 104, 110, 111, 140, 335
reaction zone, 108–110, 184, 247
Interfacial bond strength
measurement techniques, 237
Interlaminar shear strength (ILSS), 112
Intermetallics
Ti_3Al, 90, 94

L
Laminated composites, 85, 87, 91, 237, 268–272
Liquid infiltration, 55–62, 65–68, 259
Load transfer
in creep, 285, 288, 289, 293, 295, 297, 298

M
Magnesium alloys, 47, 272
Metal matrix composites (MMCs)
advantages, 1, 325
characteristics, 3–4, 37, 228
types, 2–3, 100, 102, 179, 228
typical reinforcements, 3
Metals
strengthening mechanisms, 41–45
Micropillar compression, 216, 218
MMCs. *See* Metal matrix composites (MMCs)
Monotonic behavior
composites, 215–218
discontinuously reinforced, 191–215
effect of clustering, 212, 214, 221
fiber reinforced composites, 164, 170, 176, 178, 181, 190
modeling, 187–191, 206–215

N
Nanolaminates
Al/SiC, 92
Nextel, 21, 22, 34–35, 186, 231, 348
Nicalon, 28, 29, 106, 107
Nickel, 42, 48, 49, 87, 334
Niobium, 47, 48, 53, 54, 85, 86, 88, 352
Niobium-titanium alloys, 50, 52–53, 88
Numerical methods, 129, 138–139. *See also* Finite element method

P
Particles, 2, 5, 39, 55, 99, 123, 163, 228, 284, 311, 326
Physical vapor deposition (PVD), 90–95
Poisson's ratio, 122, 124, 127, 128, 130, 131, 136, 142, 180, 273
Powder metallurgy processing, 3, 75–78, 82, 243, 261, 303–304, 328
Precipitation strengthening, 42–44. *See also* Age hardening
Processing
gaseous state, 55, 91–95
liquid state, 55–75, 101
solid state, 55, 75–91
Profilometer, 105, 106
PVD. *See* Physical vapor deposition (PVD)

R
Reinforcement clustering
effect on ductility, 201, 202, 206
effect on fatigue, 204
quantifying, 201–206
Reinforcements
fibrous materials, 5–6
Roll bonding, 85–89
Roughness
measurement techniques, 237

S
Sapphire, 20, 23, 184, 186
Scanning tunneling microscopy (STM), 105–106
Self-consistent methods, 129, 153
Shear-lag model, 138, 170, 171, 175, 191, 285–286
Shear modulus, 41, 43–44, 122, 124, 127–133, 168, 171–172, 283, 300–301
SiC/Al
  modulus, 32, 138, 192, 200, 236
Silicon carbide
  particle, 30–31
Silver, 47, 48, 51, 85–87, 89, 345, 347
Sintering, 23, 47, 76, 82–86, 200, 201, 218, 336–338
Sol-gel, 21–23
Spinel, 21, 22, 109, 111
Spray co-deposition, 55, 62–64
Squeeze casting, 55, 59–62, 289–291
STM. *See* Scanning tunneling microscopy (STM)
Steel
  Dual phase, 216, 217
Strain tensor, 121–122, 136, 137, 140–141
Strengthening mechanisms
  direct, 164–170
  indirect, 170–175
Stress tensor, 121–122, 137
Stress *versus* cycles (S-N). *See* Fatigue
Superconductivity, 49–54
Superconductor
  HTS, 49, 87–89, 344–347
  Nb3Sn, 50, 53–54, 85, 86, 88, 345
  Nb-Ti, 52, 53
Superplasticity
  grain boundary sliding, 304, 307

T
Texture, 82, 83, 87–89, 102, 174
Thermal conductivity, 1, 3, 4, 14, 47, 67, 74, 150–152, 318, 321, 333, 335, 337, 339, 342, 344
Thermal expansion mismatch, 170, 209, 272, 301, 342
Thermal stress
  Al_2O_3 fiber/Mg composite, 234–236
  fiber reinforced composites, 2, 6, 103, 110–111, 121–139, 142, 153, 157–161, 164, 170, 176, 178, 181, 190, 229
  particulate composites, 1, 132, 133, 141, 143, 144, 155–157, 170, 318
Titanium alloys, 46, 110, 237, 331
Transport properties, 151–152
Tungsten carbide
  particle, 1, 31–32, 150, 245, 313, 317–320, 352, 353

V
Variational calculus methods, 129
Viscosity, 13, 23, 45, 46, 57, 58, 61, 64, 66, 67, 75

W
WC/Co
  wear, 4, 150, 312, 317, 318, 352–354
  Young's modulus, 135, 136
W/Cu
  Young's modulus, 153, 171
Wear
  abrasive, 311, 312, 314, 318, 319, 321
  adhesive, 311, 312
  braking materials, 313, 320–322
  delamination, 236, 316, 317, 322, 330
  double cemented carbides, 318–320
  hardness, 42–44, 92, 311, 317, 352
  mechanically mixed layer (MML), 316, 317, 322
  testing, 312–314, 321, 329, 341
Wettability, 61, 101–102
Whiskers
  SiC, 3, 29–32, 76, 111, 293, 295

X
X-ray tomography, 194, 196, 198, 262, 274, 337, 340

Y
YAG. *See* Yttrium-aluminum garnet (YAG)
Young's modulus, 6, 28, 29, 32, 46, 79, 122–127, 131, 133, 135, 136, 138, 139, 151, 180, 200, 210, 237, 238, 260, 270, 273, 274, 296, 335, 349
Yttrium-aluminum garnet (YAG), 23